Development of a microimpedance pump for pulsatile flow transport - Part 1: Flow characteristics of the microimpedance pump. Part 2: A systematic study of steady and pulsatile transport in microscale cavities.

Thesis by

Derek Rinderknecht

In Partial Fulfillment of the Requirements

for the Degree of

Doctor of Philosophy

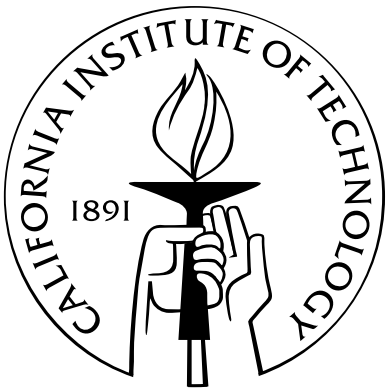

California Institute of Technology

Pasadena, California

2008

(Submitted January 18, 2008)

Acknowledgements

I would like to dedicate this thesis to my grandparents Peggy and Heinrich Rinderknecht, my Nana and Grospapa, who from an early age inspired me to pursue my interests in science, for their love and encouragement in all my endeavors and for the value they placed on family. I would like to thank my family and friends for their love and support, in particular, my mother Suzanne Austin and father John Rinderknecht, as well as my wonderful little sisters Danielle, Lauren and Ayaan all of whom have made my accomplishments possible. I would also like to recognize my cousins Rob and Andy, my uncle Dale and aunt Susie. I truly appreciate everything you have done for me during my time in Pasadena especially for the comfort and respite you have provided me during these hectic times. I would like give my endless gratitude to Ursula Jessee for her dedication, understanding and love. Thank you for the many years of happiness and continual inspiration you have given me.

Special thanks to my friend and advisor Mory Gharib for his guidance, confidence in my abilities and balanced perspective on life. I would like to thank all the members of the Gharib group past and present. In particular thanks to Elijah Samson, John Dabiri, Anna Hickerson, Michele Milano, Anya Grosberg, Arash Kheradvar, Lydia Ruiz, John Meier, Matthew Munson and last but not least to Martha Salcedo for holding us all together. It has been an honor and a pleasure.

Abstract

Microfluidics offers an effective means to carry out a wide range of transport processes within a controlled microenvironment by drawing on the benefits imparted by increasing surface area to volume ratio at the microscale. Critical to the impact of microfluidics on integrated devices in the fields of bioengineering and biomedicine is the ability to transport fluids and biomolecules effectively particularly at the size scales involved. In this context a bio-inspired pumping mechanism, the valveless impedance pump, was explored for applications in microfluidics ranging from micro total analysis systems to microchannel cooling. Adhering to the basic principles of the impedance pump mechanism, pumps have been constructed at a variety of size scales from a few centimeters to a few hundred microns. The micro impedance pump is valveless, bidirectional, and can be constructed simply from a wide range of materials. Depending on the size of the pump flow rates range from nL/min to mL/min and pressures can be generated that exceed 20 kPa. Another benefit of the impedance pump is the pulsatile flow output which can be used in the context of microfluidic applications to enhance transport at low Reynolds numbers as well as metering in drug delivery.

Pulsatile flow was therefore investigated as a method of augmenting transport in microfluidic systems. Micro PIV was used to study the affect of both steady and pulsatile flows on transport at low Reynolds number was examined in microscale rectangular cavities. Ventilation of the cavity contents was examined in terms of the residence time or average time a particle remains in the cavity region. Lagrangian coherent structures (LCS) were applied to empirical velocity fields to determine the impact of unsteadiness on time dependent boundaries to fluid transport present in the flow. Experimental results show that there are both frequencies which are beneficial and detrimental to cavity ventilation as well as certain frequencies which more evenly distribute particles originating in the cavity throughout the freestream.

Contents

List of Figures

List of Tables

Chapter 1

The Impedance Pump

1.1 Introduction

Microfluidics offers an effective means to carry out a wide range of processes within a controlled microenvironment. Much of this appeal comes from the benefits imparted by the surface area to volume ratio of microfluidic systems in terms of reagent consumption and increased transport capabilities. Critical to the implementation of microfluidic devices is the ability to drive fluid within a microenvironment, especially due to that fact microscale flows are often dominated by viscous dissipation. Fluid transport requires the ability to both pump and mix especially where transport must occur over long lengths in short timescales. The pump is therefore an integral component of any microfluidic system. In biological systems, the ability to transport fluid within the microenvironment permits biological systems a means of nourishment and waste removal, in a scientific setting it is a means to manipulate and observe both biological and chemical processes.

The impedance pump has many beneficial characteristics which make it an effective driving mechanism for microfluidic systems. The impedance pump utilizes a bioinspired mechanism for valveless pumping based on resonant wave interactions along a flexible media the therefore can easily be manufactured using current soft lithography techniques. Additionally, the wave based mechanism through which pumping occurs infers many benefits in terms of material choices, lack of moving parts and simplicity in manufacturing. There are no blades, valves or high electric fields required which make the pump safe for studies involving sensitive biomolecules. Adjustment of simple parameters such as the excitation frequency or location can reverse the direction of the flow providing a very versatile range of flow outputs. All of these characteristics make the impedance pump well suited to a variety of applications ranging from active stents and shunts for biomedical implants to providing pumping on demand for microscale thermal management devices, and a modular pump for lab-on-chip diagnostics.

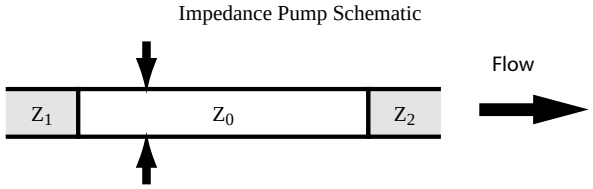

Figure 1.1: A schematic of the impedance pump. The junctions between Z_1 and Z_0 as well as Z_0 and Z_2 form the sites for wave reflection and the arrows represent the pinching location. The system asymmetry is provided both by the difference in length of the excitation from either junction and that the junctions between the different sections may have different wave reflection properties. The impedance pump is reversible, however over the first range of frequencies before any reversal flow would move from left to right in the Figure.

1.1.1 Pump Background

Although impedance based pumping has been known about for some time [1–7] the dynamics are complex and the full potential has not been realized due to the wide number of parameters which can affect performance. We are the first group to begin exploring the potential of impedance pumping as well as to demonstrate it that it is a robust and scaleable concept which can be readily adapted for use biomedical devices and applications in microfluidics [8, 9]. An extensive review of computational and experimental studies can be found in Chapter 1 section 2 of the PhD thesis of Anna Hickerson[10].

1.1.2 Impedance pump concept

1.1.2.1 Principle and Basic physics

The most fundamental principle of its operation is that the excitation occurs asymmetrically with respect to the impedance of the fluid system. The two requirements for an impedance pump in addition to a driving excitation are sites for wave reflection and the presence of systemic asymmetry. Impedance pumps are usually formed by a channel or tube composed of a thin membrane of any material coupled on either side to wave reflection sites. Coupling this membrane at either end to another material or materials of different mechanical properties, geometries or any other factor affecting wave propagation and/or reflection, creates an impedance mismatch, and therefore a site for wave reflection. Commonly, sites for wave reflection are created by changes in material properties and/or geometry and the asymmetry by a change in length. Periodic pinching at an asymmetric location at a certain frequency, waveform and duty cycle results in the accumulation of a pressure gradient from wave interference and therefore the potential to drive flow. A schematic showing the impedance pump can be seen in 1.1.

The concept in brief can be described as follows:

When the compressible section, Z_0 (shown in blue in Figure 1.2), is first pinched down, a pressure wave is emitted in both axial directions traveling at the same speed ($t_1 - t_4$ in Figure 1.2). When a pressure wave encounters a mismatch in impedance, some of the wave will continue to travel through and the rest will be reflected back towards the origin (t_5). In this case the offset in location of the pinching excitation causes the pressure waves interacting with the rigid end segments to reflect at different intervals imposing a phase lag in the reflected wave. The reflected portion of the wave will eventually combine with the next approaching pulse or attenuate out along the length of the compressible section, depending on the selected frequency and duty cycle. The first pressure wave to reflect, headed to the left in Figure 1.2 ($t_2 - t_5$) encounters the wave reflection site and inflects becoming a negative pressure wave which combines with the negative pressure wave created by the restoring force of the compressible membrane drawing fluid in from the left side (t_6). Meanwhile these waves travel to the right until the first wave headed right from the initial compression encounters the boundary moving flow out the right side of the pump before reflecting ($t_7 - t_9$). After the wave reflects it is canceled by the larger negative pressure wave from the inflection continuing to move flow from left to right (t_{10}). The repetition of these dynamic wave interactions under a variety of excitation conditions, wave interference resulting from these out of phase reflections causes the accumulation of a net pressure gradient between the two ends of the compressible section, which in turn interacts with the fluid in the rigid section to establish a mean unidirectional flow. These dynamics have recently been captured and described in computational studies [11]. The impedance pump is bidirectional, however over the first range of frequencies given the asymmetry in the excitation location shown in Figure 1.1 and Figure 1.2, fluid will flow towards the end with the longer length of the compressible section, or from left to right.

1.2 A valveless microimpedance pump driven by electromagnetic actuation

1.2.1 Introduction

Recent interest in microfluidics and microfluidic devices has been predominately driven by the need for biomedical devices on the microscale as well as applications involving chemical control, mixing, and analysis, which stem from the push towards Lab-on-Chip (LOC) methodologies. Micropumping is a necessary component of large integrated systems for sample control and mixing. A micropump requires a compact method of actuation and a mechanism to produce the flow. Commonly micropumps are driven by piezoelectric, electrostatic, electromagnetic, electrohydrodynamic or pneumatic actuators. Mechanisms of pumping vary greatly but can generally be grouped into two categories: displacement pumps and dynamic pumps [12]. These mechanisms can further be categorized in a

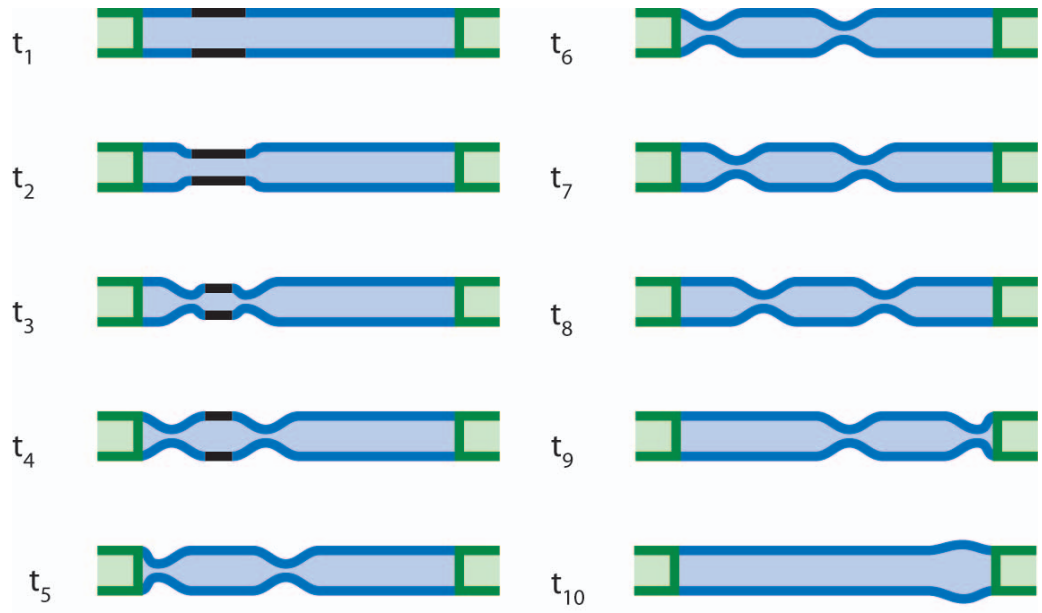

Figure 1.2: A schematic representation of wave interaction along an impedance pump at different time intervals along its length. The wave reflection sites are shown at the ends designated by a color change representing a change in impedance. The black bars indicate where the impedance pump is being excited. Note wave propagate in both directions until they reflect. Observe that due to the asymmetry along the pump length by time step 6 the wave on the right hand side has not reflected whereas on the left hand side the wave is now moving to the right.

variety of ways; one of which is the presence of valves. Conventional valves in microfluidics systems are subject to mechanical failure and, in the case of biological fluids, present further risk of malfunction due to clogging or to damage sensitive biomolecules. Current valveless pumping techniques mainly consist of peristaltic [13] and reciprocating diaphragm pumps relying on diffusers [14–18]. These systems are often fabricated on a substrate through the use of soft lithography on polymeric materials because they are flexible and allow the form and features of these devices to be created and remain functionally sound. Substrate-based systems however, occupy much more volume than is actually required by the device.

Here we present a new valveless and substrate-free impedance based technique for pumping fluid on the microscale. It should be noted that the phenomena resulting in impedance-defined flows has been known for quite some time [1–4, 7]. However, this study is the first of its kind to demonstrate the feasibility of pumping with these phenomena on the microscale, under two different flow circuit configurations, and on two different size scales, as well as report quantitative measurements of the flow performance.

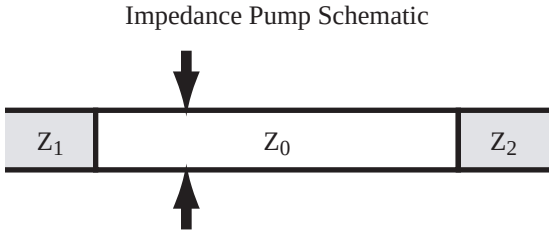

Figure 1.3: A schematic of an impedance pump. The impedances are represented by Z_0, Z_1, and Z_2 respectively. The arrows designate the location of the excitation.

1.2.2 Principle of Operation

An impedance pump is comprised of a compressible section, usually a tube, coupled at both ends to end members of different impedance. Since impedance based pumping is dependent on wave reflection, any material allowing for wave propagation is suitable for the compressible section; in experiments this section is commonly made of a silicone or latex tube. Coupling this flexible tubing at either end to another material or materials of different mechanical properties, geometries or any other factor affecting wave propagation and/or reflection, creates an impedance mismatch, and therefore a site for wave reflection. In Figure 1.3, which depicts a schematic of the pump, these impedances are represented by Z_0, Z_1, and Z_2. The most fundamental principle of its operation is that the excitation occurs asymmetrically with respect to the impedance of the fluid system. Periodic pinching at an asymmetric location at a certain frequency, waveform and duty cycle results in the accumulation of a pressure gradient from wave interference and therefore the potential to drive flow.

In our experiments this system takes the form of a thin walled elastic tube coupled at either end to two symmetric segments composed of a less compliant material, glass, and filled with water. Since the glass segments are of equal impedance the asymmetry must be caused by the location of the excitation along the length of the elastic tube. The difference in length over which the waves travel before reflecting imposes a phase difference in the traveling waves returning to the excitation site. Neglecting attenuation and the effects of viscosity for simplicity, one could imagine conditions where at a certain frequency or band of frequencies the interference of reflecting waves traveling in both directions can form pressure gradients and induce flow. Through the complete collapse of the elastic section the system can also function as a valve.

1.2.3 Experimental setup

For the remainder of this paper the following distinction will be made. Open loop will be defined as flow between two independent reservoirs on both sides of the pump, with no fluidic interconnections. Closed loop will be defined as flow within a distinct loop. Previously, the behavior of the impedance

Configuration	Tubing dimensions ID/wall	Material	Actuation type
Closed loop	2 mm / 50 μm	Silicone	Perpendicular (Fig. 1.5)
Open loop	2 mm / 50 μm	Silicone	In-line (Fig. 1.6)
μOpen loop	250 μm / 50 μm	Polyurethane	Perpendicular (Fig. 1.5)
Device	2 mm / 50 μm	Silicone	In-line (Fig. 1.6)

Table 1.1: A summary of the impedance pump testing configurations including actuation type and dimensions based on the testing configuration.

pump has been studied in both of these configurations at larger size scales [8]. In this study, the impedance pump was tested under three configurations spanning two different size scales: closed loop, open loop and micro open loop. For these configurations, two different electromagnetic actuation schemes were devised referred to as perpendicular and in-line, specifying their orientation with respect to the axis of the fluid channel. A device was also created demonstrating the feasibility of packaging a majority of the pump components into a free-standing micro pump. Table 1.2.3 summarizes the configurations and their respective electromagnetic actuator types. In all cases the glass sections attached to the micro pump are symmetric, and therefore equal in impedance. As a result of this symmetry, excitation at the midline of the elastic tube produces no net flow.

The thin walled elastic tubes used for the pump in the open loop and closed loop experiments were made of silicone with a Young's modulus of 0.4 MPa (at 100% elongation), an inner diameter (ID) of 2 mm and a wall thickness of 50 μm. The tubing used in the micro open loop study was made of polyurethane with a Young's modulus of 2 MPa (at 100% elongation), an inner diameter of 250 μm and a wall thickness of 50 μm. Unless otherwise mentioned, the elastic tubing was connected to glass tubing with an inner diameter of 0.8 mm and a 0.6 mm wall. All impedance pumps constructed using the tubing mentioned in the previous sentence were sealed on either end to the glass tube using heat shrink. A diagram of the assembly procedure can be seen in Figure 1.4.

1.2.3.1 Micro impedance pump actuation

Although any technique could have been employed, electromagnetic actuation was chosen because of its large displacement, high frequency capabilities. Two different electromagnetic actuation schemes were examined, one for experimental purposes, and the other for device oriented studies, shown in Figure 1.5 and Figure 1.6 respectively. Actuation was achieved by fixing a Neodymium Iron Boron (NdFeB) rare earth magnet cube with a side length of 2.4 mm using silicone glue to the upper surface of the tube at an asymmetrical location along the elastic tube length. This magnet was oriented such that when the coil was energized their magnetic field gradients produce a radial force compressing the tube. In the first configuration, the magnetic field of the magnet was oriented such that when the coil was energized its poles are parallel to those of the permanent magnet. A schematic illustrating the

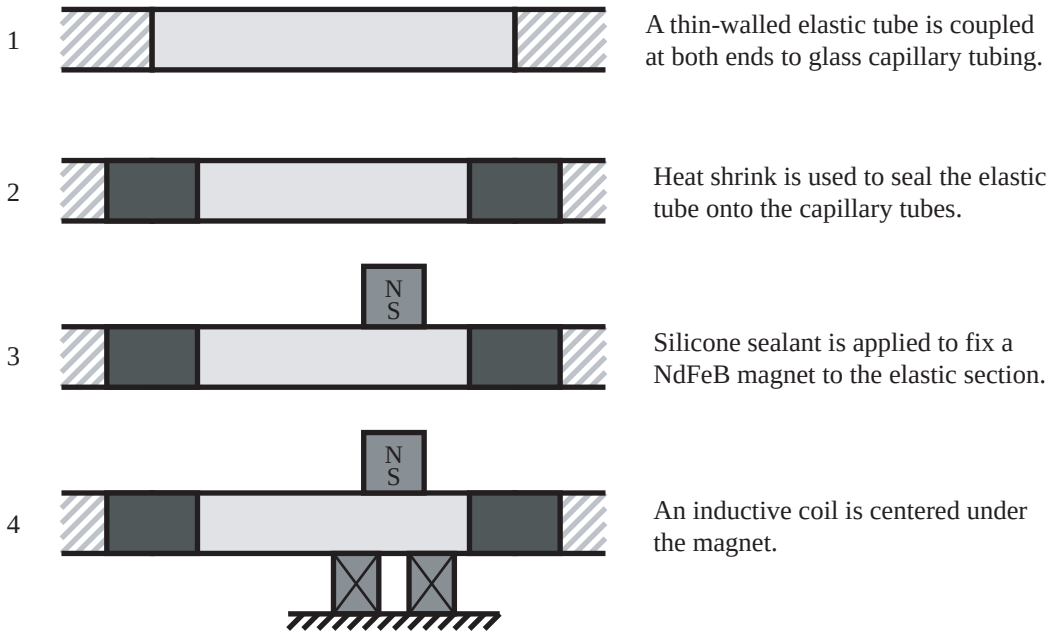

Figure 1.4: A diagram showing the assembly of an electromagnetically actuated impedance pump.

inductor-driven electromagnetic actuator in a perpendicular configuration can be seen in Figure 1.5. The second actuation scheme takes advantage of the fact that fluid passages in biological systems as well as medical devices are generally cylindrically symmetric in shape. To conserve space as well as complement the symmetry of the tube, a novel inline coil-magnet configuration was created comprised of two coils wound azimuthally symmetric with respect to the elastic tube and connected such that when energized they are in-phase. A compressive radial force can therefore be generated by locating a permanent magnet element equidistant from both coils with its magnetic pole oriented such that it is parallel to the length of the tube. A diagram of the inline coil-magnet configuration can be seen in Figure 1.6.

1.2.3.2 Closed Loop Flow

The closed loop test section was formed by coupling a thin walled elastic tube to one end of the two symmetric sections of the glass flow loop. The fluidic loop was completed by connecting the opposite ends with a latex tube with a significantly thicker wall, making it much more rigid than the elastic tube of the pump but soft enough to be crimped, isolating one section from the other. Crimping this thicker elastic tube closes one section off from the other, and creates an open loop situation in which a pressure differential can be measured between the water levels on either side of the pump. Each section also has a piece of glass tubing connected perpendicular to the plane of the flow loop on the

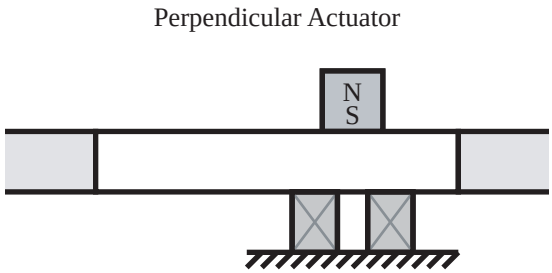

Figure 1.5: Schematic showing an impedance pump with inductance driven actuation in the perpendicular configuration. The letters N and S designate the orientation of the permanent magnet poles.

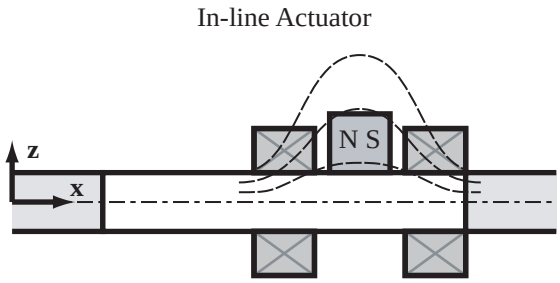

Figure 1.6: A schematic of the inductive coils wound in the in-line azimuthally symmetric format parallel to the x-axis along which flow occurs. The letters N and S designate the orientation of the permanent magnet poles.

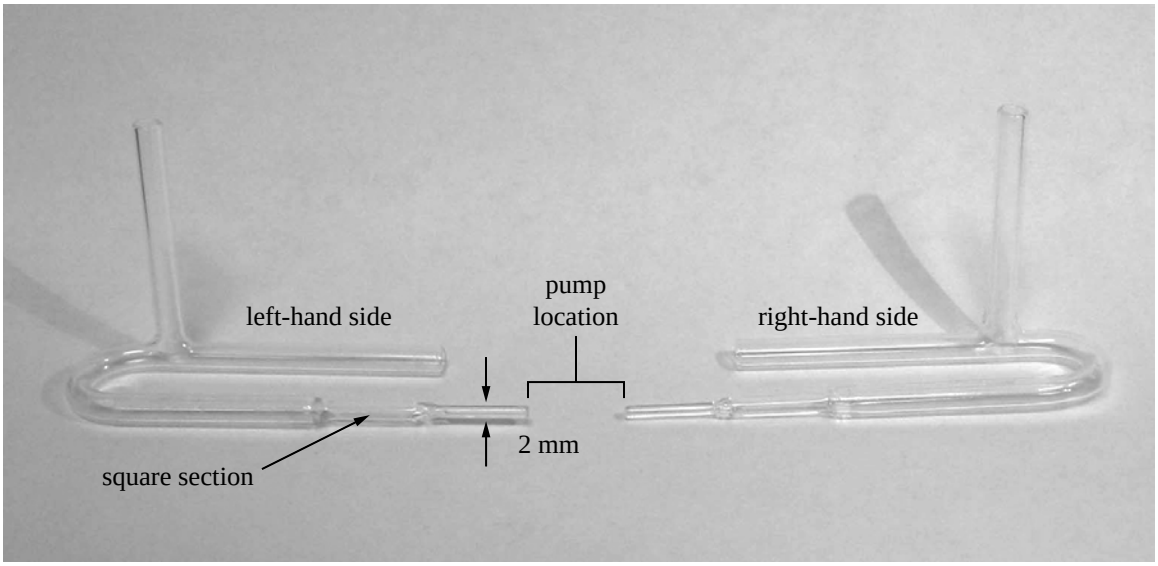

Figure 1.7: A picture of the closed loop flow circuit glass pieces. Also shown is the square section where flow velocity is measured. In operation the pump is attached between the two sides of the loop closest to the reader with an outer diameter of 2 mm. For measurements, clockwise flow within the loop, from the right-hand side to the left hand side, was taken as positive.

opposite end of the pumping site. The inner diameter along a majority of the length of the glass flow loop is 3.2 mm. On one end the tubing of the loop tapers to accommodate a 2 mm side-length square section, where the flow rates can be measured. The square section is then connected to a smaller diameter glass tube (0.8 mm ID, 0.6 mm wall) that connects the loop to the elastic tube. Figure 1.7 shows a picture of the closed loop flow circuit. In this configuration, energizing an inductive coil positioned under the magnet allows the tube to be compressed forming the pump. A schematic of the actuator can be seen in Figure 1.6. Measurements of the bulk flow velocity were taken using a Viosense Mini Laser Doppler Velocimetry (LDV) system, through the length of square tubing on the flow loop. The fluid was seeded with 3 μm neutrally-buoyant polystyrene microspheres. The best results were achieved with particles equal to or less than the fringe spacing ($\sim$ 11 μm) of the LDV. The Mini LDV has 97 % accuracy and a repeatability uncertainty of 1%. Important parameters for reliable measurements and to prevent the particles from adhering to the glass flow loop were the particle size, material, and buoyancy.

1.2.3.3 Open Loop Flow

In a device driven study similar to the environment under which a medically implantable device may operate, the inflow to the device may not contain returning fluid inertia. Open loop flow was therefore demonstrated by connecting the silicone tubing to a short length of the glass tubing (0.8 mm ID, 0.6 mm wall) through the procedure described in Figure 1.4 and placing either end into two independent water reservoirs of a known volume, dispensed through a micropipette. Flow rates were

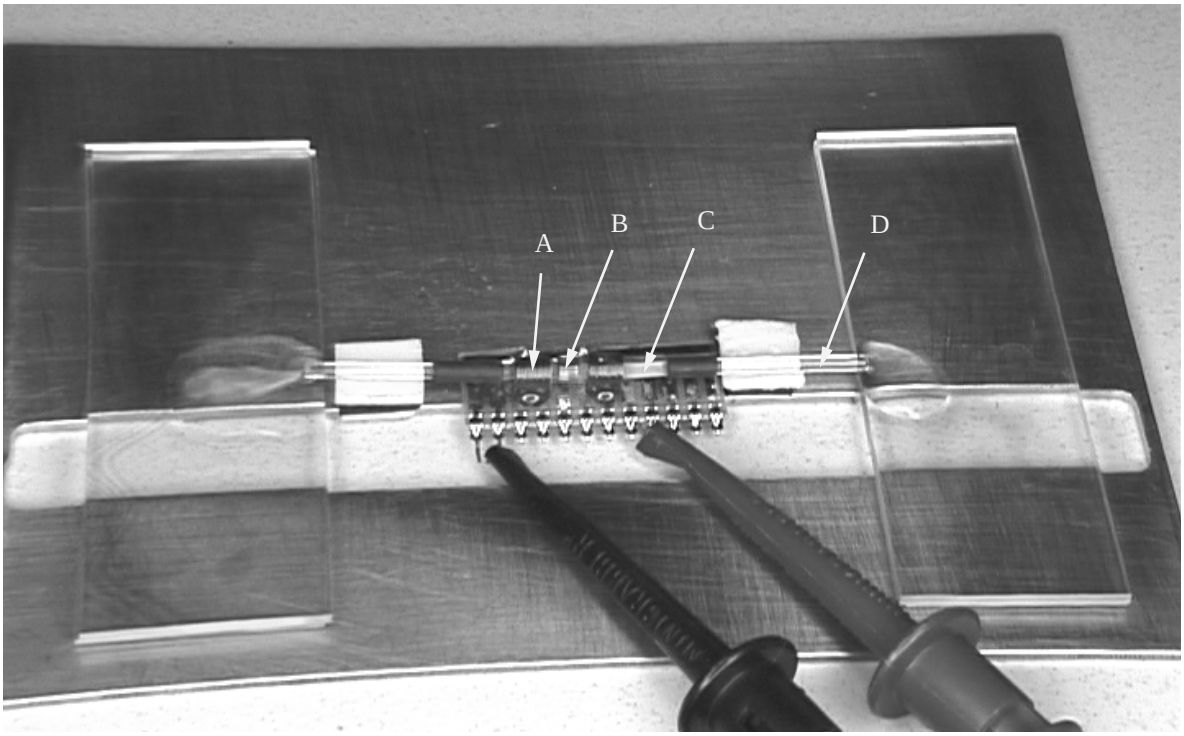

Figure 1.8: Shows the functioning pump in the open loop configuration employing the in-line actuation technique. The letters A, B, C, and D denote the coil, magnet, silicone tube and glass tube, respectively. Fluorescein dye has been used to visualize the movement of fluid from one reservoir to the other. The Teflon slides have been removed for clarity.

determined by measuring the time required for the pump to consume the entire droplet. To prevent capillary action from drawing the fluid along the bottom of the tube, the ends of the glass tubing were placed on two glass slides disconnected from the pump as well as each other. In addition, polytetrafluoroethylene (PTFE) rectangles were stuck to the slides using double-sided tape. The hydrophobicity of PTFE facilitates the visualization of the droplets. An image of such an assembly can be seen in Figure 1.8.

1.2.3.4 Micro Open Loop

The micro open loop flow experiment was constructed by pressing a short length of glass capillary tubing into either the end of the elastic section. In this case, heat shrink was not required to seal the coupled tubes, as described by the procedure above. Similar to the larger open loop study Teflon coated slides were used to visualize the flow of droplets of known volume from one side of the pump to the other. The excitation in this case was provided by cantilever style actuator based on the in-line electromagnetic scheme. A picture of the micro open loop test assembly can be seen in Figure 1.9.

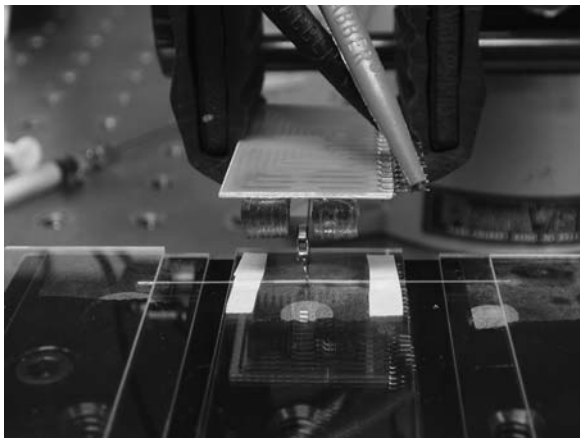

Figure 1.9: Picture of the micro open loop configuration showing the elastic section, glass tubing and actuator. The PTFE slides are not present so the glass tubing is visible.

1.2.4 Results

1.2.4.1 Closed Loop

The closed loop flow response of the impedance pump was observed to be reversible as well as highly dependent on frequency. The performance of the pump was found to be very sensitive to the waveform, offset, amplitude and duty cycle of the excitation. A typical frequency response can be seen in Figure 1.10. Clockwise flow, into the right hand side of the elastic tube was taken as positive. The magnet was located at 4.2 mm from the right hand side of a 19.6 mm tube length. The input waveform to the coil was a square waveform, 48 mA in amplitude, with a 16 mA offset and a 50% duty cycle. Consistently there was at least one flow reversal as the frequency was increased. Figure 1.10 shows three such reversals. These can be seen to occur at roughly 21 Hz, 89 Hz, and 142 Hz. Although similar net flow rates were observed at both high and low frequencies, at low frequencies the flow was highly oscillatory. As the frequency of excitation was increased, bulk flow oscillations tend to damp out resulting in unidirectional flow. Flow rates of up to 16 mL/min have been achieved. For the curve shown in Figure 1.10 the maximum flow rate was 11 mL/min at 55 Hz corresponding to a Reynolds number (Re) of 730.

1.2.4.2 Open Loop

For the open loop configuration the magnet was located 7.25 mm from the end of the 19.14 mm. The input to the coils was a 60.7 Hz a square wave 200 mA in amplitude with no offset. Flow rates exceeding 191 μL/min were achieved pumping a 100 μL droplet to the opposite end of the pump, corresponding to a Re of 5. Relatively high flow was achieved despite the fact that, in this setup, the magnet does not in any form compress the tube against a fixed opposing surface. A demonstration of flow in the open loop configuration can be observed in the sequence of frames pictured in Figure

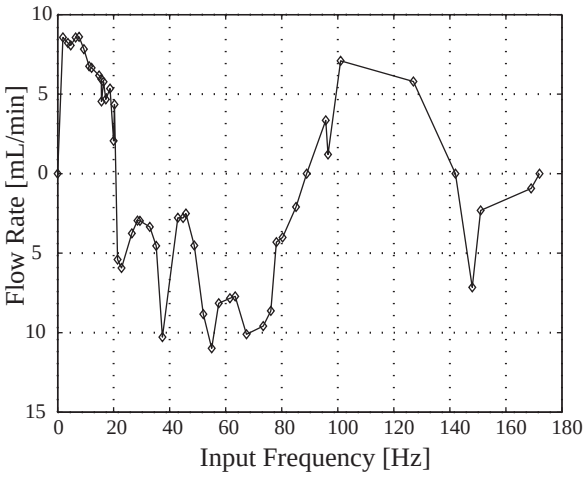

Figure 1.10: A typical frequency flow response of an impedance pump, comprised of an elastic section with an inner diameter of 2 mm and wall thickness of 50 μm coupled at either end to glass tubing of 0.8 mm in inner diameter and 0.6 mm wall thickness excited 4.2 mm from the end of the loop first to see clockwise flow.

1.11. In this sequence of frames a drop of fluorescein dye was used to visualize the flow of fluid across the pump.

1.2.4.3 Micro Open Loop

Since viscosity tends to dominate on the microscale, a study was done to determine whether impedance defined flows still function at very low Re. Tests were performed in the open loop configuration described above using a polyurethane (PU) tube, with a 250 μm inner diameter and a 50 μm wall thickness coupled to a borosilicate glass capillary tube with a 150 μm inner diameter and a 50 μm wall thickness. PU was chosen due to its large tensile strength when compared to most elastomers enabling smaller inner diameters and wall thicknesses than would otherwise be possible. Using an 82.0 Hz excitation and water as the fluid, flow rates were measured to be approximately 17 μL/min or a $Re \sim 2$. The pressure gradient created by the pump was large enough to expel droplets out of one end of the test assembly. In this configuration flow has been shown to be highly frequency dependent and reversible.

1.2.4.4 Description of the micro impedance pumping device

Currently, the design of the micro impedance pump has focused on creating a free standing device that does not rely on a supporting glass or polymeric substrate. The chosen geometry for the compressible section was a tube. Therefore, to create a freestanding device, a titanium cage was manufactured using conventional micromachining techniques. The two major factors that weighed into the design the micro impedance pump cage aside from those inherent in its principles were

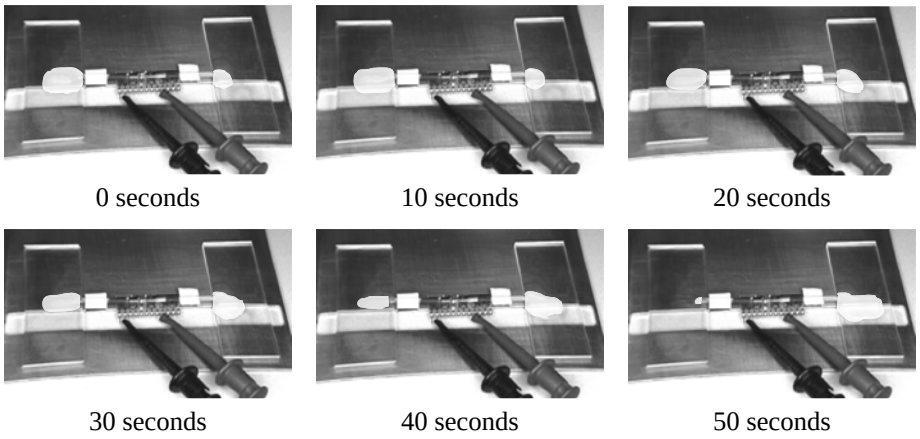

Figure 1.11: A sequence of photos demonstrating functionality of pumping fluid open loop, using the inline actuation type. The puddle on the left can be seen to contain a spot of fluorescein dye. At t = 0 seconds a square current waveform of 200 mA in amplitude at 60.7 Hz was input to the coils. Over a 50 second duration following the current input, the fluid containing the drop of dye was pumped from the slide on the left to the slide on the right.

the structural integrity of the elastic tube, and providing a compact means for the excitation. A thin wall, although beneficial to wave propagation, often meant that the tubing was collapsible and therefore required some structure to prevent buckling or collapsing. In addition, the way in which the tube was coupled to the cage was important to prevent tearing, and ensure the lifetime of the device. For the device pictured in Figure 1.12, the tubing was turned inside out and stretched over the cage, then fixed using heat shrink.

1.2.5 Discussion

High frequency excitation revealed the presence of multiple regimes of flow. The upper limit of this excitation was only limited by the attenuation of the magnetic field gradients produced by the coil at high frequency, consequently changing the excitation profile. Flow in all cases was observed to be highly dependent on frequency, waveform, duty cycle and amplitude of the input excitation. The reliance of impedance driven flows on the type of excitation provides some evidence for the occurrence of wave-based interactions being cumulatively responsible for the manifestation of flow. The dependence of the flow rate on frequency can easily be observed in the plot in Figure 1.10. Wave interference also offers some explanation as to why there was consistently a flow reversal. The presence of the elastic section implied there was at least some phase delay between the pressure and velocity waves produced with each excitation. The flow reversals as well as the flow peaks most likely correspond to frequencies where the phase delay between the reflecting waves and the source waves was the least and most optimal, respectively. The vast frequency range for which flow occurs allows for the selection of completely different, application specific flow regimes with just one pump.

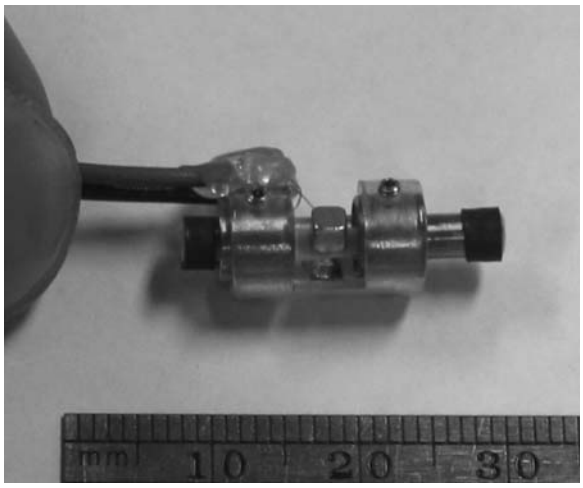

Figure 1.12: A picture of the free-standing micro impedance pump.

Functionality in the open loop configuration is also significant. In essence the inertia of the returning flow is not required to maintain pressure or flow. Instead, solely the presence of an impedance mismatch and asymmetric excitation are required to generate a pressure gradient at certain frequencies. The flow rates in either case differ by two orders of magnitude. As reported above, the micro impedance pump in the closed loop flow configuration has attained flow rates of up to 16 mL/min, whereas in the open loop configuration under similar parameters maximum flow rates have consistently been much lower ($\sim$ 191 μL/min). In contrast to other mechanisms of pumping, the increased system impedance in the closed loop configuration may actually benefit the impedance pump's performance.

1.2.6 Conclusion

Impedance based pumping has been shown to be a viable method for moving and controlling fluids on the microscale. High frequency electromagnetic actuation has revealed multiple regimes of performance which can easily be controlled as well as reversed by simply varying the frequency of excitation. As a result, micro impedance based pumping can deliver both high and low flow rates under a variety of pressure conditions. Flow rates of 16 mL/min and 191 μL/min have been demonstrated in the closed loop and open loop flow configurations respectively. In the micro open loop trials flow rates as high as 17 μL/min have been achieved. These numbers position the micro impedance pump flow performance significantly ahead of the flow rates achieved using other micro pumping mechanisms with similar dimensions.

The performance of the micro impedance pump has been observed to be dependent on a variety of parameters, namely the duty cycle, frequency, and amplitude of excitation as well as the fluid-mechanical properties of the system. However, adjusting one parameter, such as the frequency,

Table 1.2: Summarizes the parameter space of the impedance pump. **Note**: Many of the material and geometrical parameters should be considered as counting twice since they describe the compressible section of the pump and the rigid end connections.

Material Properties	Fluid Properties	Actuation	Geometry
Young's modulus	Viscosity	Shape of actuator	Length
Reflection coefficient	Pressure	Waveform	Inner diameter
Wave speed	Flow Resistance	Location	Wall thickness

enables the device to be readily tuned to achieve the desired performance. The micro impedance pump is relatively easy to construct and does not require any complex fabrication methods to build and operate. The micro impedance pump is highly resistant to clogging due in part to the pulsatile nature of the flow as well as the lack of diffusers and valves. The presence of flow in the absence of complete closure of tube, in both the open loop and closed loop configurations, may prove to be beneficial for the handling sensitive biofluids. In addition to its substrate free construction, the absence of complex parts and inner geometries makes the impedance pump well suited for integration into cost focused, space limited applications including drug delivery, cell sorting, chemical analysis, as well as act to complement current stenting and shunting techniques. Micro impedance based pumping presents an exciting new method of controlling fluids on the microscale with vast potential in a variety of applications, especially with respect to micro mixing as it relates to chemical or biological assays (DNA Chip). Although it is conceptually simple, significant future work is necessary to be able to further understand and predict the complex dynamics of impedance driven flows.

1.3 Characterizing the impedance pump

1.3.1 Introduction

The study of the electromagnetically actuated valveless microimpedance pump demonstrated the need to decouple the actuator from the pump body. Although this study was a demonstration of the ease to which impedance pumps can be implemented at the small scale the results represent the performance of two unoptimized systems. The study also elucidated the difficulties presented in comparing one pump to the next in terms of frequency response due to the large parameter space which gives rise to the pump flow output. Since the impedance pump has such a large parameter space based on material, geometric and excitation parameters it was necessary to construct an experimental system which would allow the freedom to explore the pump dynamics in a variety of configurations. The parameter space for the pump is summarized in Table 1.2. Additionally the construction of the pump mainly the limited force output and the gluing of the electromagnetic actuator prevented the exploration of the full parameter space.

Since our working hypothesis about the physics of the impedance pump was based on the interaction of pressure and velocity waves inside the body of the pump it was necessary to have measurements of the time resolved flow rate and pressure. Phase information about these pressure and velocity waves at different frequencies allows a picture of how wave interactions give rise to pumping. Since directly taking the measurement inside of the pump is not an option both pressure and flow rate were measured downstream of the pump relying on the fact that the phase relationship between the pressure and velocity waves does not change in a system with rigid boundaries.

1.3.2 Experimental Setup

An apparatus was therefore constructed to examine the flow dynamics of the impedance pump in a variety of different configurations. A schematic of the experimental setup can be seen in Figure 1.13. A Bruel and Kjaer 4810 voice coil actuator was chosen to provide large displacement, high frequency actuation at up to 10 N of force. A voltage to current amplifier was constructed to provide up to 1.8 A_{rms} or current from DC to 10 kHz. The voice coil was mounted vertically on a 3-axis micrometer stage. Position adjustments in all three directions allow for the following: transverse centering of the excitation relative to the pump body, fine adjustment of the excitation position over the entire length of the pump and adjustment of the excitation location into the pump body. The ability to adjust into the z-depth gives the apparatus the freedom to test impedance pumps of a wide range of diameters as well as ensure the excitation always remains in contact with the pump body. The displacement of the voice coil actuator is transmitted to the pump through a probe. Inset in the probe is an LVDT core, which provides displacement information about the probe through an LVDT. The probe then tapers to a 2.4 mm diameter circular surface which makes contact with the pump body. The transfer function relating displacement to frequency for the electromechanical system comprised of the voltage to current amplifier, voice coil actuator, and probe was recorded using an HP Dynamic Signal Analyzer and a transfer function was created to provide open loop control of the probe displacement. This transfer function can be viewed in Appendix B.

A two piece flow loop was also designed, the matching sides of either half providing rigid boundaries as part of the impedance pump, and a means to inserting the ultrasonic transducer into the flow loop, respectively. In addition either half has two ports which emerge perpendicular to the flow plane. Two are located on either side of the pump boundaries for a differential pressure measurement of pump output. The other two ports provide an easy means to flush the system and remove any bubbles. Dynamic flow rate measurements at low flow (μL/min to mL/min) rates are particularly difficult to measure with accuracy and sufficient bandwidth. An ultrasonic probe Transonic ME-2 PXN was chosen to provide real time flow rate measurements up to a frequency of 150 Hz with minimal end user processing. This probe is compatible with a number of fluids in particular glycerin giving the experimentalist the ability to vary the fluid viscosity.

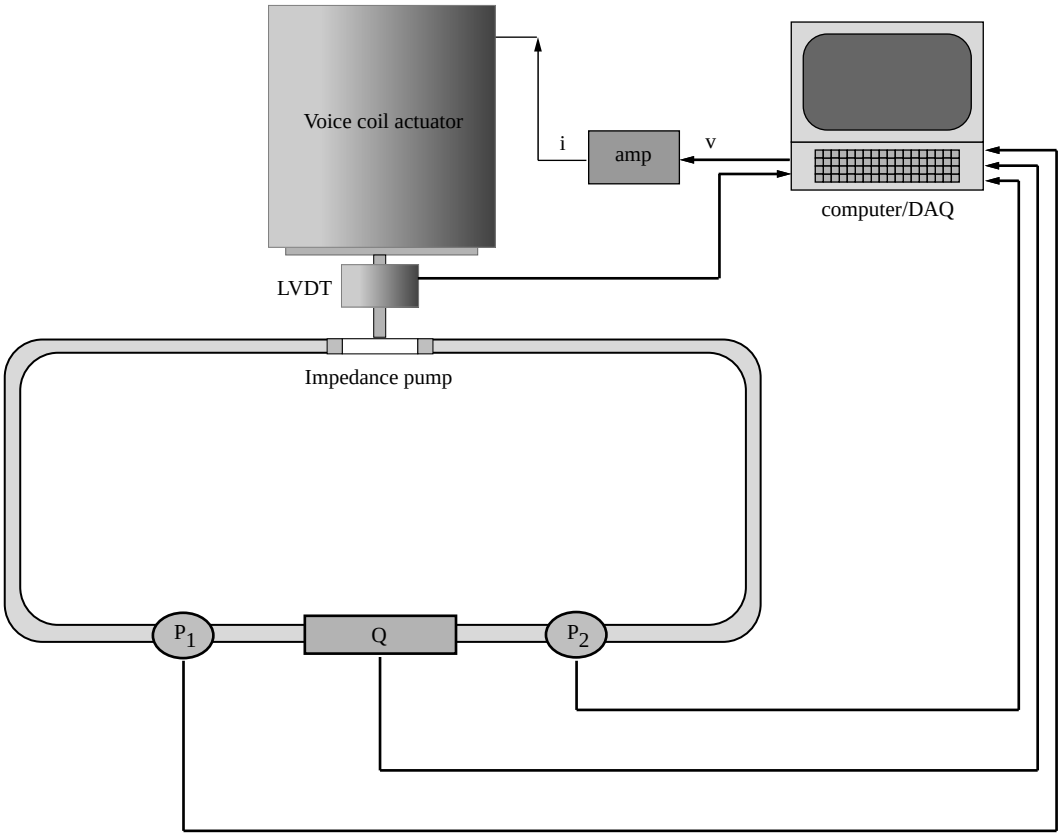

Figure 1.13: A schematic of the impedance pump characterization system. The voice coil is used to provide an excitation to the pump, the LVDT is present to measure the amplitude of the excitation. Pressure and flow were monitored by two differential pressure transducers (P_1 and P_2) and a flow meter (Q) respectively.

Time resolved fluid pressure measurements at small size scales are particularly difficult due to the fact that they are based on a stagnation pressure and the diaphragm is often many characteristic diameters away from the main channel flow. Undoubtedly the amplitude of the dynamic portion of the pressure measurement is attenuated by this affect. Most pressure measurement techniques rely on large surface area diaphragms for capacitive measurements however they are usually many times larger than the experimental system itself making coupling difficult. Silicon piezo-resistive pressure transducers were therefore chosen due to their small size, sufficient sensitivity and high bandwidth (1-3 msec). A table summarizing the technical specifications of all the various components can be found in Appendix A.

1.3.3 Results

1.3.3.1 Pressure and Flow versus frequency

The construction of the experimental apparatus provided data further demonstrating the importance of wave dynamics in the performance of the pump by providing the first empirical evidence of time resolved pressure and flow of a wide range of frequencies with a controllable waveform. The plot in Figure 1.14 shows a typical frequency response of an impedance pump tested using characterization setup. The pump was comprised of a silicone tube 20 mm in length, 2 mm in inner diameter (ID) with a 780 μm wall, coupled to two glass capillary tubes 2 mm in outer diamter (OD) and 1 mm in ID. Unlike that shown in Figure 1.10 from the LDV the frequency response is smooth due to the sampling rate of the ultrasonic transducer. Also evident from the simultaneous pressure and flow measurements is that both the maximum pressure and maximum flow occur at the same frequency demonstrating the resonant behavior of the impedance pump. In other words maximum mechanical power is transmitted to the working fluid at a specific frequency. This particular behavior was also noticed in the larger scale impedance pumps. Additionally this data represents the first empirical study to measure both the pressure and flow frequency response simultaneously to hundreds of Hertz in a closed flow loop configuration.

1.3.3.2 Impedance pump flow response versus position

Another experimental parameter relevant to characterizing the pump, provided by the new experimental setup, was the ability to examine the pump flow response versus position. Figure 1.15 shows the response of a 2 mm ID, 20 mm in length pump over a range of positions spanning 4.5 mm to 15.5 mm in 0.5 mm increments. Stepping left to right across the length of the pump produces the symmetric plot shown in Figure 1.15. The symmetric flow response of the pump to changes in the position of the excitation is another demonstratration of the wave based behavior of the pump physics another trait of impedance pumps of all size scales. As in all cases presented so forth both

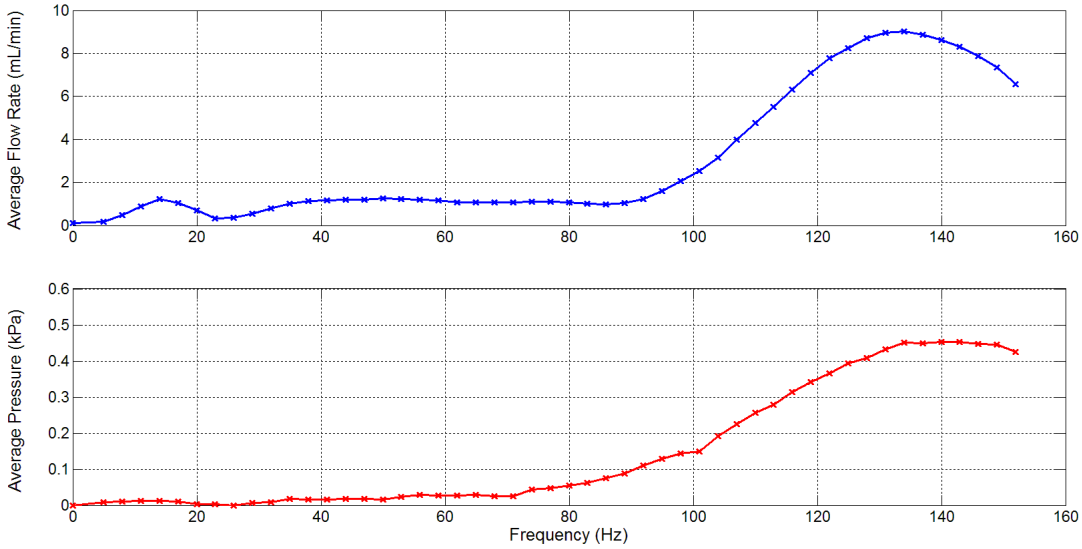

Figure 1.14: Shows a typical flow and frequency response for a millimeter scale impedance pump. The plot shows that both pressure and flow peak at the same frequency representing maximum power transmission to the fluid.

boundaries are the same so asymmetry is purely applied by change in offset position. If the excitation is located in the center the pump produces no flow since the pressure difference produced on either side of the pump cancels the other out. As the excitation location increases in asymmetry for example moves closer to one impedance mismatch boundary or the other the resonant peaks in the flow response increase.

1.3.3.3 The phase relationship between pressure and flow

The fabrication of this new setup also enabled us to examine the interaction between transient pressure and velocity waves inside of the pump. These results are illustrated in the following pressure-flow loops (P-Q). Figure 1.16 shows the frequency response of the pump from which the flow and pressure time traces were recorded. Three points are labeled on this figure denoting the various frequencies examined in Figure 1.17 - Figure 1.19. Figure 1.17 - Figure 1.19 show the phase relationship between pressure and flow at three frequencies around resonance as well as the representative P-Q loops. At 116 Hz it can be clearly seen that the pressure precedes flow in time. At this frequency the phase lag produces an open clockwise rotating P-Q loop. As the frequency is increased towards resonance at 134 Hz, it can be seen in Figure 1.18 that both pressure and flow are in phase and accordingly the P-Q loop collapses. As the excitation frequency passes over 134 Hz the P-Q loop opens up and inflects producing a counterclockwise rotation as pressure trace now lags behind the flow trace in time. This behavior can be observed in Figure 1.19 at 152 Hz.

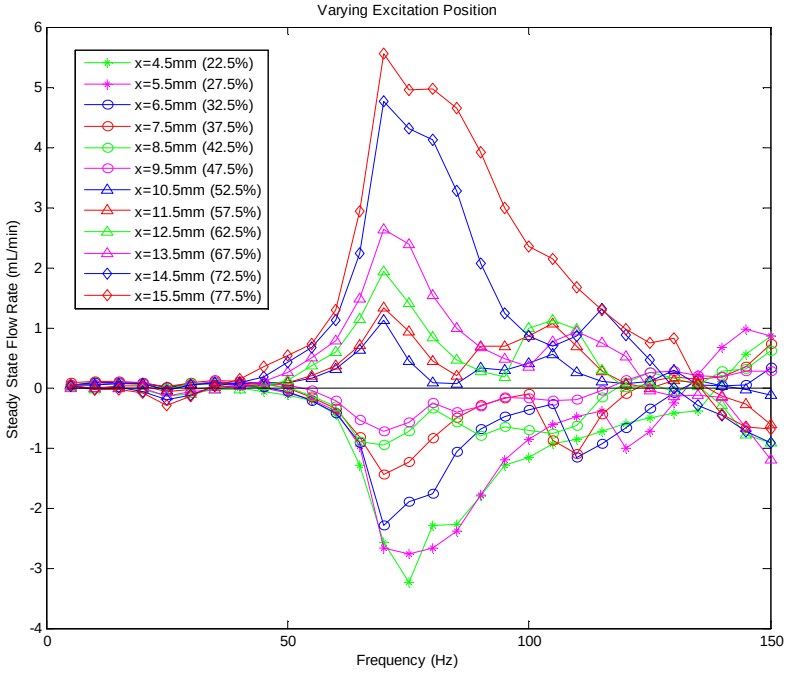

Figure 1.15: The flow response of an impedance pump translating the excitation location from left to right across the length of the body of the pump. The resonant frequency is clearly observable at 72 Hz and is persistent regardless of the position of the excitation. Note: Positive flow is denoted counterclockwise.

1.3.4 Discussion

The characterization of the millimeter scale impedance pump allowed a confirmation of many of the traits of the larger scale ($\sim$ 2 cm) impedance pumps studied by Hickerson in her thesis namely the simultaneous occurrence of peak pressure and peak flow at a single resonant frequency, the persistence of resonant frequency regardless of excitation location, the symmetrical response of the pump to the center location of the pump tube as well as the collapse of the P-Q loop at resonance. The peak flow of around 10 mL/min is typical for impedance pumps around 2 mm in inner diameter, with a typical maximum static pressure head of around 20 kPa.

The pressure-flow time traces also showed a similar behavior to larger scale impedance pumps. Spanning the resonant peak of the frequency response at close to 134 Hz, the open P-Q loops shown in Figure 1.17 and Figure 1.19 at frequencies of 116 Hz and 152 Hz respectively demonstrate how pressure and flow interact to give rise to conditions of maximal flow. The clockwise open loop at 116 Hz and the counterclockwise loop at 152 Hz represent fluid mechanical power not being transmitted to the flow. The subsequent collapse of this loop near resonance at 134 Hz represents full power transmission to the fluid in terms of mean flow as well as static pressure head.

1.3.5 Conclusion

The construction of the characterization apparatus greatly improved the parameter space which could be explored for a single pump. Improvements to the actuation and instrumentation enabled data to be acquired more quickly as well as a versatile platform for testing pumps of many different size scales. The improvement to the flow data is clearly evident in comparing Figure 1.10 to Figure 1.14. The combination of the voice coil and LVDT allowed for open loop control of the displacement and position information about the actual displacement of the voice coil probe at frequencies up to 160 Hz, an order of magnitude larger than any previous experimental study. The combination of the pressure transducers and ultrasonic flow velocity probe allowed for rapid measurements of pressure and flow allowing the large frequency space up to 160 Hz to be spanned accurately accommodating the dynamic flow response of the pump where changes of a few Hertz can result in flow spikes, flow reversals or both. The apparatus also allowed for the observation of key features of the flow dynamics of the impedance pump relating the pressure to the flow in time and how their relationship in phase gives rise to flow. However the exact dynamics and interaction of pressure and flow inside the thin walled tube remain unknown the pressure flow data give some insight into the importance of their phase relationship and their net affect external to the pumping region.

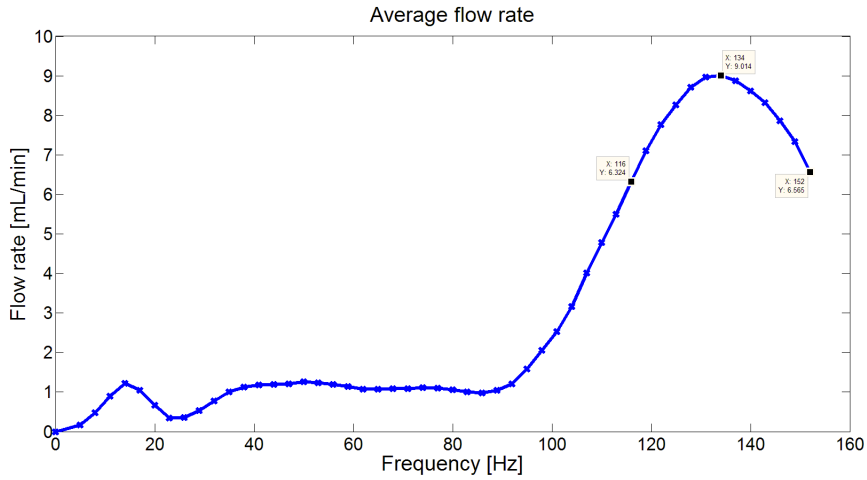

Figure 1.16: Shows a typical frequency response for the impedance pump and highlights three frequencies 116 Hz, 134 Hz, and 152 Hz.

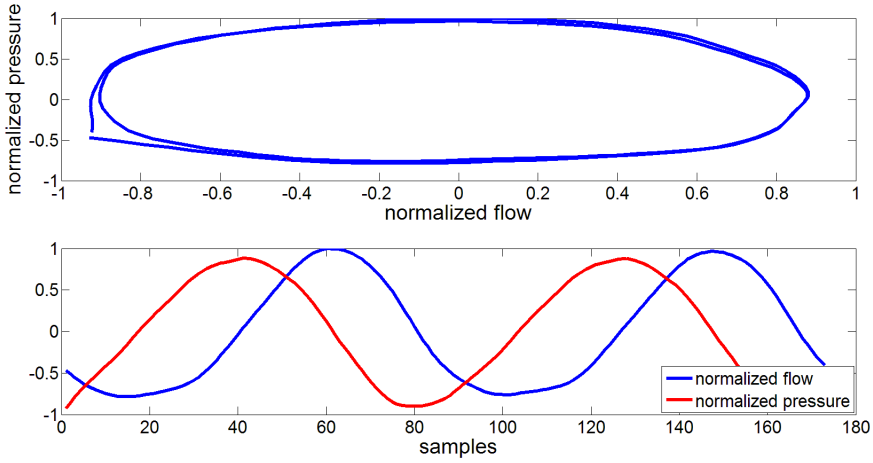

Figure 1.17: Pressure flow phase relationship at 116 Hz. Notice that in this case pressure precedes flow in phase generating an open P-Q loop.

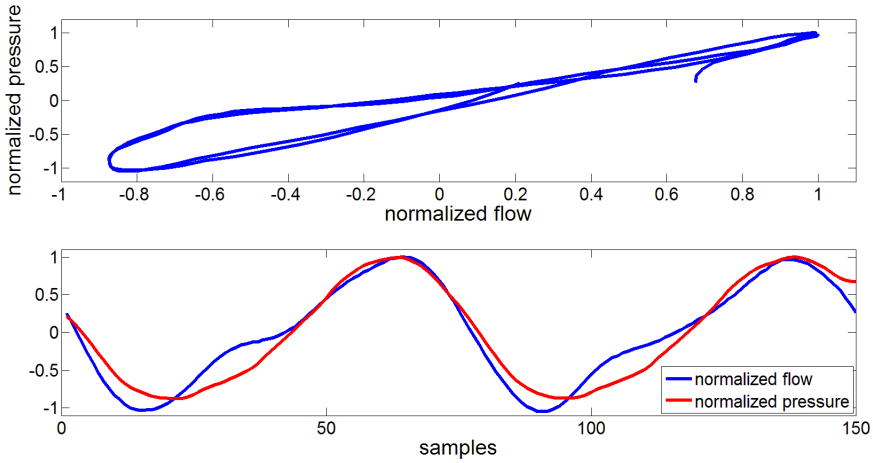

Figure 1.18: The pressure flow trace at 134 Hz, very close to resonance. Notice in this case pressure and flow are nearly in phase and the pressure flow loop collapses.

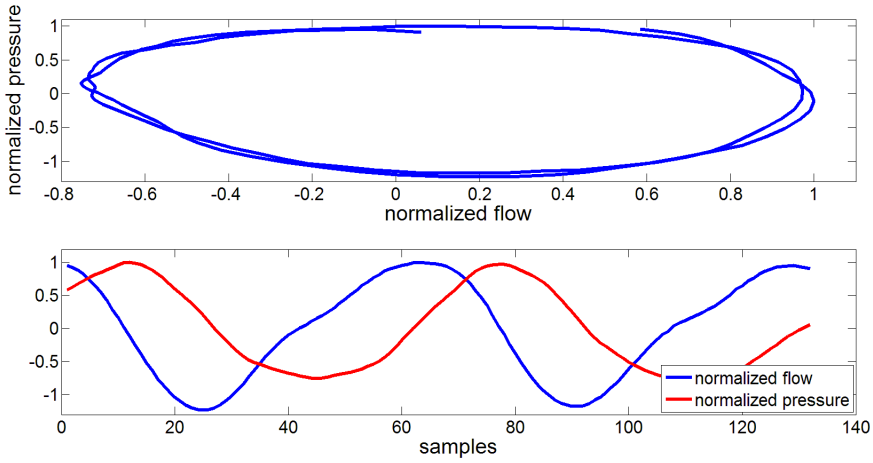

Figure 1.19: Pressure flow phase relationship at 152 Hz. Notice that in this case instead flow precedes pressure in phase once again generating an open P-Q loop.

1.4 Implementing the impedance pump on the microscale

1.4.1 Introduction

The basic concept of an impedance pump requires at least a single wave reflection site, a media functioning as the pump body to propagate the excitation as well as that the excitation occurs asymmetrically with respect to systemic impedance. Therefore when the question of scaleablity is posed there is nothing regarding the basic concept of the pump which is violated in going to smaller size scales. Additionally the proof of concept study presented in Micro Open Loop flow of Section 1.2.4.3 provided the evidence that using the impedance pump as a micropump was feasible. This evidence was further strengthened by observations of a purely biological system, the embryonic zebrafish which uses the mechanism of the impedance pump to move blood during the early post fertilization stages of cardiogenesis once diffusion alone has become inadequate to sustain development

The dimensionless parameter which describes the relative size of the inertial core relative to the boundary layer in a pulsatile flow is the Wormersley number (Wo). For the impedance pump the Wormersley number is taken in its original for given by:

$$\mathrm{Wo} = \mathrm{R}\sqrt{\frac{\omega}{\upsilon}} \tag{1.1}$$

where R is the channel radius, ω the rotational frequency in radians/sec, and ν the kinematic viscosity. Examining the Wo of both the 2 mm ID impedance pump and the roughly 2 cm ID impedance pump studied by Hickerson we can see that although these responses have different resonant frequencies due to the larger number of parameters which together produce the flow frequency response these flow responses occur over a similar range of Womersley numbers roughly Wo = 0 - 30. Therefore the argument could be made that given an actuator with sufficient frequency bandwidth a similar range of Wo numbers could be attained for a pump of a smaller characteristic inner diameter. For a 100 μm pump a Wo of 10 would require a frequency of roughly 6.3 kHz, well within range of the response of many common actuators.

1.4.2 Design considerations

Since ultimately the goal is to translate the pumping concept to working devices the benefits in scaling down the pump tend to be better viewed from a design standpoint. Smaller size dimensions favor the choice of actuators. The principle of the impedance pump is one of resonance small excitation amplitude can result in substantial flow output, however there is a threshold minimum displacement required to generate flow. Presumably this threshold, although it has not been measured experimentally, can be described by the relative ratio of that threshold displacement amplitude and the

characteristic internal diameter of the pump. This threshold has also been a resulting draw back to implementing the larger scale ($\sim$ 2 cm ID) impedance pump in a stand alone implantable device. The large dimensions limit the choice of actuators and frequency over which they are effective. The implications of this are seen in the experimental study by Hickerson[10] in that the frequency range was limited to below 20 Hz due to the speed of the motor. In her study an elegant mechanism composed of a series of gears with pins guided in a grooved slot to reciprocate the pinchers in a sinusoidal motion were designed to apply large displacements however due to issues of reliability and size such a mechanism would not be practical in an implantable device. Piezoelectrics and electrostatic actuation is impractical at those dimensions and electromagnetic mechanisms which apply such large displacements and can handle the inertia of actuation at high frequency tend to be extremely large, relative to the 1.9 cm by 15.2 cm pump. At smaller size scales below a millimeter there is better harmony between the apparent resonant frequency of the pump and that of common actuator materials, which affects the potential for maximal energy transmission to the working fluid.

As with any design problem there are tradeoffs regarding manufacturing and geometry at small size scales. Thin walled tubes elastic tubes are limited to wall thickness greater than 50 microns due the manufacturing processes involved in their fabrication. This has huge implications if one desires to create tubular impedance pumps at the microscale. In this case the wall thickness to inner diameter ratio is on the order of a factor or 10 greater than the pumps studied in Hickerson et al.[8], or Rinderknecht et al. [9] where the ratio is 0.041 and 0.025 respectively. However our hypothesis about the impedance pump concept tells us that there is nothing specific about the geometry of the wave propagating media. Additionally with the advent of microfluidics and manufacturing for Micro Electro Mechanical Systems (MEMs) many fabrication techniques are in existence which could easily be extrapolated to building a microscale impedance pump.

1.4.3 The effect of fluid viscosity on pump performance

Given that there was evidence that the impedance pump continued to function well at low Re there was a need to examine the effect of fluid viscosity on the performance on the pump. Two independent experiments were conducted. First the frequency response of the impedance pump was characterized versus varying viscosities from 1 cP to 40.55 cP. The viscosity was adjusted by varying ratio of glycerin to water by weight from 0 to 80%. The impedance pump tested was 27.0 mm in length and the excitation position was 3.89 mm from the right hand side wave reflection site. The pump had an inner diameter 2mm and a wall thickness of 780 μm. The excitation waveform applied to the pump was a sinusoid of 0.6 mm amplitude. The probe tip was lowered one half the amplitude of the excitation or 0.125 mm so that the tube is only completely open during the peak of the excitation cycle. The resulting frequency response can by seen in Figure 1.20. Flow from the right hand side wave reflection site to the left hand side wave reflection site is given as positive in

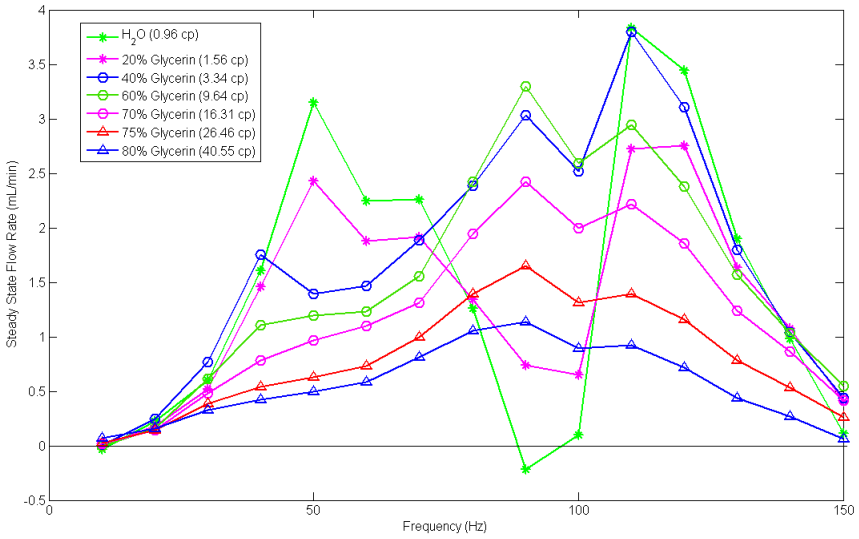

Figure 1.20: Flow frequency response of a 2 mm impedance pump scanned in increments of 10 up to 150 Hz. The individual color traces show the response of the pump to increasing fluid viscosity.

Figure 1.20. Given the frequency response of the 0.96 cP case it is easy to recognize the resonant peaks of 3.1 mL/min at 50 Hz and 3.8 mL/min at around 110 Hz as well as the small reversal of 0.3 mL/min at 90 Hz. Observing the frequency response the affect of increasing viscosity has an averaging-like affect of the frequency to frequency response of the pump. After only an increase from 0.96 cP to 1.56 cP in viscosity the flow reversal at 90 Hz is completely eliminated. The most prominent flow peak, at 110 Hz, continues to dominate until 26.46 cP or 60% glycerin where is it then overshadowed by the emergence of a new peak at 90 Hz. When this frequency response is plotted against the Womersley number and the flow output is nondimensionalized by half the rate of the volume displaced by the pinchers as suggested by Thomann (1978) and adopted by Hickerson et. al. the respective frequency responses are compacted as shown in Figure 1.21. Otherwise the plots display similar features to the dimensional frequency response. Next an experiment was carried out with the same setup as that presented in the micro open loop Section 1.2.4.3 to attempt to establish some lower end Reynolds number limit to where the impedance pump principle ceases to function. Three different pumps were tested whose geometries are summarized in Table 1.4.3. The current input to the electromagnetic cantilever style actuator was 84.3 Hz sinusoid with an amplitude of 32 mA.

The plot in Figure 1.22 shows that the impedance pump at 60 times the viscosity of water still produces a flow rate of 3.42 μL/min, or steady Reynolds number of 0.02. Scaling this back in terms of the dimensionless parameter the Reynolds number this represents an effective inner diameter of

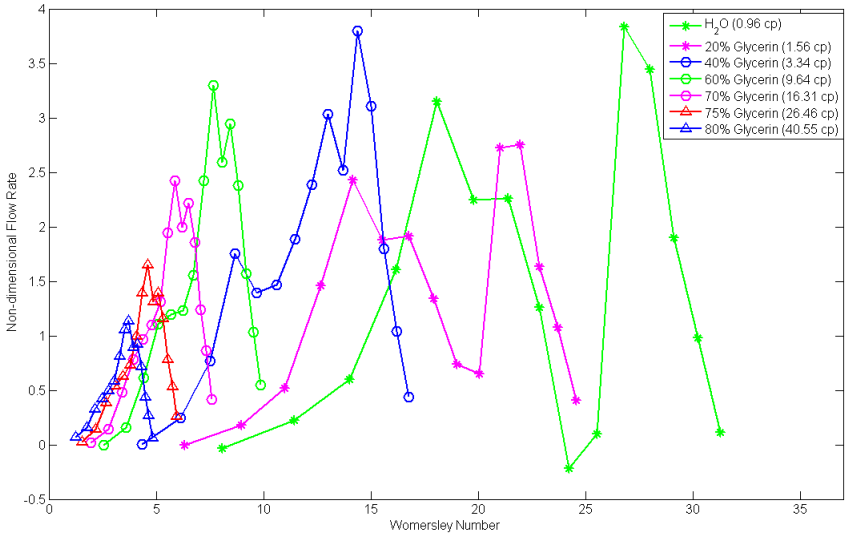

Figure 1.21: The same plot as Figure 1.20 but non dimensionalized according to the methods of Thomann 1978 and plotted versus the Wo.

	Rigid coupling		Elastic Tube			
Pump	ID [μm]	Wall [μm]	L [mm]	ID [μm]	Wall [μm]	*EL [mm]
1	250	50	8.42	250	50	1.56
2	400	35	8.10	300	150	1.40
3	400	35	10.52	300	150	2.11

Table 1.3: Summarizes the parameters of the three pumps used in the micropump viscosity study. * **Note**: EL denotes excitation location as defined from the left hand side wave reflection site.

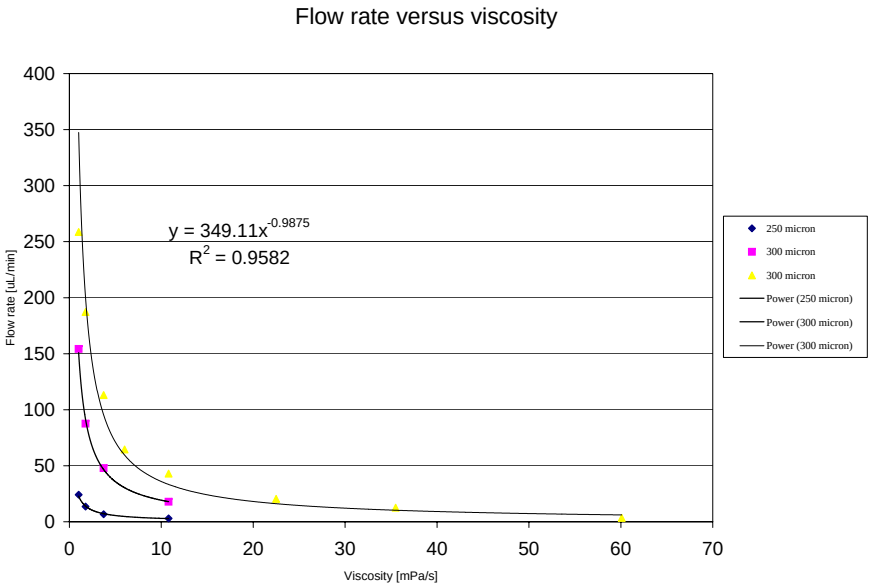

Figure 1.22: Shows the output flow rate of three impedance pumps at a frequency of 84.3 Hz versus increasing fluid viscosity.

approximately 5 μm.

1.4.4 Conclusion

Construction of the characterization system and the proof of concept experiments based around the electromagnetically actuated impedance pump were able to lay the ground work to consider the impedance pump for applications other than strictly a biomedical device for active stents and shunts. The favorable response of the impedance pump to increases in fluid viscosity shows that although the output is attenuated the impedance pump concept still functions down to Reynolds numbers of 0.02. Considering the impedance pump as a micropump opens many new avenues for exciting applications ranging from Lab-on-Chip diagnostics to microscale thermal management.

1.5 Microfluidic platforms and applications

1.5.1 Impedance pumps in Lab-on-chip microfluidics

Microfluidics offers a unique opportunity to observe biological and chemical events in an environment which can easily be controlled and manipulated. Since the early 1990's scientist and researchers have discovered that microfluidic devices can be useful in a plethora of applications ranging from thermal management systems for cooling microprocessors to screening and analysis for pharmaceutical discovery, polymerase chain reaction (PCR), and protein crystallization. As demand drives integrated microfluidic systems to pack increasingly more components per unit area, microfluidic systems must be able to perform operations with smaller volumes and on shorter time scales allowing a larger number of operations to occur on a single chip. Since integration is a key issue and a limiting one in the overall success of microfluidic components, in addition to being effective and space conservative, microfluidic components must easily operate in a planar format, where integrated systems are built up from a series of layers. This format creates a synergy between all microfluidics components as well as agrees with the next obvious step in large scale integration, 3-D fabrication.

Given the basic principles of the impedance pump, there is no required geometry therefore standard soft lithography offers us a fabrication technique to begin producing impedance pumps in a planar format which can easily be prototyped with other microfluidic components within the context of Lab on Chip diagnostics.

A variety of different impedance pumps have been fabricated in polydimethylsiloxane (PDMS) microchips for applications ranging from heat transfer to blood glucose sampling. An example of such devices can be seen in Figure 1.23. The device on the left was made to demonstrate that the impedance pump principle could easily be implemented within the context of a closed microfluidic system. The device on the right was made as a sample diagnostics demonstration for sampling a

biological fluid such as blood. Here the fluid to be sampled could be drawn in through the inlet and stored in a series of reservoirs which can be opened and closed through a series of valves. One of the problems with Lab on chip sampling devices is the volume required to form the sampling line, which in the case of a glucose monitoring device would most likely the hollow body of a needle. From sample to sample this line needs to be flushed to ensure accurate sampling such that no residual stagnant fluid is left in the sample line between samples. The impedance pump lends itself well to this problem in that by taking advantage of the bidirectionality of the impedance pump a single pump can be used to reverse the flow flushing the sampling chambers to prevent coagulation and ensure that a fresh sample was stored. A second pump was also placed on the device to allow previously stored samples to be transported to other areas on the chip for diagnostic operations such as measuring HCO_3-, pH or other physiological markers. Adhering to the basic principles of having a wave reflection site, wave carrying media and an asymmetric excitation location with respect to systemic impedance a microscale impedance pump on a chip was constructed out of PDMS. In this case the wave carrying media is created not by a tube but by a flexible membrane. The pump dimensions are 20 mm in length by 3mm in width with a 200 μm channel depth. Wave reflection sites are created by two affects: one an abrupt geometrical length change as the 3mm pump width couples to the 300 micron flow channel as well as thickening of the PDMS material over the whole boundary to reflect any energy carried by at the center of the propagating surface wave. If the latter affect was not addressed, the layered fashion of PDMS manufacturing would result in an entire microfluidic channel has an upper wall which was free to deflect with changes in pressure and hence could remove energy from the pumping process which could otherwise be rectified and used to drive the flow. The micro impedance pump on the left in Figure 1.23 was tested using the perpendicular coil arrangement specified in Section 1.2.3.1. The NdFeB magnet was positioned on top of the pump and actuated using a 119 Hz square wave with 16 mA offset and 60 mA amplitude at a position of 4.6 mm from the right hand side wave reflection site. The flow output produced by the microimpedance pump was 16 μL/min.

1.5.2 Impedance pumps in rigid systems

Recently we have demonstrated that these principles work equally well in more rigid systems. Early prototypes have been manufactured using standard micro machining techniques from brass and aluminum however can easily be adapted to silicon based fabrication. A picture of a metallic micro impedance pump prototype can be seen in Figure 1.24. Preliminary studies have yielded flow rates of 190 μL/min.

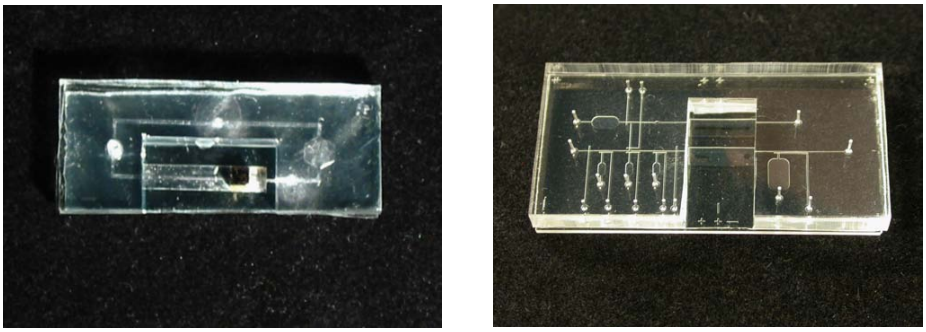

Figure 1.23: Two different PDMS devices with integrated microimpedance pumps. The device on the left was built to demonstrate the ability to generate flow using microimpedance pump in a closed loop microsystem the second was built to demonstrate a series of microimpedace pumps implemented in complex microfluidic system for sampling and diagnostics.

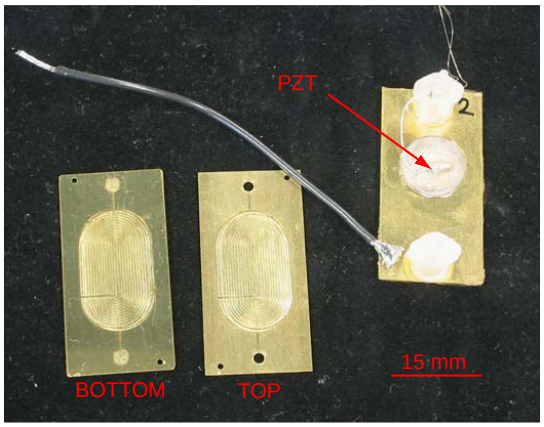

Figure 1.24: A picture of the inside of a rigid micro impedance pump. The material is brass. A small pocket has been machined out to form the body of the pump. Wave reflection sites are created by the change in geometry. Excitation still occurs asymmetrically with respect to the length of the pump body.

1.5.3 A case study: Optimization of microscale heat transfer

1.5.3.1 Introduction

Understanding the mechanisms of thermal transport at the microscale is important to applications ranging from chip level cooling of microprocessors and power amplifiers (PAs) to effective rapid cycling of polymerase chain reaction (PCR) for DNA amplification. In these applications the heated area is usually along a single planar surface within a microchannel. Maximal uniform heating or cooling of the working fluid is often critical to effective operation. The most common system for studying heat transfer in microchannel heat sinks involves a surface with constant heat flux over which an integrated heat sink is used to remove heat. These systems are either open loop or closed loop referring to whether flow occurs within a closed circuit or between two independent thermal or fluid reservoirs. In addition to the flow parameters such as pressure drop and flow rate, three temperatures are usually monitored: the inlet temperature, outlet temperature and the die temperature (chip surface temperature.) Many studies have been undertaken to optimize the geometry of microchannel heat sinks [19]. As a result, much of the trend in microchannel heat sinks has been to ignore the fluid dynamics, electing to enhance heat transfer by means of a pure decrease in size of the microchannels, which increases surface area to volume ratio thus reducing the effects of the thermal boundary layer. The price paid for this, however, is a drastically increasing pressure drop across the heat sink, which leads to costly packing and safety issues in addition to a thermal management system which requires a large amount of input power. Pulsatile flows circumvent this problem, because they can manipulate the thermal boundary layer by increasing the interfacial area between the hot and cold fluid, with no need to change the channel geometry.

1.5.3.2 Background

Along these lines many methods to enhance single-phase heat transfer devices have been proposed, such as developing flow, swirl flow, vibration, secondary flow and mixing; however very few of these methods have been implemented experimentally, or systematically explored, at the microscale. Therefore there is a large body of relatively unexplored thermal transport problems. Heat transfer augmentation methods have been reviewed by a variety of authors including Tao et al. [20]. Tao divided heat transfer augmentation methods into three mechanisms: decreasing the thermal boundary layer, increasing flow interruptions and increasing the velocity gradient near the heated surface. Many of these flow augmentation methods can be achieved through pulsatile flows.

Pulsatile flows have been explored in a variety of contexts for enhancing heat transfer. Numerical studies by Moschandreou and Zamir[21] and Kim et al.[22] have suggested that oscillatory flows can enhance convective heat transport by as much as 20%. A 50% increase in heat transfer enhancement for pulsatile flows with flow reversals[23]. Analogous experiments have been performed on the

large scale on oscillating cylinders in cross-flow. The experimental results performed by Pottebaum show that the wake mode created by vortex shedding from a cylindrical body in cross-flow plays a significant role in determining heat transfer coefficient; this work demonstrated that an oscillating cylinder in cross-flow can augment heat transfer coefficients by as much as 8 times[24]. These studies reveal the importance of flow/structure interaction in aiding in convective heat transfer, given that heat transfer from the cylinder into the surrounding fluid can be significantly enhanced by modifying the flow field to augment the transport of heated fluid out of the thermal boundary layer. We find merit in exploring the mechanisms of heat transfer augmentation in these pulsatile flow systems, when considering that even a 50 % increase in the heat transfer coefficient for pulsatile flow conditions translates into an increase in the dimensions of a channel heat sink equivalent to a reduction in pressure drop by a factor of 3 or more; effects at the microscale may be even more substantial.

1.5.3.3 Experimental apparatus

Since the aim of this experiment was to investigate the effect of pulsatile flow profiles on heat transfer in microscale geometries. Preliminary studies were conducted to optimize the heat transfer in a custom designed micromachined heat sink with a channel depth of 100 μm. The heat sink is attached to the backside of a Riedon Inc. TF1218H-A 100 Ω power resistor with a supply voltage of 20 V in order to dissipate a heat flux of 4 W/cm2. The inlet and outlet of the heatsink were connected within the characterization flow loop described in Figure 1.13. Thermocouples were installed on the inlet to the heatsink, outlet to the heat sink and in the thermal junction between the heatsink and the sinking surface of the power resistor. Downstream of the outlet of the micromachined heatsink was a large water bath which functioned as thermal reservoir to maintain constant inlet temperature to the heatsink as well as allow the optimization to work over long time periods. The temperature of the incoming water from this reservoir is monitored by the inlet heatsink thermocouple. The difference between the inlet and outlet thermocouple gives a measurement of the average thermal power removed by the fluid flow. The junction thermocouple allows us to monitor the junction temperature, a critical temperature for establishing the thermal resistance to heat flow into the working fluid.

The pump used in this study was a 2 mm ID impedance pump with a 780 μm wall driven by the characterization system described Figure 1.13. The impedance pump was 14.87 mm in length with a excitation location of 2.52 mm from the left hand side wave reflection site. The frequency input was a sine wave that was allowed to vary from 10 -150 Hz and amplitude limited to the range of 0.1 to 0.5 mm. No electrical offset was applied to the waveform however a mechanical offset of 1.397 mm was applied through the z-traverse. The heater was activated for 3 secs before the pump was activated.

To explore the large parameter space comprised of the pump and heatsink system an optimizer based on an evolutionary algorithm was employed. In this study the optimizer sought to maximize the temperature difference between the inlet and outlet bulk fluid temperatures of the heat sink, while minimizing the average flow rate, a linear combination of the flow rate and the inverse of the temperature difference are minimized. To allow the optimizer to run for long periods of time and preserve the initial conditions of the experiment, if the amplitude frequency choice of the optimizer produced insufficient flow to prevent the fluid in the heatsink from boiling, the point was discarded. After every run a cooling cycle was applied to lower the heatsink temperature to within 99% to that of the inlet thermocouple reading.

1.5.3.4 Results and Discussion: System specific optimal points for heat transfer

The performance of the impedance pump, similar to the pulsatile flow heat transfer problem, varies with the excitation frequency and amplitude. This combination of systems results in an optimal region for heat transfer, which is the intersection of two regions: one which results in efficient heat transfer characteristics, and another which contains optimal points which produce effective flow performance for the pump. The left part of Figure 1.25 shows a contour plot of the optimal region, found by the optimizer. The plot on the right in Figure 1.25 shows the temperature difference produced by one point belonging to the converged solution of the optimizer for the pump/heat sink system compared to the temperature difference which results from steady flow. The mean flow rate for both the steady and oscillatory cases is 8.37 mL/min. The excitation frequency and amplitude for the pulsatile flow case are 122 Hz and 0.37 mm, respectively.

Examining the plot on the right of Figure 1.25 it is noticeable that the pulsatile flow case is more effective at removing heat versus the steady case. Comparing the ΔT of this point to the steady flow case there is a 25 % increase in ΔT for the optimal pulsatile flow with a negligible change in system pressure (760 Pa steady/768 Pa pulsatile). These optimal points are largely affected by the frequency response of the pump due to the fact the points insufficient to cool the heatsink are discarded however a larger frequency and amplitude domain still exists. Unfortunately the brass heatsink did not allow visual access therefore it is difficult to determine the exact physics responsible for the increase however such points providing enhanced heat transfer do exist under pulsatile flow conditions.

1.5.3.5 Conclusion

An experiment was conducted to examine whether pulsatile flow can be used as a method of heat transfer enhancement in microchannel heatsinks. The frequency and amplitude space of heat transfer were examined for the combination system of an impedance pump and a custom machined brass microchannel heatsink to determine whether pulsatile flow points existed which provided enhanced

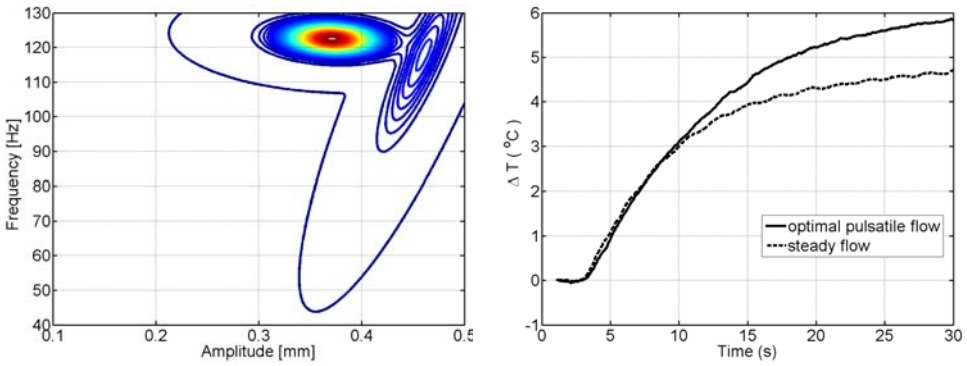

Figure 1.25: Shows preliminary data, on the left is the contour plot of the distribution of optimal points found by the optimizer. The plot on the right compares the optimal point of the contour plot on the left to steady flow. For both cases the mean flow rate is 8.37 mL/min the change in pressure drop was negligible.

heat transfer for the pump-heatsink system versus steady flow. In order to search the large parameter space an evolutionary optimization routine was employed. The cost function looked for points where heat transfer was maximized while the power input to the fluid was minimized. One of the predicted optimal points, a frequency of 122 Hz and 0.37 mm amplitude, shows a 25% increase in the temperature difference inlet to outlet versus steady flow of an equal mean flow rate.

1.6 Summary

The impedance pump functions through dynamic wave interactions allowing a pressure gradient to be created across the ends of the pump. The concept has been shown to require the presence of one or more wave reflection sites functioning as boundaries located along a compressible section as well as an excitation occurring asymmetrically with respect to systemic impedance. To tackle the huge parameter space of the pump the characterization system was constructed to measure time resolved pressure and flow in order to provide an understanding of how these parameters influence their interaction and how these dynamics give rise to flow. As a result many of the studies invovled in the characterization of the large scale impedance pump by Hickerson in her thesis were able to be repeated at millimeter size scales and smaller. These experiments include:

1. Measurement of the flow response of the impedace pump to open loop and closed loop flow conditions.

2. Observation of the symmetry of the flow reponse to excitation location.

3. Pressure-flow loops describing the contribution of potential work to the flow.

4. Response of the pump to increases in fluid viscosity.

5. Response of the flow output to transmural pressure.

The concept of the impedance pump was demonstrated to be scaleable down to a few hundred microns and tested under increased viscosity demonstrating that the concept is robust to the dominance of viscous forces at the microscale. Microscale impedance pumps were then fabricated using current microfabrication and micromachining techniques demonstrating that the impedance pump concept can drive fluid in microfluidic systems. The basic concepts were then extrapolated further to create impedance pumps composed entirely of rigid materials. This work opened the door to consider impedance pumps in a wide range of applications spanning micro implantable pumps for treating glaucoma and hydrocephalus, to lab-on-chip diagnostics or even for applications in drug delivery and microscale heat transfer.

Chapter 2

Enhancing transport in microfluidic systems

2.1 A systematic study of mixing and transport in microscale cavity flows

2.1.1 Introduction

The problem of mixing is fundamental to the miniaturization and effective operation of microfluidic circuits for biological and chemical diagnostics and analyses. Mixers, like valves and pumps, are integral components of microfluidic systems. Recently, with the increasing interest in controlling fluidic events in volumes on the order of 10^{-6} to 10^{-9} L an increasing amount of attention has been paid to the design of both passive and active mixers for microfluidic circuits. Low Reynolds numbers are characteristic of flows at the microscale (Re < 1) indicating that inertial effects are small and that the flow is dominated by viscous dissipation. Under constant pressure-driven, fully developed low shear laminar flow conditions, the velocity profile will be parabolic. Another characteristic of laminar flow is that there is very little communication between particles in different streamlines; for example, fluid in the center of the channel and fluid near the wall. In a purely laminar flow, two miscible fluids mix purely by diffusion. The Peclet number, relating convective to diffusive transport, for microfluidic systems are commonly much greater than 100, diffusive mixing is therefore slow in contrast to the axial velocity of the fluid along the channel. The penetration depth, δ, of diffusing fluid particles grows as $(D^*t)^{1/2}$ at the interface of the two fluids. For simplicity we will assume a square channel with a side length of 100 μm, flow velocities of $\sim$ 5 mm/sec, and diffusion constant $D \sim 10^{-6}$ cm^2/sec resulting in a Peclet number, Ul/D, of 105. Given that diffusion time scales across the channel are on the order of 25 seconds particles have already moved 125 mm in the axial flow direction. Clearly these time scales and distances are not compatible with microfluidic systems. A low shear laminar parabolic profile means that the average residence times of fluid particles near

the wall are much greater. Since mixing between fluids near the wall is particularly poor, clearly there are limitations on speed with which two reactants can mix in a purely laminar microfluidic environment. Besides the use of 3-D geometries, exploiting time periodic or unsteady flows is a common technique to overcome these limitations on mixing.

2.1.2 Background

Microscale flows can more or less be considered 2D, or varying only in x and y. The problem of mixing therefore becomes one of adding disturbances to perturb and therefore alter flow within the cross section of an otherwise laminar viscosity dominated 2D flow. By imposing flow components in the cross section of the flow the interface between the two mixing fluids can be increased, decreasing the distance over which diffusion occurs. Folding and stretching of the fluids to be mixed into extremely narrow striations has the advantage of maintaining the concentration gradients resulting in rapid diffusion due to the very small distances. For chaotic flows stretching and folding occurs exponentially as a function of the distance moved down the flow channel drastically reducing mixing times. These concepts have been successfully demonstrated in a variety of different micro mixers involving complex spatially varying geometries, or a series of periodically forced cross streams.

2.1.3 Principles of microscale mixing

Flows in microchannels are persistently laminar therefore the streamwise or cross-sectional velocities of particles within such flows are often negligible. Mixing commonly involves the homogenization of two initially separated fluids streams the basic idea being to maximize the interfacial area between two miscible fluids while expending the least amount of time and energy. Interfacial contact area is often increased by simple stretching and folding of the fluid. Stretching is more or less the strain on an individual fluid element. In a given flow field there may be sections where fluid elements are expanding and others where elements are contracting. In a simple shear flow this stretching occurs linearly in time. In other flows stretching may occur exponentially. Flows which display this exponential stretching have been linked to chaotic flows. A mathematical discussion of chaotic flows is given by Ottino[25].

Recently the interest in microscale mixing has prompted a reexamination of much of the literature produced on mixing theory during the 1980s and early 1990s. Many of these different theoretical constructs were proposed for enhancing mixing in 2D flows such as the blinking vortex[26] model and the pulsed source-sink model [27]. These theoretical schemes have normal spatio-temporal flow fields however have been proven mathematically to demonstrate exponential growth of fluid elements termed, chaotic advection. Chaotic advection can be seen in both 3D flows as well as unsteady 2D flows. Other constructs involve the deforming of laminated fluid streams whorls or tendrils thereby

Symbol	Parameter	Equation	Description
Re	Reynolds number	$\mathrm{Re} = \frac{\mathrm{Ud}}{\nu}$	Inertial to viscous
Sc	Schmidt number	$\mathrm{Sc} = \frac{\nu}{\mathrm{D}}$	Diffusion of momentum to diffusion of dye
Pe	Peclet number	$\mathrm{Pe} = \frac{\mathrm{Ud}}{\mathrm{D}}$	Convective to diffusive transport
Fo	Fourier number	$\mathrm{Fo} = \frac{\mathrm{LD}}{\mathrm{Ud}^2}$	Residence time of particle to diffusive time
Wo	Womersley number	$\mathrm{Wo} = \mathrm{R}\sqrt{\frac{\omega}{\nu}}$	Frequency dependent Reynolds number

Table 2.1: Shows a summary of the important dimensionless parameters for micro mixing and pulsatile micro flows.

increasing the contact area[25]. Much of this early work seems to be captured by a single kinematic concept embodied in the linked twist map (LTM) which has recently applied to micromixers[28]. The basic idea behind the LTM is that in a time or spatially varying flow streamline portraits at different instances in space and time that have crossing streamlines will generate chaotic flows. From a design or optimization standpoint the concept of crossing streamlines is the most direct and easily applied heuristic to mixing enhancement.

2.1.4 Dimensionless parameters

Dimensionless parameters such as the Reynolds number (Re), describing the relative contributions of inertial to viscous forces are another tool commonly used to understand and characterize mixing problems. Additionally, there are a number of other dimensionless parameters which are relevant convective/diffusive mixing problems such as the Peclet number (Pe), the ratio of convective to diffusive transport within the fluid and the Fourier number (Fo), the ratio of the average residence time to the diffusive mixing time. Additionally, since the aim is to study fluid mixing in the context of pulsatile flows, the Womersley (Wo) number used to describe pulsatile flows. Table 1 below summarizes the important dimensionless parameters and the properties that describe them. Here U, D, L, d, ω and υ denote the average velocity, diffusion coefficient, axial length, hydraulic diameter, frequency and kinematic viscosity respectively.

2.1.5 Micro mixers

Although it is generally difficult to classify micro mixers, they can generally be divided into two groups: passive and active mixers. Passive mixers basically rely on passive flow to reconfigure the fluid by passing it through a prescribed geometry. Active mixers rely on energy input to enhance mixing in an otherwise passively mixing flow.

2.1.5.1 Passive mixers

Passive micro mixing schemes tend to employ the lamination of parallel fluid streams or split and recombine techniques which use obstacles placed in the flow to separate and recombine lamellar fluid streams. Passive mixers can further be categorized into those that are composed of a single plane lamination and those employing three dimensional geometries. The simplest case of a passive micro mixer is the T- or Y-junction which have been used for both fluid and gas mixing. Gobby et al. studied the T mixer at a variety of inlet stream angles as well as using a throttle to stretch the mixing streams before entering the mixing chamber[29]. Other passive mixers have used hydrodynamic focusing using two perpendicular streams to squeeze the fluid into a thin jet over which diffusion occurs very rapidly[30]. In this case mixing times were reduced to a few microseconds using very high advection velocities $\sim 1 - 10$ m/s. The rapid mixing times achieved by this mixing technique have been used to study protein folding dynamics[31]. Passive mixers with obstacles have been demonstrated with mixing times on the order of 20 μs for rapid freeze quenching[32]. Optimizations of obstacle layouts for mixing in microchannels have also been performed[33].Other passive mixing systems have explored using a series of spatially varying impinging jets[34], recirculating flows (Jeon et al., 2005), in zig-zagging microchannels with interconnecting cross channels to encourage lateral transport [35, 36] or even a series of S-shaped channels to generate secondary flow circulation within the cross-section of the mixing streams.

Quite a few passive chaotic three dimensional mixers have been successfully used for effective micro mixing in several different geometries [37–41]. The staggered herringbone micro mixer[40], is a well known example that employs a spatially varying geometry of a series of angles L-shaped ridges along the bottom of the channel, referred to as herring bones, which periodically alternate direction adding asymmetry to the mixing flow. In another example a 3D square spiral towers were created within a network of microchannels[42]. Unfortunately, spatially varying geometry-based micro mixers, although effective, are difficult to fabricate, have a large amount of dead volume and require significant space with respect to microfluidic systems.

2.1.5.2 Active mixers

Active mixers use external energy to stir or agitate the flow. Many methods have been devised to mix fluids on the microscale these include: externally driven magnetic microstirrers[43], acoustic streaming [44], a flapping plates to stir the flow [45], thermocapillary flows [46], electrokinetic instabilities [47–49], dielectrophoretic [50], pulsed source-sink [51], pulsed flow [52–54], and shear superposition mixing [55]. Under the proper conditions many of these designs have been able to achieve chaotic flow.

Of the examples mentioned many of these employ oscillatory flows to enhance mixing. The

pulsed source-sink mixer of [56] embodies the theories suggested by [27], that a series of 180 out of phase combinations of time periodically forced sources and sinks could induce chaotic advection in a 2D flow. The shear superposition micro mixer (SSM)[55] is an example of a periodically forced cross-stream mixer, consisting of one main channel intersected orthogonally by a series of cross-channels. These systems are fabricated with a series of inputs to provide the periodic shear flows are successive lengths down the channel. Other studies have focused on a single unit of the SSM [57–60]. Each of these experiments has yielded chaotic advection as predicted by the LTM concept[28]. Micropumps have been used to provide a high frequency on/off switching between the two inlet channels up to 1 kHz, in effect creating a transverse layering the two fluids, where the thickness of the layer was determined by the on/off switching frequency[54]. Oscillatory mixing in a T-junction under continuous flow from both channels, as well as the effect of phase on pulsed input from the two channels have been investigated previously[52, 53]. Both studies employ micropumps to drive the oscillatory flow, however neither of these studies examines frequencies in excess of 3 Hz.

2.1.6 Formulation of the cavity problem

2.1.6.1 Large scale cavity studies

Since this work concerns a study on micro scale cavity flows therefore a brief review of cavity flows will be given. Flows within cavities are well known and often even used to gauge the validity of computational studies however in contrast there are relatively few experimental studies, especially those restricted to rectangular cavities. The most well known study of flows in cavities is probably that of Taneda[61]. Charwat categorized cavity flows into two types, open and closed, where the shear layer spans the cavity and where it reattaches at the bottom of the cavity, respectively[62, 63]. Moffat showed that an infinite sequence of vortices occur in a wedge shaped void if the angle was less than approximately146[64]. Strong oscillations in the shear layer have been observed for fixed parameters relating to the boundary layer, shear layer, free stream velocity one the cavity width exceeded a critical value[65–67]. The effect of flow oscillations on cavity drag has been investigated in a symmetric cavity on the surface of an ellipsoidal cone[68]. The basic geometry of a cavity flow is captured by 2.1. Shown are the width and height of the cavity, b and d respectively. U8 the free stream velocity and $\delta 0$ and $\theta 0$ the boundary layer thickness and momentum thickness respectively.

Here we will adopt the terminology of Gharib, 1983 in which the flow structure in cavity flows is divided into three modes for a given a fixed U8, $\delta 0$ and $\theta 0$:

1. Mode I: Is the non oscillating regime characterized by a weak, steady vortex circulating inside the cavity. Here there residence time of particles inside the cavity is expected to be very long.

2. Mode II: Once a minimum cavity width has been reached the shear layer interacts with downstream corner to create self-sustaining oscillations. Responsible for this interaction is the en-

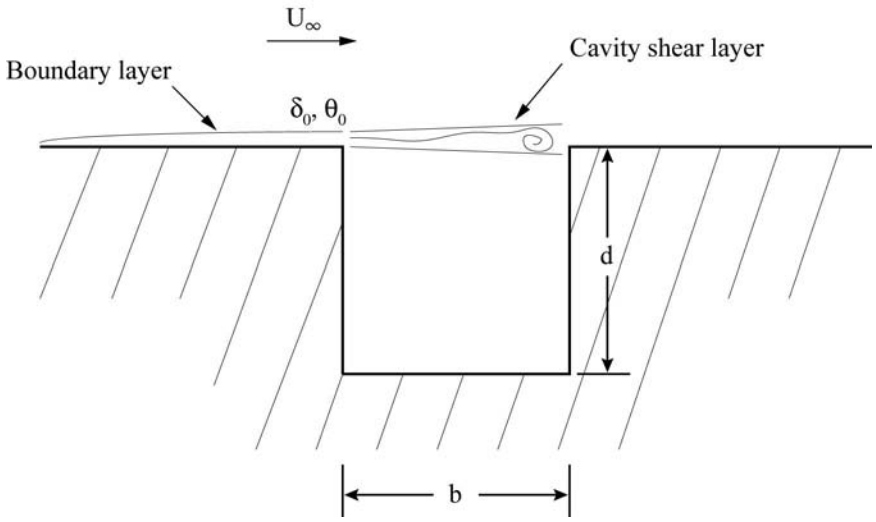

Figure 2.1: A geometric description of flow over a cavity.

trainment of fluid by the shear layer and its redirection into the cavity to replace the entrained fluid as a result of mass conservation. Under these conditions the overall phase difference between the corners of the cavity satisfied the relation $\varphi/2\pi$ = Fb/Uc= N. Where φ is the phase, F is the frequency of oscillation, b the cavity width, Uc the phase velocity of the shear layer and N the integer number of wavelengths contained by the cavity during oscillation[68].

3. Mode III: By increasing the cavity width the flow eventually transforms into wake mode where the flow reattaches at the bottom of the cavity ahead of the downstream edge. In this case the shear layer is forced to reattach at the bottom of the cavity because it can no longer sustain its entrainment. This mode is characterized by the splitting of the center vortex and the formation of two corner vortices.

2.1.6.2 Cavity flows at the microscale

Cavity flows have been studied at the microscale mainly for the manipulation of cells and other biological molecules[69–71]. However, very few measurements relating to the fluid mechanics were made. Only single particle measurements were conducted such as by optically trapping a particle and measuring its rotational velocity. From these measurements quantities such as the estimating rotational shear stress and circulation velocity were approximated. Since the focus of these studies was the manipulation of biological molecules inside of the cavity, different geometries were examined to maximize the rotationally velocities or forces experienced by the molecules within the cavity. These studies however provided no detailed results regarding the fluid mechanics of transport in and out of the cavity nor was there any examination of the parameter space under steady or pulsatile conditions.

2.2 Problem statement

Many previous studies have been able to definitively show the effectiveness of microscale mixing under pulsatile flow conditions (Dodge et al., 2003; Truesdell et al., 2003; Glasgow et al., 2004; Tabeling et al., 2004). In terms of cavity studies, elliptical cavities have been examined at the microscale however only for the purposes of manipulating cells and other biomolecules. While low Reynolds number cavity flows have been conducted on infinitely deep cavities, no parametric investigation exists on microscale cavity flows which focus on the fluid mechanics of the cavity with out-of-plane boundary layers, a situation more relevant to real world flows. Similarly, there is no investigation of pulsatile flows in microscale cavities.

Microscale cavities were therefore investigated to determine how the frequency and amplitude conditions of the flow field affect the ventilation or mixing of the cavity contents with the freestream. The homogenization of two intially separtated fluids will be adopted as a general definition of mixing. However this study seeks to examine the mixing of two intially separated fluids, one in the freestream and one in the cavity, not to directly to examine mixing inside the cavity region. The goal is to understand how to better mix the ventilated cavity contents with the freestream aside from the situation observed in steady, purely laminar flow where contents advected out of the cavity remain near the wall.

To overcome the geometrical complexities of many of the microfluidic mixers a simple rectangular cavity was chosen for the purposes of the study. Although the aforementioned studies do exist in which some comparisons can be made, in terms of the fluid mechanics and microfluidic fabrication, elliptical cavities are difficult to parameterize namely due to the definition of their intersection with the freestream and the ability to resolve this boundary accurately with current microfabrication techniques, and the huge impact this has on flow separation, making case by case comparisons difficult.

In addition these experiments sought to develop techniques to control cavity ventilation purely through the manipulation of the flow field. To accomplish this study the following three objectives were set:

1. To understand the relationship between ventilation and Reynolds number and cavity geometry under steady flow conditions steady.

2. To investigate the affect of pulsation frequency on the ventilation properties of the cavity.

3. To determine the relevance of pulsation amplitude on cavity ventilation.

Besides the problem of mixing in Lab-on-Chip microfluidics, there are many real world examples where this form of analysis is particularly useful. For example, the elution of a drug and subsequent mixing of the drug with the fluid of interest such as blood. What is the most effective means of

distributing a substance throughout the main body of the flow in order to distribute the drug evenly to the target tissues? Unsteady cavity flows also have analogs in other biofluids flows such as in the junctions of grafts and stents or the alveolus of the lungs. Take the latter case for example, in the alveolus of lung, ventilation of gas into or out of microenvironment, and the degree of mixing or ventilation of alveolus is important to maintaining blood oxygen levels. This investigation also holds merit in the search for effective strategies to control transport in microfluidic systems in that many of the current mechanisms for pumping fluid at the microscale are inherently pulsatile in nature.

2.2.1 Approach

The systematic study of microscale cavities requires the ability to provide high frequency large amplitude oscillation onto a mean flow as well as methods to acquire information about the flow fields. PIV remains the most widely used measurement technique for acquiring velocity fields of microflows due to its ability to be implemented optically without disturbing the flow and its versatility in terms of its application. Accurate measurements of the cavity flow fields are crucial to predicting particle trajectories for the residence time calculations which will be used to estimate the ventilation properties of the flow conditions. These PIV measurements will also be used to feed Finite Time Lyapunov exponent calculations to aid in identifying flow boundaries explaining the ventilation and mixing behavior.

2.3 Description of the experimental setup

The goal of the experimental setup was to provide a known high frequency oscillation with a fixed mean flow into microfluidic chip which could be imaged in an inverted microscope. Since push pull syringe pumps are limited to around 10 Hz, high frequency, large amplitude oscillatory flow will be provided by a voice coil (Brel and Kjr, 4810 mini-shaker) used to pinch an elastic tube downstream of a syringe pump (Harvard Apparatus, Holliston, MA.) providing a mean flow. A fluidic capacitor will be installed between the syringe pump and the elastic tube to damp out any fluctuations created by the operation of the pump. The inner diameter of the elastic tube is 2 mm with a 780 μm wall. The voice coil probe has a diameter of 2.4 mm resulting in a displacement volume of approximately 8 μL. Data is acquired using a National Instruments data acquisition card and the motion of the probe is controlled in open loop by using a Matlab script which provides 2 mm displacements of the probe up to 150 Hz. Microscale flows will be observed using an Olympus IX-70 inverted microscope. Image acquisition will be performed using an Imperx Lynx. Flows will be illuminated using a 200 mJ Nd:YAG New Wave Gemini lasers allowing for a 15 Hz double exposure repetition time and phase averaged reconstruction of high velocity flows. A schematic of the experimental system is shown in Figure 2.2. A diagram of the relevant cavity geometry can be seen in Figure 2.2.

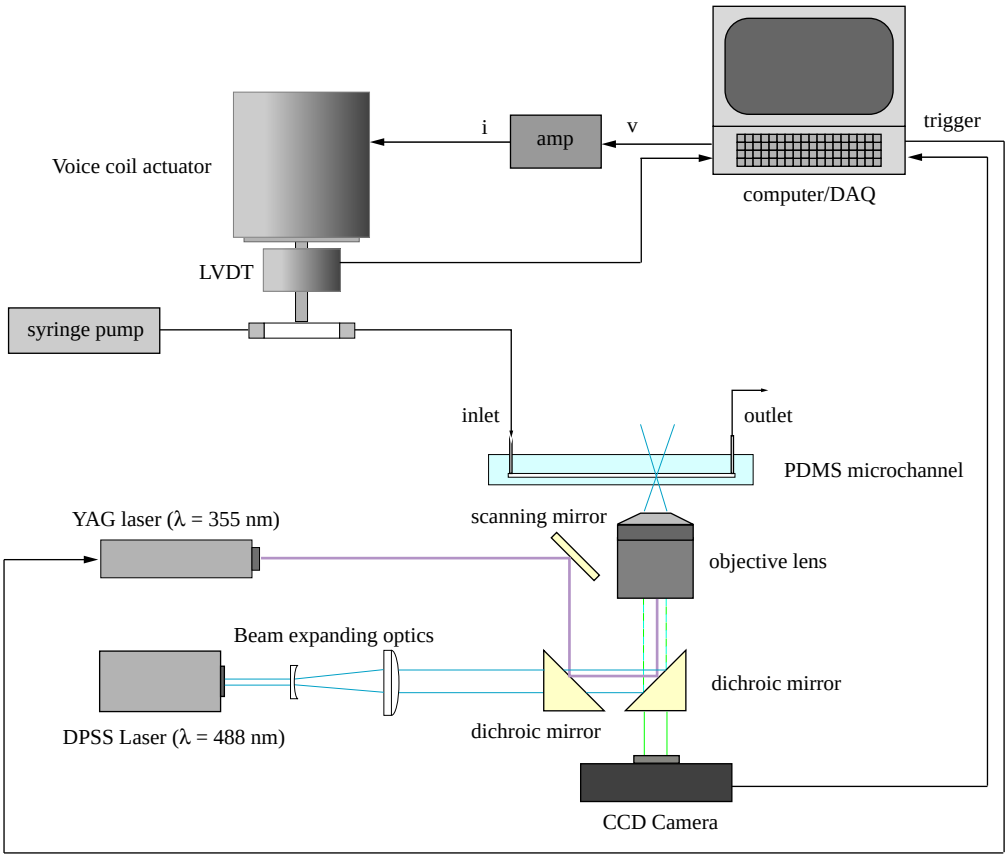

Figure 2.2: A diagram of the experimental setup to be used for the microscale cavity flow studies. The voice coil and LVDT will be used to provide precise frequency and flow velocity amplitude inputs over the steady flow provided by the syringe pump.

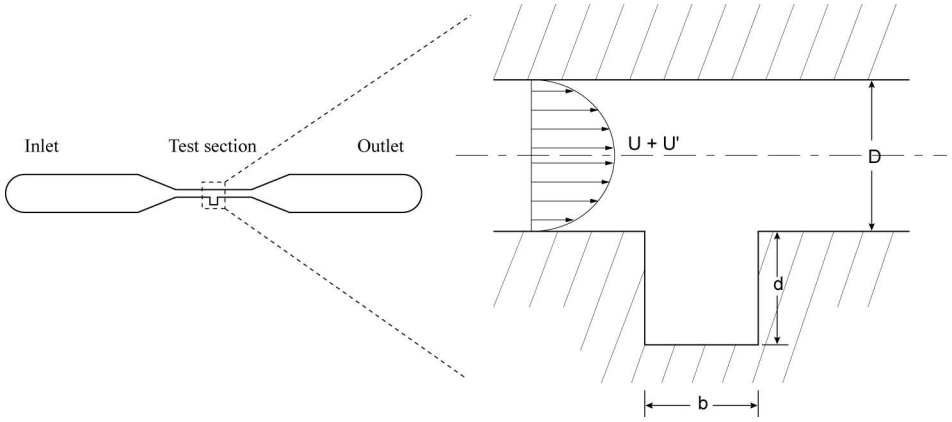

Figure 2.3: Shows the geometry of the microscale cavity including the width and depth of the cavity, b and d respectively as well as the width of the main channel, D. The height of the cavity in the out of plane dimension was fixed at 100 μm. Also shown are the relevant fluid parameters U and U'.

2.3.1 Optical setup

To clean up the laser pulse from the Nd:YAG the laser light was first passed though a weak spatial filter with an optical pinhole of size of 50 μm. The beam was then expanded and passed through a 5° holographic diffuser. The diffuser has the function of evening out any regions of unusually high energy density left in the beam producing a close to Gaussian output. Flows were imaged using a 100x oil immersion apochromatic lens from Olympus. In order to condense the image onto the camera CCD, a 0.63 x tube coupler was used to couple the image to a Imperx Lynx. The camera and lasers were triggered using a National Instruments PCI-6602 timing card.

2.3.2 Microfluidic chip design

The microfluidic channels were designed to contain single cavities such that there was no cross talk between structures in the flow. To minimize any 3-dimensionality to the flow the microchannel was fabricated to a depth of 30 μm. Since the flow enters through a vertical inlet and outlet and is pulsatile flow first enters a larger section of the microchannel with a 750 μm width before tapering to 50 μm in the test section containing the cavity. The length of the flow channel after the cavity is 2 mm to ensure that any potential instabilities remaining in the flow from the inlet and outlet, producing an even laminar flow over the surface of the cavity.

The microfluidic chip was fabricated through well documented methods of soft lithography. SU8-25 Photoresist was applied to a Si wafer to produce a thickness of 30 μm and exposed to the cavity pattern using a 20000 dpi photomask. Once the mold was developed, a two part RTV 617B was poured over the mold and baked in the oven at 80°C to cure the polymer. The PDMS chip was then sealed to a glass cover slip using O_2 Plasma treatment to ensure adequate bonding.

Large scale fluid mechanics studies have the benefit of relative size with regards to having sharp edges and minimal surface roughness. These attributes cannot always be taken for granted with work at the microscale. Since this study is concerned with the fluid mechanics of cavity flows the mold was measured using SEM measurements to confirm the channel height was well as examine the relative smoothness of the mold. A representative SEM image of the bottom of a 50 μm wide cavity can be seen in Figure 2.4.

2.3.3 Micro Particle Image Velocimetry

Micro PIV studies yield velocity fields of particles moving within the flow. The methodology for applying DPIV to microchannel flows is well established [72, 73]. Results from μPIV experiments on micro cavities were used to quantify values such as the mean and oscillatory velocity components and channel profiles as well as analyze properties such as shear stress within the cavity. Much of the complexity in imaging microscale cavity flows comes from the huge velocity gradient spanning

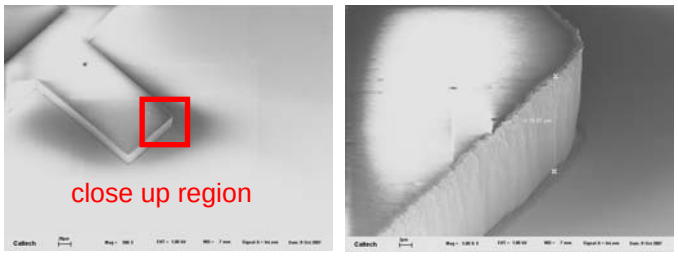

Figure 2.4: An SEM of the cavity. On the left is a zoomed out view showing the region given for the close up. On the right is the side profile of the cavity. The image is taken at a 30 viewing angle so the sine of the view angle makes the actual mold height 31.1 μm.

the freestream to the base of the cavity. Complete reconstruction of the velocity field within a microscale cavity depending on the freestream velocity and cavity geometry can involve performing μPIV measurements with time increments spanning 4 orders of magnitude. PIVview a PIV analysis package was used to mask the PIV frames isolating areas of common velocity within the cavity as well as process contained in them. The velocity fields from the μPIV experiments were then applied to particle tracking schemes to identify the residence times of the particles and quantify the time averaged Lyapunov exponents of particle trajectories within the flow.

2.3.4 Analysis of microscale transport

2.3.4.1 Definition of Particle Residence time

PIV velocity fields were used to provide particle tracking trajectories in order to compute the residence time of particle, or the time the particle remains within the cavity for different flow input conditions. The following equation was used to calculate the particle residence time:

$$T_R = \sum_i \frac{|x_i - x_{i-1}|}{|v_i|}; x_i \in X \tag{2.1}$$

where x and v are the displacement and velocity vectors for each particle, respectively. TR represents particle residence time, i denotes the number of time steps that the particle is still in the area of interest, and X the region of interest. Residence times will be used as a tool to examine the ventilation or mixing process between the cavity and free stream.

The residence time code was written in Matlab. Particle velocities were determined by a weighted average based on the particles distance to the nearest 16 surrounding grid points. Time series for the steady cases were reconstructed by replaying time averaged steady velocity over and over again into the residence time simulator. Steady cases analyzed the residence times of 5000 particles seeded randomly in the lower half of the cavity. Each particle was tracked for a total of 10000 time steps. If a particle did not exit the cavity within the allotted 10000 time increments the residence time was flagged as infinite.

Phase averaged velocity data was taken to collect 10 phase increments of each at pulsatile flow frequency examined Pulsatile flow cases examine random distributions of only 1000 particles however they were tracked over 50000 time steps. The reason for this is the small phase increment of subsequent velocity fields in the time series.

2.3.4.2 Lagrangian Coherent Structures

Lagrangian Coherent Structures (LCS) was used to identify separatrices within the flow that form boundaries to transport in order to visualize structures present in the microscale cavity which may affect the ventilation process. The Lyapunov Exponent is an average measure of the exponential rate of divergence of the trajectories of two closely located particles within the flow field. LCS are the local maxima of the FTLE field and refer to the manifolds that exist as parts of hyperbolic structures within the phase space of the flow (Shadden et al., 2005).

Velocity information from the μPIV data was processed using MANGEN to produce the FTLE fields. MANGEN is publicly available software created by Francois Lekien and Chad Coulliette. Steady flows were processed by replaying a single time averaged steady PIV repeatedly for a given time period. The steady data was processed using 60 frames with a time step of 0.0714 seconds for a total of 4.28 seconds. The integration time was adjusted according to the freestream flow rate to prevent a large number of particles from exiting the FTLE region during integration. Pulsatile flows were processed using 100 phase slices per cycle over a time frame of 2.5 periods.

This form of analysis was able to elucidate key flow features which affect the transport properties of microscale cavities as well as aid in the identification of areas of flow separation, and stagnation that exist on different timescales. In the case of the pulsatile flows LCS proved particularly useful to in revealing the instantaneous boundaries in the rapidly changing flow field and how their evolution through time influences mixing between the cavity and freestream.

2.4 Experimental results

2.4.1 Steady flow in microscale cavities

An investigation into steady flows microscale cavities was performed to determine the dominant modes of transport under steady flow conditions. These studies were also useful in identifying separations and the onset of circulation in the cavity under steady flow conditions for varying cavity geometries. The investigation into steady flows also provides us a starting point for interpreting the pulsatile flow results presented in the Section 2.4.2. A compilation of all residual plots for all steady cases examined can be found in Appendix E.

Three cavity aspect ratios were examined 0.5, 1, and 2 spanning Reynolds numbers 0.1 – 100.

Aspect Ratio	Freestream Reynolds Number								
0.5	0.1	1	10	15	16.7	20	30	50	100
1	0.1	1	10	20	22.2	23.3	24.4	30	50
2	0.1	1	10	20	30	40	50	75	100

Table 2.2: A summary of the various cavity flow configurations investigated under steady flow.

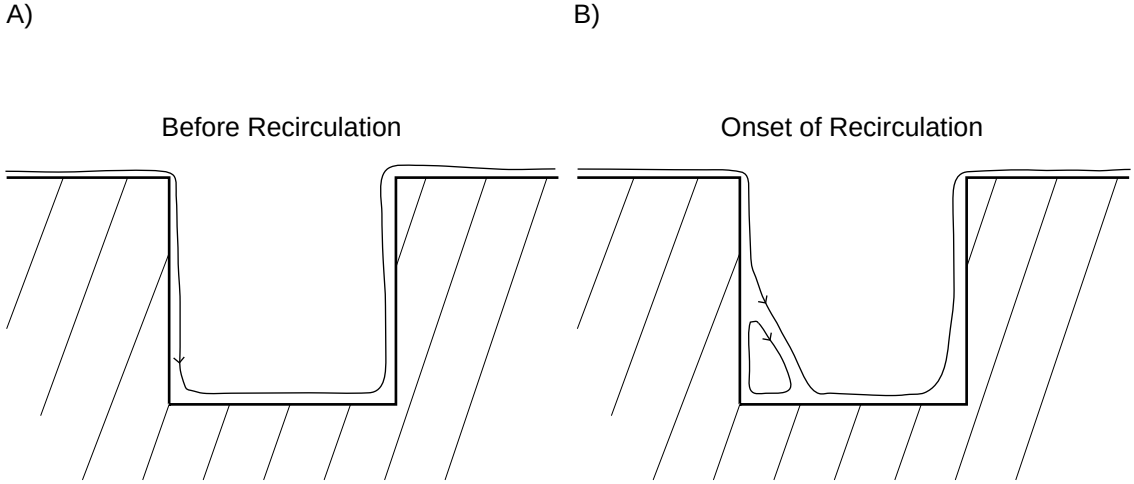

Figure 2.5: A schematic representation of the onset of recirculation in the microscale cavity under steady flow conditions. A) Shows flow before the onset. B) Show flow after the onset of recirculation.

A summary of the particular flow rates examined for every cavity case is presented in Table 2.4.1. Particular attention was paid to capture the transition region to separated flow.

2.4.1.1 Separation and reattachment versus Re and geometry

For Reynolds numbers less than 10 there is no separation for cavites of any of the aspect ratios examined. The relatively low Reynolds number of the flows examined combined with the similarity in dimensions between the freestream channel depth and the boundary layer thickness, results in a very diffuse separation compared to that normally observed or simulated in cavity flows. Careful attention was paid to capture the onset of circulation for cavity aspect ratio 0.5, 1 and 2 the onset of recirculation occurred at Reynolds number 16.7, 23.3 and 40 respectively. The onset of recirculation is defined schematically in Figure 2.5. A plot of these two parameters can be found in Figure 2.6. A rough fit of onset of recirculation versus Reynolds number shows a linear trend, however such a relationship is probably the result of the number of points and not an existing physical trend in the data. Streamline images generated from PIV velocity fields enabled the visualization of the separation and reattachment regions along the boundaries of the cavity. Typically for aspect ratio 1 and 2 cavities at the onset of recirculation the separation has a triangular form, separating from the leading edge of the cavity and reattaching to the cavity base. As the freestream Reynolds number

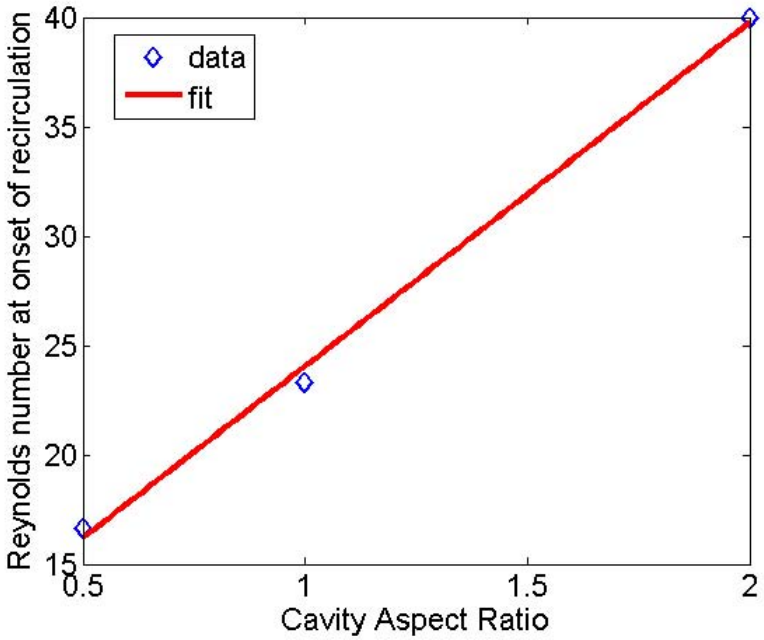

Figure 2.6: A plot of the onset of recirculation versus cavity aspect ratio revealing the linear relationship between the two parameters.

is increases first the location of separation and the reattachment expand moves along the base of the cavity until reattaching on the trailing edge wall. Upon reattaching to the trailing edge the separation does not immediately jump to the trailing edge. At this state the morphology of the recirculation maintains its oblong character until the freestream velocity is increased sufficiently to reattach the separation on the trailing edge. The position of the reattachment away from the leading edge cavity wall was measured for cavity aspect ratios 1 and 2. The plot of this behavior is shown in Figure 2.7. The relative stability of the separation is visible in the rate at which the curves in Figure 2.7 reach full separation or 1. The steeper rise indicates that the shorter width of cavity aspect ratio 1 versus 2 makes the separation in this case more stable. Aspect ratio 0.5 was not examined due to the depth of the cavity the separation is stable and always located on the trailing cavity edge wall.

2.4.1.2 Shear layer penetration depth and the affect of freestream Reynolds number

Another affect examined at the microscale, especially predominant at lower Reynold numbers in the range was the apparent diffusion or broadening of the shear layer over wide region relative to the cavity. The recession depth is represented schematically in Figure 2.8 and the data is shown in Figure 2.9. When examined closer it can be seen that in these cases the separation point is actually located at a position along the height of the leading edge wall. Due to the relative simarlity in dimensions between most fluid geometries in the flow the microscale cavity is more resistant to separation due to the presence of the opposing wall. On the other end of the spectrum towards higher Reynolds

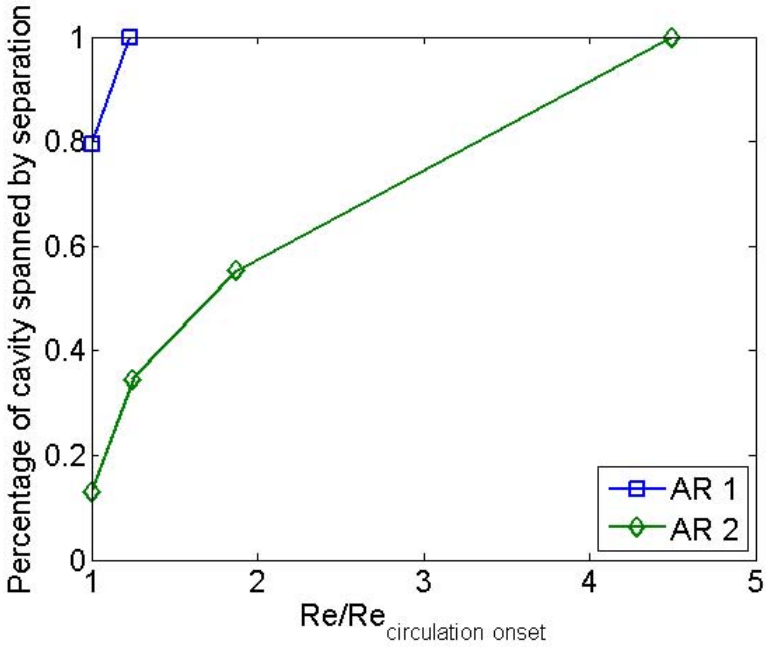

Figure 2.7: Displays the percentage of the cavity spanned by the reattachment for AR = 1 and 2.

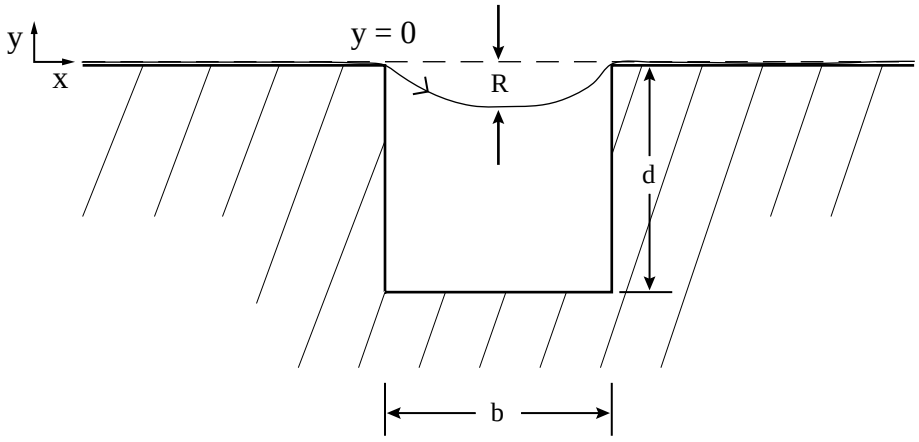

Figure 2.8: A schematic representation of the cavity recession depth, R. The y = 0 line is taken as the top of the cavity.

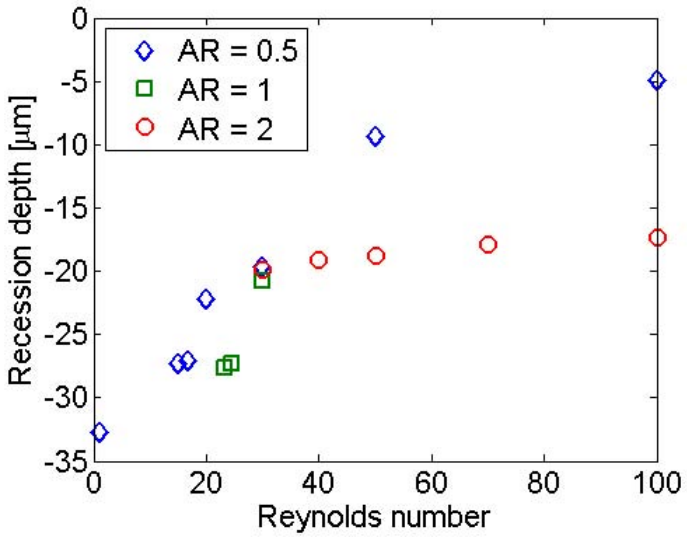

Figure 2.9: The recession depth of the shear layer versus Reynolds number for steady cavity flows.

numbers, we see the affect of fluid entrainment into the shear layer in that much higher Reynolds numbers are required for the higher aspect ratio cavities to minimize the penetration depth to the top of the cavity. For example rise of the aspect ratio 0.5 much more rapidly approaches the cavity top located at 0 μm. Whereas at Re = 100, the maximum Reynolds number examined, the penetration depth in the aspect ratio 0.5 cavity equals 4.9 μm, the penetration depth of the shear layer in the aspect ratio 2 cavity is 17.3 μm.

2.4.1.3 Tangential circulation velocity and freestream Reynolds number

The tangential circulation velocity was examined for the full range of Reynolds numbers and cavity aspect ratios after the onset of recirculation in the cavity in order to attain an estimate for the circulation in the cavity. Since establishing a precise boundary for the recirculation was difficult circulation was not directly measured. Examining the plot shown in Figure 2.10, initially the circulation velocity increases slowly. Towards higher Reynolds numbers in excess of the curve continues to climb in an almost linear fashion. This effect seems representative of the isolation from the freestream velocity provided by the cavity depth and related to the broadness of the shear layer. As the free stream velocity increases the circulation grows in size and moves toward the top of the cavity until it reaches a minimum bounded by the streamlines of the freestream. One of the relationships established by the studies of Shelby et al. was a linear relationship between radial acceleration and rotational frequency of a particle trapped in the cavity circulation to volumetric flow rate. In this study, the completely linear trend is most likely the result of the fact that over the range of Reynolds numbers in their study the circulation is already located at the cavity top and hence responsed linearly to linear increases in freestream flow rate.

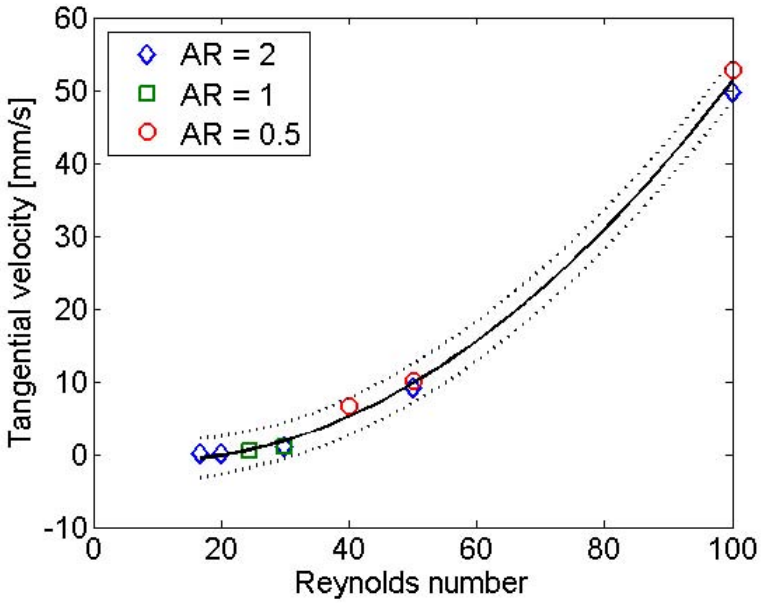

Figure 2.10: A plot of the tangential velocity of the circulation versus Reynolds number. The dashed lines show the 95 % confidence interval for the data.

2.4.1.4 The influence of Reynolds number and geometry on shear stress across the top of the cavity

The affect of increasing Reynolds number showed that the shear across the top of the cavity increases linearly with Reynolds number. The top of the cavity is defined as the y = 0 line represented in Figure 2.8. Plotting the points seems to indicate that independent of aspect ratio all points seem to collapse onto a single line, meaning that shear at the top of the cavity is independent of the cavity aspect ratio as well as the location of the recirculation. Figure 2.11 shows a scatter plot of average shear values across the top for various cavity experiments as well as a linear fit. The dashed lines above and below the linear fit represent a 95% confidence interval, showing fairly good agreement between measurements. Additionally, in light of the tangential velocity data, circulation velocity is not a linear function of the shear stress for Reynolds numbers less than 100. It however remains to be determined whether this relationship becomes linear at Reynolds number in excess of 100.

2.4.1.5 Residence times of steady cavity flows

The average velocity fields were used to compute the average residence times of particles seeded inside the bottom half of the cavity region. Two flow regions are present in the cavity and their relative size affects the number of instances in the distribution as well as varies the number of peaks from 1 to 2. These two regions are represented in Figure 2.12. The first peak represens particles seeded in a region outside or near the boundary of the separation where the streamlines from the

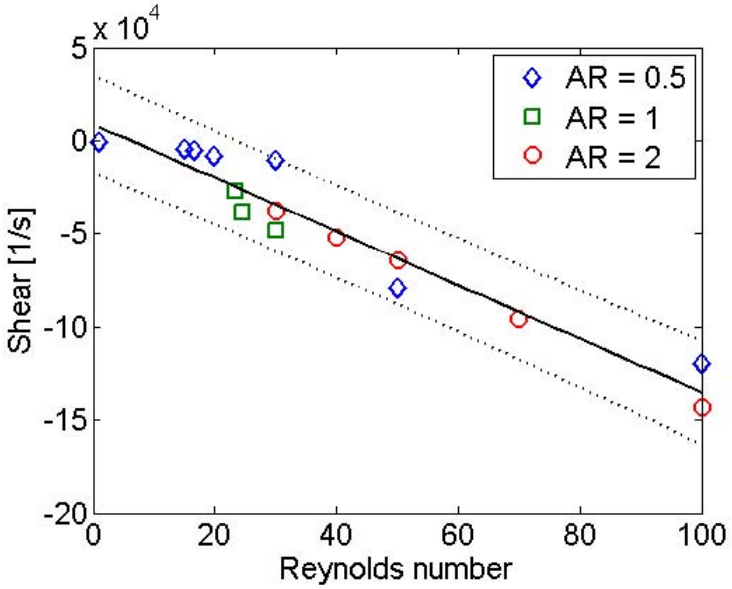

Figure 2.11: A plot of the average shear stress at the top of the cavity versus Reynolds number for cavity AR = 0.5, 1, 2.

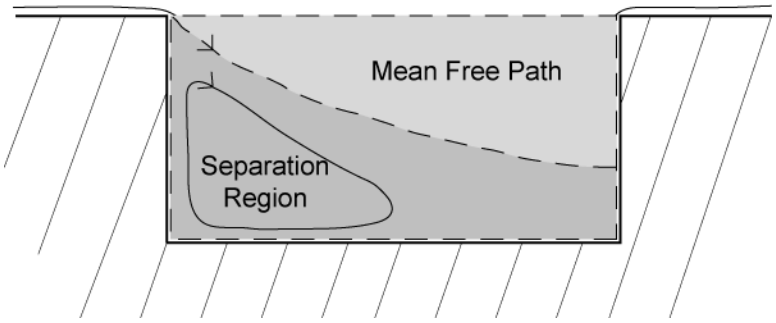

Figure 2.12: A schematic of the two regions representing the individual peaks in the residence time plots. The first peak correlated to particles in the mean free path. The second to particles in the recirculation region.

Aspect Ratio	Freestream Reynolds number					
0.5	1	15	16.7	20	30	100
1	23.3	24.4	30			
2	40	50	75	100		

Table 2.3: Summarizes the residence time calculations performed under steady flow conditions.

freestream enable them to quickly find a path to the main part of the flow, referred to as the mean free path back to the freestream. The second, for particles seeded inside the separation region. Particles here can do one of two things, escape or remain trapped infinitely in the circulation or a region of stagnation near the boundaries of the cavity.

The residence time plots show the affect of the growing size and strength of this circulation region by the appearance of the second peak, a growth in its relative size to the mean time of flight path and lastly by a decrease in the number of instances in the histogram, representing the fraction of particles that were not infinitely trapped inside the separation. These affects are illustrated in Figure 2.13 through Figure 2.14. These regions individually are also representative of the two extremes of the cavity flows. At Reynolds numbers where there is no separation present particles are advected with the streamlines out of the cavity producing a mean time of flight path peak. At very high Reynolds numbers the circulation fills the entire width or height of the cavity depending on its limiting dimension as a result of its aspect ratio, trapping all particles inside. Table 2.4.1.5 summarizes the steady flow conditions for which residence times were calculated.

The residence times were normalized by a timescale assigned by dividing the cavity width by the freestream velocity. When plotted on a log scale versus the freestream Reynolds number the residence time calculations produced the plot in Figure 2.15. Figure 2.15 shows the presence of peak in the normalized residence time right before the onset of recirculation. In this range the fluid goes through a transition. At Reynolds numbers far below the transition the flow the boundary layer of the freestream is able make the corner and adhere the base of the cavity. In this case nearly all the particles escape from the cavity. As the flow accelerates, the velocity gradient from the top to the bottom of the increases meaning residence times change only slightly while the velocity of the freestream increases significantly producing an increase in the normalized residence time. This can be seen in the transition from Re = 1, to Re = 27 in the AR = 0.5 case. These Reynolds numbers are equivalent to flow rates of 1.8 μL/min and 27 μL/min. Here the flow rate increases by a factor of 10 but the residence times only increase by a factor of 2 or so, indicating the growth of a stagnation region. Right before the onset of circulation the normalized residence times reach a maximum before dropping as the circulation begins. Somewhere past this point the residence time reaches a minimum where the circulation is strong enough to introduce particles in the base of the cavity to the freestream flow but not trap them. As the strength of the recirculation increases the result on the residence time has two affects: first the number of particles in the distribution drop significantly

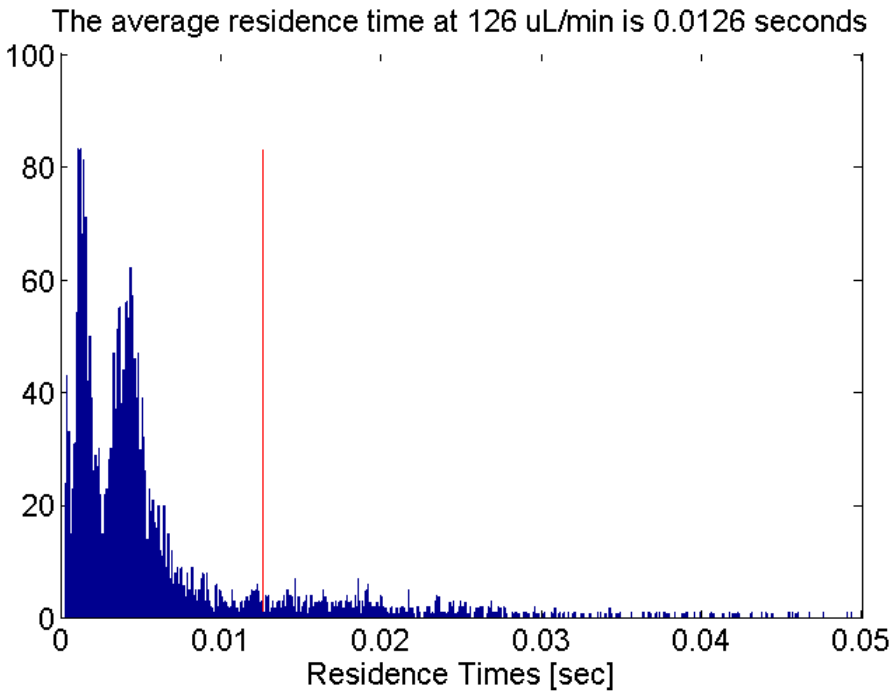

Figure 2.13: The residence time distribution for the AR 2 cavity at 126 μL/min or a Re of 75. The two peaks representing the mean free path and the escape route through the recirulation. The relative size of the peaks represents the relative size of the recirculation region versus the mean free path region. The average residence time in this case is 0.0126 seconds.

representing the fact that very few particles are located in a position where their trajectory presents a path to the freestream, if it does they exit very quickly, and second if the particle does not begin on one of these trajectories the tendency is for particles to be trapped indefinitely in the recirculation. It is difficult to interpret the residence time plot without prior knowledge of the flow occurring in the cavity therefore the residence time distributions are presented in Appendix E. For example, residence time calculations such as at AR = 0.5, Re = 100 produced an infinite residence time and therefore are not represented on the plot. The residence times indicate that in terms of timescale the best cavity ventilation occur at very low Reynolds numbers where no separation is present as well as right past the onset of recirculation where the weak circulation is able to move particles in the base of the cavity on trajectories where they can be entrained by the free stream flow. Since a purely laminar flow has the affect of poor communication between particles in different streamlines it suggests that the second minimum right past the onset of recirculation is best in terms of the mixing and ventilation of the cavity under steady flow conditions.

2.4.1.6 Lagrangian Coherent Structures in steady cavity flows

For the steady flow cases the FTLE fields displayed the presence of the separation, reattachment as well as the trapping region formed by the circulation region. Although Lagrangian Coherent

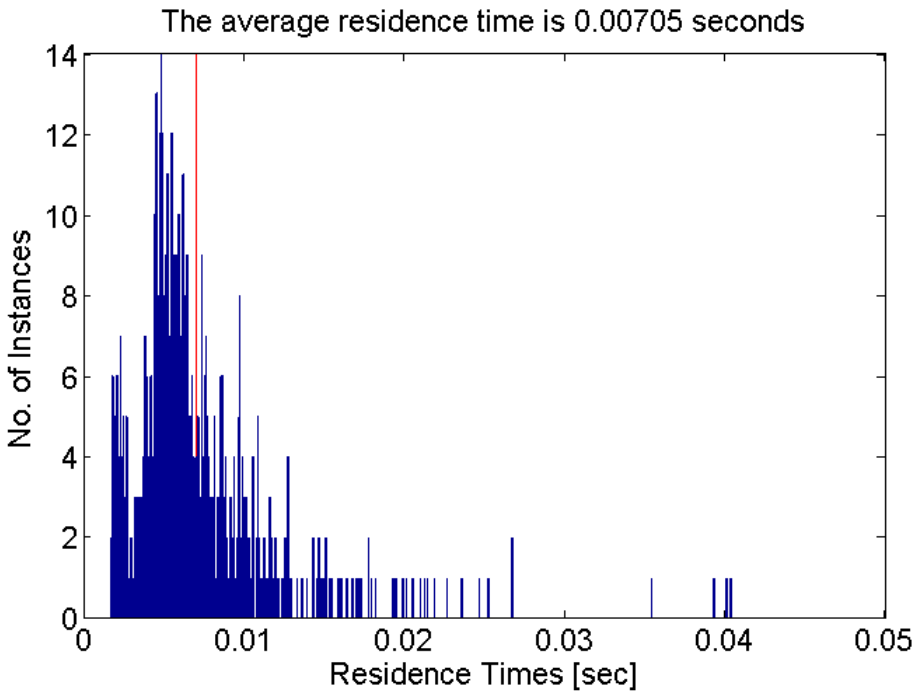

Figure 2.14: The residence time distribution for the AR 2 cavity at 180 μL/min or a Re of 100. The two peaks representing the mean free path and the escape route through the recirulation. The relative size of the peaks represents the relative size of the recirculation region versus the mean free path region. The average residence time in this case is 0.007 seconds.

Structures were applied for the visualization of the flow structures in all steady cases, for the purpose of this discussion the LCS at 180 μL/min or Re = 100 will be examined. At Re = 100 the forward time LCS clearly reveals the reattachment on the trailing edge of the cavity wall as well as an repelling LCS related to a stagnation region in the lower right corner of the cavity. The reattachment is more easily visualized by examining the full FTLE field in Figure E.20. The corresponding backward time FTLE field in Figure E.19 reveals the presence of the separation towards the upper extent of the leading edge wall. The overlay of the backward time and forward time FTLE fields can be viewed in Figure 2.16. The overlay was produced by masking all but the highest values in the FTLE field for both the forward time and backward time calculations. The colormap on the forward time FTLE field was then flipped in order to distinguish between attracting and repelling LCS. In the LCS overlay in Figure 2.16 the backward time LCS are colored pink and the forward time structures are colored to the blue end of the colormap. The overlay allows the visualization of the trapping region formed by the attracting and repelling LCS within the cavity. Also apparent from the overlay is the difficulty particles have in leaving the recirculation region due to the transport boundary formed by repelling LCS surrounding the recirculation region.

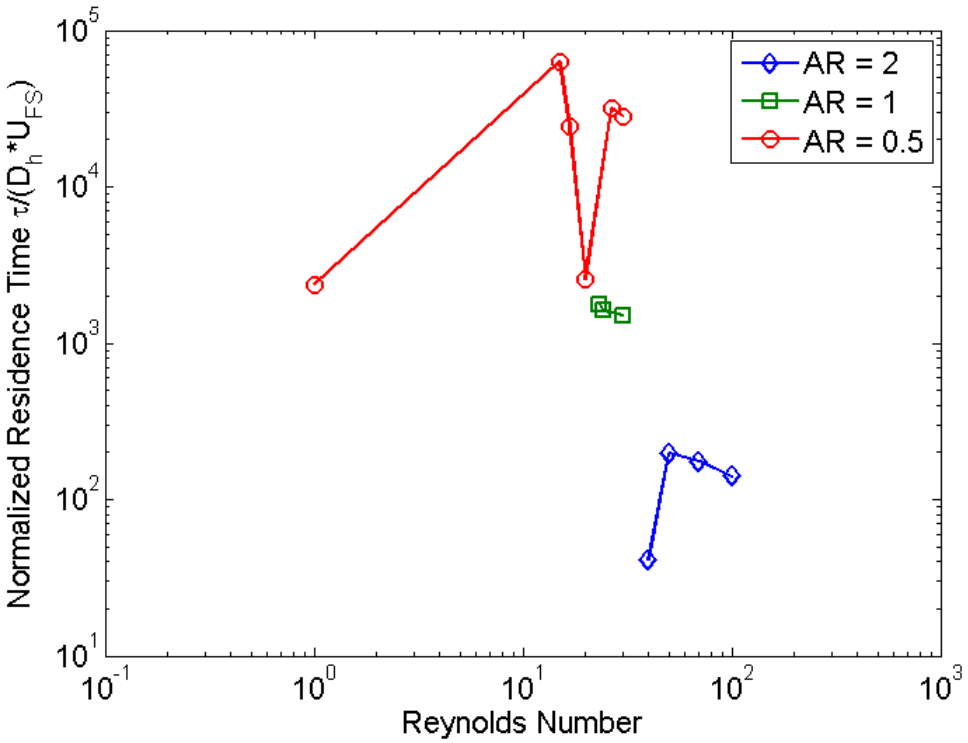

Figure 2.15: A log plot of the normalized residence times versus Reynolds number for cavity AR = 0.5, 1, 2. Residence times are normalized by the cavity with divided by the freestream velocity.

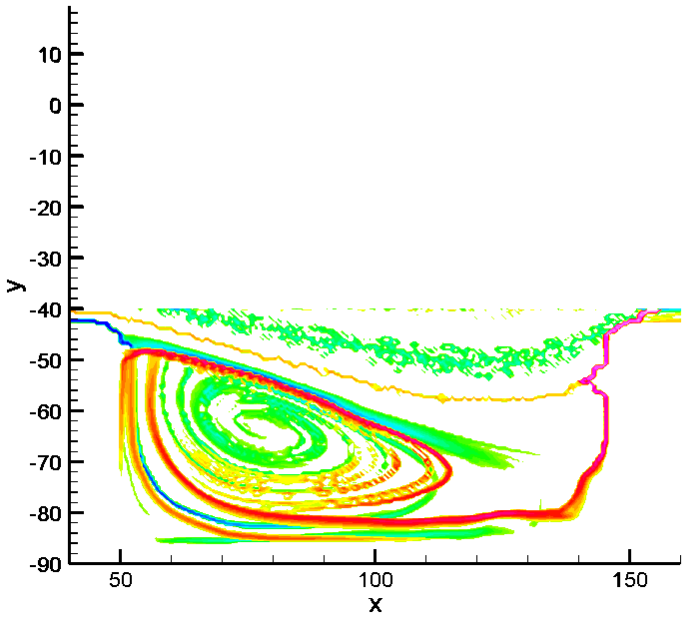

Figure 2.16: Shows the FTLE field at AR = 2 and a flow rate of 180 μL/min.

2.4.1.7 Dimensionality of microscale flows - affect of out-of-plane dimension 30 μm and 100 μm.

One of the benefits of this study is it allows us to comment on the affect limited channel depth and its influence on cavity circulation. Compared to previous microscale cavity studies conducted at 100 μm cavity depth, the transition to circulation occurred much earlier. In this instance we see a reduction from 16.7 to approximately 1 for an out-of-plane depth of 30 μm and 100 μm respectively. These results are further confirmed by the results of Shelby and Chiu where in order to get increased cavity rotational frequency they move from a channel depth of 30 microns to a channel depth of 50 μm. This increase in cyclical frequency is in response to a decrease in length of the out-of-plane boundary layer.

2.4.1.8 Dimensionality of microscale flows - affect of out-of-plane dimension 30 μm and 100 μm.

One of the benefits of this study is it allows us to comment on the affect limited channel depth and its influence on cavity circulation. Compared to previous microscale cavity studies conducted at 100 μm cavity depth, the transition to circulation occurred much earlier. In this instance we see a reduction from 16.7 to approximately 1 for an out-of-plane depth of 30 μm and 100 μm respectively. These results are further confirmed by the results of Shelby and Chiu where in order to get increased cavity rotational frequency they move from a channel depth of 30 microns to a channel depth of 50 μm. This increase in cyclical frequency is in response to a decrease in length of the out-of-plane boundary layer.

2.4.1.9 Shape of z-profile

The objective lens of the microscope due to is thin focal depth allows us to examine the shape of the out-of-plane boundary layer by imaging through the depth of the cavity and the freestream. Cavity flows were imaged for a cavity AR = 1 for flow rates of 1.8 μL/min and 54 μL/min or Re = 1 and 30 respectively. Seven slices of the cavity were imaged to reconstruct the flow. The first velocity profile slice was taken approximately 500 nm off the channel base, another at 1.5 μm off the channel base and the rest in 4 μm increments until 22.5 μm into the cavity depth. The complete z-profile was not acquirable due to the presence of out focus particles limiting the depth that could be images. Figure 2.17 shows the reconstruction of the 2D slices for the entire AR = 1 cavity at Re = 1. The entire cavity at Re = 30 was not plottable due to the large gradient in the velocities from the top of the cavity to the bottom and the limitations of the vector scaling properties of the 3D vectorfield plotter in Matlab. Figure 2.18 shows a reconstruction of the u-velocity profile in the x-z plane. The profile as expected is parabolic, the same as in the x-y plane. The peak velcocity is 2 times the mean

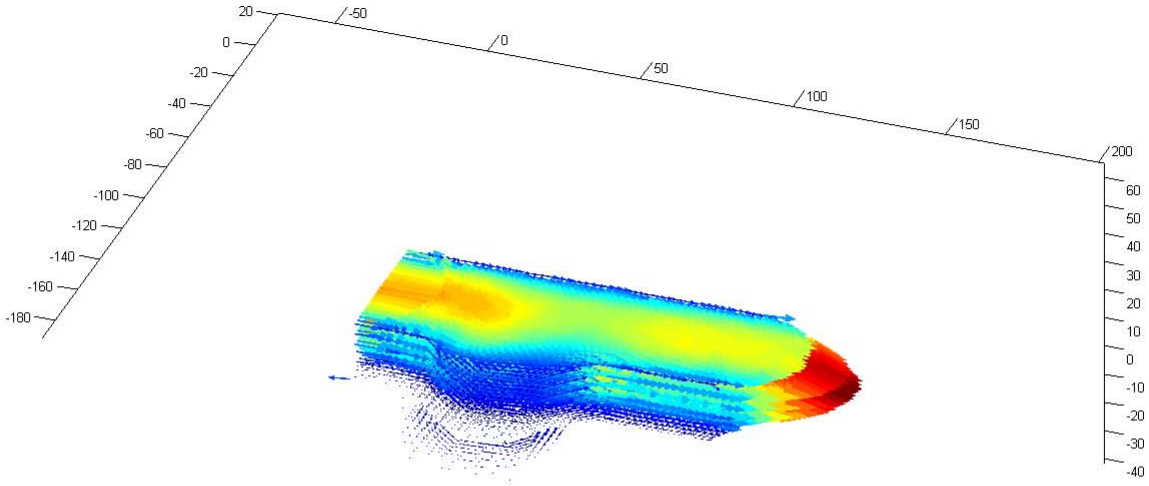

Figure 2.17: A reconstruction of the 3D flow profile of the cavity at 1.8 μL/min or Re= 1.

of 20 mm/s, exactly what is predicted by Pouseille flow.

2.4.2 Enhancing transport through pulsatile flow

Pulsatile flows were examined to determine the affect of unsteadiness on transport out of microscale cavities. For this investigation 4 frequencies, 13 Hz, 64 Hz, 80 Hz, and 113.1 Hz were examined for a mean flow of 1.8 μL/min in the AR = 0.5 cavity. These frequencies correspond to Wo numbers of 0.33, 0.75, 0.84, and 1. Here the Womersley number is defined slightly differently for cavity flows than for channel flows. The modified Womersley number used in this study was defined as,

$$\mathrm{Wo} = \mathrm{D_h}\sqrt{\frac{\omega}{\upsilon}} \tag{2.2}$$

where Dh is the hydraulic diameter of the cavity top, ω is the frequency in rad/s and ν the kinematic viscosity. The affect of amplitudes was also examined at 113.1 Hz at two voice displacements 0.4 mm and 0.2 mm corresponding to flow peak to peak amplitudes of 80 mm/s and roughly 5 mm/s respectively. It is readily obvious that is ratio is not equivalent indicating that the response is not linear. The reason for this is the experiments were started at 0.4 mm, which provided 80 mm/s peak to peak amplitude. The assumption prior to what is indicated by the data was that this response should proceed linearly given the incompressibility of the fluid. The peak to peak amplitude did not remain constant in the case of the pulsatile cases at 0.4 mm amplitude either. Possibly this affect

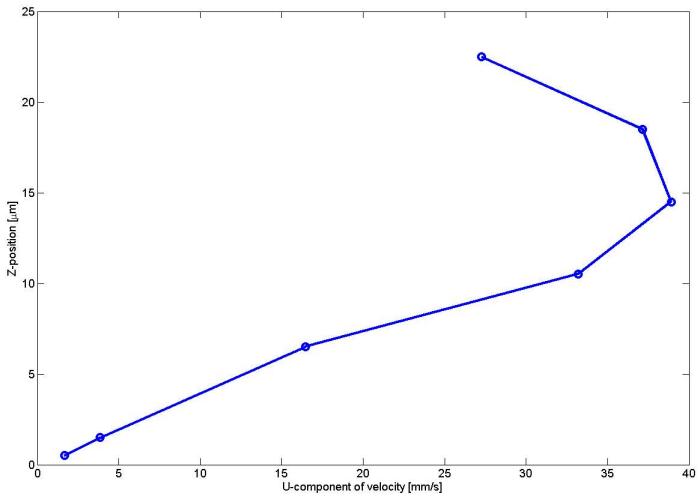

Figure 2.18: A plot of the z-profile in the cavity freestream at 1.8 μL/min or Re = 1. The peak u-velocity is roughly twice the mean of 20 mm/s, as predicted by Pouseille flow.

was due to some phase lag in the response of the tube to high frequency excitation in addition to the fact that there are most likely unknown system dynamics associated with the transfer of that pulsation to the cavity flow area through the many couplings required to connect to cavity flow channel.

Reconstructing velocity fields for the pulsatile cases was particularly difficult for any particular phase increment because the unusually high velocity gradient in microscale cavities was only accentuated by the presence of the oscillatory component. Additionally at specific frequencies, 13 Hz for example a significant phase lag was observed between flow in the cavity and flow in the freestream creating a shearing motion. Velocity fields were helpful in examining the pulsatile flow velocity profile in time for the flow approaching in the freestream however due to the large variation in flow velocities were difficult to scale onto a viewable plot within the cavity. To visualize time periodic flow in the cavity streamlines were calculated. These streamlines revealed the presence of circulations among other flow features at different increments of phase within the cavity which did not exist under steady conditions. Figure 2.19 shows two timesteps of the streamline images sequence at 80 Hz.

2.4.2.1 Influence of Wo and amplitude on pulsatile transport with Re = 1

The influence of pulsatile flow frequency was examined through the variation of the Wormersley numbers over a range of 0 to 1. At very low Reynolds numbers in the limit of stokes flow the input of an oscillatory component should superimpose linearly over the mean flow and the flow should remain reversible at all times. Therefore in this regime quantities such as residence times should

remain unaffected by the input of pulsation. However since the flows examined are not Stokes flows there is an inherent irreversibility which should be affected by the input of unsteadiness and hence the mixing properties of cavity ventilation. Examining the velocity fields for the pulsatile flow cases it is easy to see the oscillatory flow imposed on top of the mean flow provided by the syringe pump. A summary of these velocity fields can be found in Appendix F. Additionally since Wo are in the range of 0 to 1 the velocity profile remains roughly parabolic through all phase increments are predicted for pulsatile flow in a rigid system. The time averaged peak velocities as well as velocity profiles throughout two periods are also found in the Appendix F for all pulsatile flow cases.

2.4.2.2 Time averaged shear stress versus Wo

Time averaged shear was examined for the four frequency conditions spanning Womersley numbers as well as both amplitudes. Time averaged shear in the pulsatile cases was defined the same as the shear for the steady case except averages were taken along the top of the cavity for all phase increments. These spatial averages were then averaged in time to obtain the values plotted in Figure 2.20. Figure 2.20 show the time averaged shear for Womersley numbers of 0, 0.34, 0.84 and 1 as well as 1 under the reduced amplitude conditions. Although the amplitude did not remain constant throughout the range of frequencies the peak in shear does not correspond to the peak in flow amplitude. In all cases the affect of pulsation was to increase the time averaged shear experienced by the cavity. The mean flow in all cases was measured to be 30 mm/s +/- 1 mm/s. Suggesting that the data was not imaged in the direct center of the flow channel. The increase in time averaged shear was only 30 % relative to normal mean shear in the cavity under steady flow conditions at Re = 1. The uncertainty of the shear measurements is estimated to be on the order of 5%. The peak flow amplitude versus frequency decreases whereas the plot in Figure 2.20 suggests there is a peak within Wo 0 to 1. Fitting the data with a cubic spline we find an approximate Wo of 0.7 as the location of the peak as well as point to the existence of a resonant peak for time averaged shear across the top of the cavity under pulsatile flow conditions. As the Wo passes over the peak the shear begins to decrease, contrary to intuition, demonstrating that frequencies may exist in which time averaged shear at the top of the cavity could be equal to or less than the shear in steady flow conditions. The influence of amplitude on time averaged shear in the pulsatile cases was explored by examining two amplitudes corresponding to peak to peak of 80 mm/s and 5 mm/s. Although these peak to peak amplitudes differ by a factor of 16 and with 80 mm/s amplitude the flow reverses whereas at 5 mm/s peak to peak flow amplitude it does not the time averages shear stress values at the top of the cavity differ only by 5%.

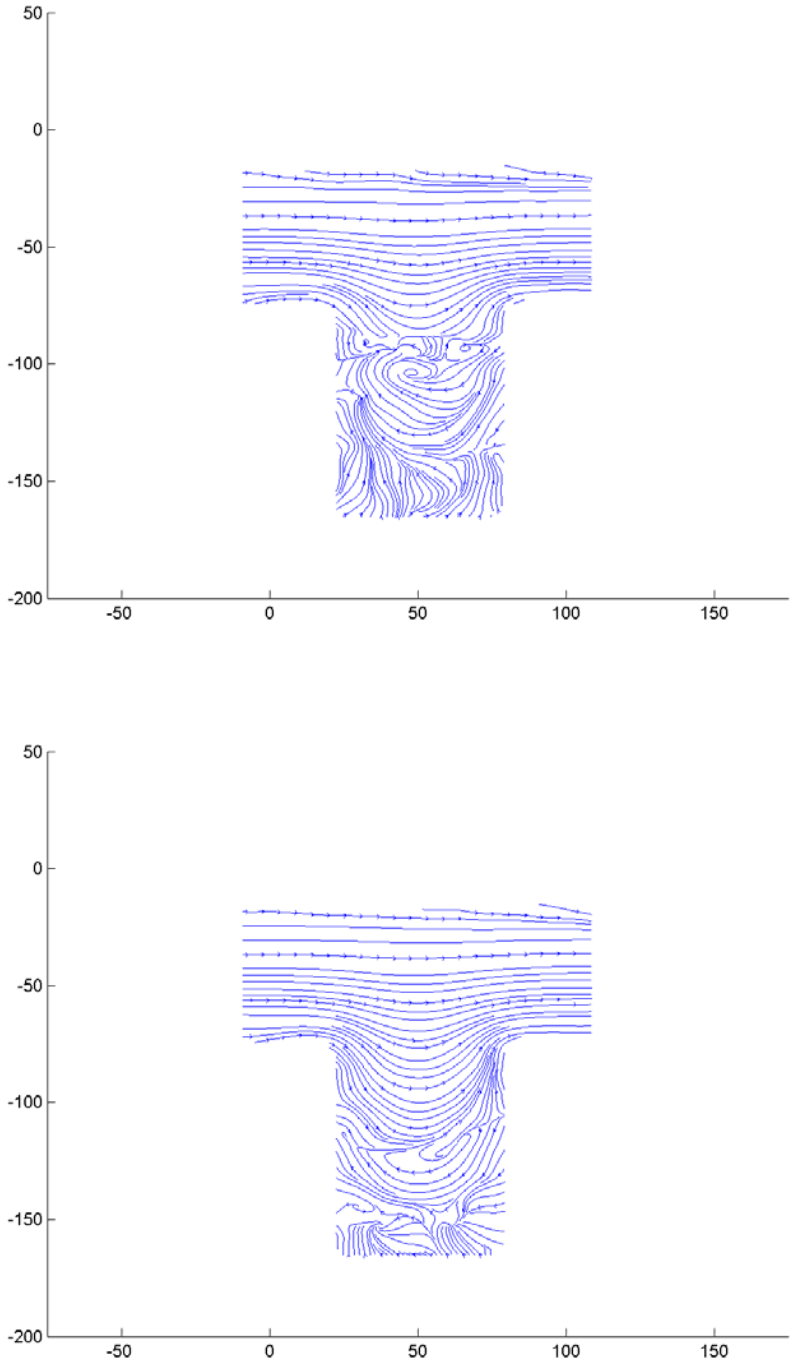

Figure 2.19: Two streamline images at phase time steps t = 0.00 seconds and t = 0.00125 seconds. These frames show the dynamic nature of the streamlines throughout time in the cavity.

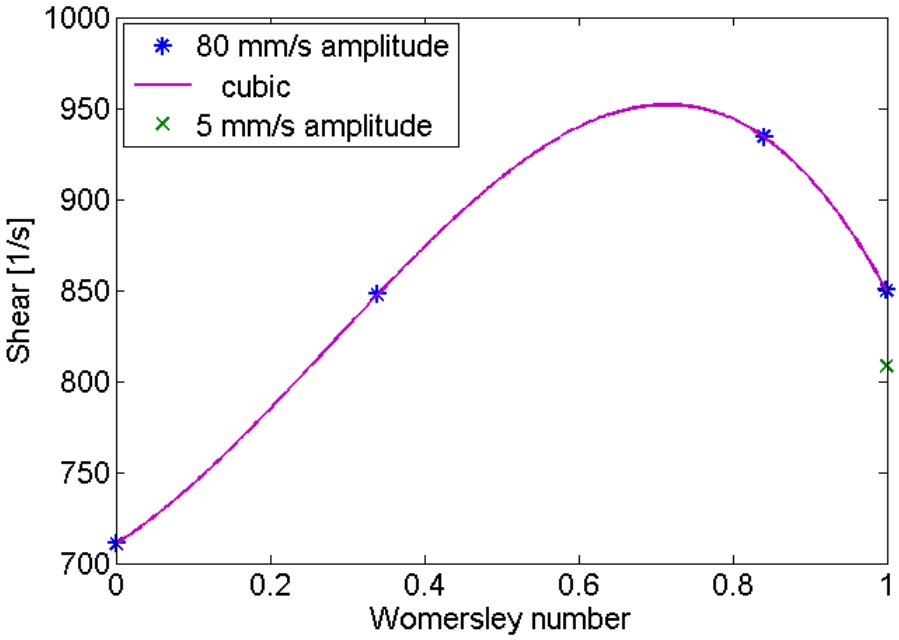

Figure 2.20: A plot of the pulsatile time averaged shear versus Womersley number for Wo = 0, 0.34, 0.84 and 1 for amplitudes of 0.4mm and 0.2 mm with respect to the voice coil probe displacement.

2.4.2.3 Residence times under pulsatile conditions

Residence time calculations were also performed for the pulsatile flow cases. In these cases the motion of the particles was largely dominated by the oscillatory component due to its relative size to the mean component locally inside of the cavity. The plot in Figure 2.21 shows the data points from the both the 0.4 mm amplitude and 0.2 mm amplitude trials. A rough cubic fit to the residence time calculation data also suggested the presence of a peak around Wo = 0.7 similar to the peak found in the average shear plot. Residence times were not normalized in this case due to the fact that the mean shear was approximately equal in all cases. The persistence of this apparent peak in two completely independent calculations suggests it is a real affect experienced by flow within the cavity opposed to just a strict increase in the residence time of particles versus the steady case as would be expected if for all times particles remained on the same streamlines. The affect of amplitude on the residence times of particles in the cavity was examined at a frequency of 113.14 Hz. Strangely but similar to the time averaged shear stress the amplitude had little to no distinguishable affect on the residence times and actually increased slightly.

2.4.2.4 Lagrangian coherent structures in pulsatile cavity flows

The FTLE fields for the pulsatile flow cases were able to define rough boundaries for the visualization of the fluid exchange occurring periodically through time within the cavity. Similar to the steady

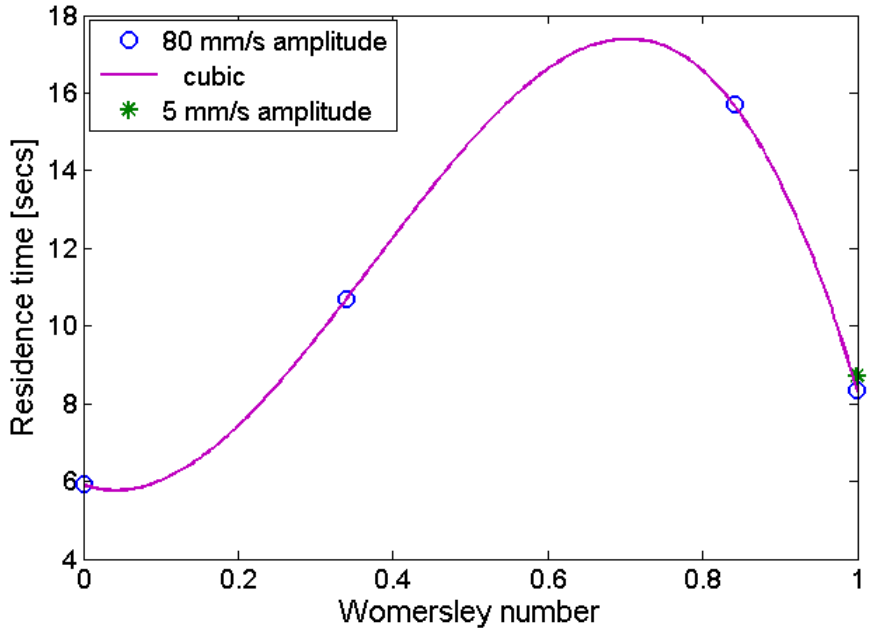

Figure 2.21: A plot of pulsatile residence times for different Wo numbers at amplitudes of 0.2 mm and 0.4 mm. The data suggests the possibility of a frequency dependent peak for the residence times of particles in the cavity. A spline fit to the data locates this peak at a Wo of approximately 0.7.

FTLE fields in portions of the phase where there is a large unidirectional flow the FTLE fields reveal LCS at the separation and reattachment at the top of the cavity for the backward time and forward time calculations respectively. At other increments within each period interesting flow structures were revealed that exist on millisecond timescales. Since the complete time series of FTLE fields is approximately 100 frames in length a few example overlays processed the same as was described for the steady case will be discussed. Also posing a difficulty was the large velocity gradient from the top of the cavity to the bottom making picking one integration time which clearly resolved structures into the lower reaches of the cavity but short enough to prevent particles near the top of the cavity from leaving the boundary. Figure 2.22 depicts the overlay of the forward time and backward time LCS at a frequency of 80 Hz. At t = 0.000375 sec the attracting or backward time LCS creates an attracting tentacle like structure which sweeps upward over the next 125 μsec. In the frame on the top of Figure 2.22, this tentacle along with the backward time LCS emerging from the trailing edge of the cavity enclose a packet of fluid which is squeezed between these two LCS structures during the next time step, shown in Figure 2.22 on the bottom. This tentacle also entrains particles from the base of the cavity promoting the expulsion of particles into the freestream. This behavior can be seen in the particle images in Figure 2.23. Notice how the influence of the pulsatililty is to distribute particles more evenly throughout the freestream depicted in part a) and b) in Figure 2.23. The entire motion of the LCS throughout the period is difficult to describe with only a few

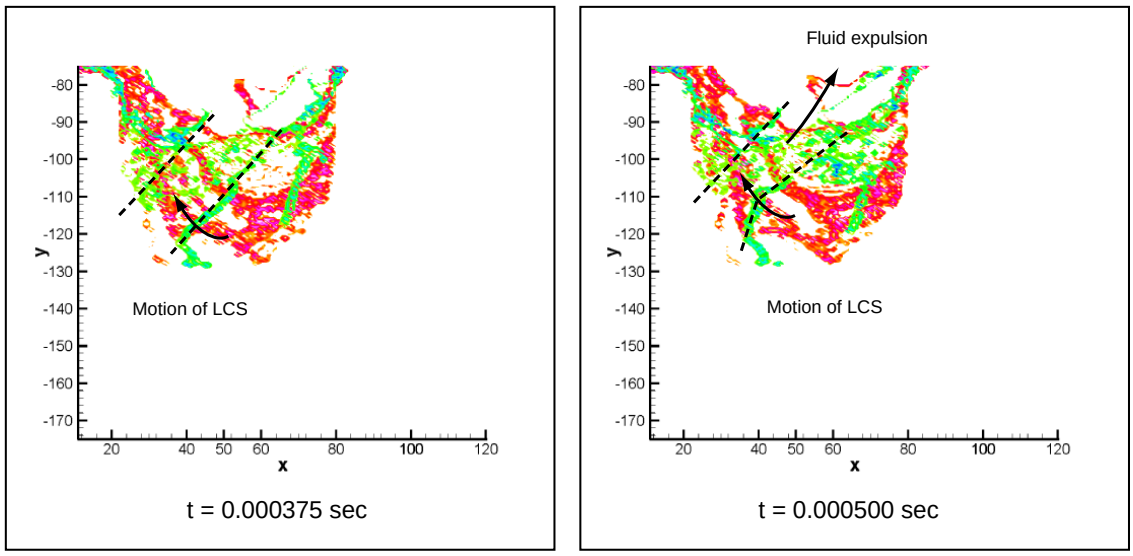

Figure 2.22: The forward and backward time LCS overlaid at two different time steps. On the left t = 0.000375 sec and on the right t = 0.000500 sec at 80 Hz.

frames, however these types of interactions between structures present within the cavity occur over multiples time steps in multiple phase increments throughout any given period and are prevalent in all pulsatile cases examined, 13 Hz, 80 Hz, and 113.14 Hz. Although far from identical to the 113.14 Hz large amplitude case with only 5 mm/s of pulsation amplitude the affect generally is to decrease the length to which tentacle like structures penetrate into the cavity and decrease the sharpness of the FTLE ridges and hence the LCS.

2.5 Conclusion

Microscale cavity flows were examined over a wide range of parameters for both steady and pulsatile flows. Transport was examined using both residence time calculations and Lagrangian Coherent Structures to reveal boundaries to transport within the flow. For steady cases the affects of cavity aspect ratio and mean freestream flow rate were examined for AR = 0.5, 1, 2 and mean freestream flow rates from 0.18 μL/min to 180 μL/min, equivalent to a Re range of 0.1 to 100. Pulsatile flows were examined at a mean freestream Re = 1 for a range for frequencies from DC to 113.14 Hz, equivalent to a Wo spanning 0 to 1.

1. Steady flow studies showed the stability of the separation in smaller aspect ratio cavities.

2. This stability was also represented in the penetration depth study where the the effective destablization of the separation by fluid entrainment is increased at higher aspect ratios meaning that higher Reynolds numbers are required for higher aspect ratio cavities to resist reat-

tachment to the cavity base as well as to minimize the penetration depth.

3. Time averaged shear stress in steady flow at the top of the cavity increases linearly with freestream Reynolds number.

4. In the steady cases ventilation into and out of the cavity reached a maximum slightly after the onset of recirculation pointing to a narrow region where the presence of a recirculation aids in the washout of particles from the cavity.

5. Contrary to the time averaged shear results in the steady case, pulsatile results of time averaged shear revealed a resonance for cavities under pulsatile flow forcing.

6. The residence time calculations in the pulsatile cases displayed a similar resonant peak pointing to some correlation between time averaged cavity shear and the inhibition of transport into or out of the cavity. The presence of this peak also points to the fact that there are frequencies which will have little or even a possibly negative affect on transport.

7. LCS calculations performed on the pulsatile flow studies revealed the presence of time periodic boundries emanating from the freestream and extending into the cavity depth. Their back and forth action periodically in time provides a qualitative mechanism for the expulsion of particles from the cavity and their distribution throughout the freestream.

This study show the affect of pulsation in microscale cavity flows can be both beneficial and detrimental to transport into and out of the cavity. Further investigation is desired to fully quantify the extent of mixing within the cavity under pulsatile flow conditions in particular emphasizing the affect of pulsation amplitude.

Microscale cavity flows are relevant to many flows on the microscale ranging from microfabrication to biofluid flows in grafts and stents. Here it has been demonstrated that a simple parameter such as the frequency of the flow can have a profound influence on the transport in microscale voids and cavities and in many cases the fluid mechanics of this relationship may determine the efficacy of the device in the case of a graft or stent or the throughput in the case of microfluidics. Although more detail is necessary before the parameter space is completely understood this work serves to illustrate some of the basic modes transport and serve as a starting point for understanding how pulsatile flows can be used to provide enhanced performance for applications such as thermal management, or sorting and filtration at the microscale.

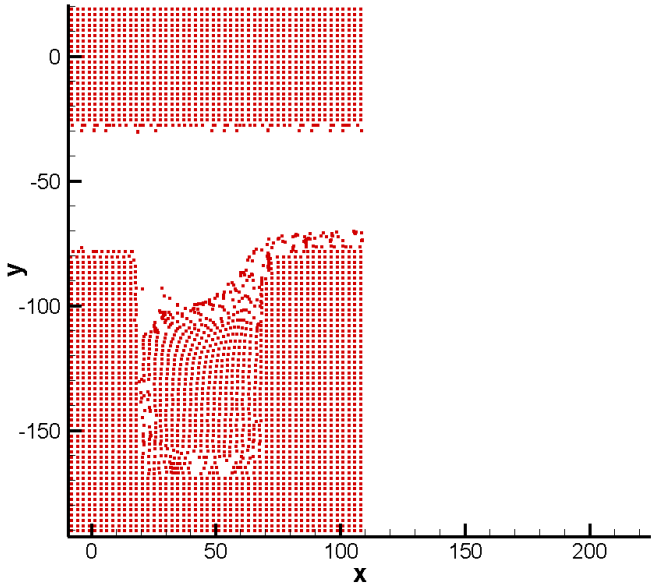

(a) A

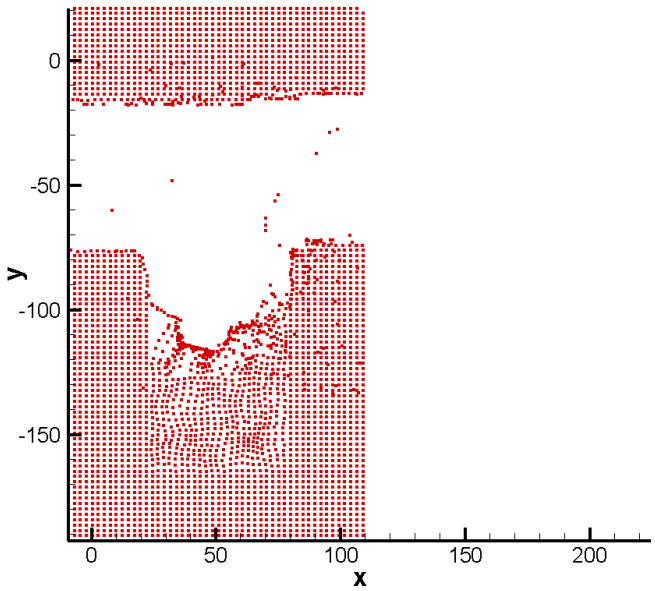

(b) B

Figure 2.23: The behavior of the ventilation process under a) steady and b) pulsatile conditions at 80 Hz. Note the tendency of particles remain near the wall in the steady case.

Appendix A

Summary of characterization system metrics

Parameter		Value	Units
System Bandwidth	**Characterization System**	150	**Hz**
Force	**Dynamic Range**	10	**N**
Displacement	**Resolution of LVDT**	5.8	**μm**
	Dynamic Range of LVDT	$\pm$ 3.2	**mm**
	Dynamic Range of Minishaker 4810	$\pm$ 3	**mm**
	Bandwidth of LVDT	500	**Hz**
	Dynamic Range/Displacement Resolution Ratio	1103	
Flow Rate	**Resolution of Flow Rate**	$\pm$ 0.02	**mL/min**
	Dynamic Range of Flow Rate	$\pm$ 200	**mL/min**
	Bandwidth of Flow Rate	150	**Hz**
	Dynamic Range/Flow Resolution Ratio	10000	
Differential Pressure	**Resolution of Pressure Sensor**	0.25	**%FS**
	Dynamic Range of Pressure Sensor	$\pm$ 5	**psi**
	Response Time of Pressure Sensor	1	**msec**
	Dynamic Range/Pressure Resolution Ratio	400	

Table A.1: Summary of the impedance pump characterization system metrics.

Appendix B

Design of the voltage to current amplifier to drive inductive micro-actuators

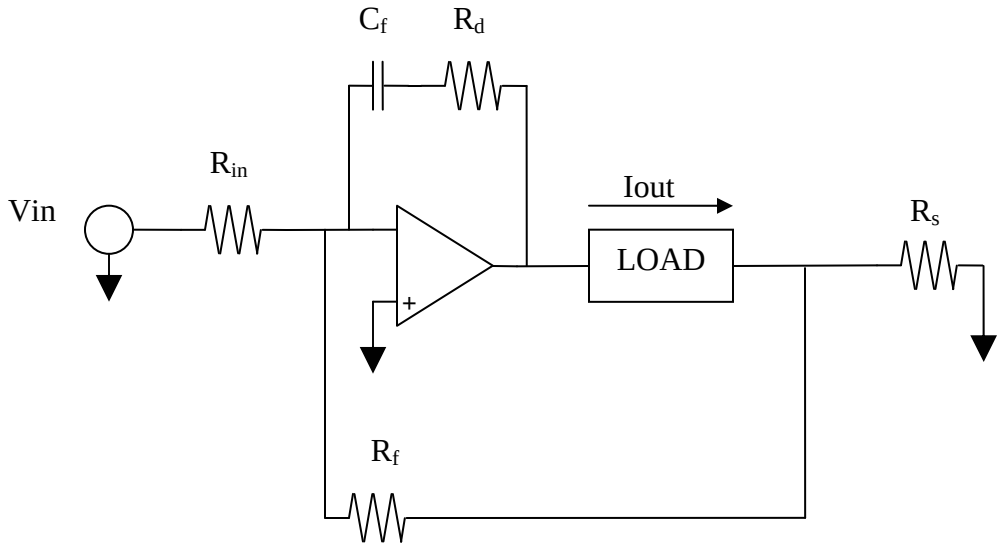

Figure B.1: A schematic of thevoltage to current amplifier used to drive the voice coil in the characterization system and inductive micro-actuators.

The voltage to current amplifier was designed to have a gain of 0.4 A/V and a bandwidth of DC to 10 kHz. The output of the amplifier is given by the following equation:

$$I_o = \frac{-R_f}{R_s R_{in}} V_{in} \tag{B.1}$$

Appendix C

Impedance pump characterization system dynamic response and control system

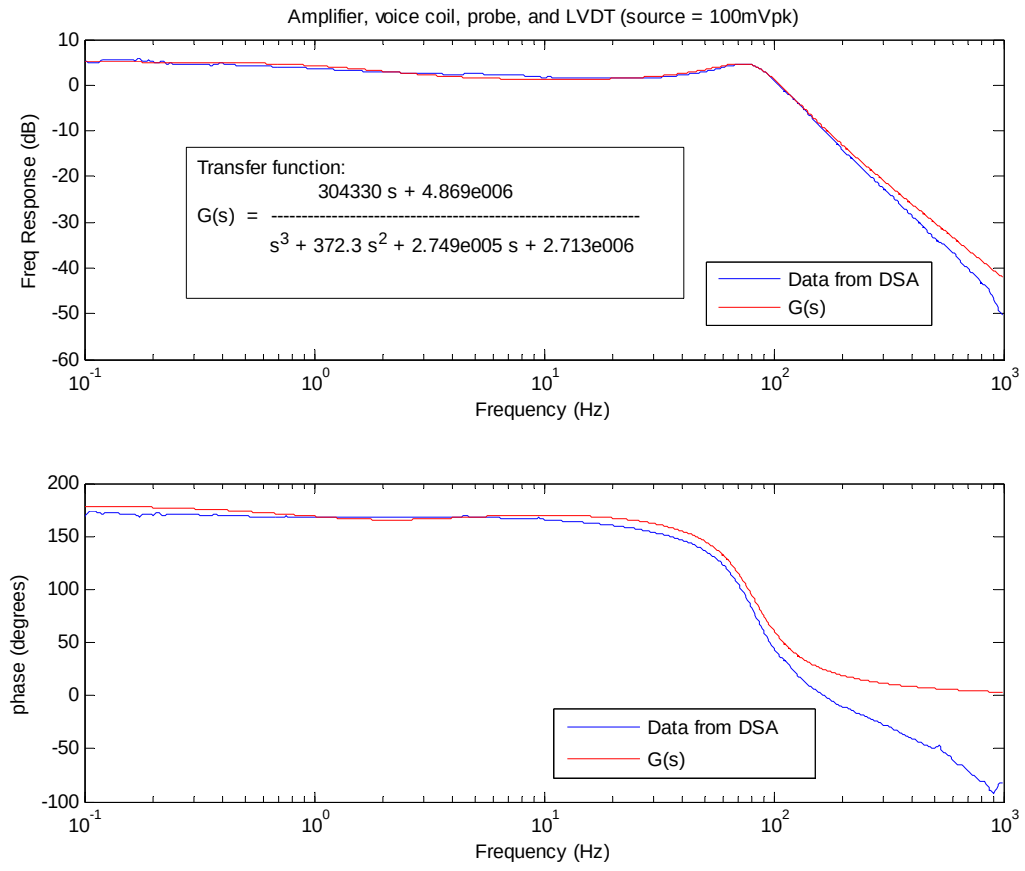

Figure C.1: The frequency response of the amplifier, voice-coil probe and LVDT system.

Appendix D

Derivation of the Finite Time Lyapunov Exponent

Consider an arbitrary fluid particle $x(t)$ in a given domain $\in X$ at time t. Let Φ_t^{t+T} define a function which maps a particle at time $x(t)$ to time $x(t+T)$. Given that fluid is a continuum and behaves according to conservation of mass and conservation of momentum particles near $x(t)$ will behave similarly in time.

Consider the location $y(t)$ on the opposite side of a divergent manifold where:

$$y(t) - x(t) = \delta x(t) \tag{D.1}$$

Where $\delta x(t)$ is an infinitismal distance in an arbitrary orientation. After some time period T the particle has moved a distance of

$$\delta x(t+T) = y(t+T) - x(t+T) = \Phi_t^{t+T}(y) - \Phi_t^{t+T}(x) \tag{D.2}$$

Performing a Taylor expansion about x:

$$\delta x(t+T) = \Phi_x^{t+T} + \frac{d\Phi_x^{t+T}}{dx}(y(t) - x(t)) + ...O\left\|\delta x(t+T)\right\|^2 - \Phi_t^{t+T}(x) \tag{D.3}$$

$$\delta x(t+T) = \frac{d\Phi_x^{t+T}}{dx}\delta x(t) \tag{D.4}$$

$$\left\|\delta x(t+T)\right\| = \sqrt{\left\langle \frac{d\Phi_x^{t+T}}{dx}\delta x(t), \frac{d\Phi_x^{t+T}}{dx}\delta x(t) \right\rangle} \tag{D.5}$$

$$\left\|\delta x(t+T)\right\| = \sqrt{\left\langle \delta x(t), \frac{d\Phi_x^{t+T}}{dx}^* \frac{d\Phi_x^{t+T}}{dx}\delta x(t) \right\rangle} \tag{D.6}$$

Now we define the symmetric matrix ϵ given by:

$$\epsilon = \frac{d\Phi_x^{t+T}}{dx}^* \frac{d\Phi_x^{t+T}}{dx} \tag{D.7}$$

Since we are investigating stretching, we notice $\delta x(t)$ is maximum when aligned with the eigenvector associated with the maximum eigenvalue of ϵ.

If $\lambda_{max}(\epsilon)$ is the maximum eigenvalue of ϵ then:

$$\max_{\delta x(t)} \|\delta x(t+T)\| = \sqrt{\left\langle \overline{\delta x(t)}, \lambda_{max}(\epsilon)\overline{\delta x(t)} \right\rangle} \tag{D.8}$$

$$\max_{\delta x(t)} \|\delta x(t+T)\| = \sqrt{\overline{\delta x(t)}^2 \lambda_{max}(\epsilon)} \tag{D.9}$$

$$\max_{\delta x(t)} \|\delta x(t+T)\| = \left\| \overline{\delta x(t)} \right\| \sqrt{\lambda_{max}(\epsilon)} \tag{D.10}$$

Now define the finite time Lyapunov exponent (FTLE) at location x at time t with integration time T as:

$$\sigma_t^T(x) \equiv \frac{1}{|T|} \ln \sqrt{\lambda_{max}(\epsilon)} \tag{D.11}$$

Therefore the factor by which the flow is maximally stretched is given by:

$$e^{\sigma_t^T(x)|T|} = \sqrt{\lambda_{max}(\epsilon)} \tag{D.12}$$

Substituting equation (D.12) into (D.11) yields:

$$\max_{\delta x(t)} \|\delta x(t+T)\| = \left\| \overline{\delta x(t)} \right\| e^{\sigma_t^T(x)|T|} \tag{D.13}$$

Appendix E

Supplementary data for Chapter 2 - Steady cavity flow

E.1 Data for the AR = 2 cavity

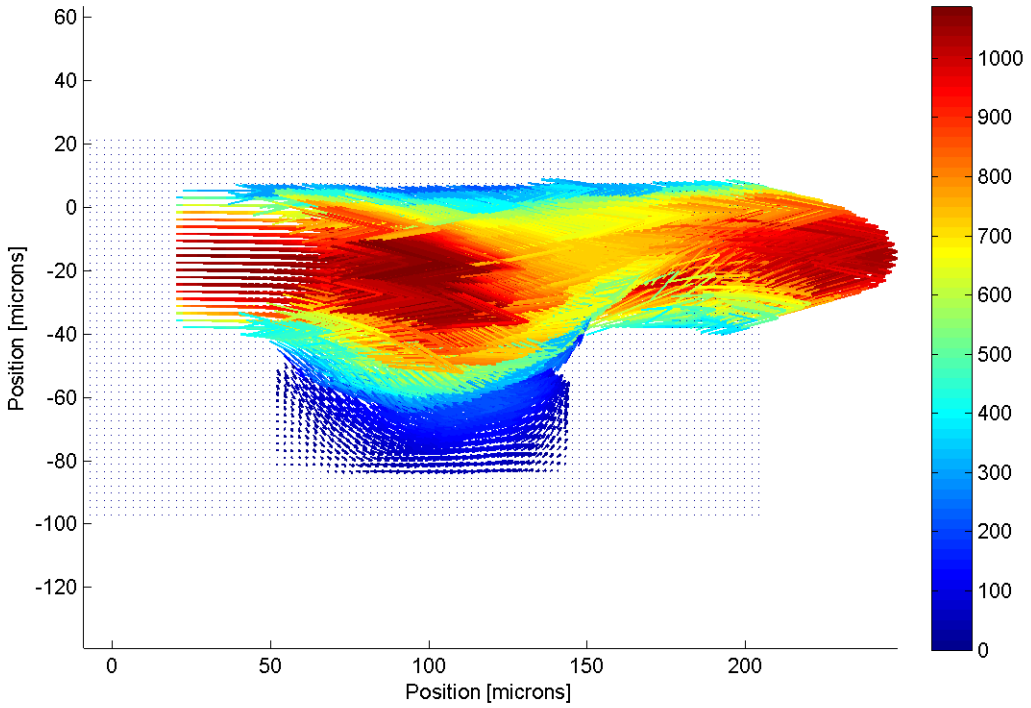

Figure E.1: Velocity field in the AR 2 cavity at Re 30.

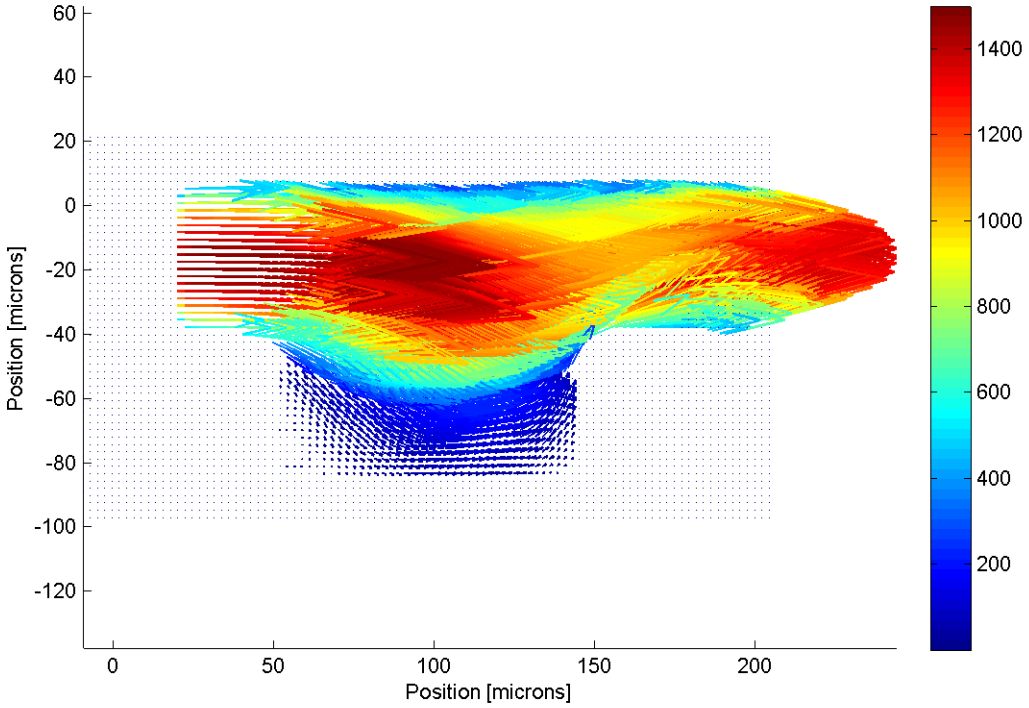

Figure E.2: Velocity field in the AR 2 cavity at Re 40.

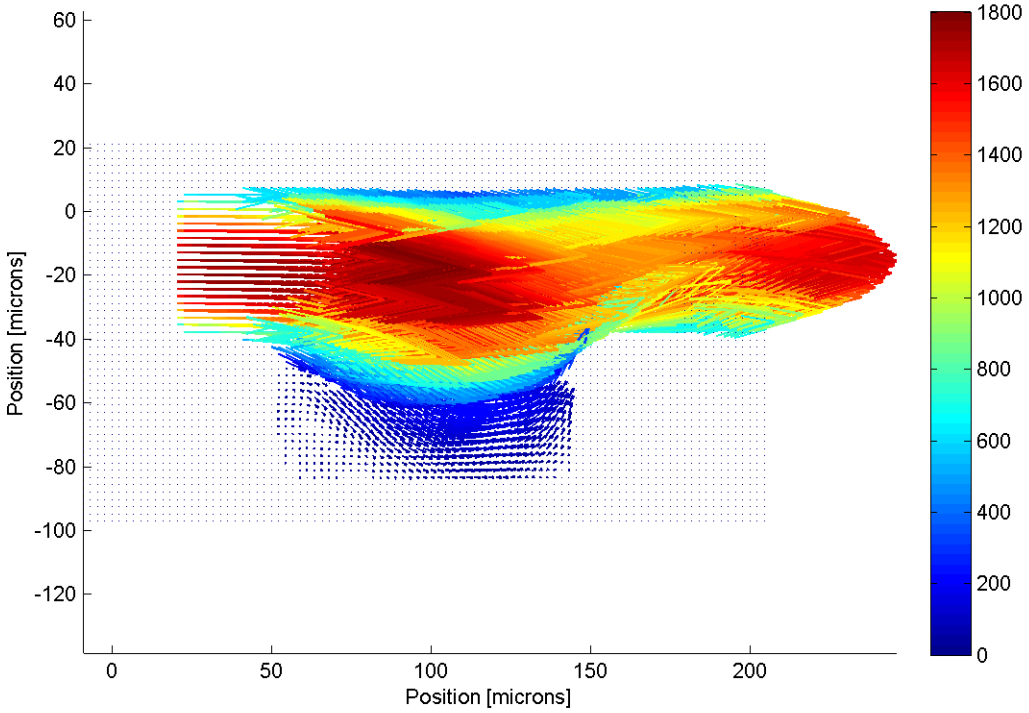

Figure E.3: Velocity field in the AR 2 cavity at Re 50.

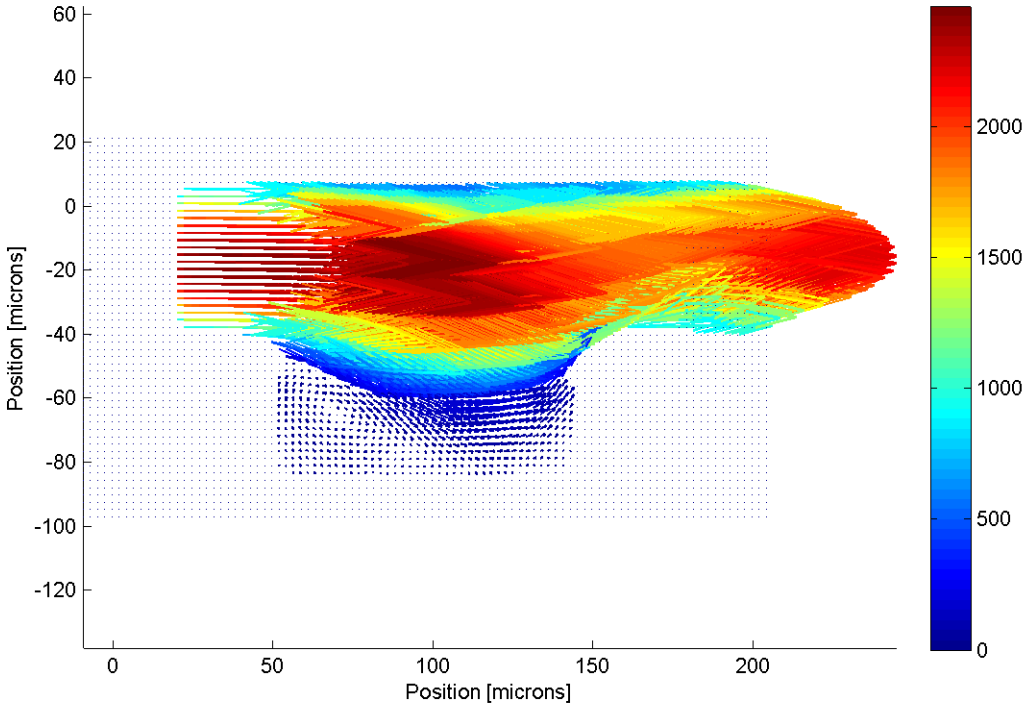

Figure E.4: Velocity field in the AR 2 cavity at Re 75.

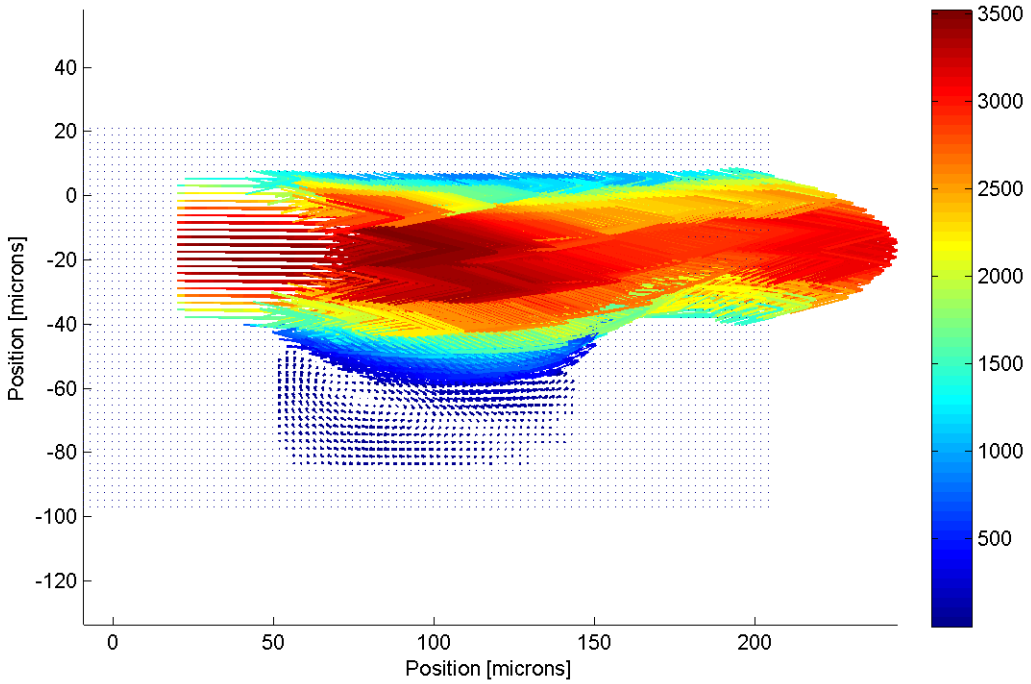

Figure E.5: Velocity field in the AR 2 cavity at Re 100.

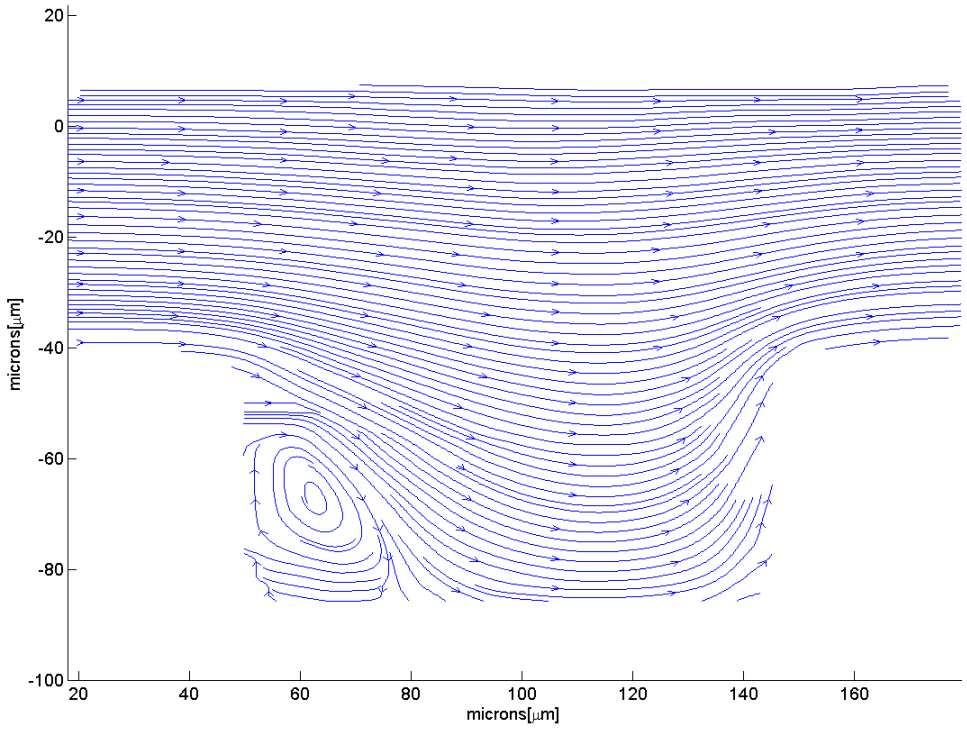

Figure E.6: A streamline plot of steady flow in the AR = 2 cavity at Re 50.

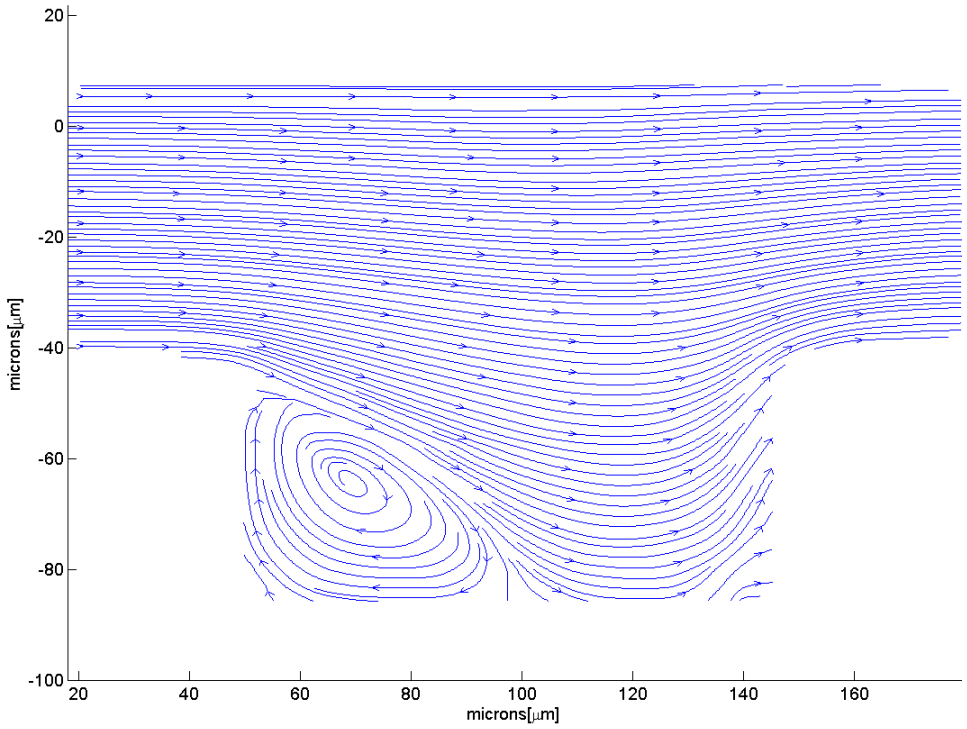

Figure E.7: A streamline plot of steady flow in the AR = 2 cavity at Re 75.

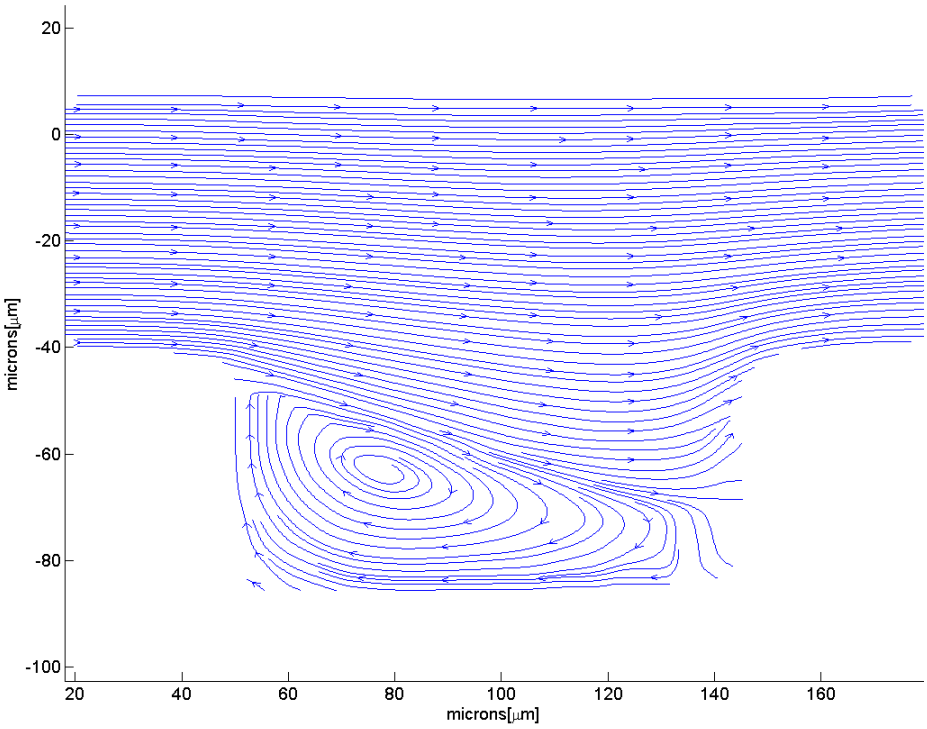

Figure E.8: A streamline plot of steady flow in the AR = 2 cavity at Re 100.

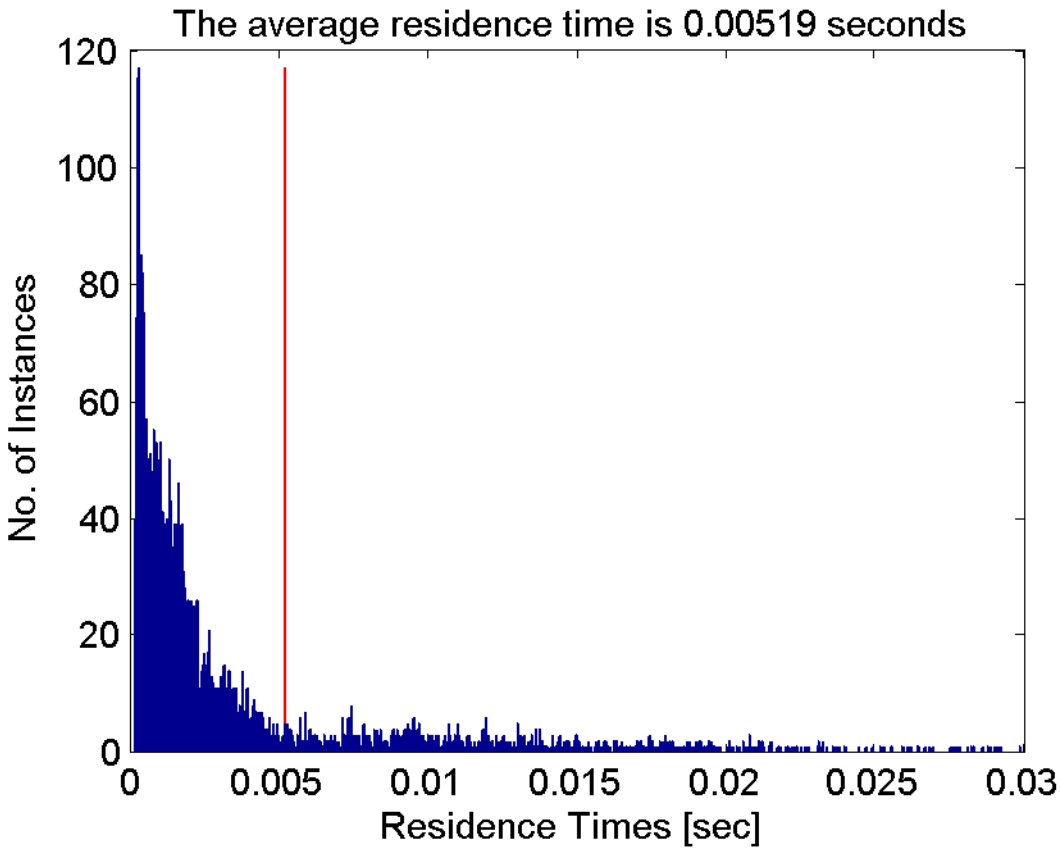

Figure E.9: The residence time distribution for the AR = 2 cavity at Re 40. The average residence time is 0.0052 secs.

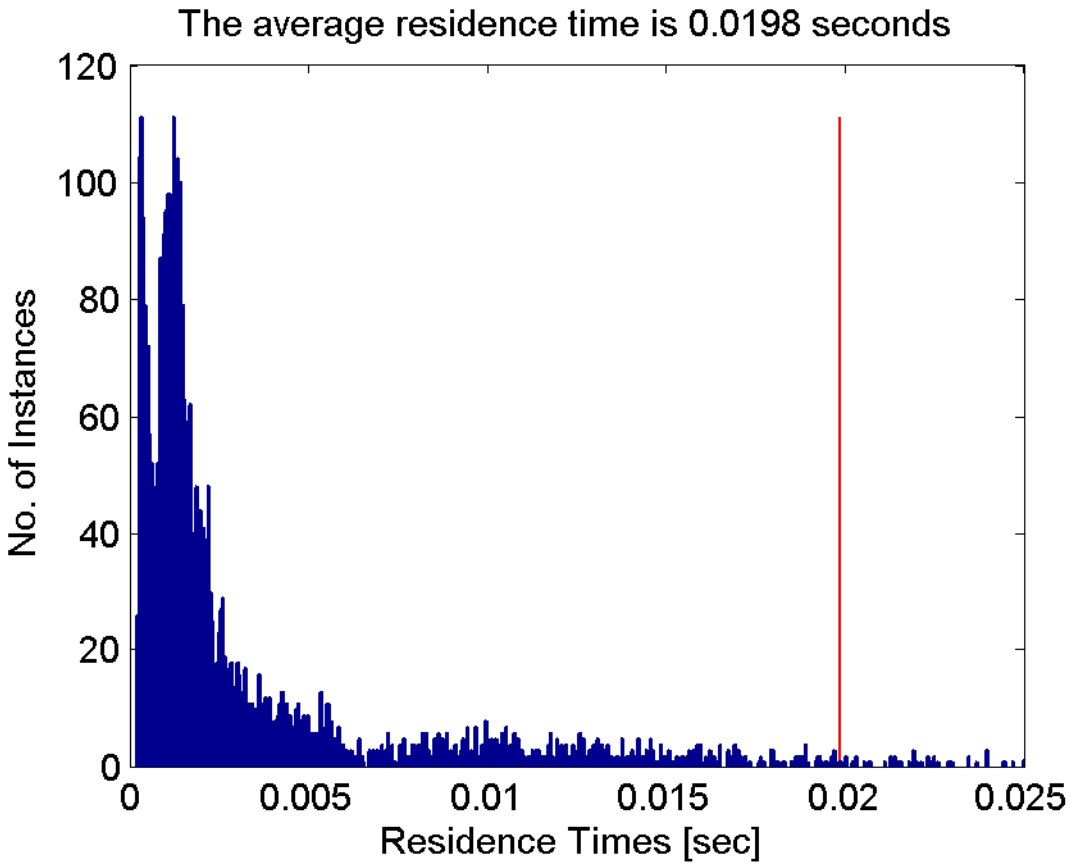

Figure E.10: The residence time distribution for the AR = 2 cavity at Re 50. The average residence time is 0.0198 secs.

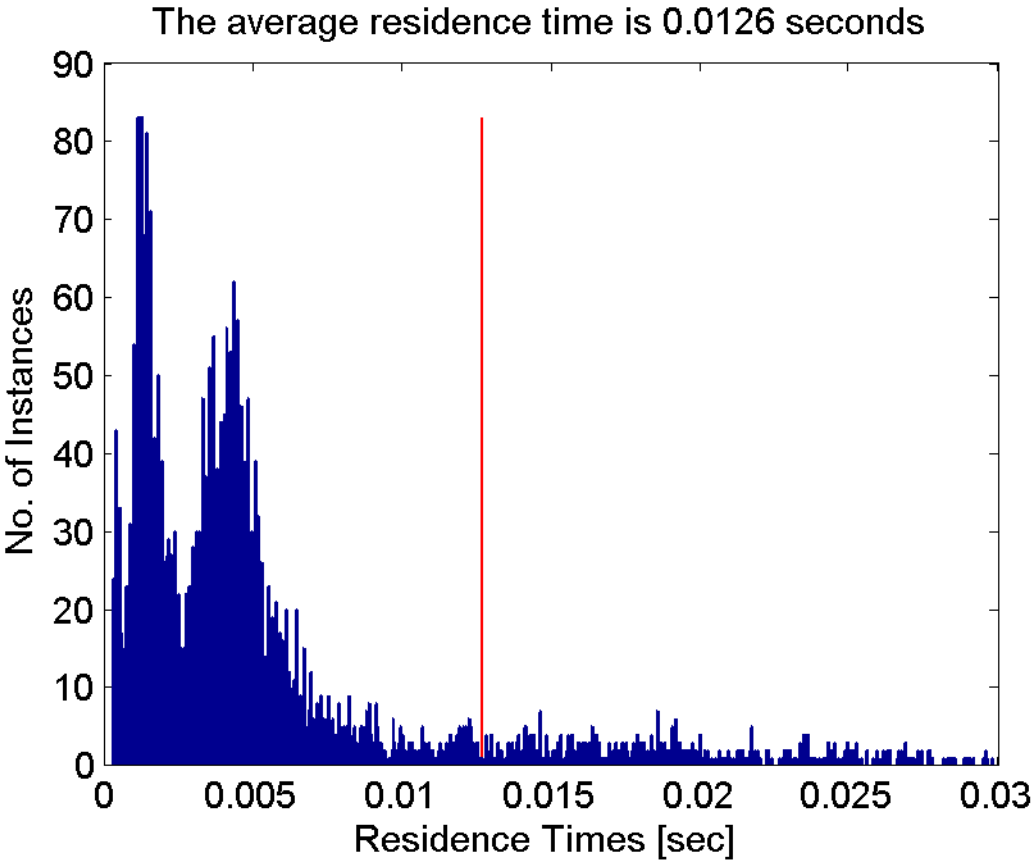

Figure E.11: The residence time distribution for the AR = 2 cavity at Re 75. The average residence time is 0.0126 secs.

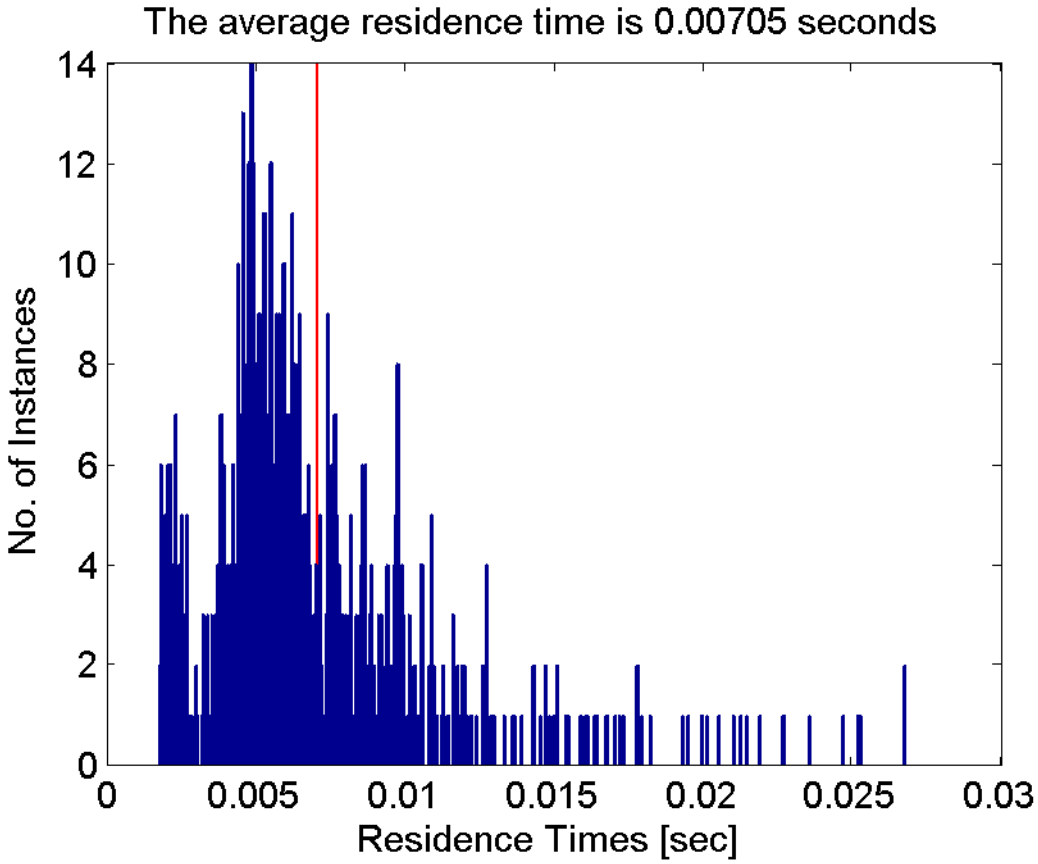

Figure E.12: The residence time distribution for the AR = 2 cavity at Re 100. The average residence time is 0.00705 secs.

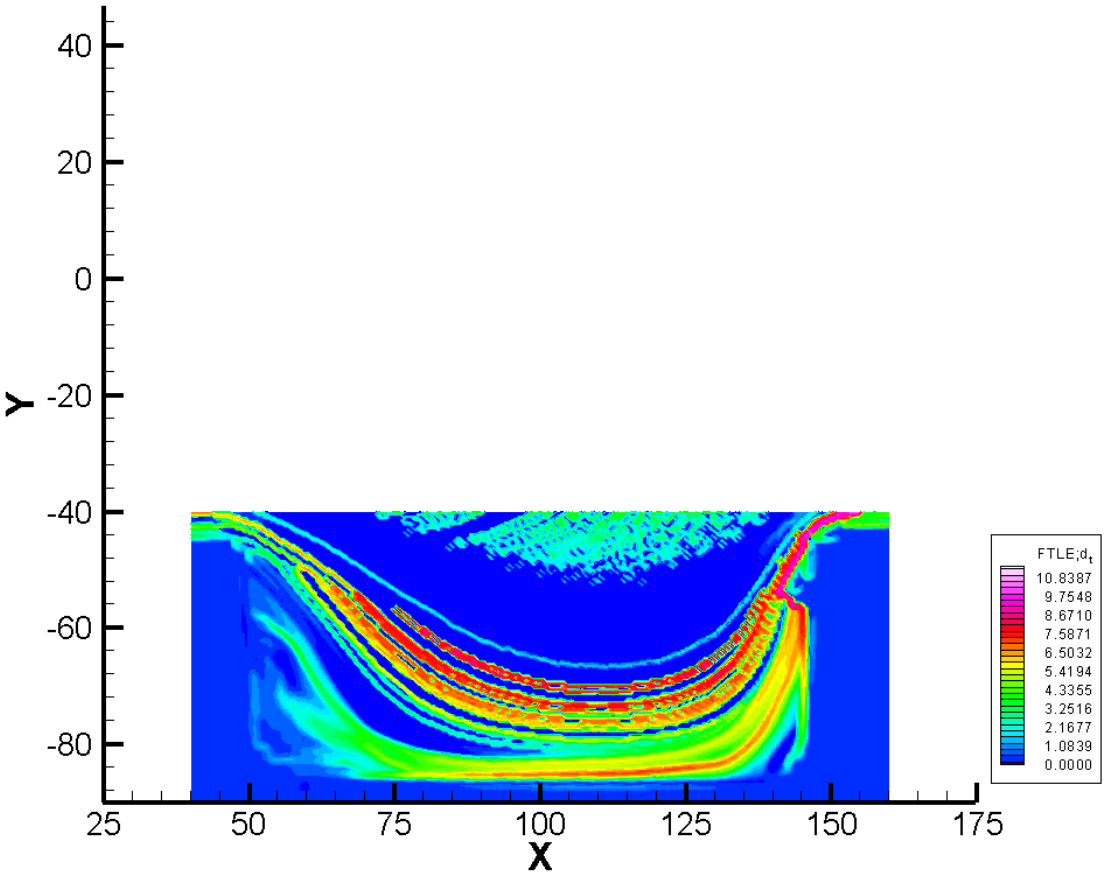

Figure E.13: The backward time LCS for the AR = 2 cavity at Re 40.

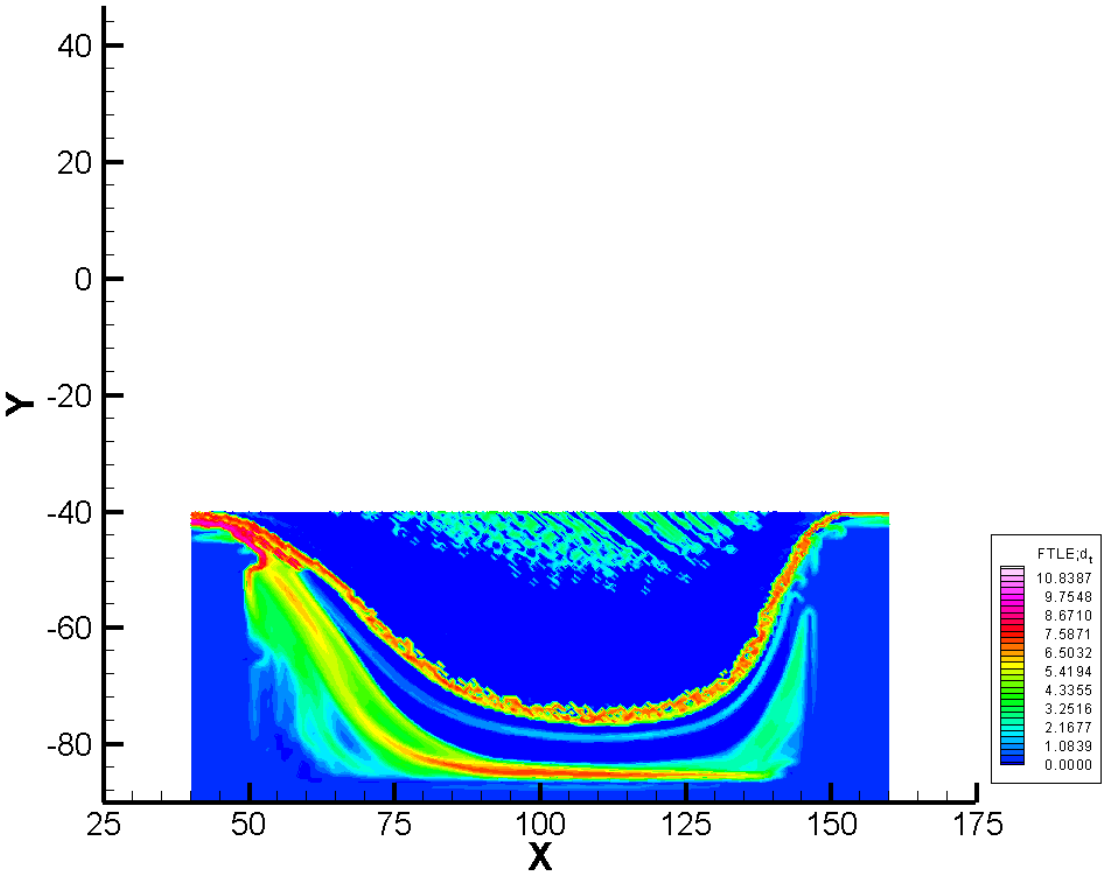

Figure E.14: The forward time LCS for the AR = 2 cavity at Re 40.

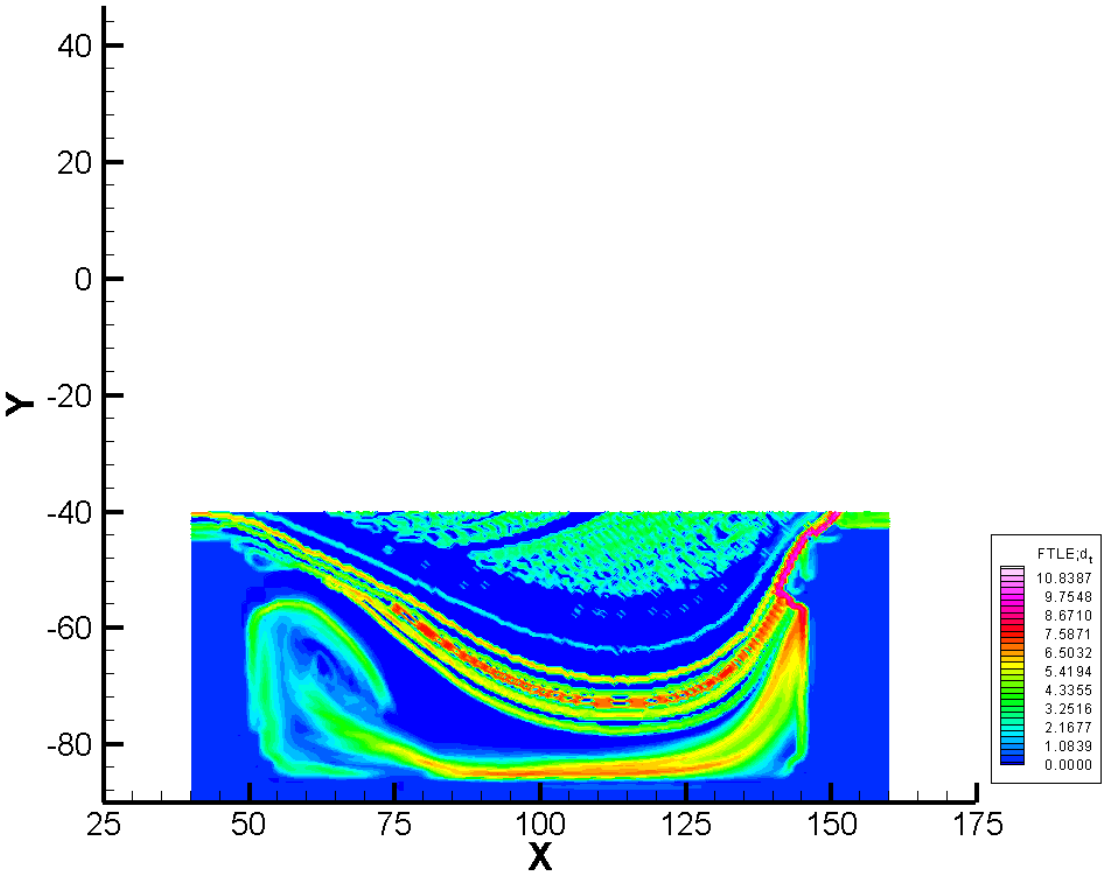

Figure E.15: The backward time LCS for the AR = 2 cavity at Re 50.

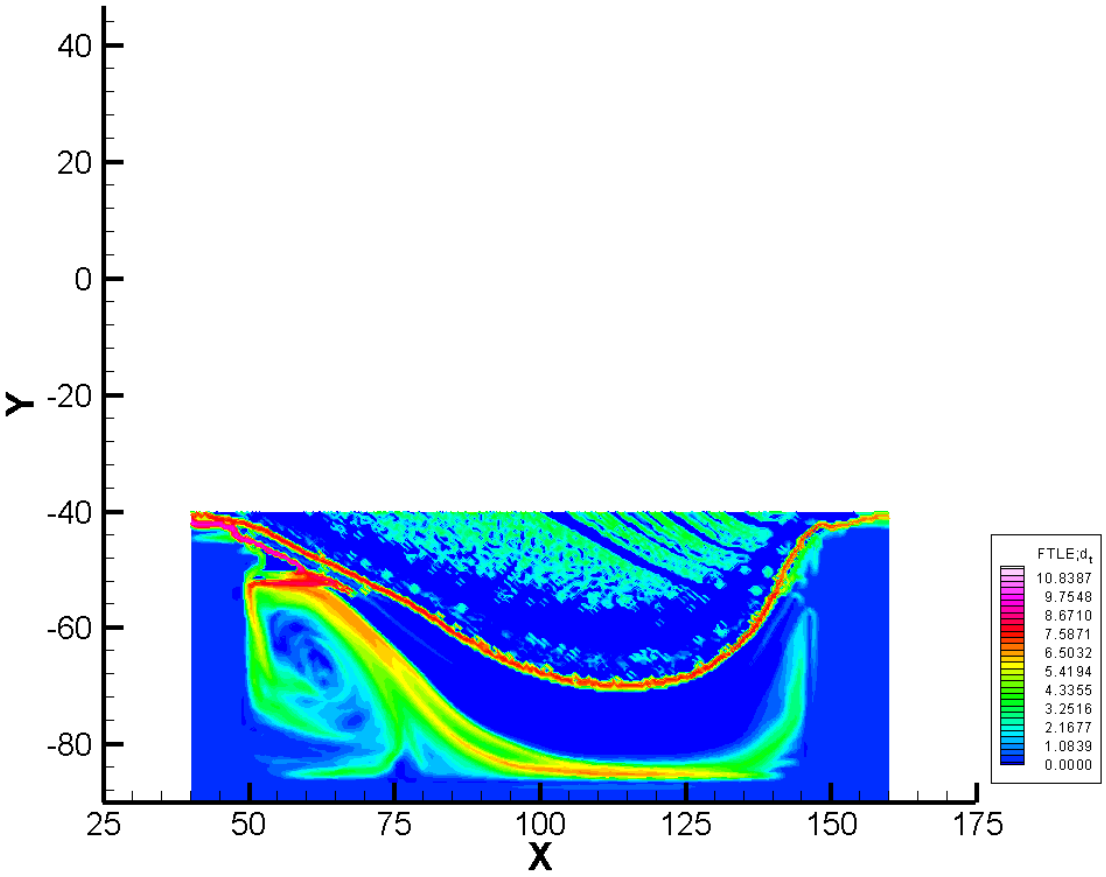

Figure E.16: The forward time LCS for the AR = 2 cavity at Re 50.

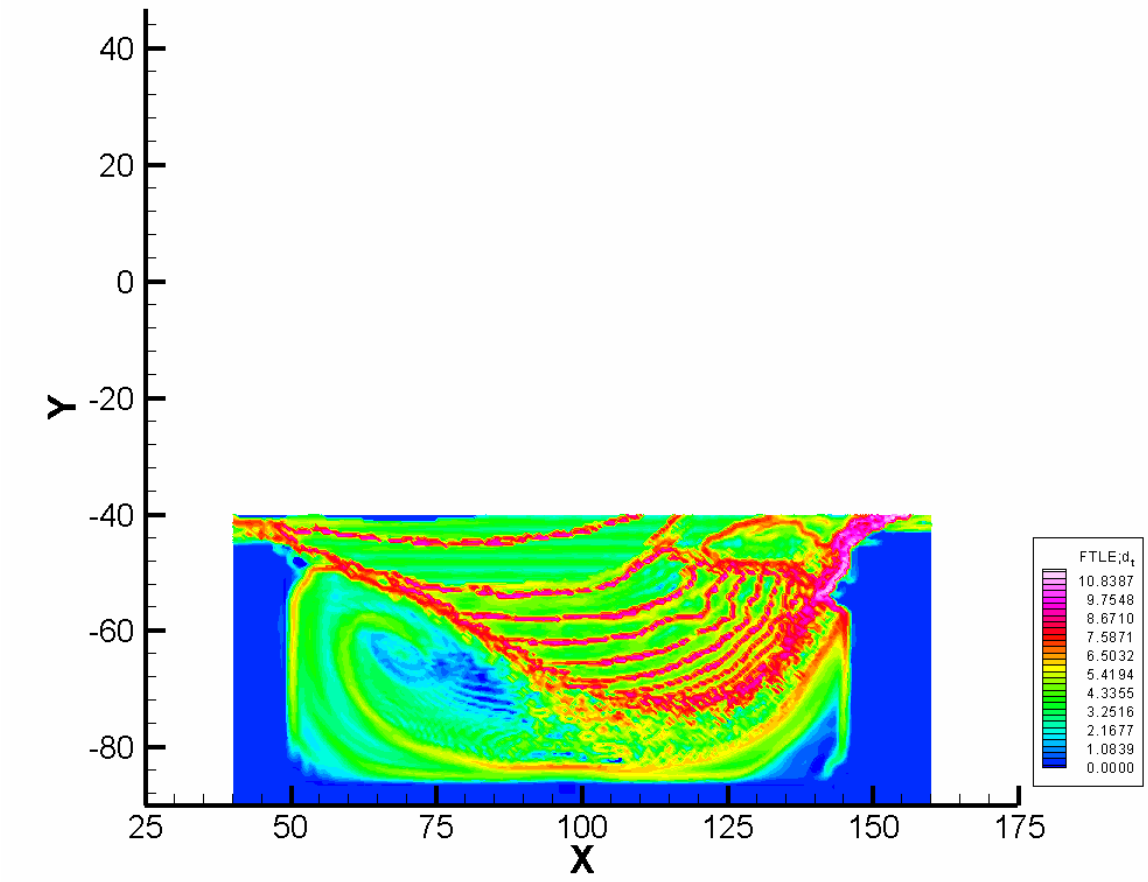

Figure E.17: The backward time LCS for the AR = 2 cavity at Re 75.

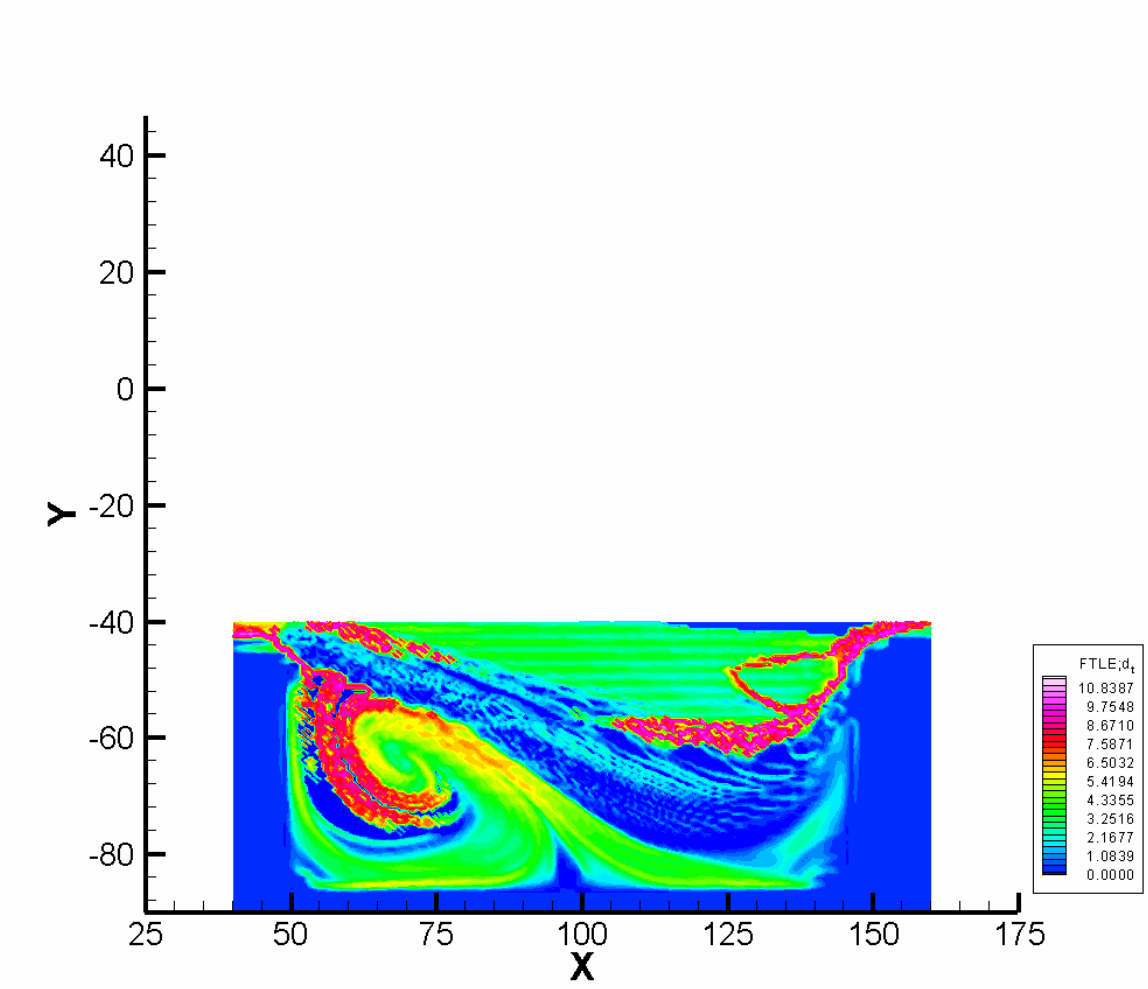

Figure E.18: The forward time LCS for the AR = 2 cavity at Re 75.

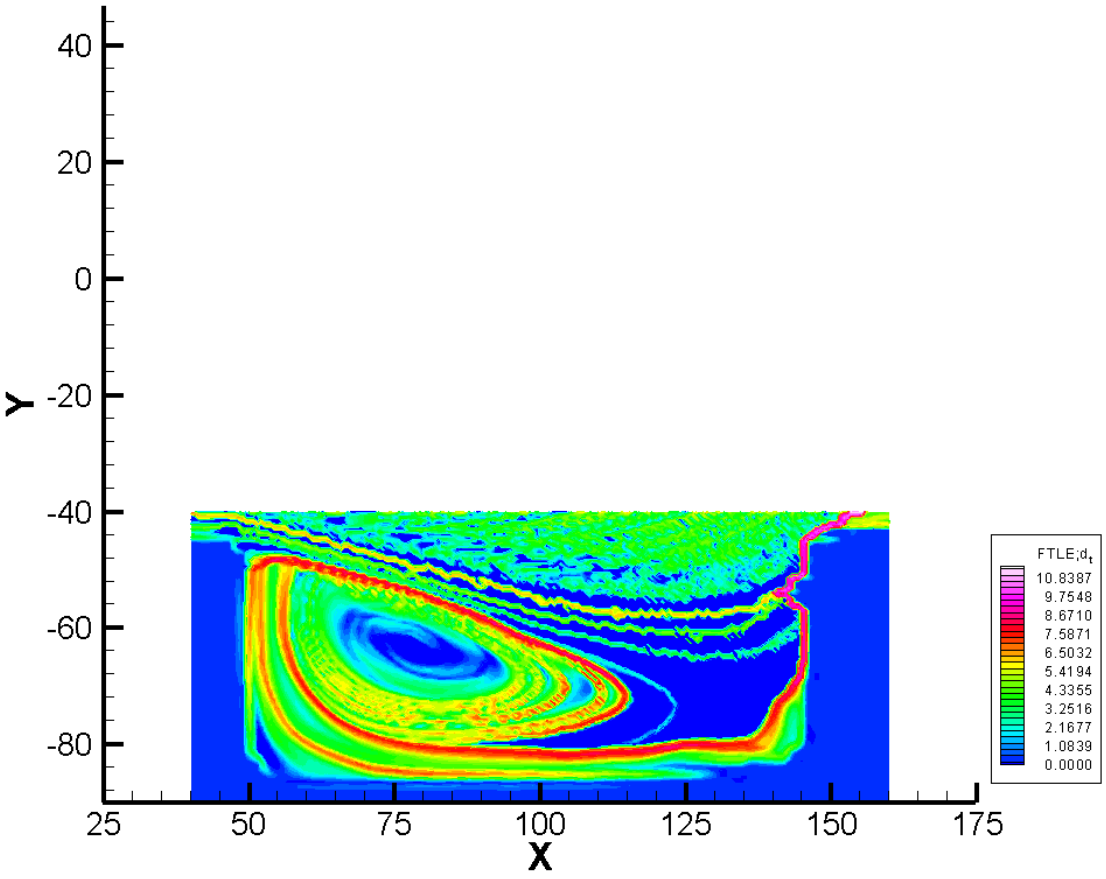

Figure E.19: The backward time LCS for the AR = 2 cavity at Re 100.

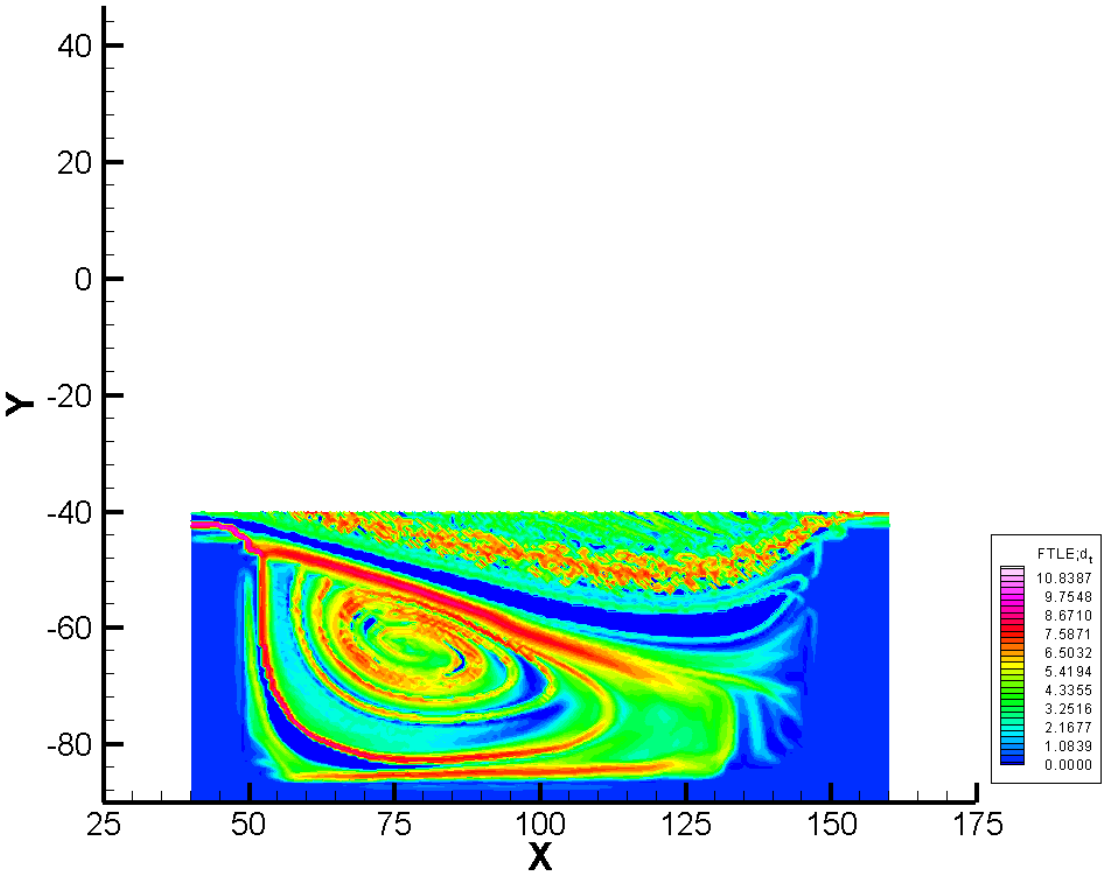

Figure E.20: The forward time LCS for the AR = 2 cavity at Re 100.

E.2 Data for the AR = 1 cavity

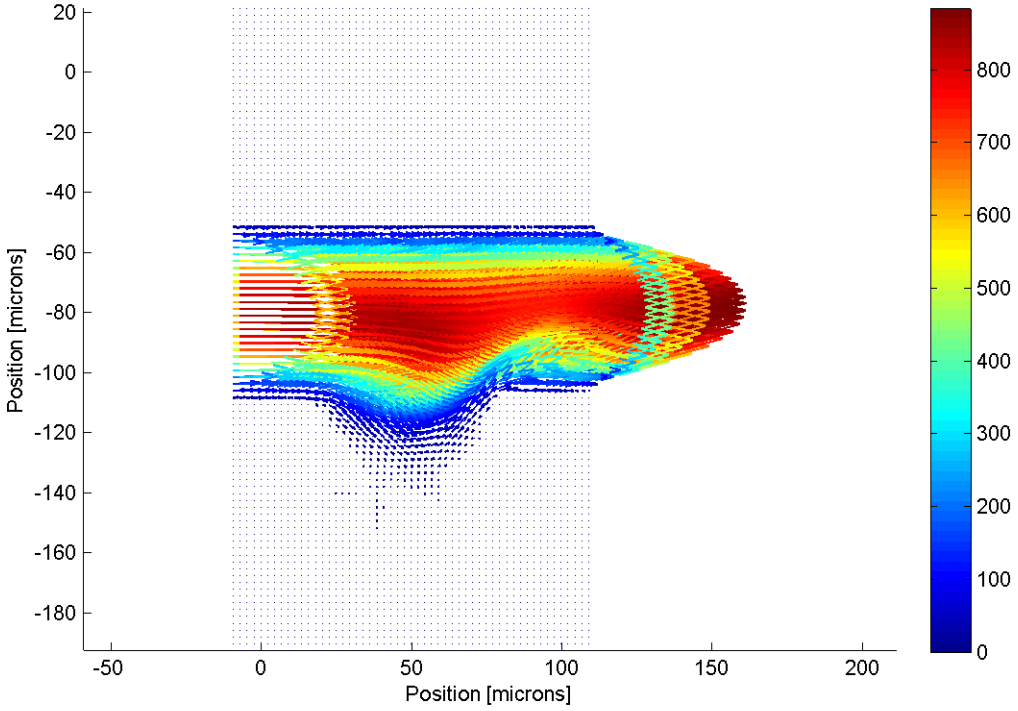

Figure E.21: Velocity field for the AR = 1 cavity at Re 24.

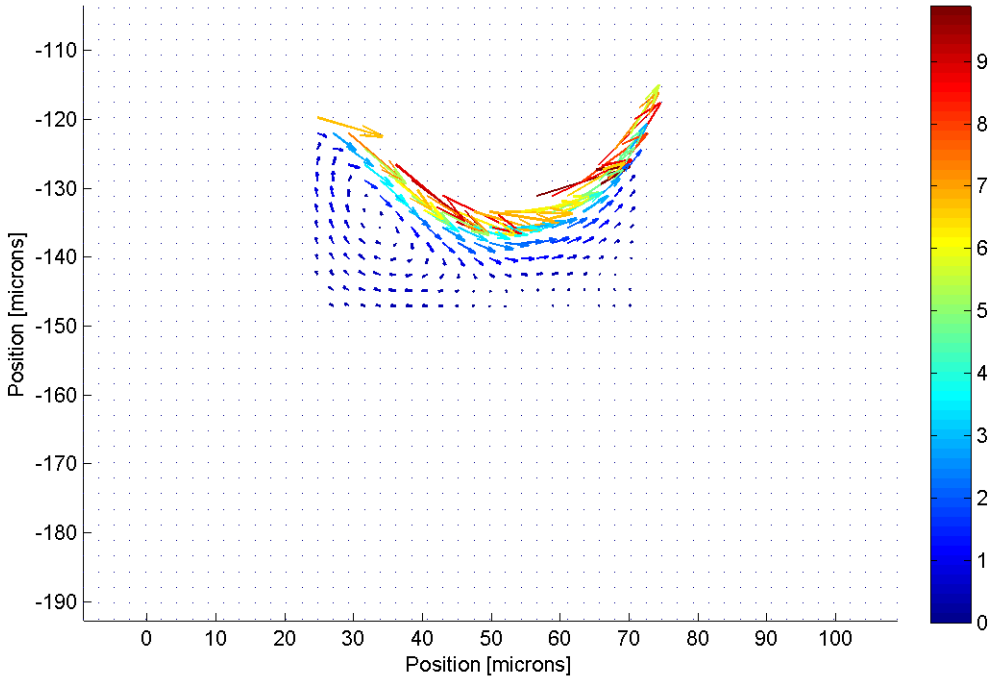

Figure E.22: Velocity field in the lower portion of the AR = 1 cavity at Re 24.

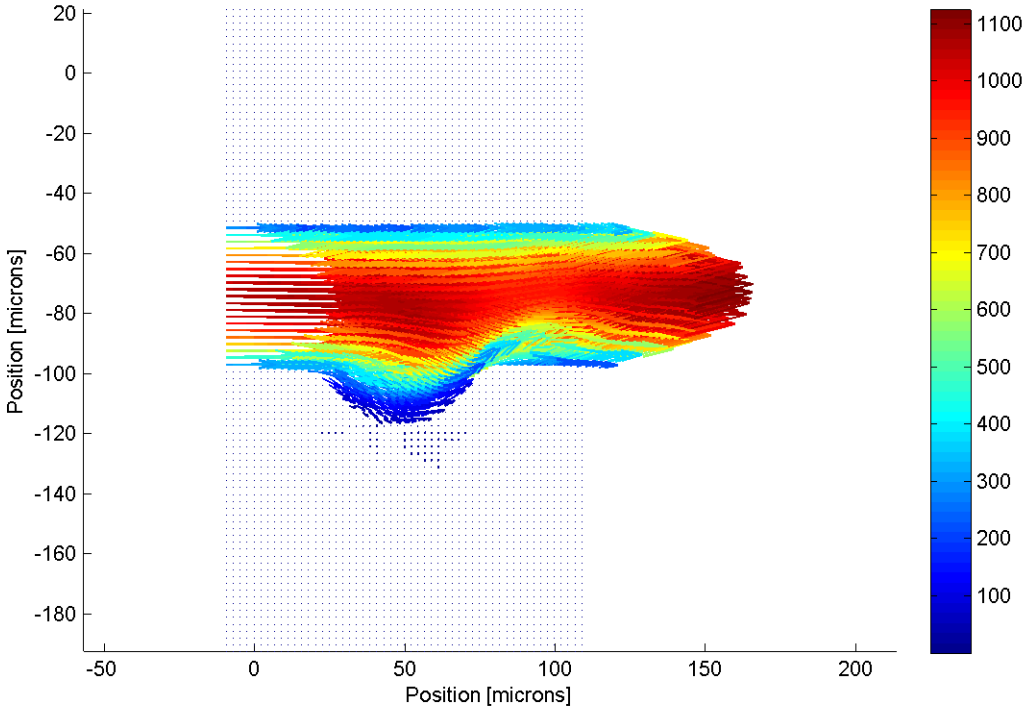

Figure E.23: Velocity field for the AR = 1 cavity at Re 30.

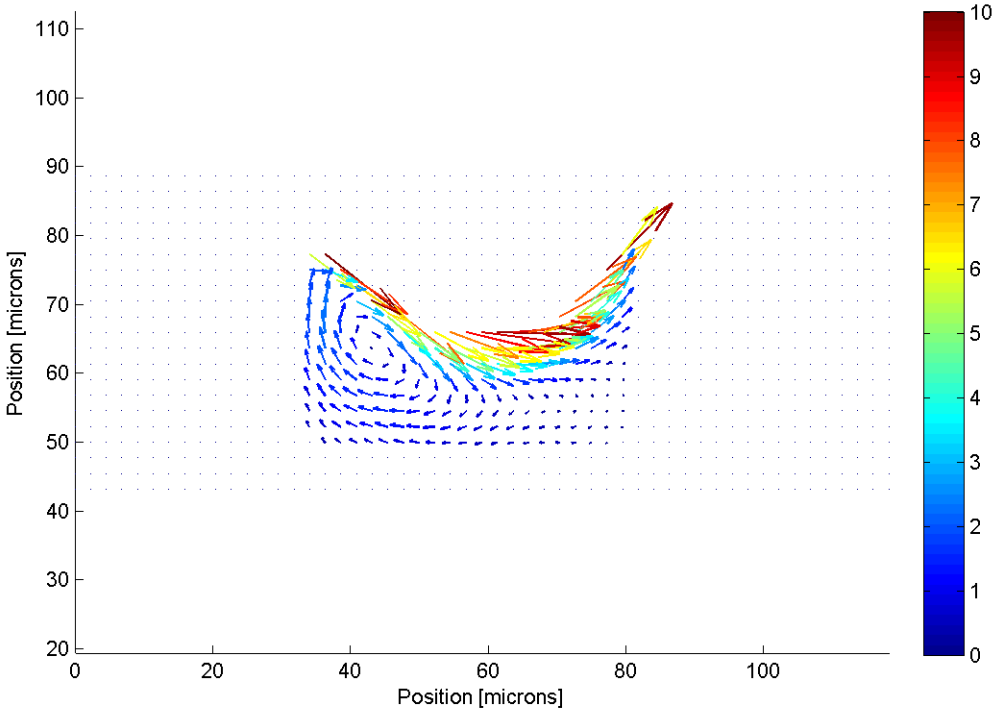

Figure E.24: Velocity field in the lower portion of the AR = 1 cavity at Re 30.

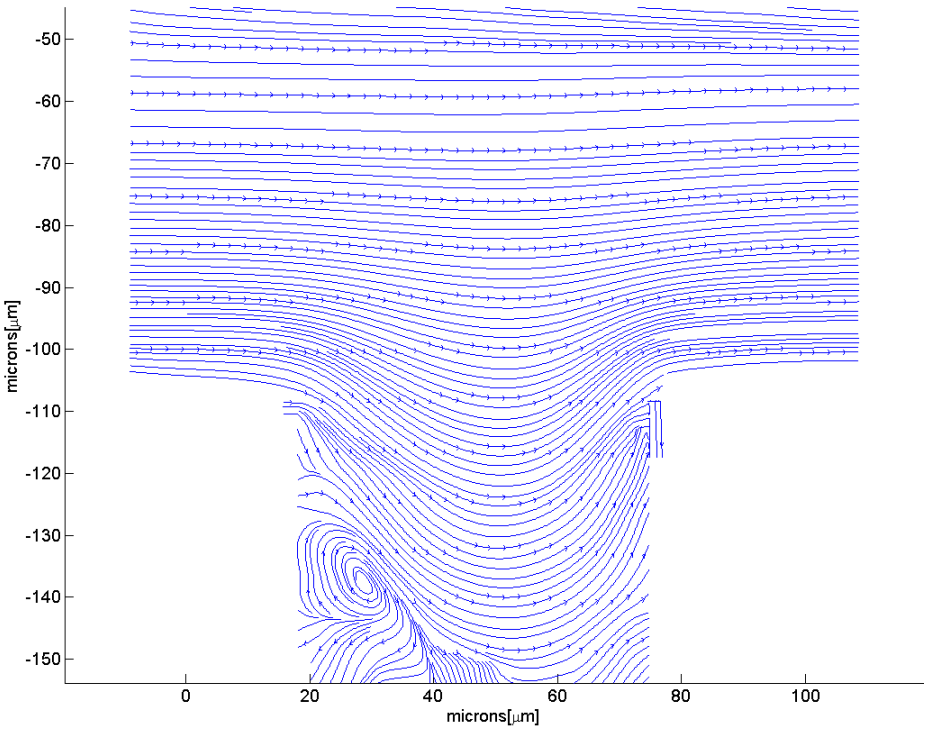

Figure E.25: A streamline image of steady flow in the AR = 1 cavity at Re 23.

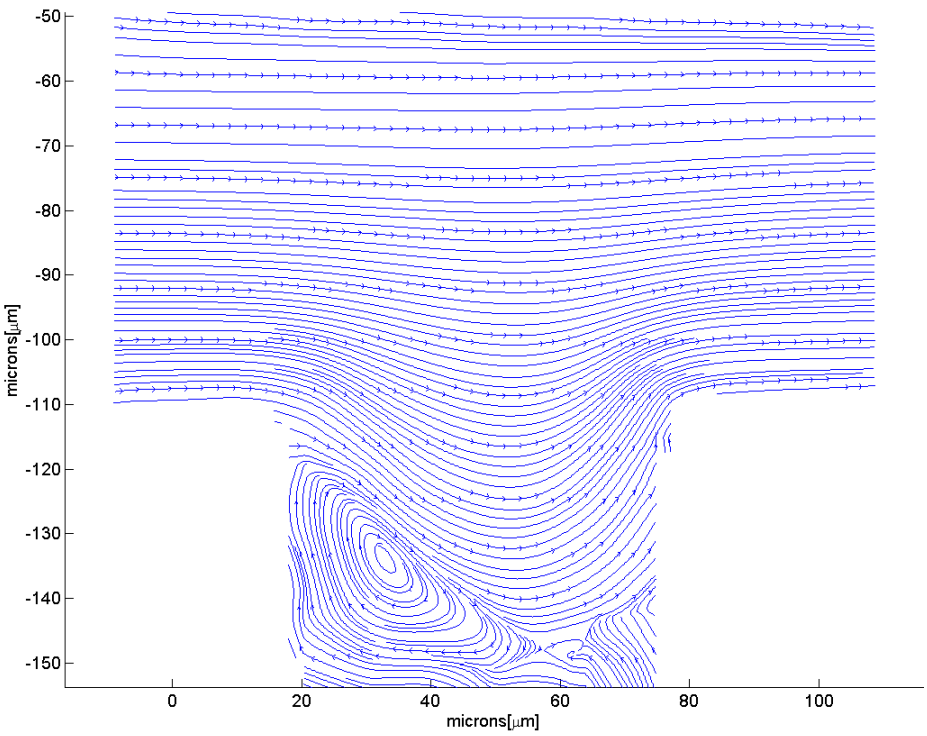

Figure E.26: A streamline image of steady flow in the AR = 1 cavity at Re 24.

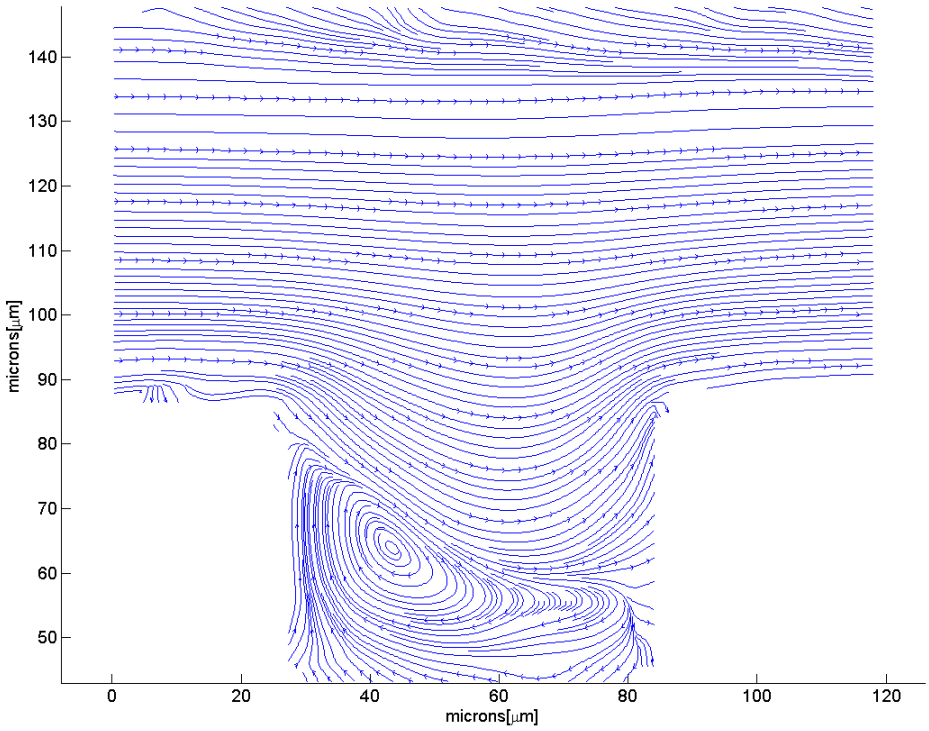

Figure E.27: A streamline image of steady flow in the AR = 1 cavity at Re 30.

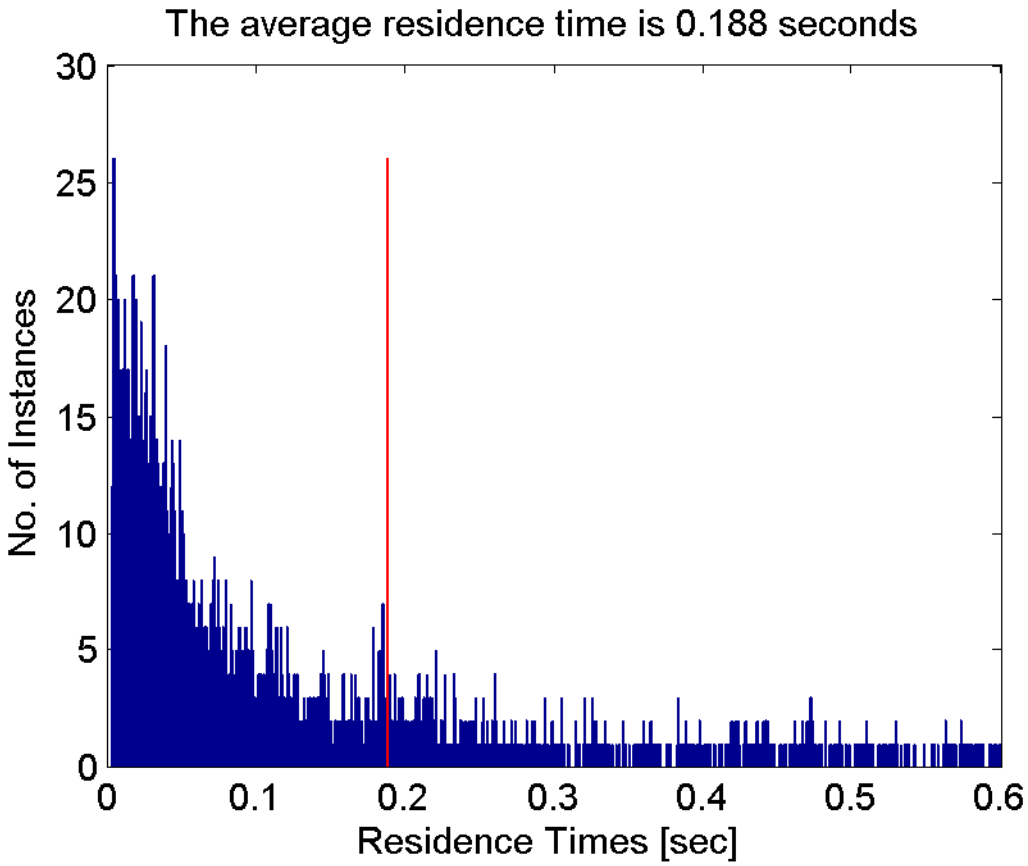

Figure E.28: The residence time distribution for the AR = 1 cavity at Re 23. The average residence time is 0.188 secs.

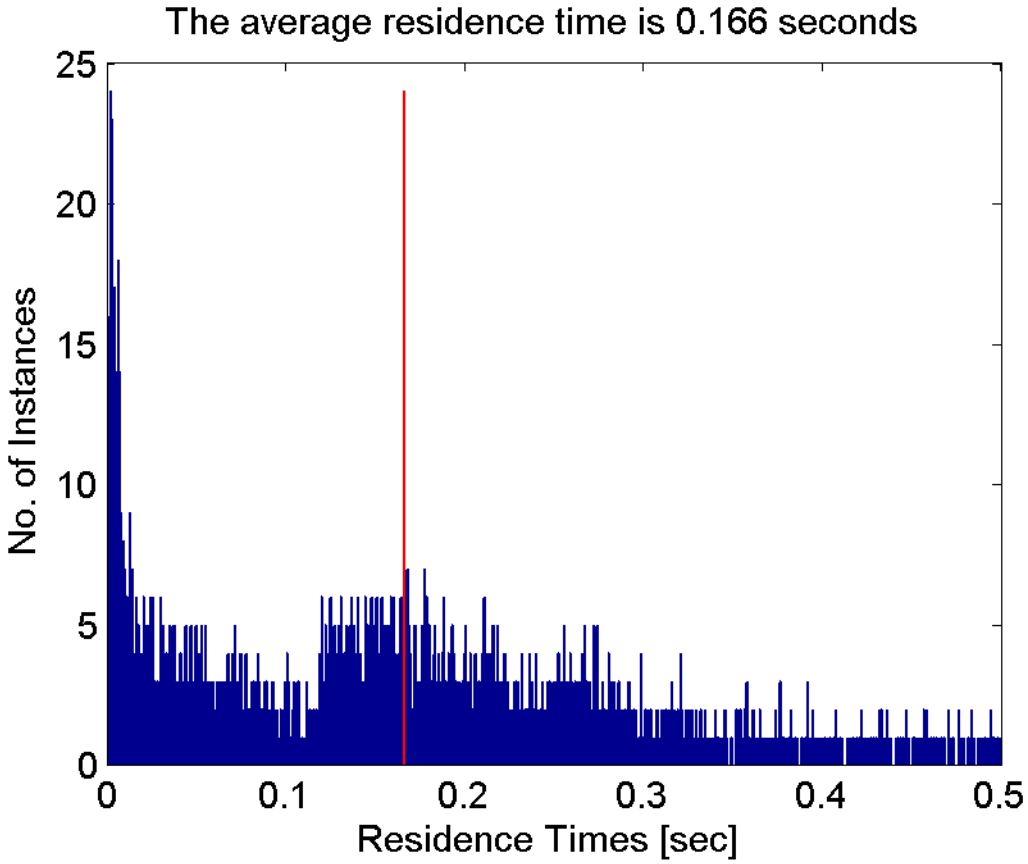

Figure E.29: The residence time distribution for the AR = 1 cavity at Re 24. The average residence time is 0.166 secs.

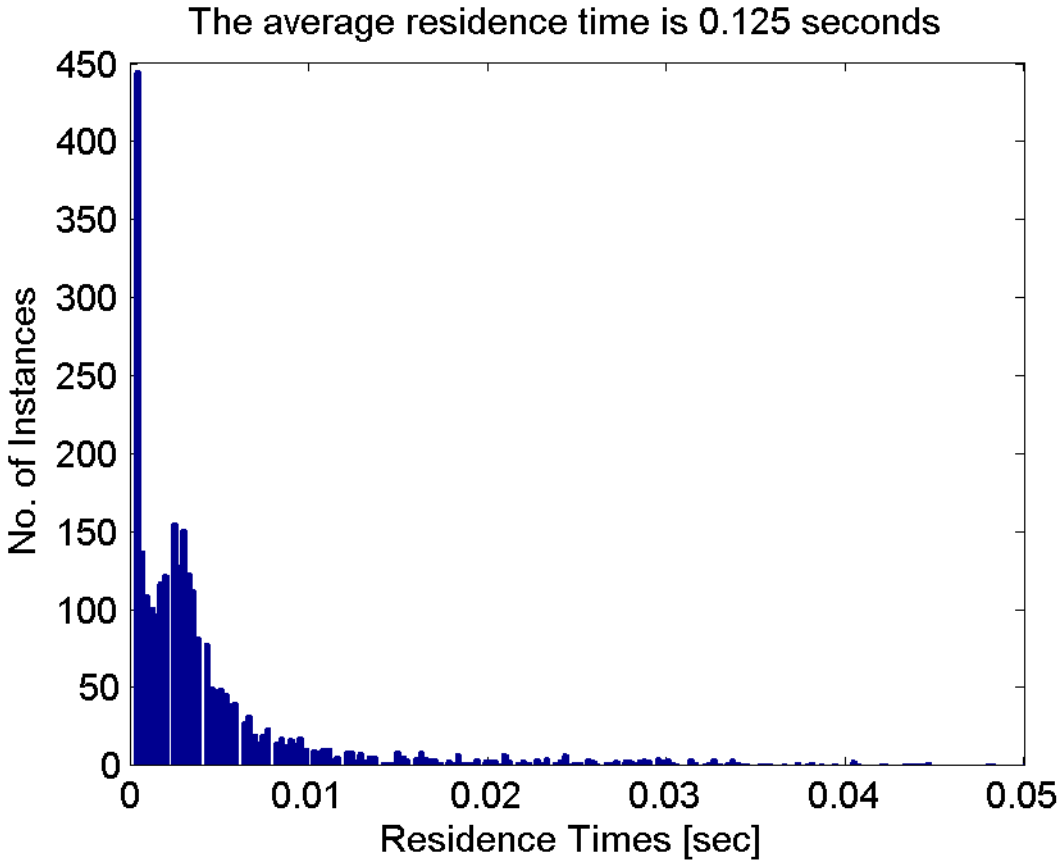

Figure E.30: The residence time distribution for the AR = 1 cavity at Re 30. The average residence time is 0.125 secs.

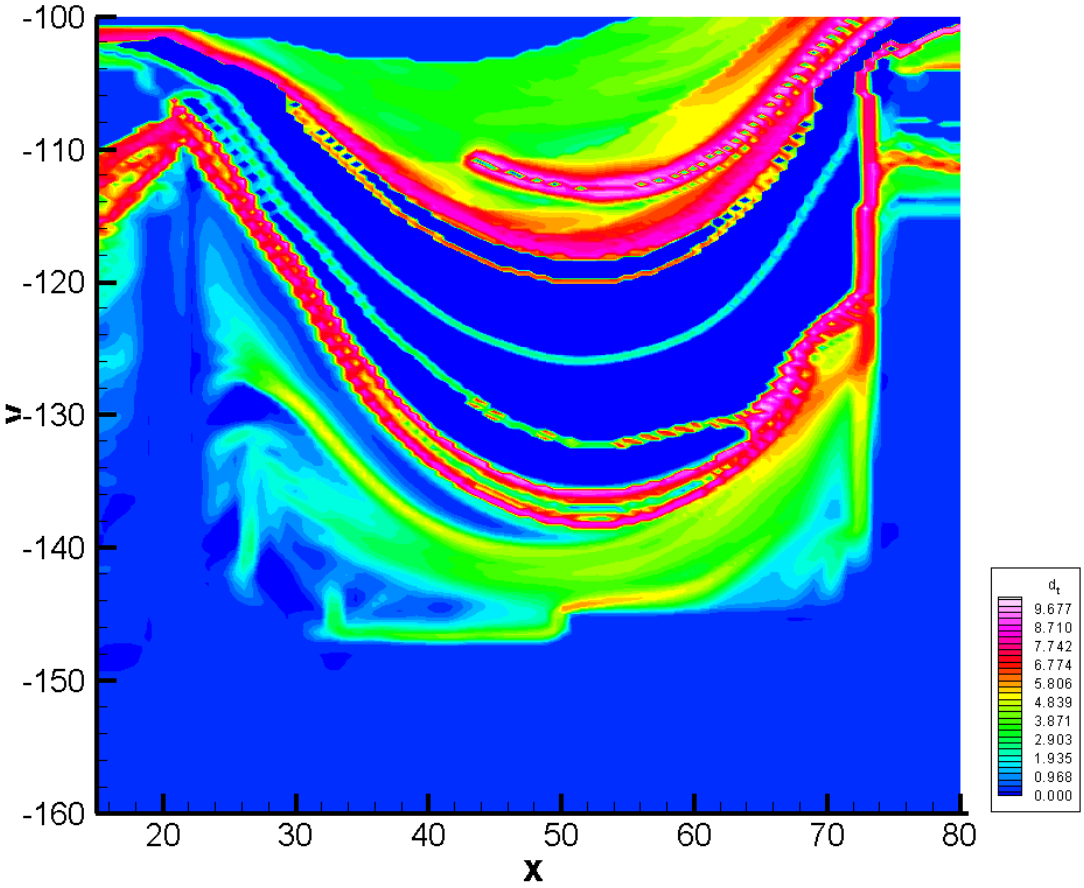

Figure E.31: The backward time LCS for the AR = 1 cavity at Re 23.

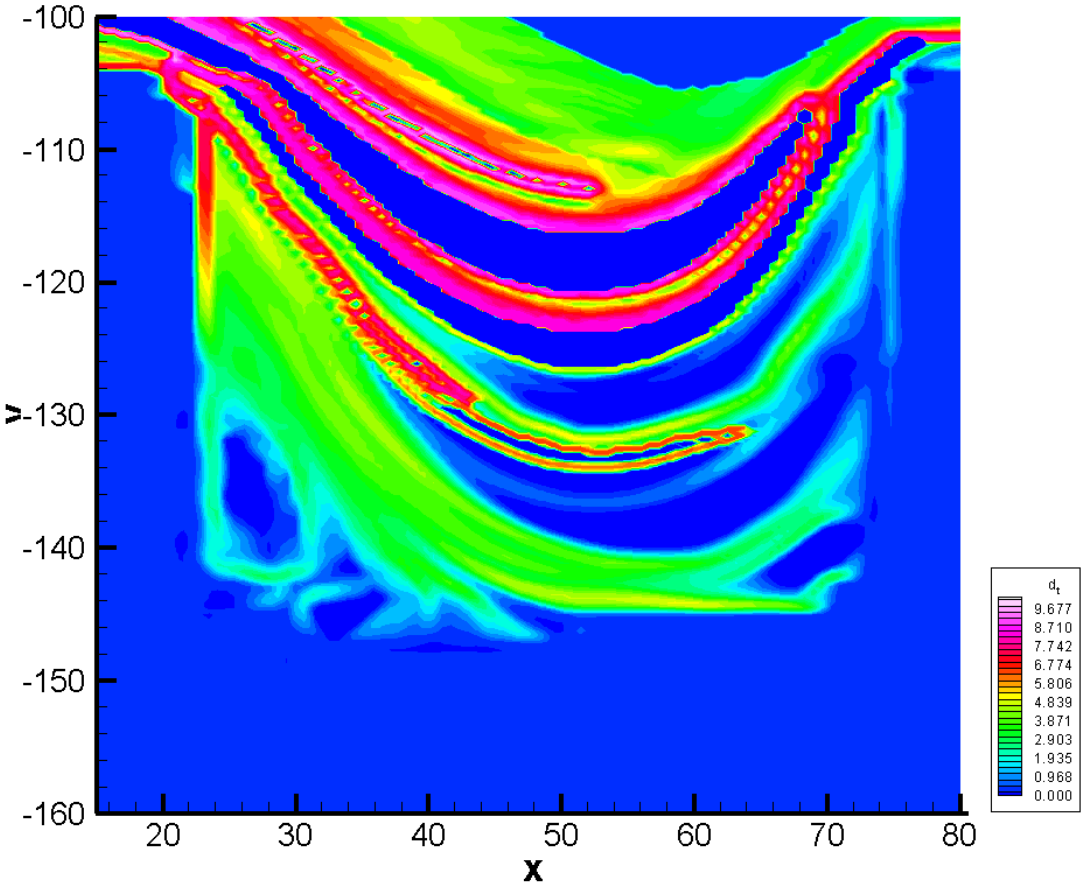

Figure E.32: The forward time LCS for the AR = 1 cavity at Re 23.

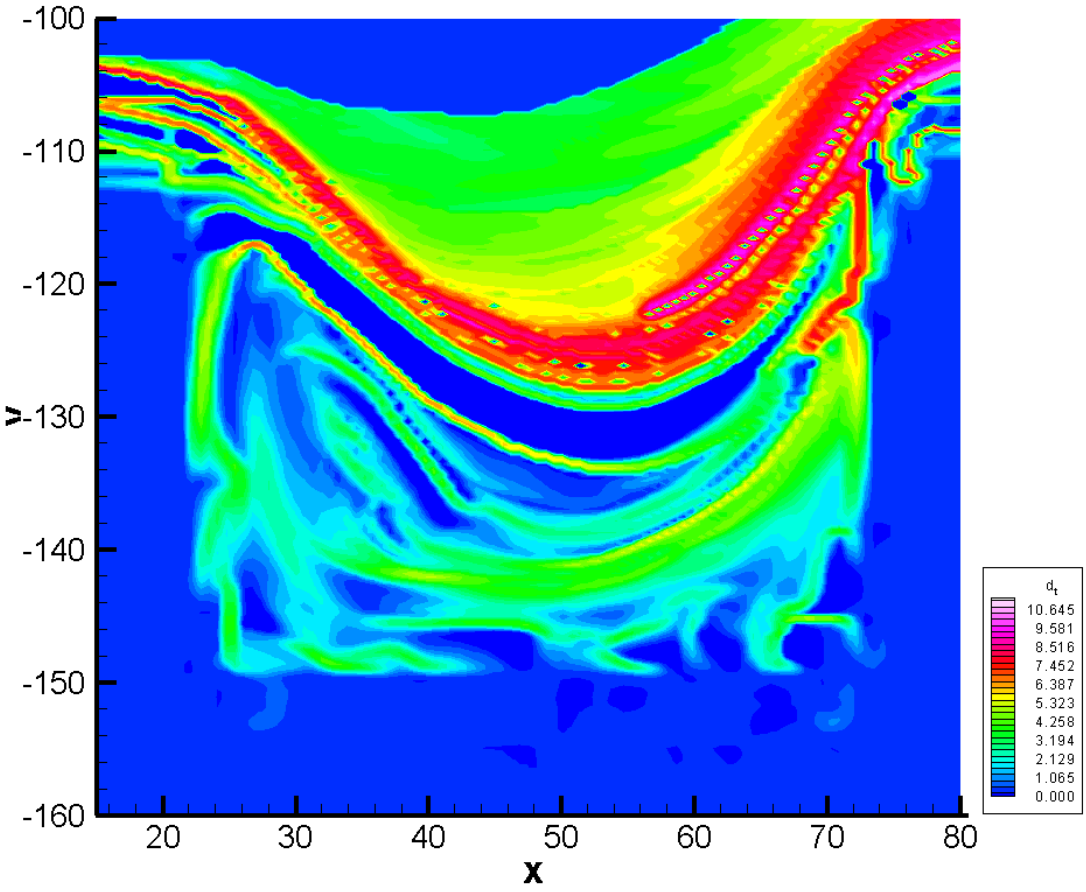

Figure E.33: The backward time LCS for the AR = 1 cavity at Re 24.

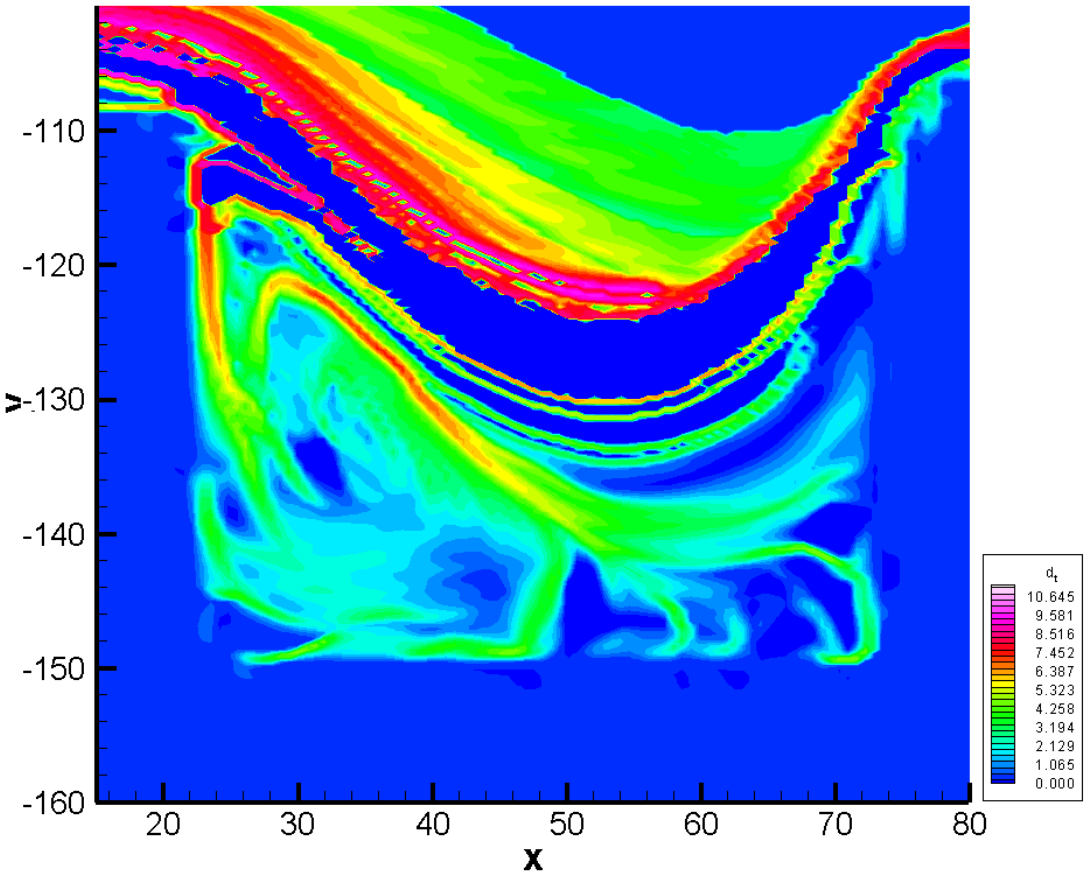

Figure E.34: The forward time LCS for the AR = 1 cavity at Re 24.

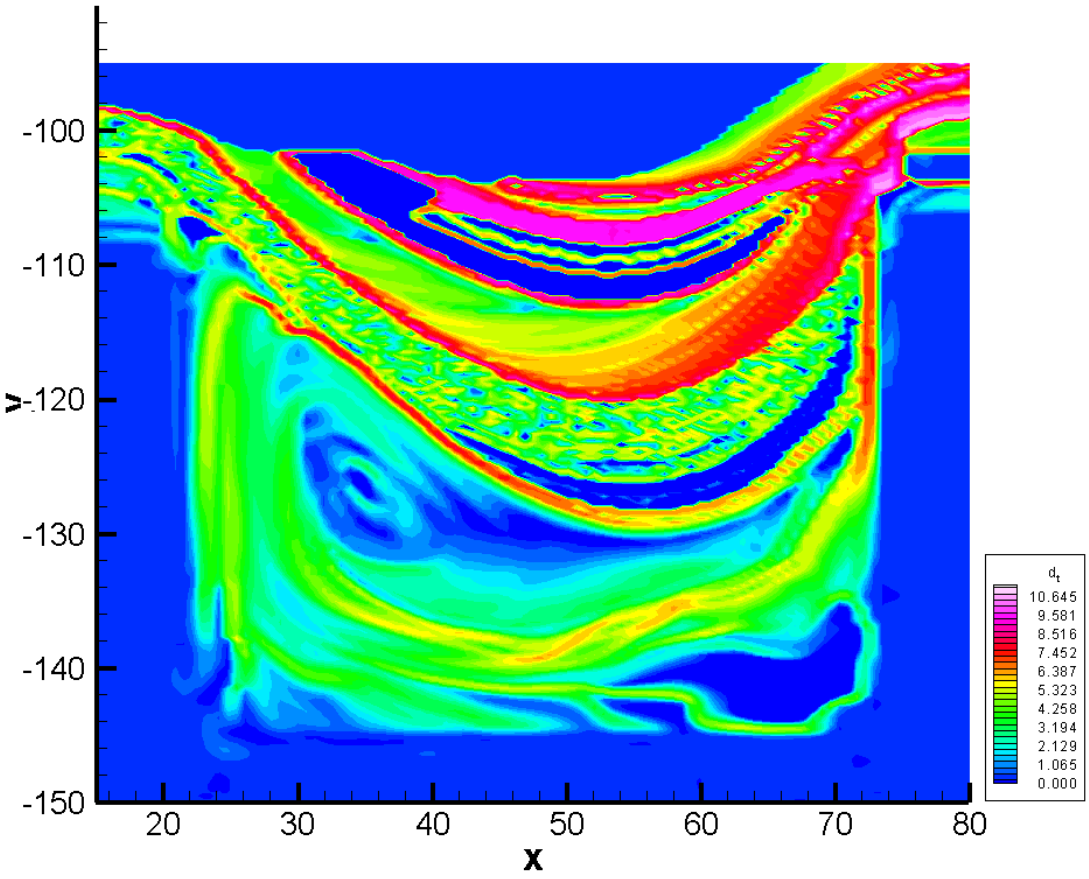

Figure E.35: The backward time LCS for the AR = 1 cavity at Re 30.

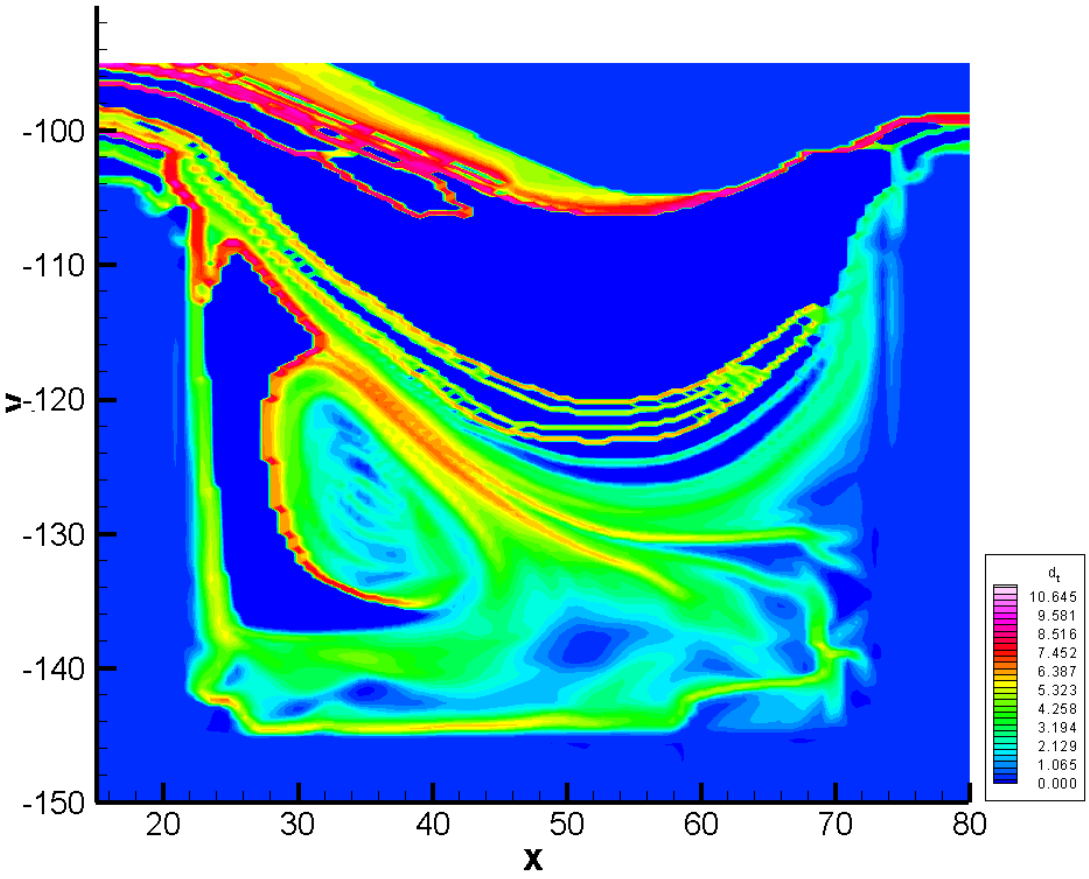

Figure E.36: The forward time LCS for the AR = 1 cavity at Re 30.

E.3 Data for the AR = 0.5 cavity

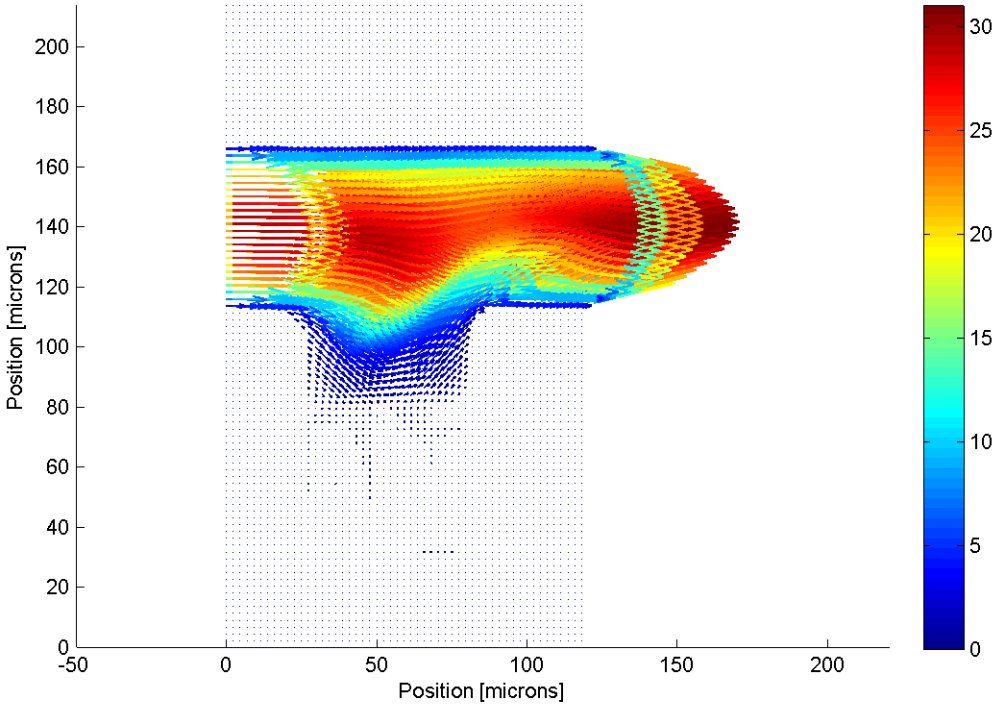

Figure E.37: Velocity field in the AR = 0.5 cavity at Re 0.1.

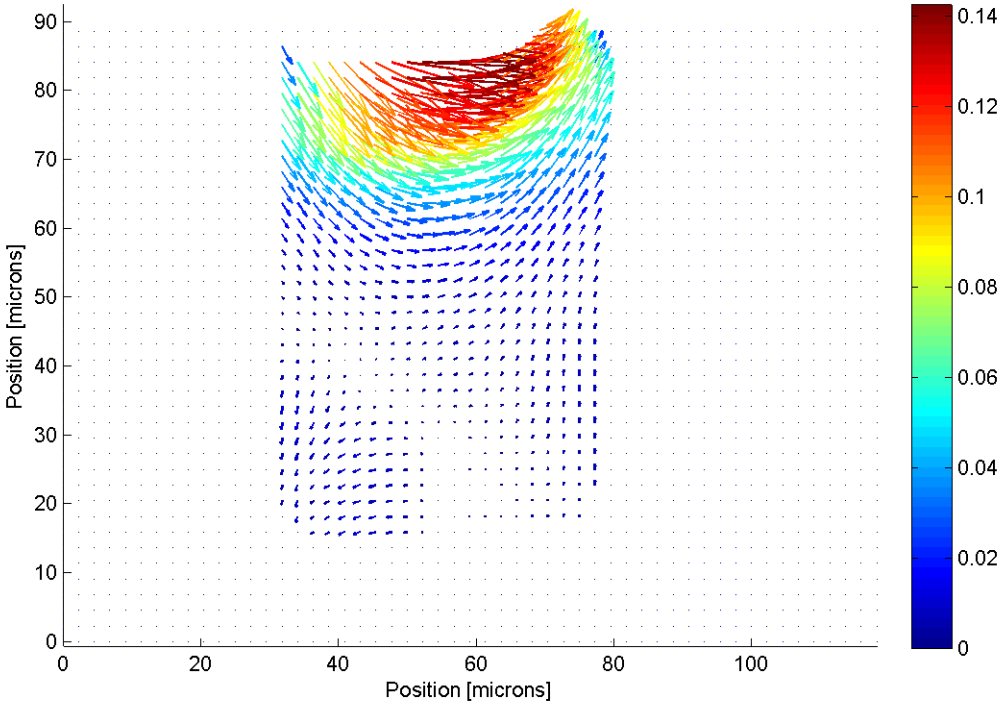

Figure E.38: Velocity field in the lower portion of the AR = 0.5 cavity at Re 0.1.

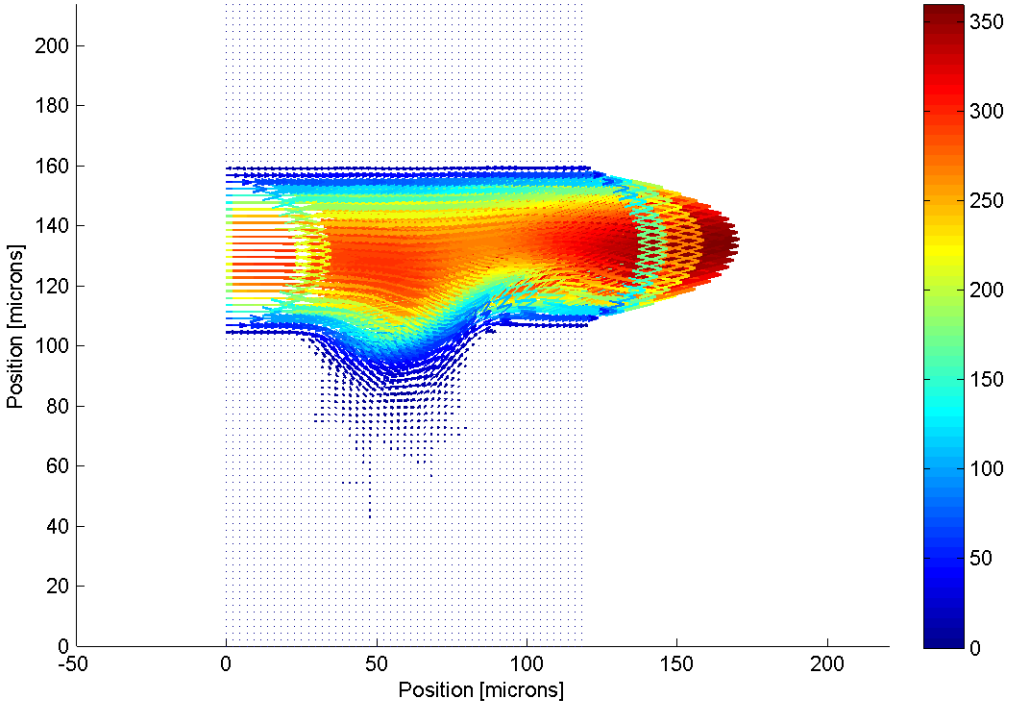

Figure E.39: Velocity field in the AR = 0.5 cavity at Re 15.

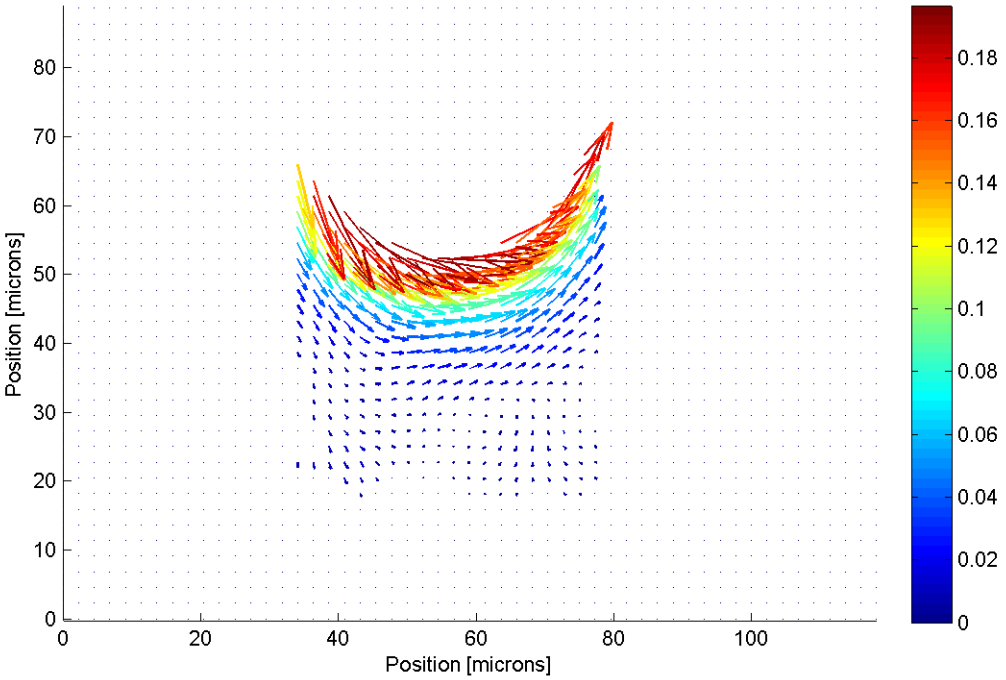

Figure E.40: Velocity in the lower portion of the AR = 0.5 cavity at Re 15.

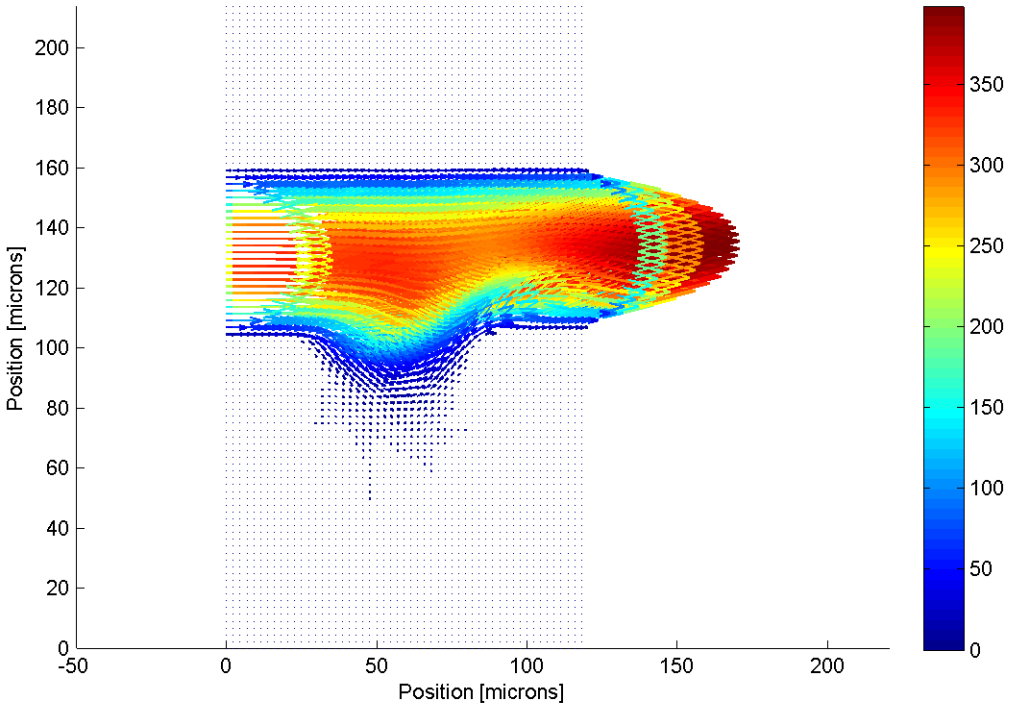

Figure E.41: Velocity field in the AR = 0.5 cavity at Re 17.

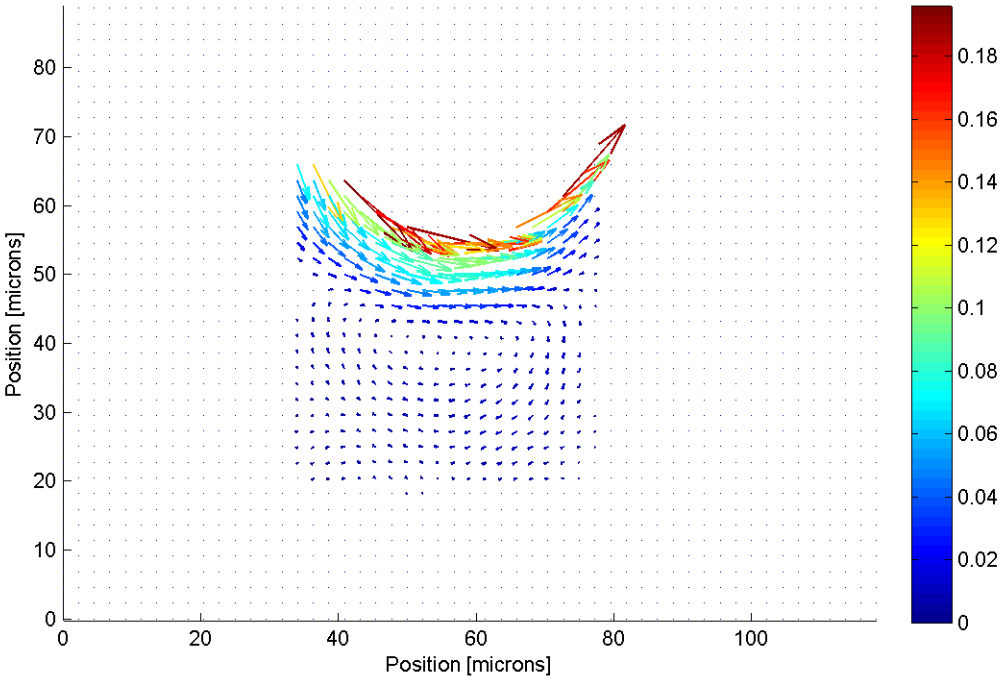

Figure E.42: The velocity field in the lower portion of the AR = 0.5 cavity at Re 17.

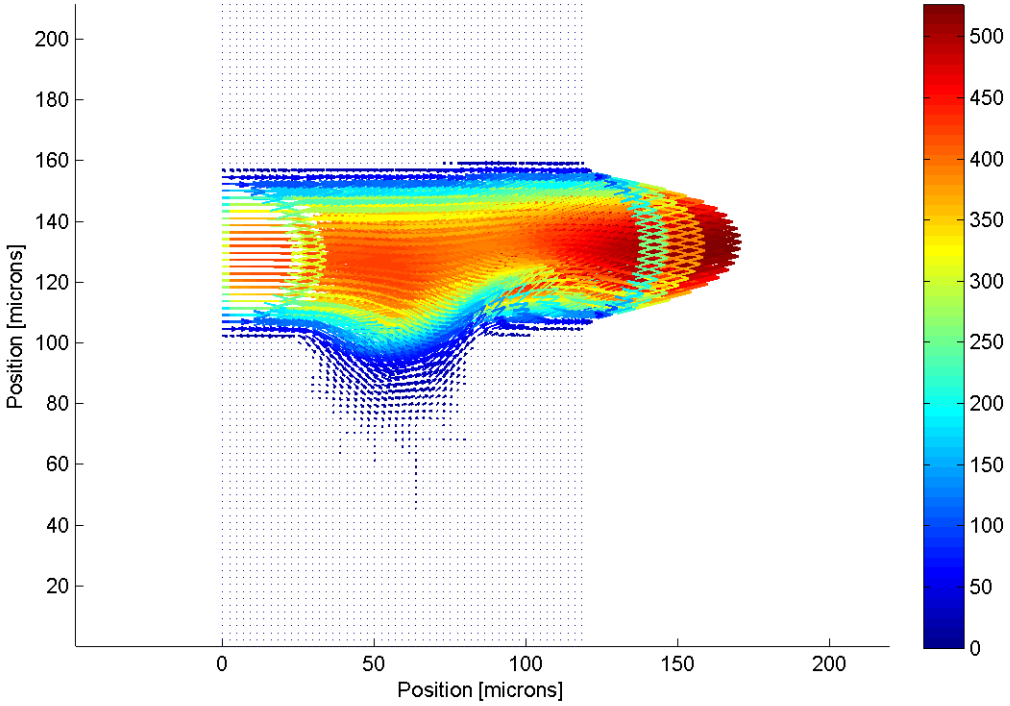

Figure E.43: Velocity field in the AR = 0.5 cavity at Re 20.

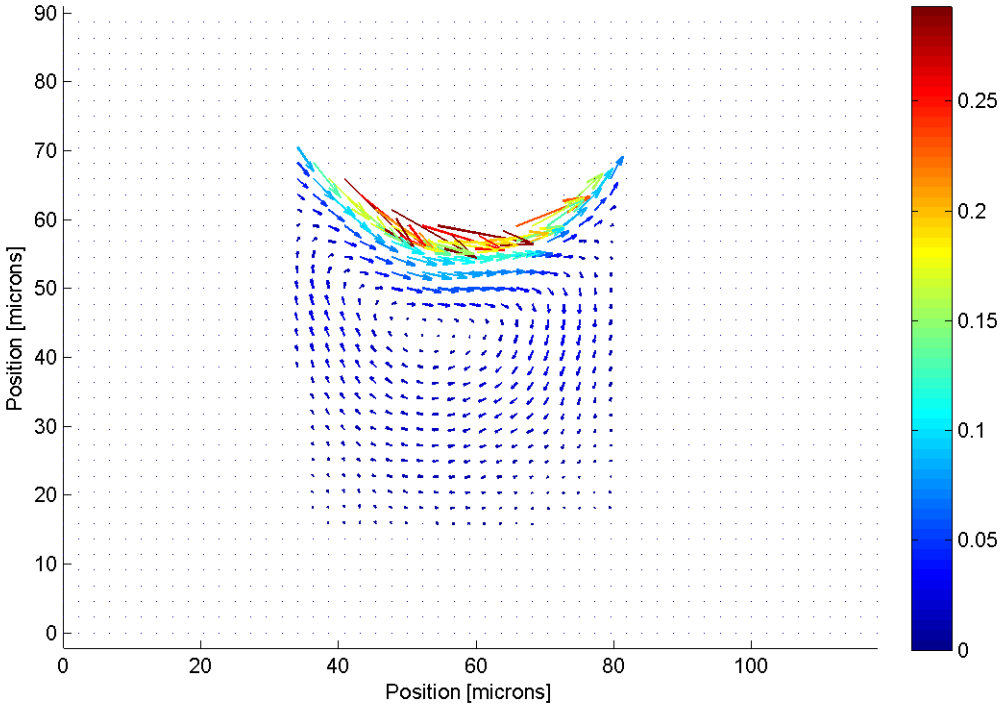

Figure E.44: Velocity field in the lower portion of the AR = 0.5 cavity at Re 20.

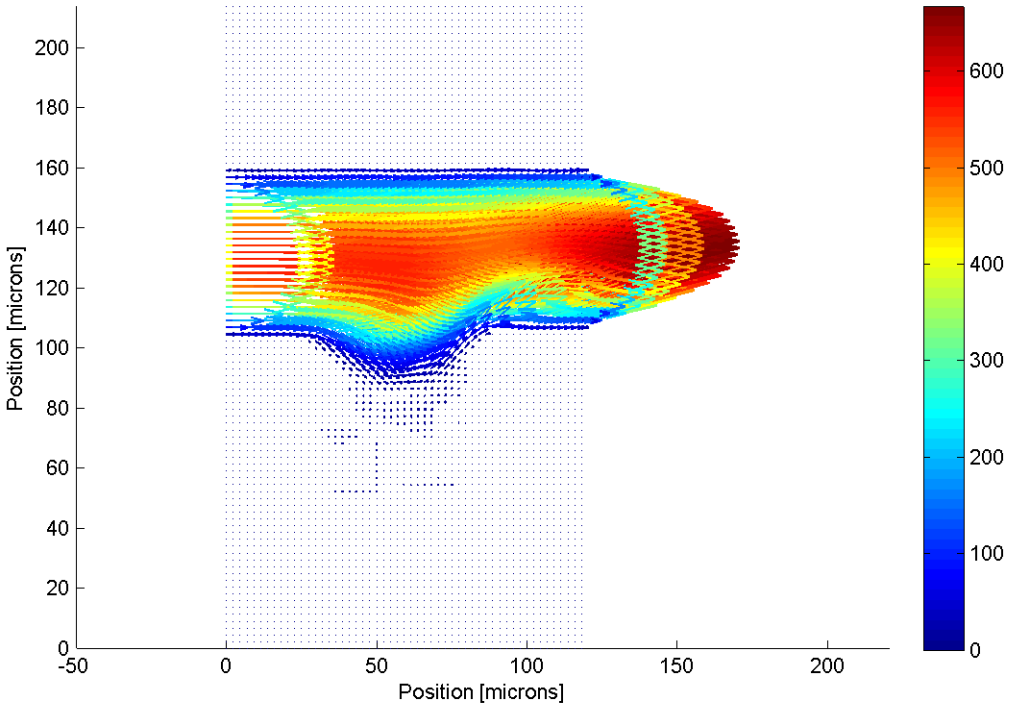

Figure E.45: Velocity field in the AR = 0.5 cavity at Re 30.

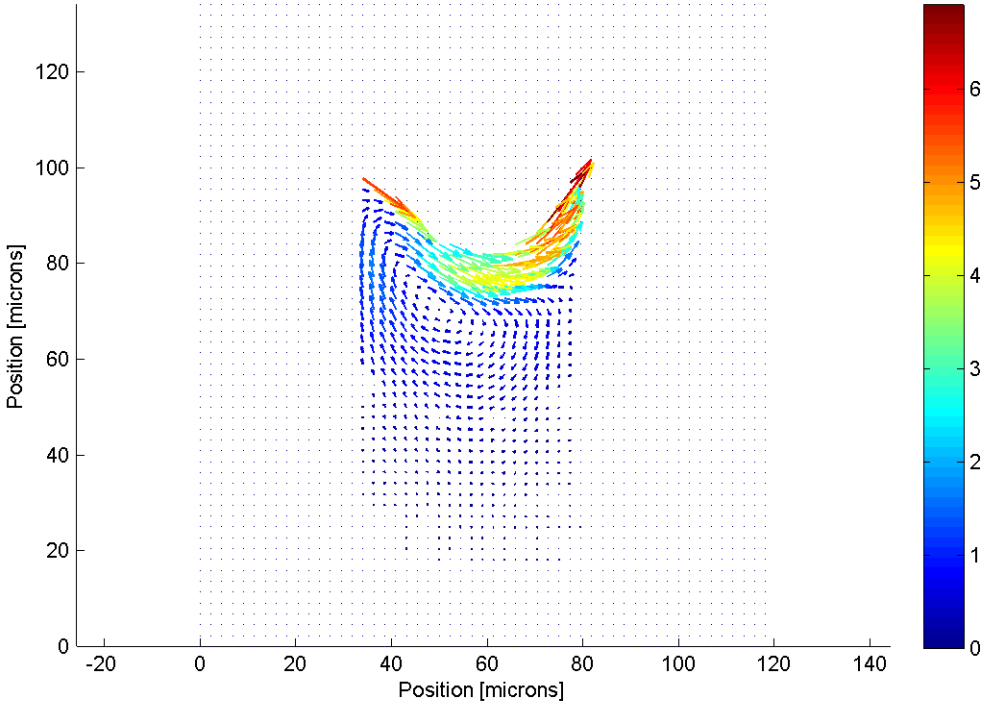

Figure E.46: Velocity field in the AR = 0.5 cavity at Re 30

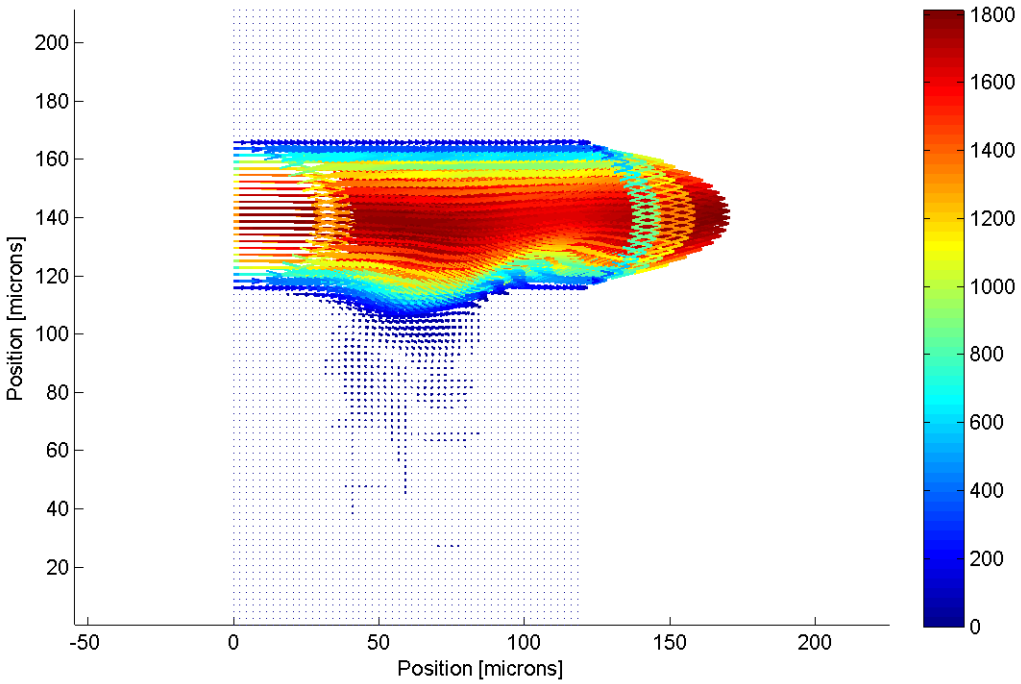

Figure E.47: Velocity field in the AR = 0.5 cavity at Re 50.

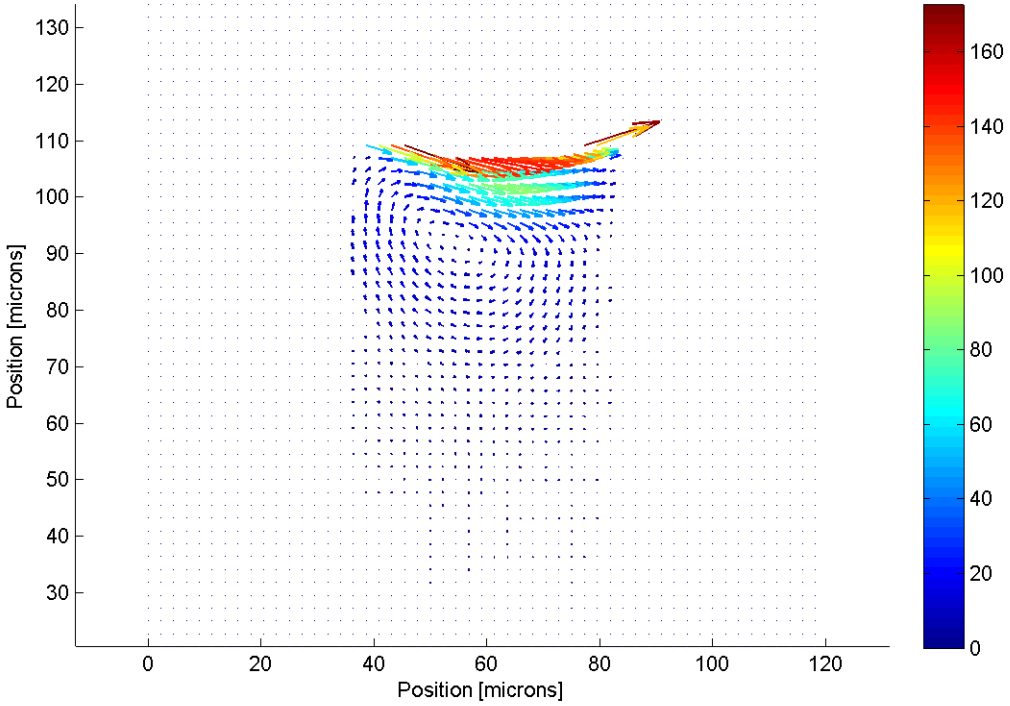

Figure E.48: Velocity field in the lower portion of the AR = 0.5 cavity at Re 50.

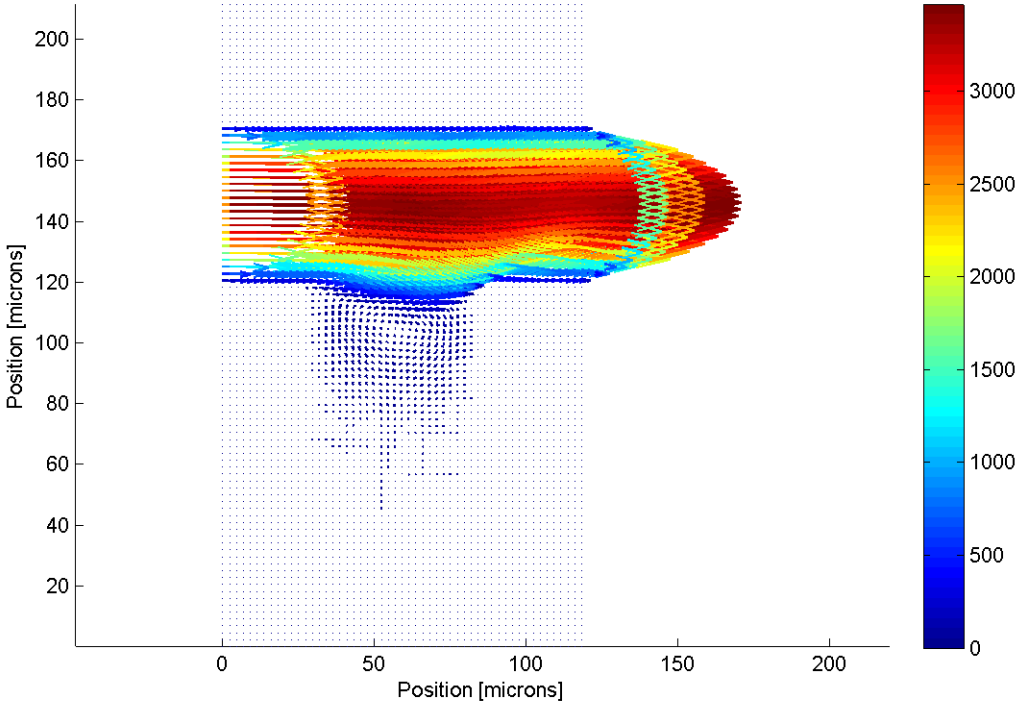

Figure E.49: Velocity field in the AR = 0.5 cavity at Re 100.

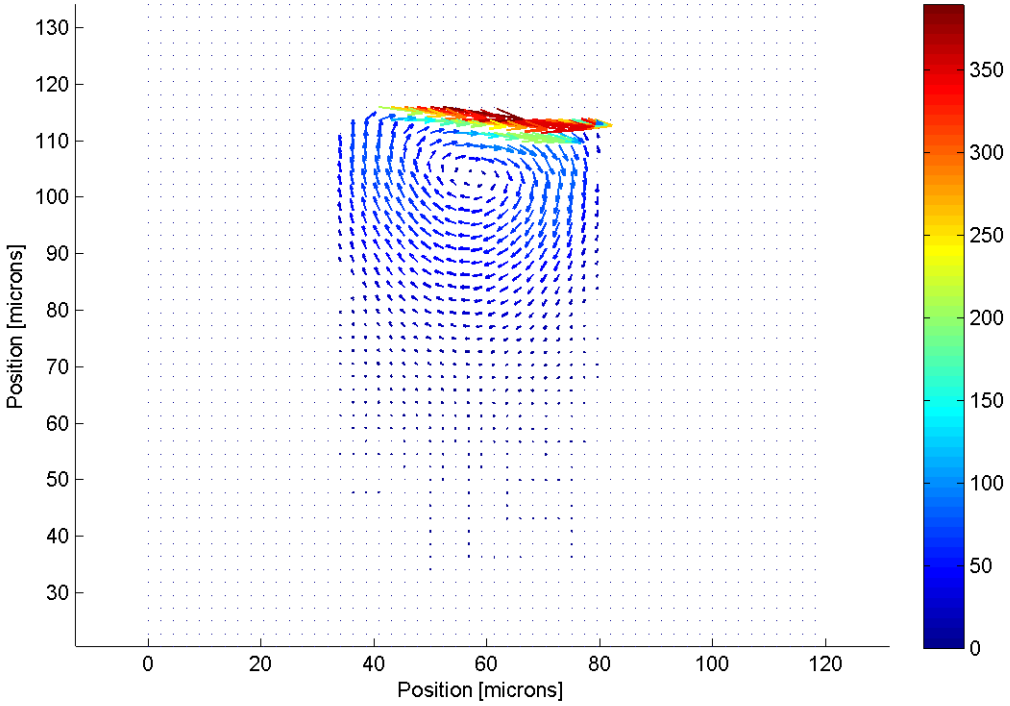

Figure E.50: Velocity field in the lower portion of the AR = 0.5 cavity at Re 100.

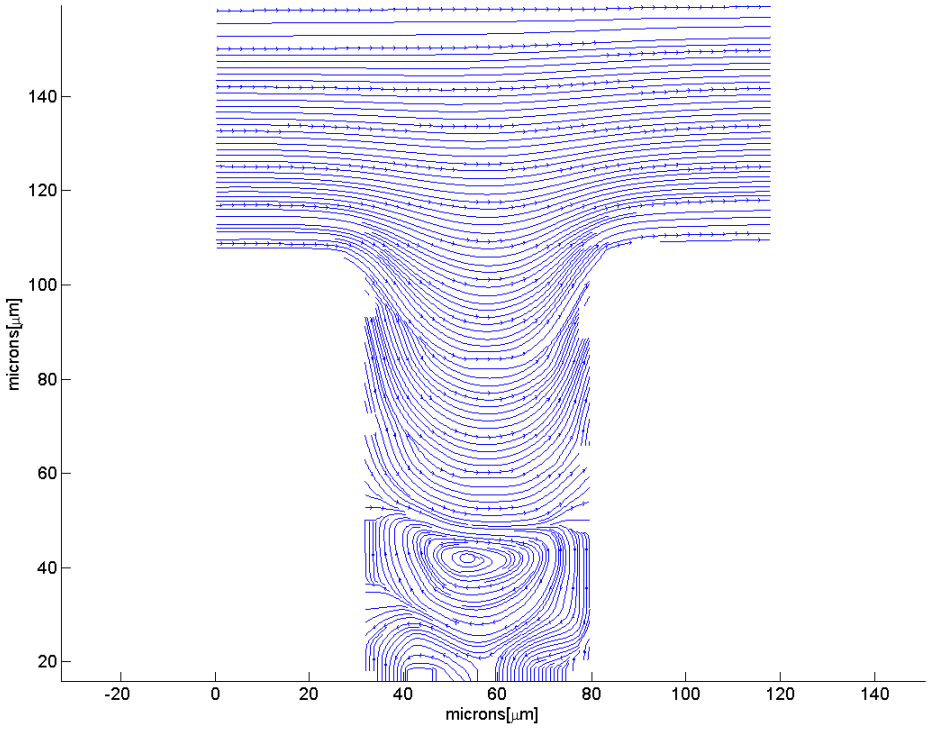

Figure E.51: A streamline image of steady flow in the AR = 0.5 cavity at Re = 17.

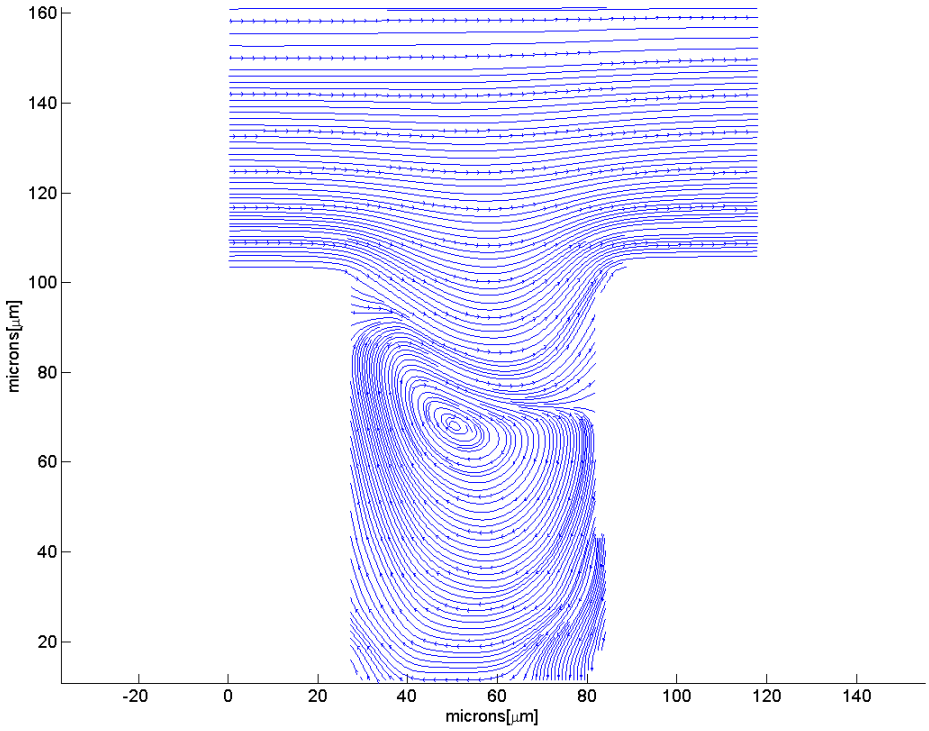

Figure E.52: A streamline image of steady flow in the AR = 0.5 cavity at Re 30.

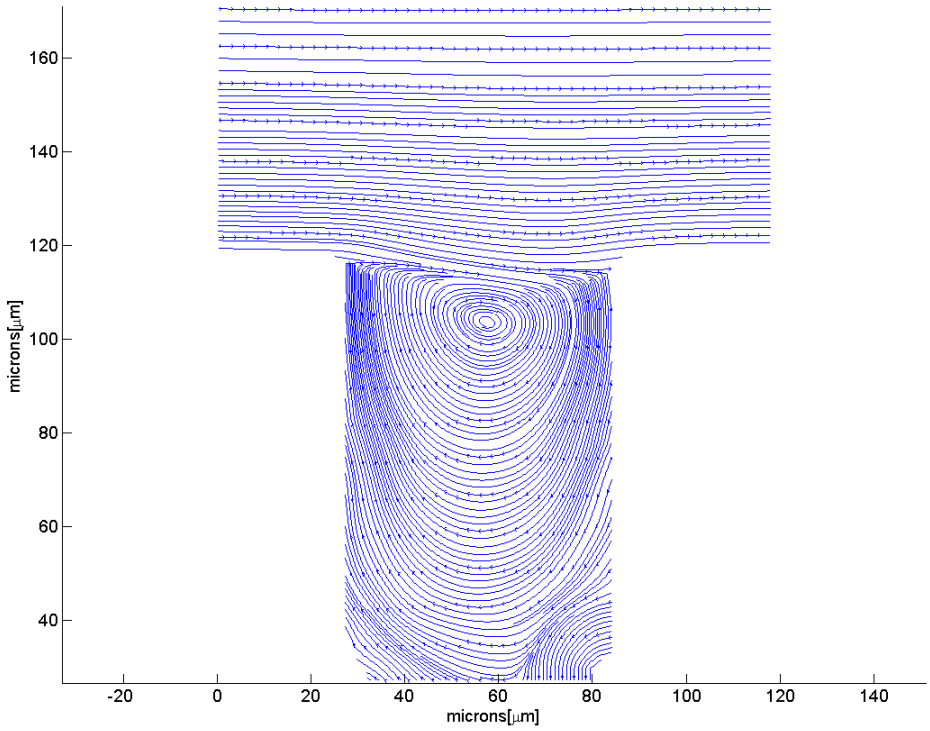

Figure E.53: A streamline image of steady flow in the AR = 0.5 cavity at Re 100.

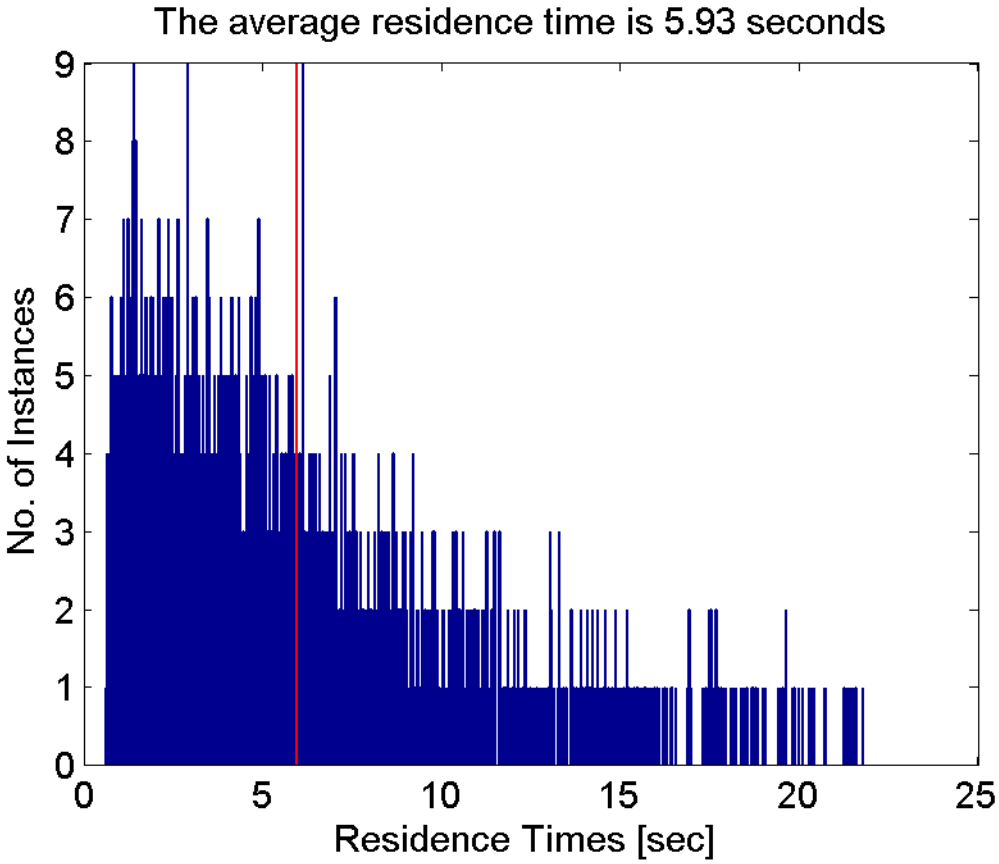

Figure E.54: The residence time distribution for the AR = 0.5 cavity at Re 0.1. The average residence time is 5.93 secs.

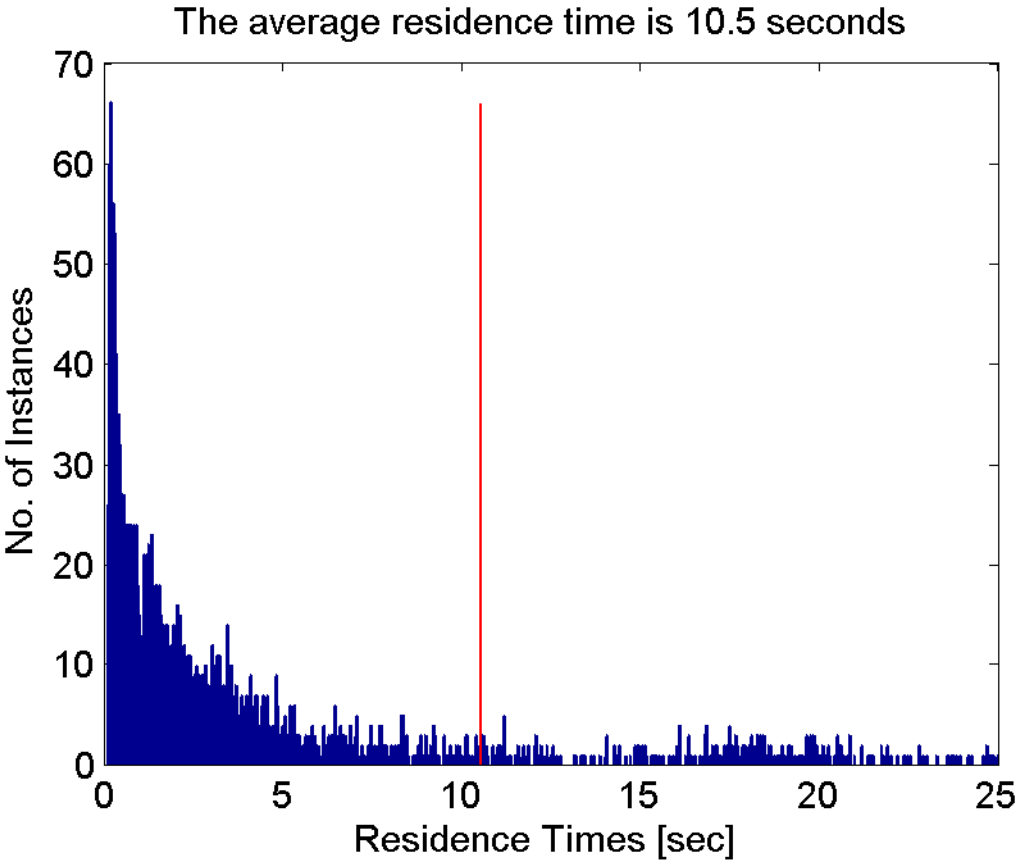

Figure E.55: The residence time distribution for the AR = 0.5 cavity at Re 15. The average residence time is 10.5 secs.

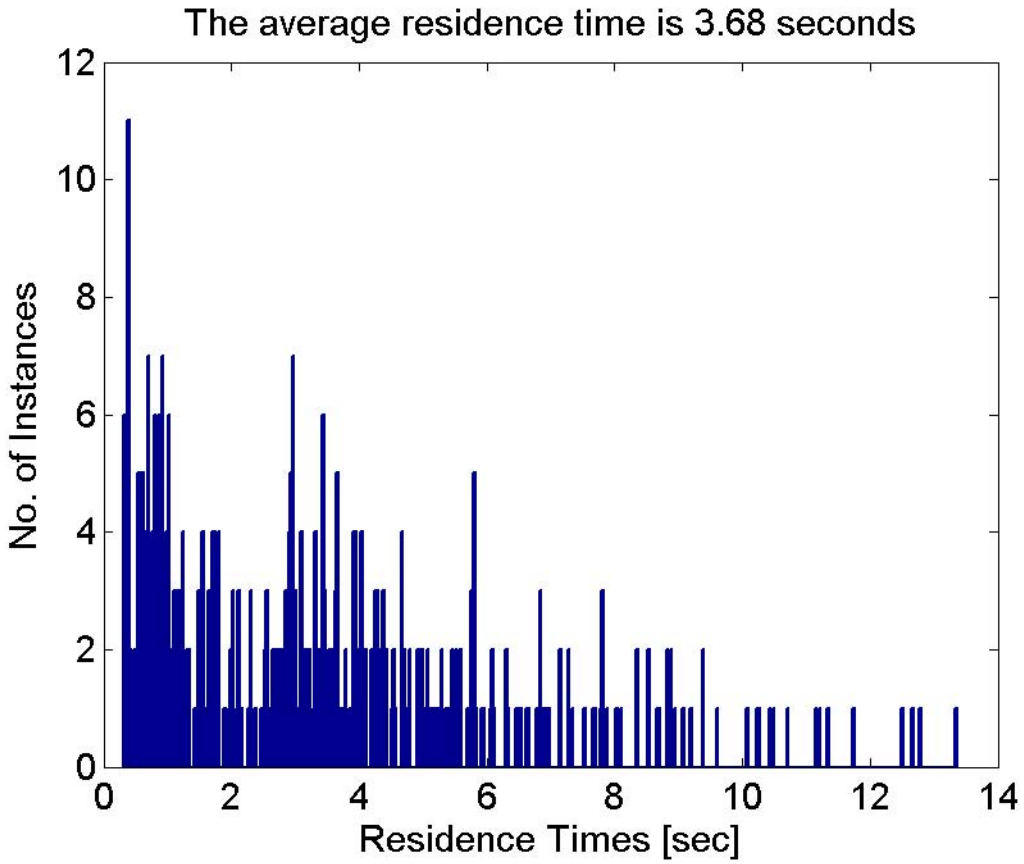

Figure E.56: The residence time distribution for the AR = 0.5 cavity at Re 17. The average residence time is 3.68 secs.

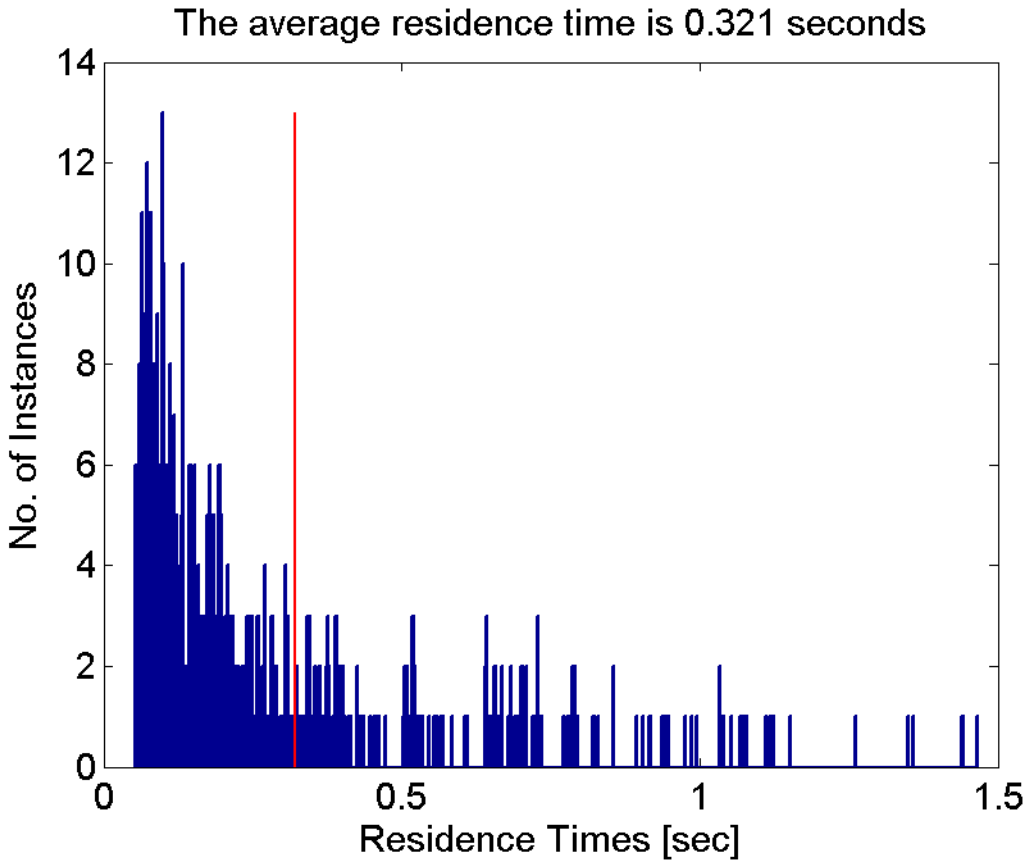

Figure E.57: The residence time distribution for the AR = 0.5 cavity at Re 20. The average residence time is 0.321 secs.

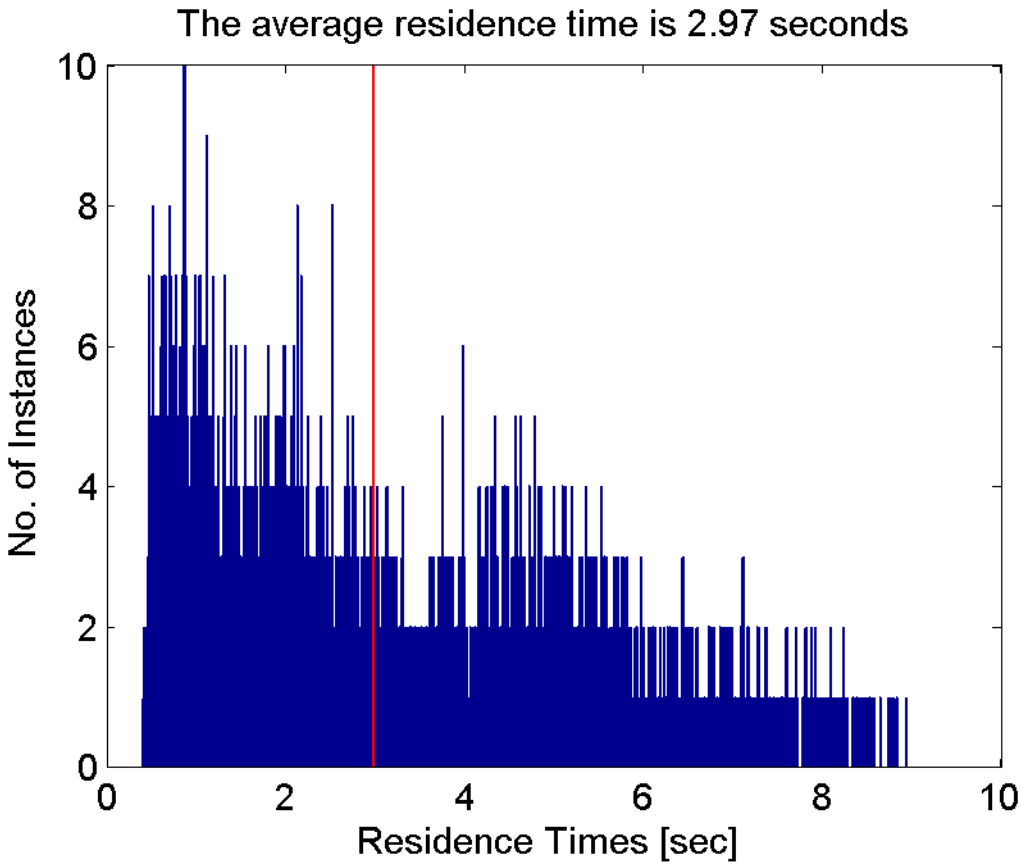

Figure E.58: The residence time distribution for the AR = 0.5 cavity at Re 27. The average residence time is 2.97 secs.

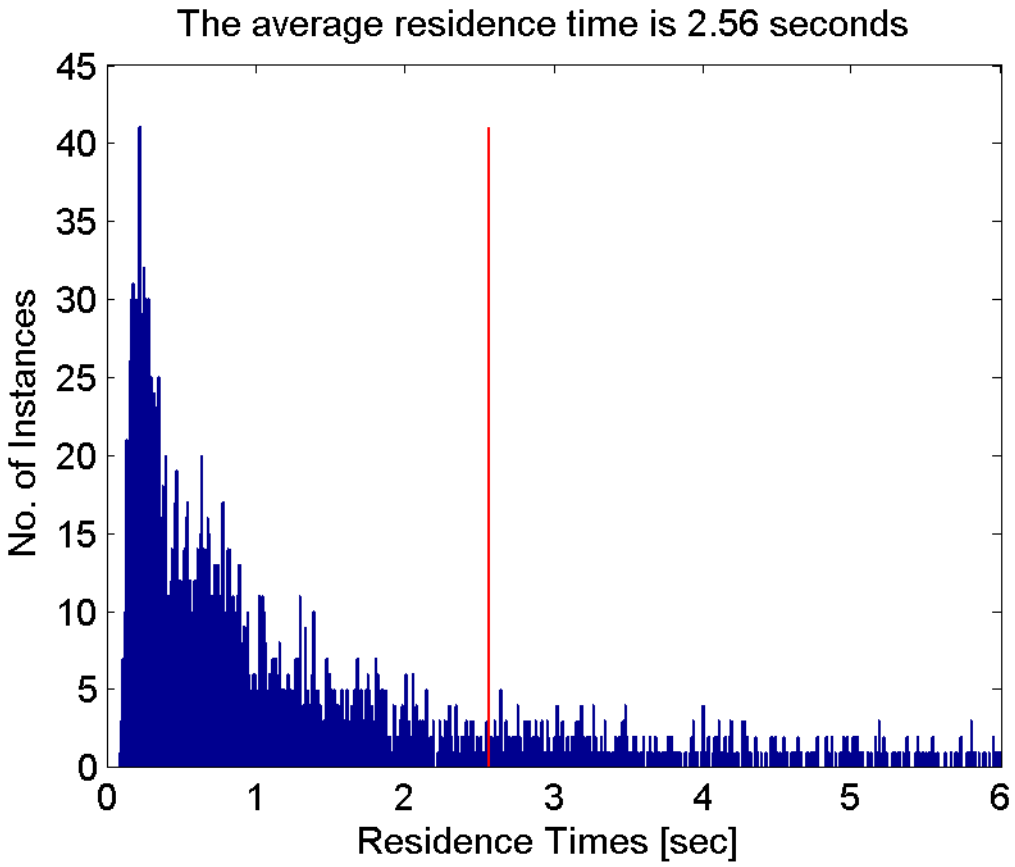

Figure E.59: The residence time distribution for the AR = 0.5 cavity at Re 30. The average residence time is 2.56 secs.

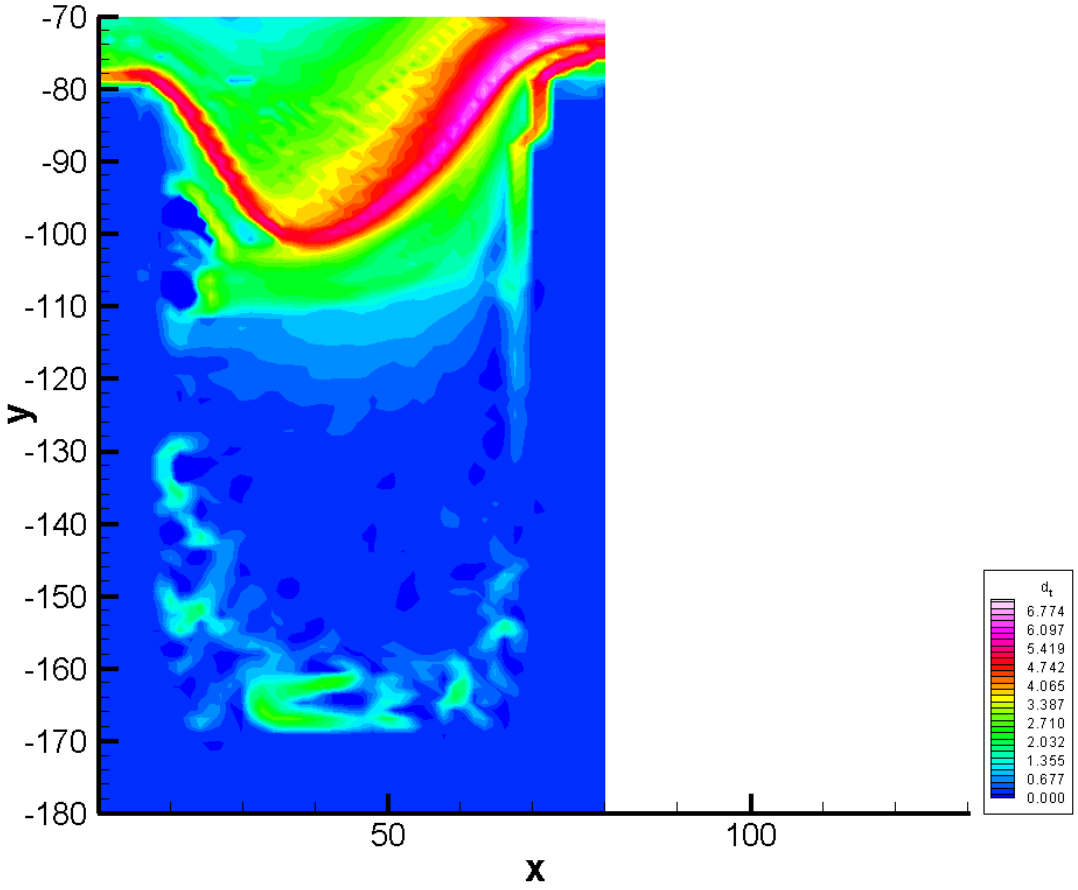

Figure E.60: The backward time LCS for the AR = 0.5 cavity at Re 0.1.

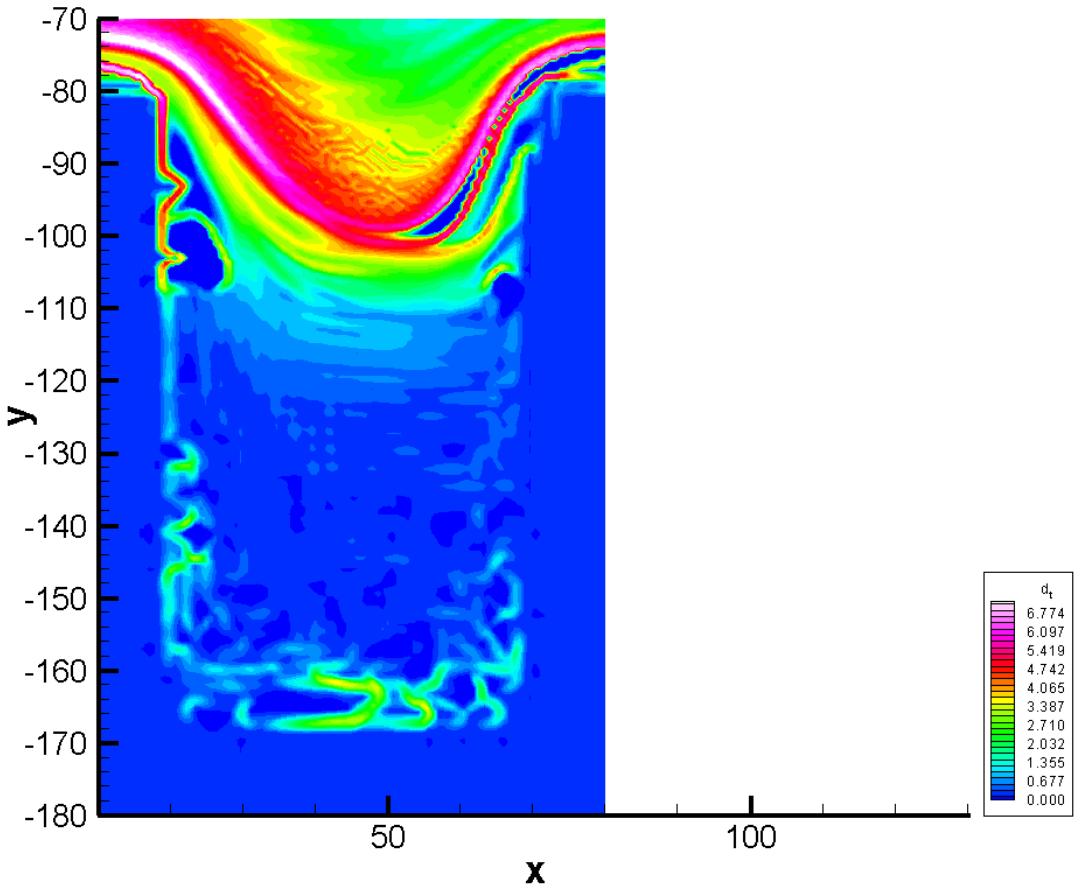

Figure E.61: The forward time LCS for the AR = 0.5 cavity at Re 0.1.

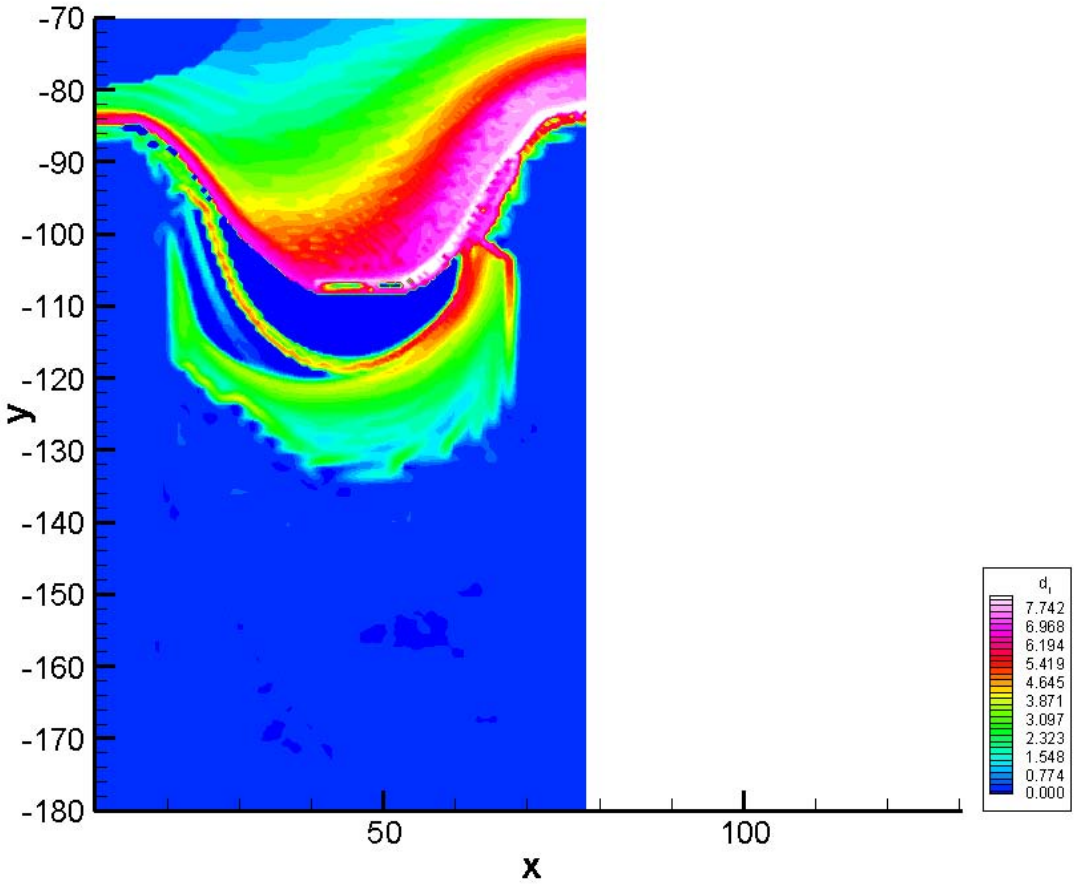

Figure E.62: The backward time LCS for the AR = 0.5 cavity at Re 17.

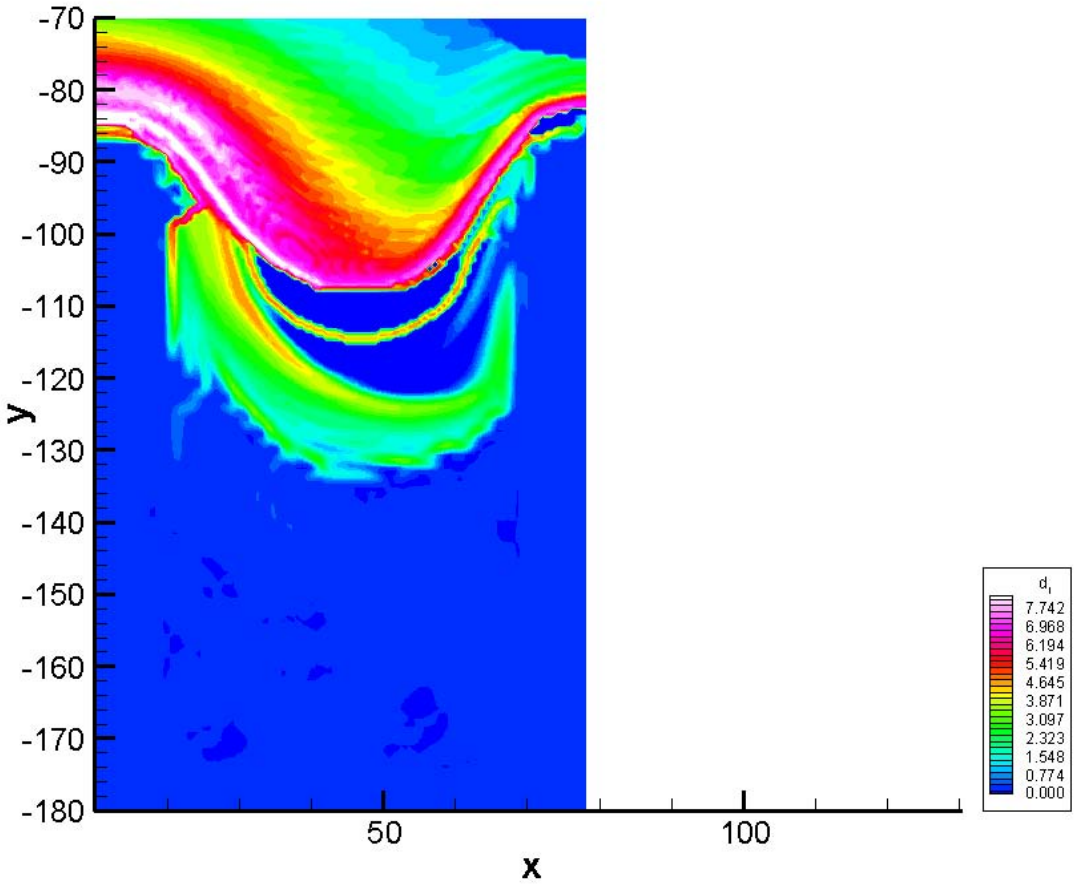

Figure E.63: The forward time LCS for the AR = 0.5 cavity at Re 17.

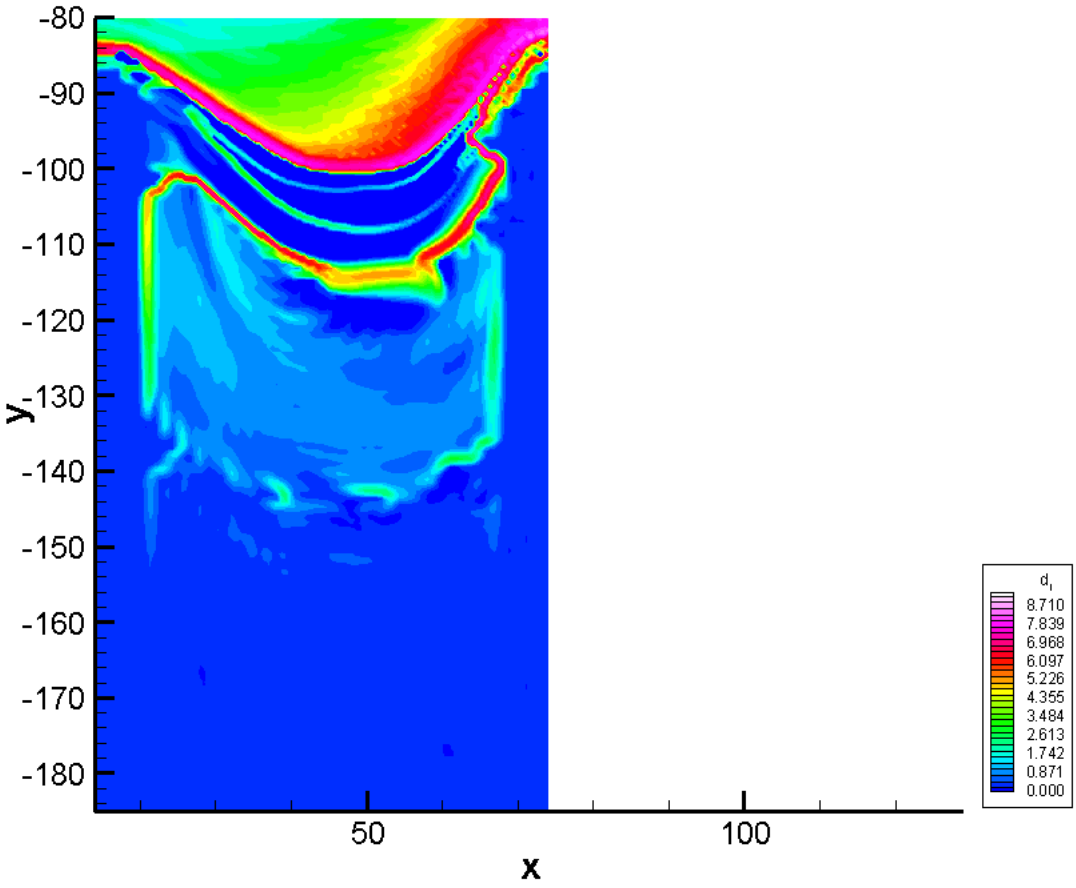

Figure E.64: The backward time LCS for the AR = 0.5 cavity at Re 30.

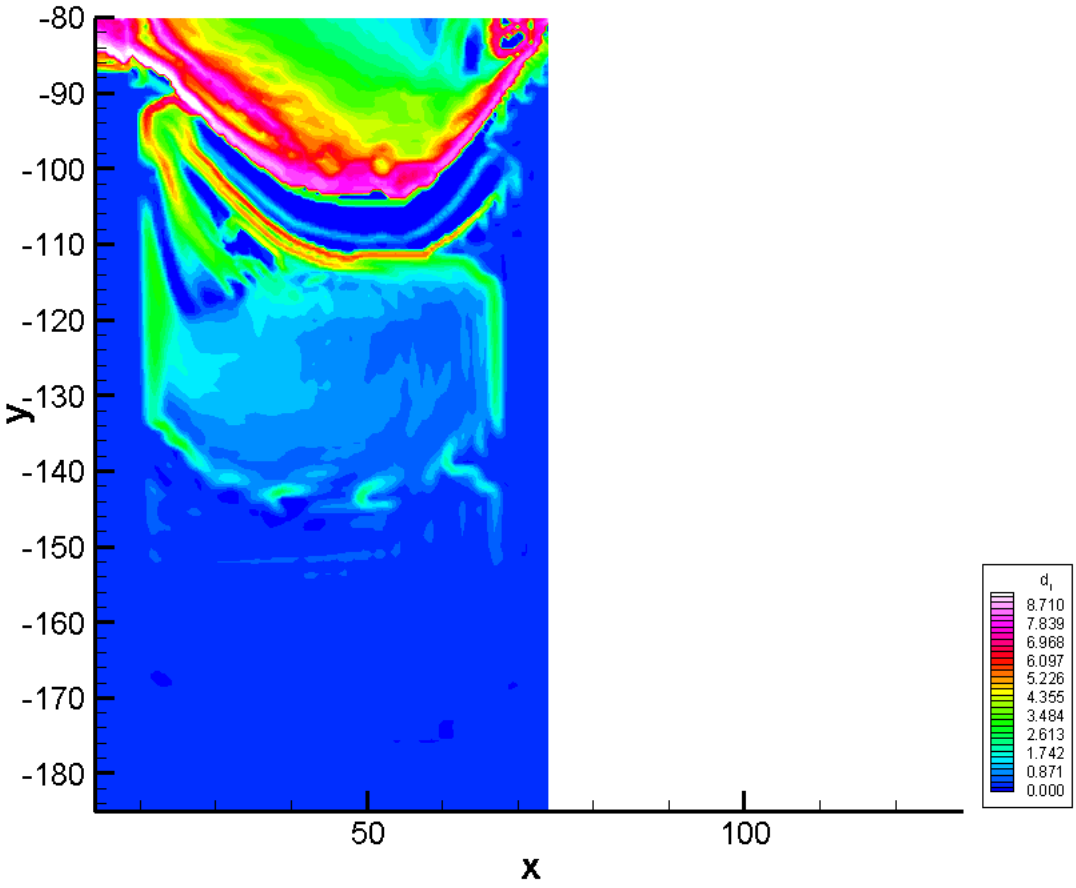

Figure E.65: The forward time LCS for the AR = 0.5 cavity at Re 30.

Appendix F

Supplementary data for Chapter 2 - Pulsatile cavity flow

F.1 13 Hz

F.1.1 Velocity field data at 13 Hz

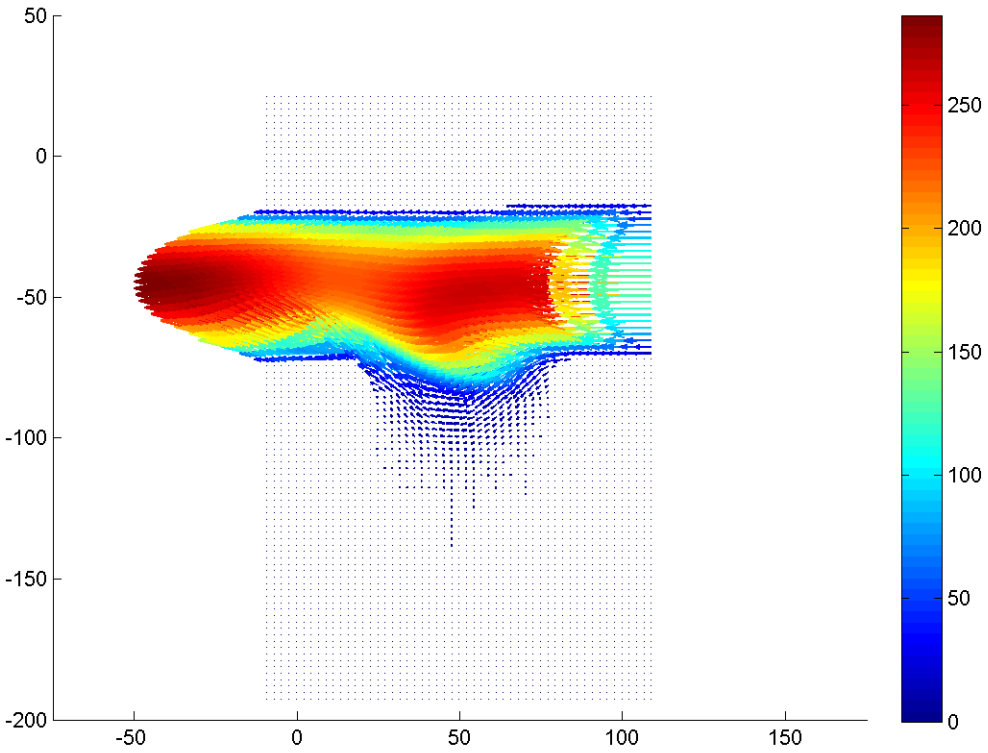

Figure F.1: Velocity field during phase increment 1 at 13 Hz with a Re of 0.1.

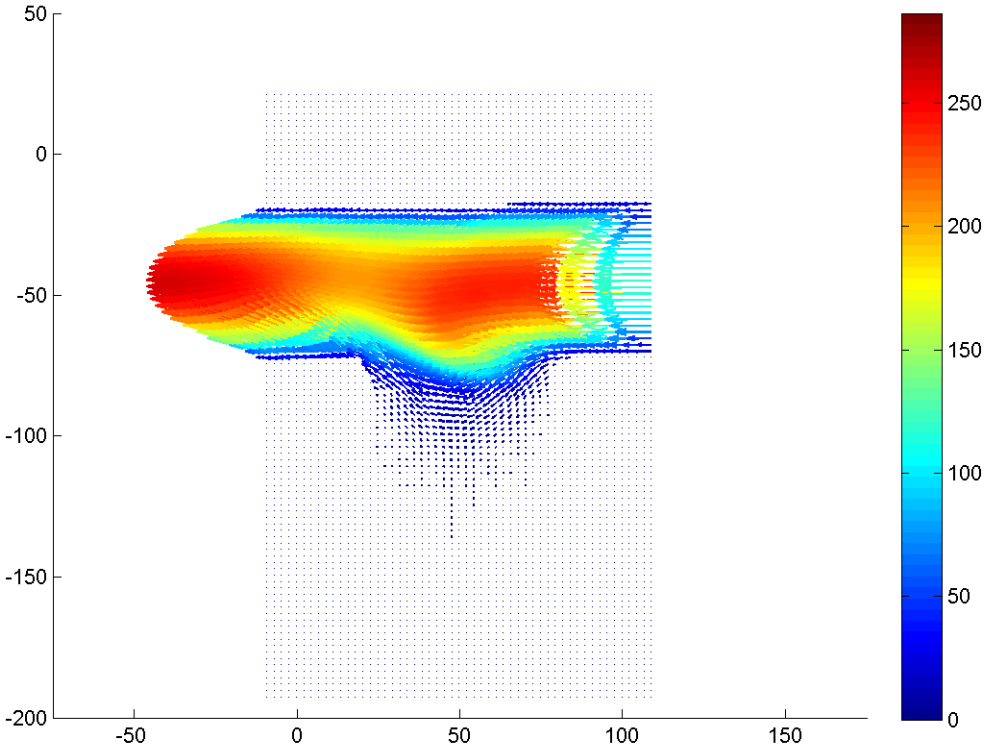

Figure F.2: Velocity field during phase increment 2 at 13 Hz with a Re of 0.1.

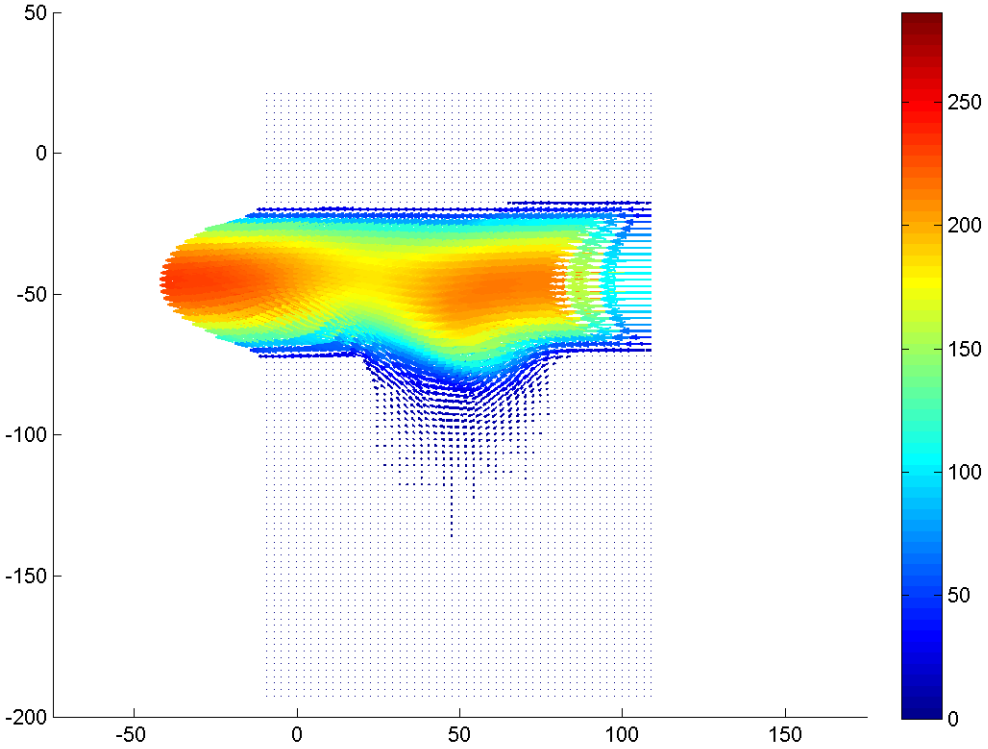

Figure F.3: Velocity field during phase increment 3 at 13 Hz with a Re of 0.1.

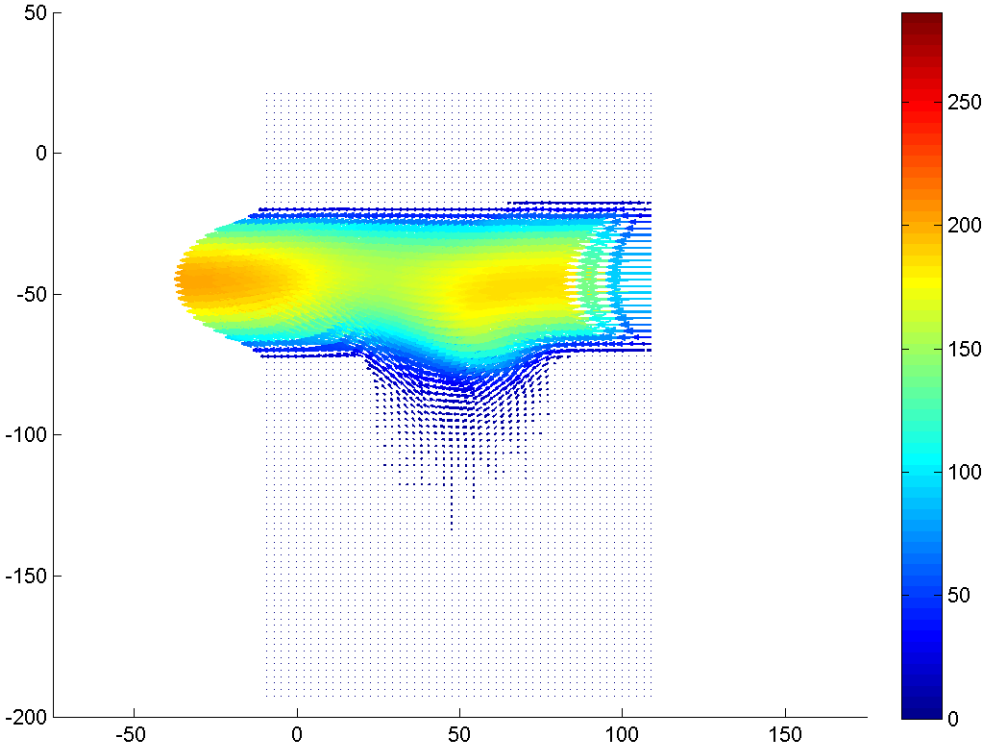

Figure F.4: Velocity field during phase increment 4 at 13 Hz with a Re of 0.1.

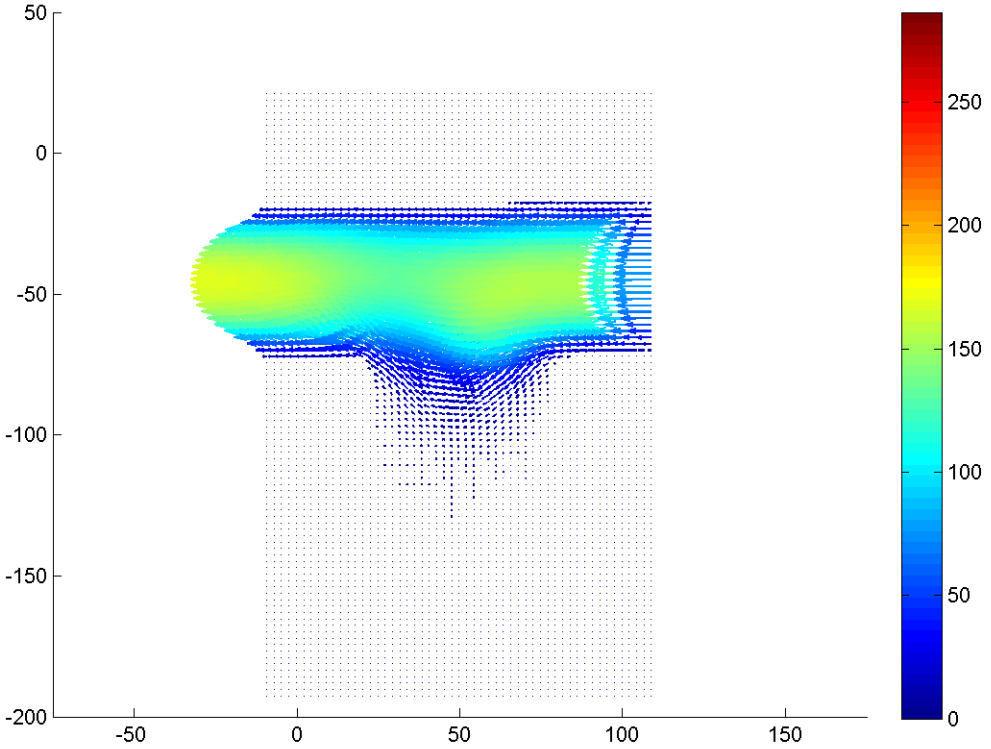

Figure F.5: Velocity field during phase increment 5 at 13 Hz with a Re of 0.1.

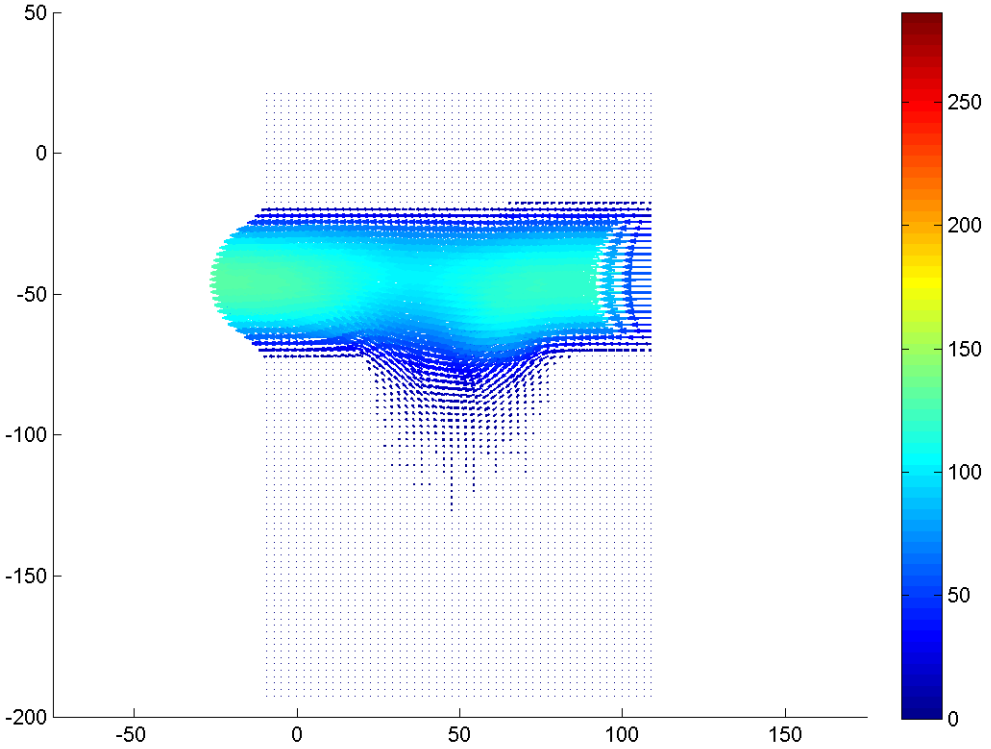

Figure F.6: Velocity field during phase increment 6 at 13 Hz with a Re of 0.1.

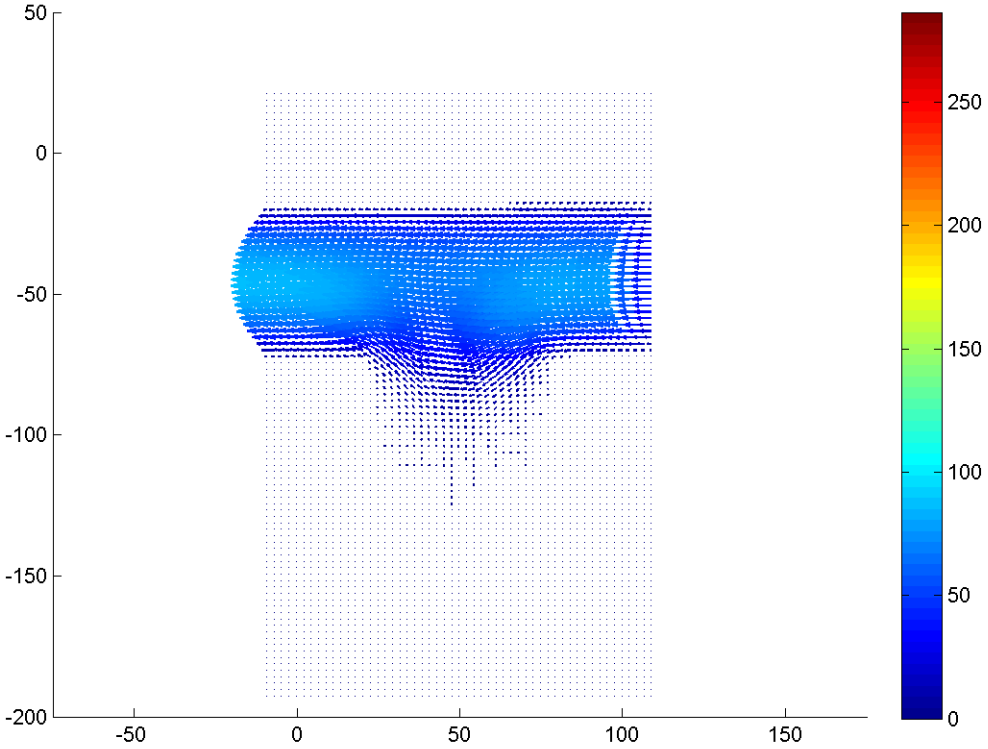

Figure F.7: Velocity field during phase increment 7 at 13 Hz with a Re of 0.1.

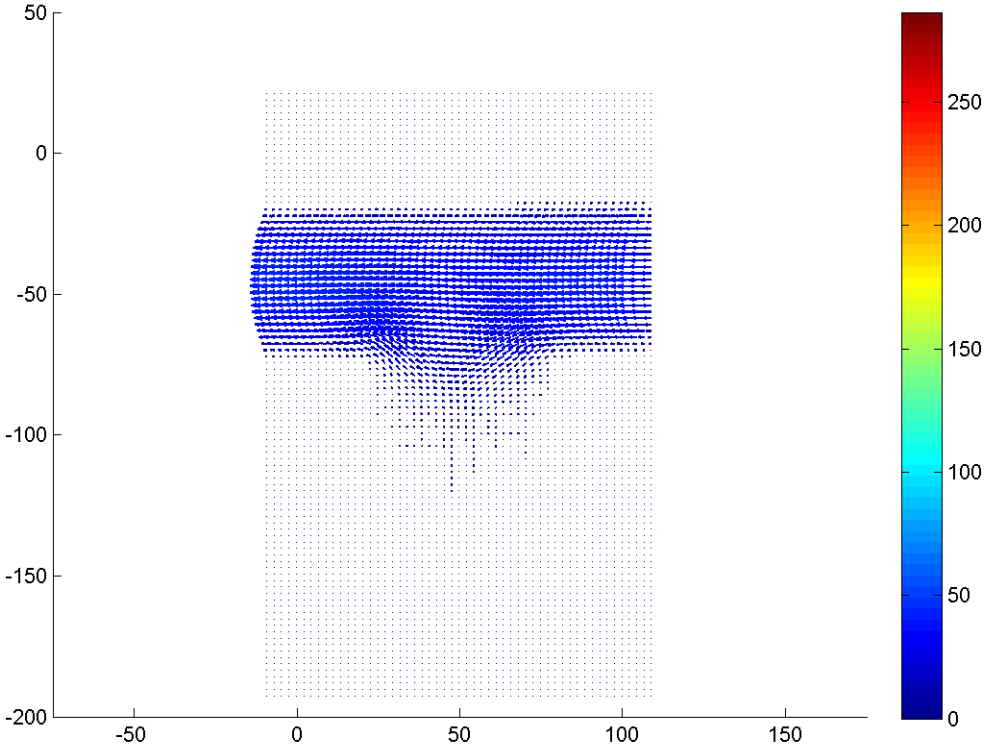

Figure F.8: Velocity field during phase increment 8 at 13 Hz with a Re of 0.1.

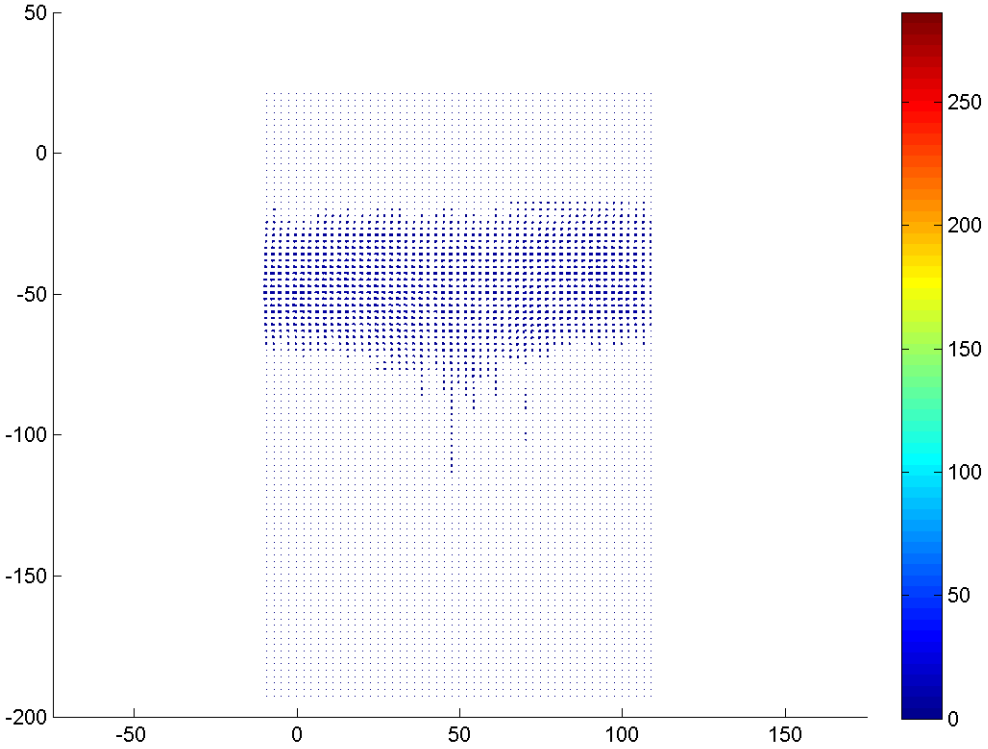

Figure F.9: Velocity field during phase increment 9 at 13 Hz with a Re of 0.1.

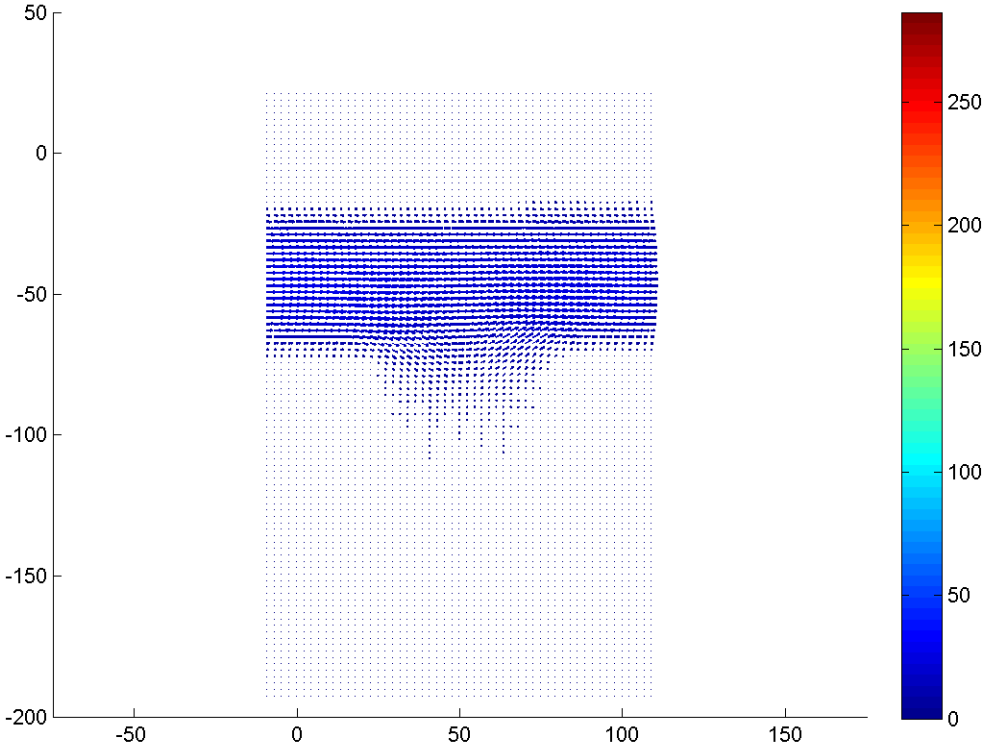

Figure F.10: Velocity field during phase increment 10 at 13 Hz with a Re of 0.1.

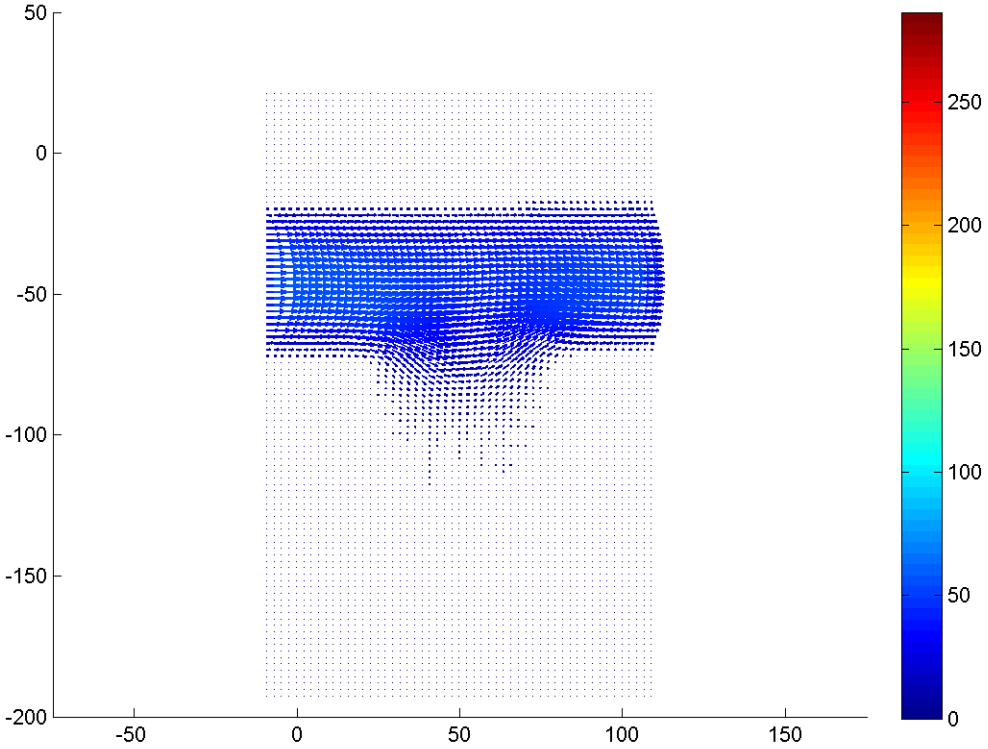

Figure F.11: Velocity field during phase increment 11 at 13 Hz with a Re of 0.1.

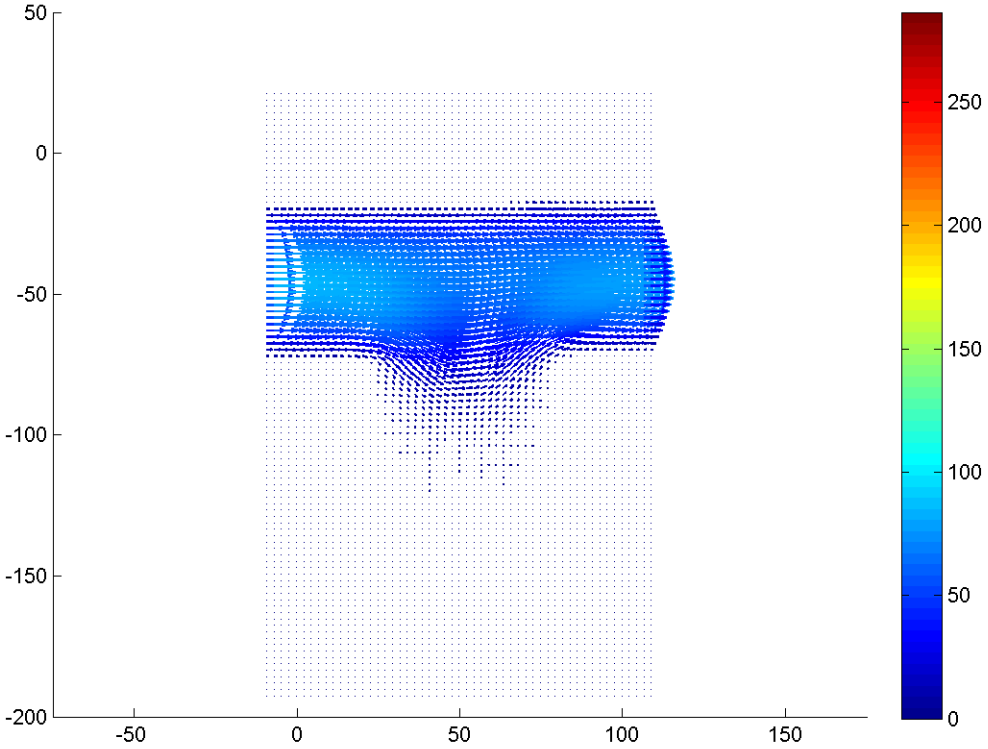

Figure F.12: Velocity field during phase increment 12 at 13 Hz with a Re of 0.1.

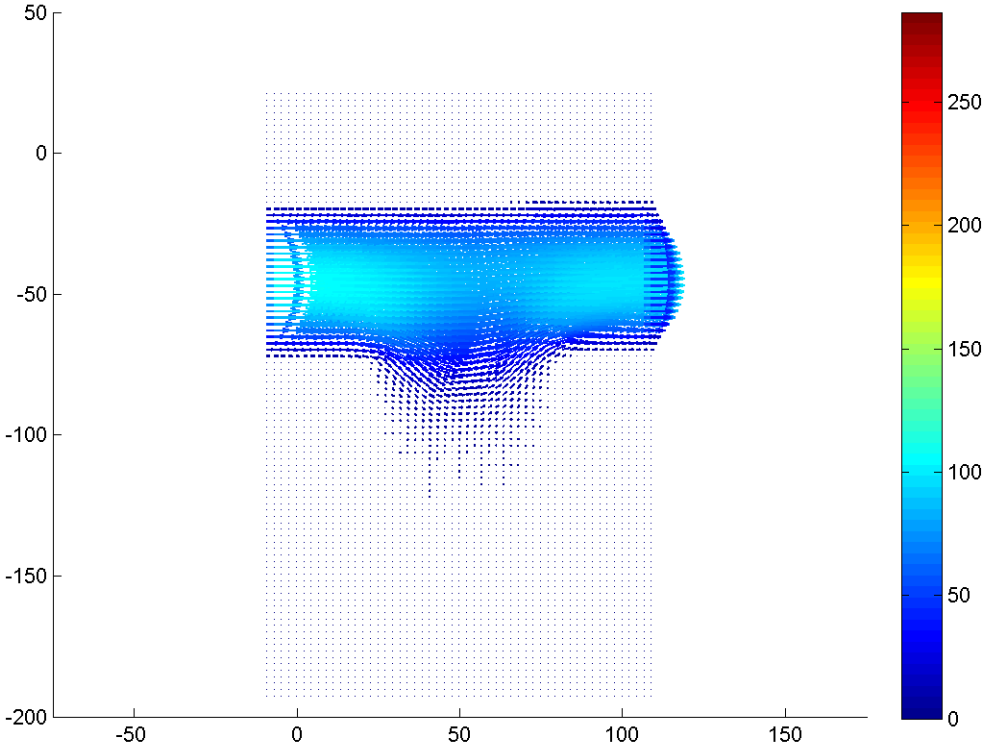

Figure F.13: Velocity field during phase increment 13 at 13 Hz with a Re of 0.1.

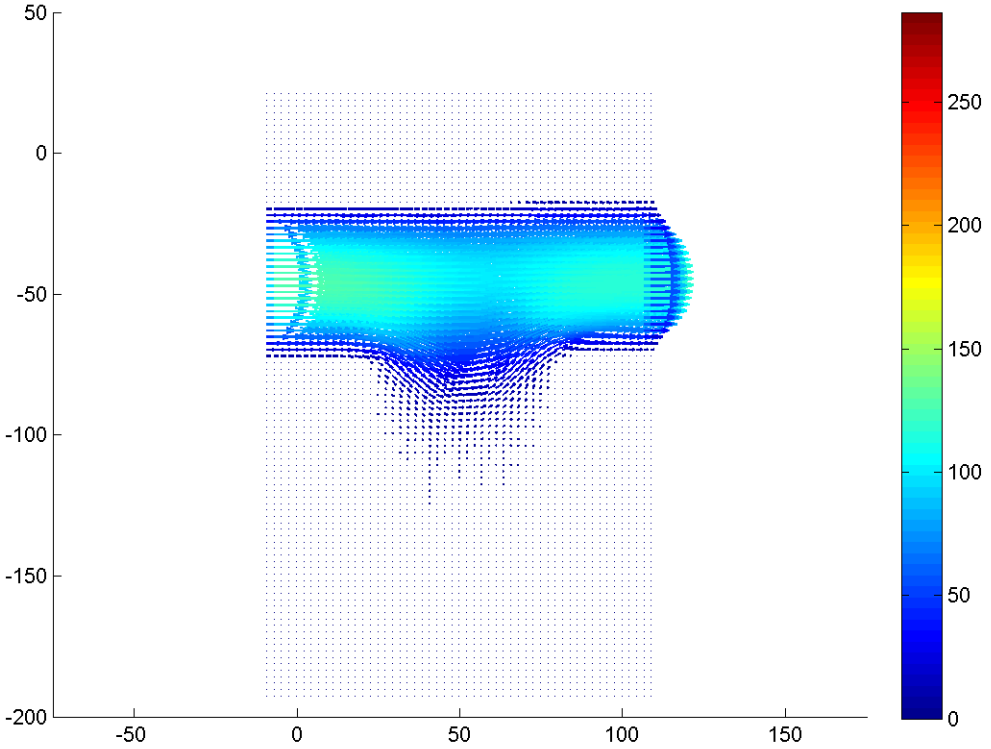

Figure F.14: Velocity field during phase increment 14 at 13 Hz with a Re of 0.1.

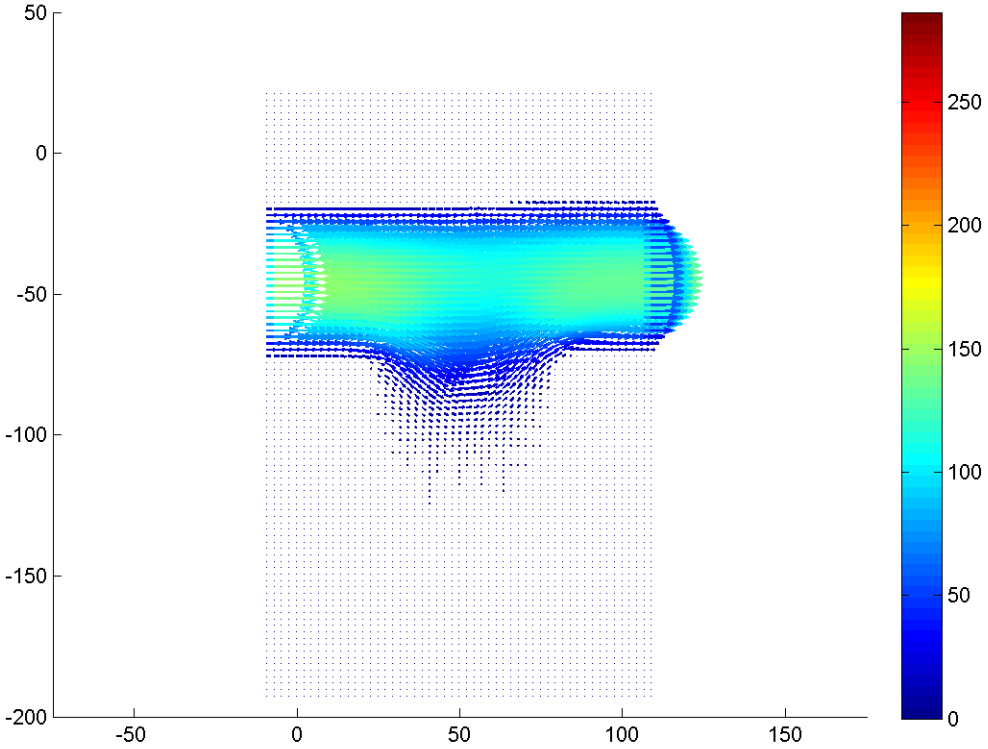

Figure F.15: Velocity field during phase increment 15 at 13 Hz with a Re of 0.1.

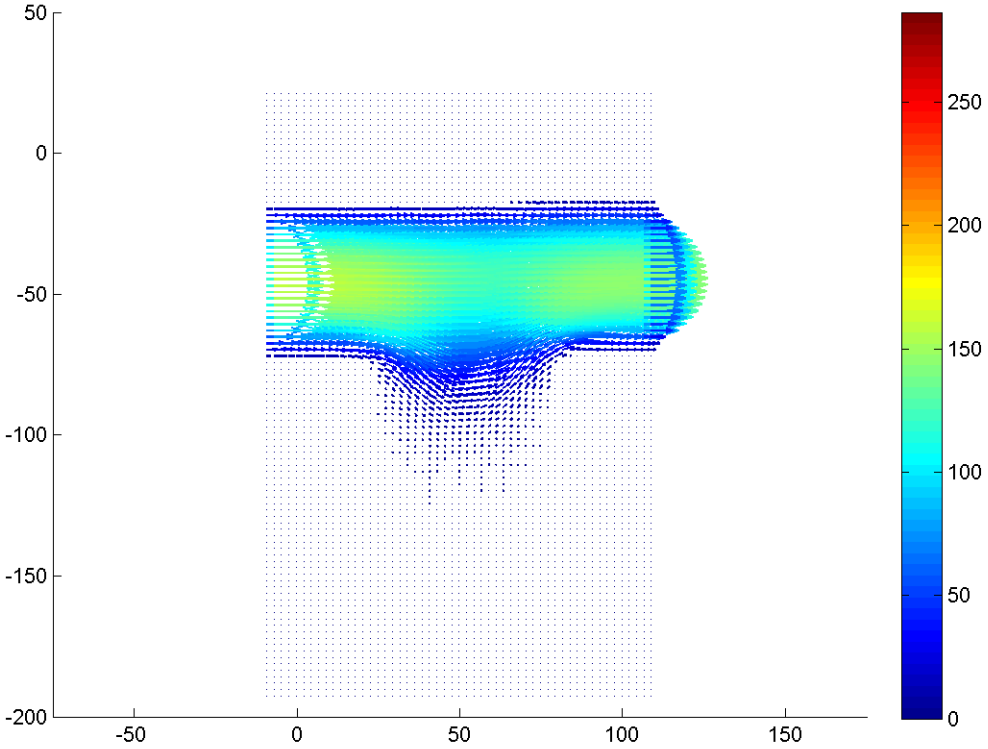

Figure F.16: Velocity field during phase increment 16 at 13 Hz with a Re of 0.1.

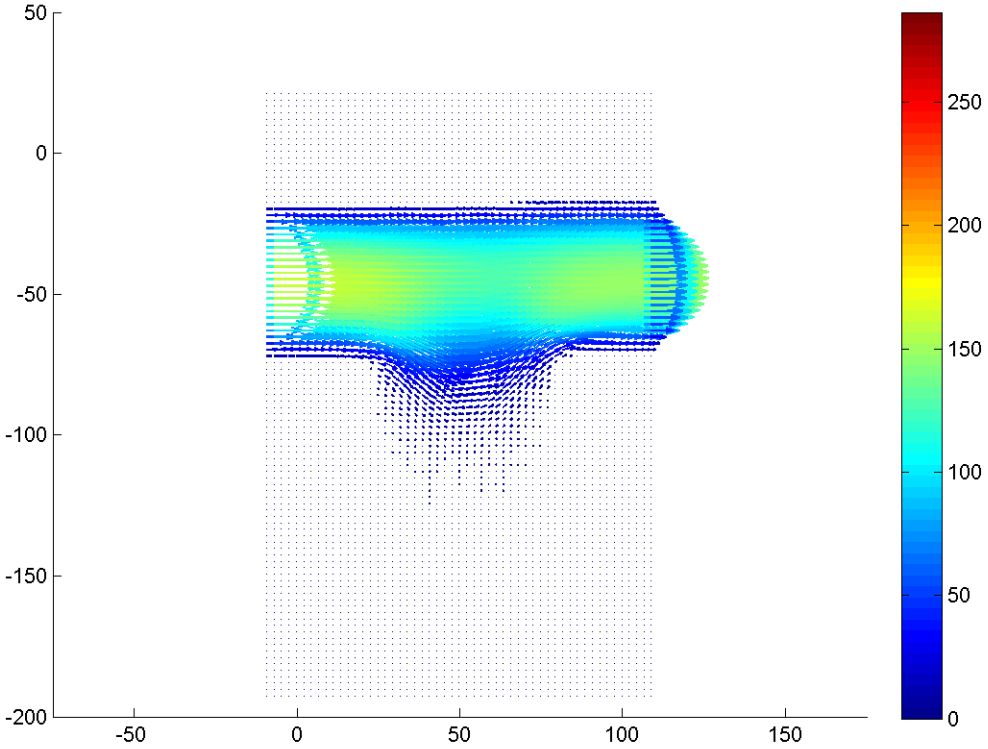

Figure F.17: Velocity field during phase increment 17 at 13 Hz with a Re of 0.1.

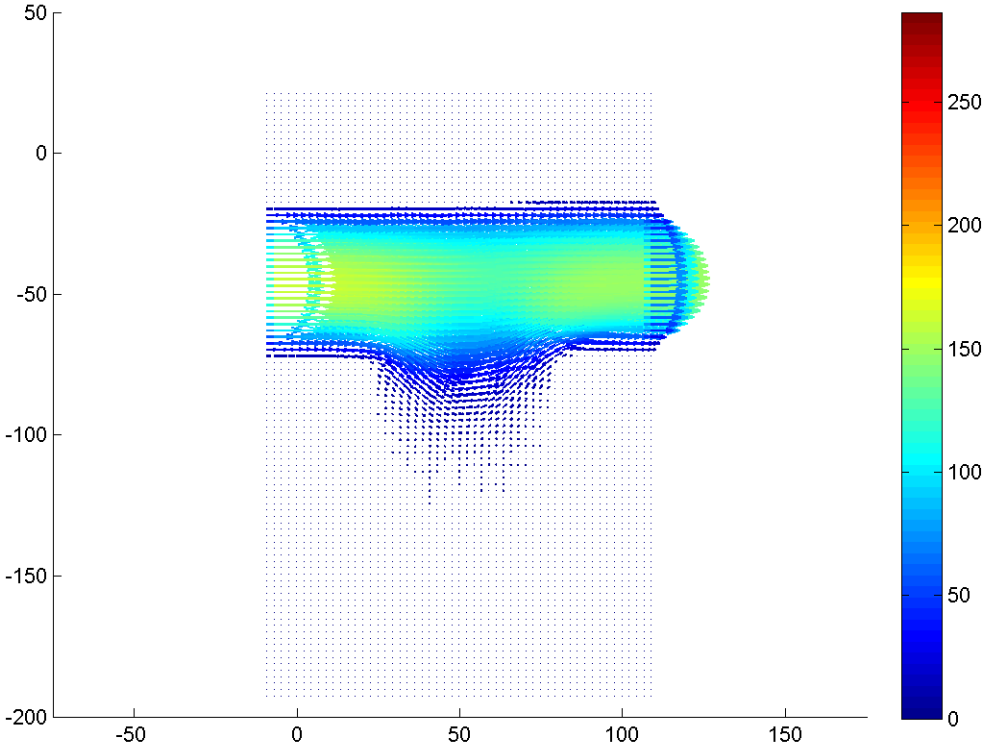

Figure F.18: Velocity field during phase increment 18 at 13 Hz with a Re of 0.1.

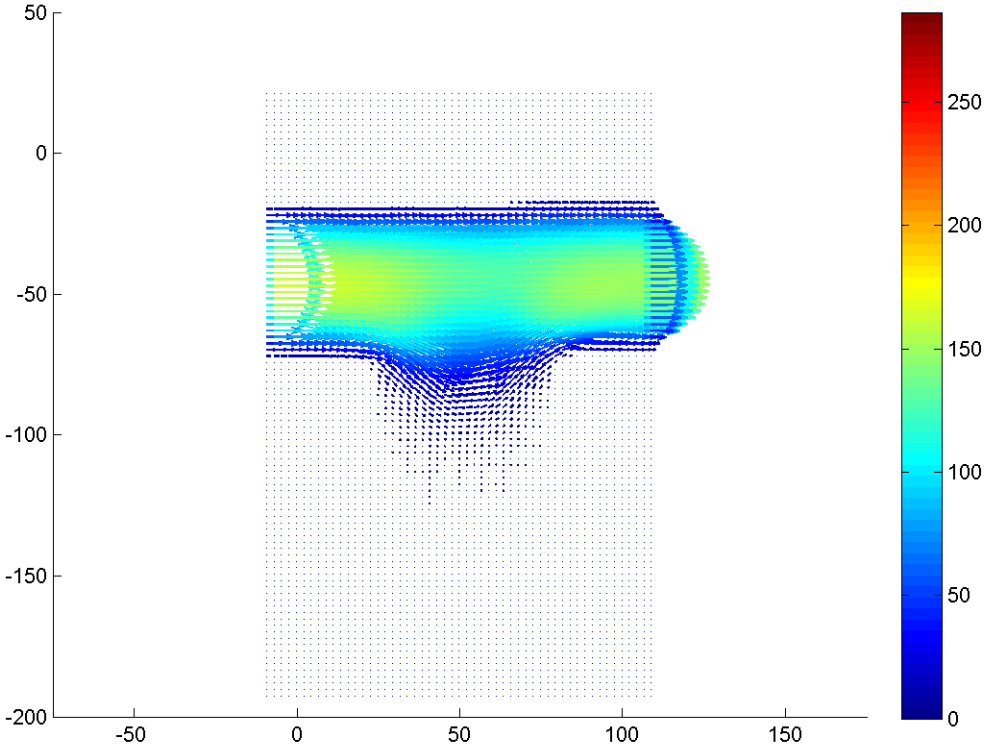

Figure F.19: Velocity field during phase increment 18 at 13 Hz with a Re of 0.1.

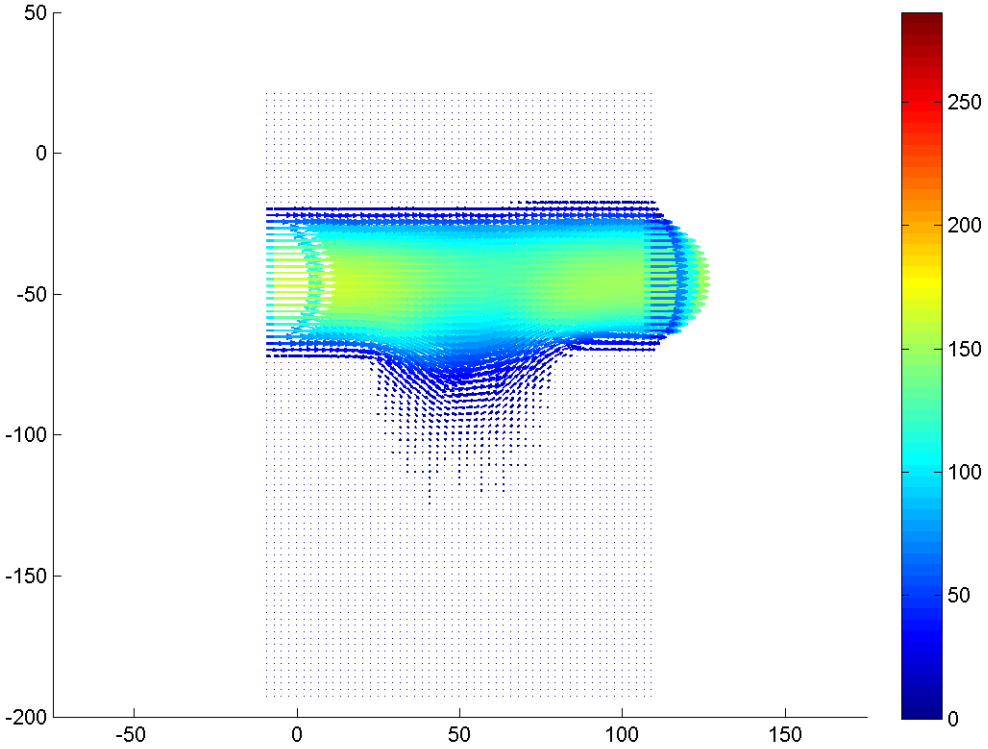

Figure F.20: Velocity field during phase increment 20 at 13 Hz with a Re of 0.1.

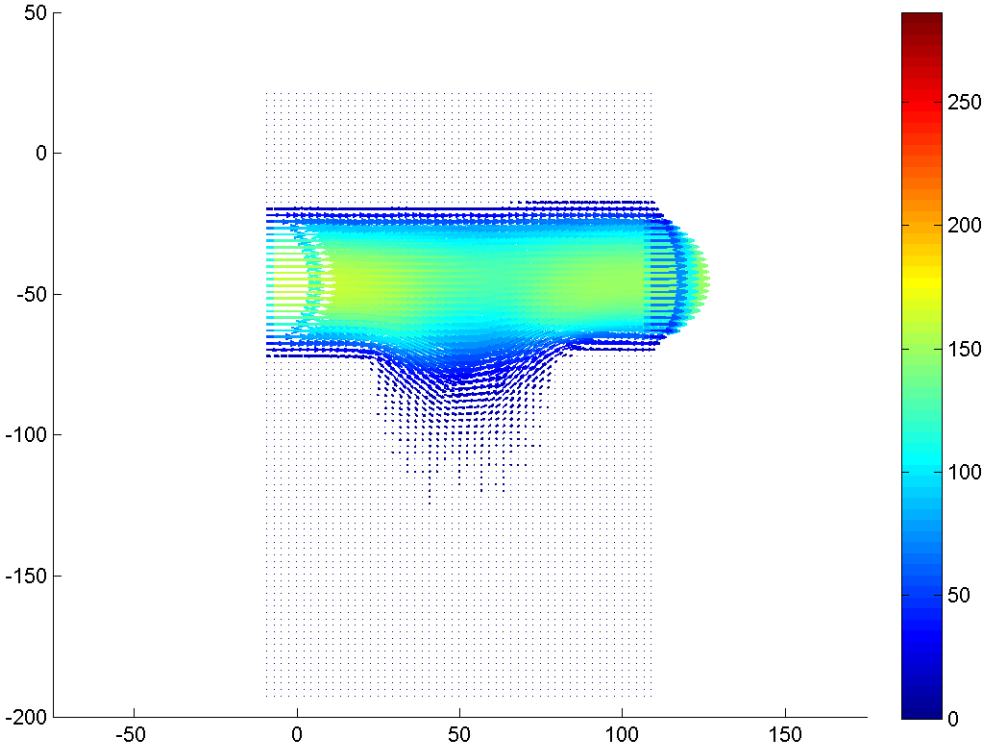

Figure F.21: Velocity field during phase increment 21 at 13 Hz with a Re of 0.1.

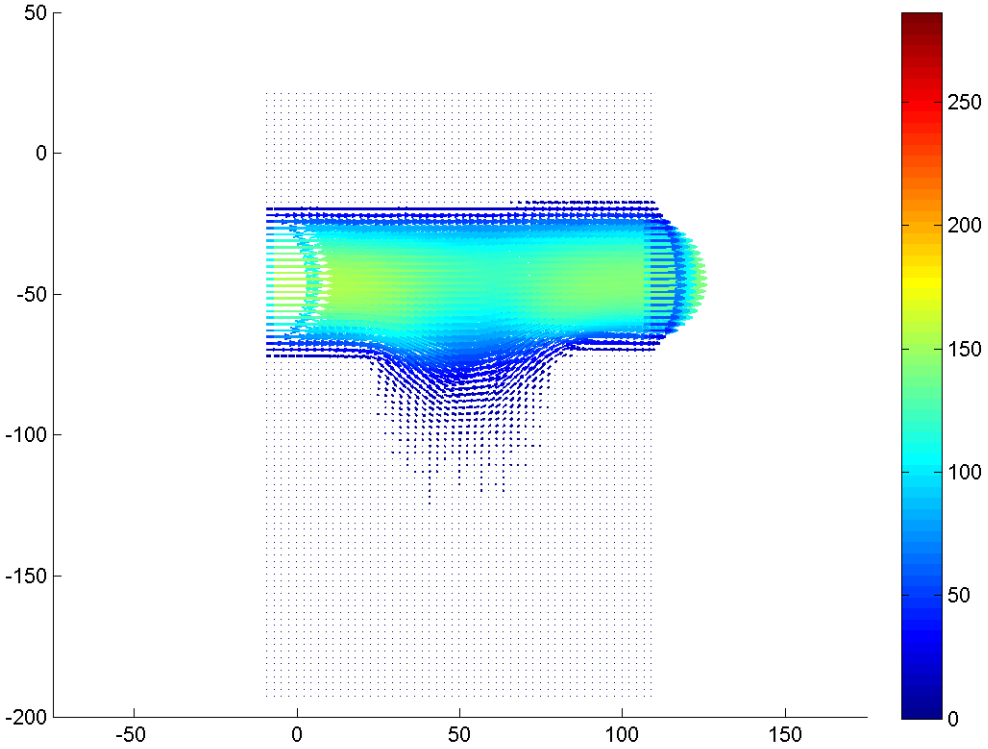

Figure F.22: Velocity field during phase increment 22 at 13 Hz with a Re of 0.1.

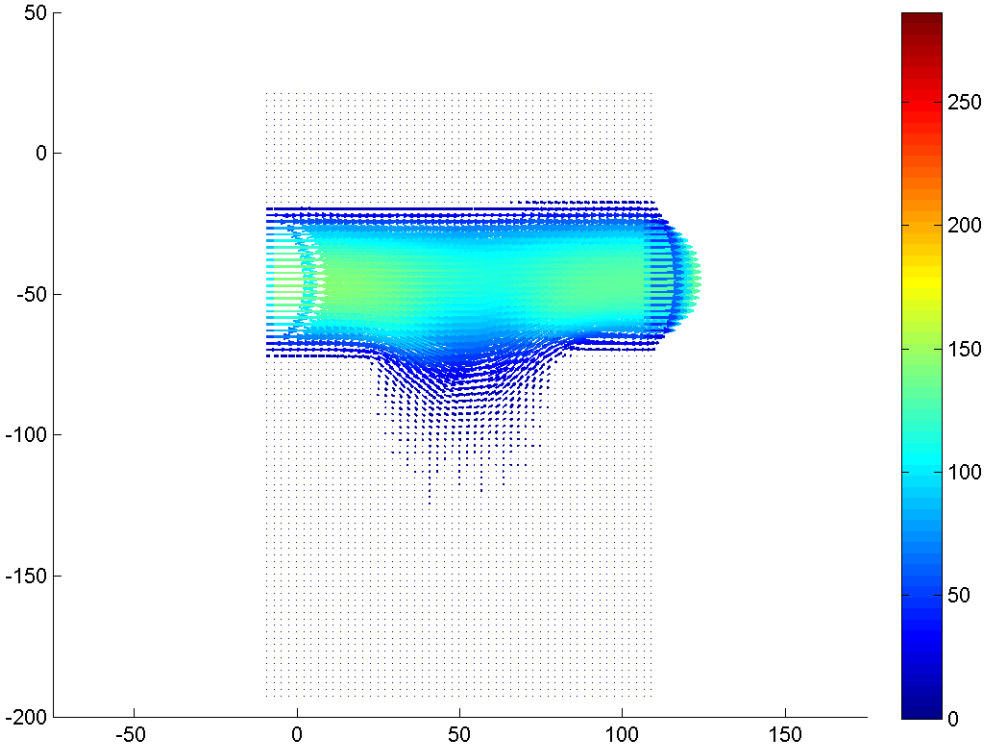

Figure F.23: Velocity field during phase increment 23 at 13 Hz with a Re of 0.1.

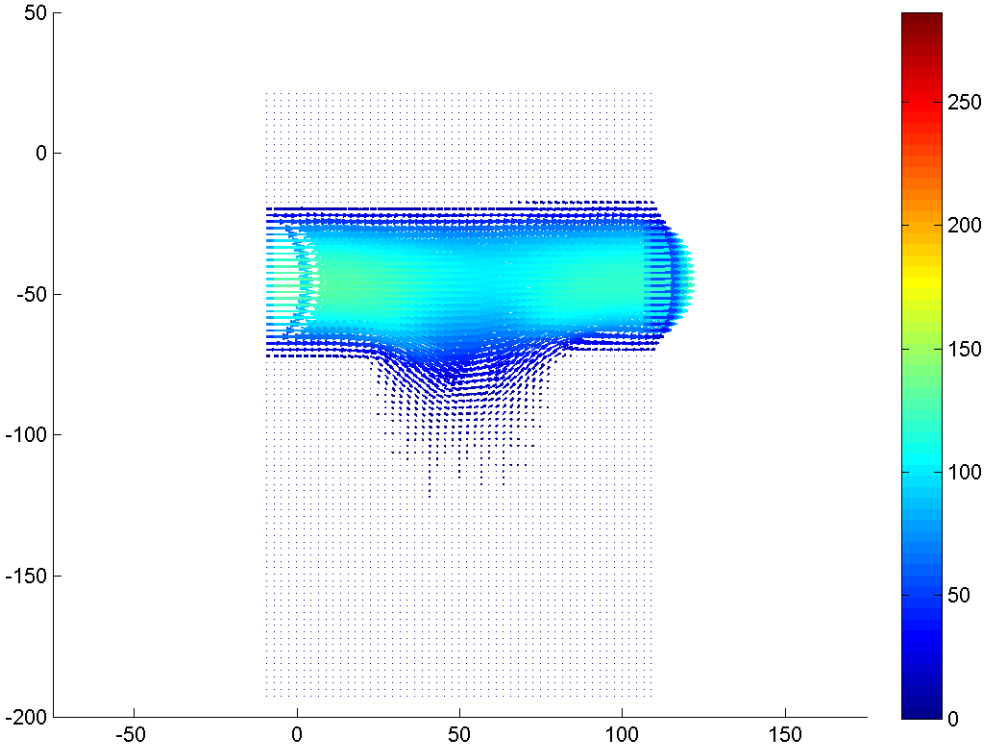

Figure F.24: Velocity field during phase increment 24 at 13 Hz with a Re of 0.1.

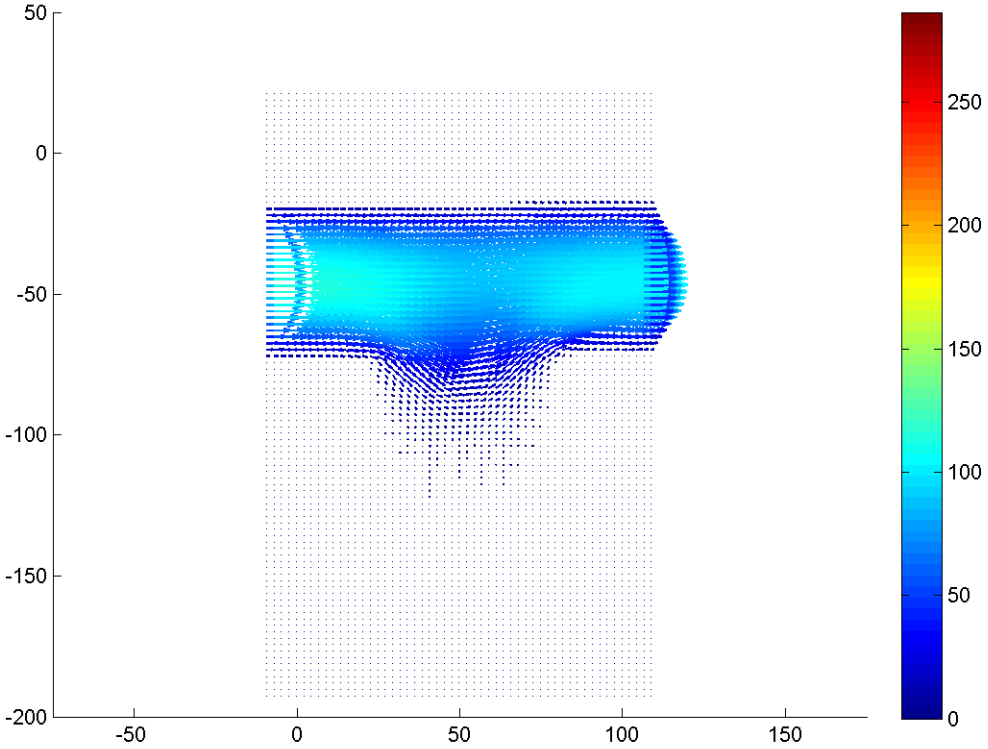

Figure F.25: Velocity field during phase increment 25 at 13 Hz with a Re of 0.1.

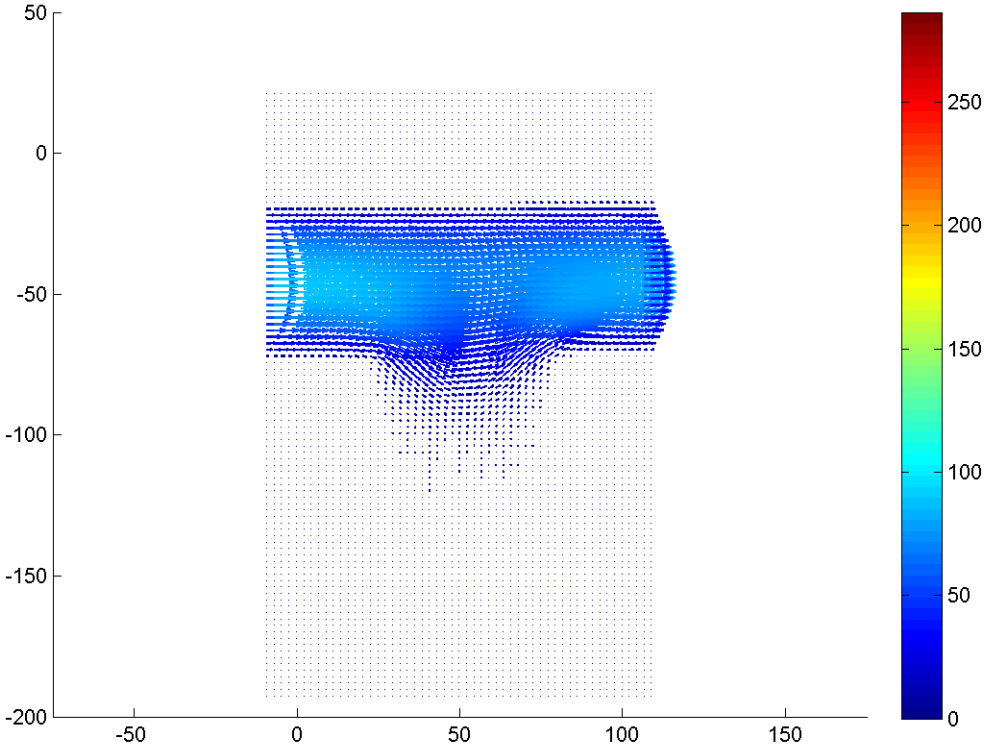

Figure F.26: Velocity field during phase increment 26 at 13 Hz with a Re of 0.1.

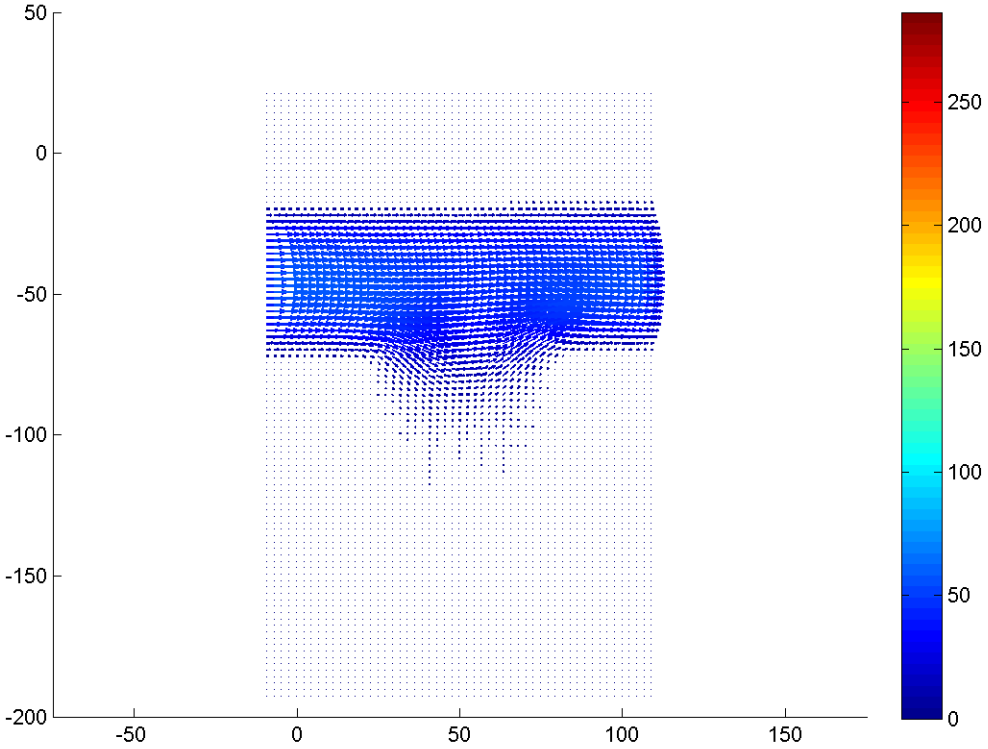

Figure F.27: Velocity field during phase increment 27 at 13 Hz with a Re of 0.1.

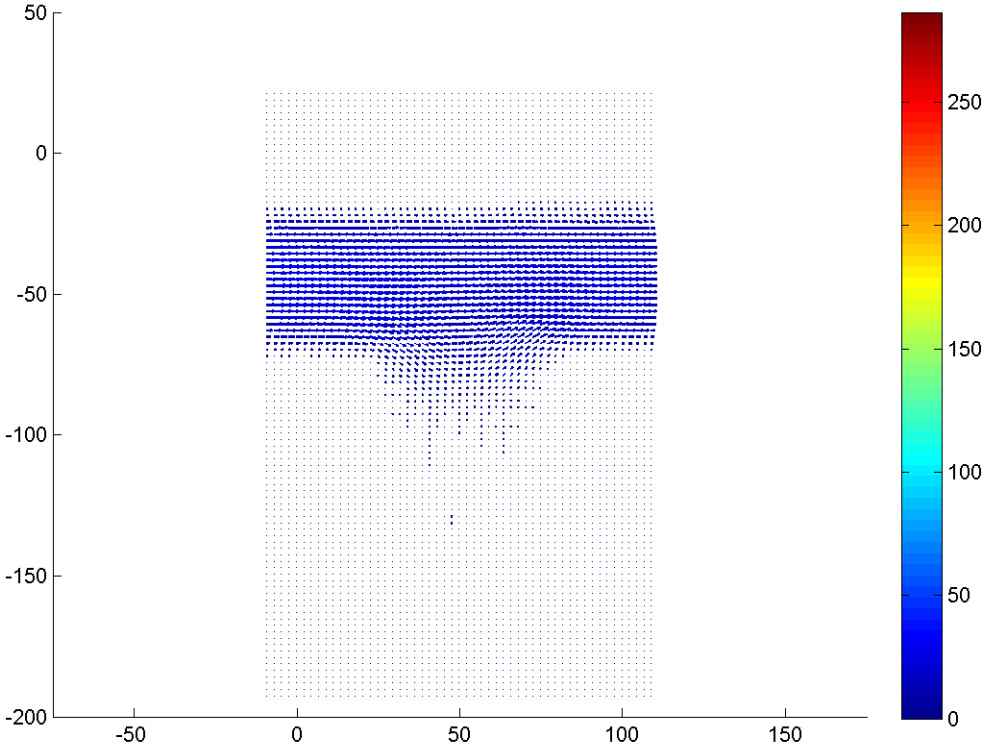

Figure F.28: Velocity field during phase increment 28 at 13 Hz with a Re of 0.1.

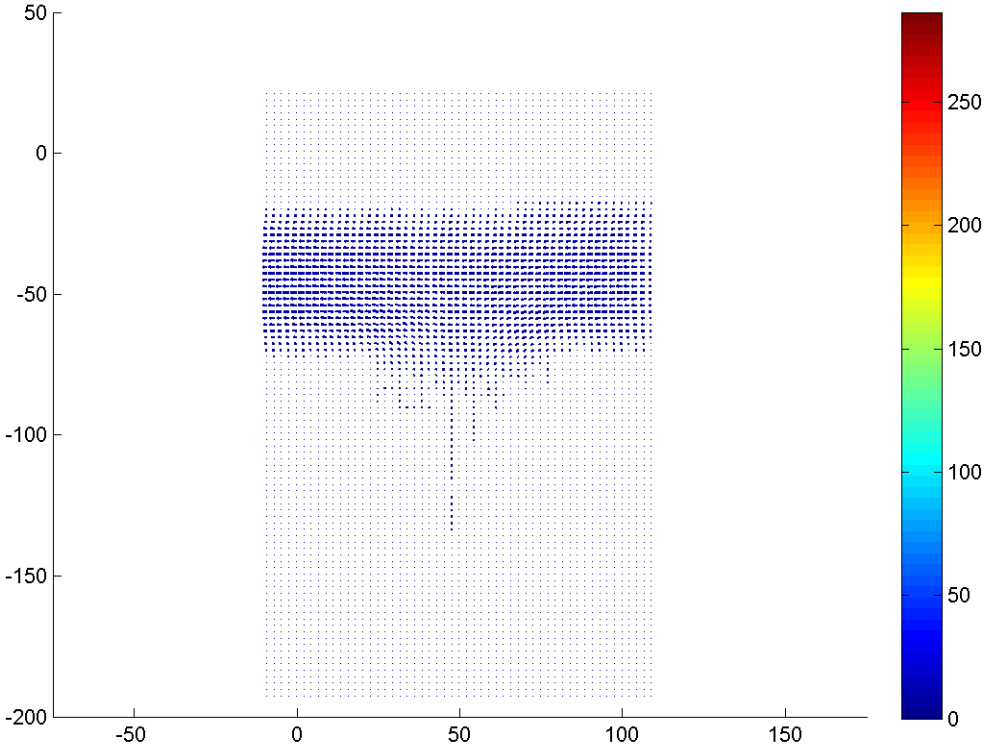

Figure F.29: Velocity field during phase increment 29 at 13 Hz with a Re of 0.1.

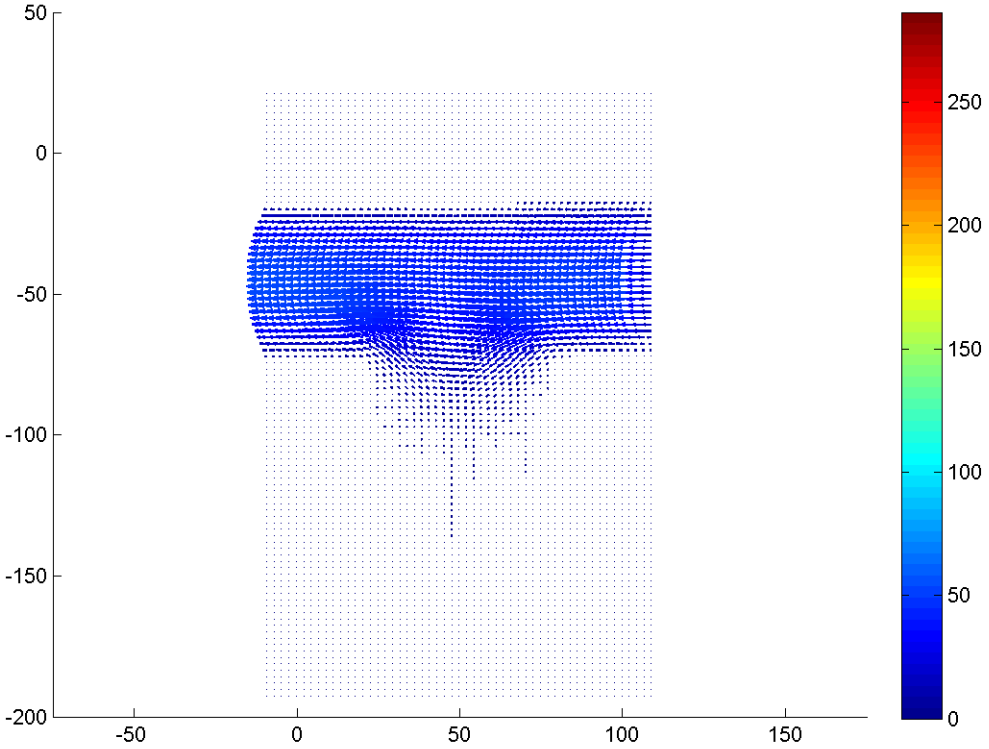

Figure F.30: Velocity field during phase increment 30 at 13 Hz with a Re of 0.1.

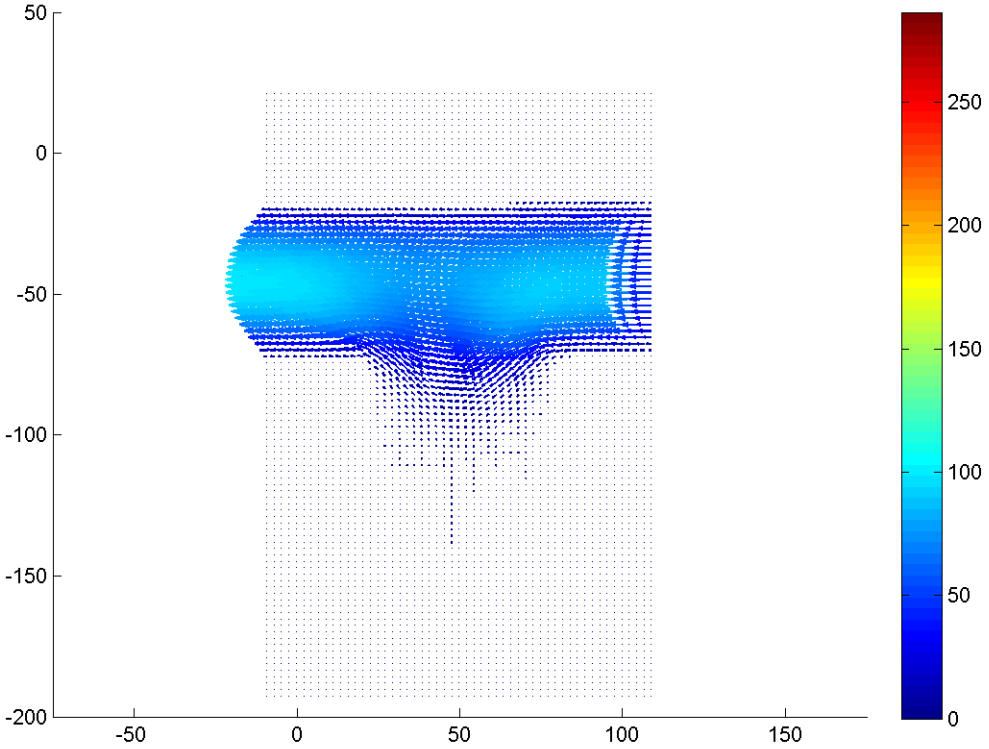

Figure F.31: Velocity field during phase increment 31 at 13 Hz with a Re of 0.1.

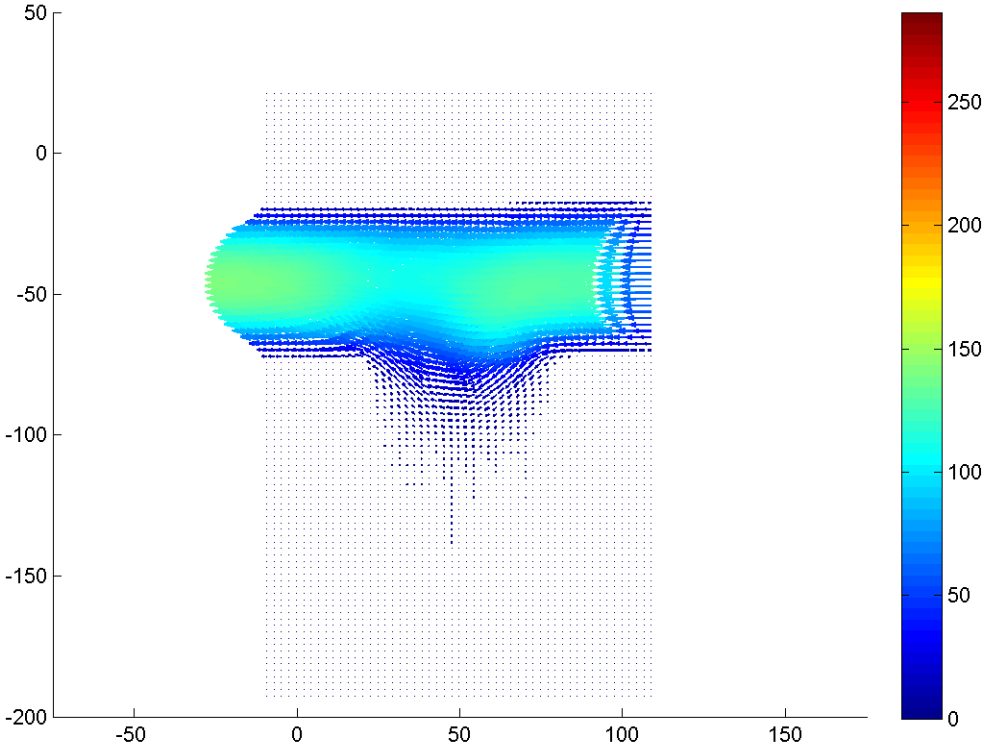

Figure F.32: Velocity field during phase increment 32 at 13 Hz with a Re of 0.1.

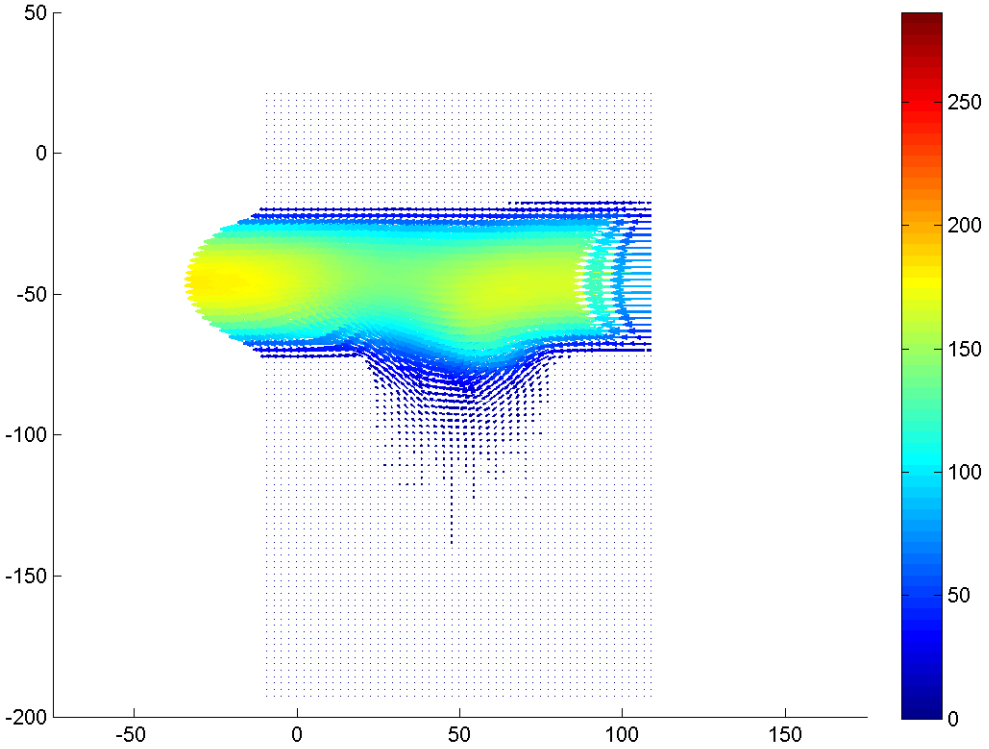

Figure F.33: Velocity field during phase increment 33 at 13 Hz with a Re of 0.1.

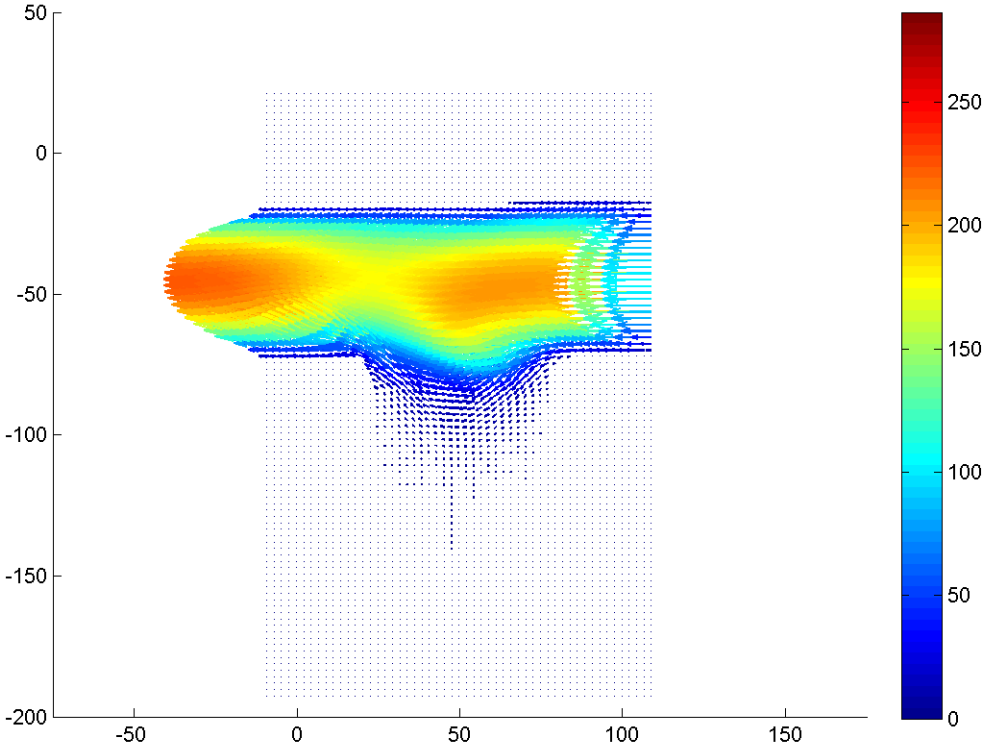

Figure F.34: Velocity field during phase increment 34 at 13 Hz with a Re of 0.1.

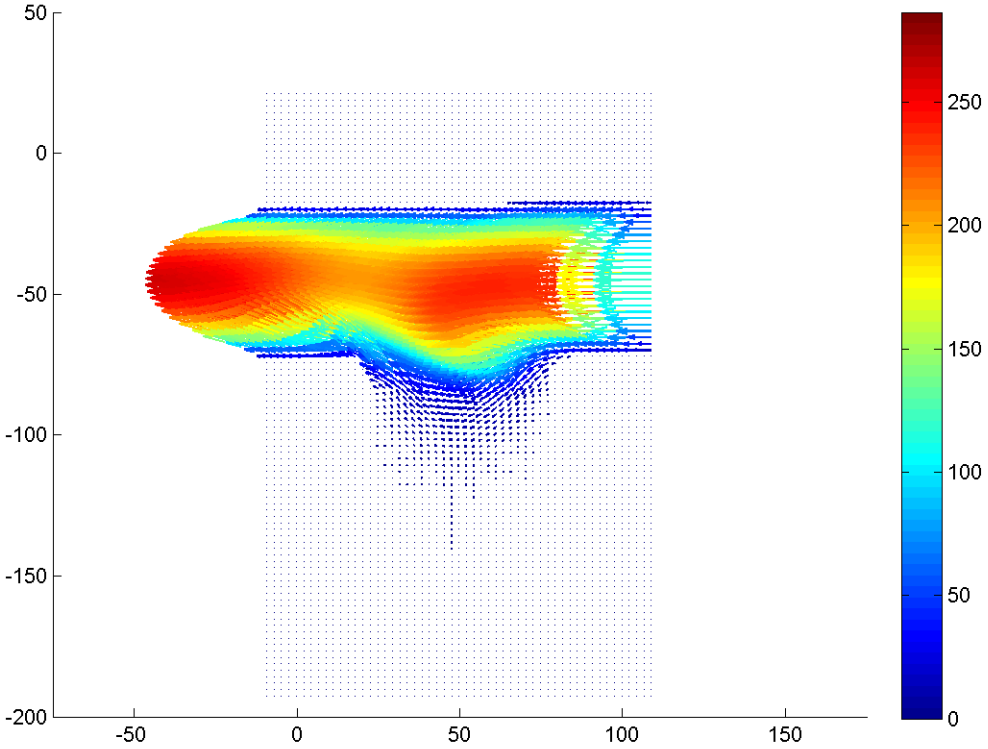

Figure F.35: Velocity field during phase increment 35 at 13 Hz with a Re of 0.1.

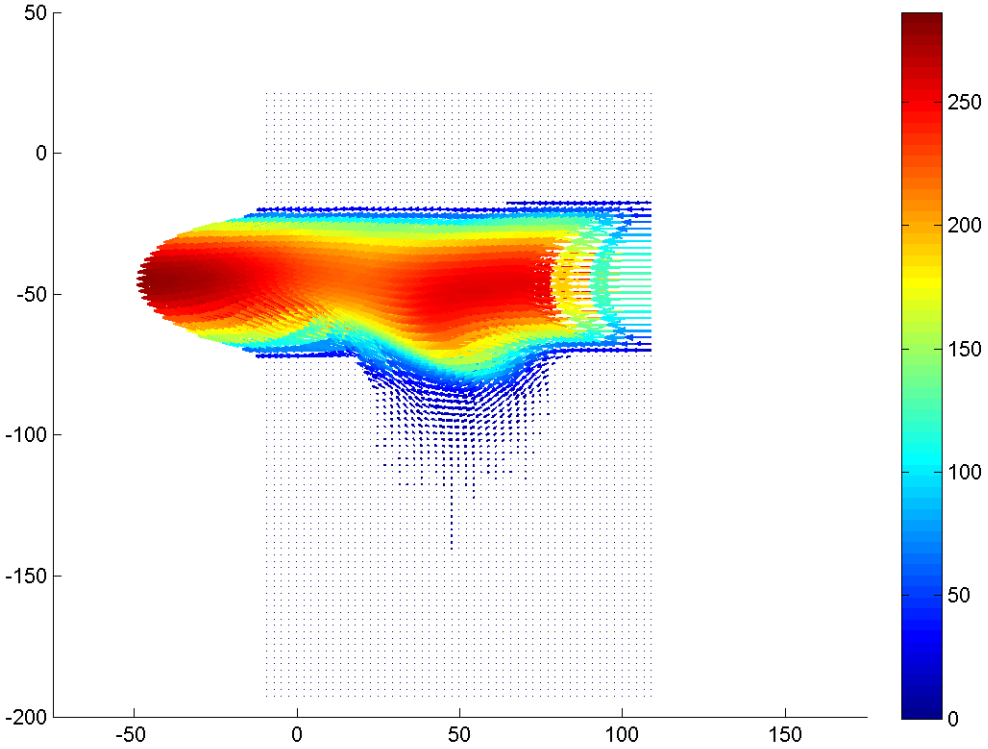

Figure F.36: Velocity field during phase increment 36 at 13 Hz with a Re of 0.1.

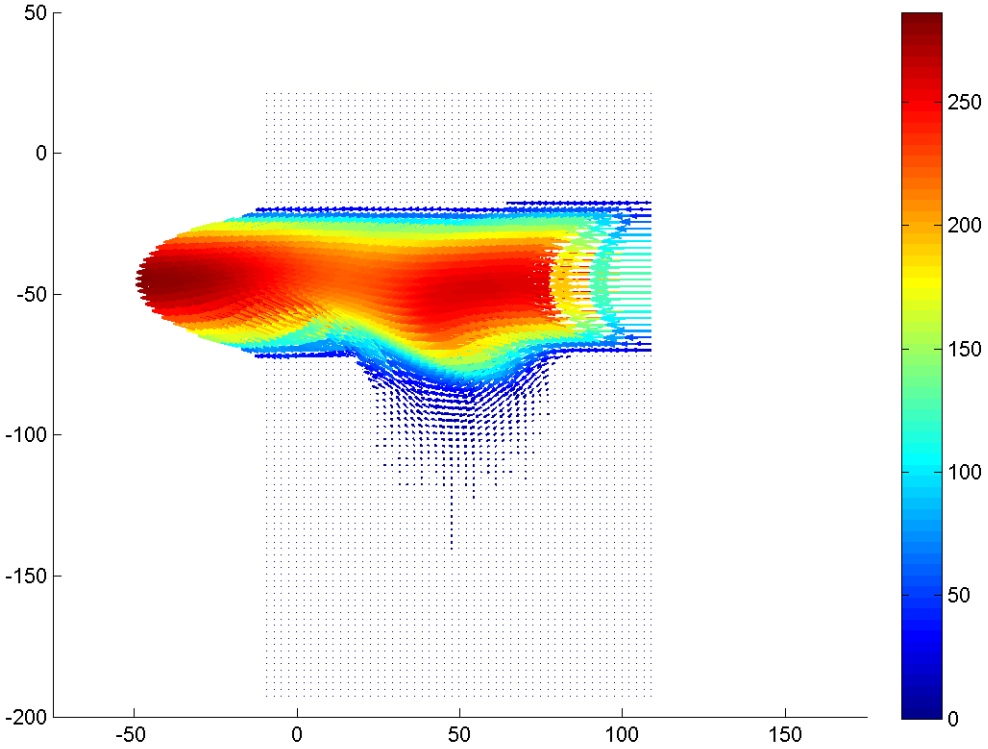

Figure F.37: Velocity field during phase increment 37 at 13 Hz with a Re of 0.1.

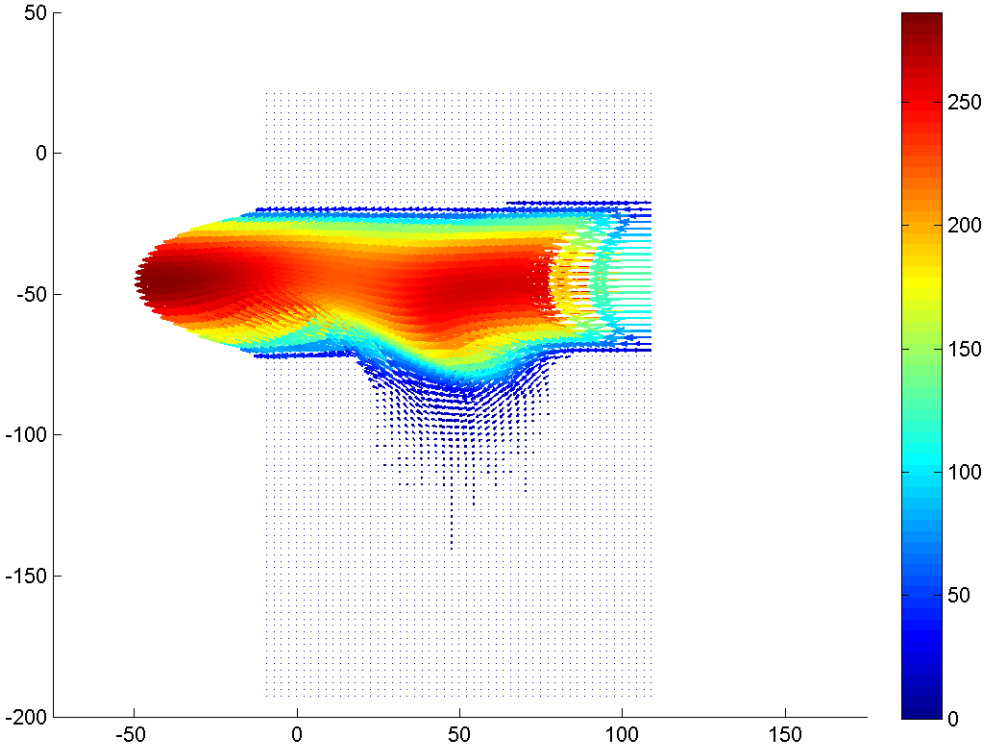

Figure F.38: Velocity field during phase increment 38 at 13 Hz with a Re of 0.1.

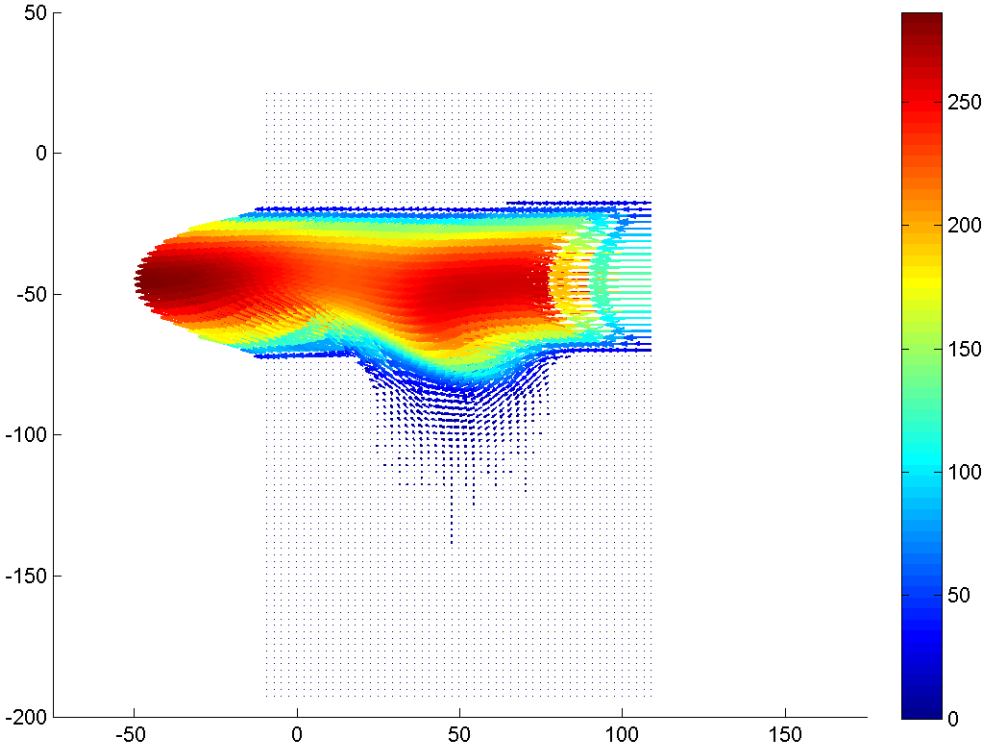

Figure F.39: Velocity field during phase increment 39 at 13 Hz with a Re of 0.1.

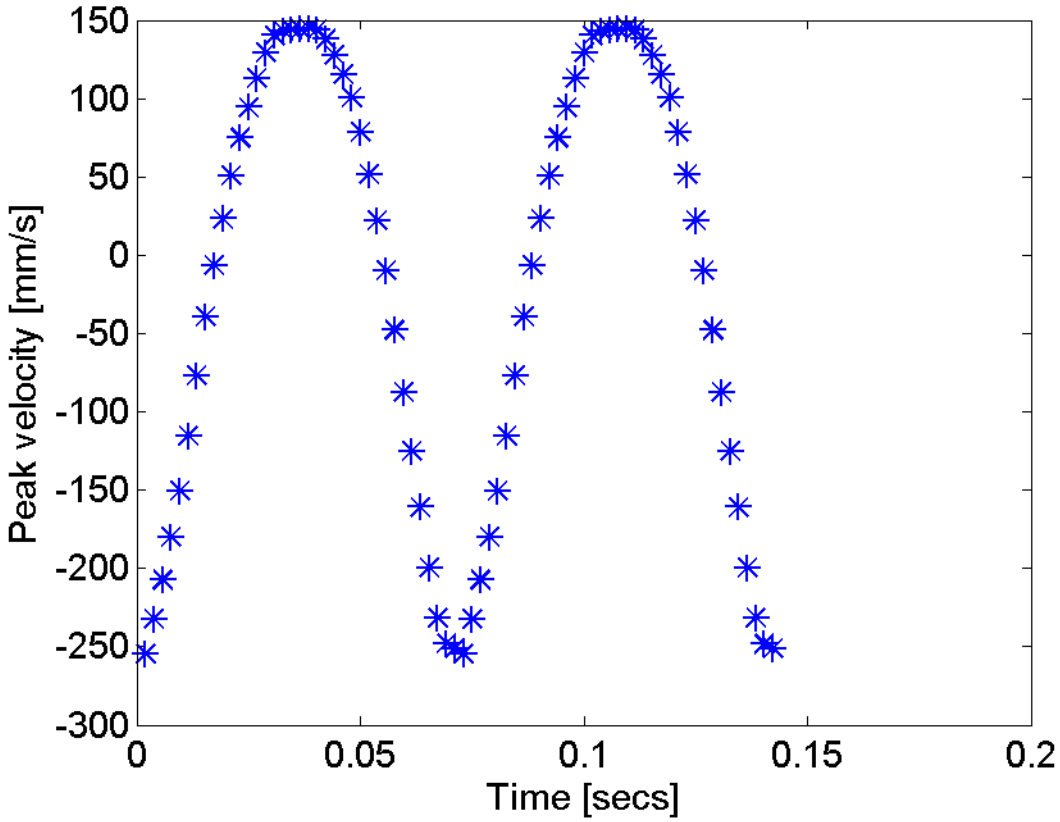

Figure F.40: The peak velocity in the free stream region in time at 13 Hz.

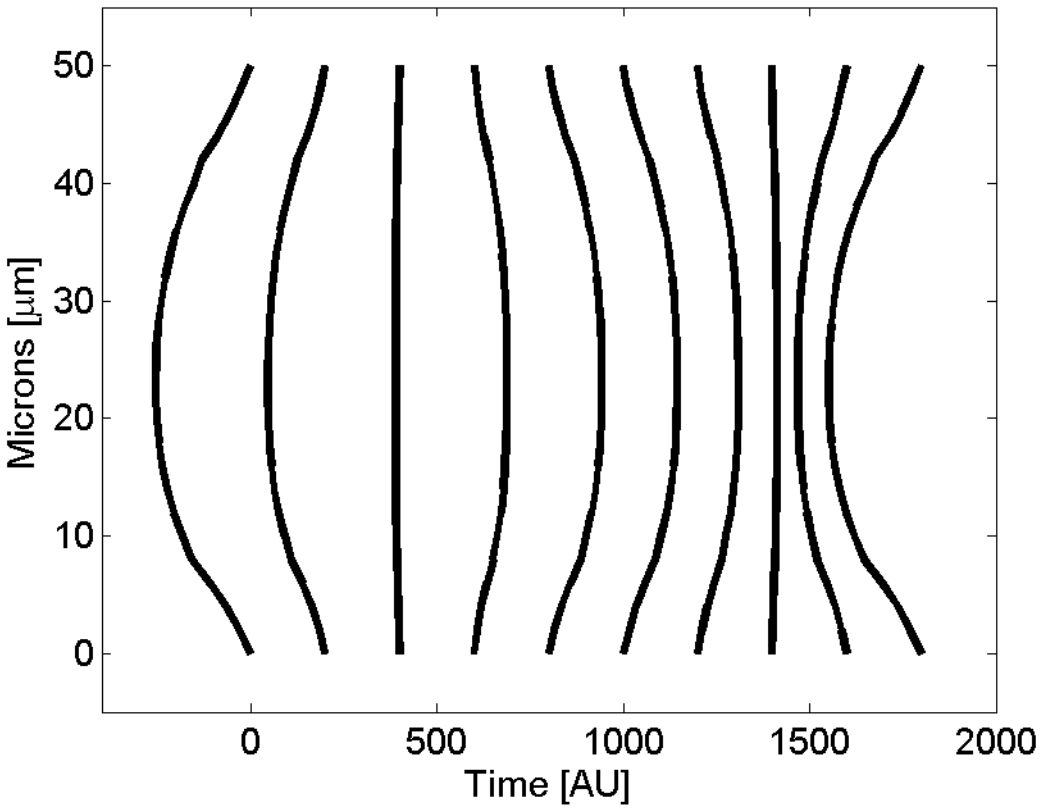

Figure F.41: The velocity profile in the free stream versus time at 13 Hz.

F.1.2 Streamline images at 13 Hz

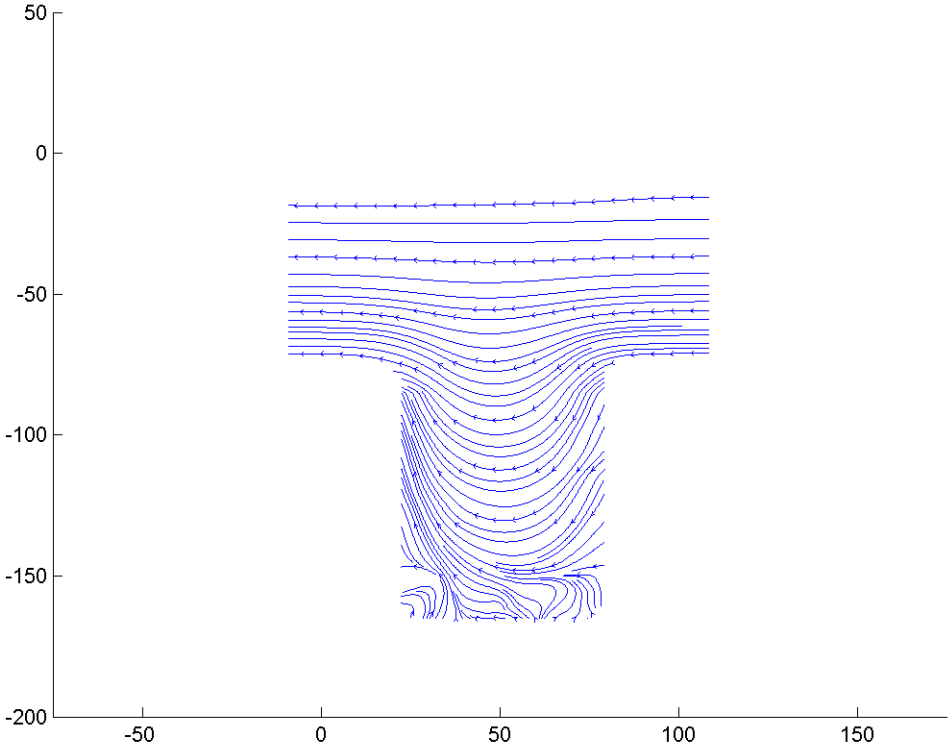

Figure F.42: Streamline image during phase increment 1 at 13 Hz and a Re of 0.1.

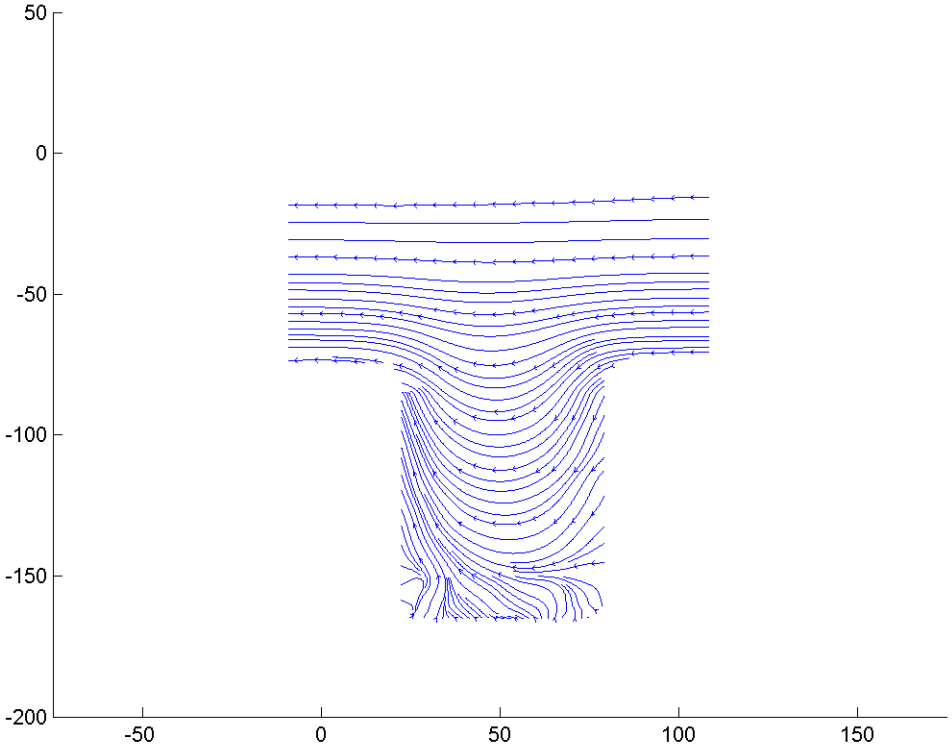

Figure F.43: Streamline image during phase increment 2 at 13 Hz and a Re of 0.1.

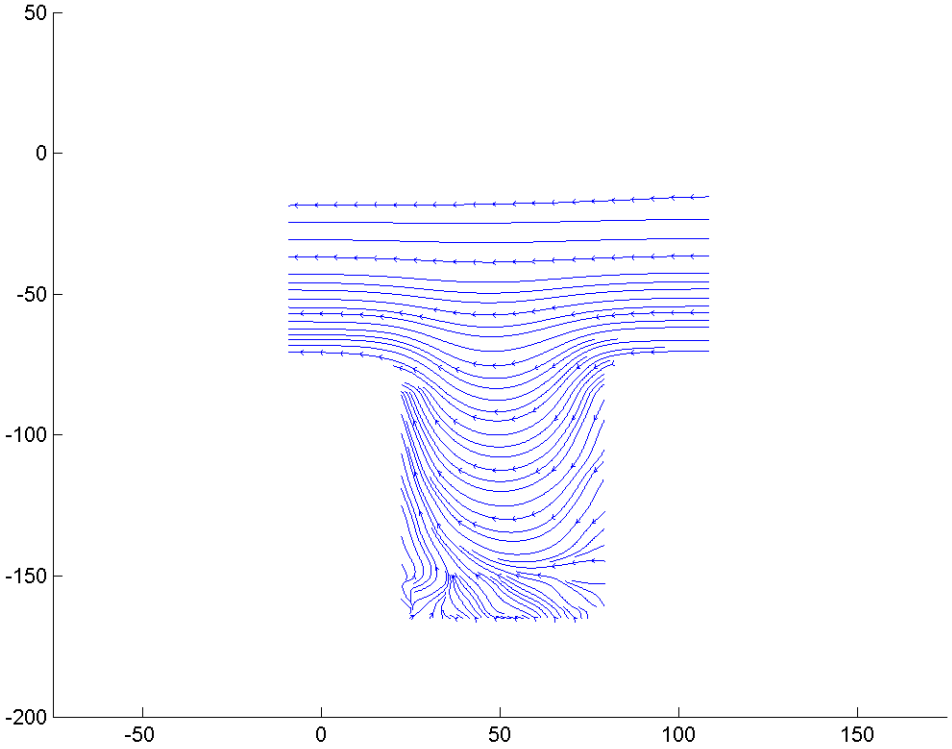

Figure F.44: Streamline image during phase increment 3 at 13 Hz and a Re of 0.1.

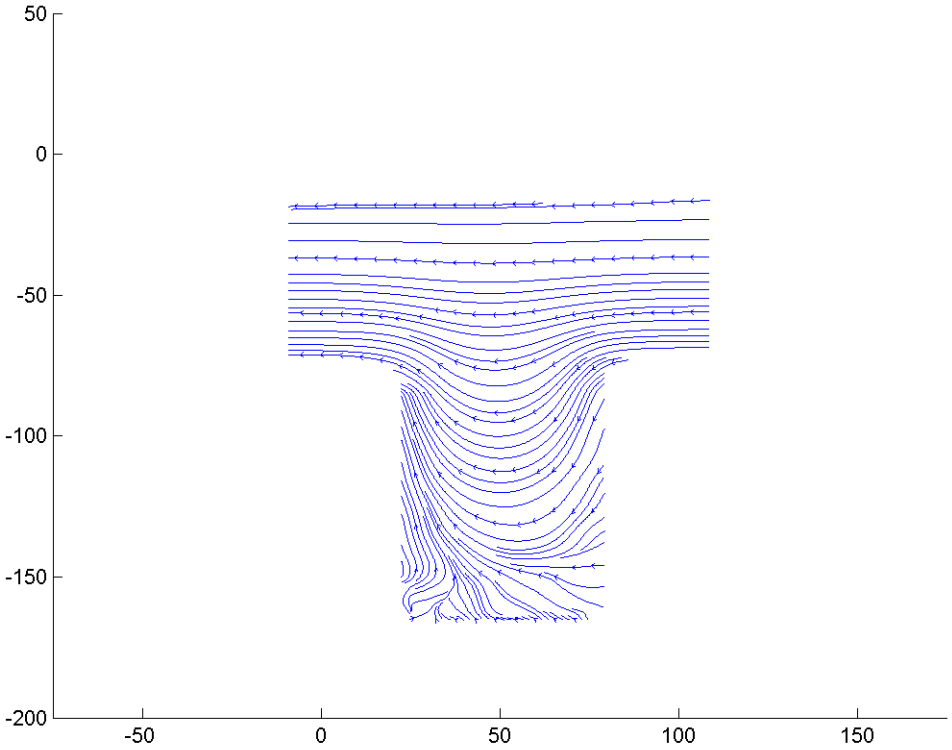

Figure F.45: Streamline image during phase increment 4 at 13 Hz and a Re of 0.1.

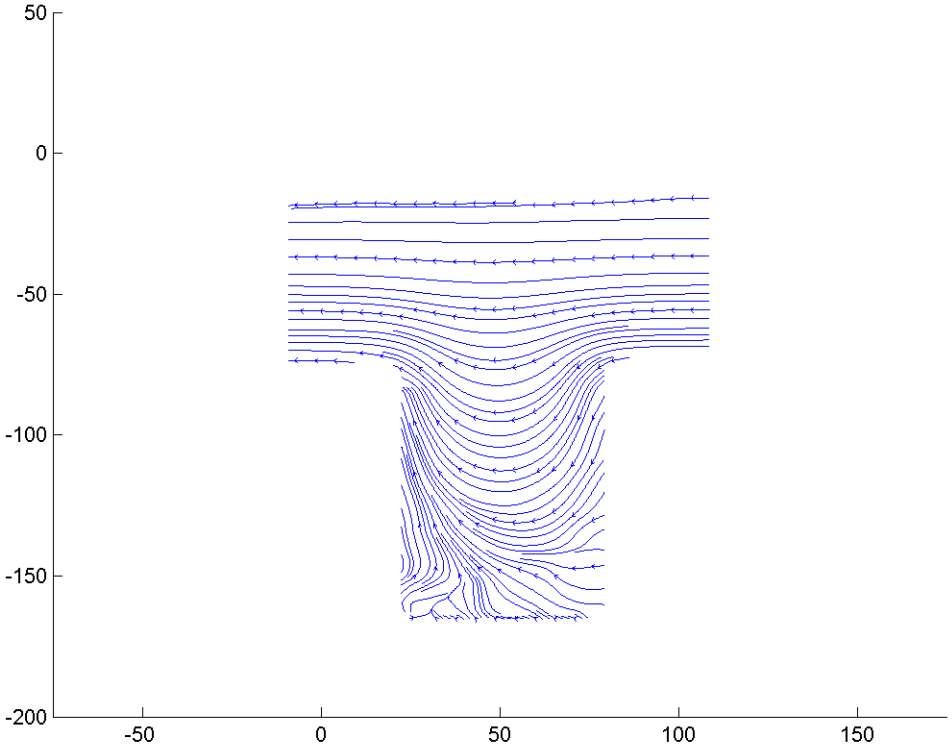

Figure F.46: Streamline image during phase increment 5 at 13 Hz and a Re of 0.1.

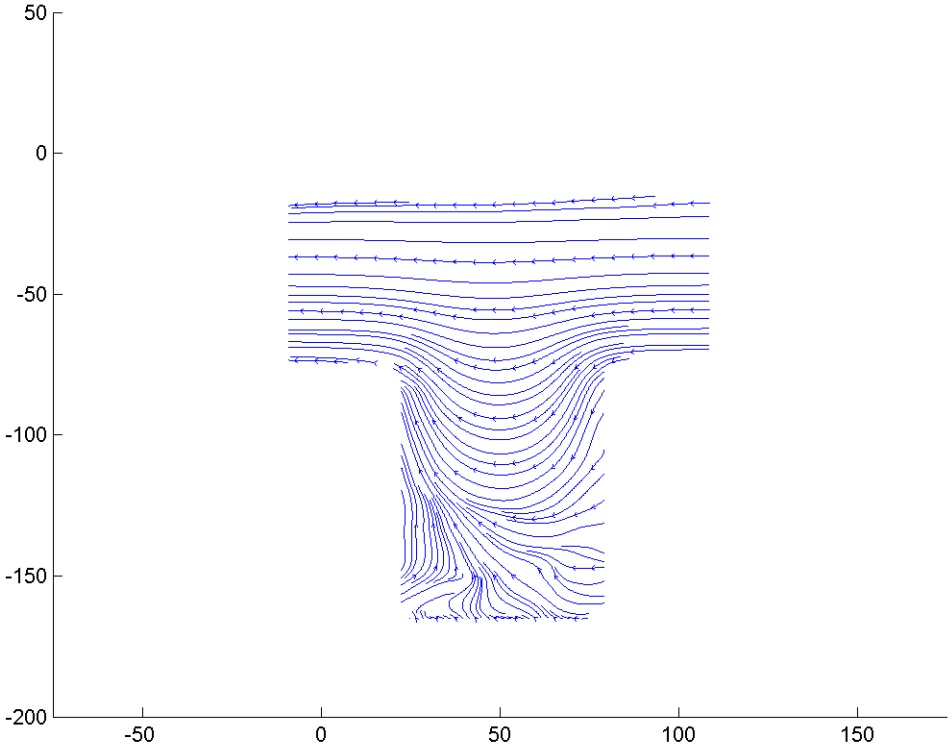

Figure F.47: Streamline image during phase increment 6 at 13 Hz and a Re of 0.1.

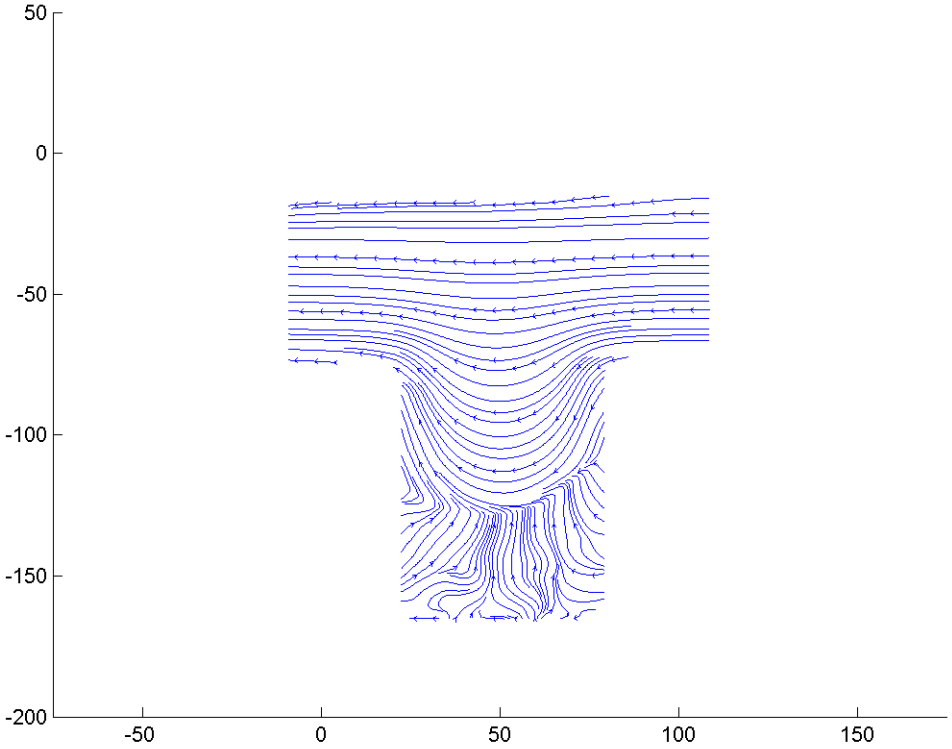

Figure F.48: Streamline image during phase increment 7 at 13 Hz and a Re of 0.1.

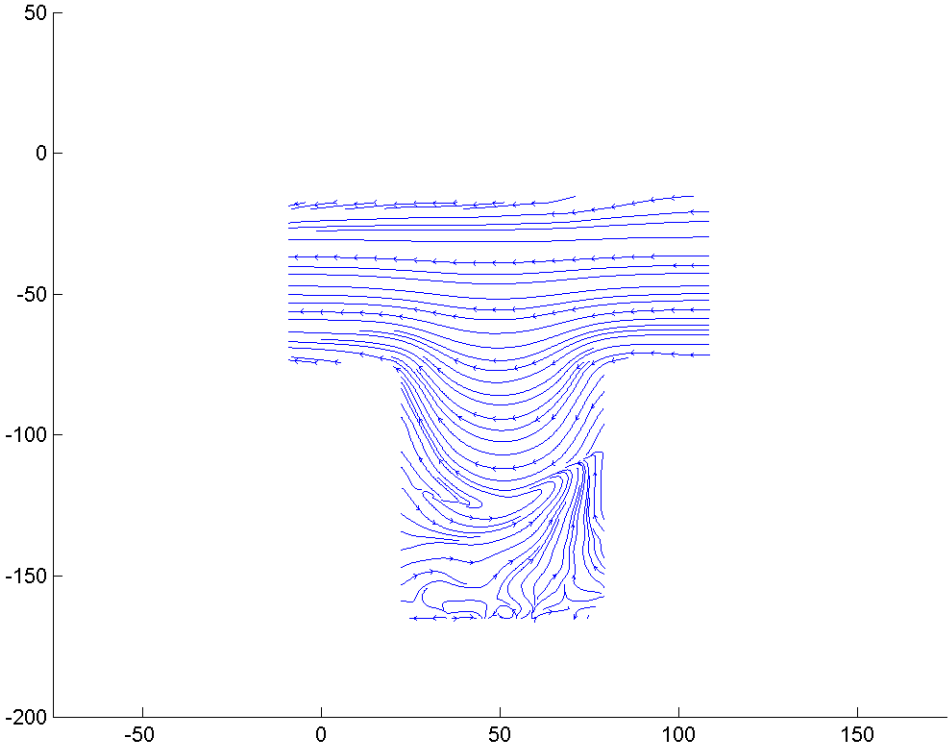

Figure F.49: Streamline image during phase increment 8 at 13 Hz and a Re of 0.1.

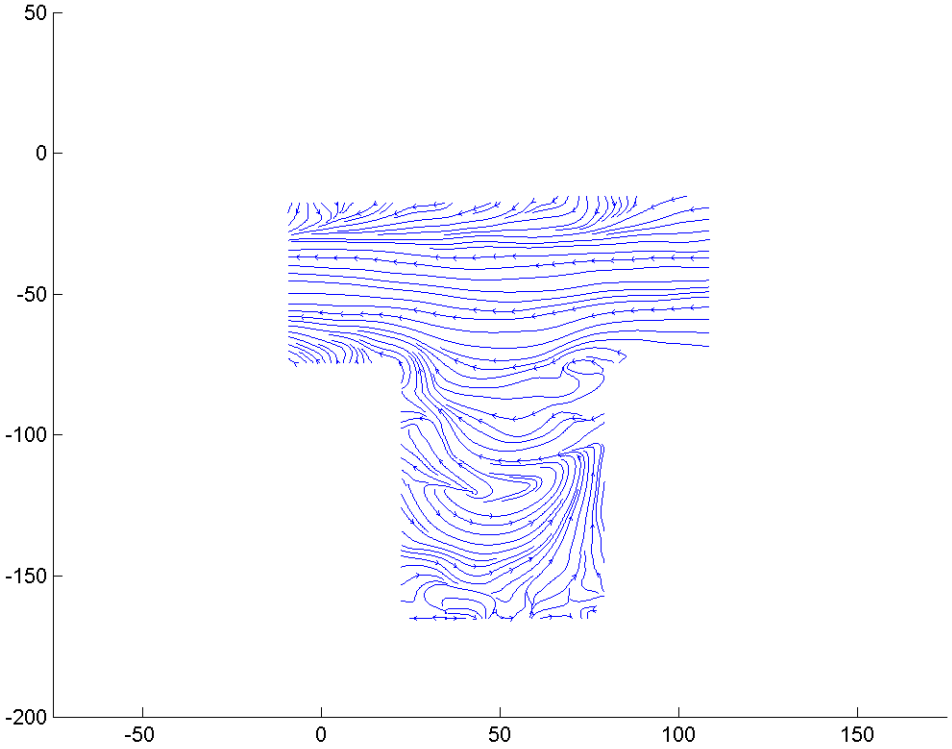

Figure F.50: Streamline image during phase increment 9 at 13 Hz and a Re of 0.1.

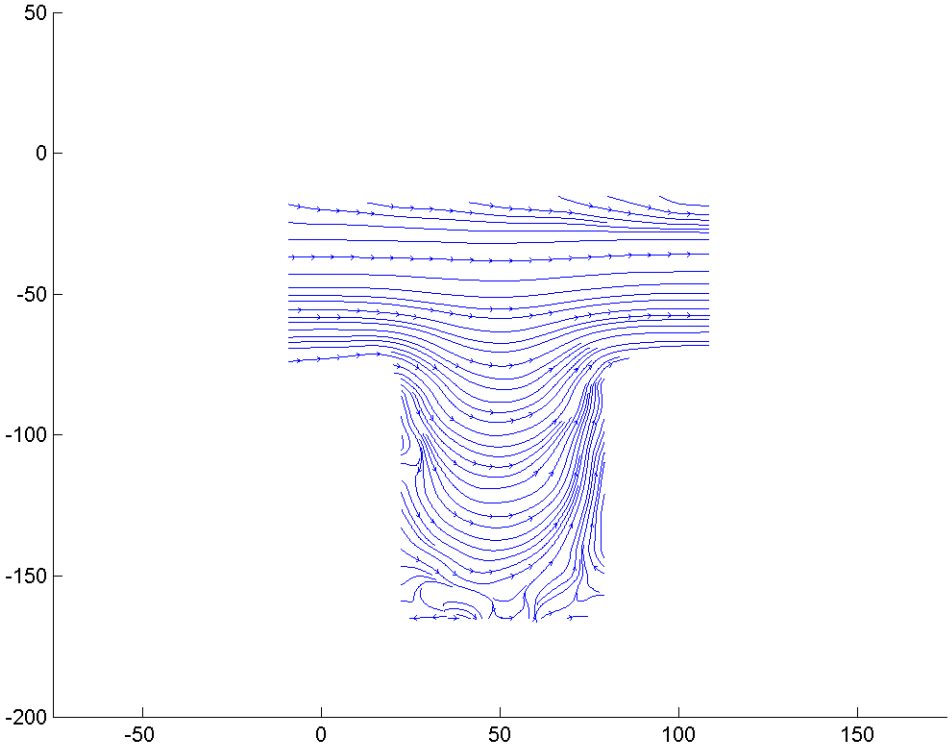

Figure F.51: Streamline image during phase increment 10 at 13 Hz and a Re of 0.1.

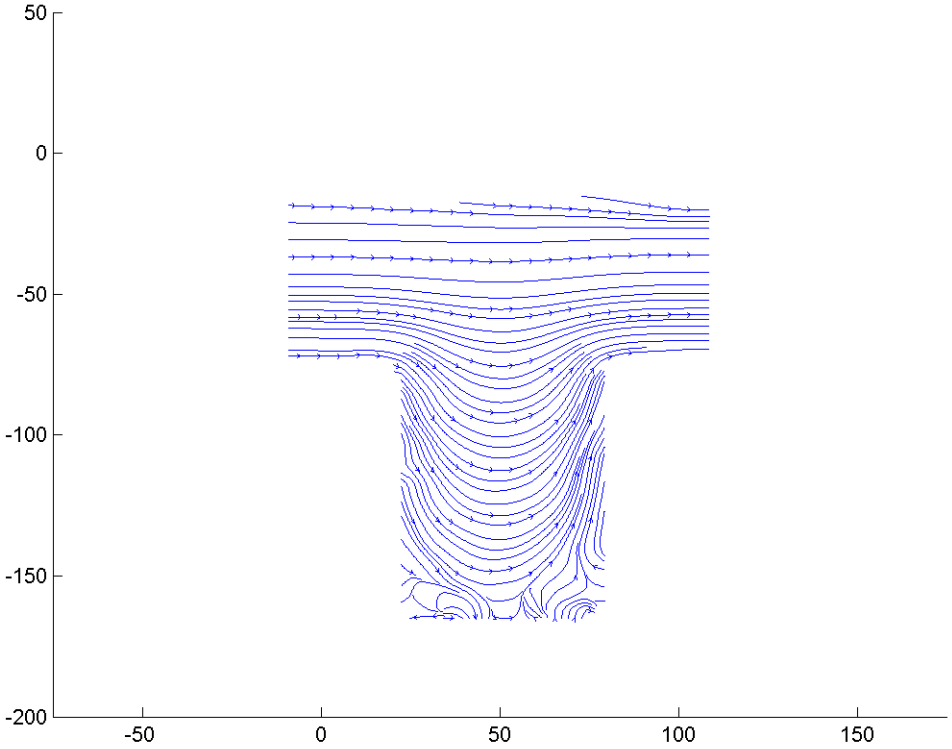

Figure F.52: Streamline image during phase increment 11 at 13 Hz and a Re of 0.1.

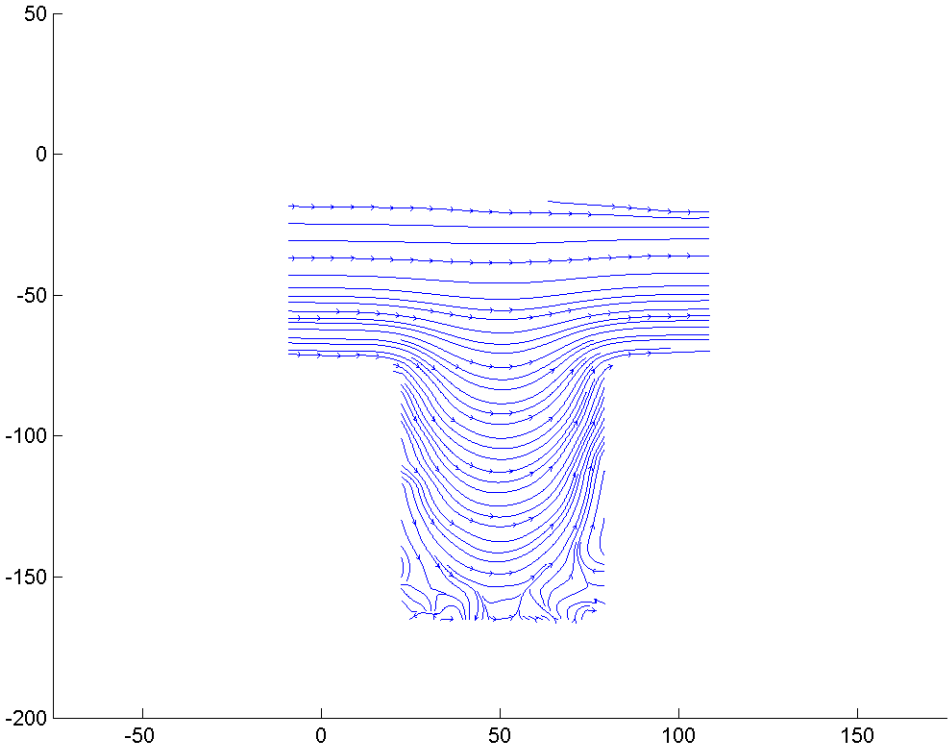

Figure F.53: Streamline image during phase increment 12 at 13 Hz and a Re of 0.1.

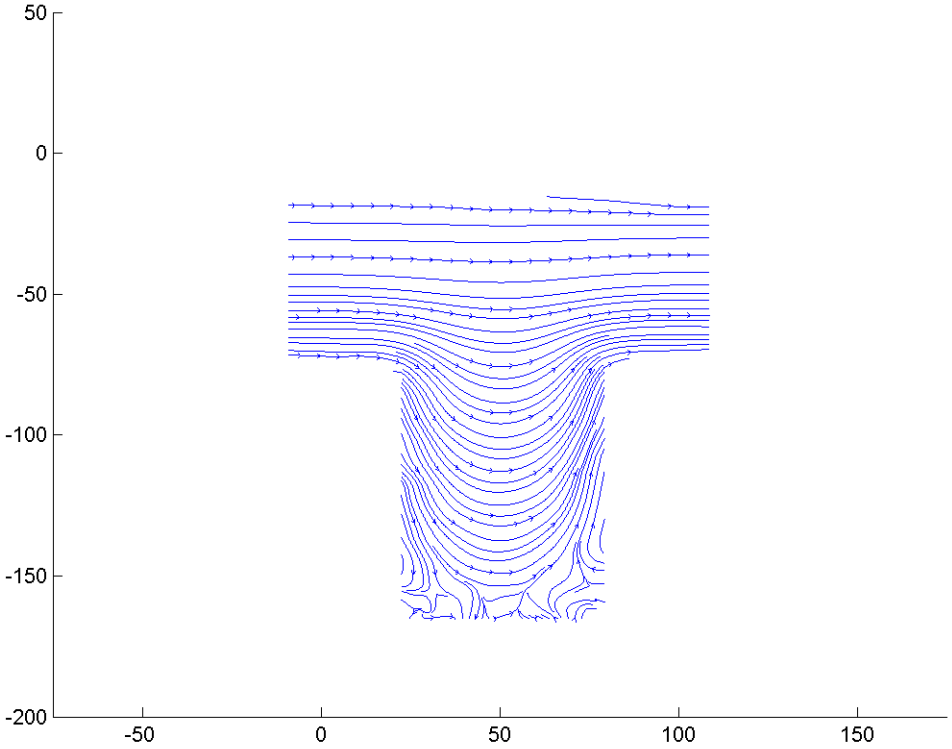

Figure F.54: Streamline image during phase increment 13 at 13 Hz and a Re of 0.1.

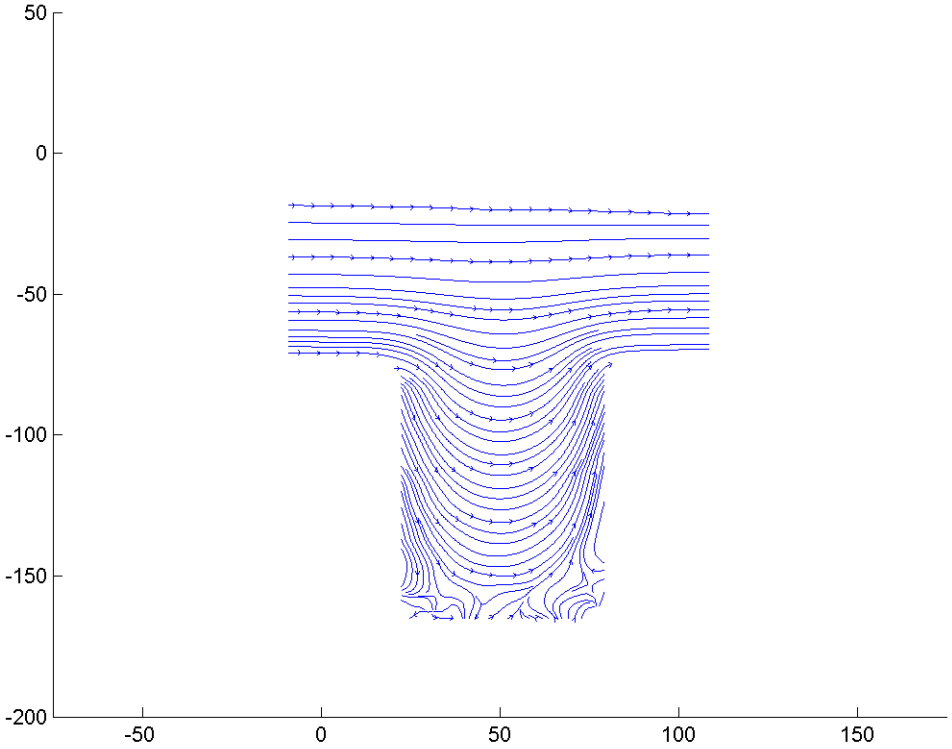

Figure F.55: Streamline image during phase increment 14 at 13 Hz and a Re of 0.1.

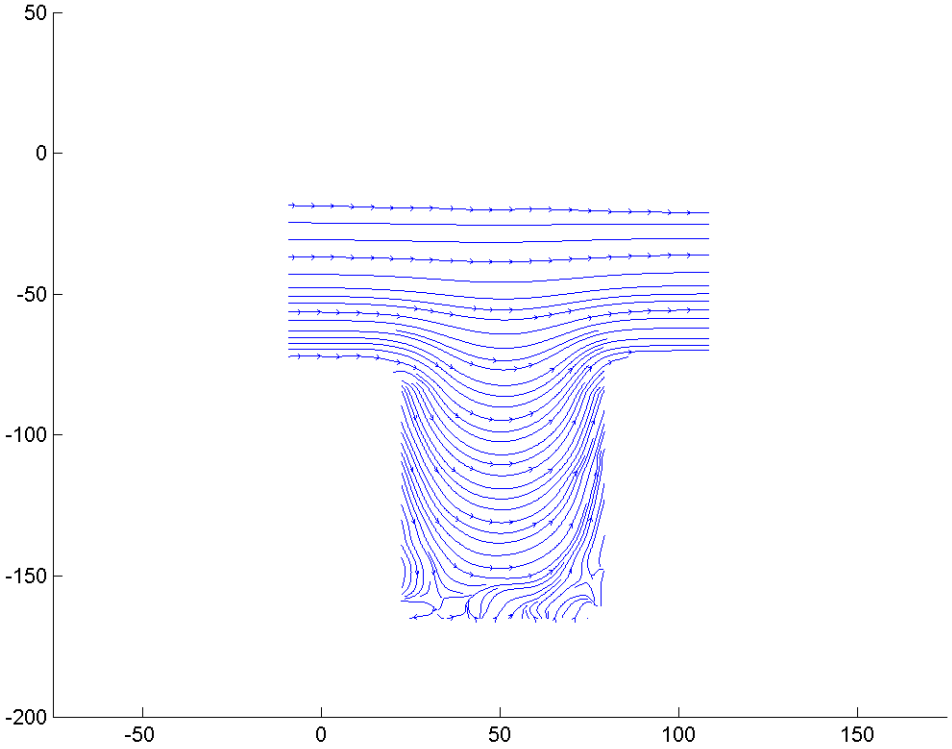

Figure F.56: Streamline image during phase increment 15 at 13 Hz and a Re of 0.1.

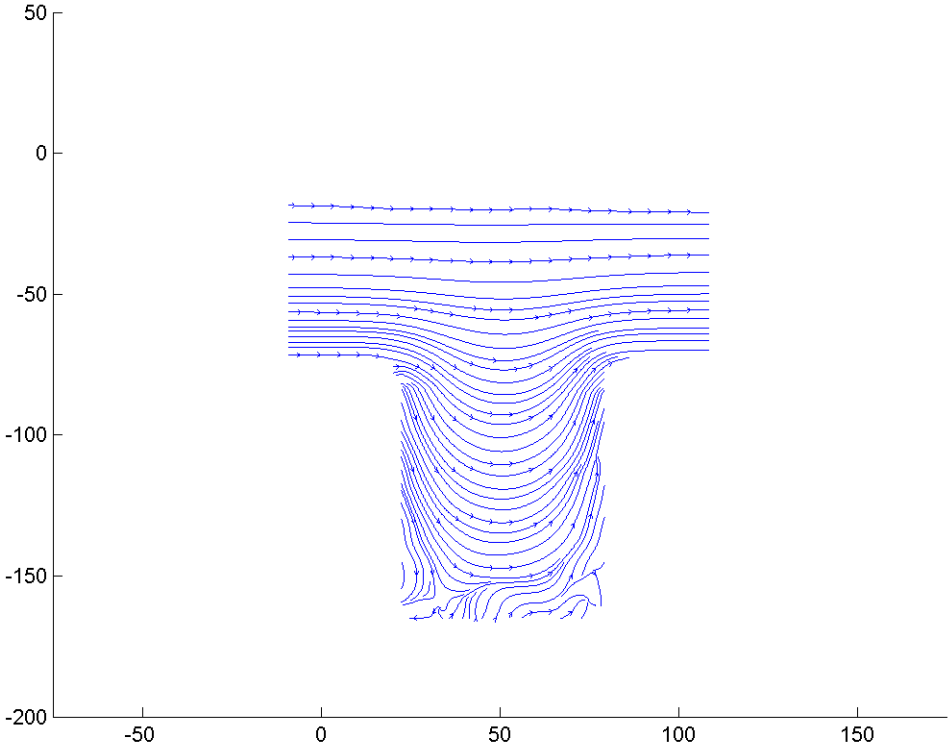

Figure F.57: Streamline image during phase increment 16 at 13 Hz and a Re of 0.1.

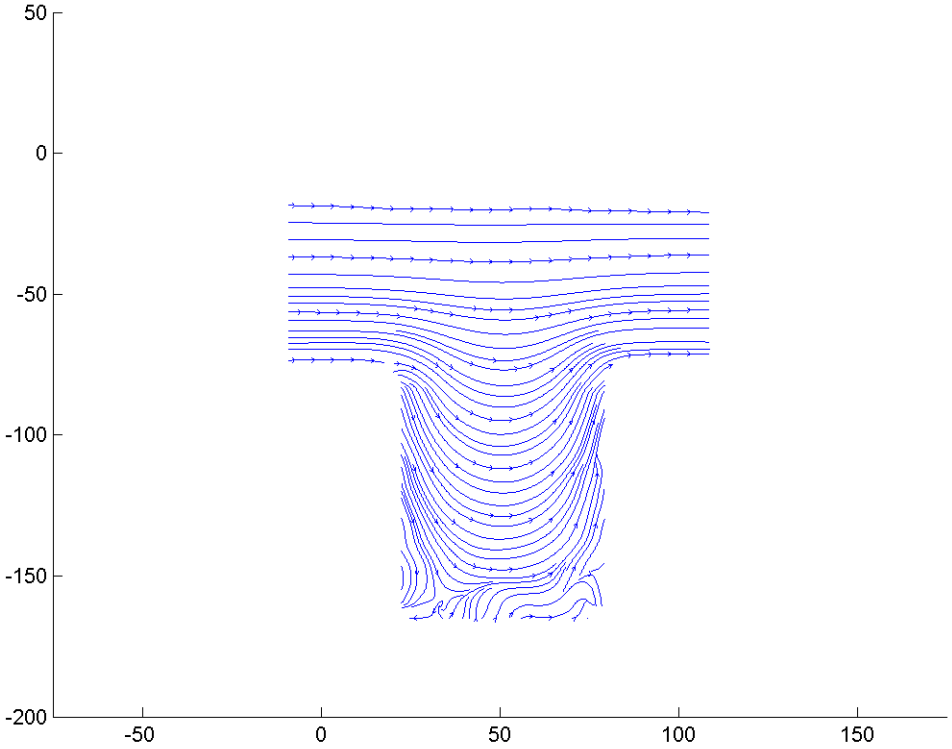

Figure F.58: Streamline image during phase increment 17 at 13 Hz and a Re of 0.1.

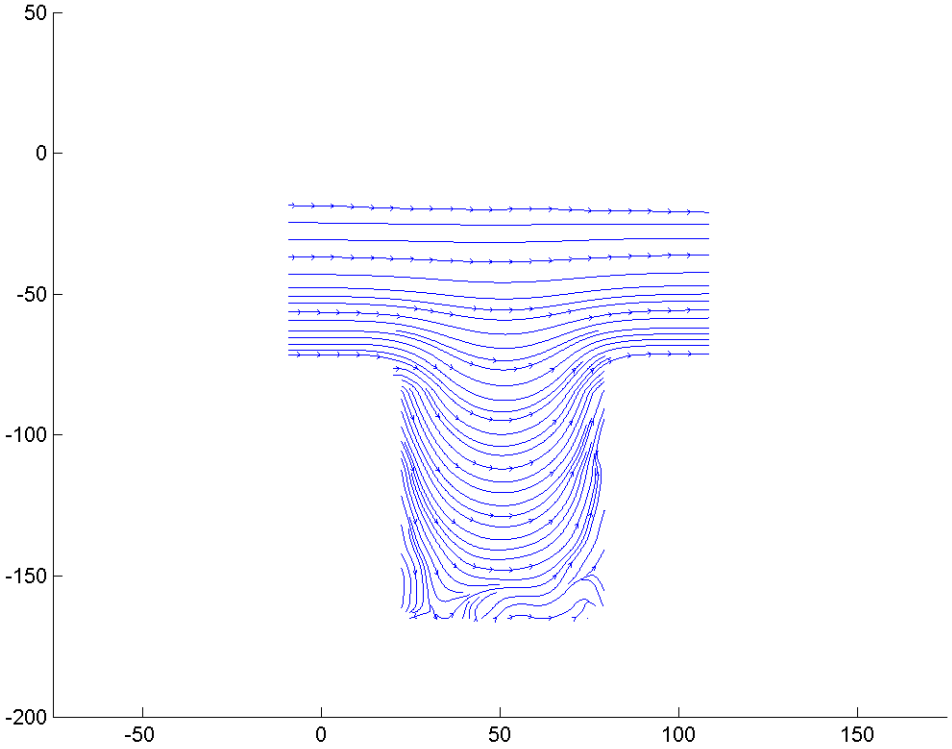

Figure F.59: Streamline image during phase increment 18 at 13 Hz and a Re of 0.1.

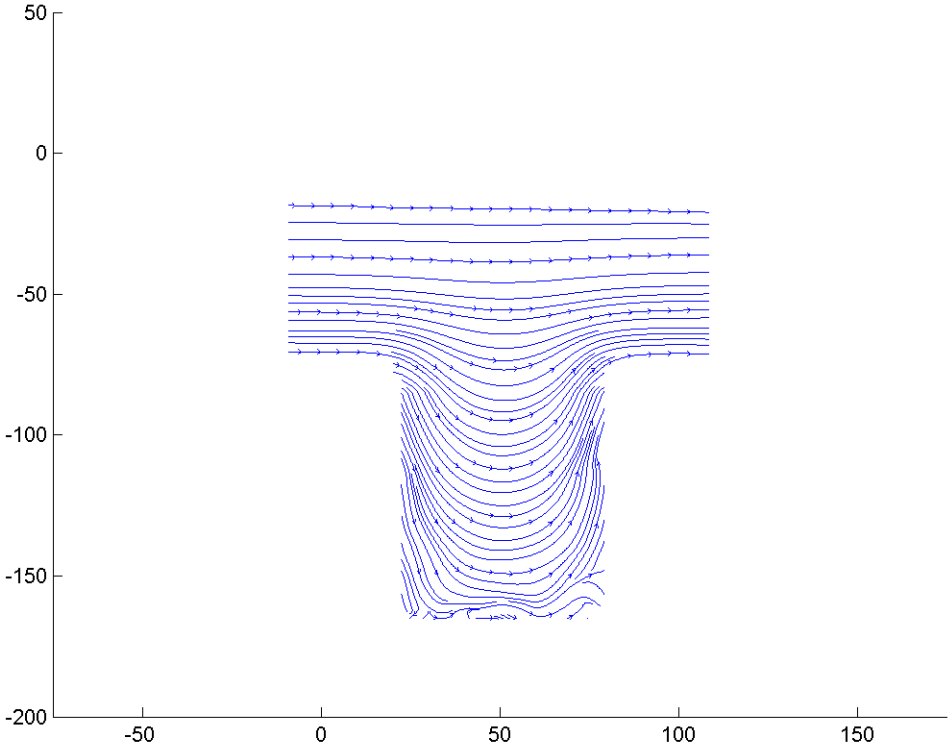

Figure F.60: Streamline image during phase increment 18 at 13 Hz and a Re of 0.1.

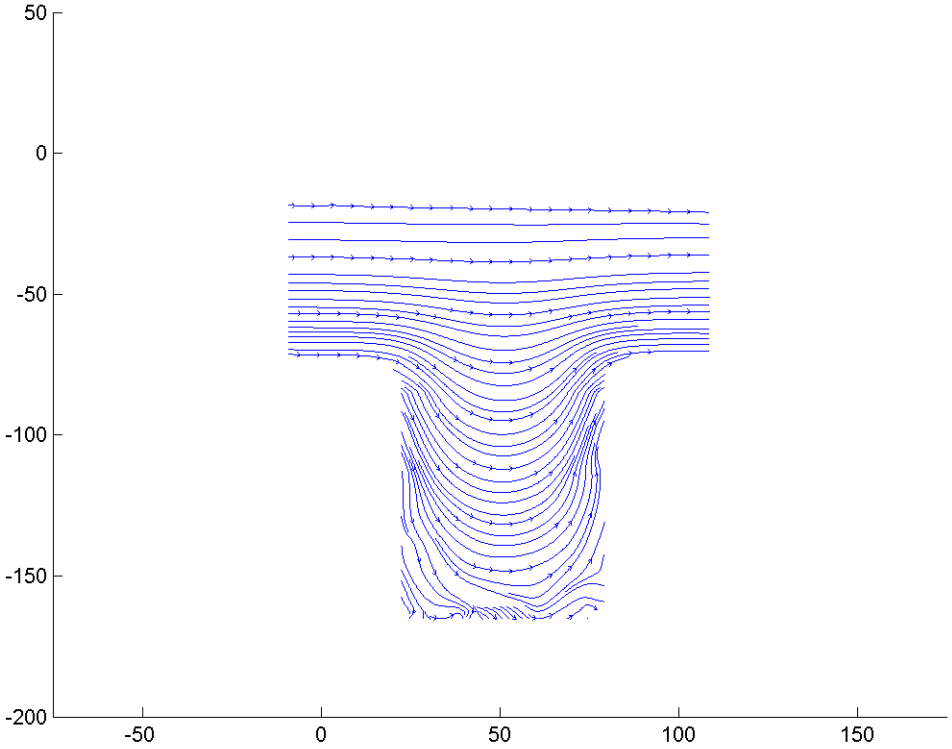

Figure F.61: Streamline image during phase increment 20 at 13 Hz and a Re of 0.1.

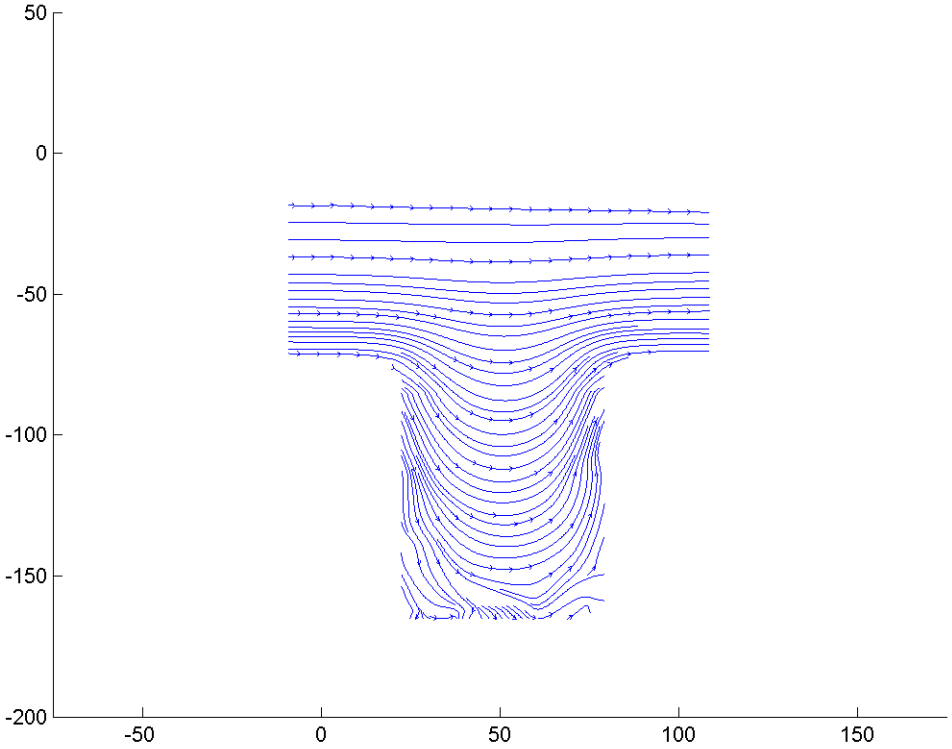

Figure F.62: Streamline image during phase increment 21 at 13 Hz and a Re of 0.1.

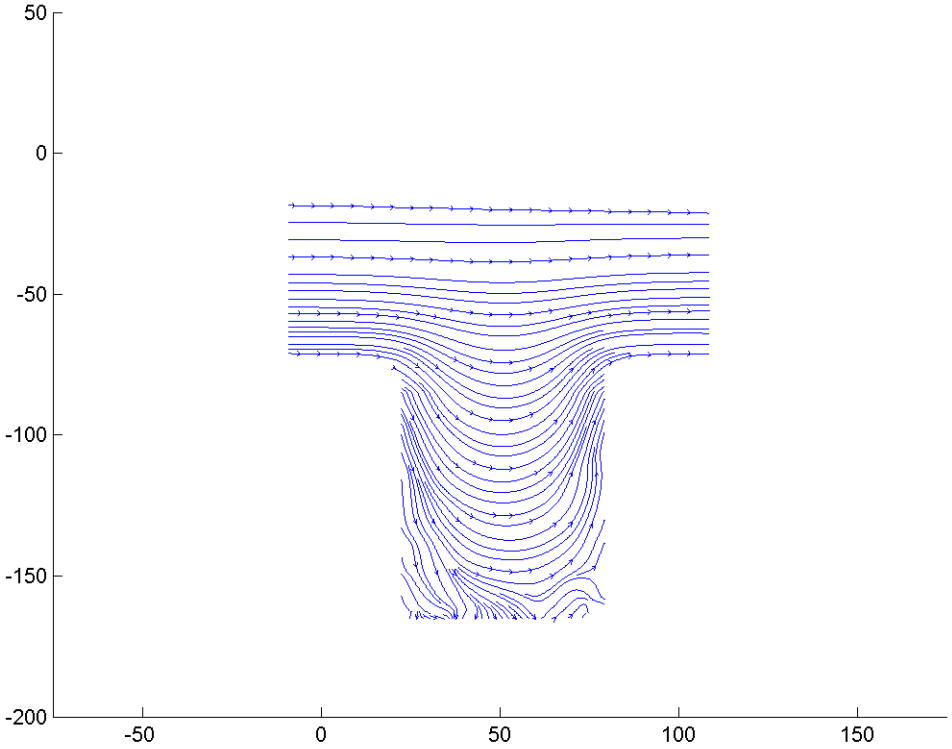

Figure F.63: Streamline image during phase increment 22 at 13 Hz and a Re of 0.1.

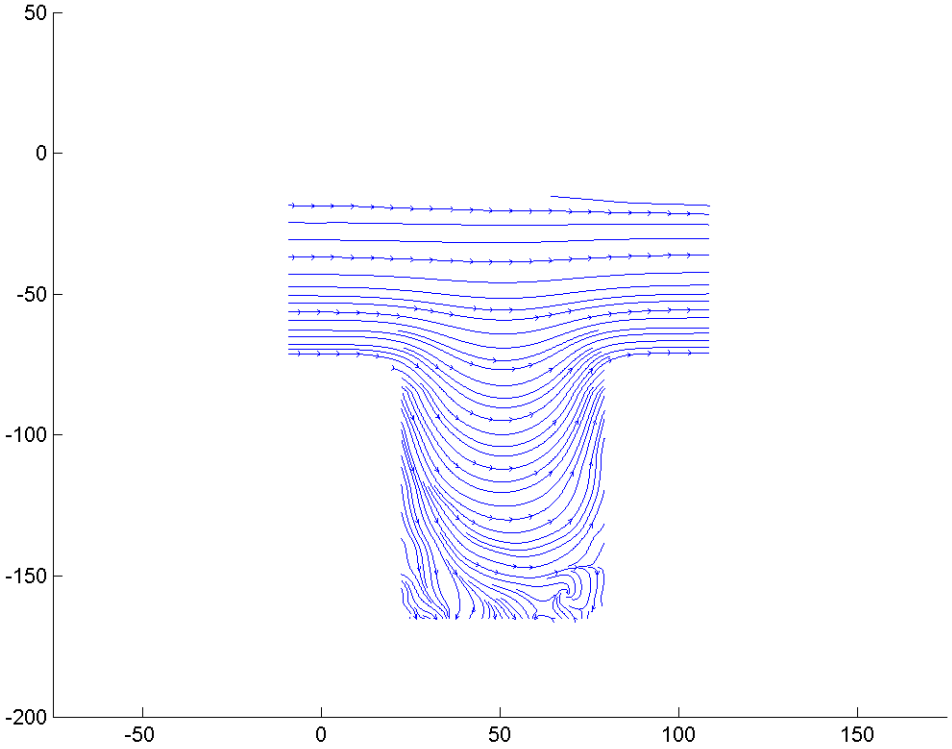

Figure F.64: Streamline image during phase increment 23 at 13 Hz and a Re of 0.1.

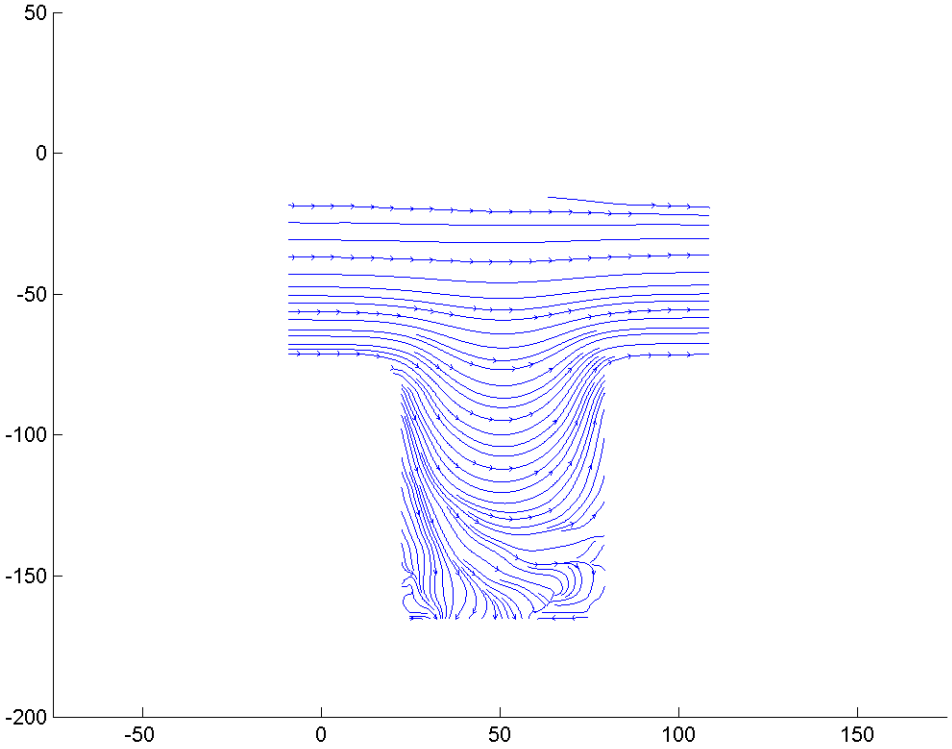

Figure F.65: Streamline image during phase increment 24 at 13 Hz and a Re of 0.1.

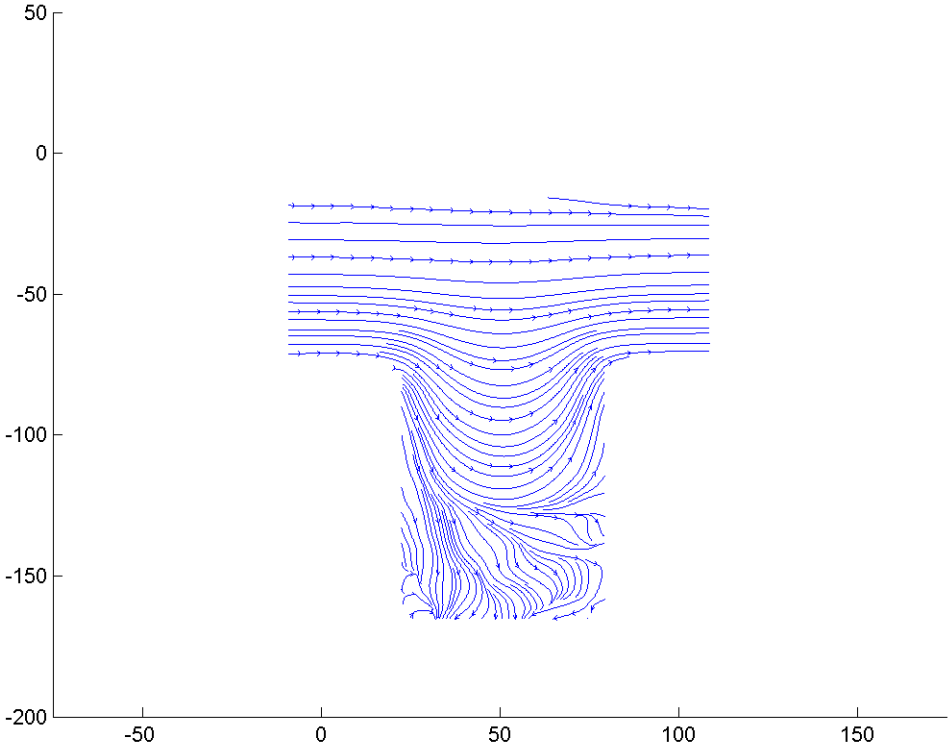

Figure F.66: Streamline image during phase increment 25 at 13 Hz and a Re of 0.1.

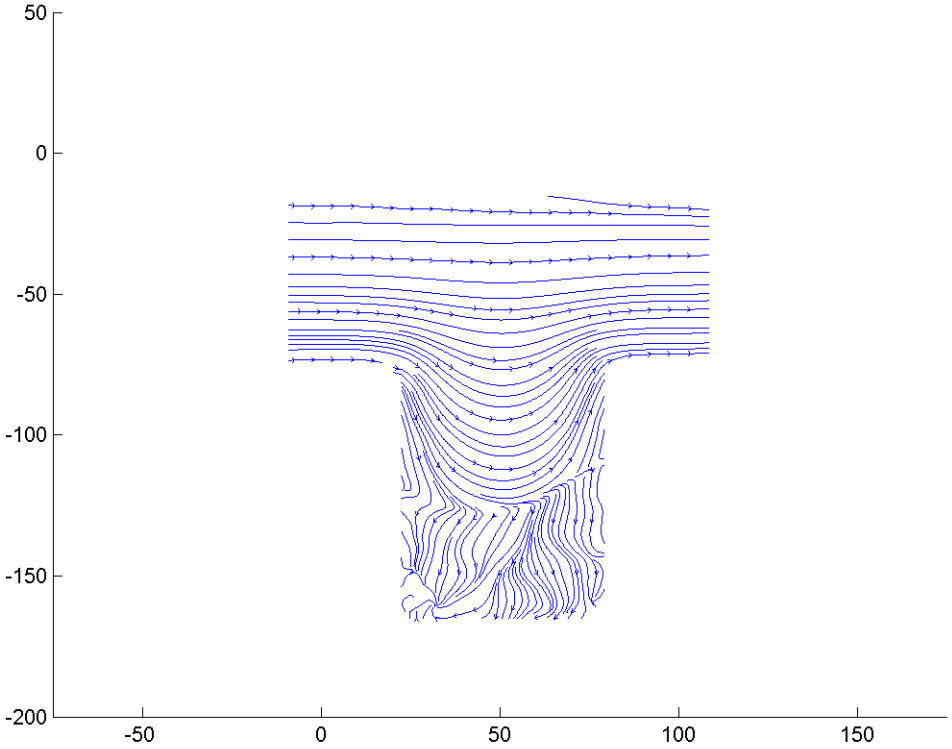

Figure F.67: Streamline image during phase increment 26 at 13 Hz and a Re of 0.1.

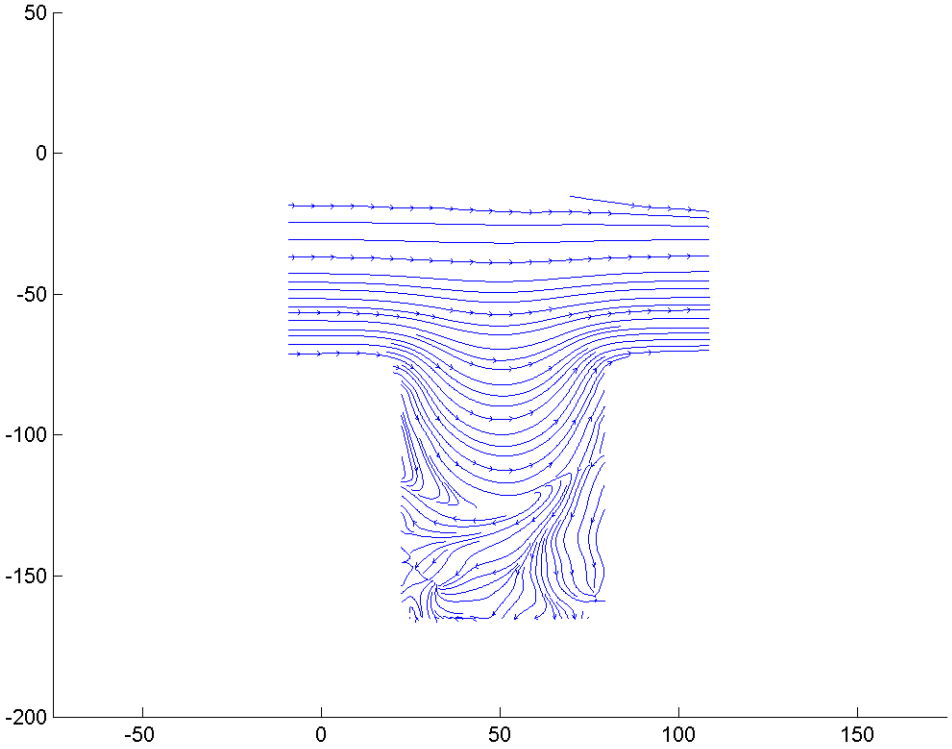

Figure F.68: Streamline image during phase increment 27 at 13 Hz and a Re of 0.1.

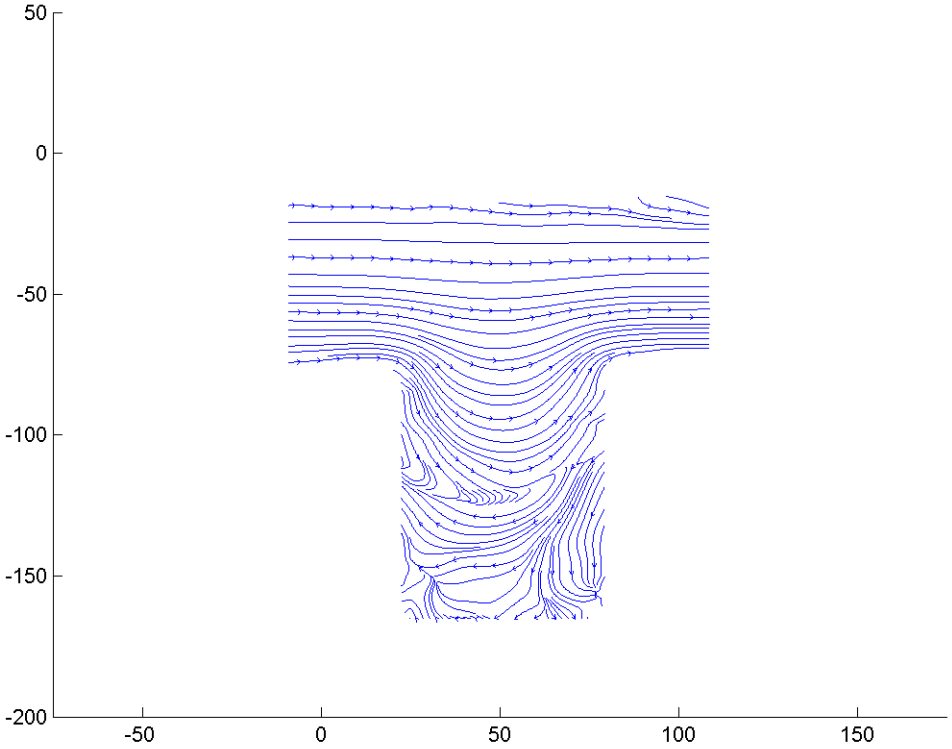

Figure F.69: Streamline image during phase increment 28 at 13 Hz and a Re of 0.1.

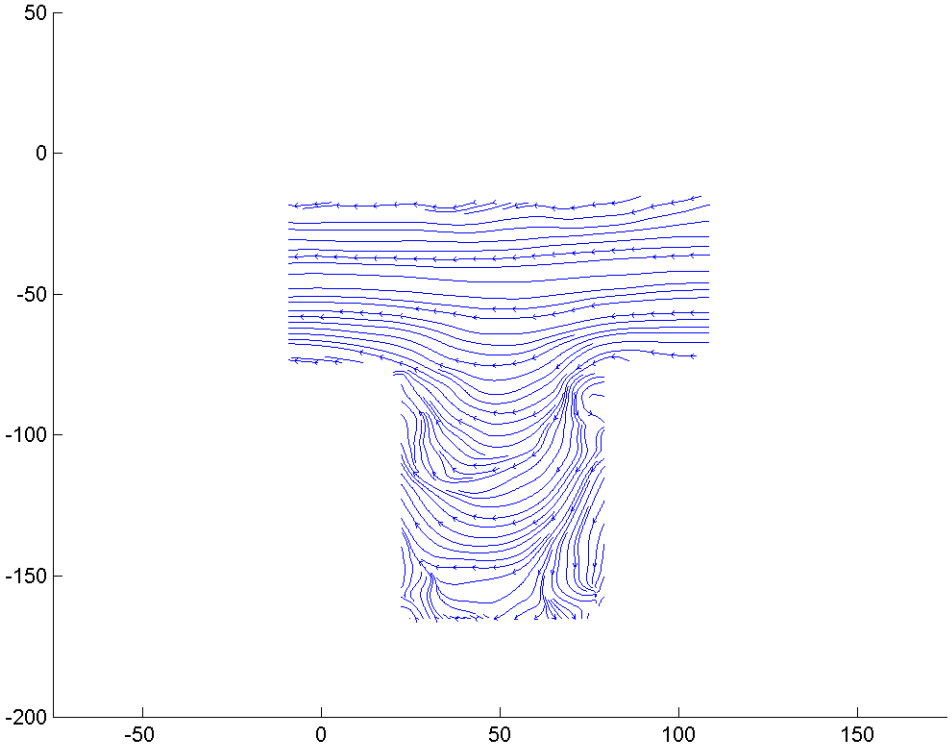

Figure F.70: Streamline image during phase increment 29 at 13 Hz and a Re of 0.1.

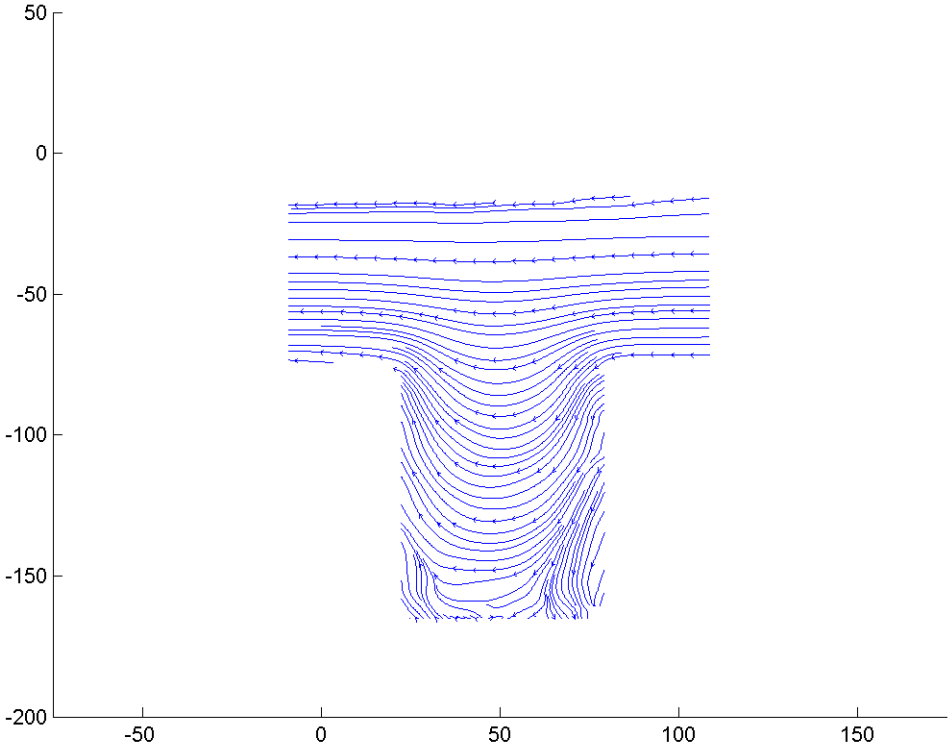

Figure F.71: Streamline image during phase increment 30 at 13 Hz and a Re of 0.1.

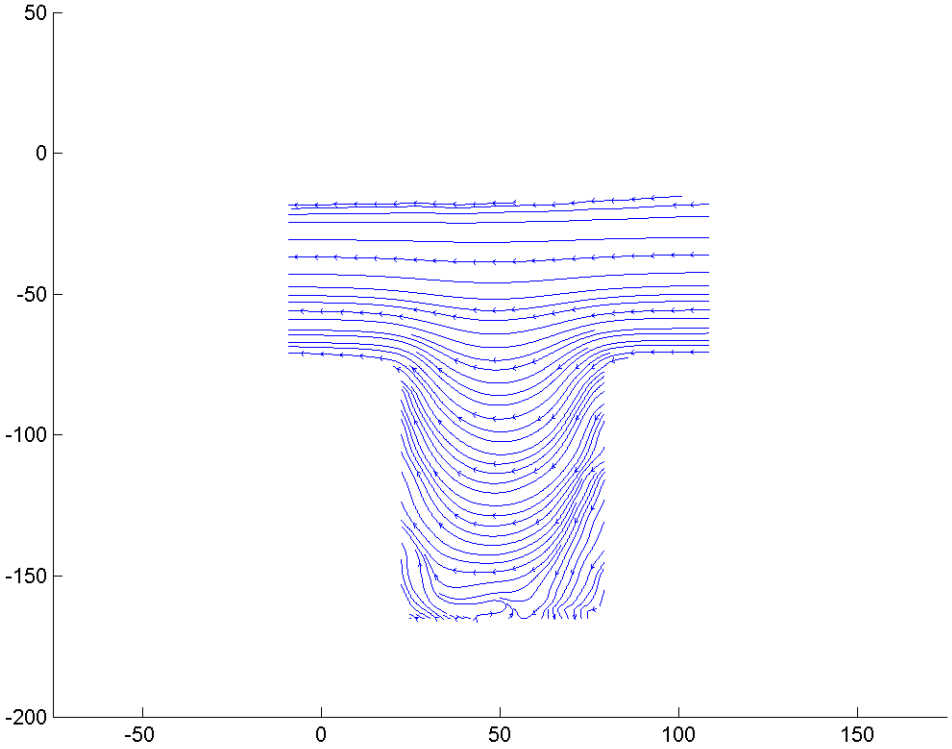

Figure F.72: Streamline image during phase increment 31 at 13 Hz and a Re of 0.1.

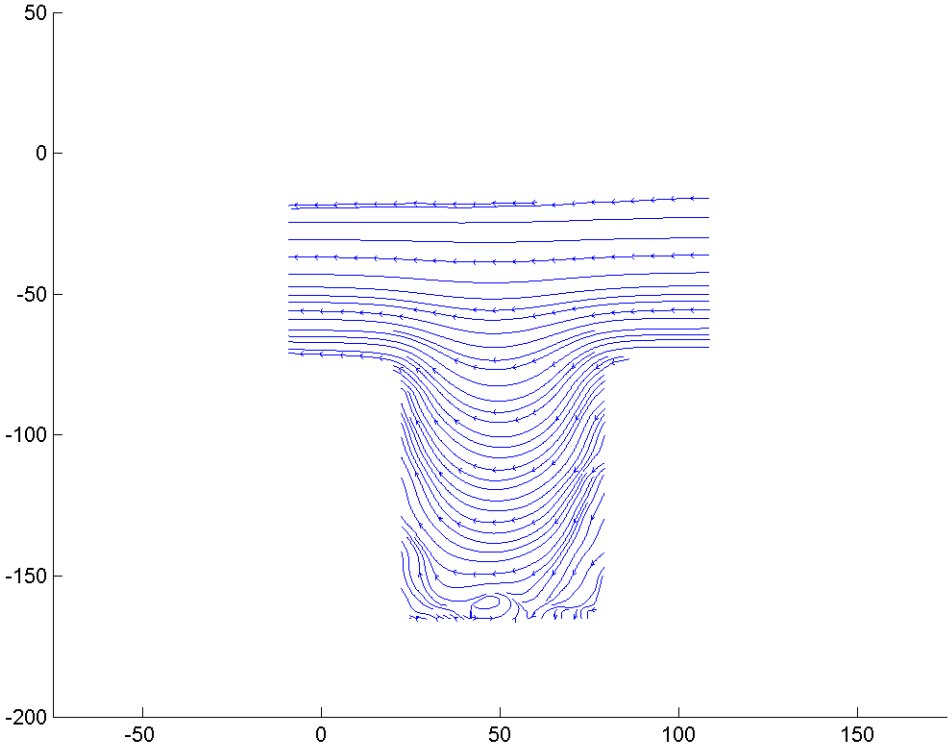

Figure F.73: Streamline image during phase increment 32 at 13 Hz and a Re of 0.1.

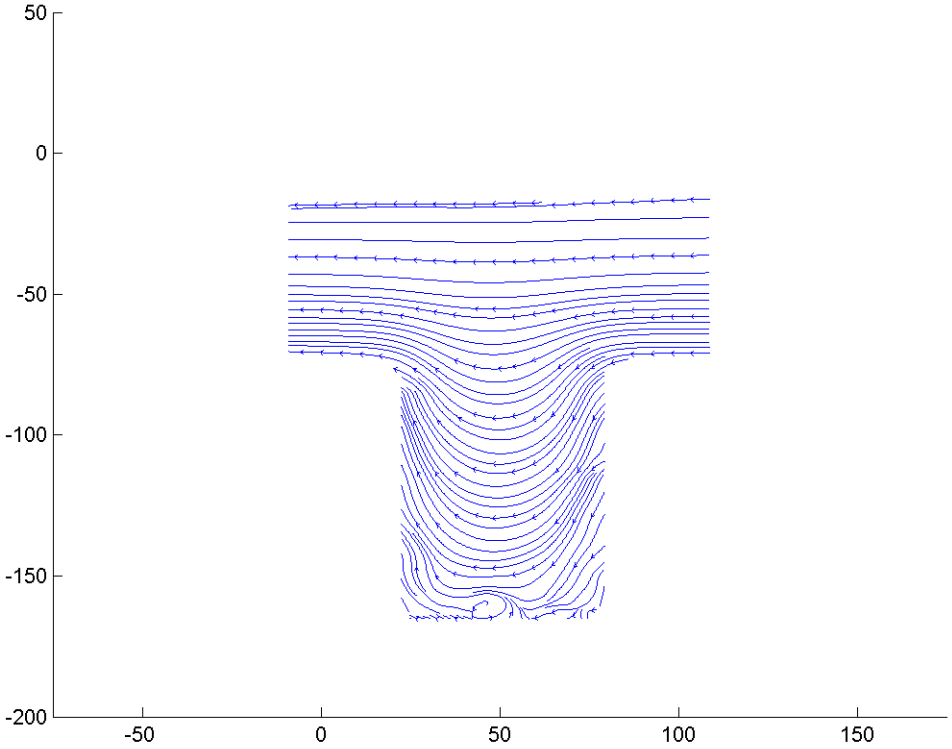

Figure F.74: Streamline image during phase increment 33 at 13 Hz and a Re of 0.1.

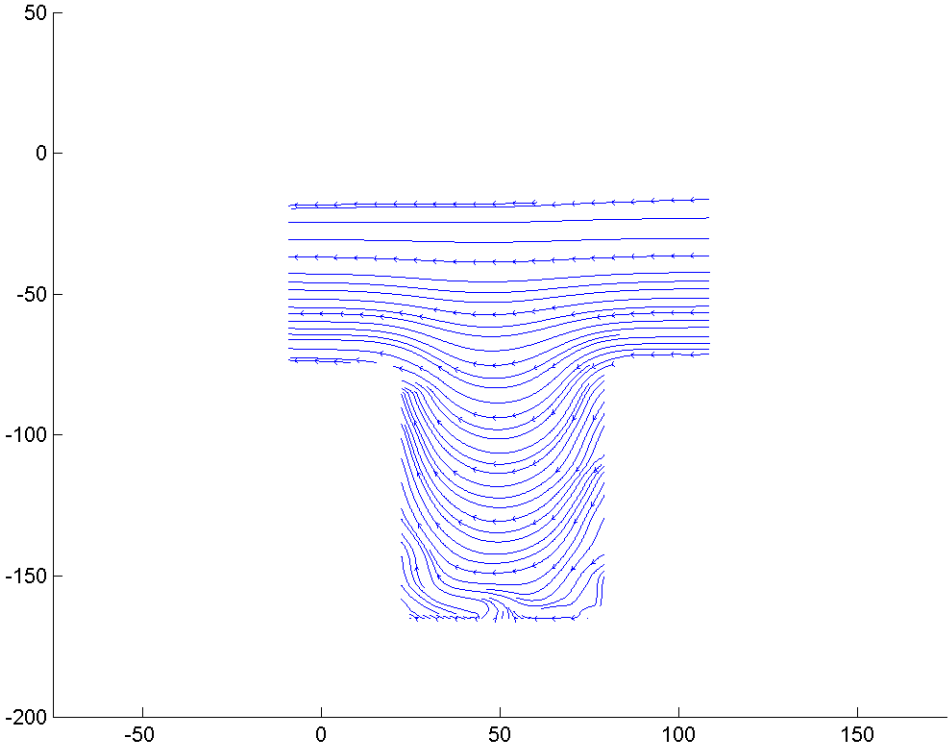

Figure F.75: Streamline image during phase increment 34 at 13 Hz and a Re of 0.1.

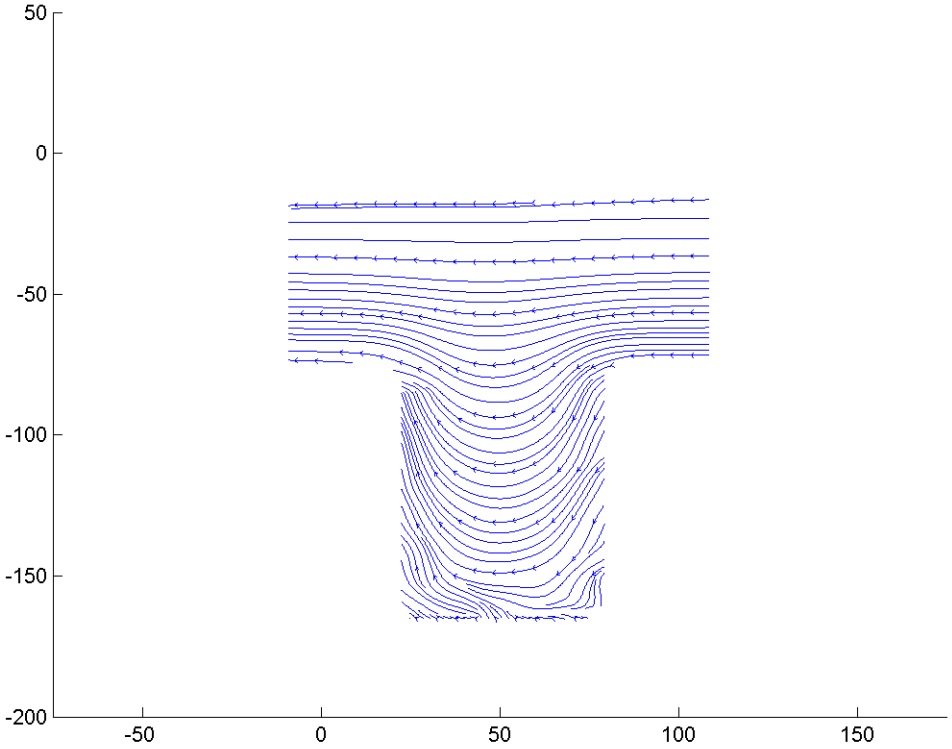

Figure F.76: Streamline image during phase increment 35 at 13 Hz and a Re of 0.1.

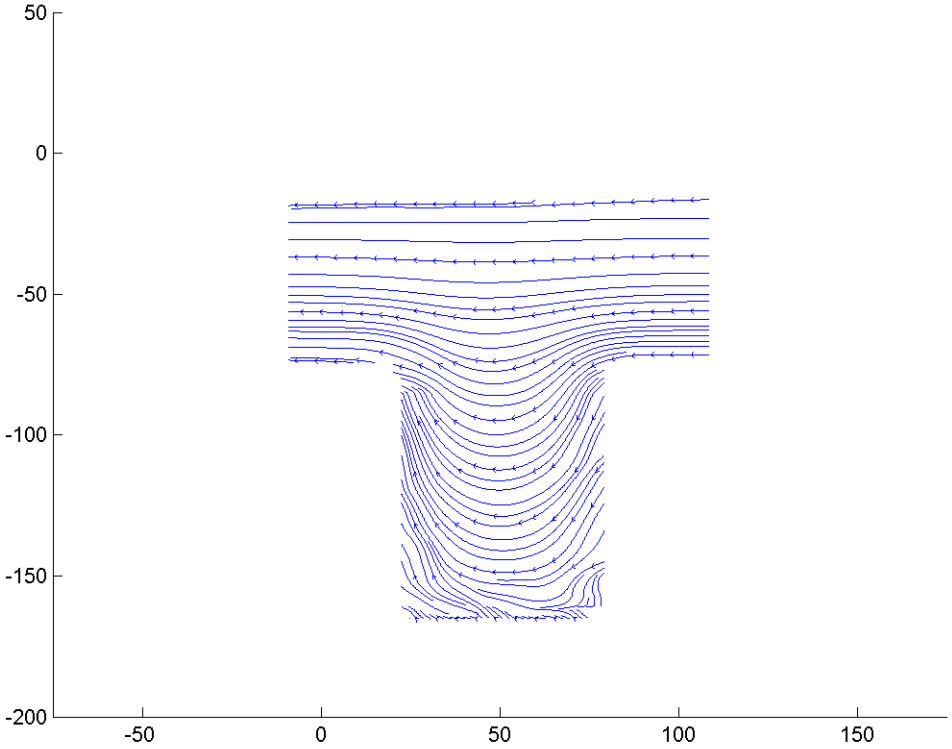

Figure F.77: Streamline image during phase increment 36 at 13 Hz and a Re of 0.1.

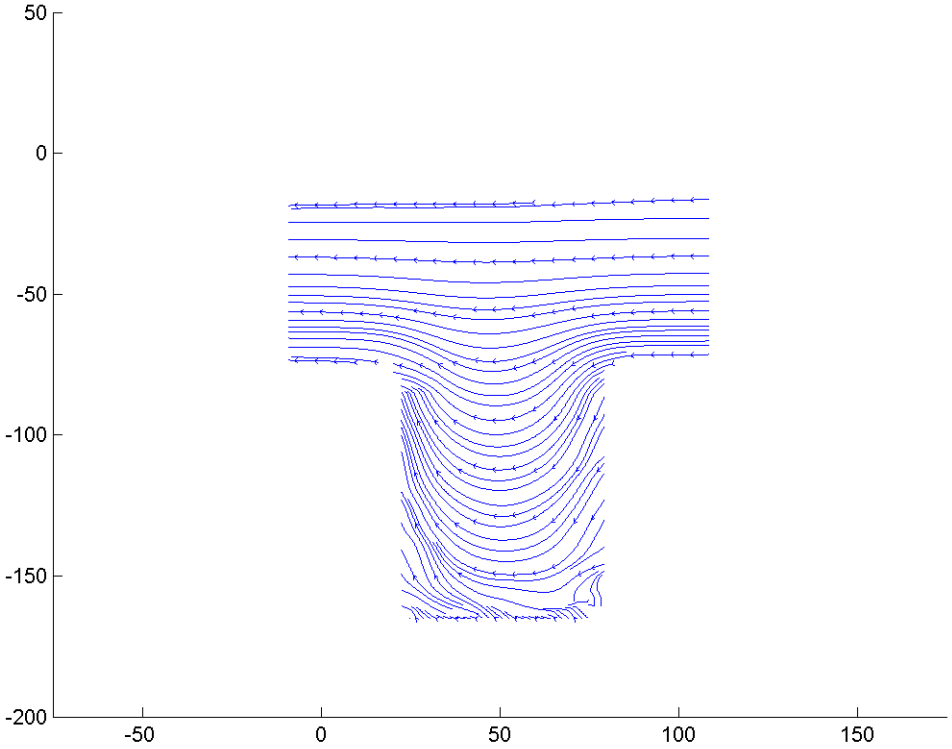

Figure F.78: Streamline image during phase increment 37 at 13 Hz and a Re of 0.1.

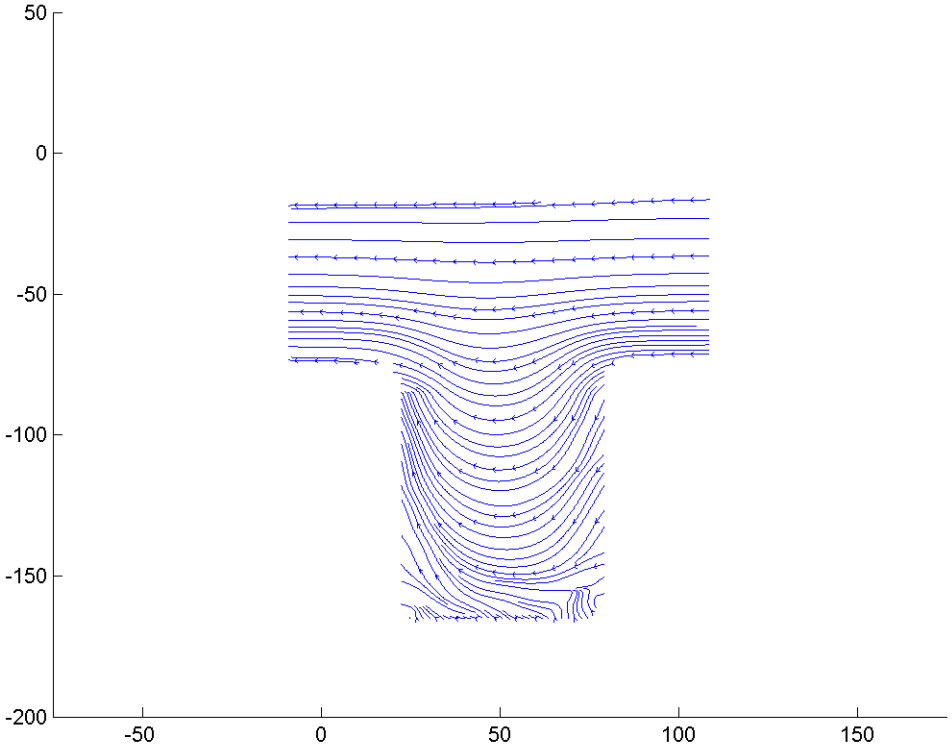

Figure F.79: Streamline image during phase increment 38 at 13 Hz and a Re of 0.1.

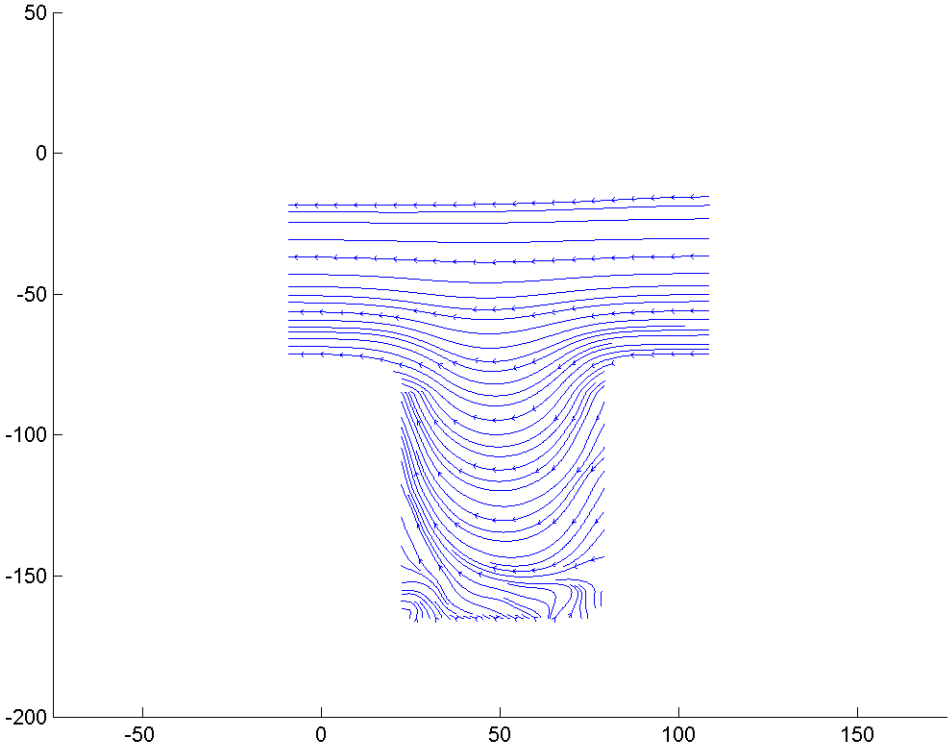

Figure F.80: Streamline image during phase increment 39 at 13 Hz and a Re of 0.1.

F.1.3 Residence time of particles in the cavity at 13 Hz

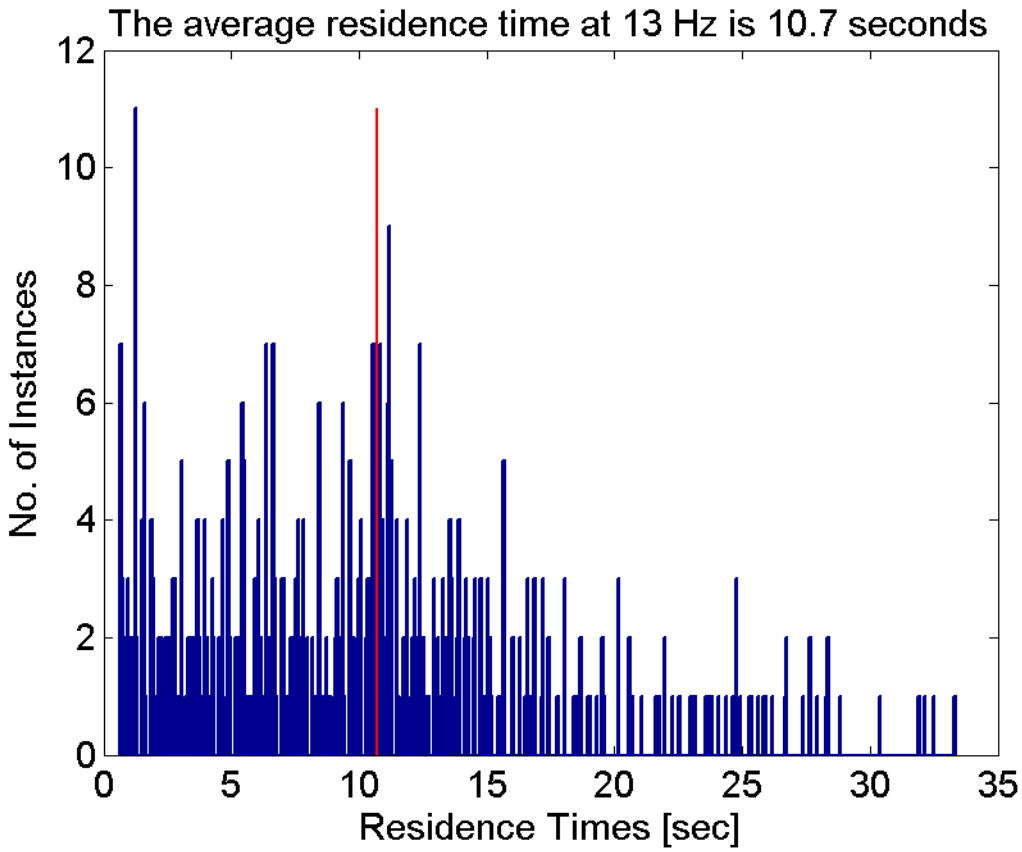

Figure F.81: The residence time distribution for the AR = 0.5 cavity at Re 0.1 at 13 Hz. The average residence time is 10.7 secs.

F.1.4 Lagrangian coherent structures at 13 Hz

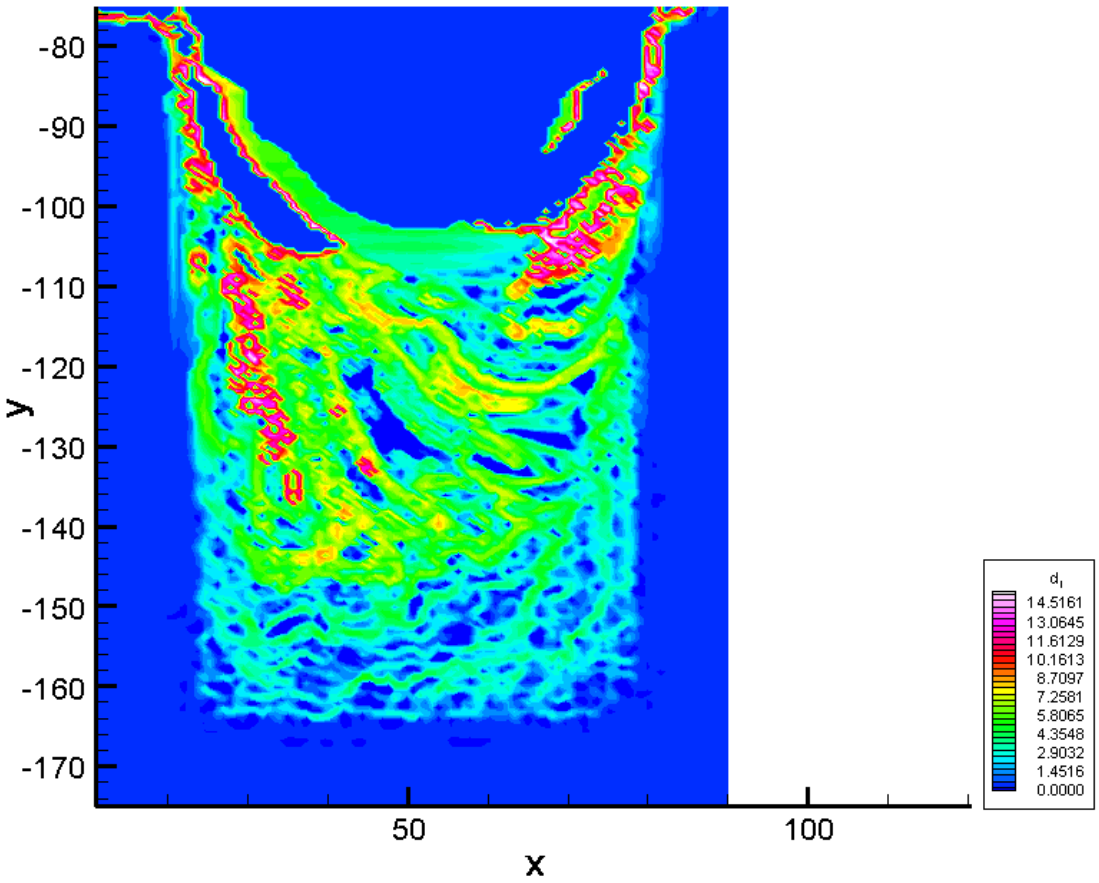

Figure F.82: The backward time LCS during phase increment 1 at 13 Hz.

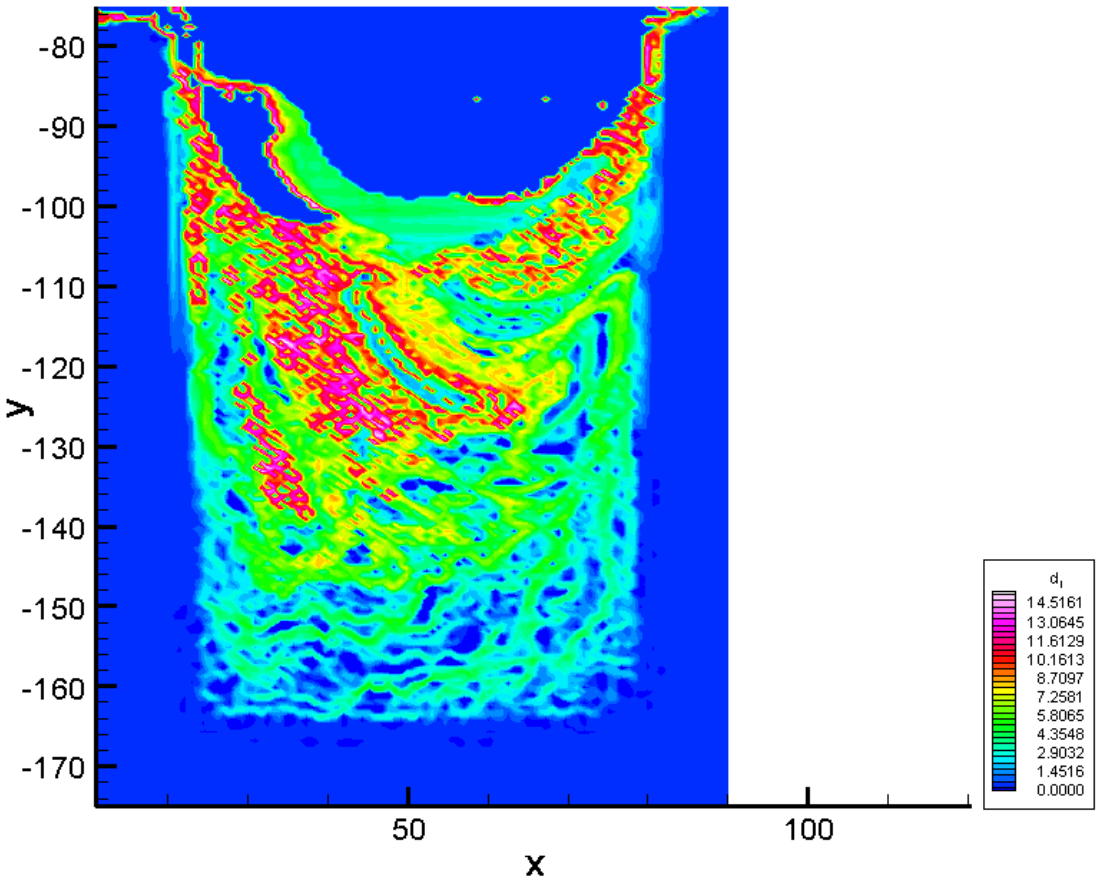

Figure F.83: The backward time LCS during phase increment 2 at 13 Hz.

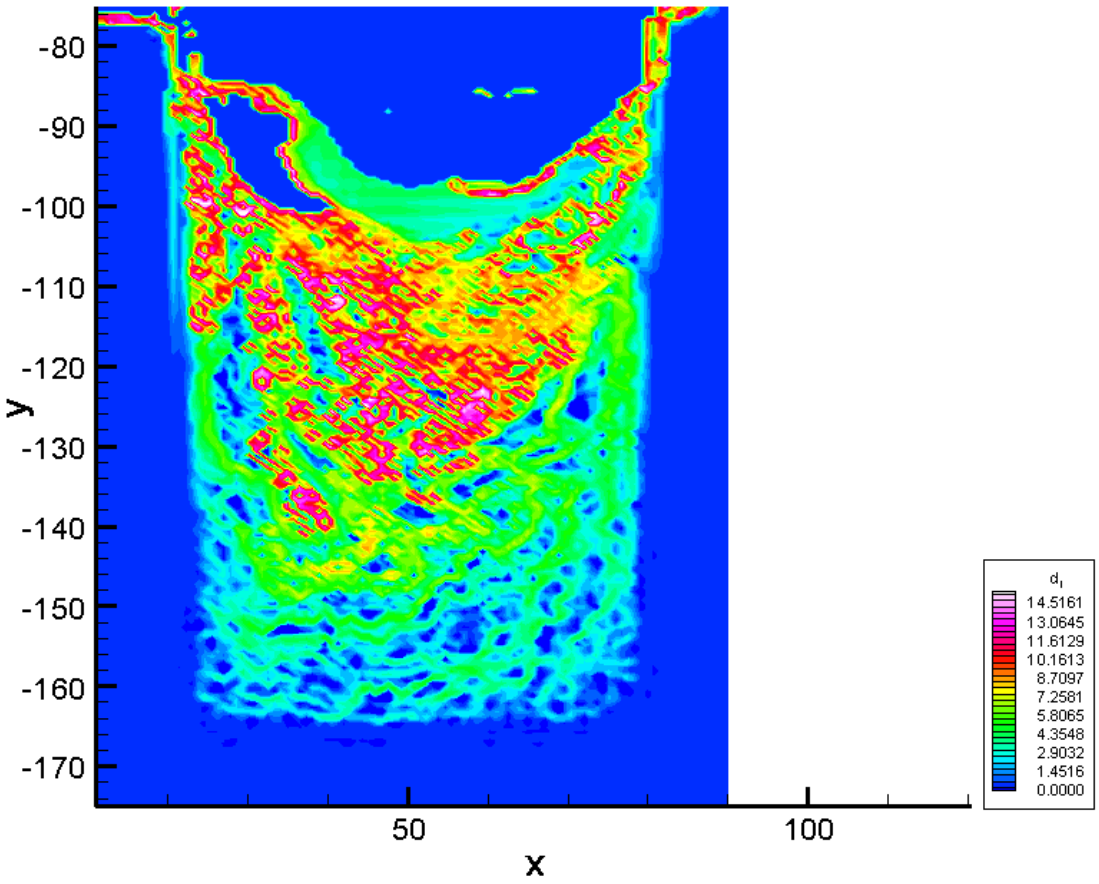

Figure F.84: The backward time LCS during phase increment 3 at 13 Hz.

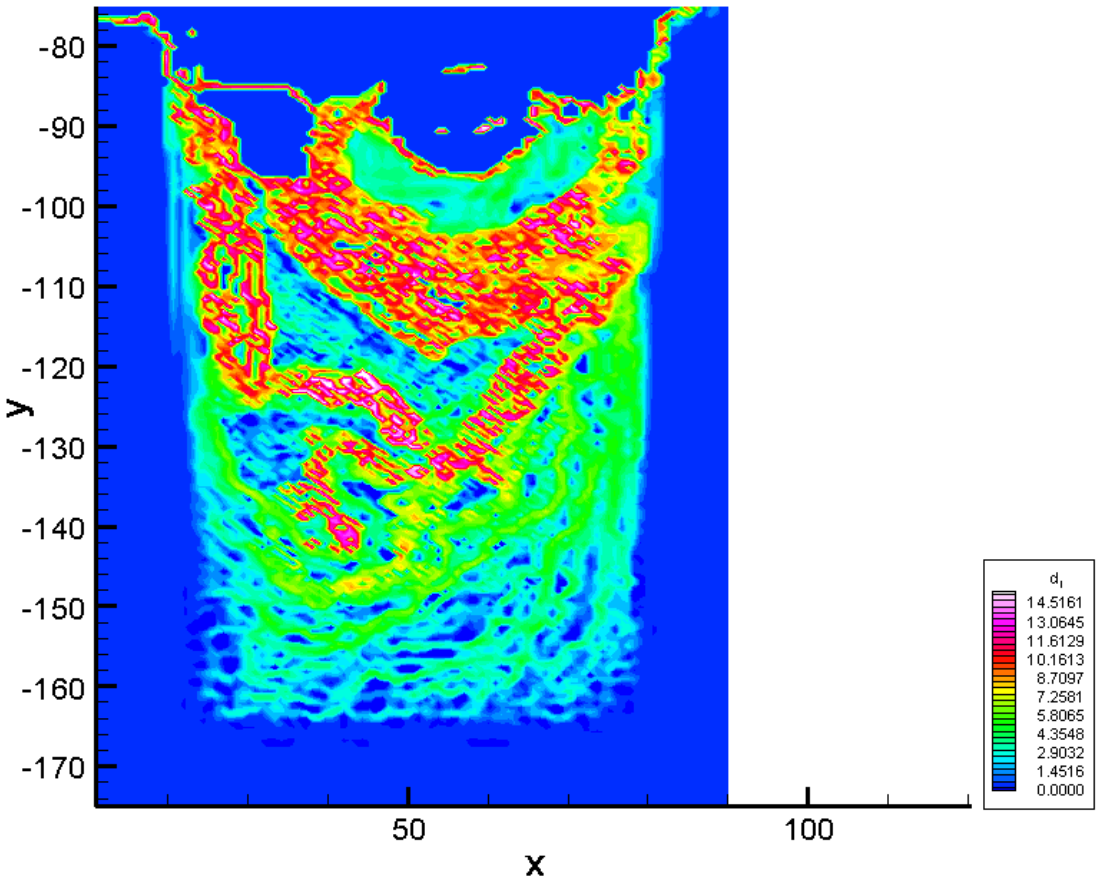

Figure F.85: The backward time LCS during phase increment 4 at 13 Hz.

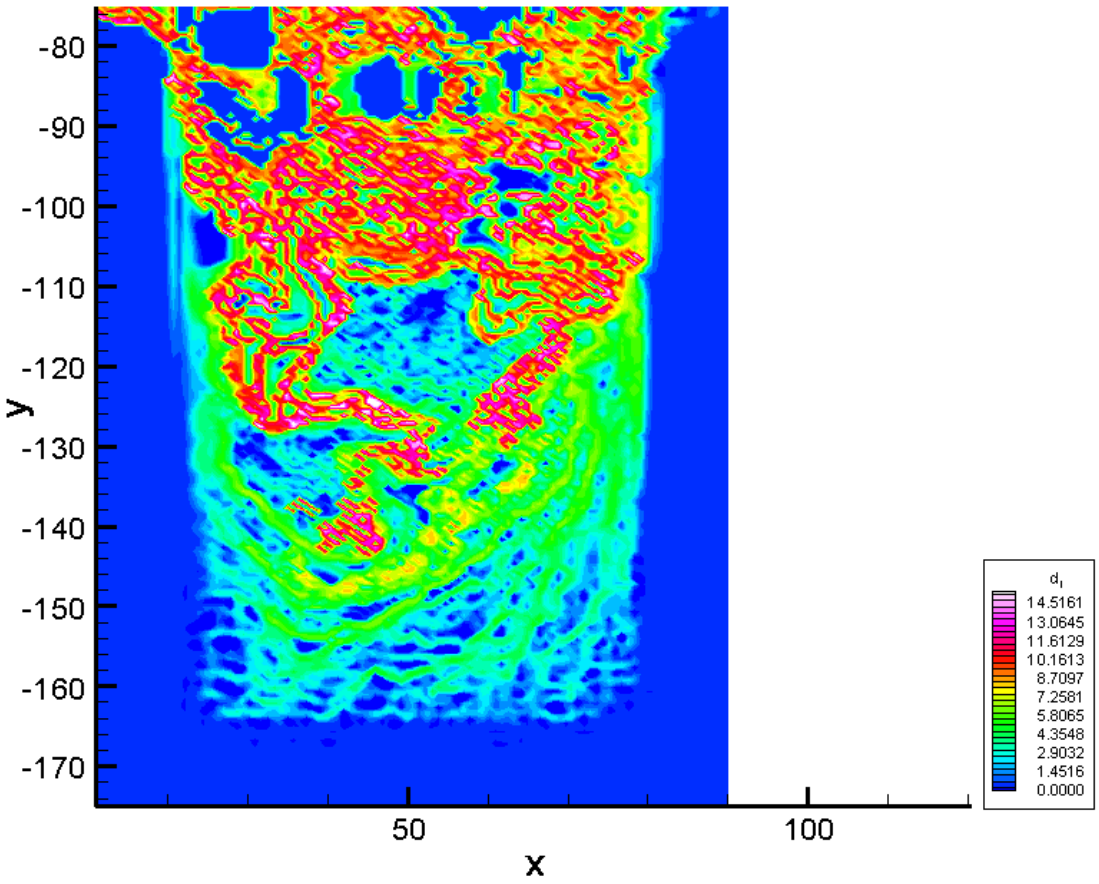

Figure F.86: The backward time LCS during phase increment 5 at 13 Hz.

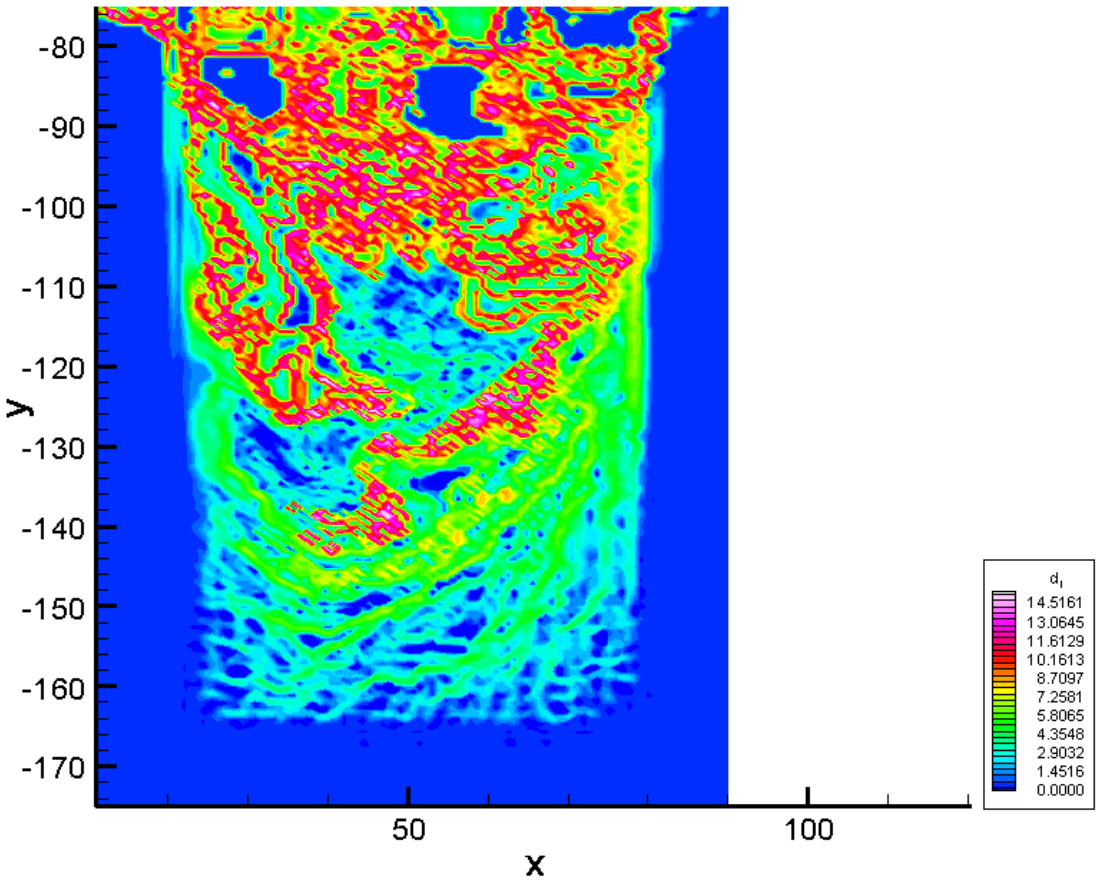

Figure F.87: The backward time LCS during phase increment 6 at 13 Hz.

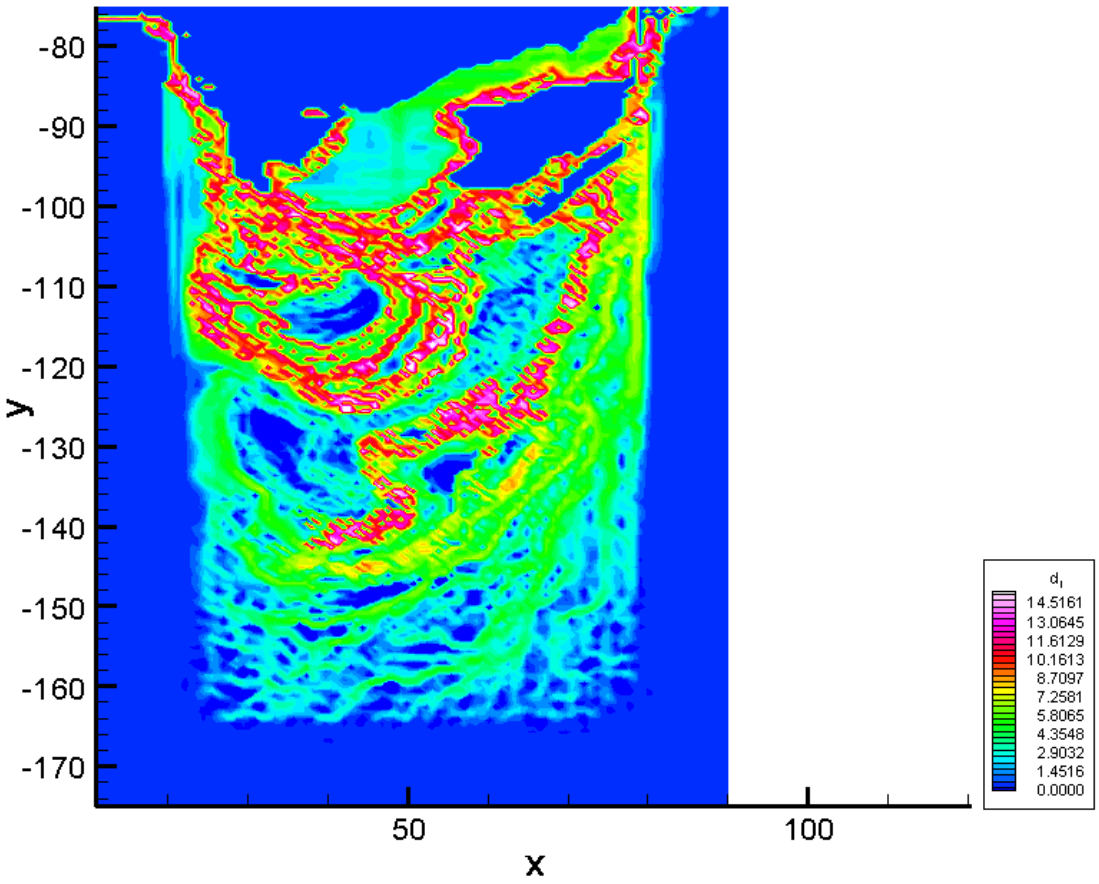

Figure F.88: The backward time LCS during phase increment 7 at 13 Hz.

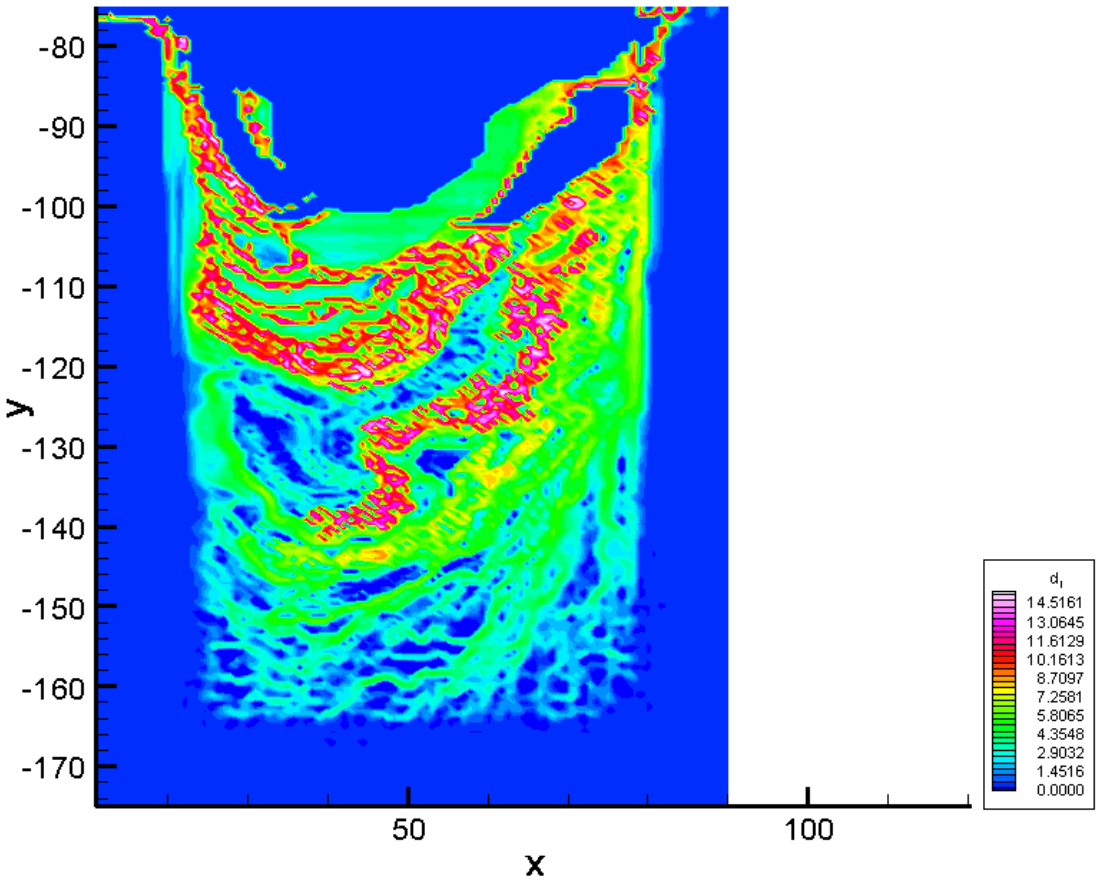

Figure F.89: The backward time LCS during phase increment 8 at 13 Hz.

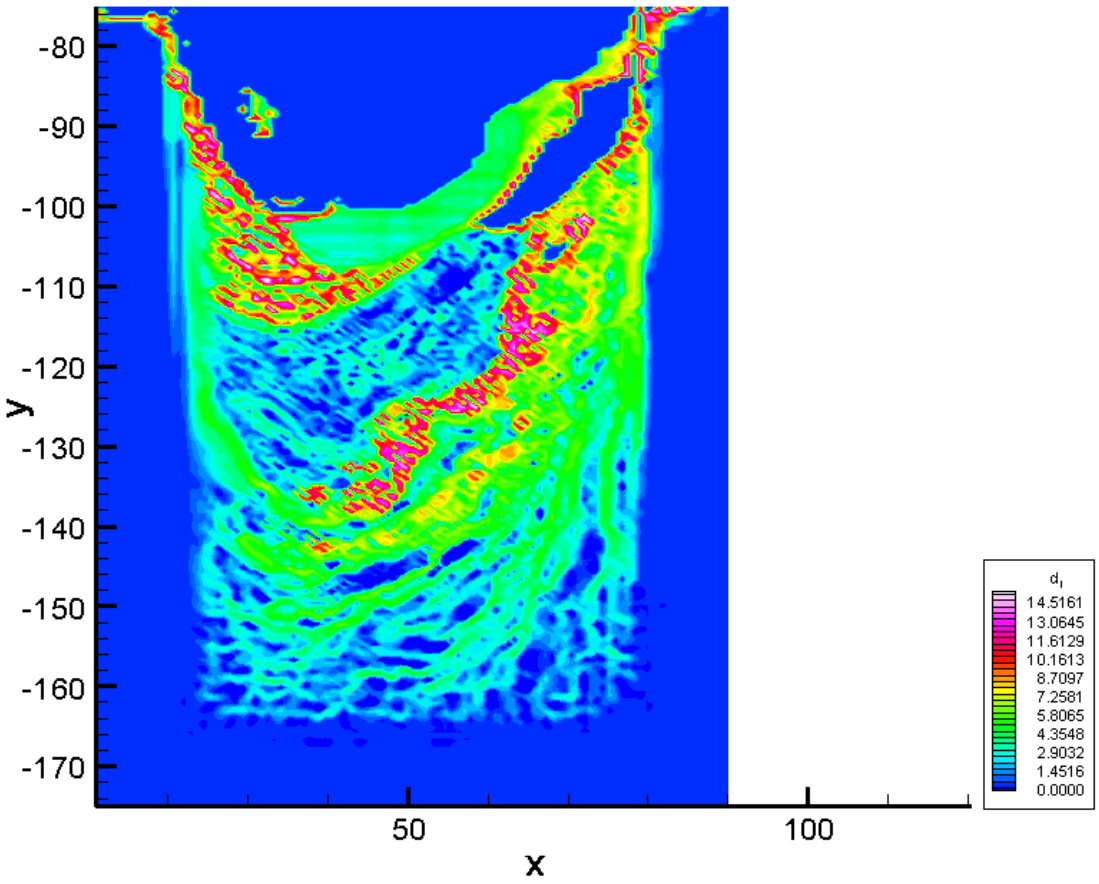

Figure F.90: The backward time LCS during phase increment 9 at 13 Hz.

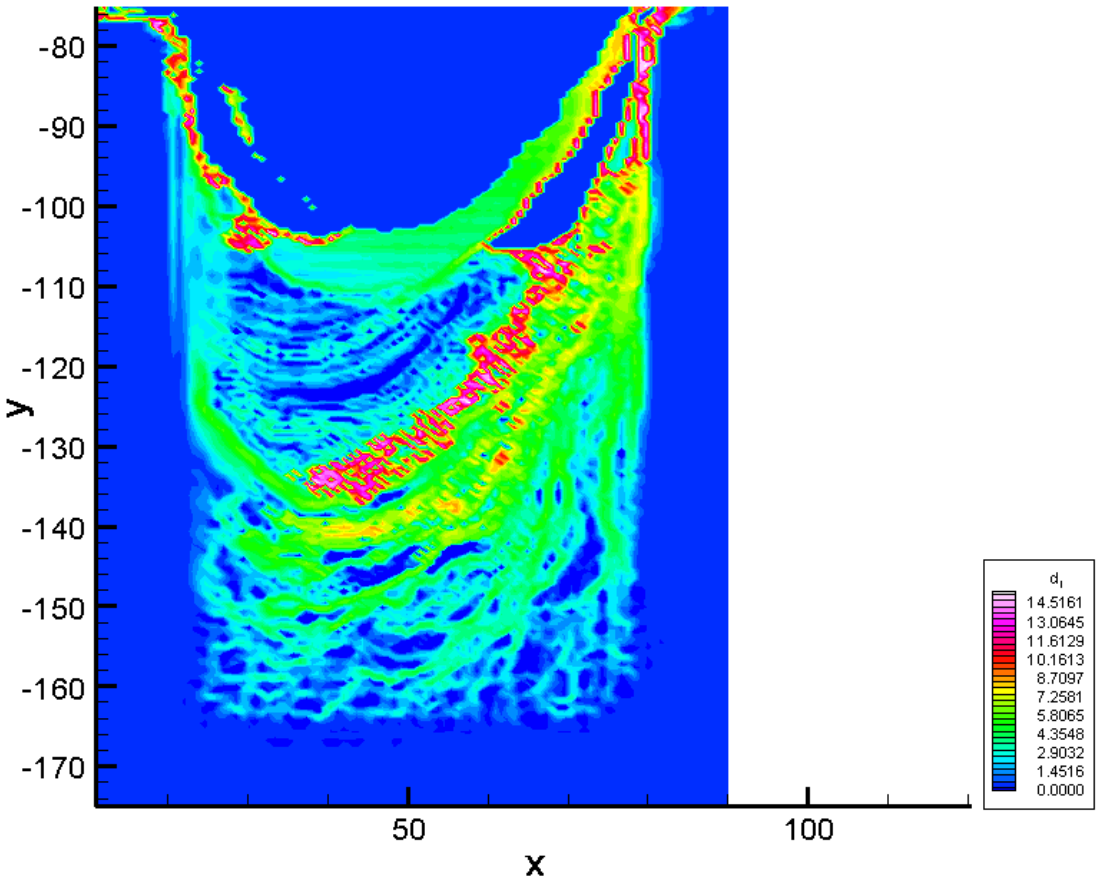

Figure F.91: The backward time LCS during phase increment 10 at 13 Hz.

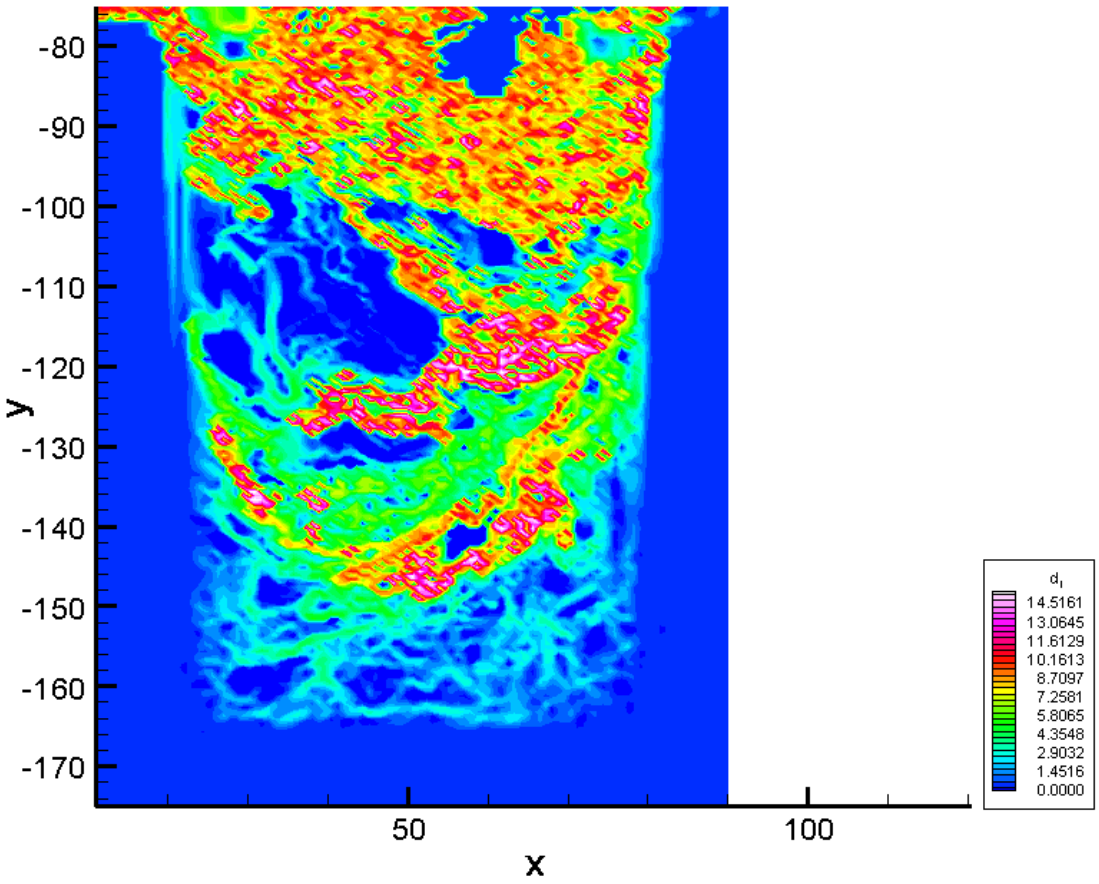

Figure F.92: The forward time LCS during phase increment 1 at 13 Hz.

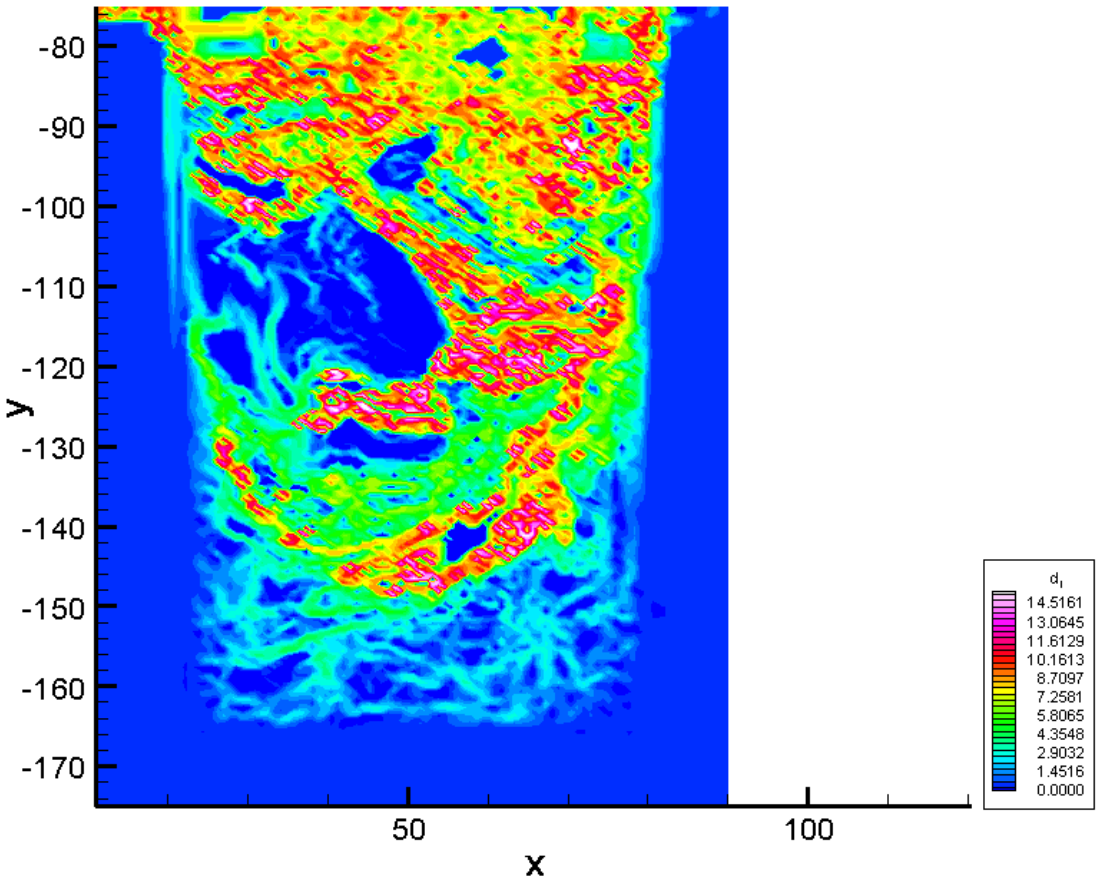

Figure F.93: The forward time LCS during phase increment 2 at 13 Hz.

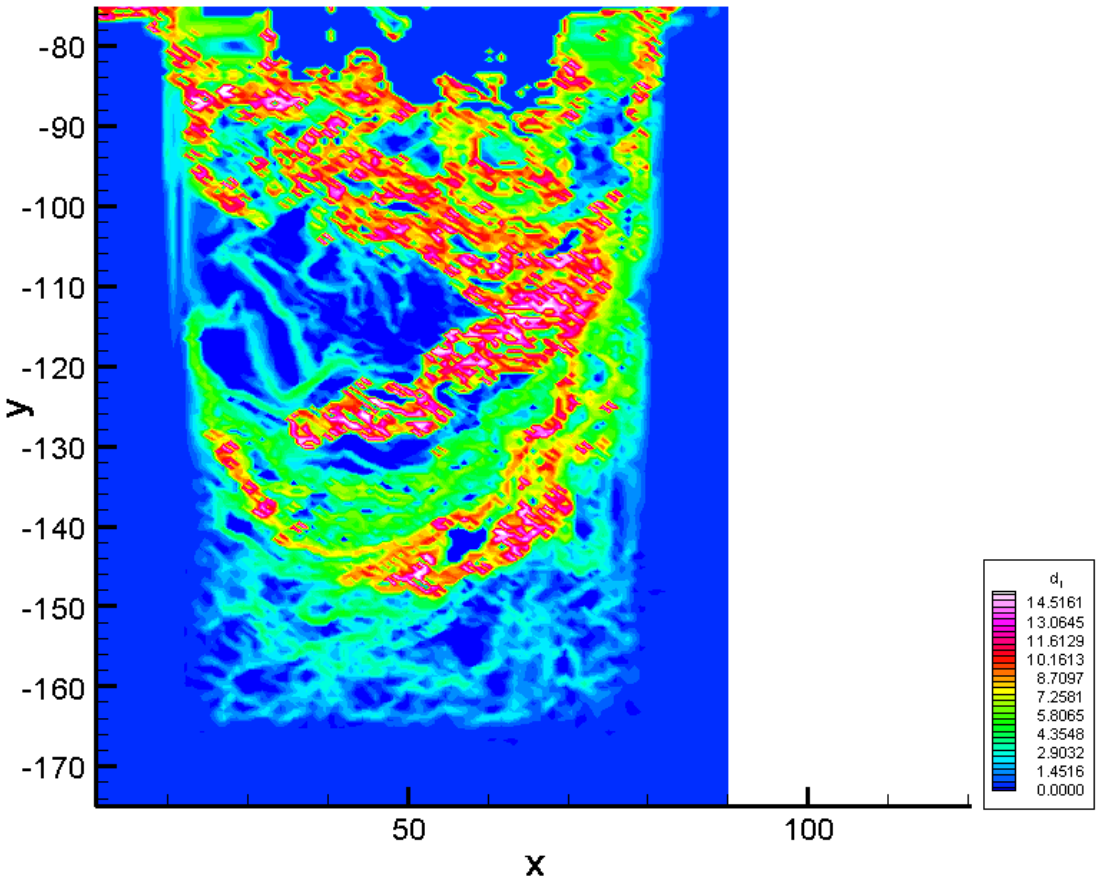

Figure F.94: The forward time LCS during phase increment 3 at 13 Hz.

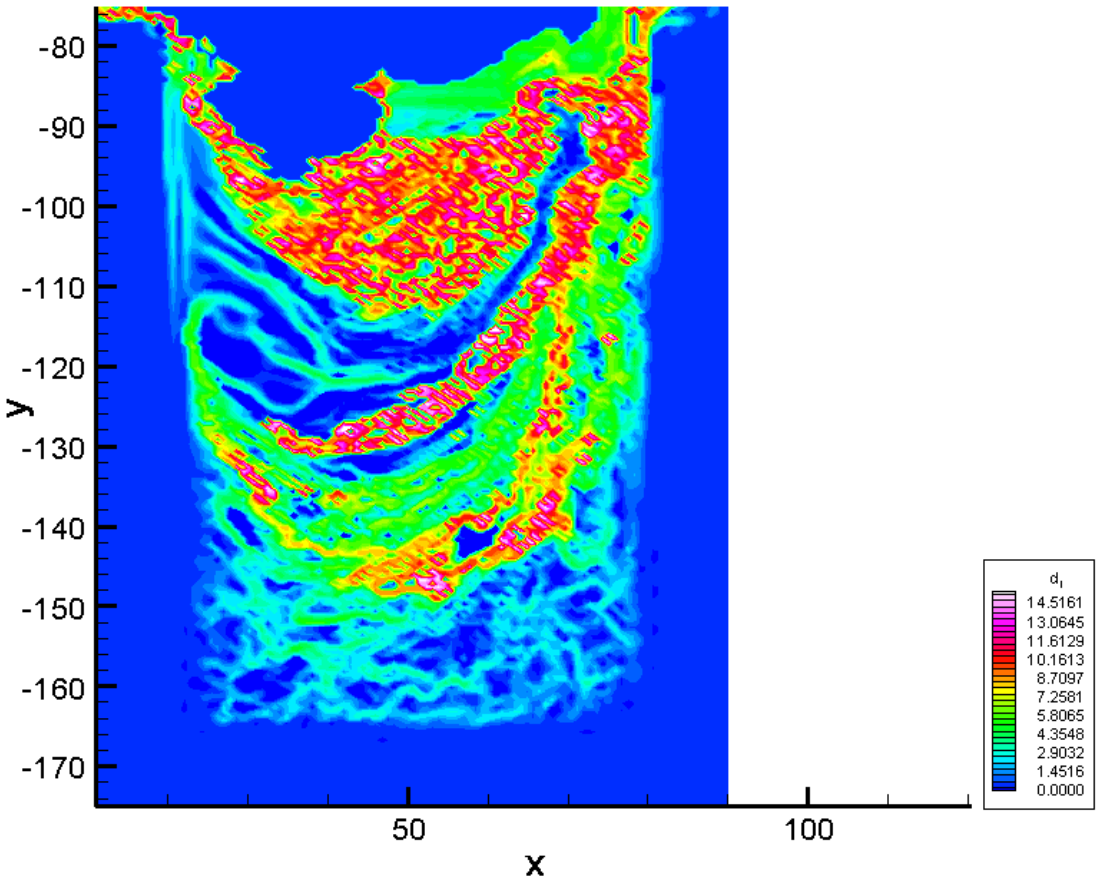

Figure F.95: The forward time LCS during phase increment 4 at 13 Hz.

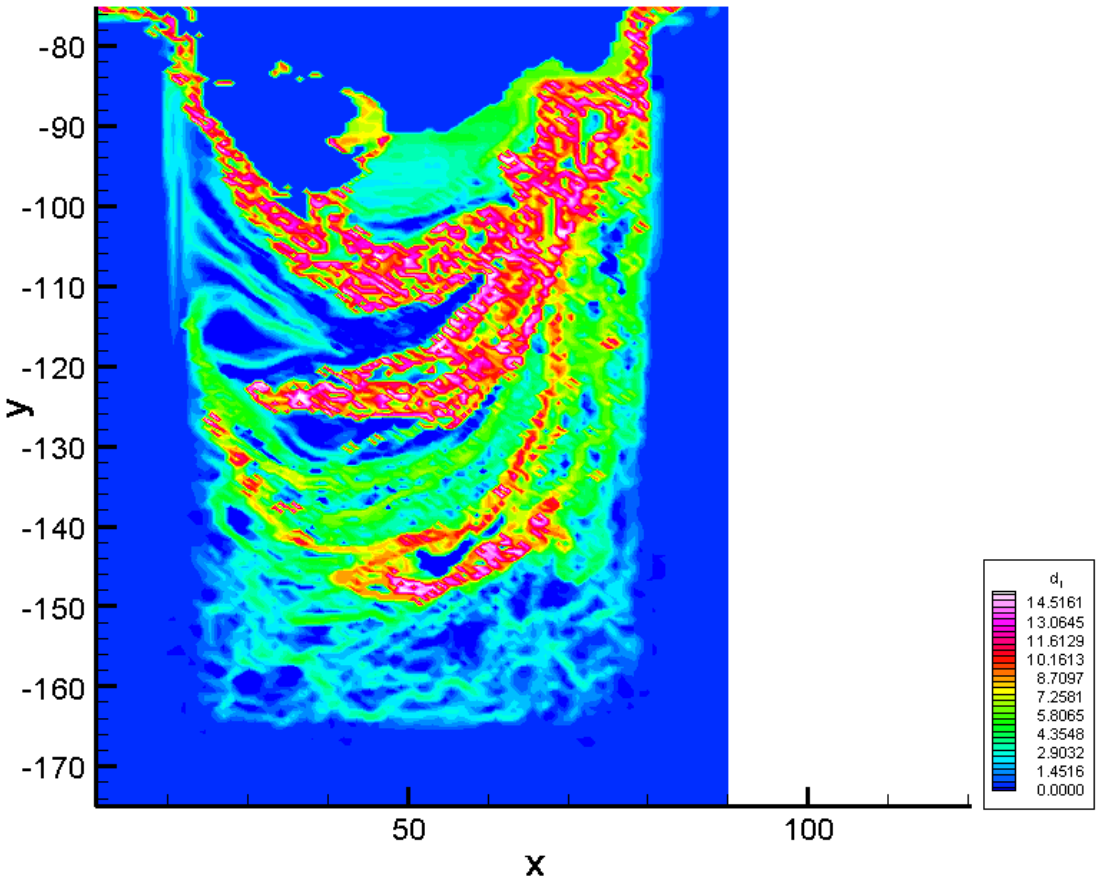

Figure F.96: The forward time LCS during phase increment 5 at 13 Hz.

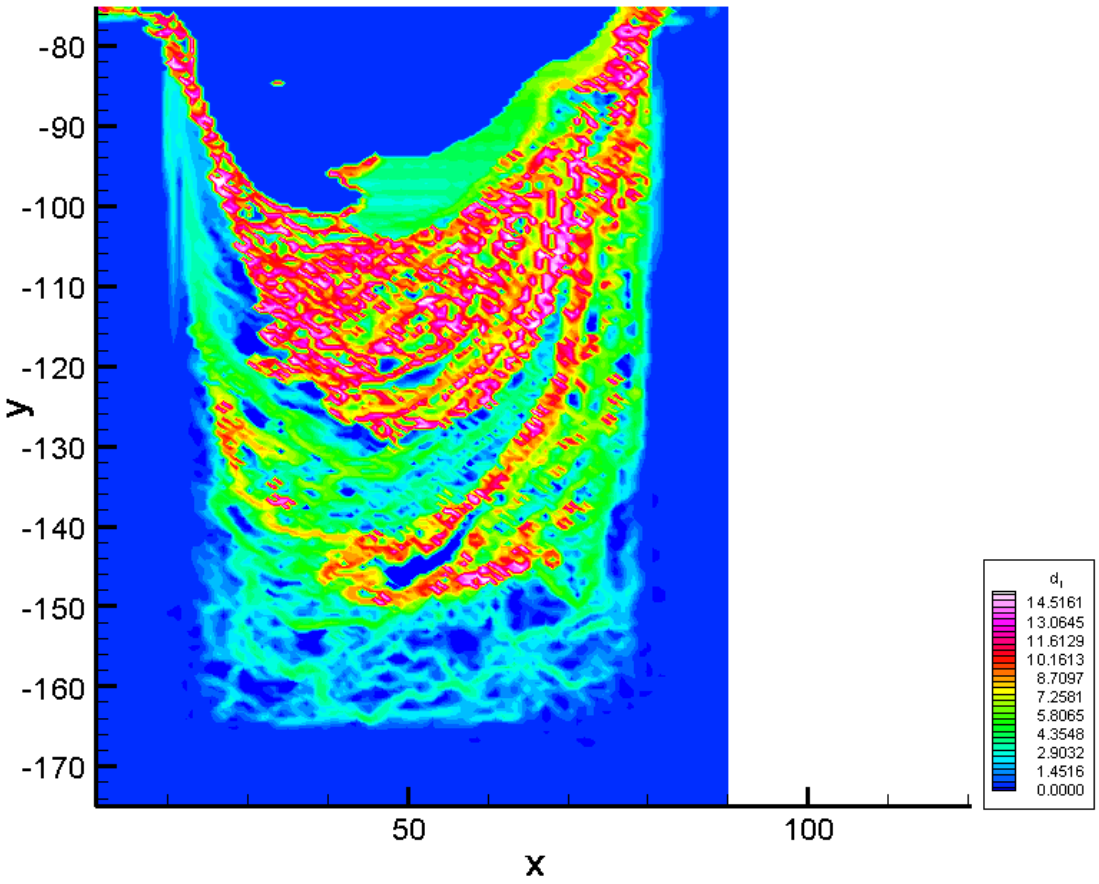

Figure F.97: The forward time LCS during phase increment 6 at 13 Hz.

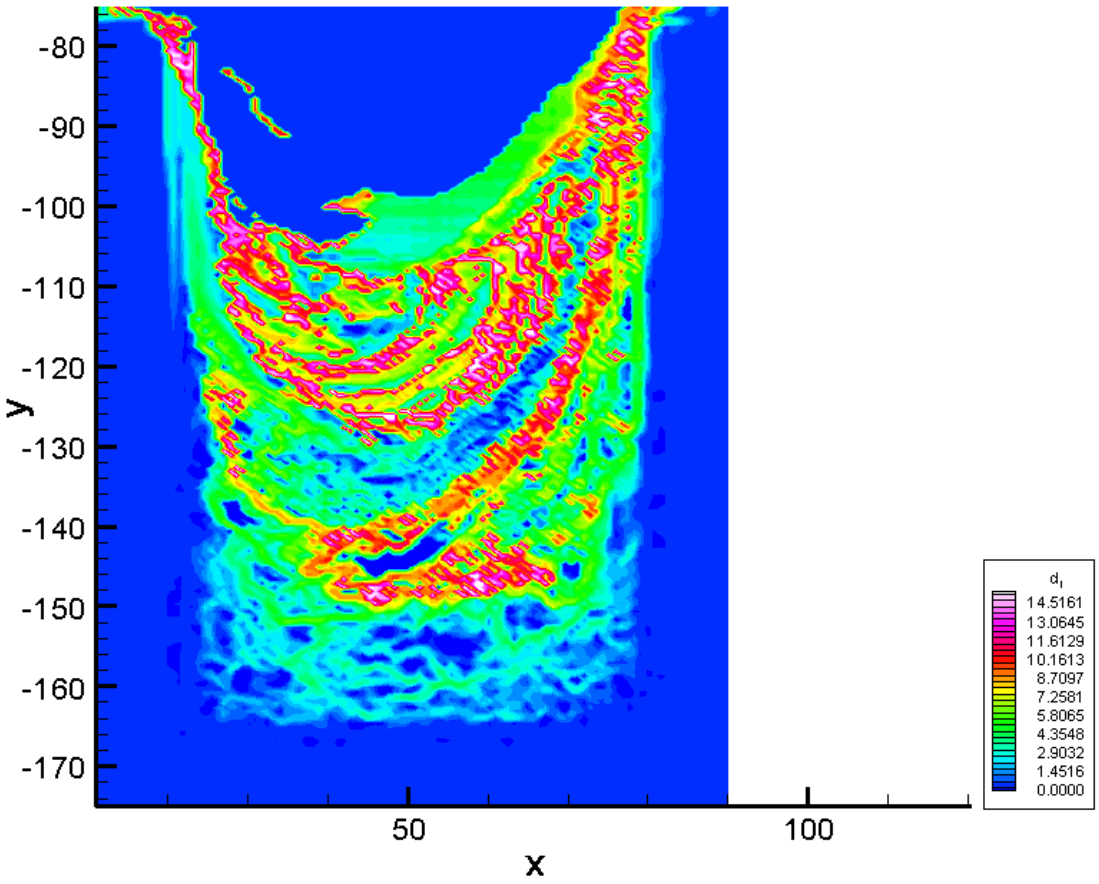

Figure F.98: The forward time LCS during phase increment 7 at 13 Hz.

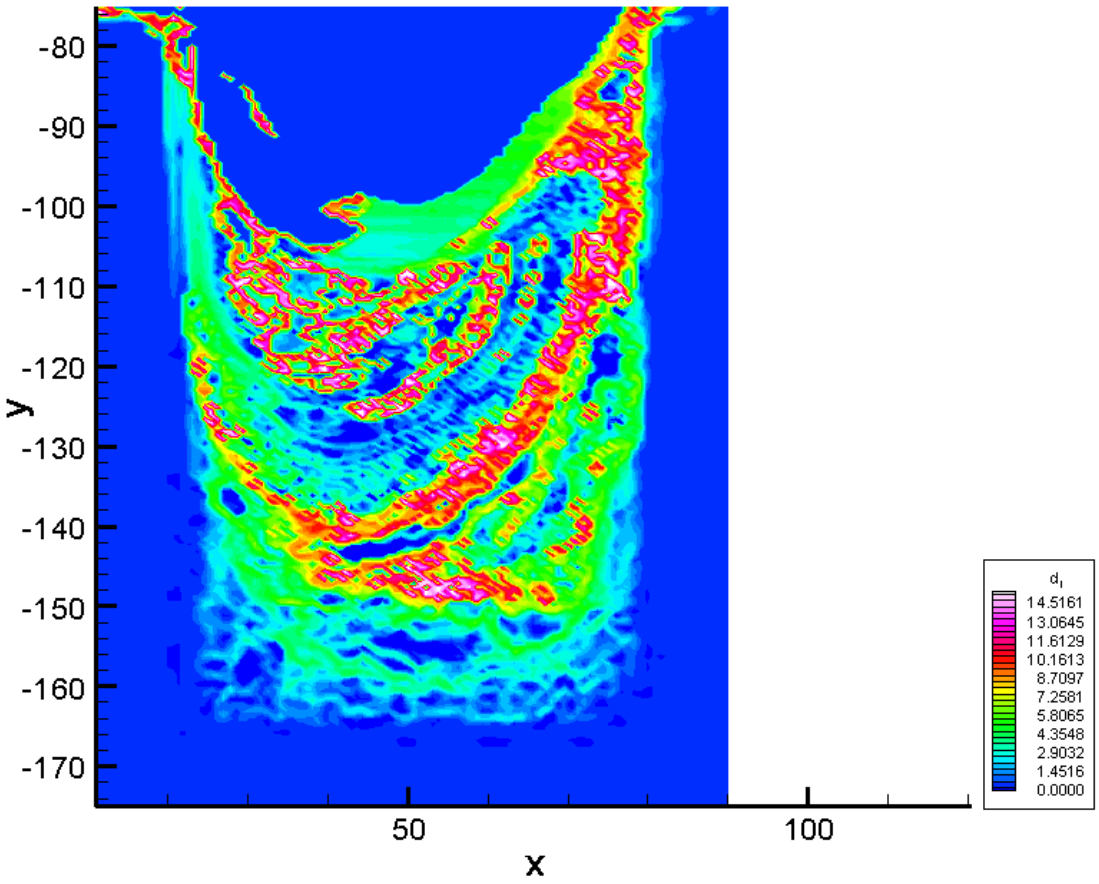

Figure F.99: The forward time LCS during phase increment 8 at 13 Hz.

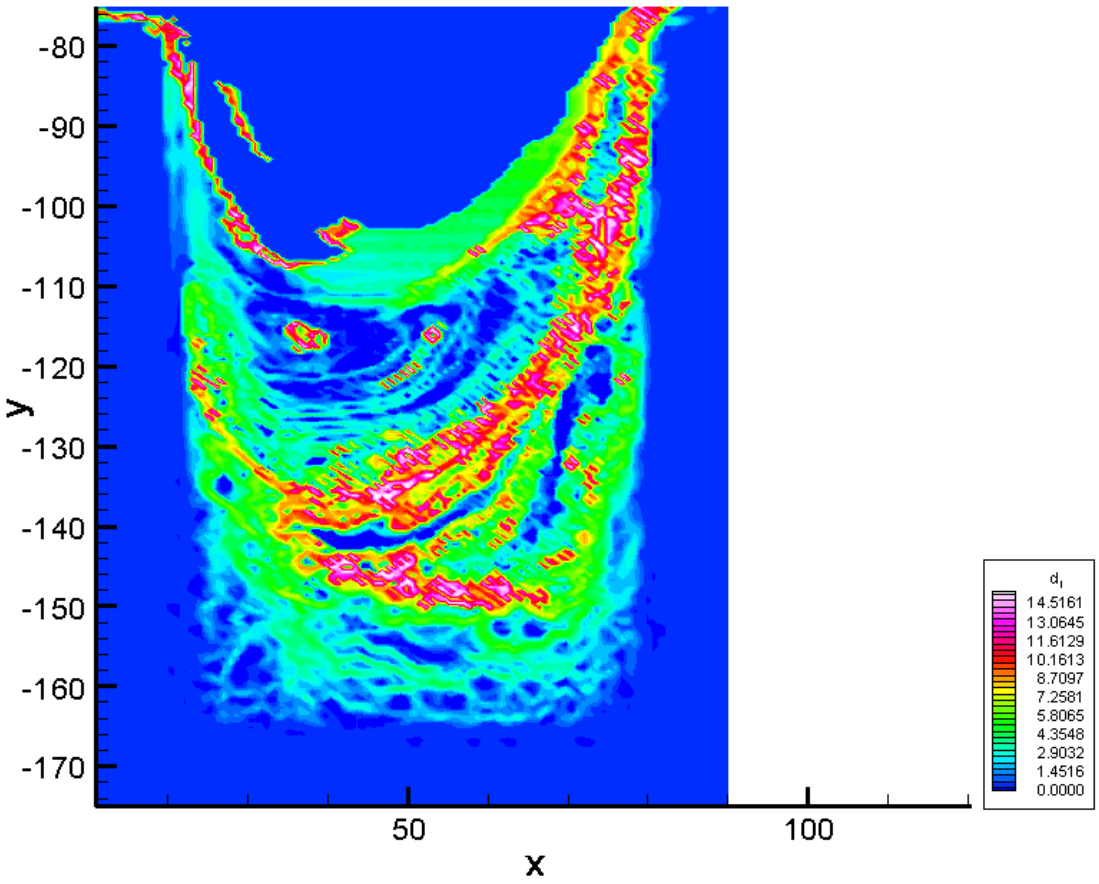

Figure F.100: The forward time LCS during phase increment 9 at 13 Hz.

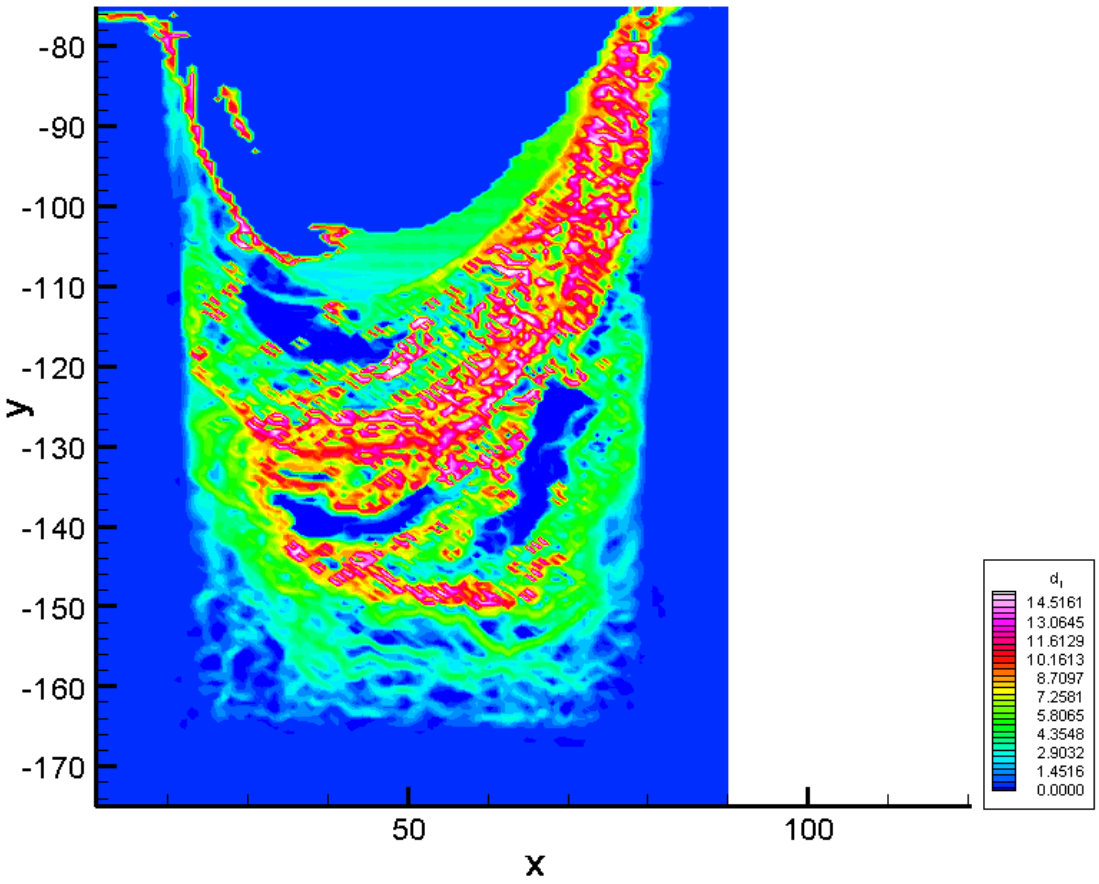

Figure F.101: The forward time LCS during phase increment 10 at 13 Hz.

F.2 80 Hz

F.2.1 Velocity field data at 80 Hz

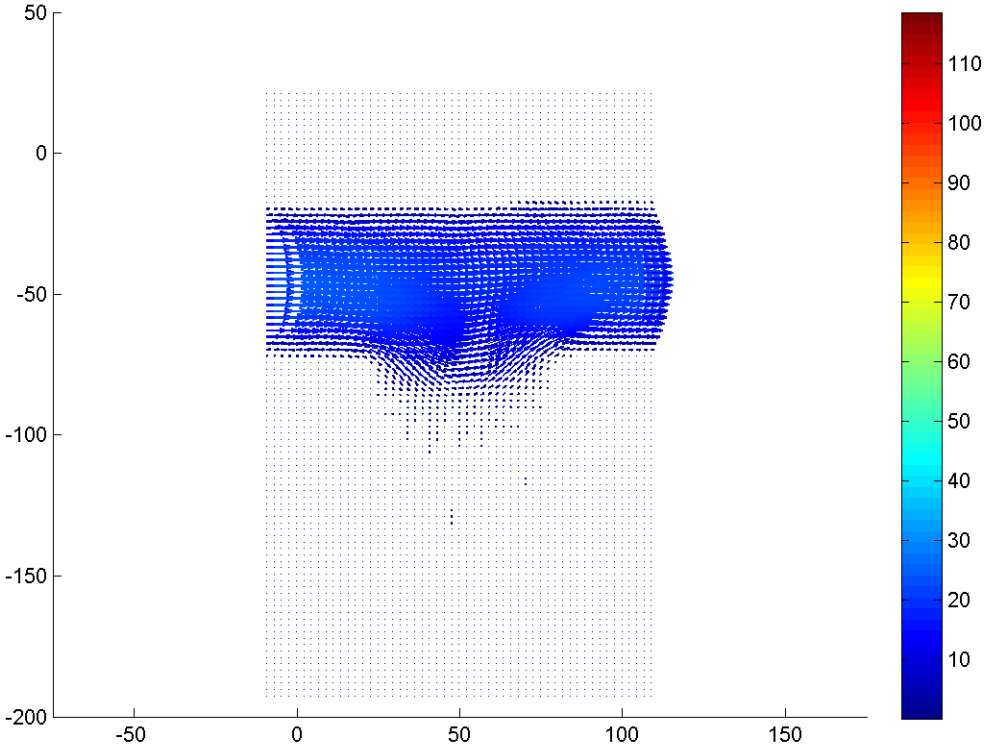

Figure F.102: Velocity field during phase increment 1 at 80 Hz with a Re of 0.1.

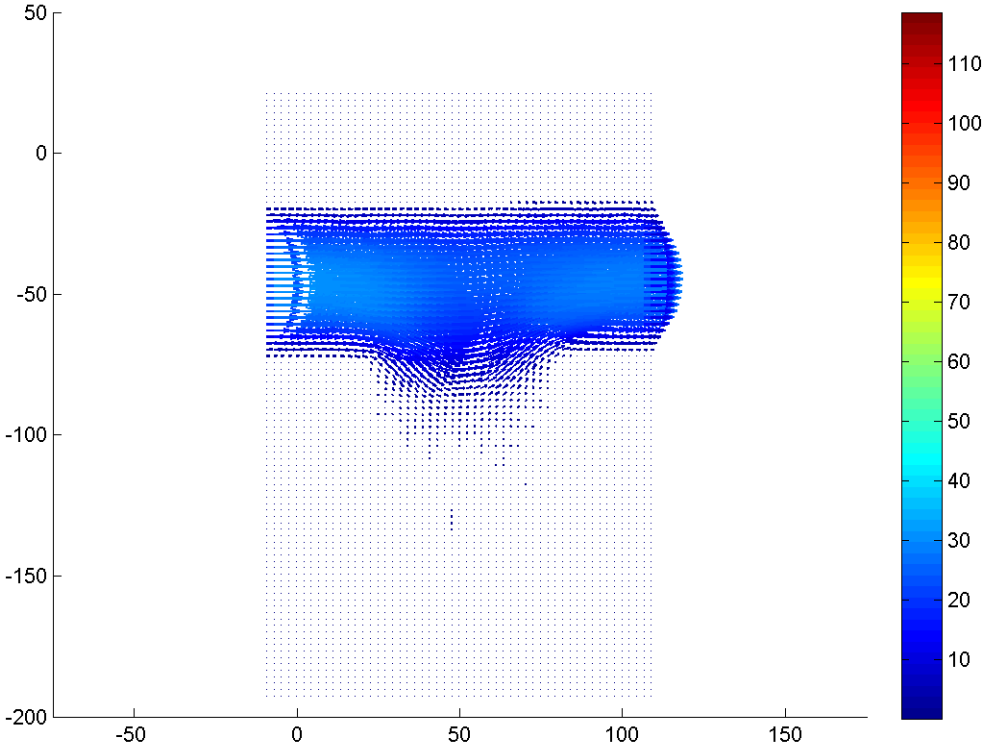

Figure F.103: Velocity field during phase increment 2 at 80 Hz with a Re of 0.1.

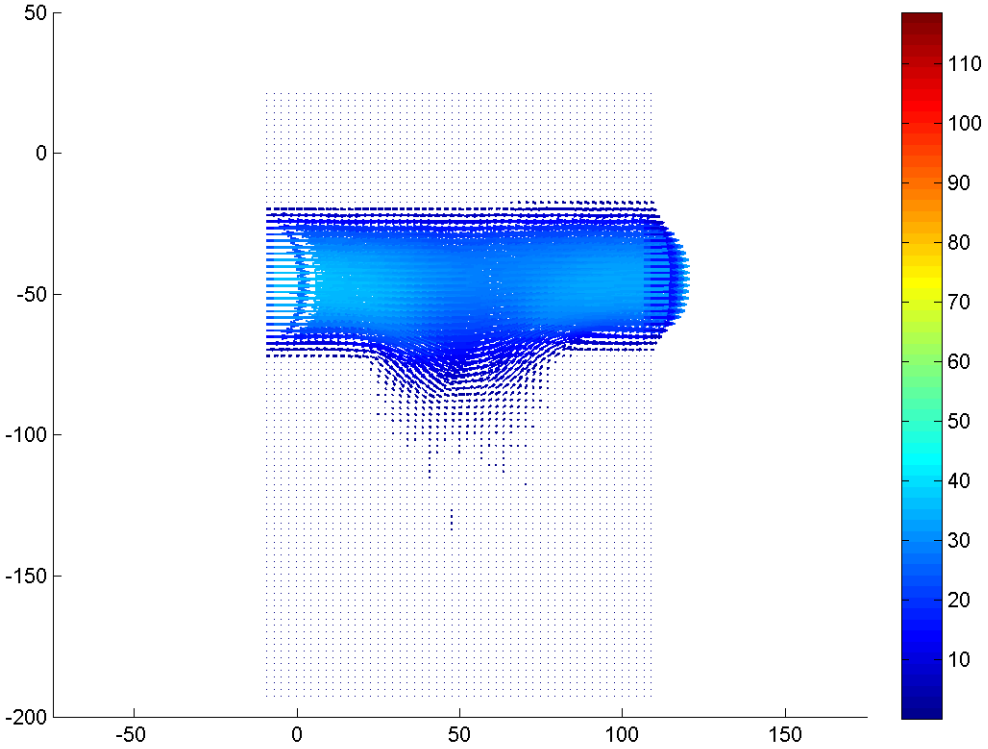

Figure F.104: Velocity field during phase increment 3 at 80 Hz with a Re of 0.1.

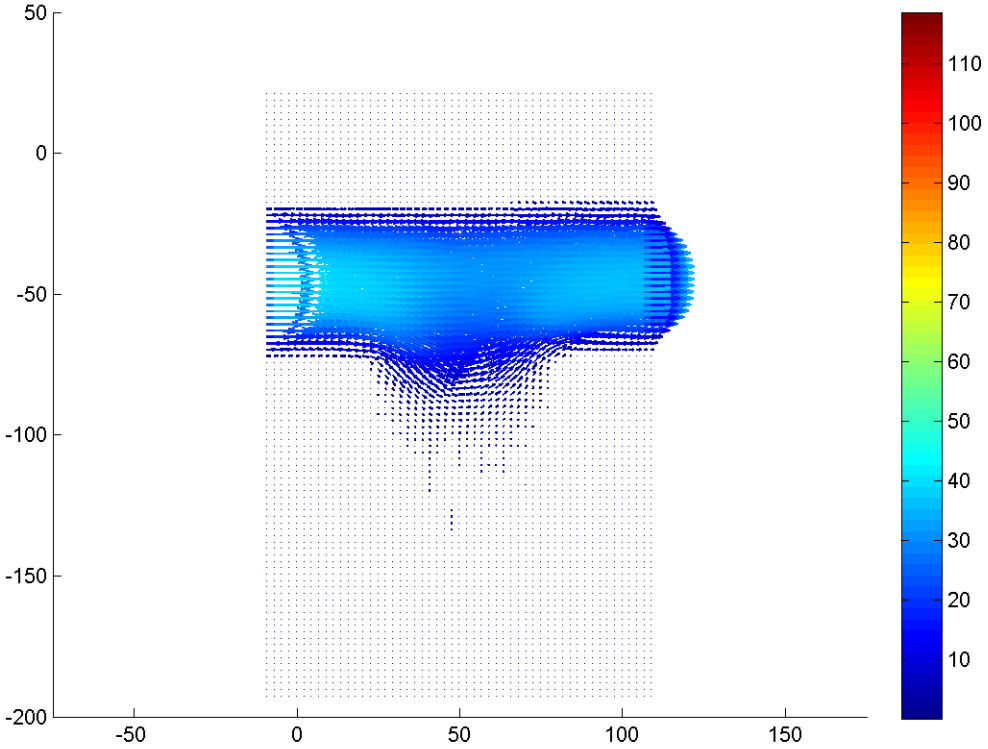

Figure F.105: Velocity field during phase increment 4 at 80 Hz with a Re of 0.1.

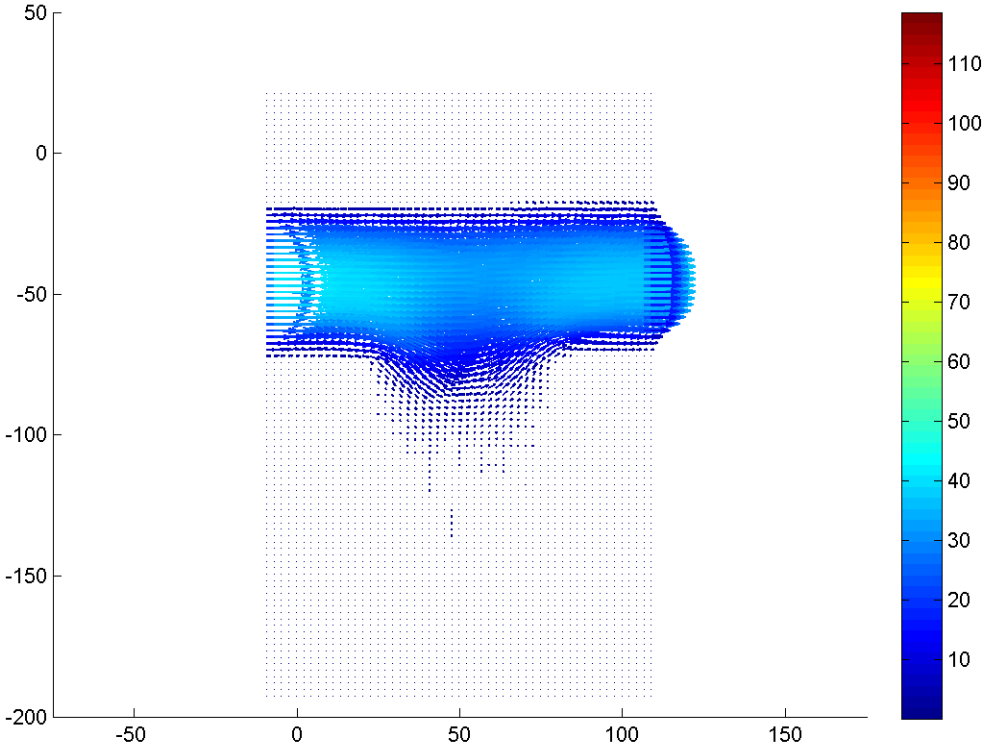

Figure F.106: Velocity field during phase increment 5 at 80 Hz with a Re of 0.1.

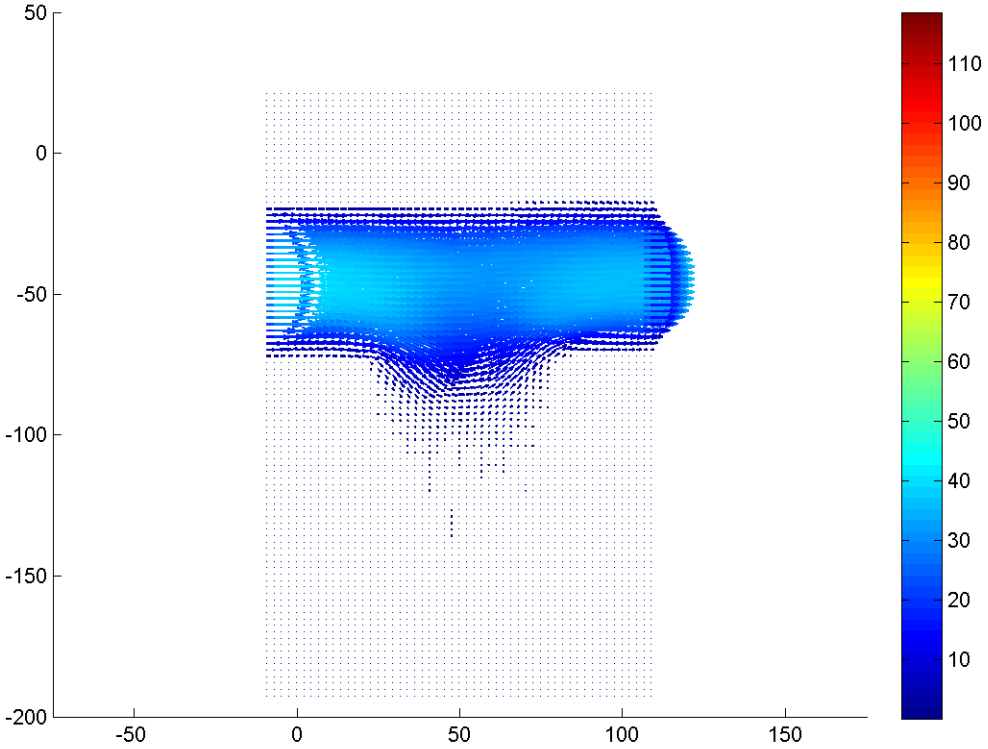

Figure F.107: Velocity field during phase increment 6 at 80 Hz with a Re of 0.1.

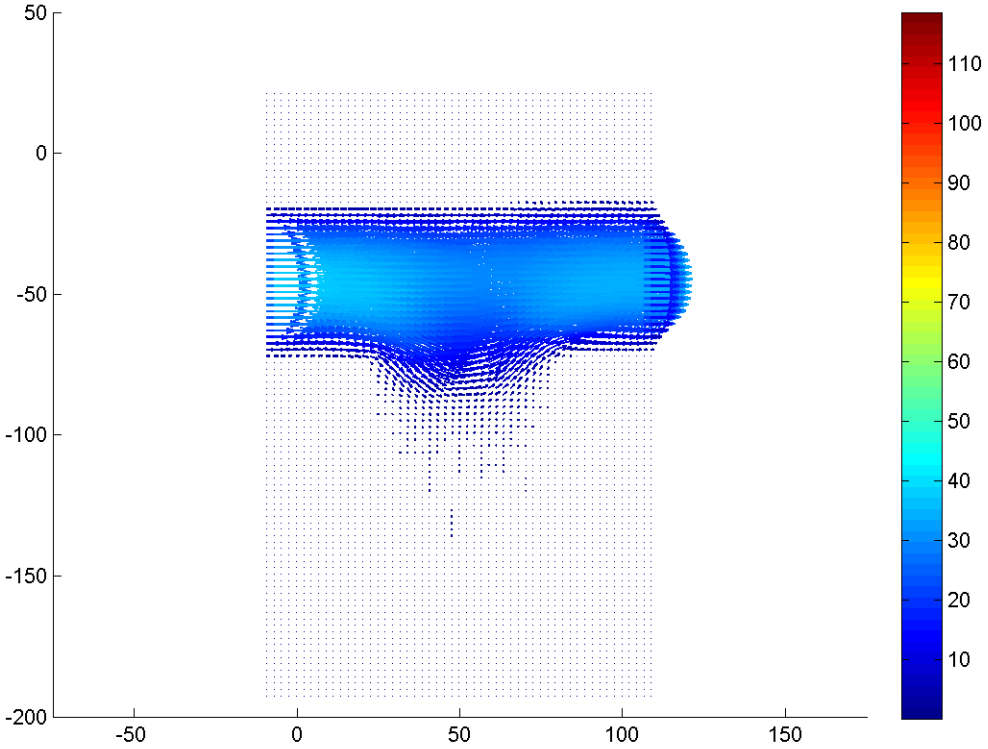

Figure F.108: Velocity field during phase increment 7 at 80 Hz with a Re of 0.1.

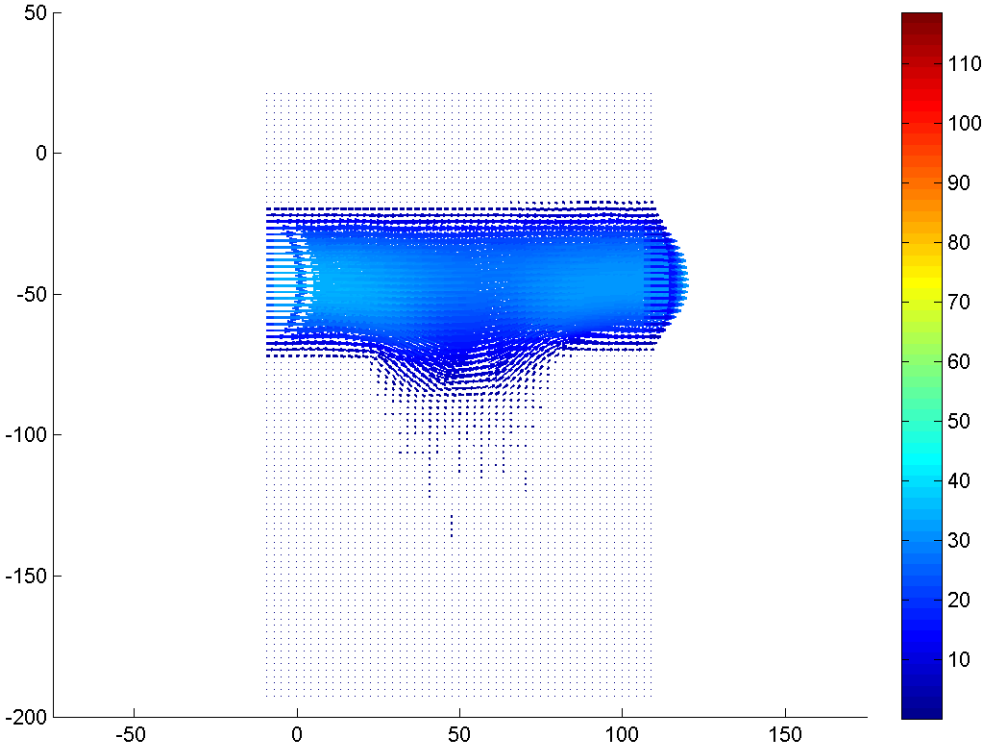

Figure F.109: Velocity field during phase increment 8 at 80 Hz with a Re of 0.1.

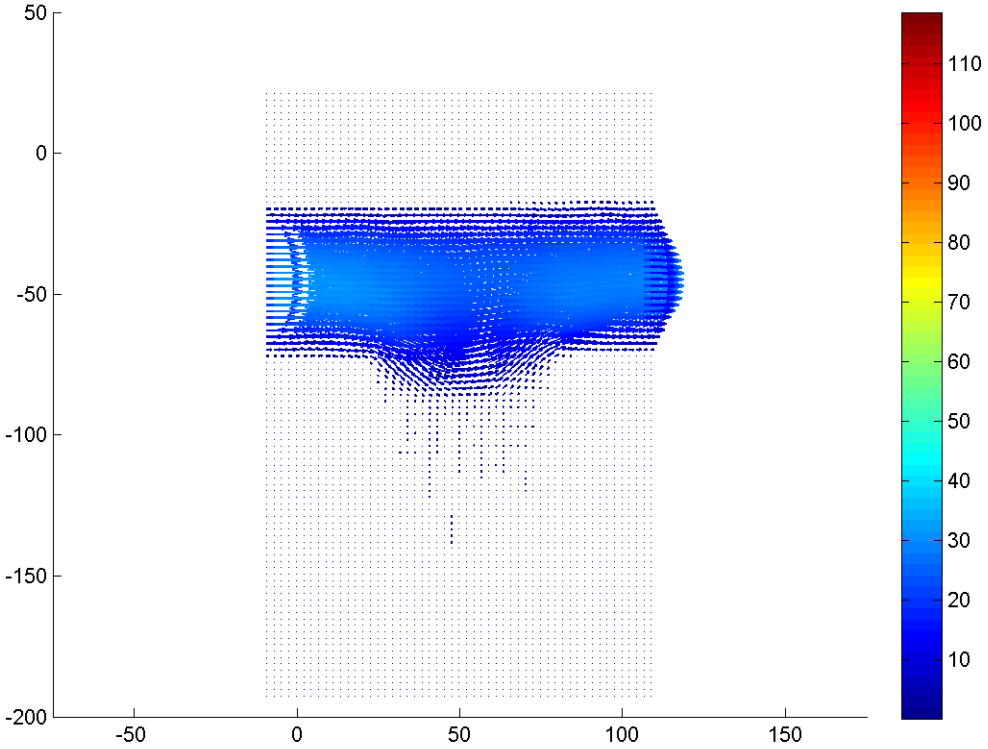

Figure F.110: Velocity field during phase increment 9 at 80 Hz with a Re of 0.1.

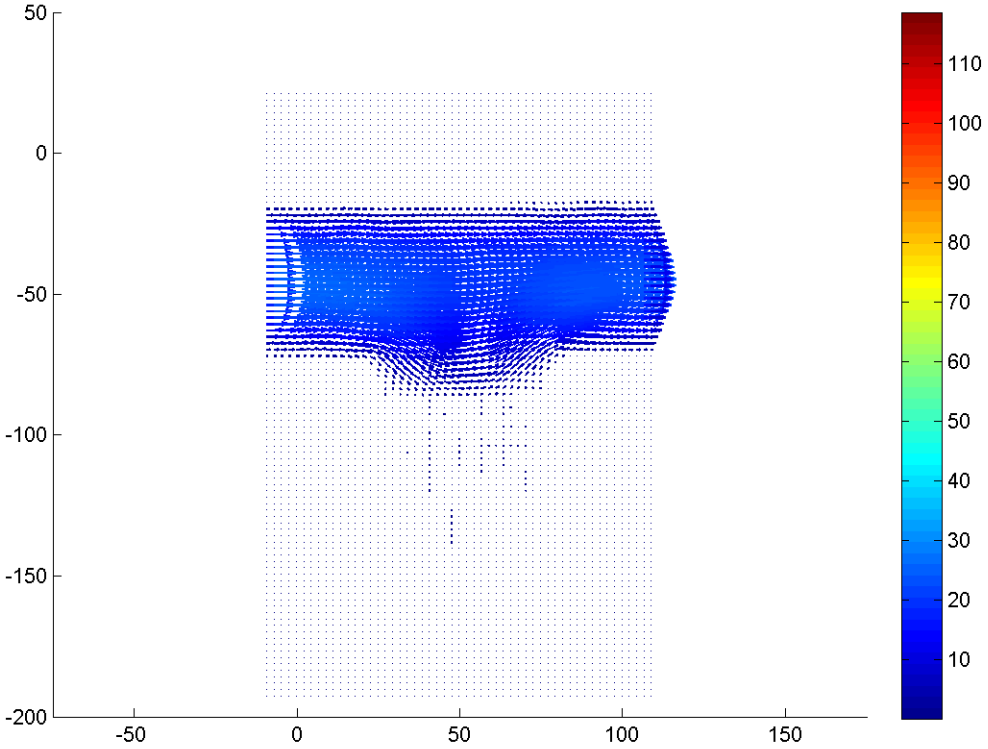

Figure F.111: Velocity field during phase increment 10 at 80 Hz with a Re of 0.1.

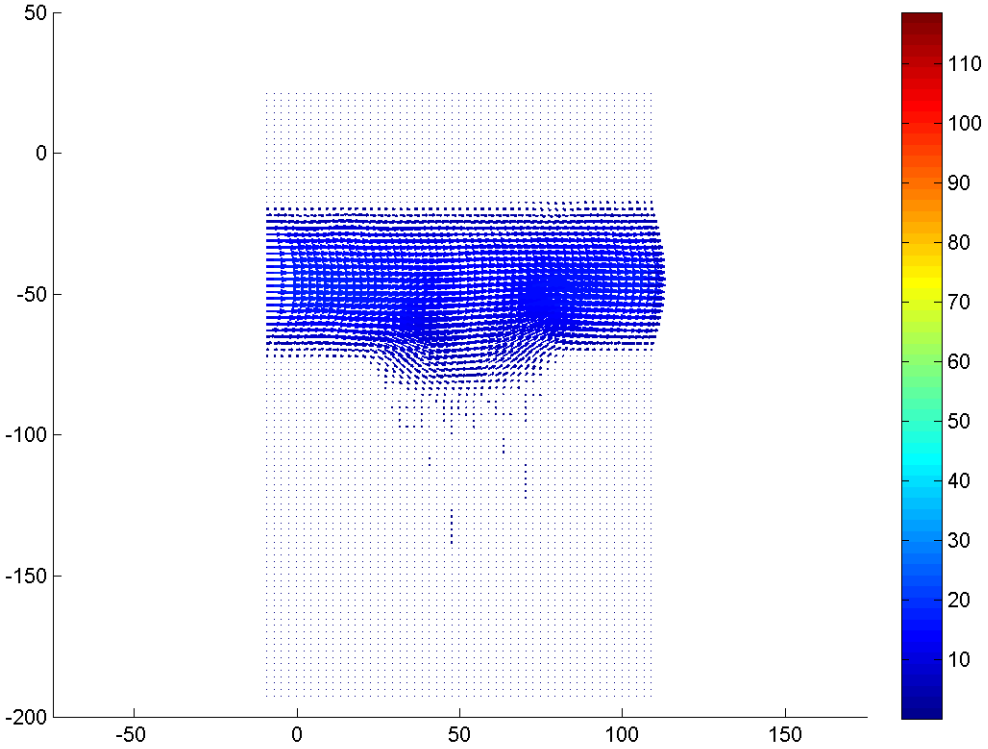

Figure F.112: Velocity field during phase increment 11 at 80 Hz with a Re of 0.1.

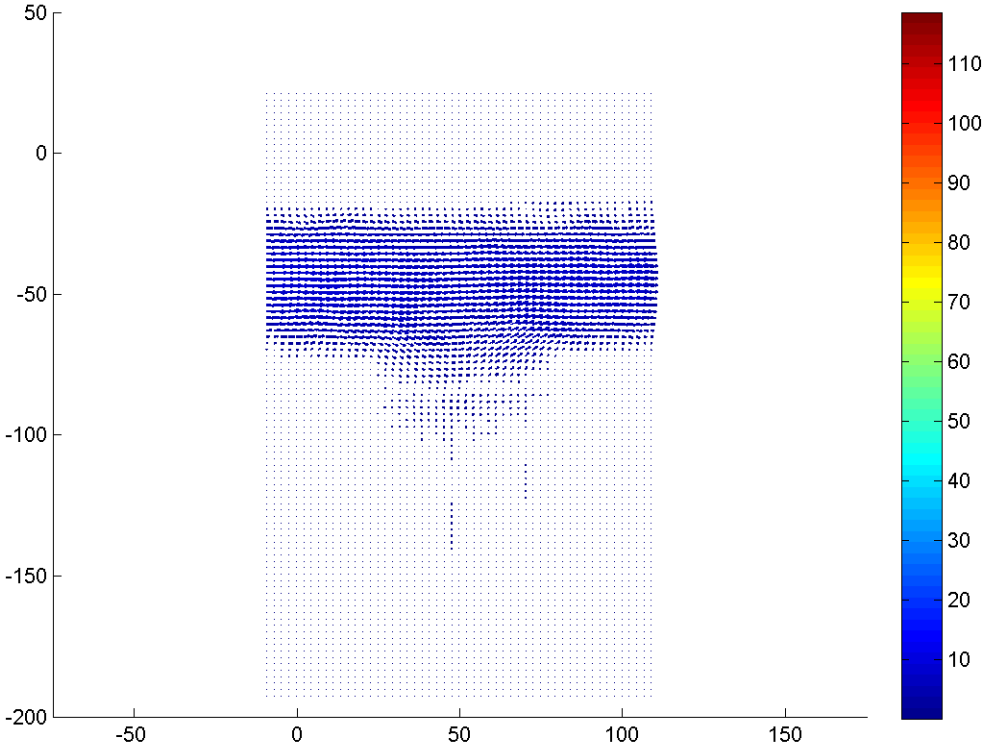

Figure F.113: Velocity field during phase increment 12 at 80 Hz with a Re of 0.1.

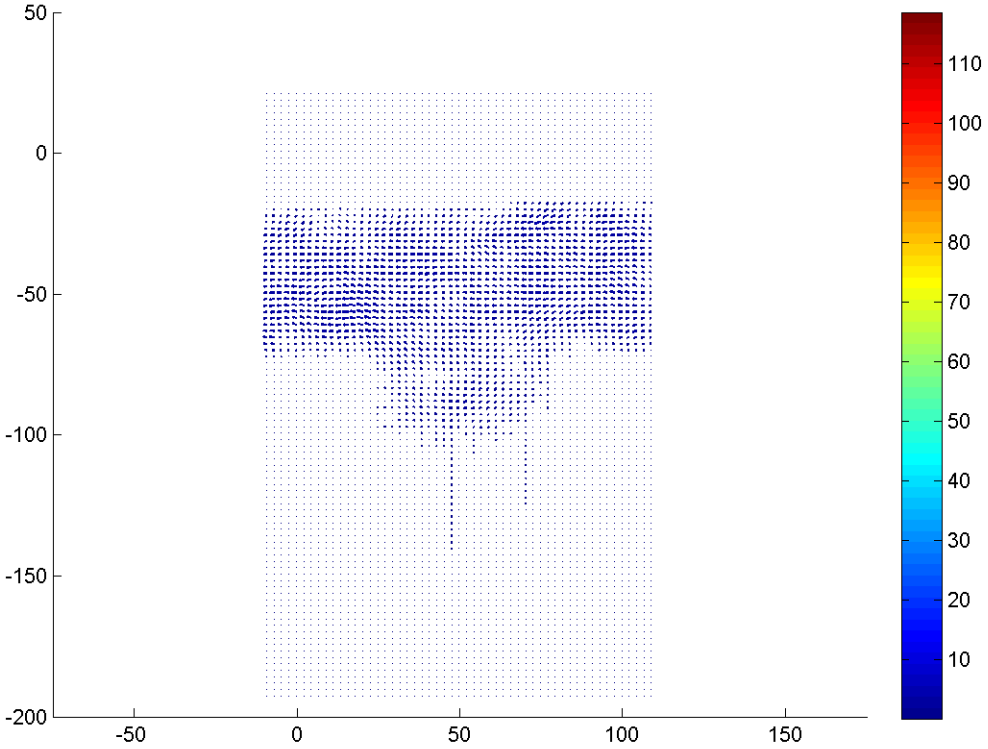

Figure F.114: Velocity field during phase increment 13 at 80 Hz with a Re of 0.1.

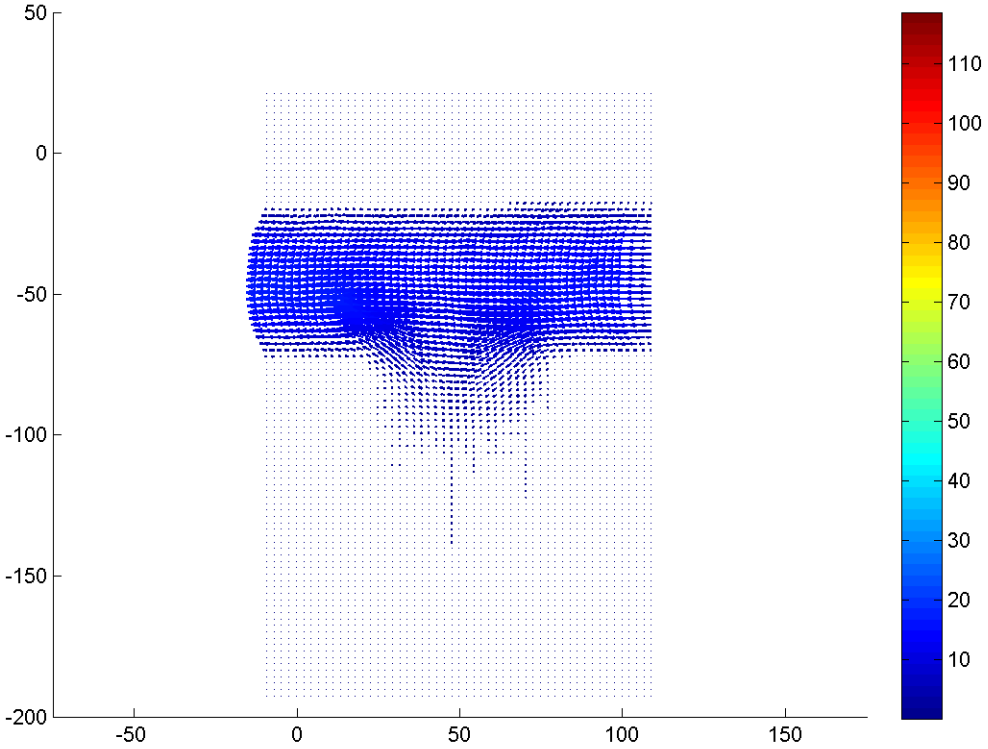

Figure F.115: Velocity field during phase increment 14 at 80 Hz with a Re of 0.1.

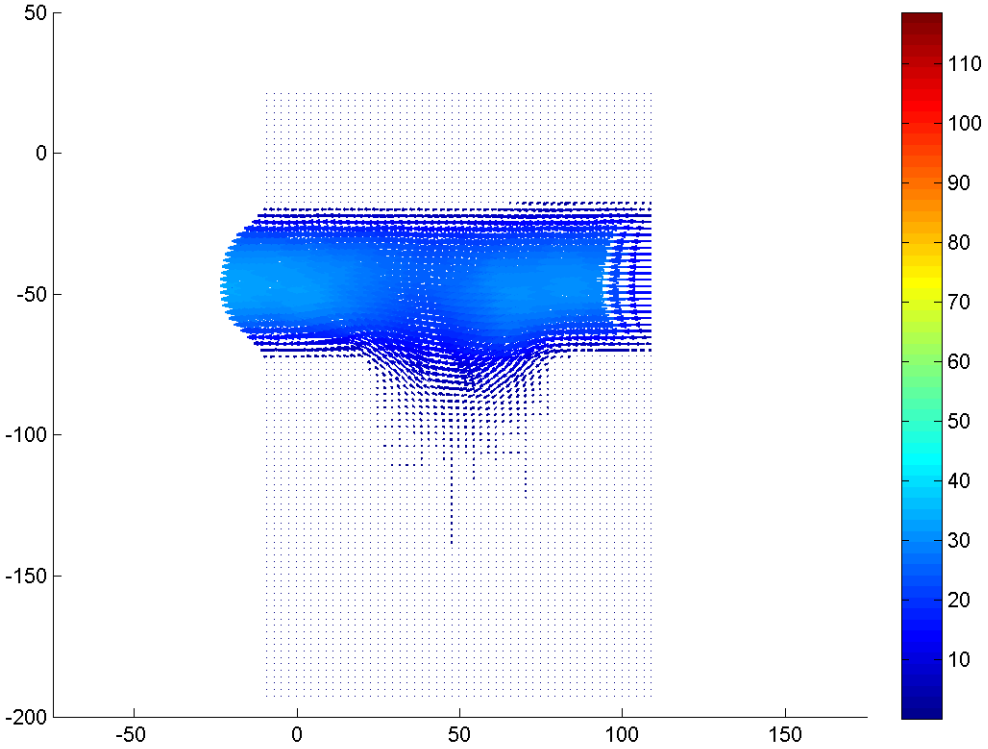

Figure F.116: Velocity field during phase increment 15 at 80 Hz with a Re of 0.1.

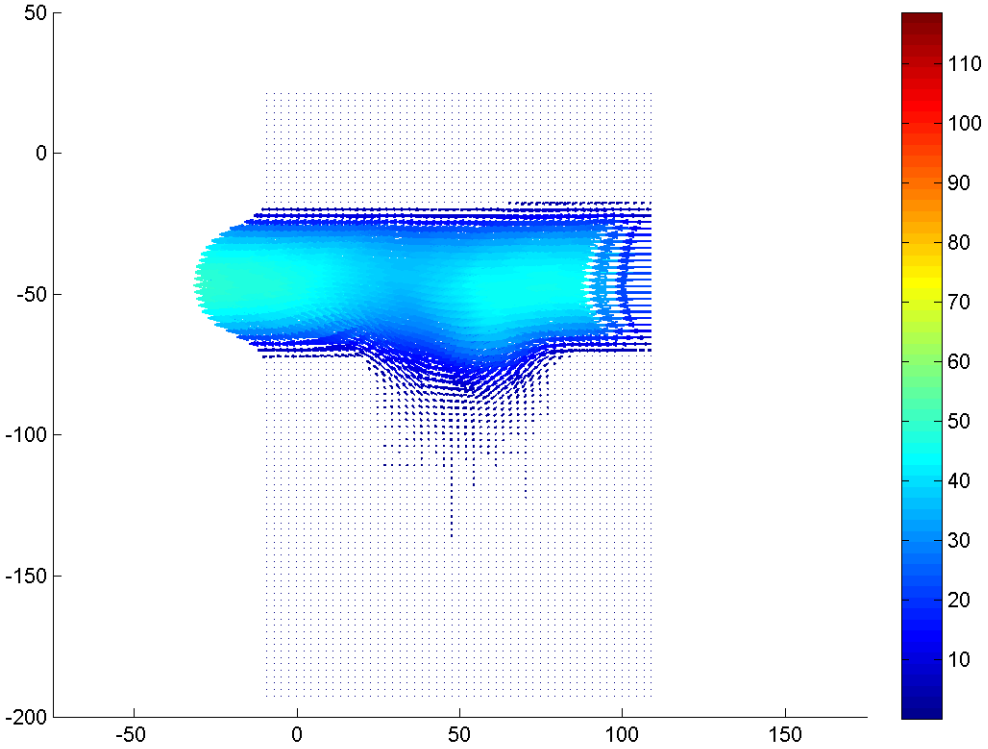

Figure F.117: Velocity field during phase increment 16 at 80 Hz with a Re of 0.1.

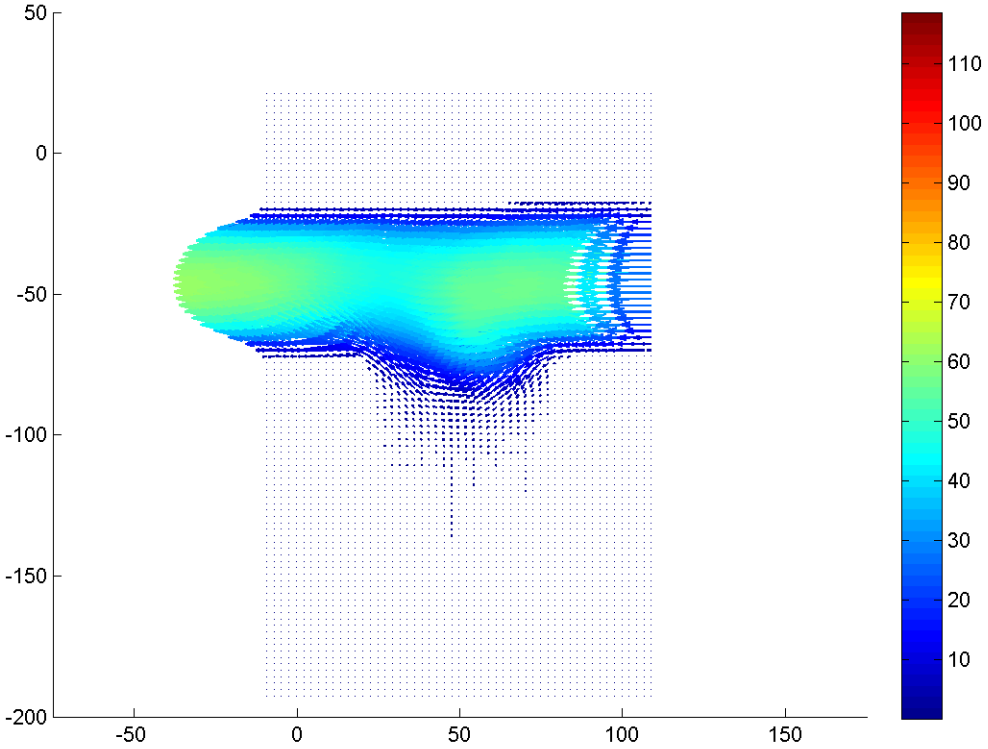

Figure F.118: Velocity field during phase increment 17 at 80 Hz with a Re of 0.1.

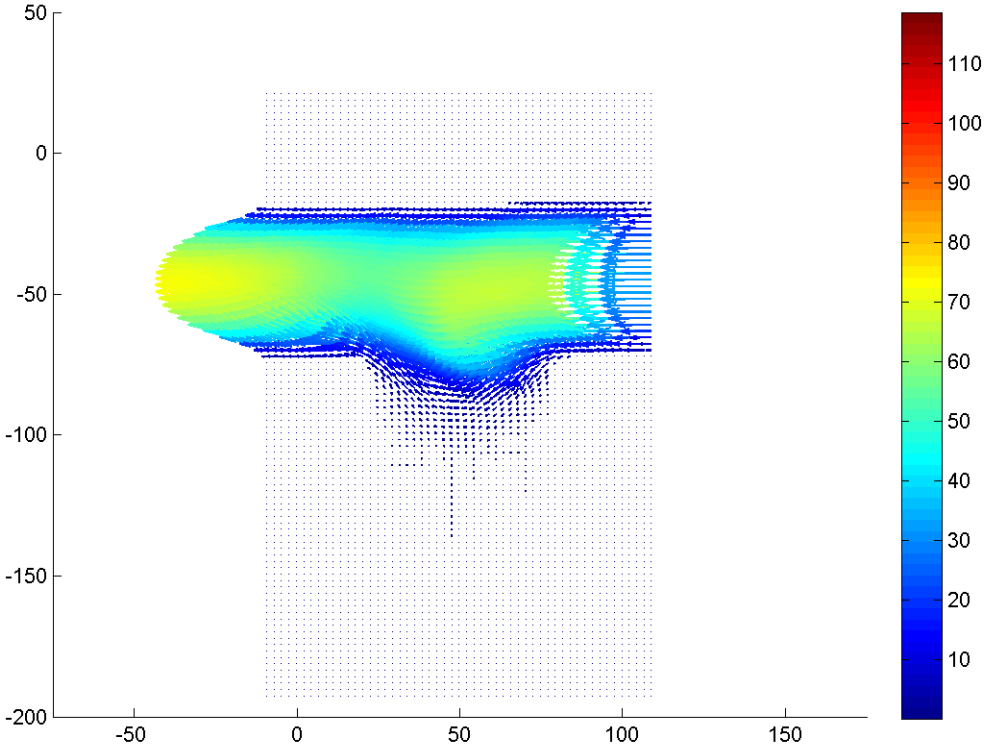

Figure F.119: Velocity field during phase increment 18 at 80 Hz with a Re of 0.1.

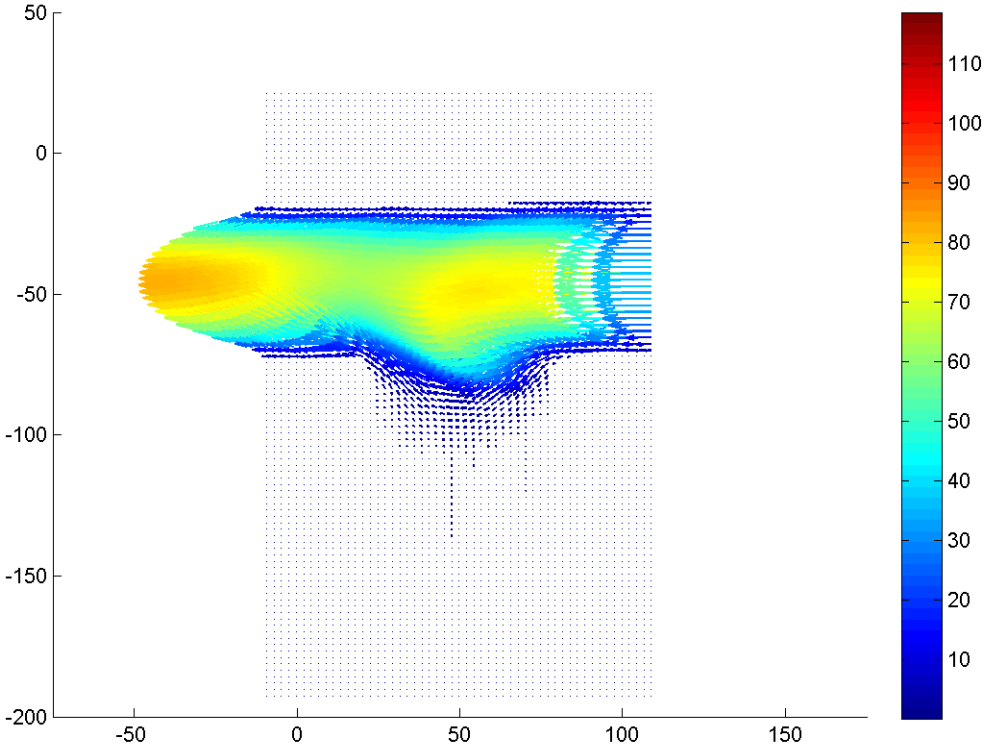

Figure F.120: Velocity field during phase increment 18 at 80 Hz with a Re of 0.1.

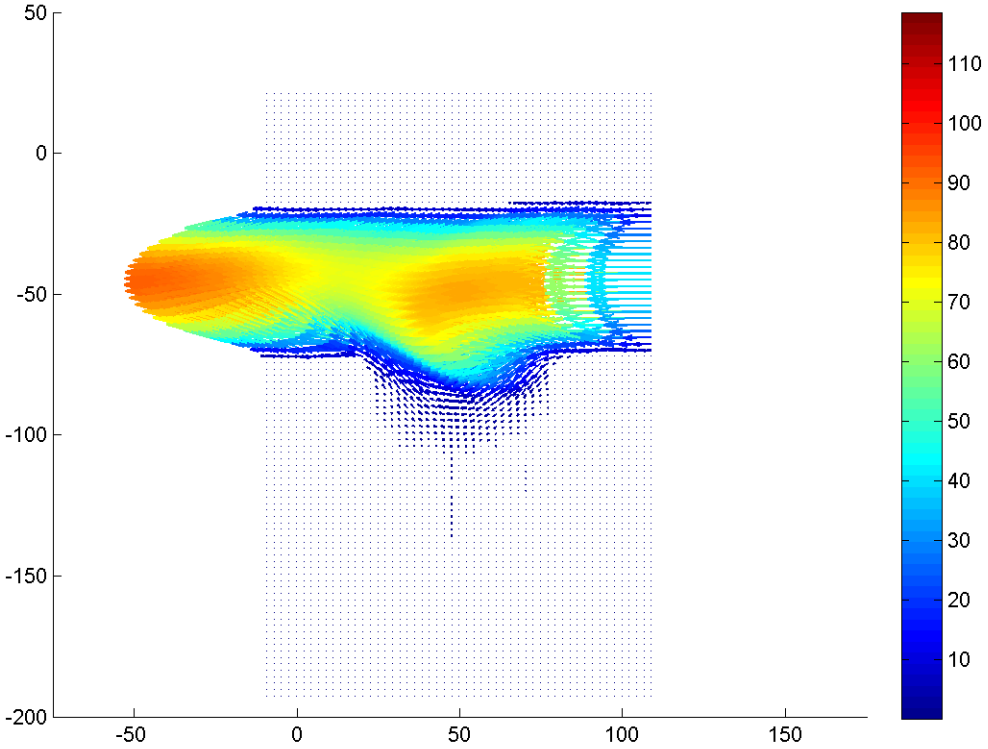

Figure F.121: Velocity field during phase increment 20 at 80 Hz with a Re of 0.1.

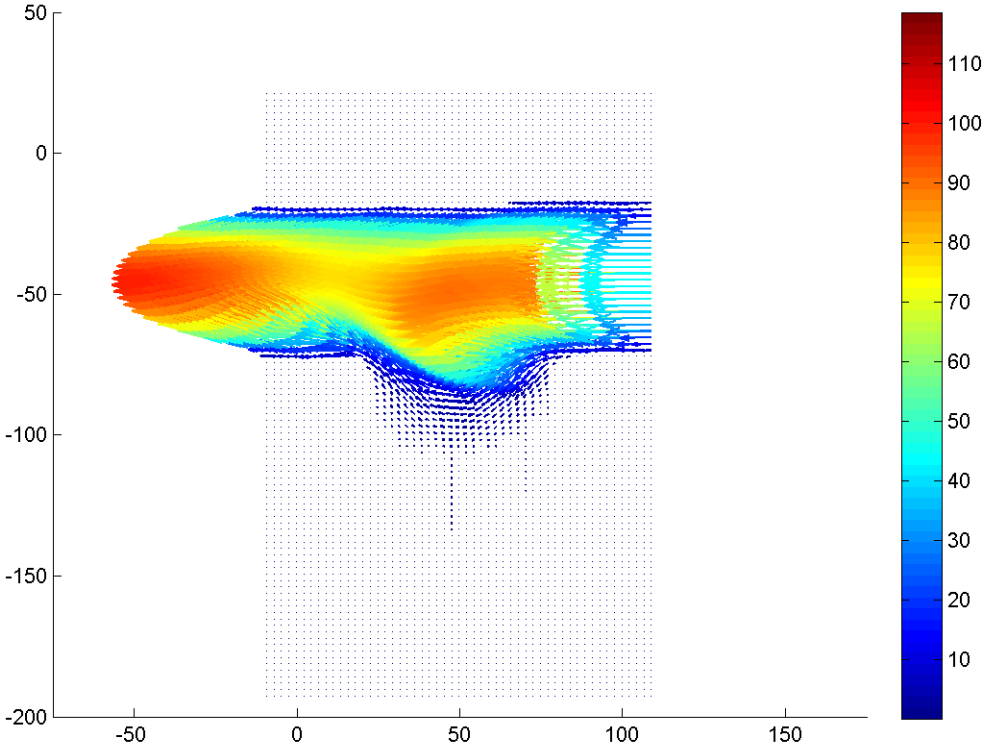

Figure F.122: Velocity field during phase increment 21 at 80 Hz with a Re of 0.1.

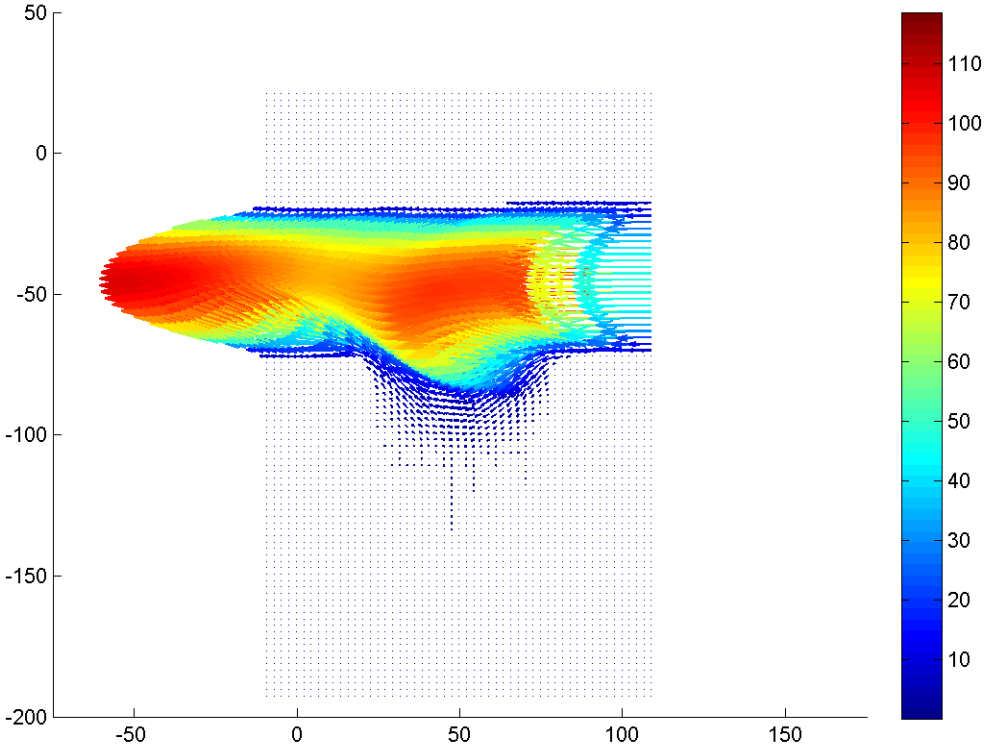

Figure F.123: Velocity field during phase increment 22 at 80 Hz with a Re of 0.1.

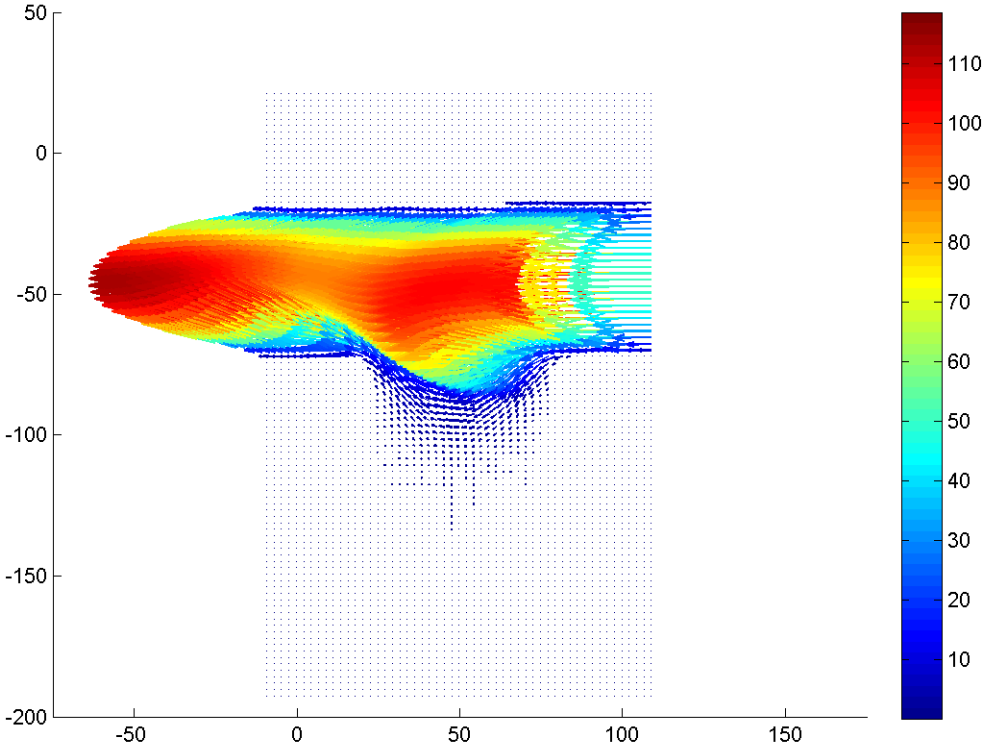

Figure F.124: Velocity field during phase increment 23 at 80 Hz with a Re of 0.1.

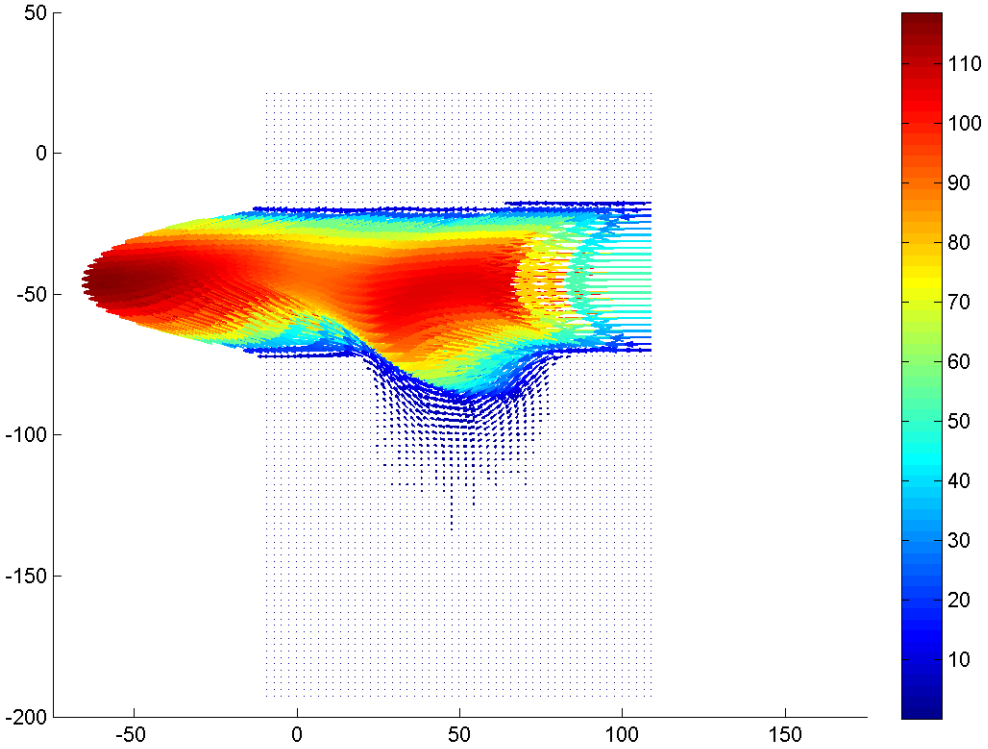

Figure F.125: Velocity field during phase increment 24 at 80 Hz with a Re of 0.1.

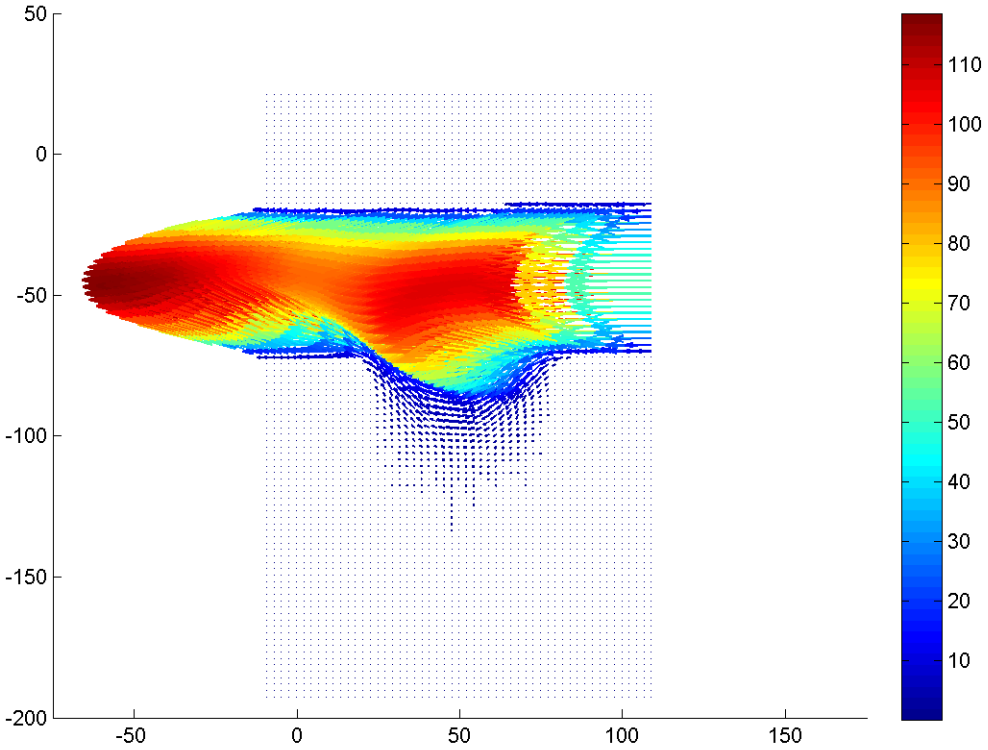

Figure F.126: Velocity field during phase increment 25 at 80 Hz with a Re of 0.1.

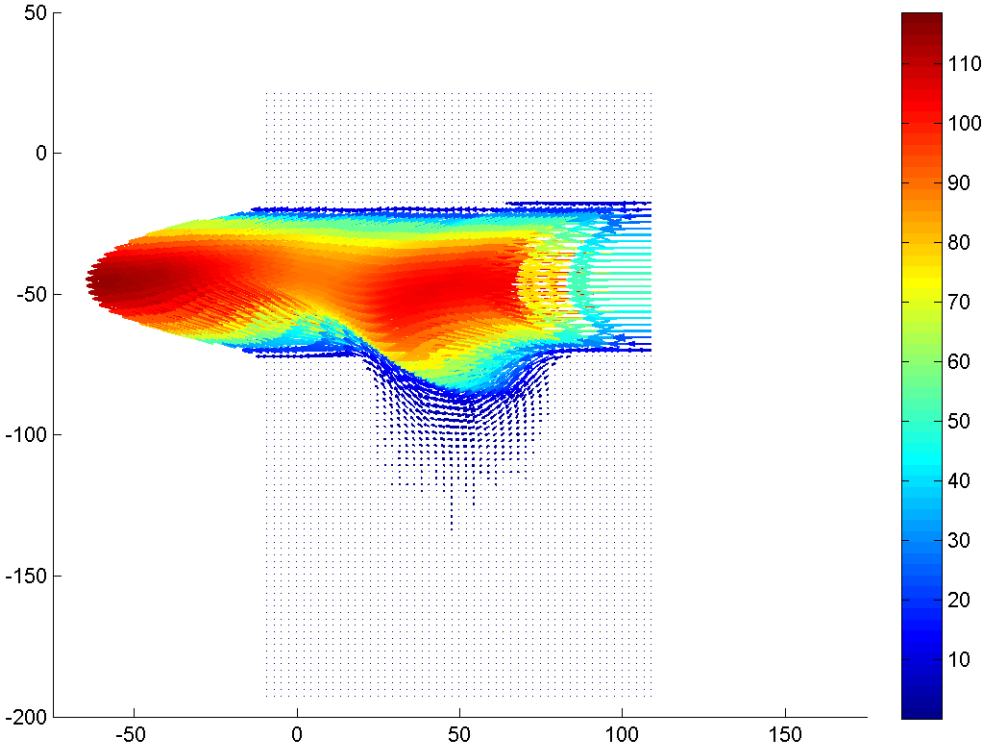

Figure F.127: Velocity field during phase increment 26 at 80 Hz with a Re of 0.1.

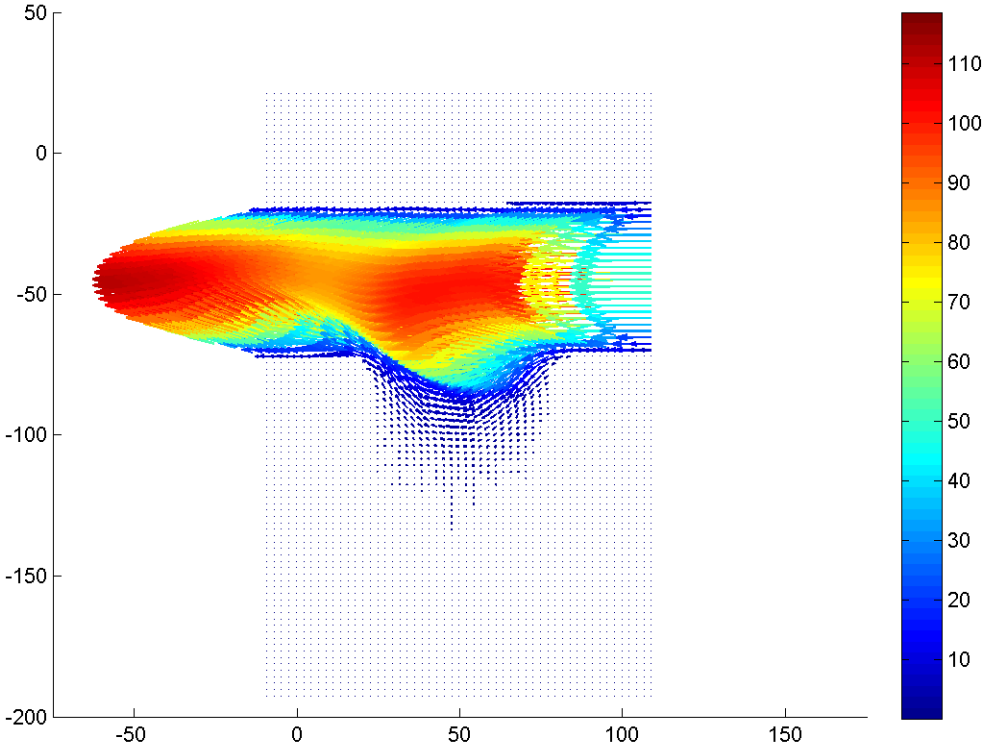

Figure F.128: Velocity field during phase increment 27 at 80 Hz with a Re of 0.1.

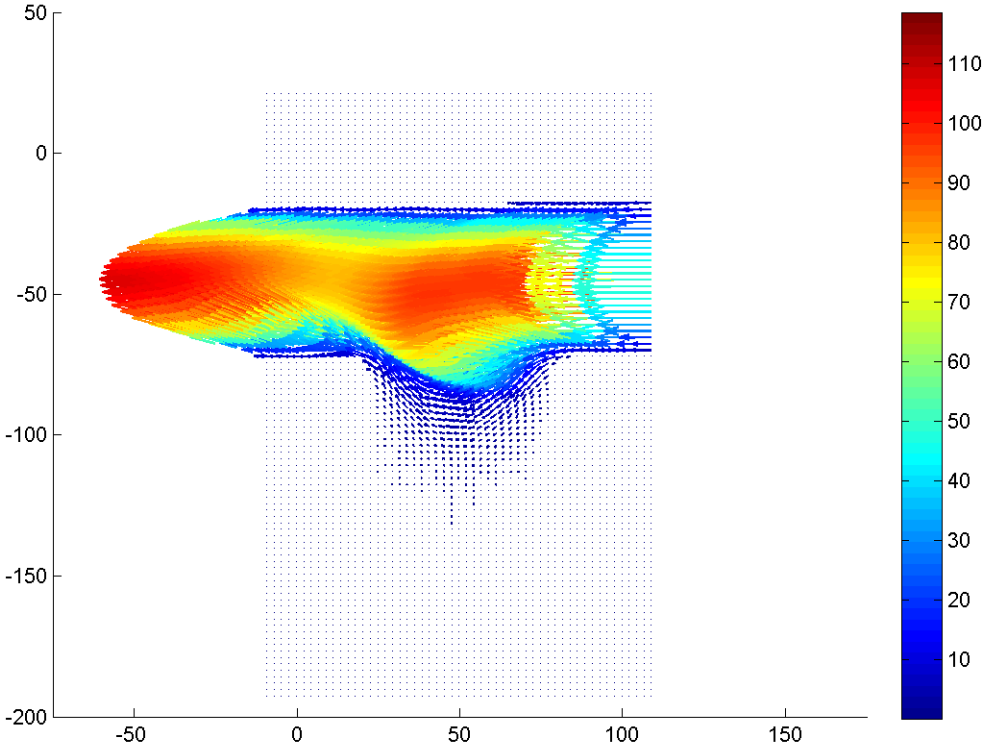

Figure F.129: Velocity field during phase increment 28 at 80 Hz with a Re of 0.1.

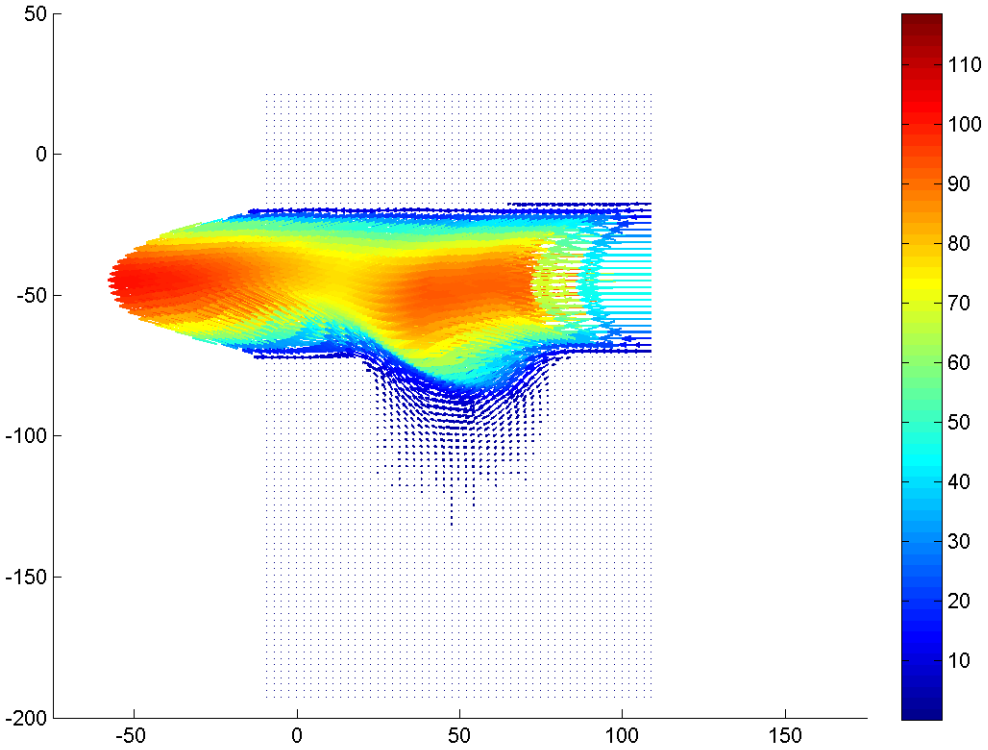

Figure F.130: Velocity field during phase increment 29 at 80 Hz with a Re of 0.1.

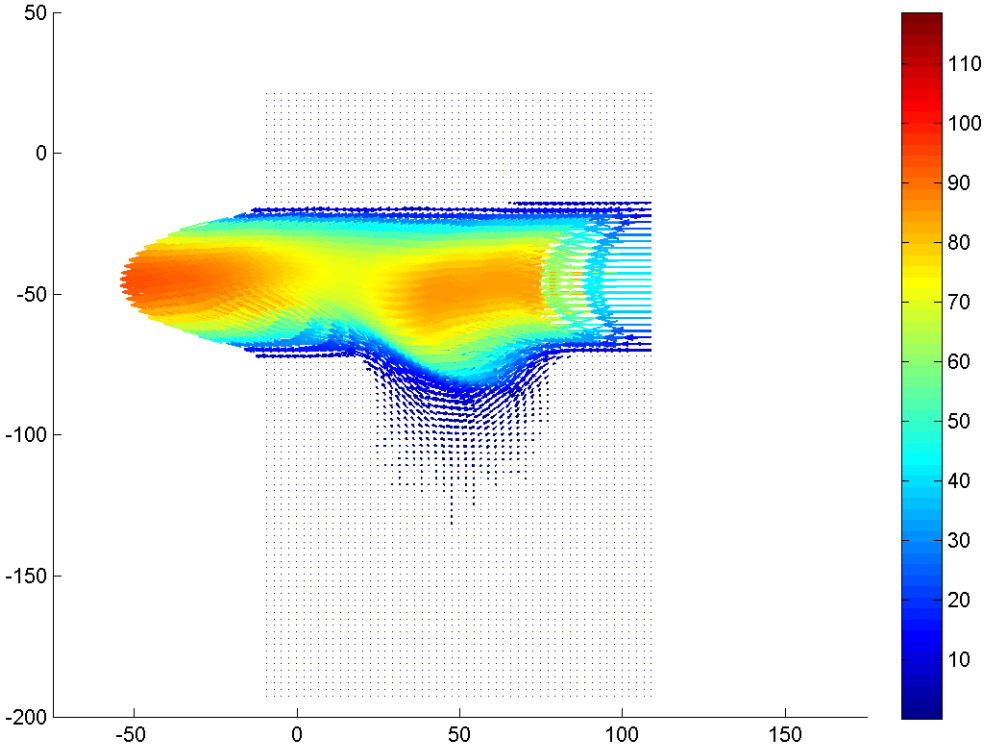

Figure F.131: Velocity field during phase increment 30 at 80 Hz with a Re of 0.1.

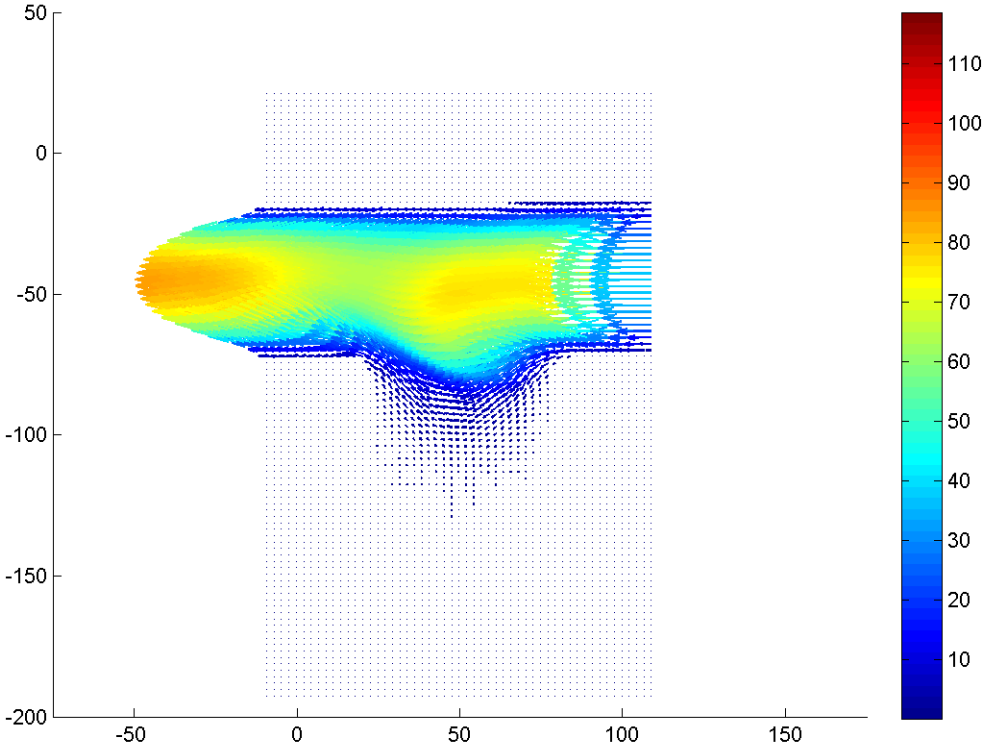

Figure F.132: Velocity field during phase increment 31 at 80 Hz with a Re of 0.1.

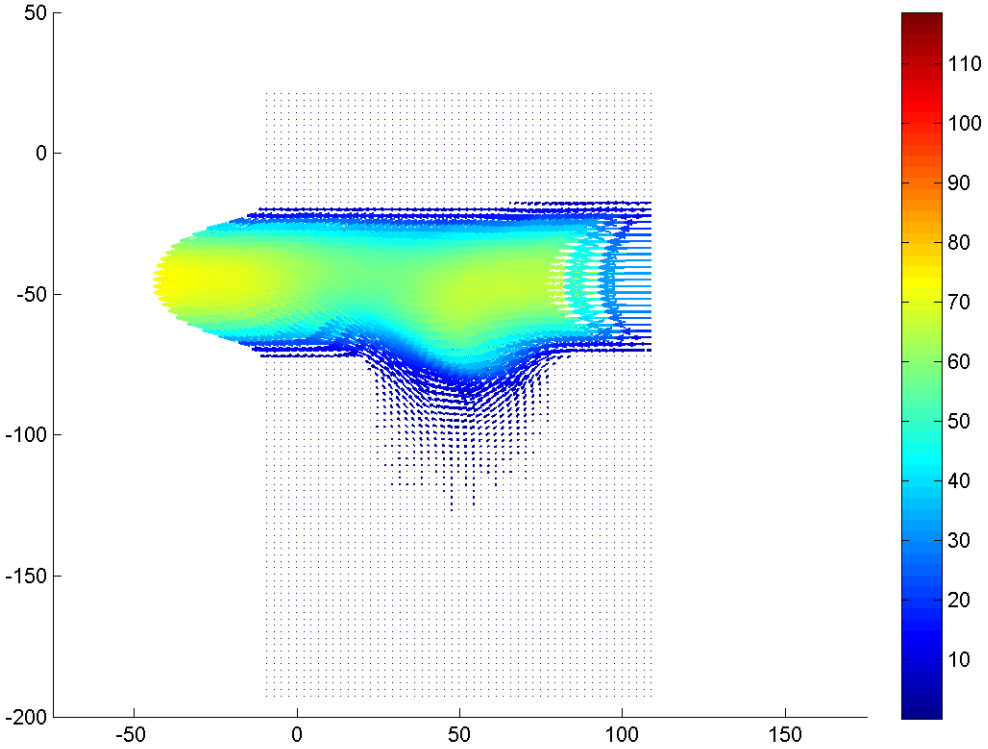

Figure F.133: Velocity field during phase increment 32 at 80 Hz with a Re of 0.1.

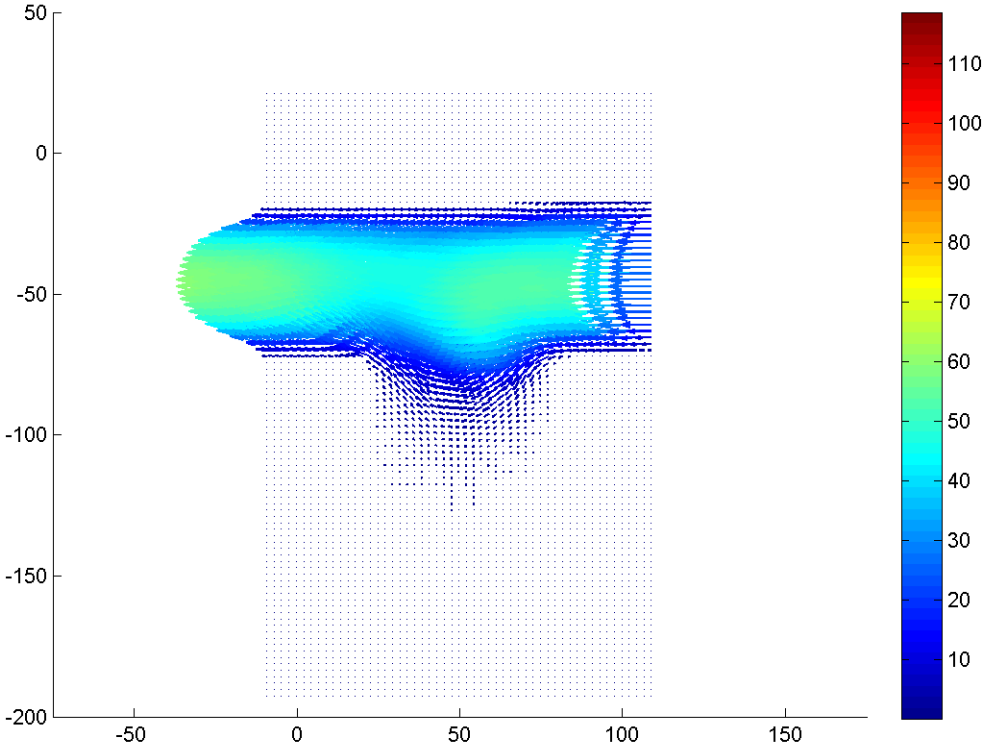

Figure F.134: Velocity field during phase increment 33 at 80 Hz with a Re of 0.1.

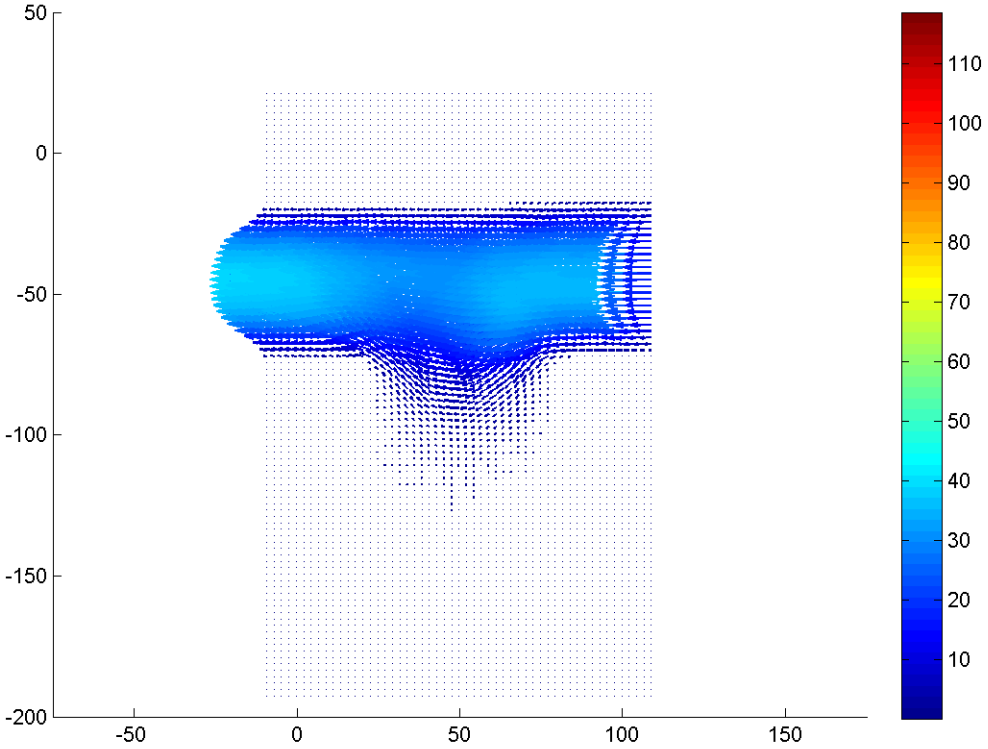

Figure F.135: Velocity field during phase increment 34 at 80 Hz with a Re of 0.1.

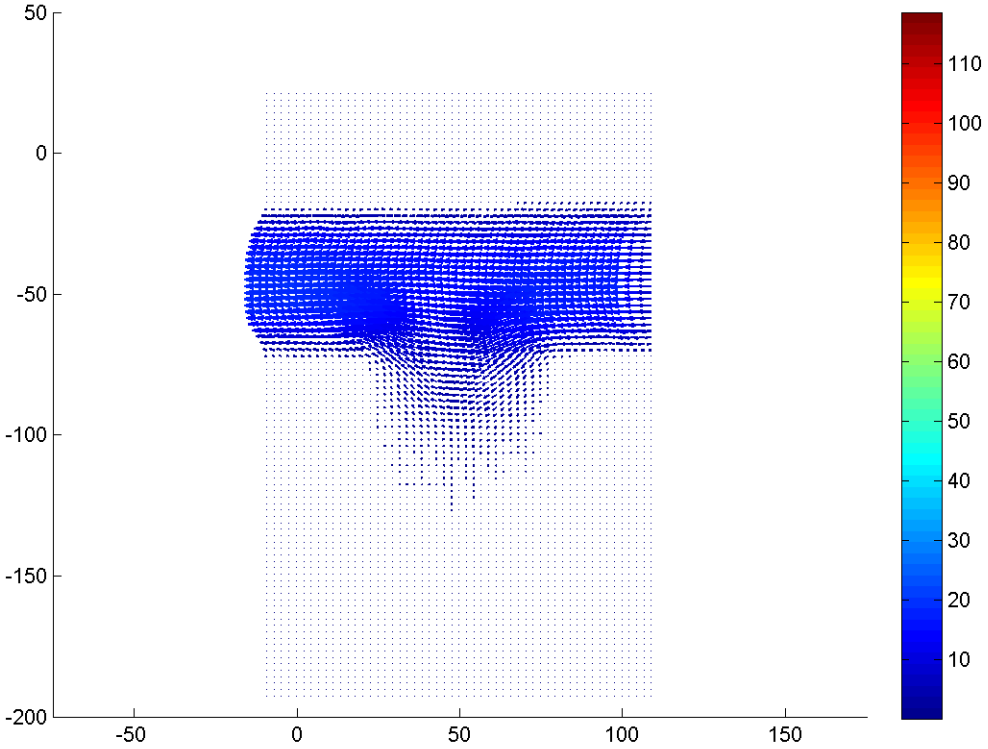

Figure F.136: Velocity field during phase increment 35 at 80 Hz with a Re of 0.1.

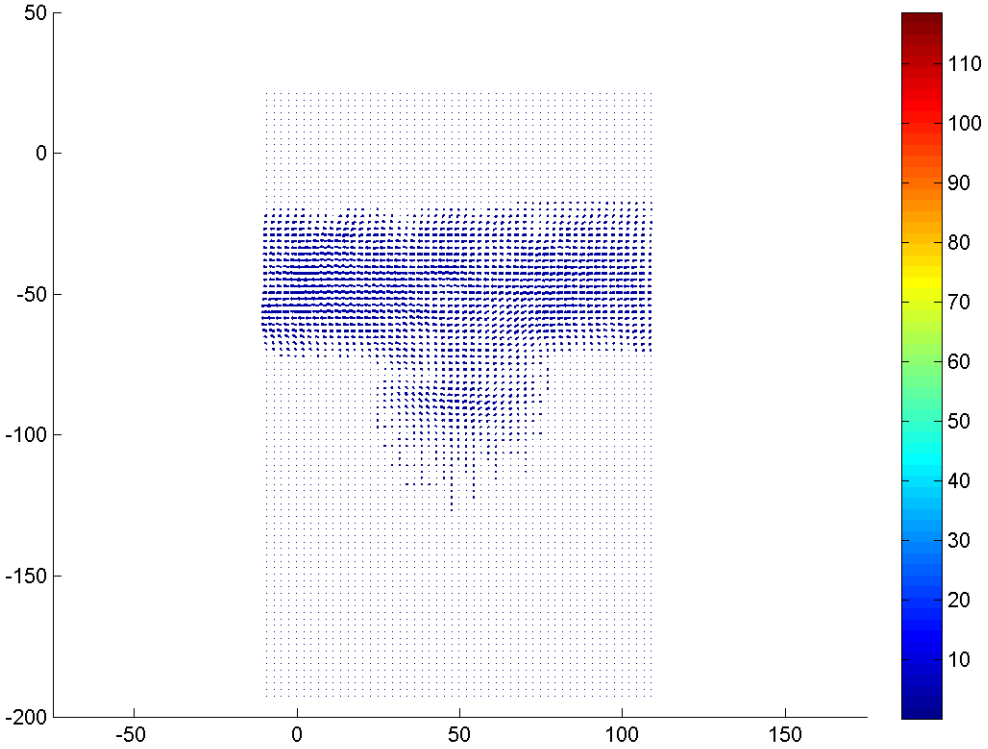

Figure F.137: Velocity field during phase increment 36 at 80 Hz with a Re of 0.1.

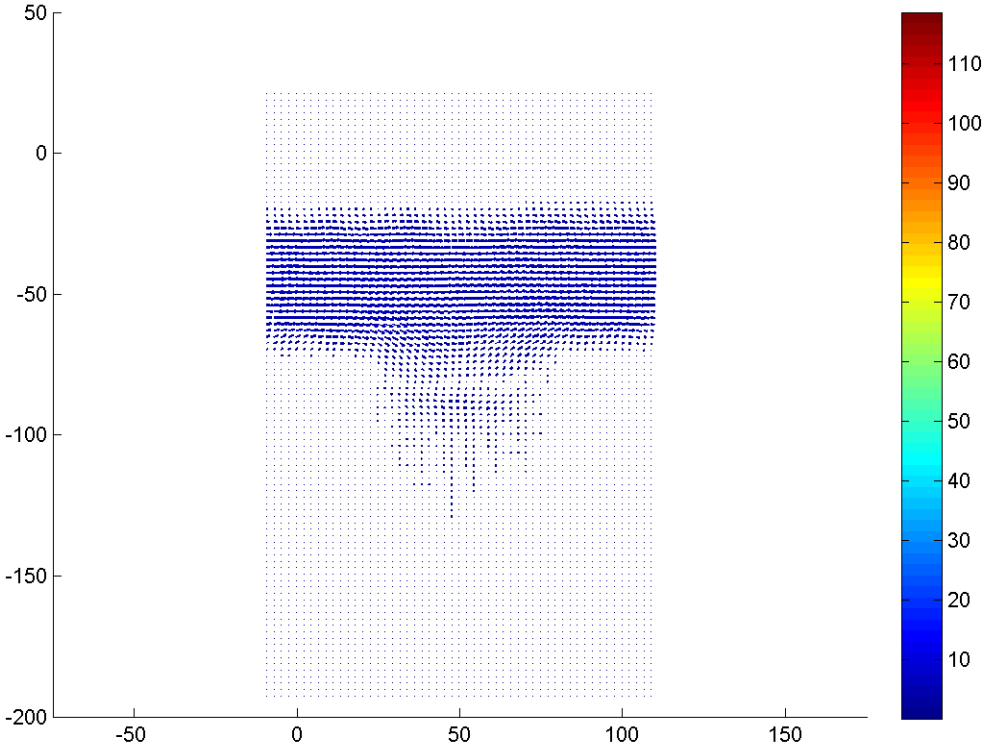

Figure F.138: Velocity field during phase increment 37 at 80 Hz with a Re of 0.1.

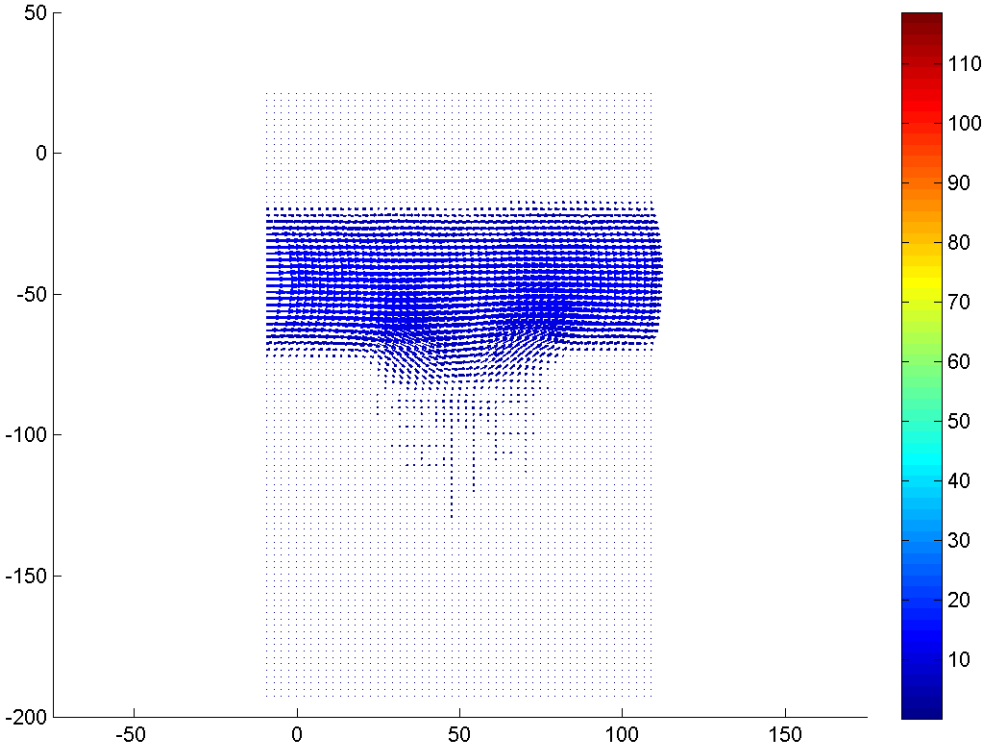

Figure F.139: Velocity field during phase increment 38 at 80 Hz with a Re of 0.1.

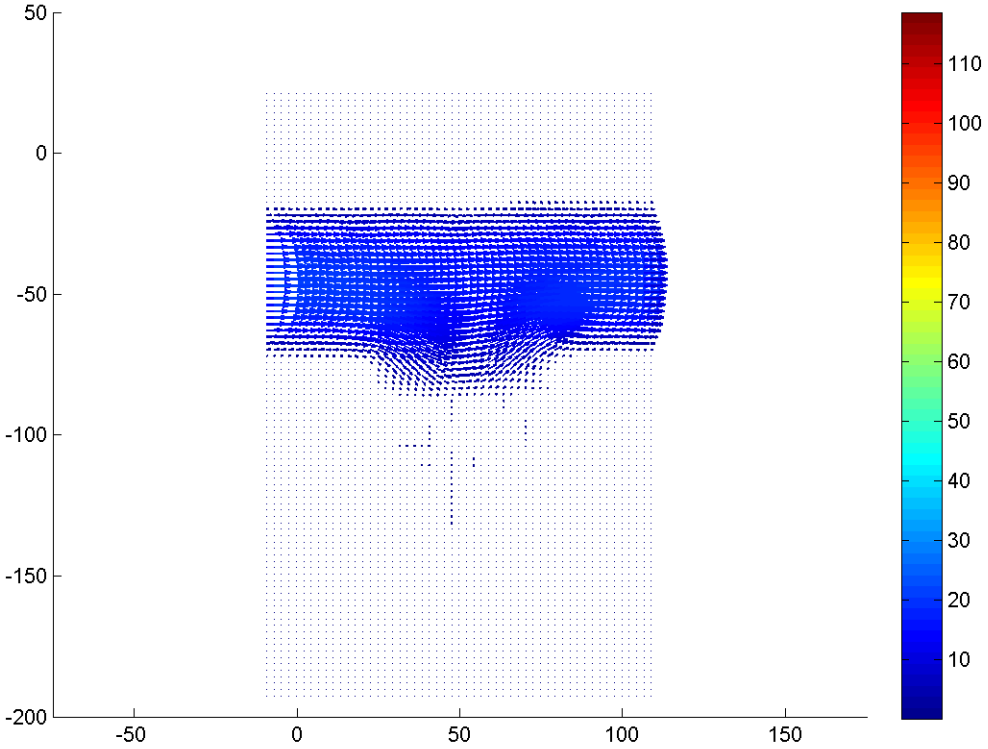

Figure F.140: Velocity field during phase increment 39 at 80 Hz with a Re of 0.1.

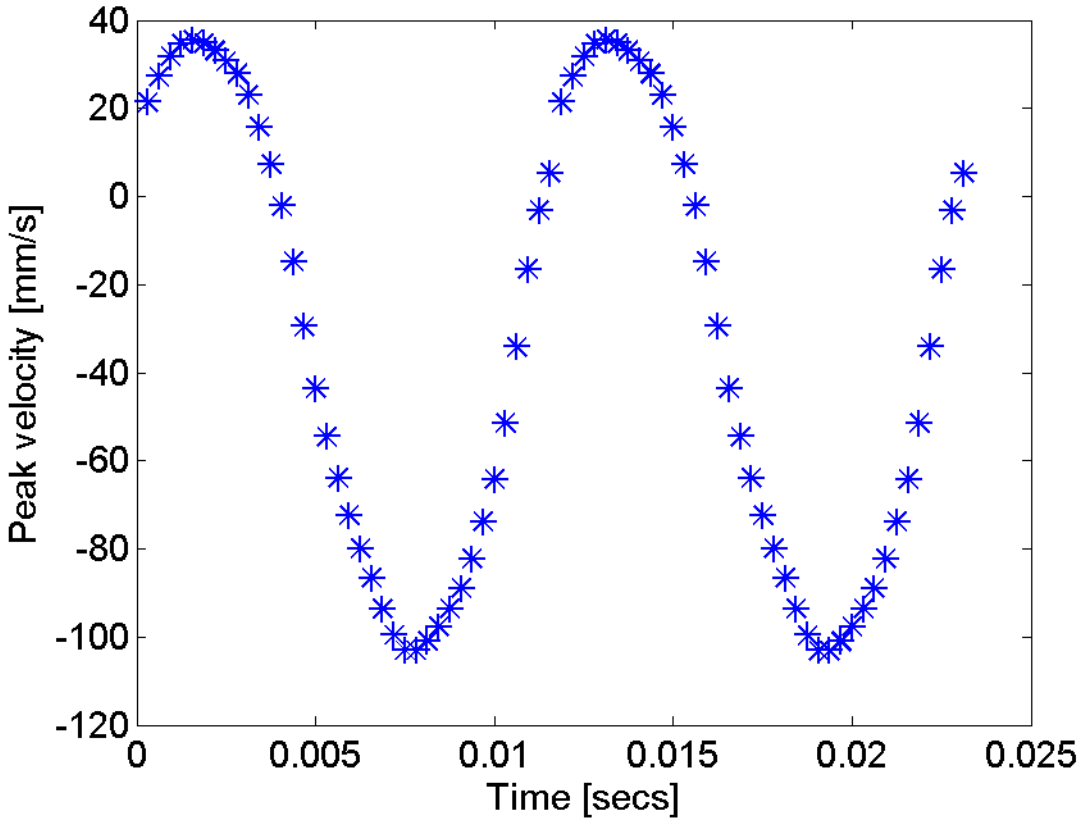

Figure F.141: The peak velocity in the free stream region in time at 80 Hz.

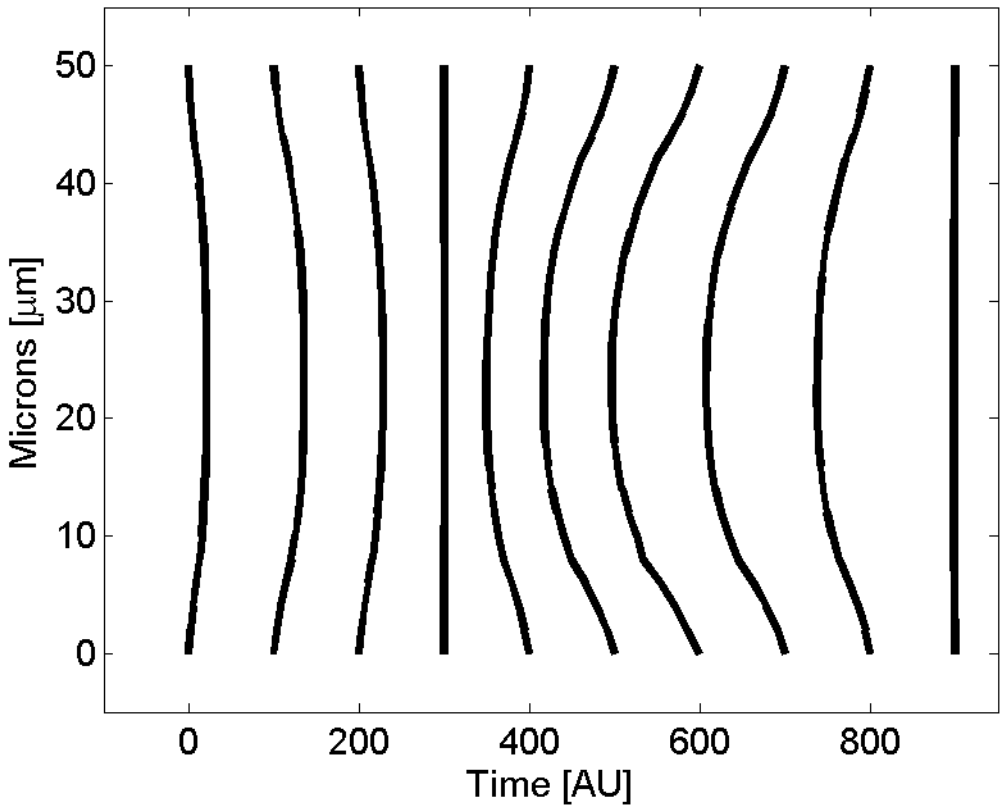

Figure F.142: The velocity profile in the free stream versus time at 80 Hz.

F.2.2 Streamline images at 80 Hz

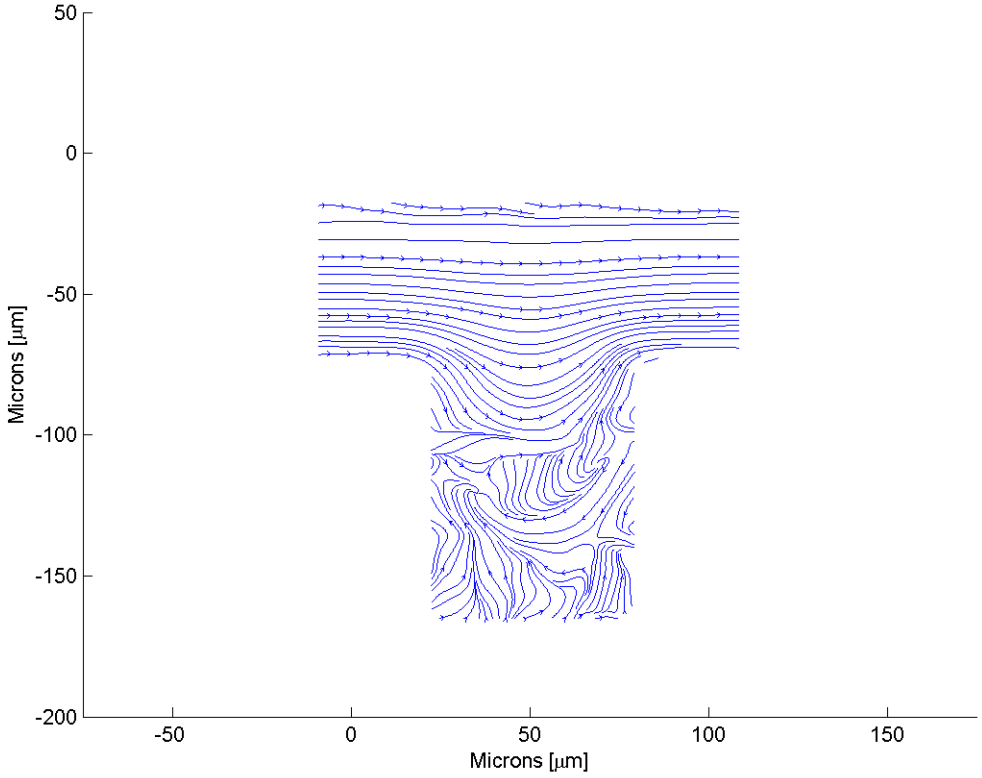

Figure F.143: Streamline image during phase increment 1 at 80 Hz and a Re of 0.1.

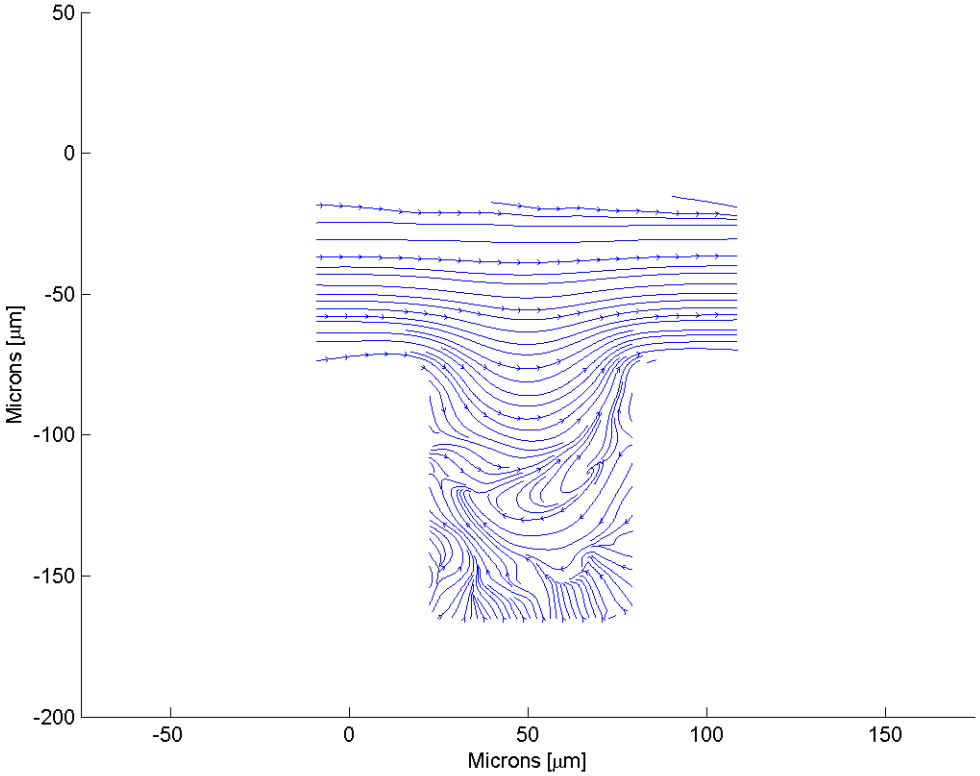

Figure F.144: Streamline image during phase increment 2 at 80 Hz and a Re of 0.1.

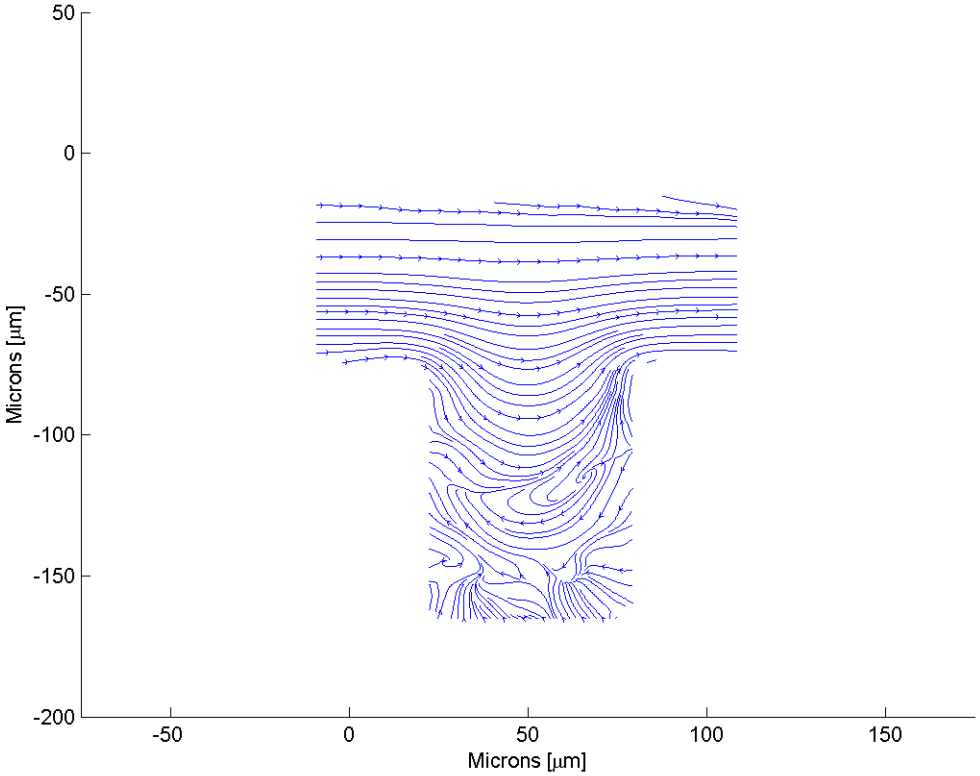

Figure F.145: Streamline image during phase increment 3 at 80 Hz and a Re of 0.1.

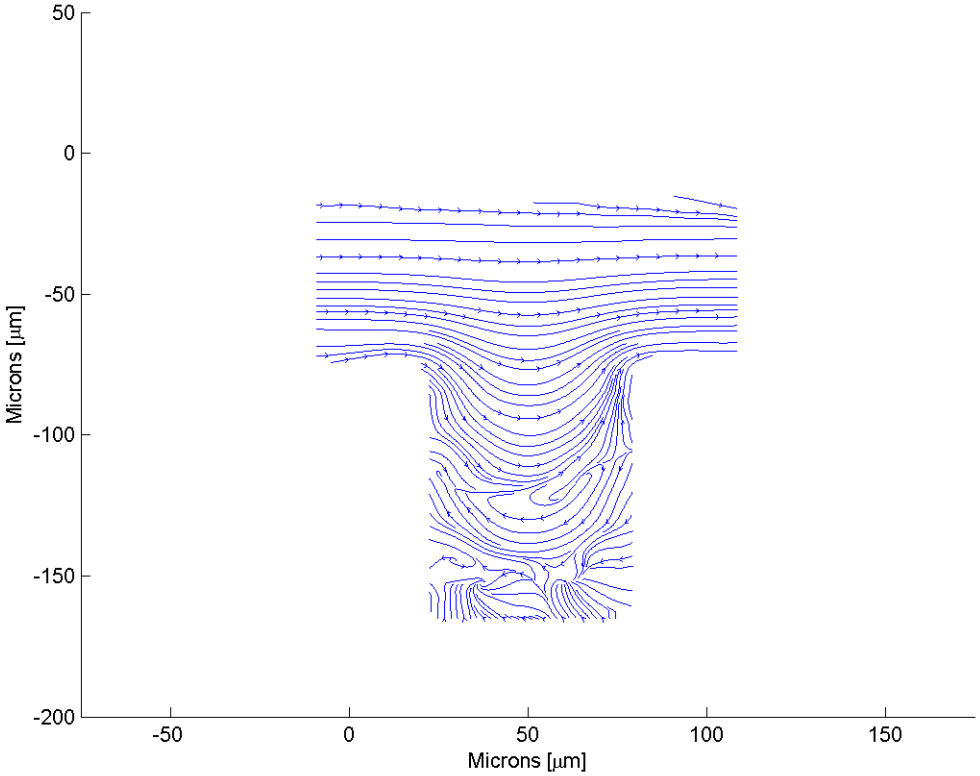

Figure F.146: Streamline image during phase increment 4 at 80 Hz and a Re of 0.1.

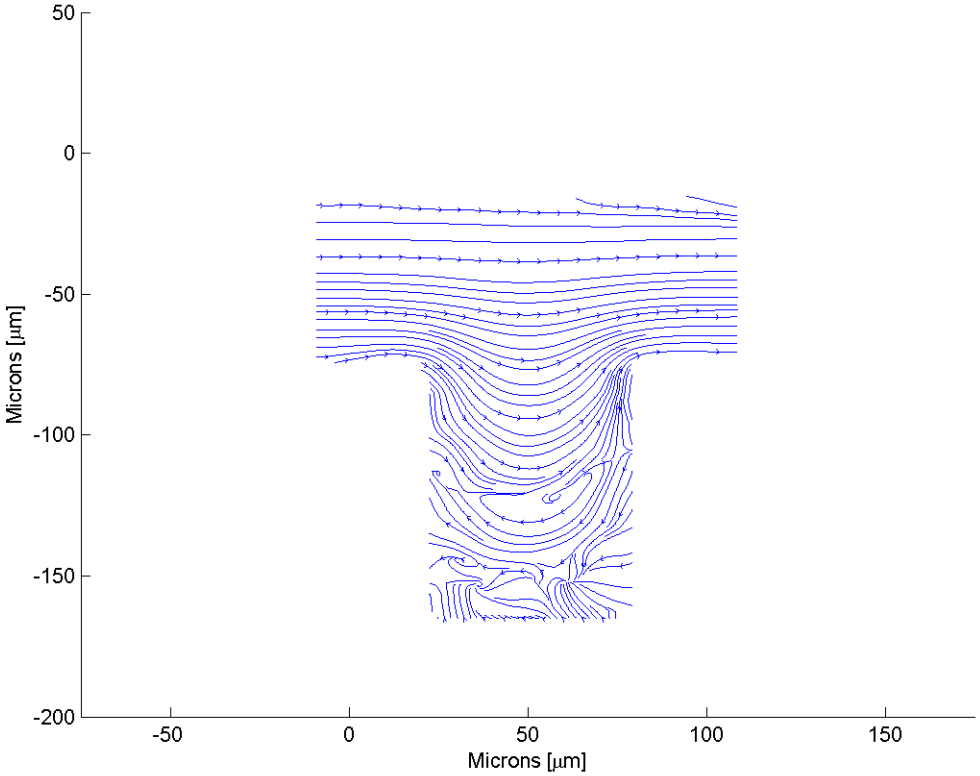

Figure F.147: Streamline image during phase increment 5 at 80 Hz and a Re of 0.1.

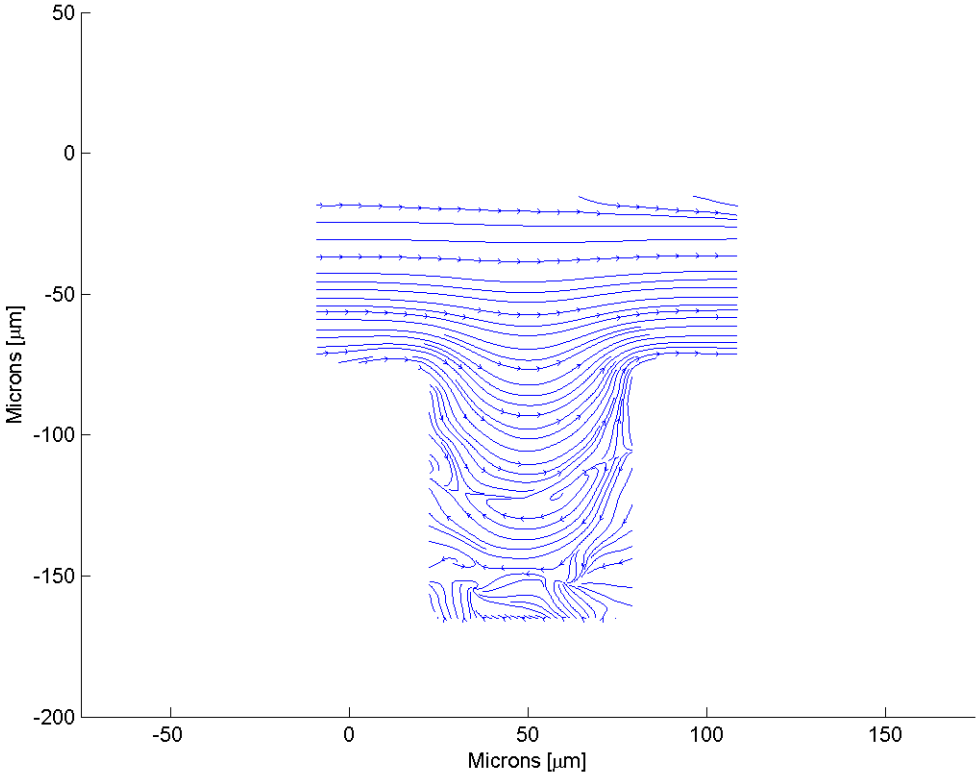

Figure F.148: Streamline image during phase increment 6 at 80 Hz and a Re of 0.1.

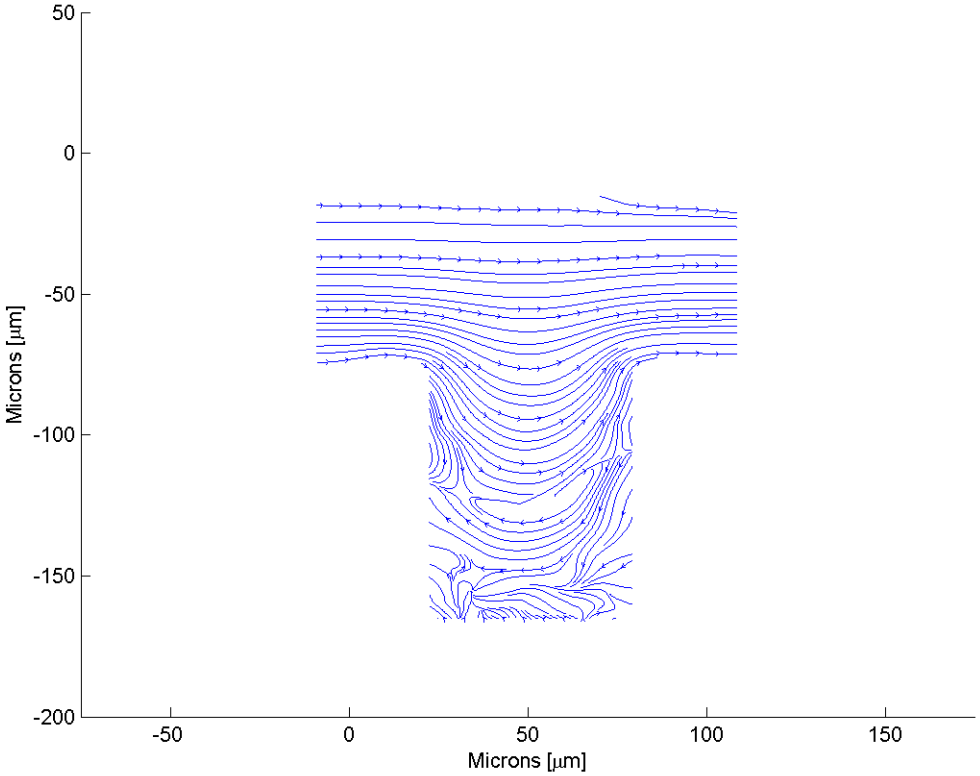

Figure F.149: Streamline image during phase increment 7 at 80 Hz and a Re of 0.1.

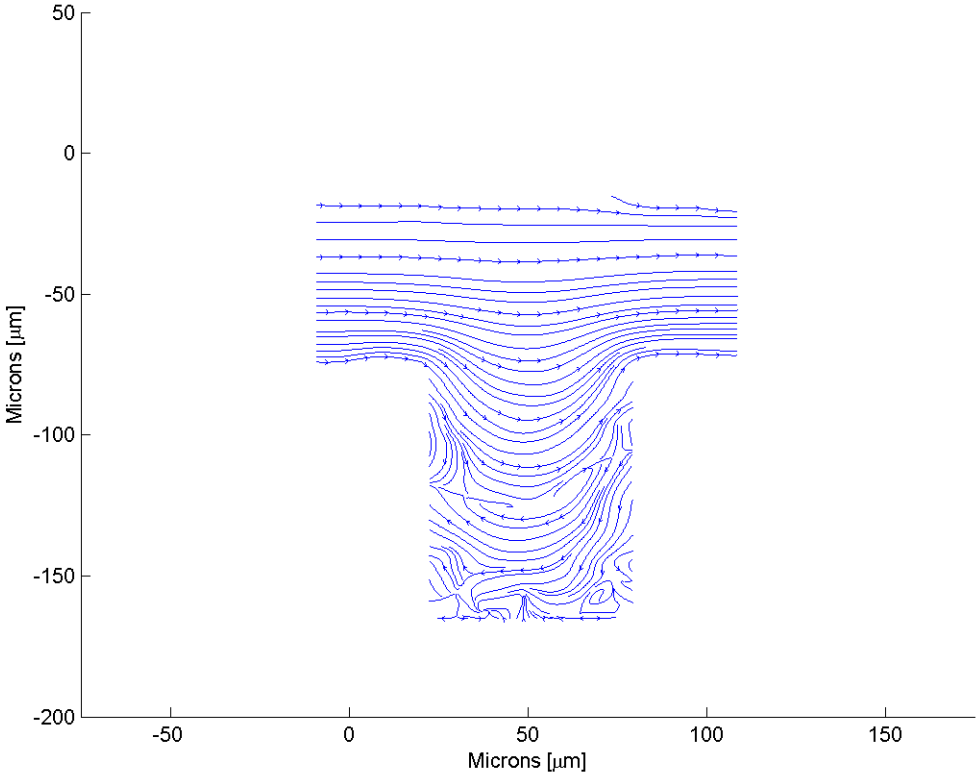

Figure F.150: Streamline image during phase increment 8 at 80 Hz and a Re of 0.1.

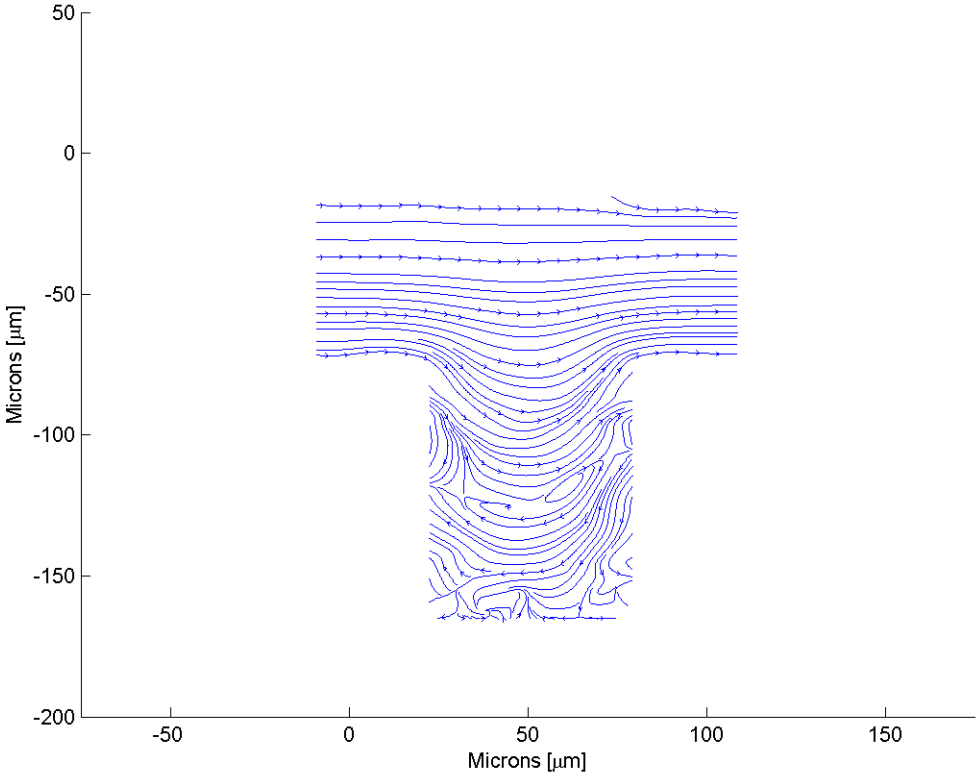

Figure F.151: Streamline image during phase increment 9 at 80 Hz and a Re of 0.1.

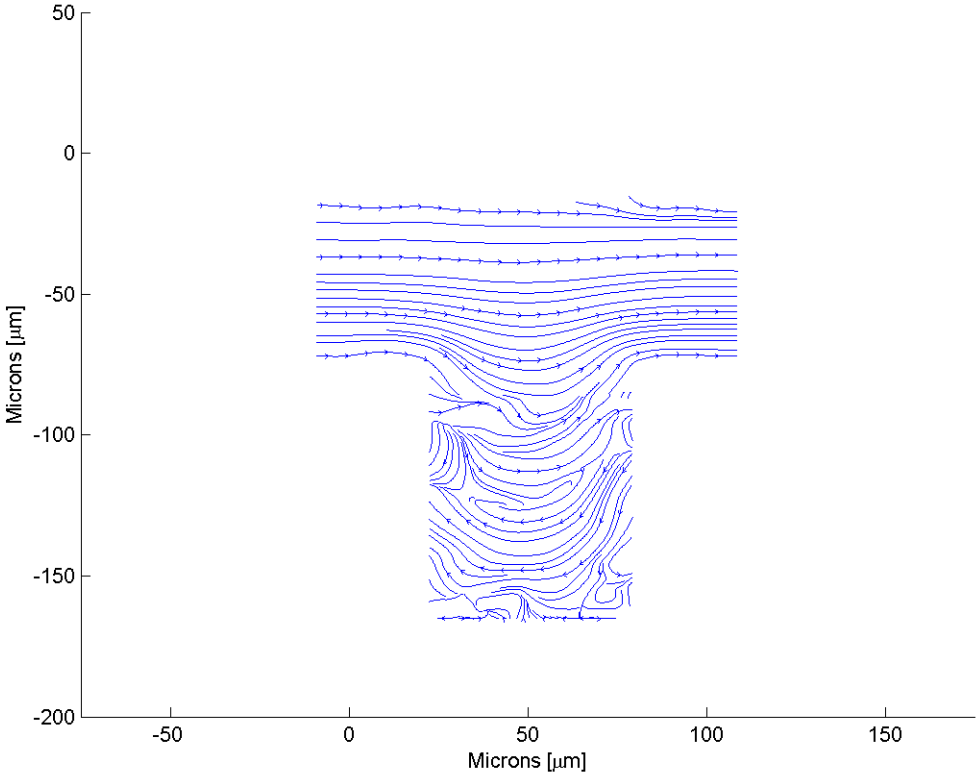

Figure F.152: Streamline image during phase increment 10 at 80 Hz and a Re of 0.1.

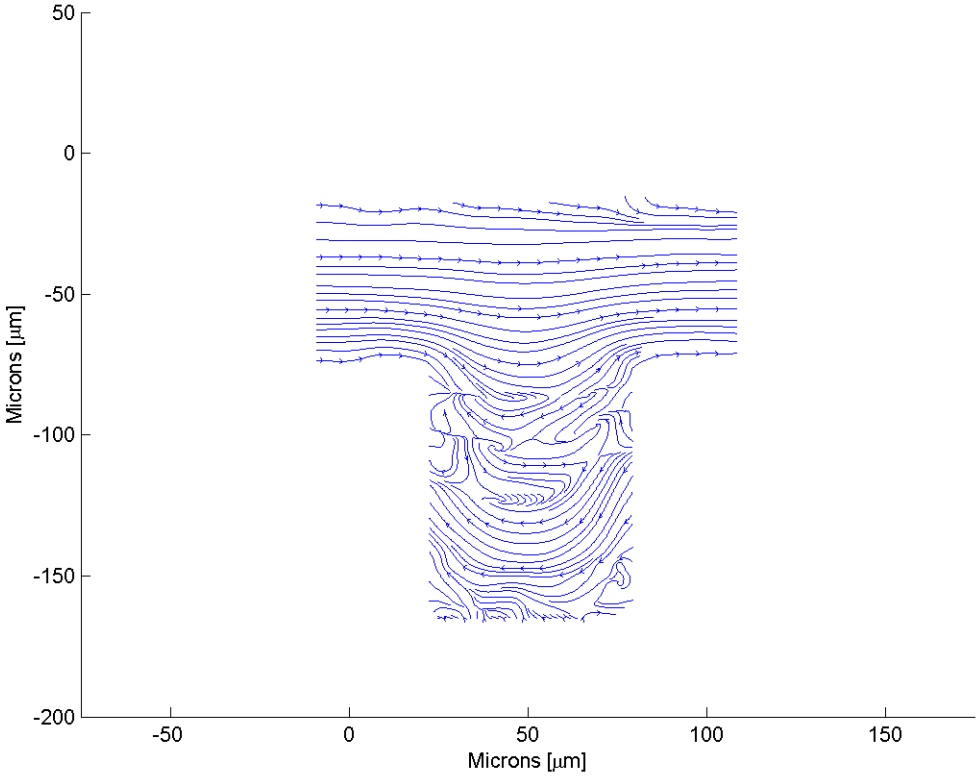

Figure F.153: Streamline image during phase increment 11 at 80 Hz and a Re of 0.1.

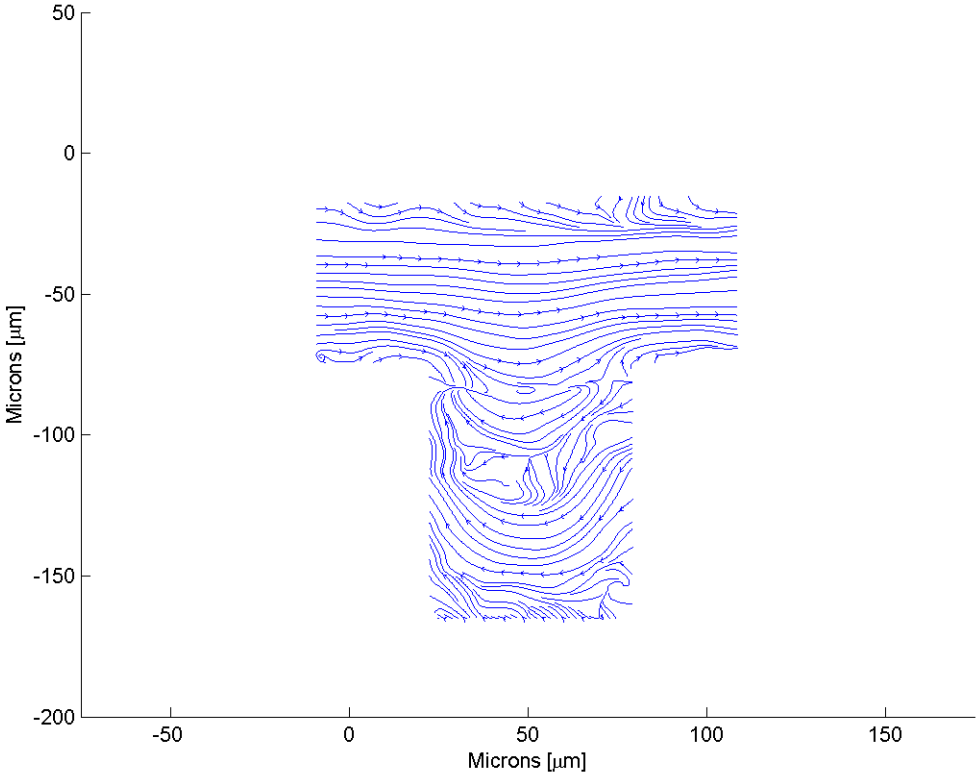

Figure F.154: Streamline image during phase increment 12 at 80 Hz and a Re of 0.1.

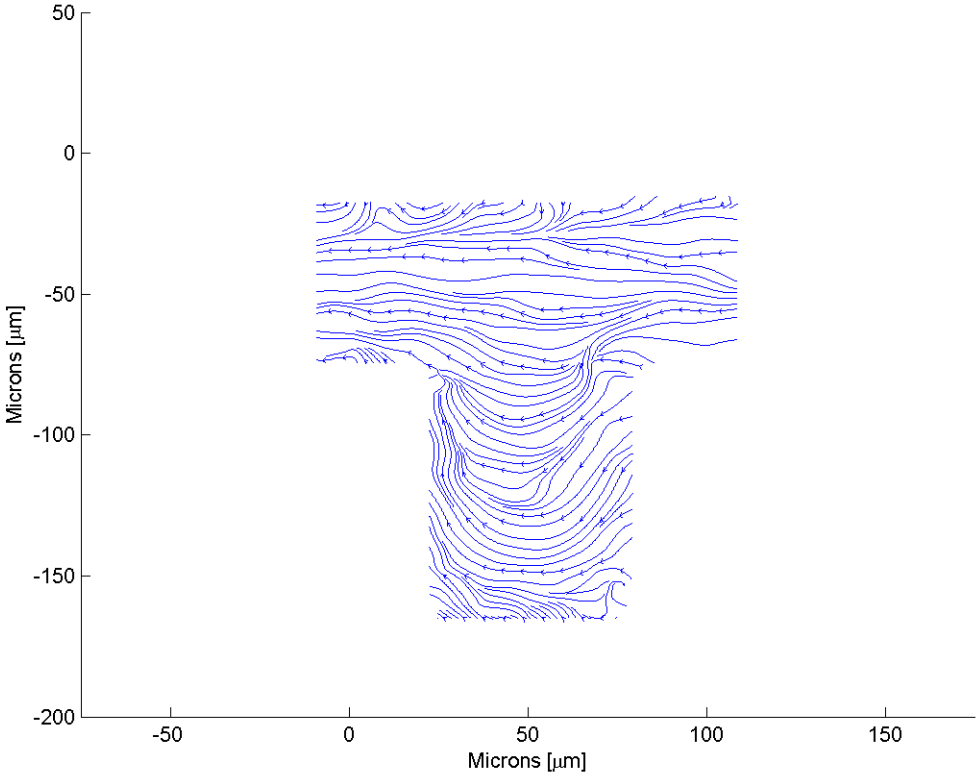

Figure F.155: Streamline image during phase increment 13 at 80 Hz and a Re of 0.1.

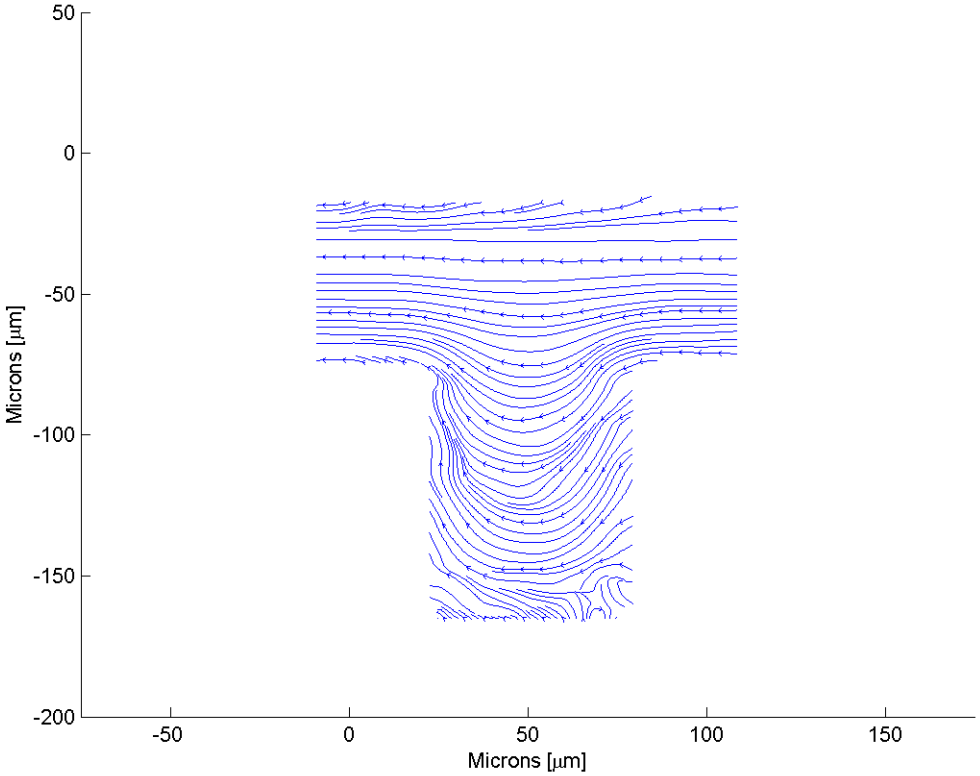

Figure F.156: Streamline image during phase increment 14 at 80 Hz and a Re of 0.1.

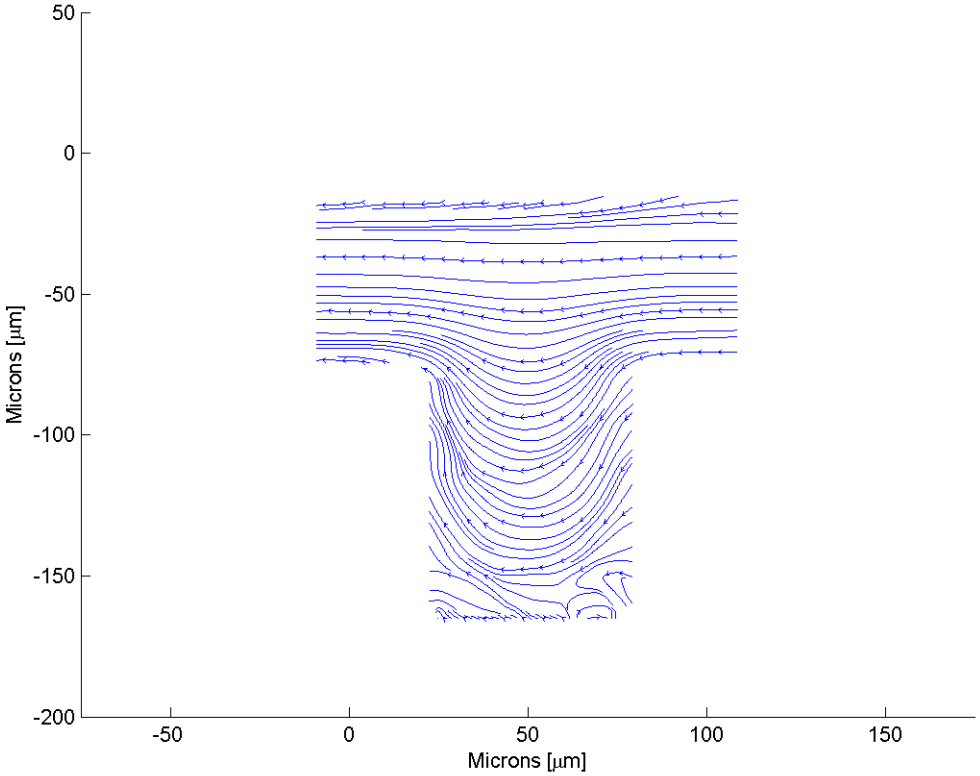

Figure F.157: Streamline image during phase increment 15 at 80 Hz and a Re of 0.1.

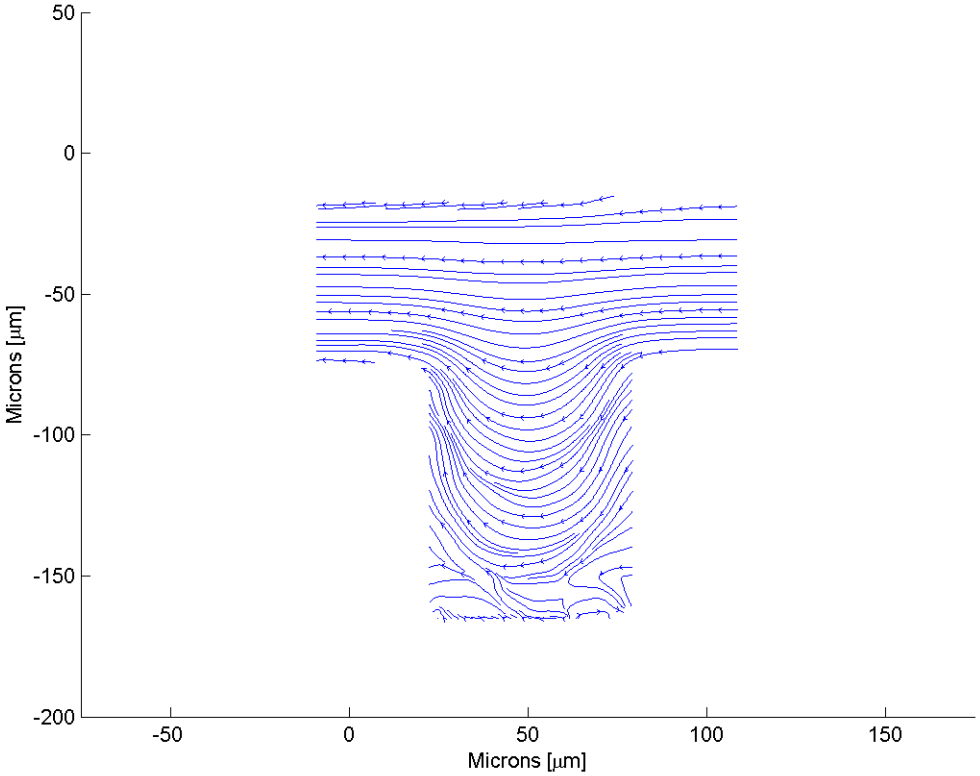

Figure F.158: Streamline image during phase increment 16 at 80 Hz and a Re of 0.1.

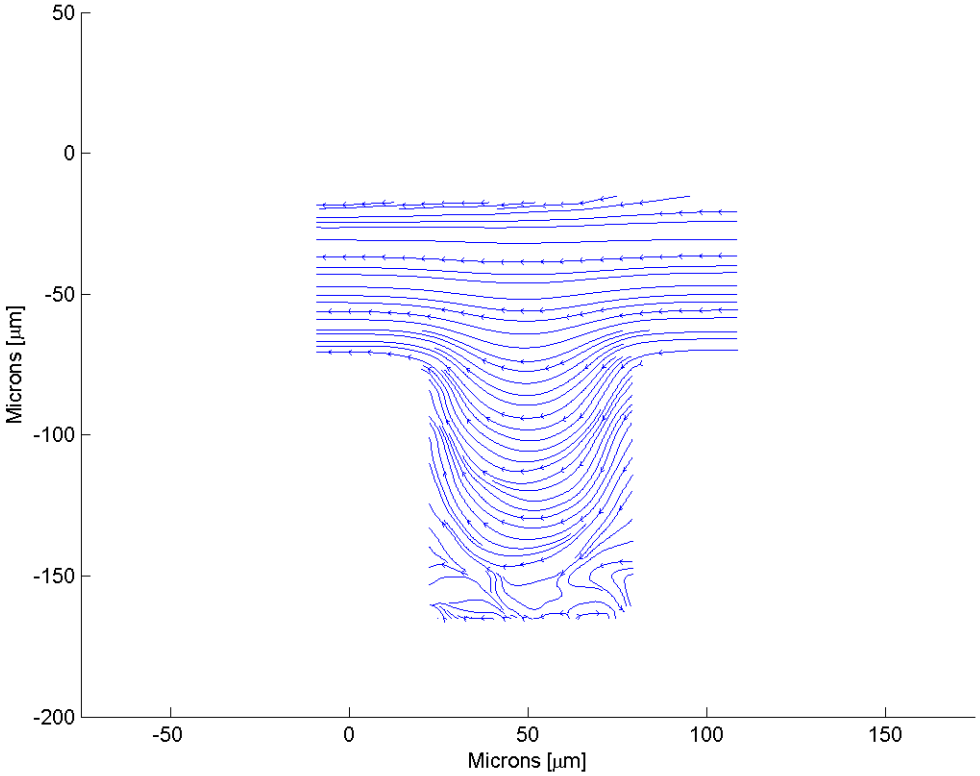

Figure F.159: Streamline image during phase increment 17 at 80 Hz and a Re of 0.1.

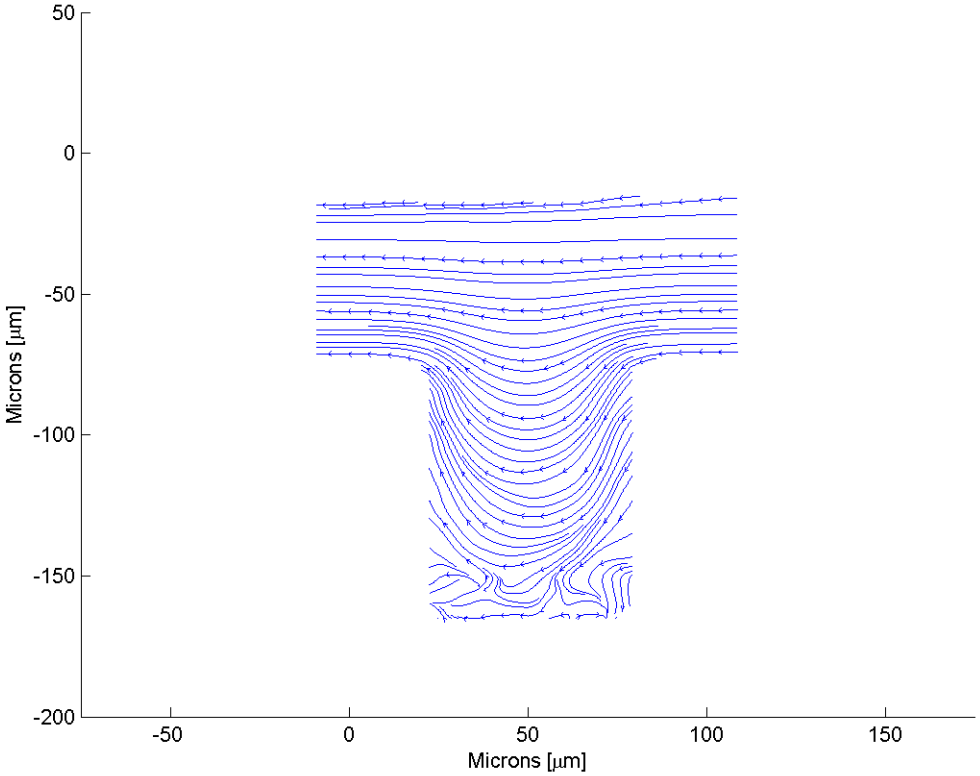

Figure F.160: Streamline image during phase increment 18 at 80 Hz and a Re of 0.1.

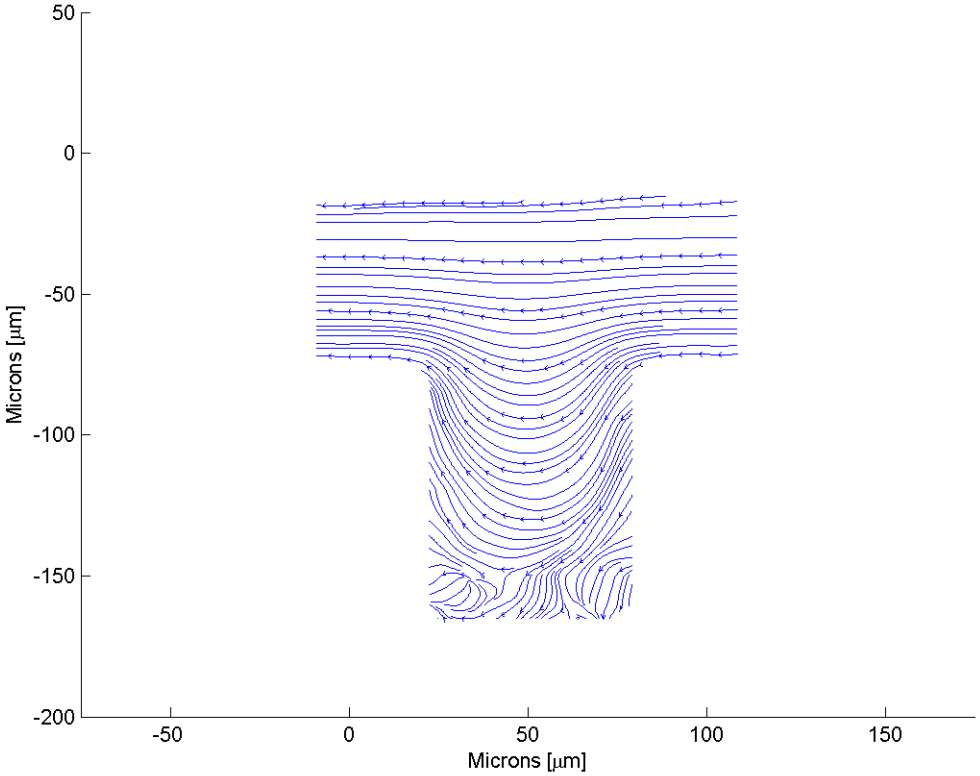

Figure F.161: Streamline image during phase increment 18 at 80 Hz and a Re of 0.1.

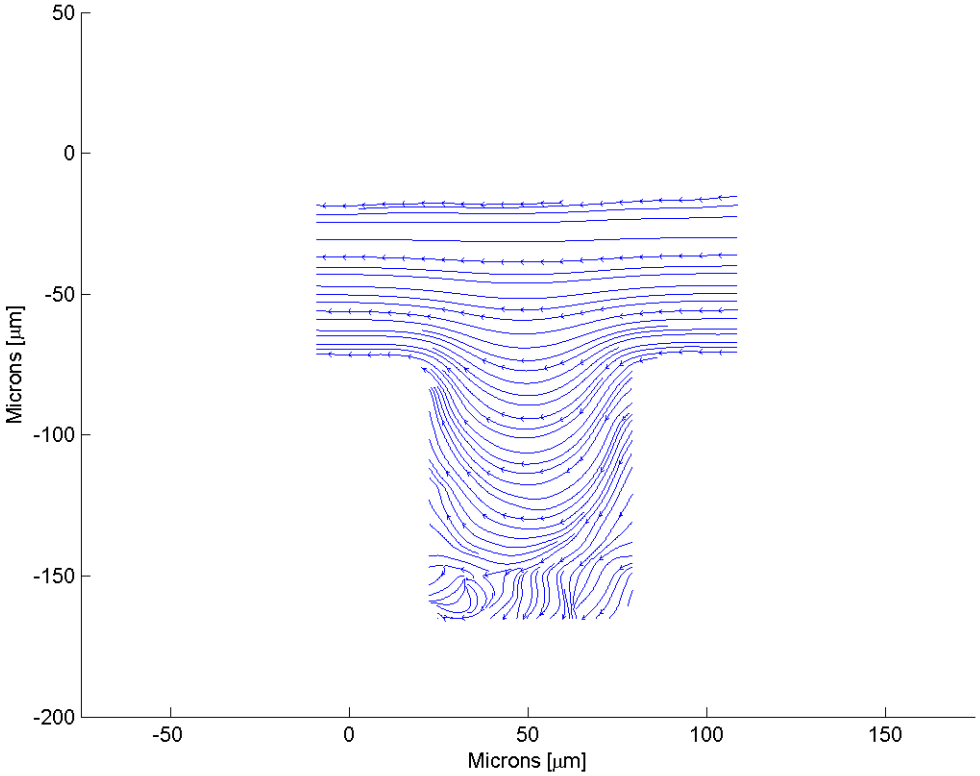

Figure F.162: Streamline image during phase increment 20 at 80 Hz and a Re of 0.1.

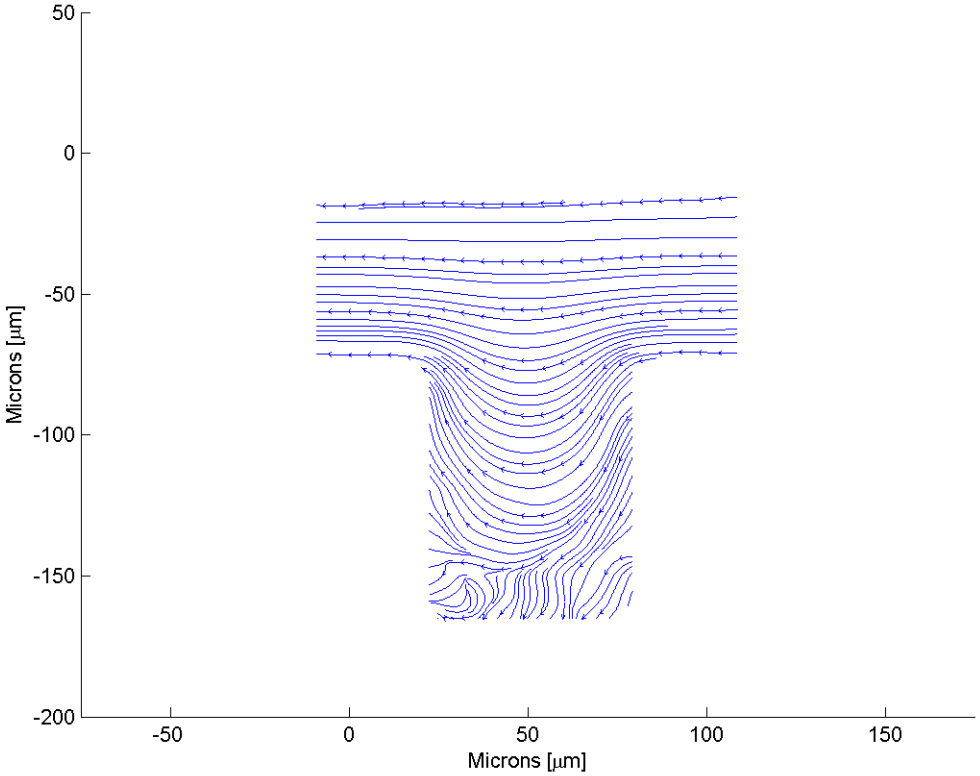

Figure F.163: Streamline image during phase increment 21 at 80 Hz and a Re of 0.1.

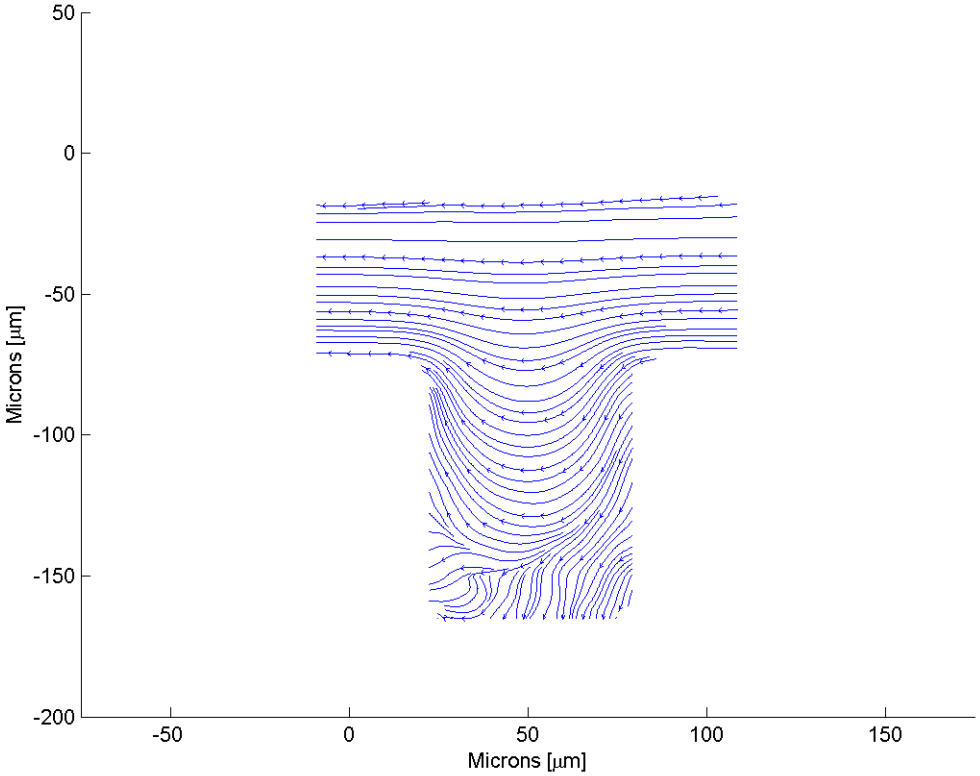

Figure F.164: Streamline image during phase increment 22 at 80 Hz and a Re of 0.1.

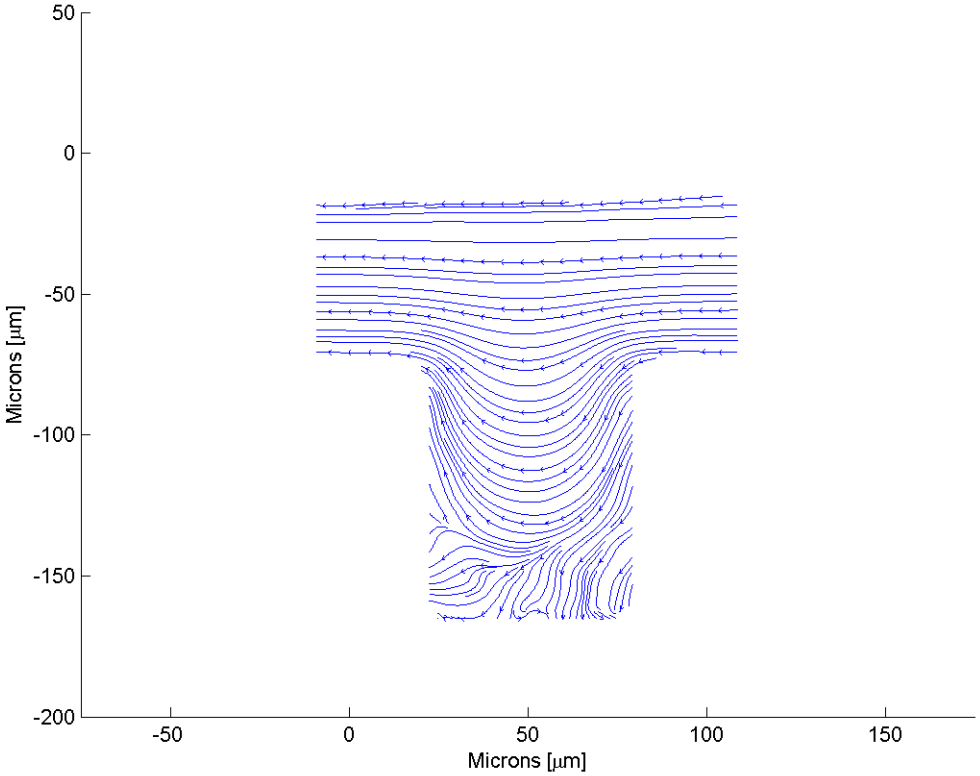

Figure F.165: Streamline image during phase increment 23 at 80 Hz and a Re of 0.1.

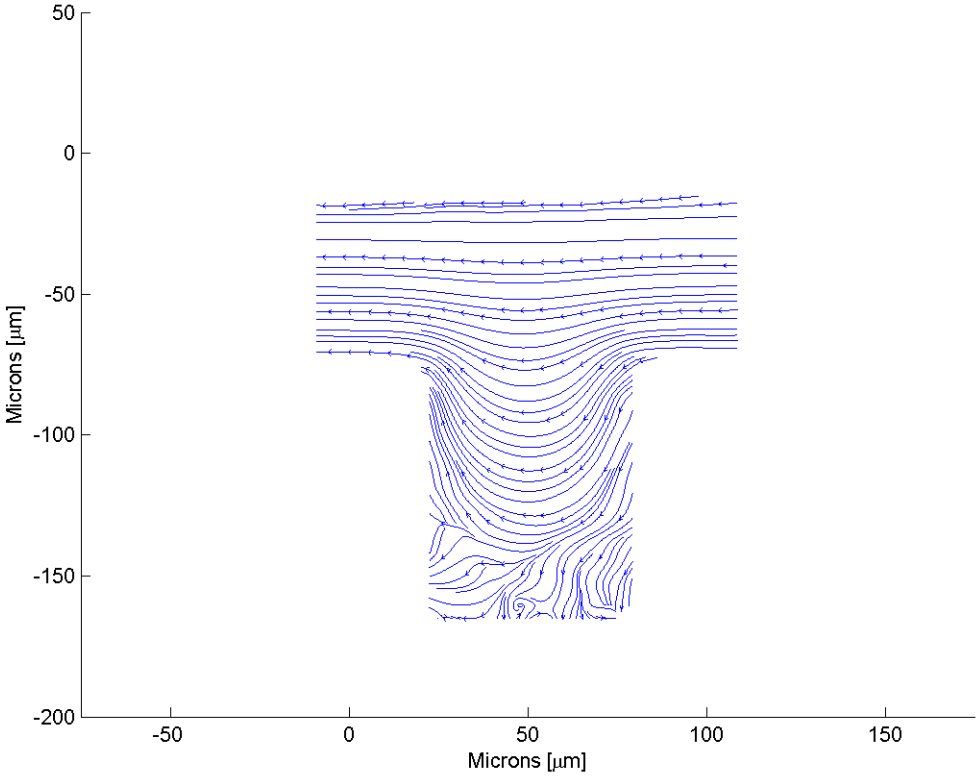

Figure F.166: Streamline image during phase increment 24 at 80 Hz and a Re of 0.1.

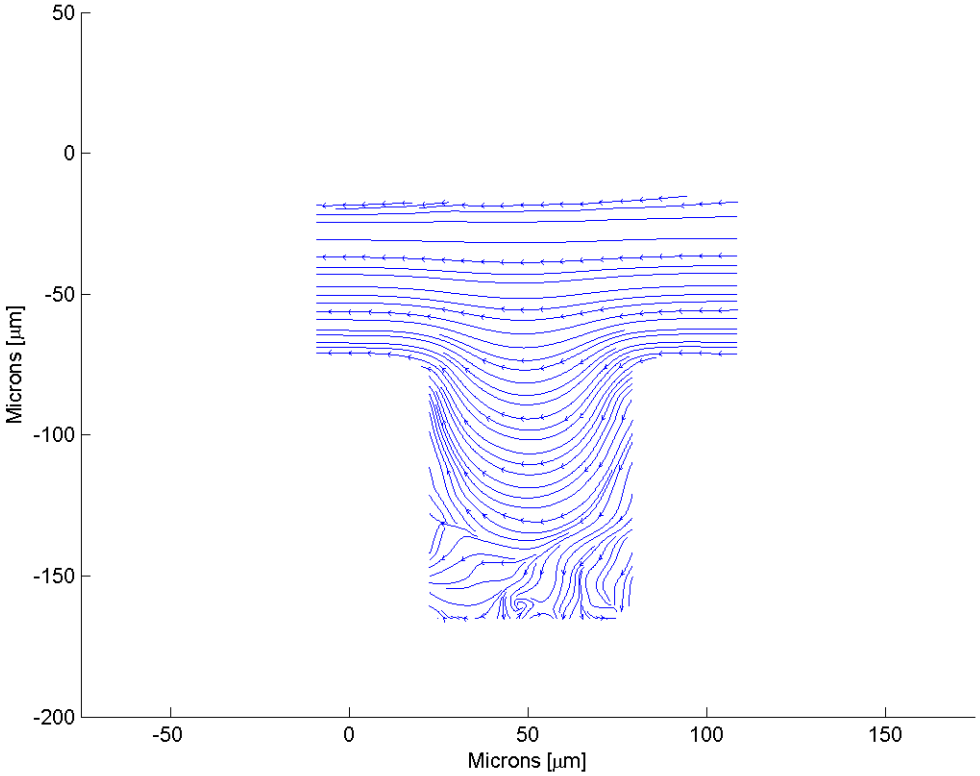

Figure F.167: Streamline image during phase increment 25 at 80 Hz and a Re of 0.1.

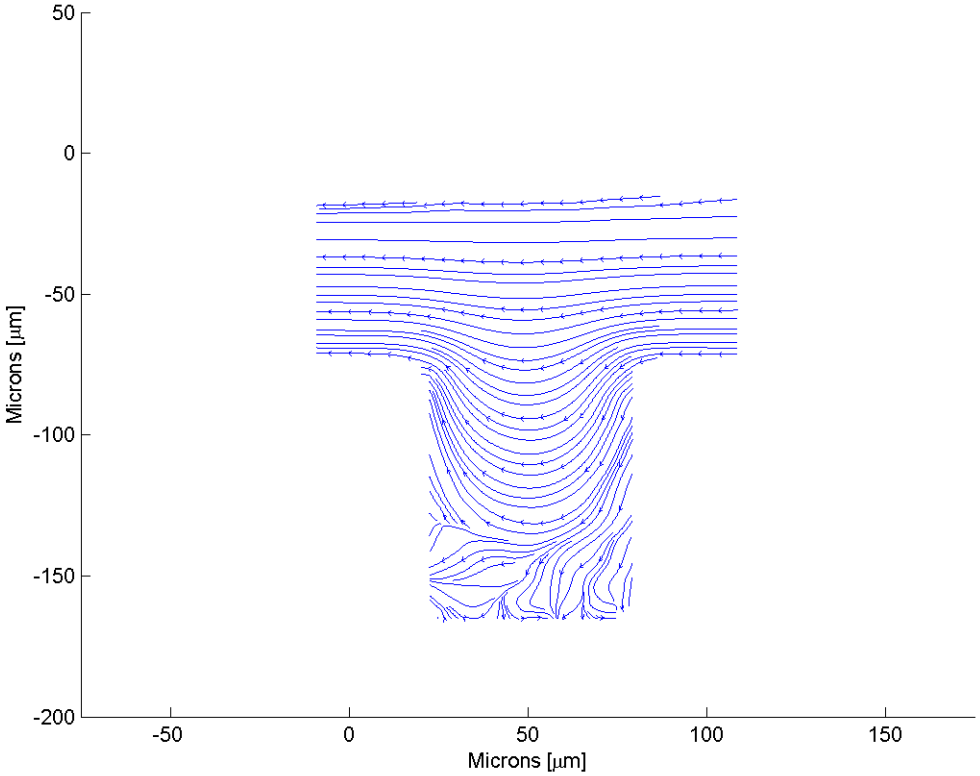

Figure F.168: Streamline image during phase increment 26 at 80 Hz and a Re of 0.1.

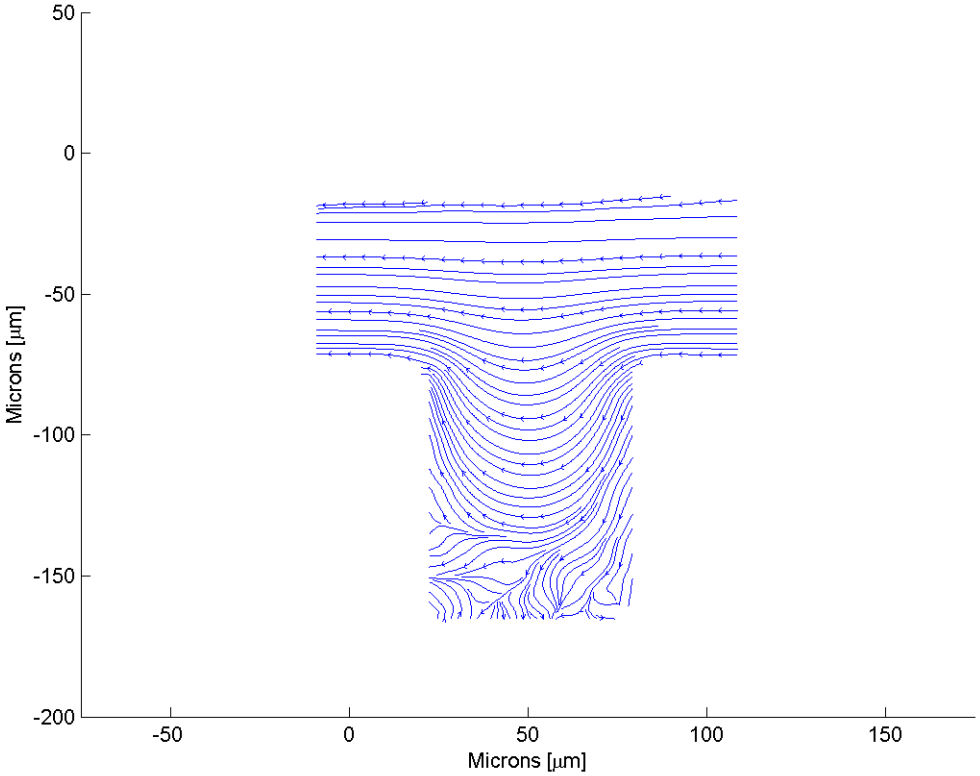

Figure F.169: Streamline image during phase increment 27 at 80 Hz and a Re of 0.1.

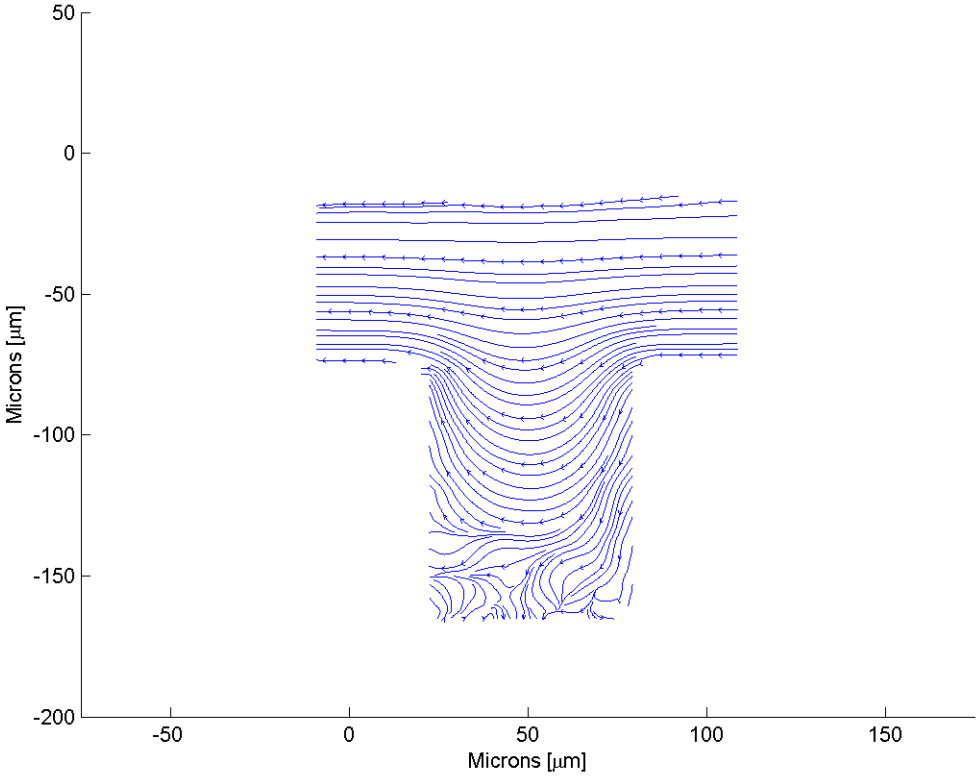

Figure F.170: Streamline image during phase increment 28 at 80 Hz and a Re of 0.1.

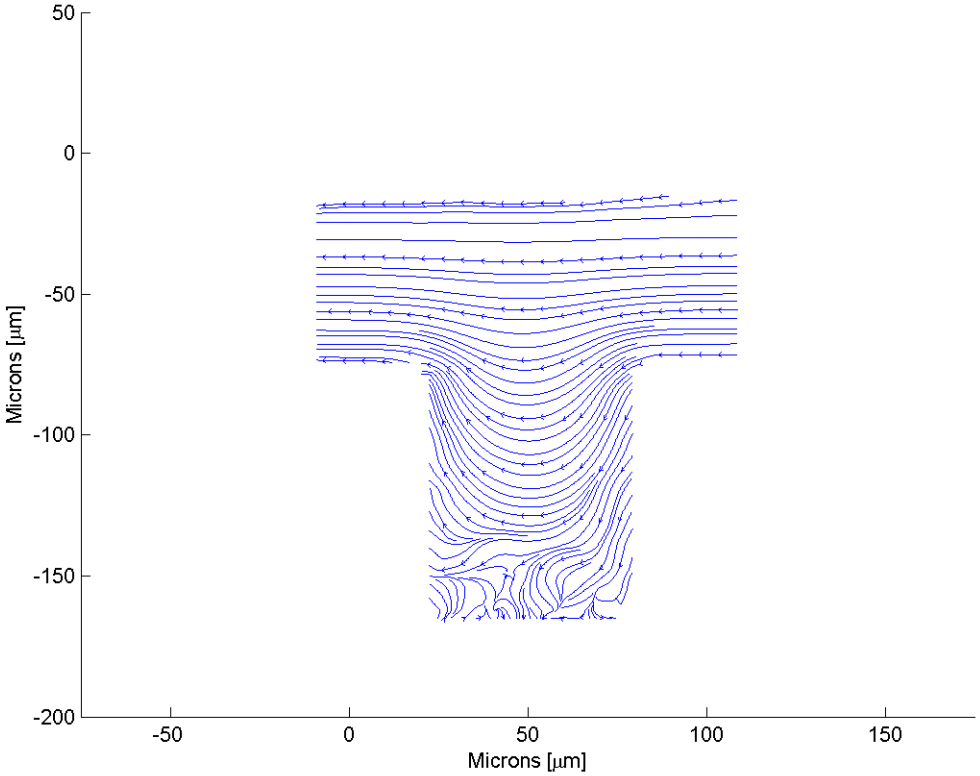

Figure F.171: Streamline image during phase increment 29 at 80 Hz and a Re of 0.1.

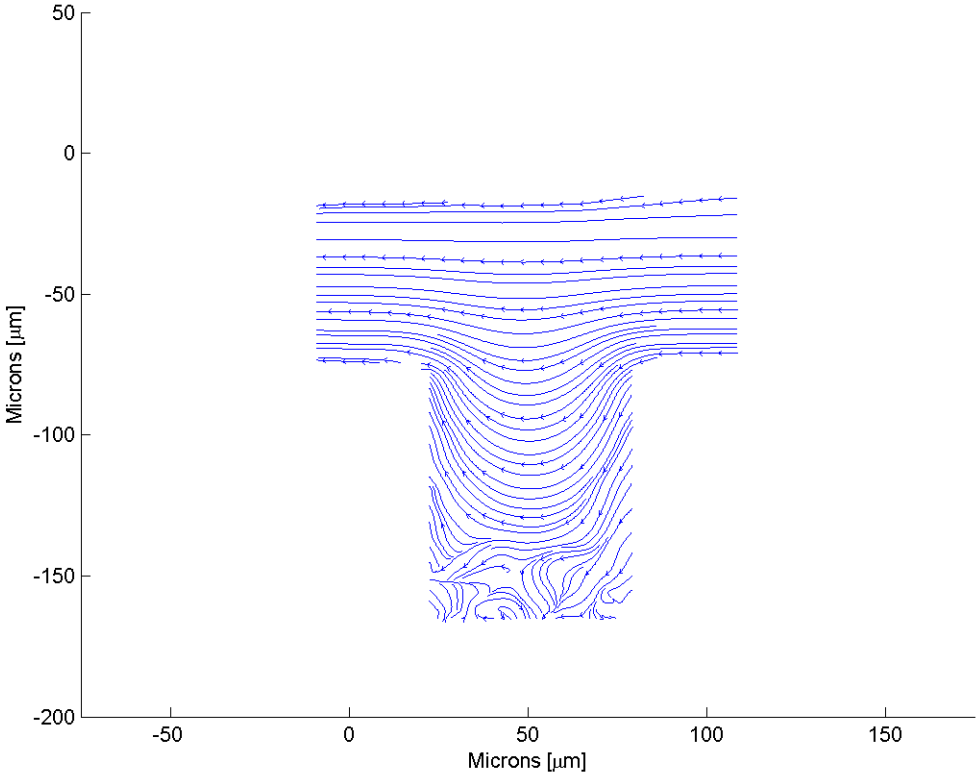

Figure F.172: Streamline image during phase increment 30 at 80 Hz and a Re of 0.1.

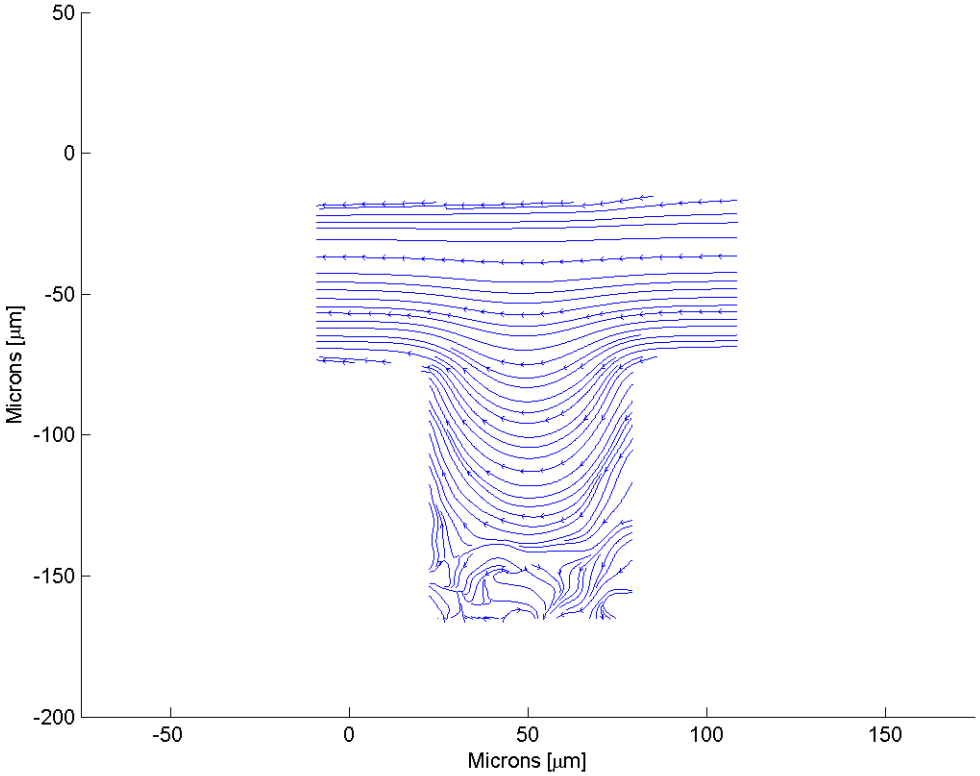

Figure F.173: Streamline image during phase increment 31 at 80 Hz and a Re of 0.1.

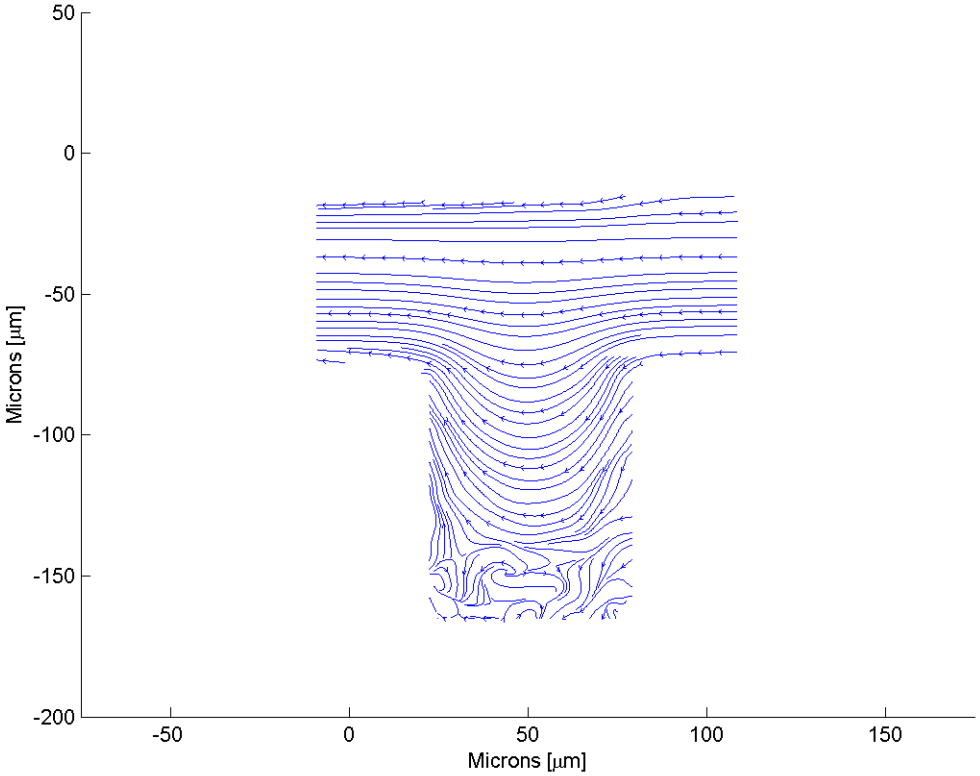

Figure F.174: Streamline image during phase increment 32 at 80 Hz and a Re of 0.1.

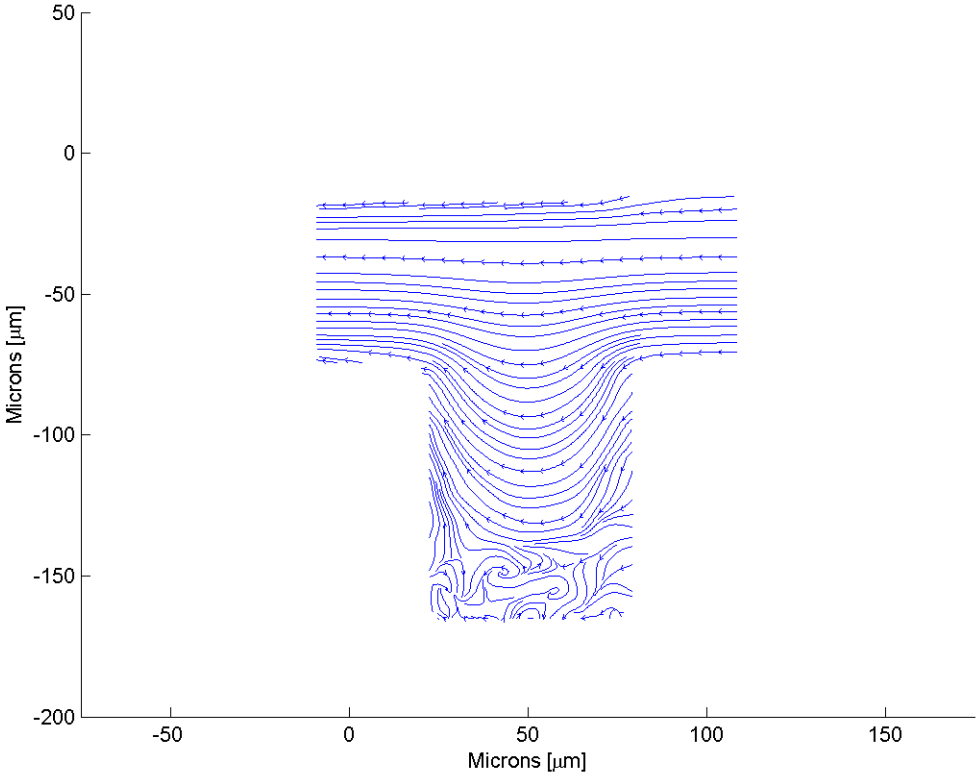

Figure F.175: Streamline image during phase increment 33 at 80 Hz and a Re of 0.1.

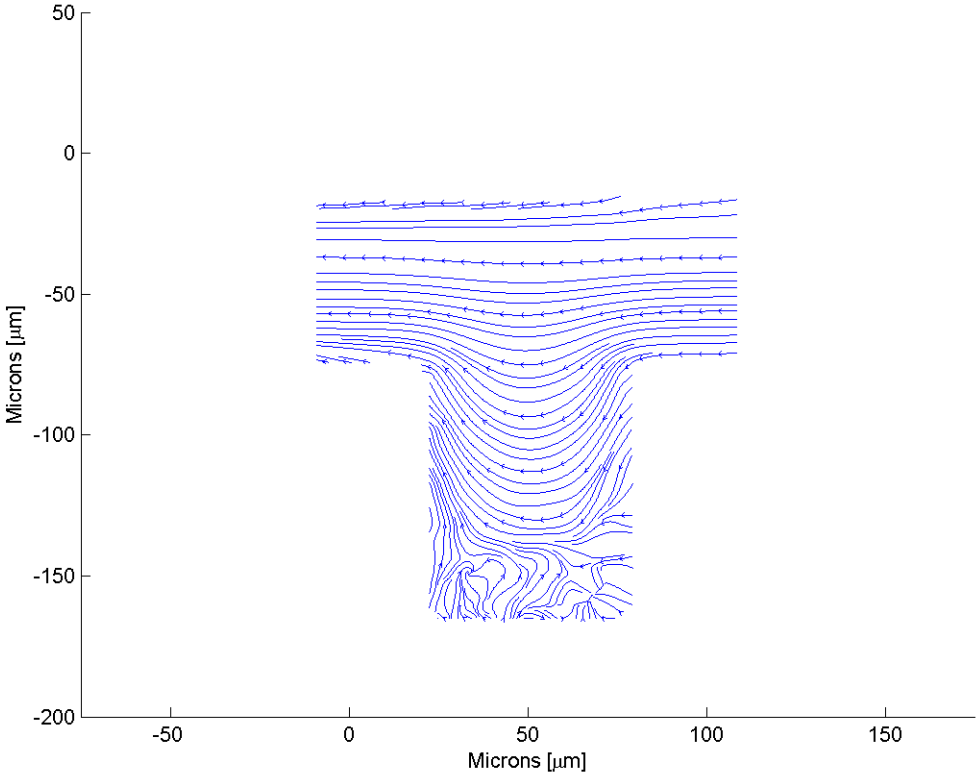

Figure F.176: Streamline image during phase increment 34 at 80 Hz and a Re of 0.1.

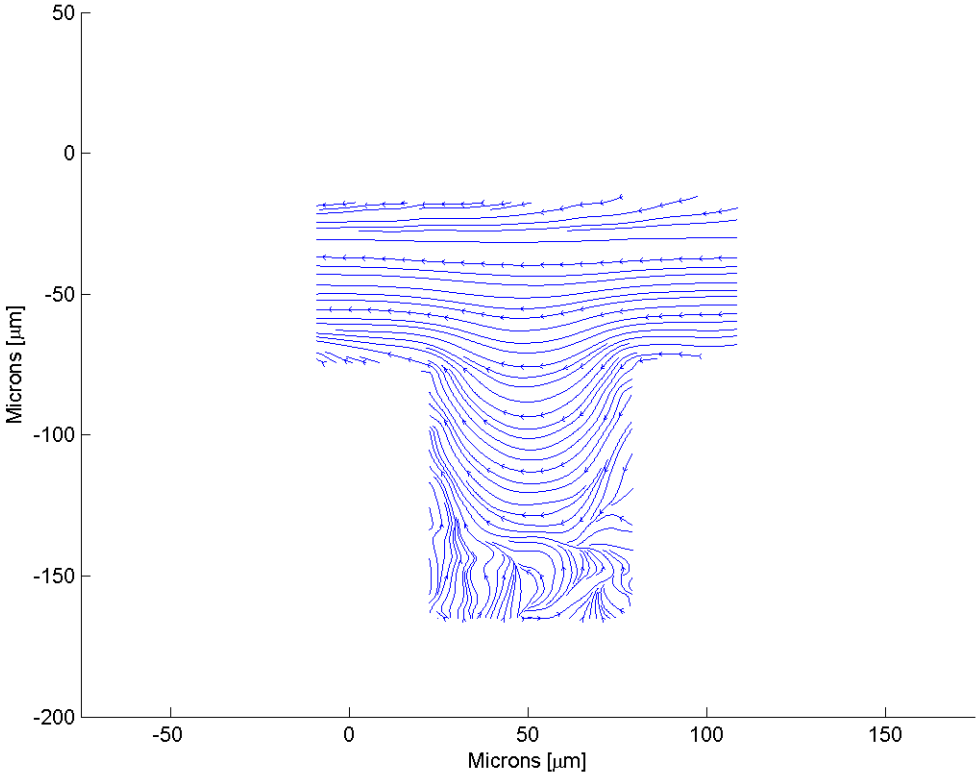

Figure F.177: Streamline image during phase increment 35 at 80 Hz and a Re of 0.1.

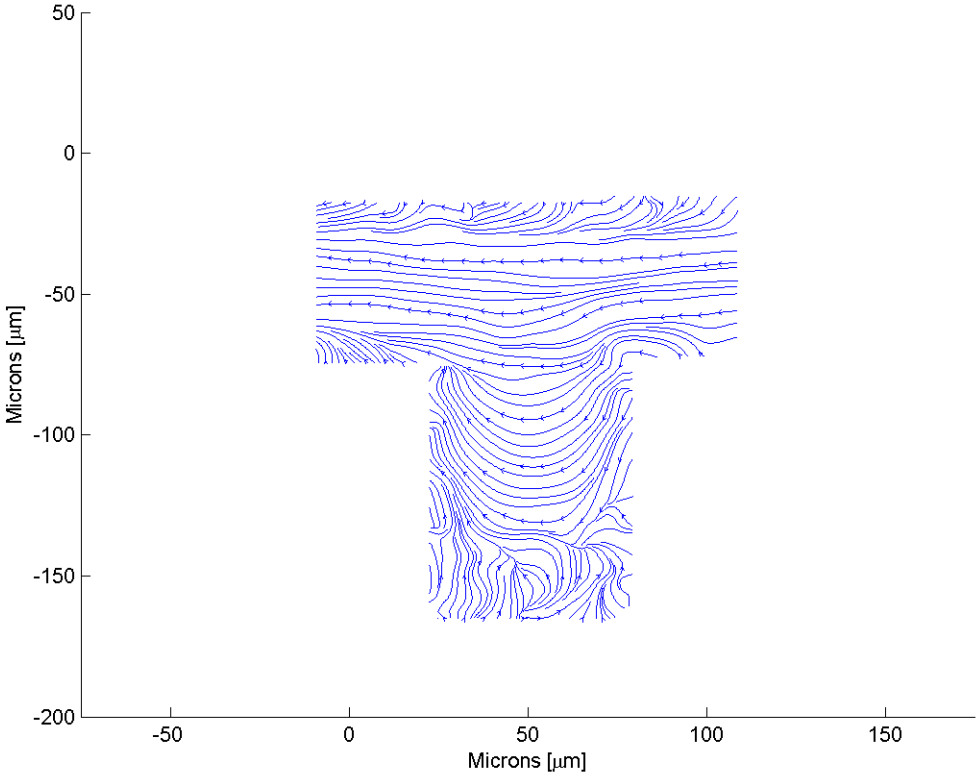

Figure F.178: Streamline image during phase increment 36 at 80 Hz and a Re of 0.1.

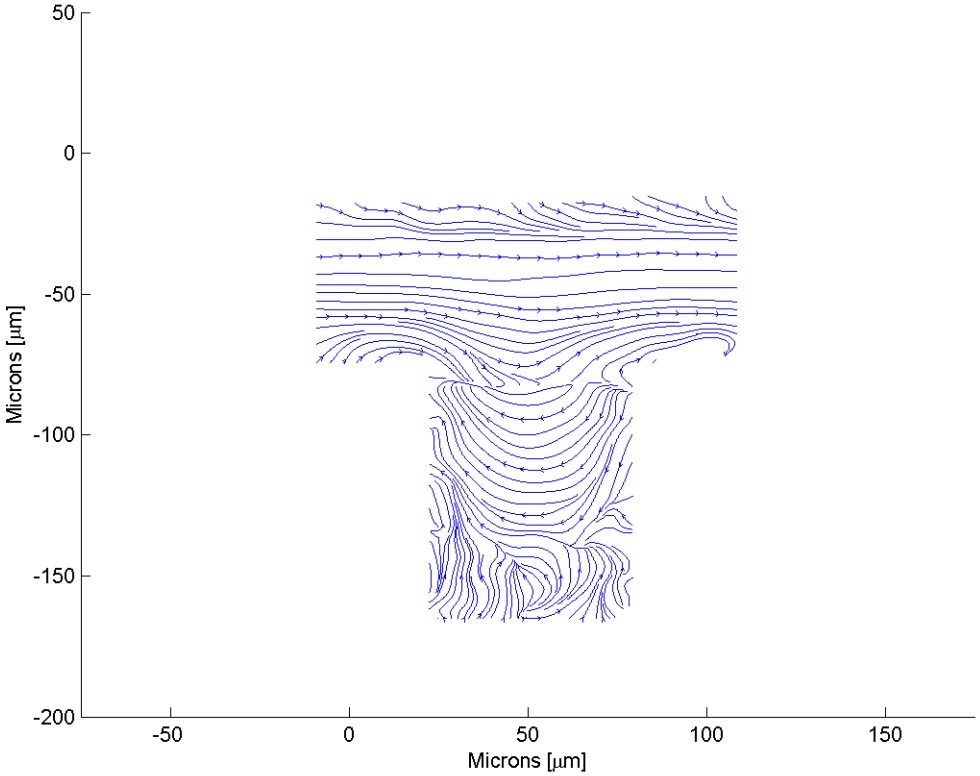

Figure F.179: Streamline image during phase increment 37 at 80 Hz and a Re of 0.1.

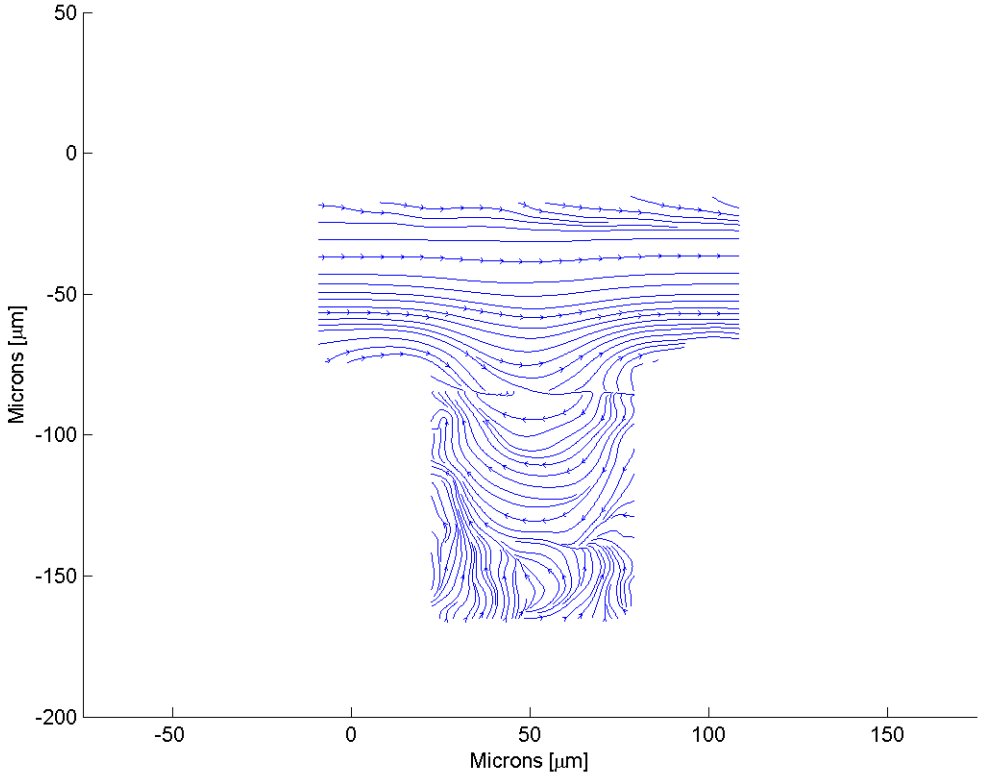

Figure F.180: Streamline image during phase increment 38 at 80 Hz and a Re of 0.1.

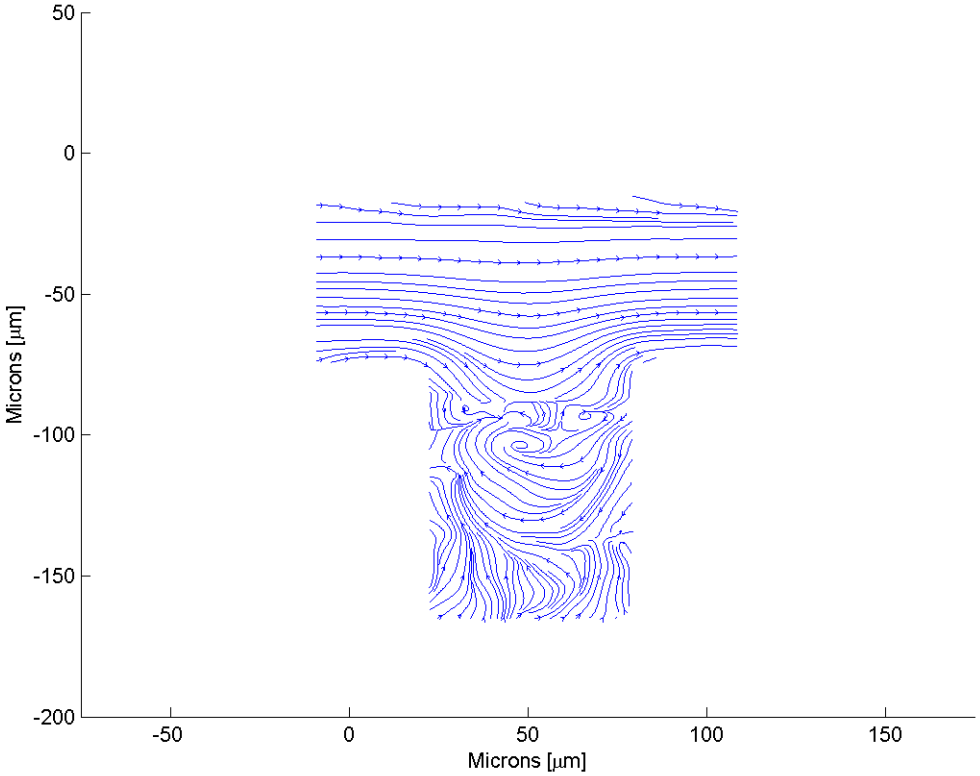

Figure F.181: Streamline image during phase increment 39 at 80 Hz and a Re of 0.1.

F.2.3 Residence time of particles in the cavity at 80 Hz

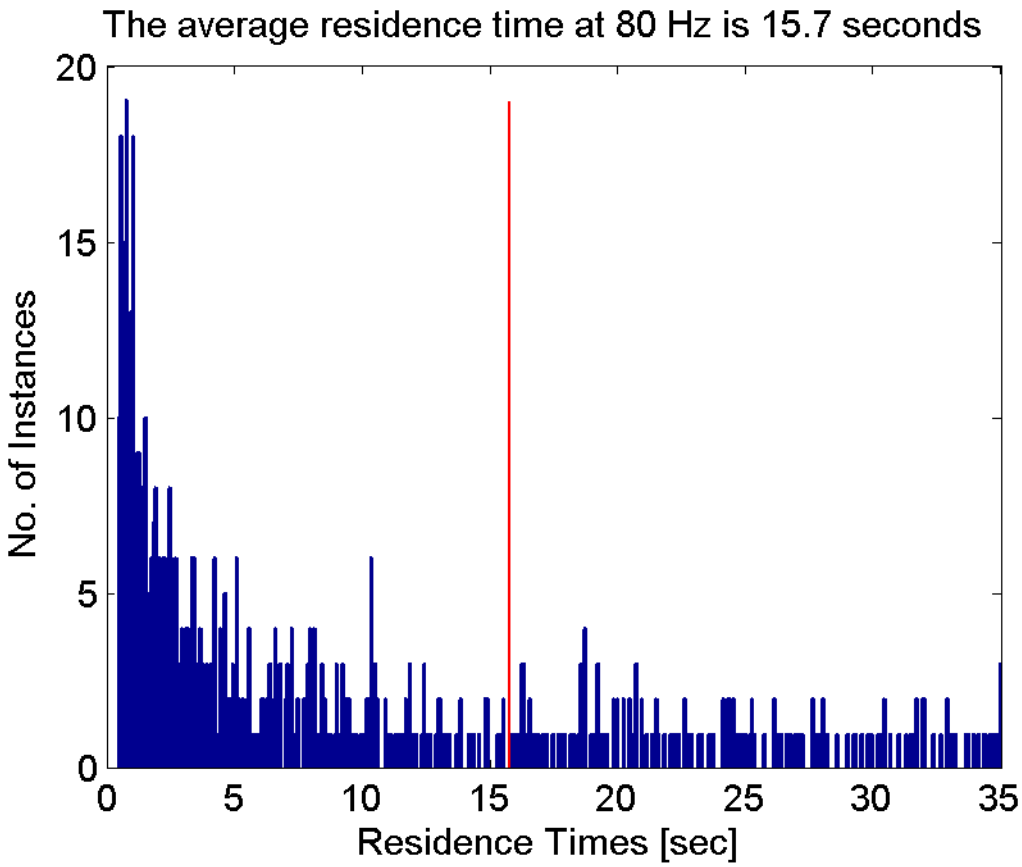

Figure F.182: The residence time distribution for the AR = 0.5 cavity at Re 0.1 at 80 Hz. The average residence time is 15.7 secs.

F.2.4 Lagrangian coherent structures at 80 Hz

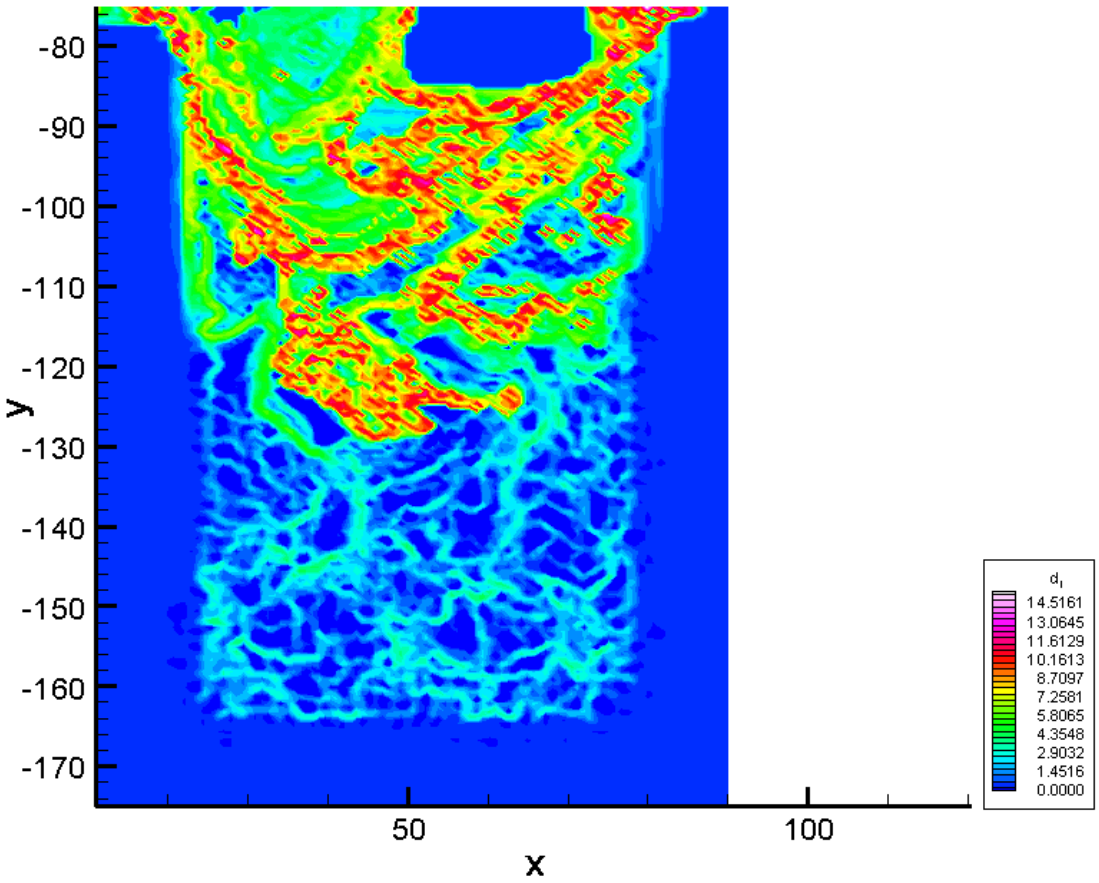

Figure F.183: The backward time LCS during phase increment 1 at 80 Hz.

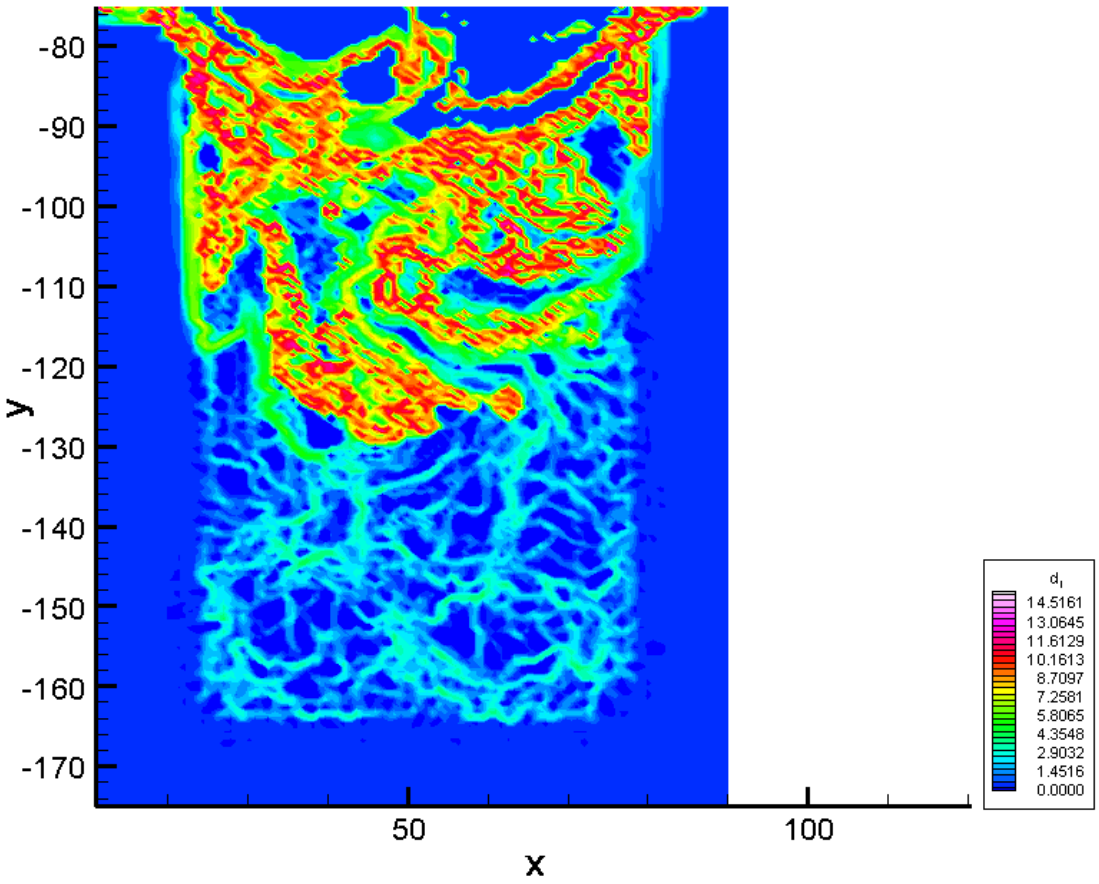

Figure F.184: The backward time LCS during phase increment 2 at 80 Hz.

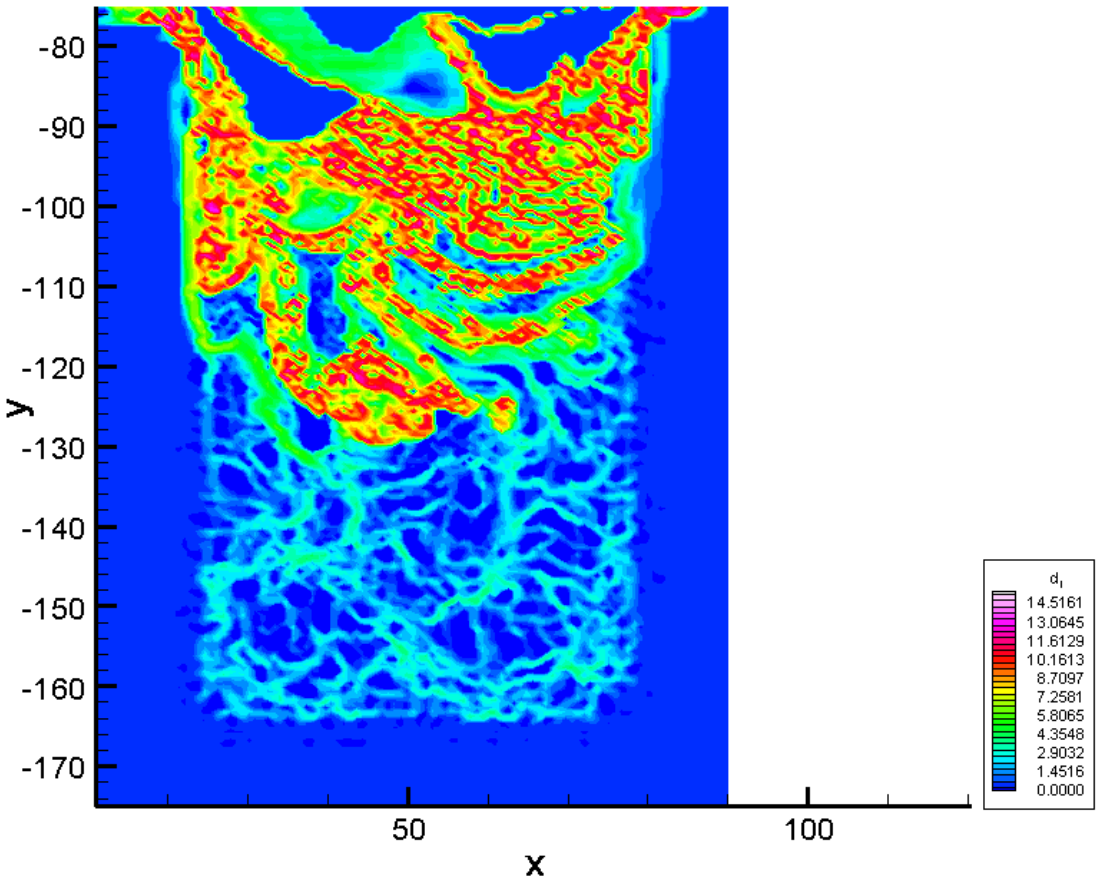

Figure F.185: The backward time LCS during phase increment 3 at 80 Hz.

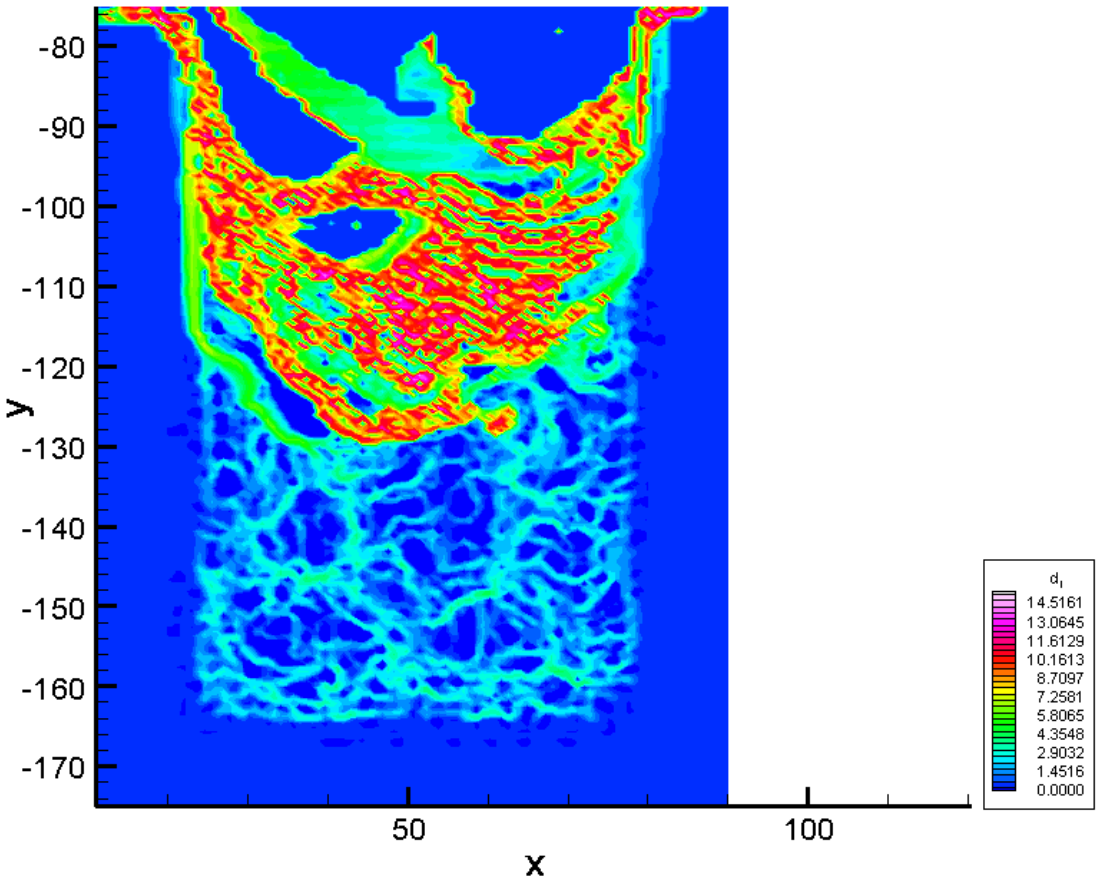

Figure F.186: The backward time LCS during phase increment 4 at 80 Hz.

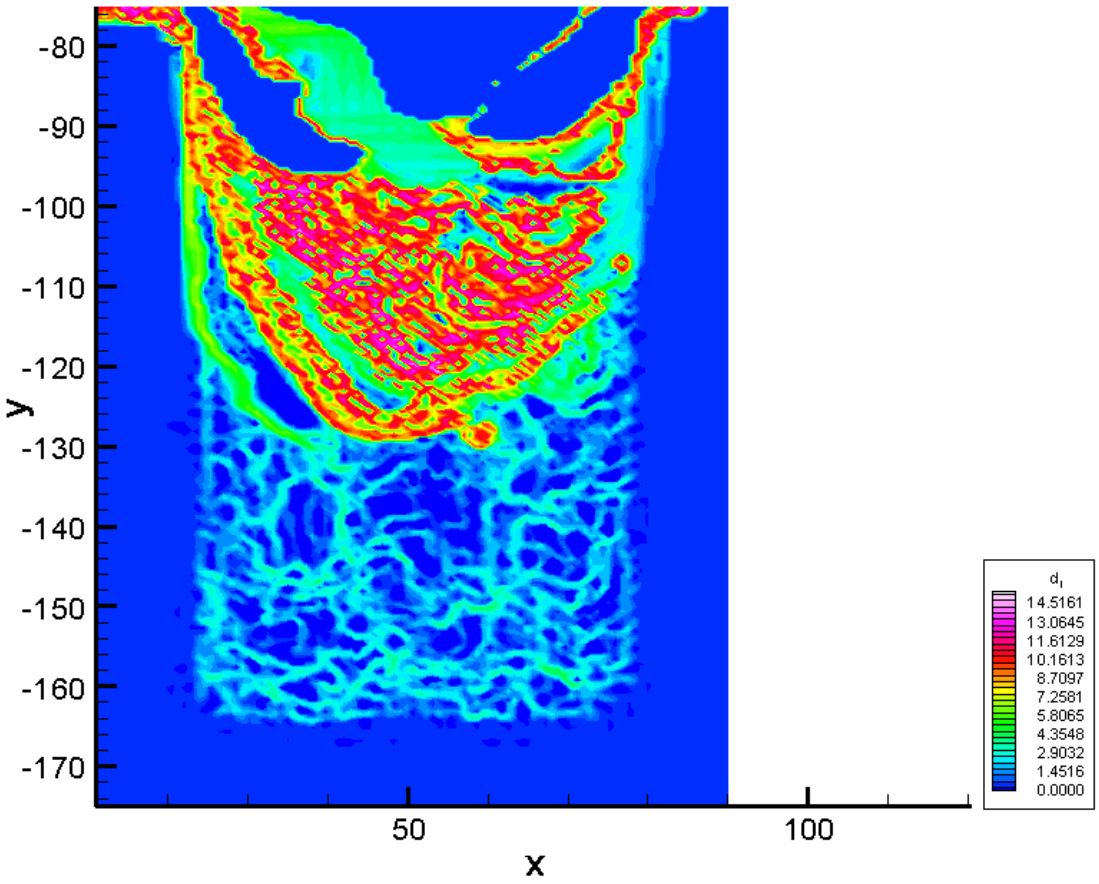

Figure F.187: The backward time LCS during phase increment 5 at 80 Hz.

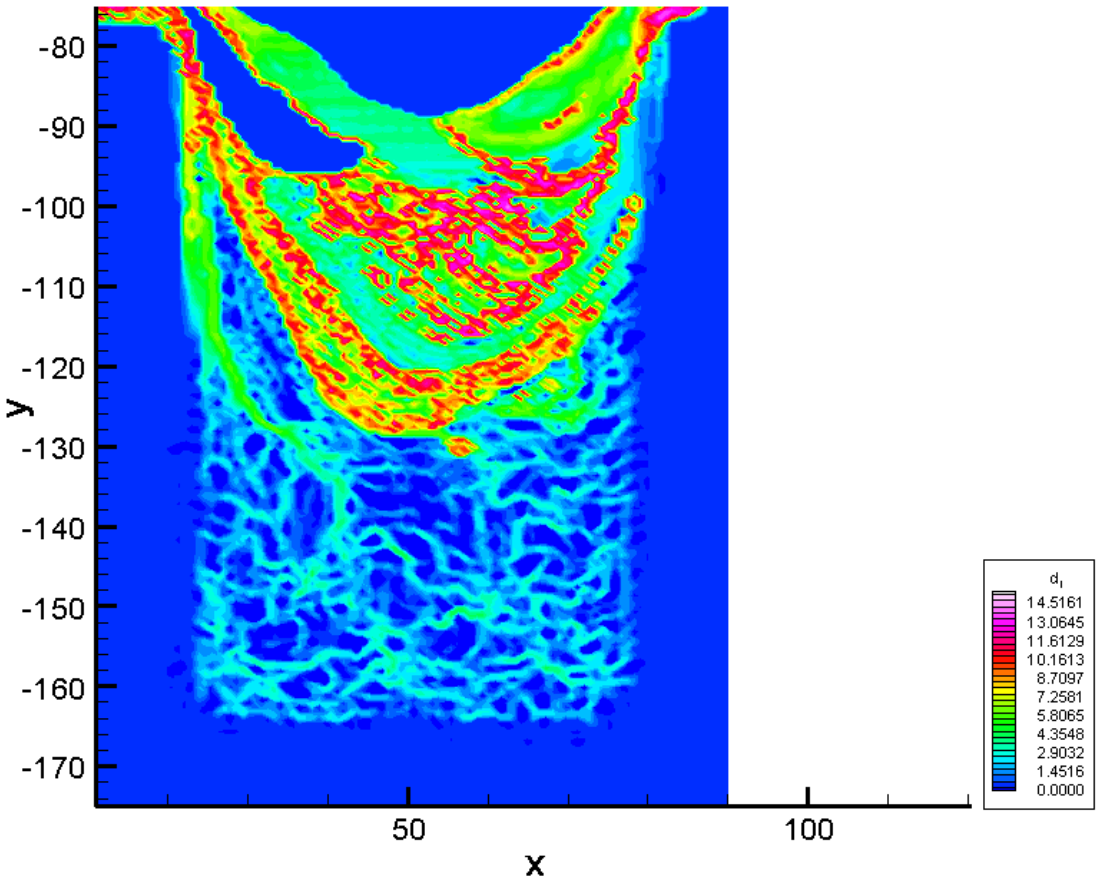

Figure F.188: The backward time LCS during phase increment 6 at 80 Hz.

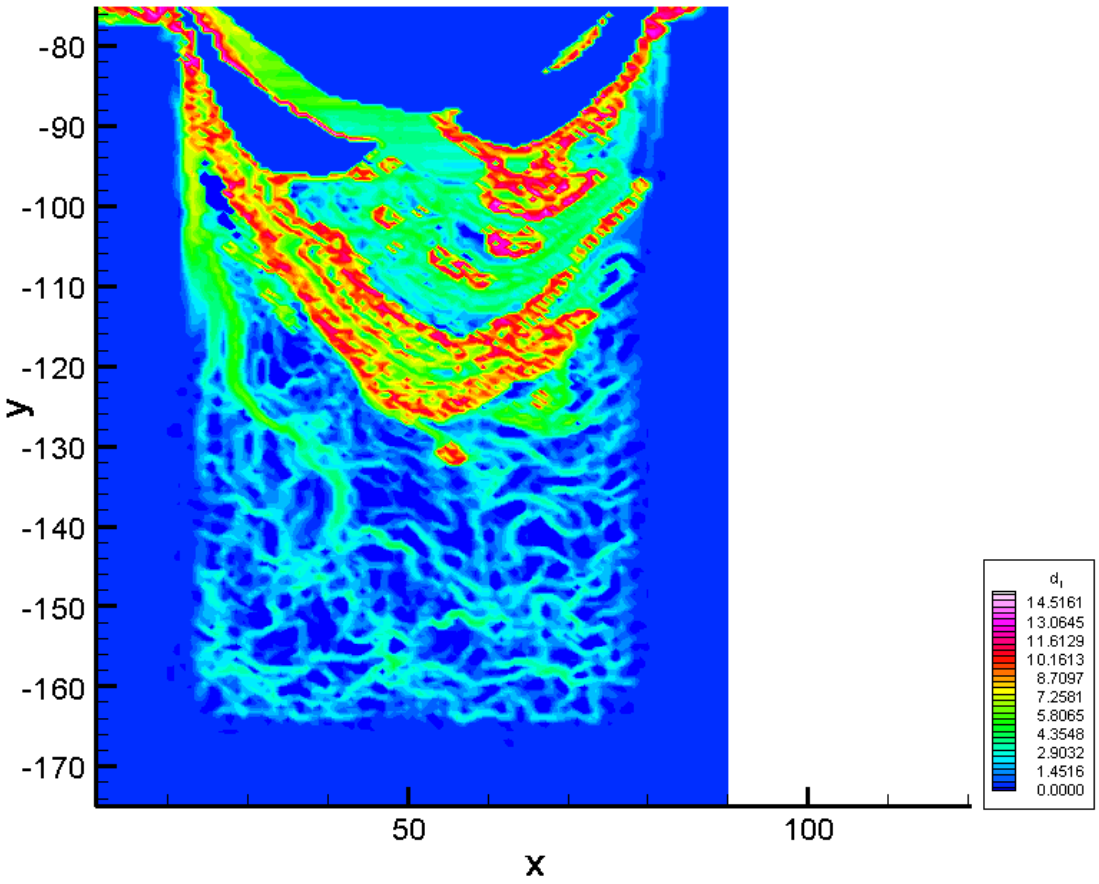

Figure F.189: The backward time LCS during phase increment 7 at 80 Hz.

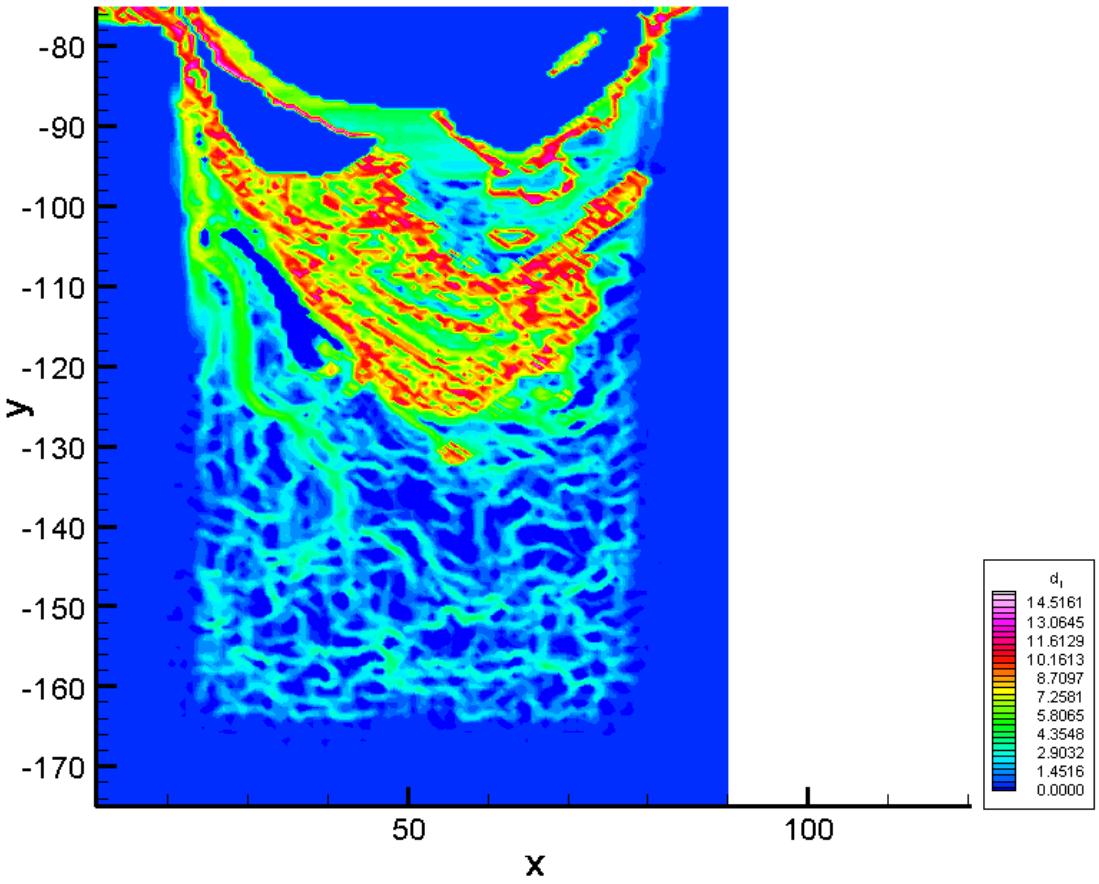

Figure F.190: The backward time LCS during phase increment 8 at 80 Hz.

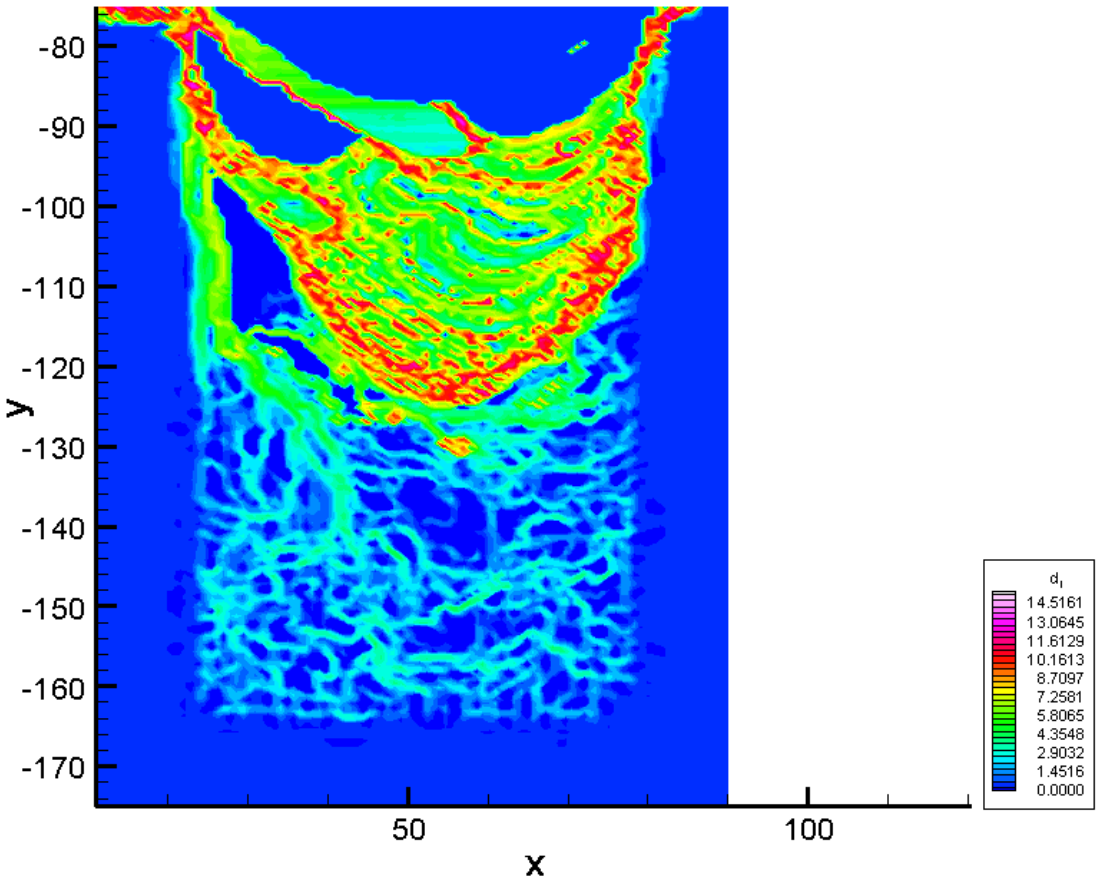

Figure F.191: The backward time LCS during phase increment 9 at 80 Hz.

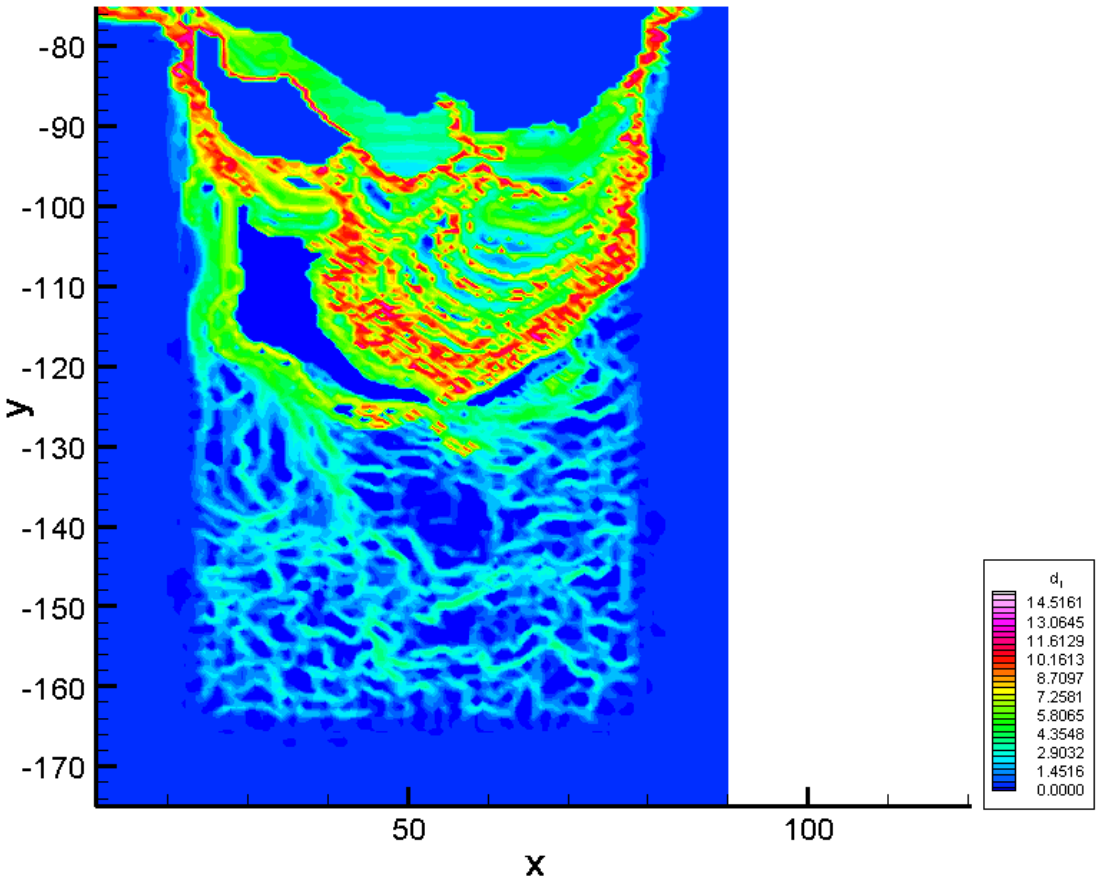

Figure F.192: The backward time LCS during phase increment 10 at 80 Hz.

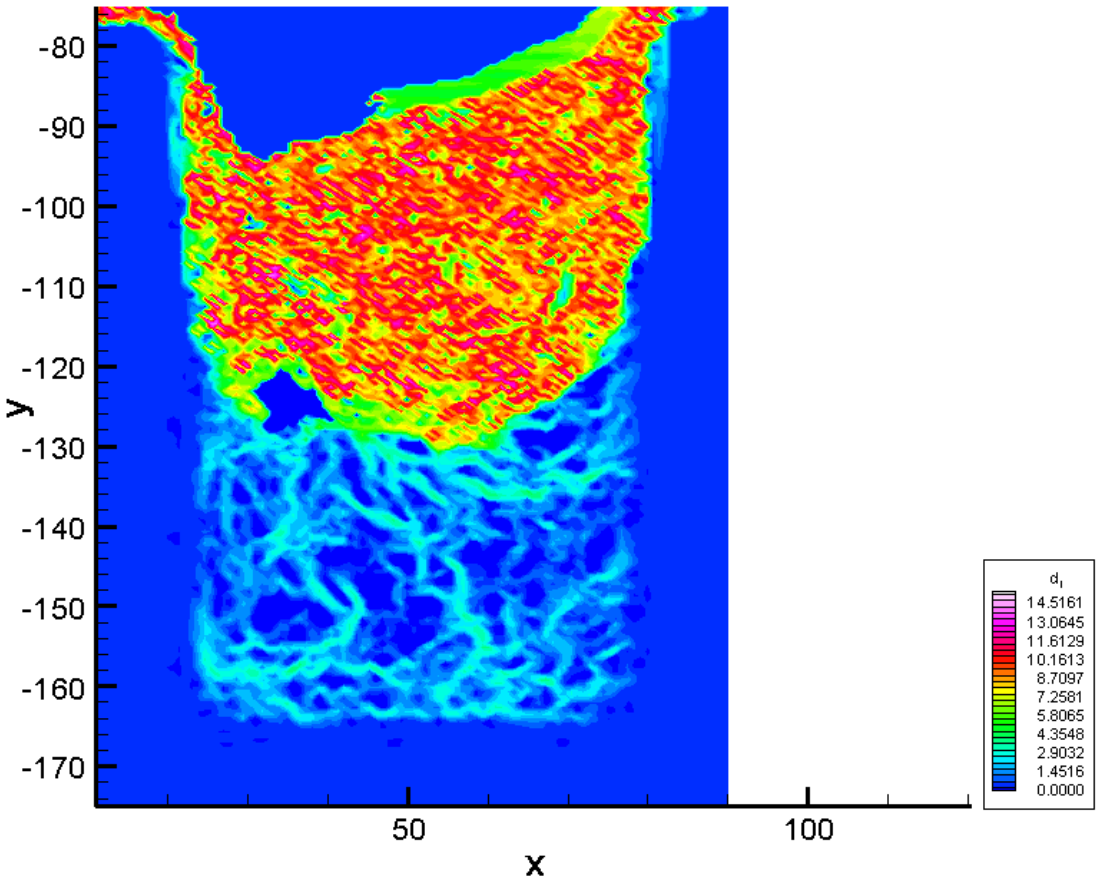

Figure F.193: The forward time LCS during phase increment 1 at 80 Hz.

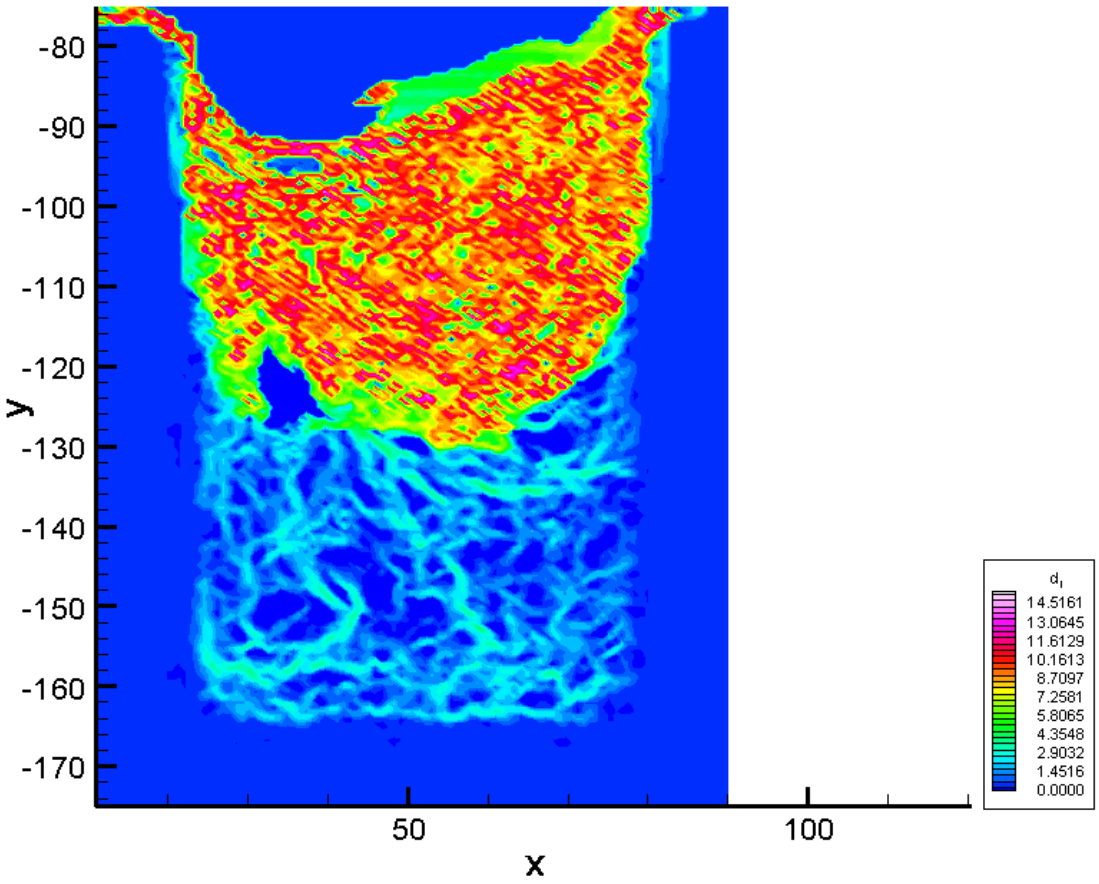

Figure F.194: The forward time LCS during phase increment 2 at 80 Hz.

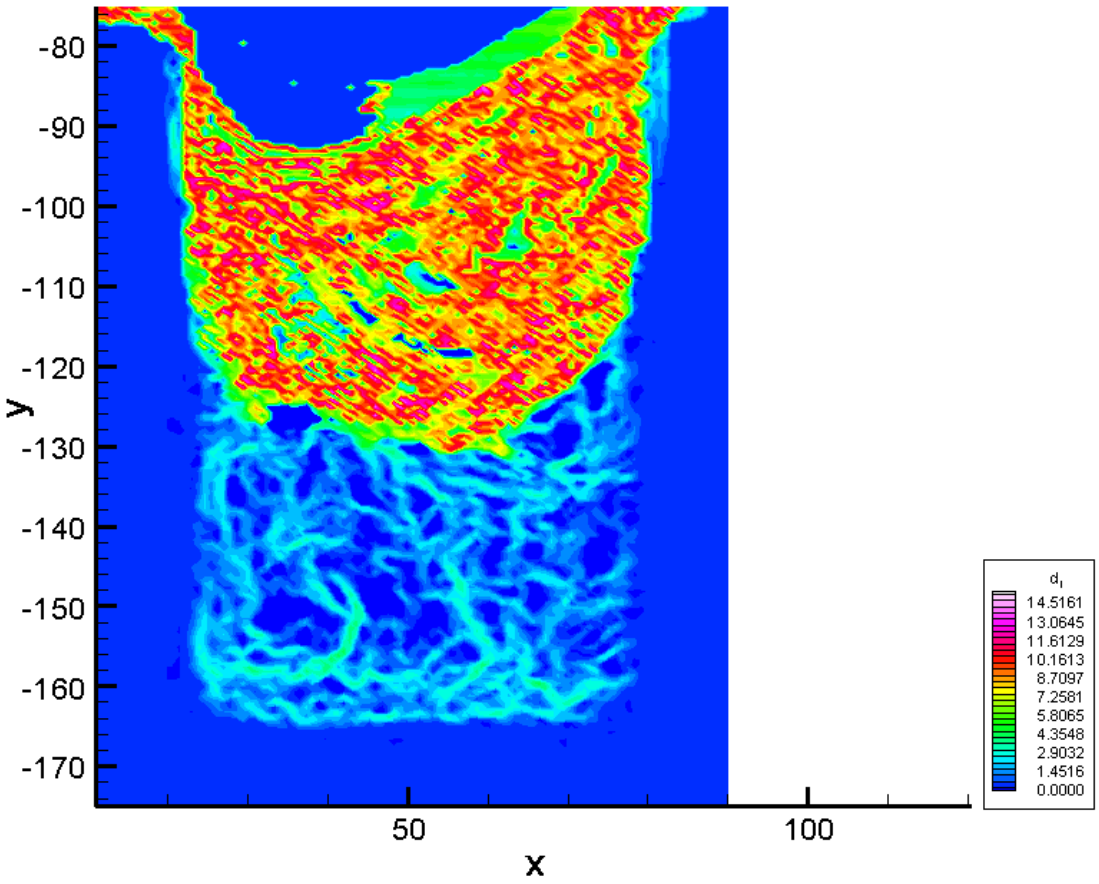

Figure F.195: The forward time LCS during phase increment 3 at 80 Hz.

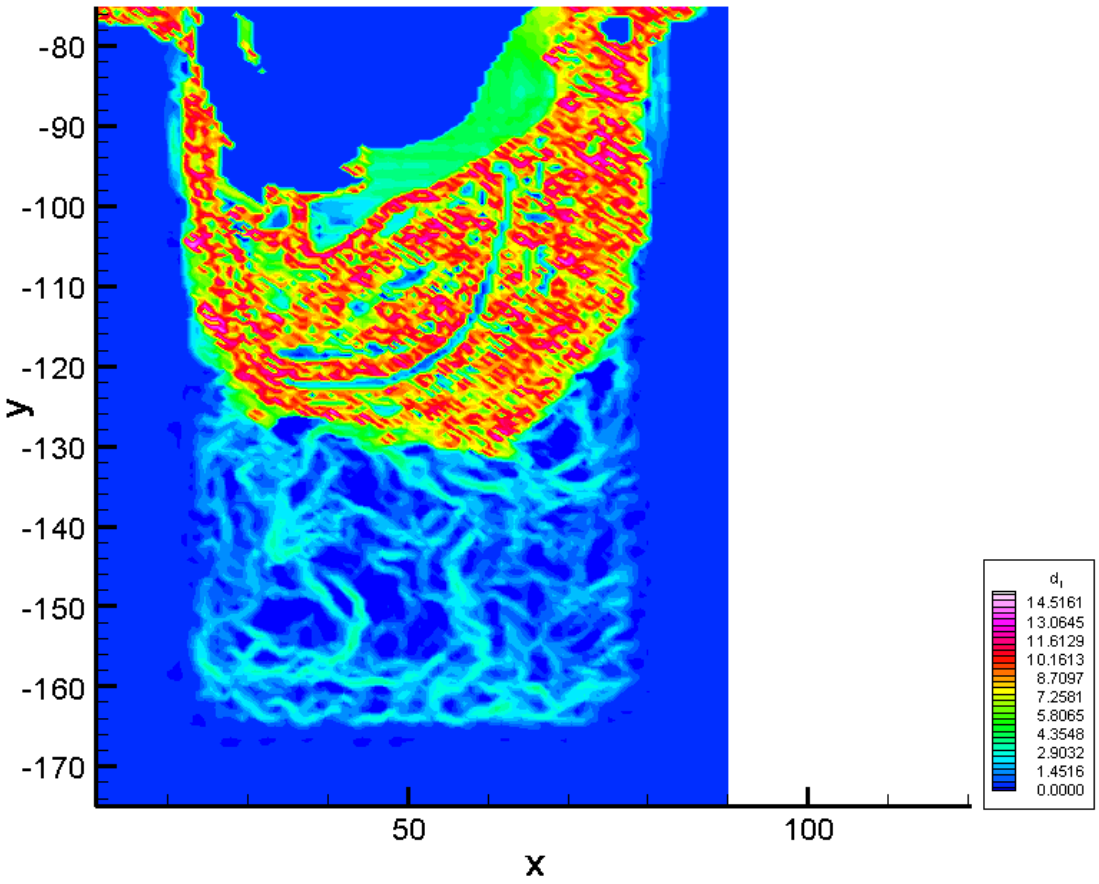

Figure F.196: The forward time LCS during phase increment 4 at 80 Hz.

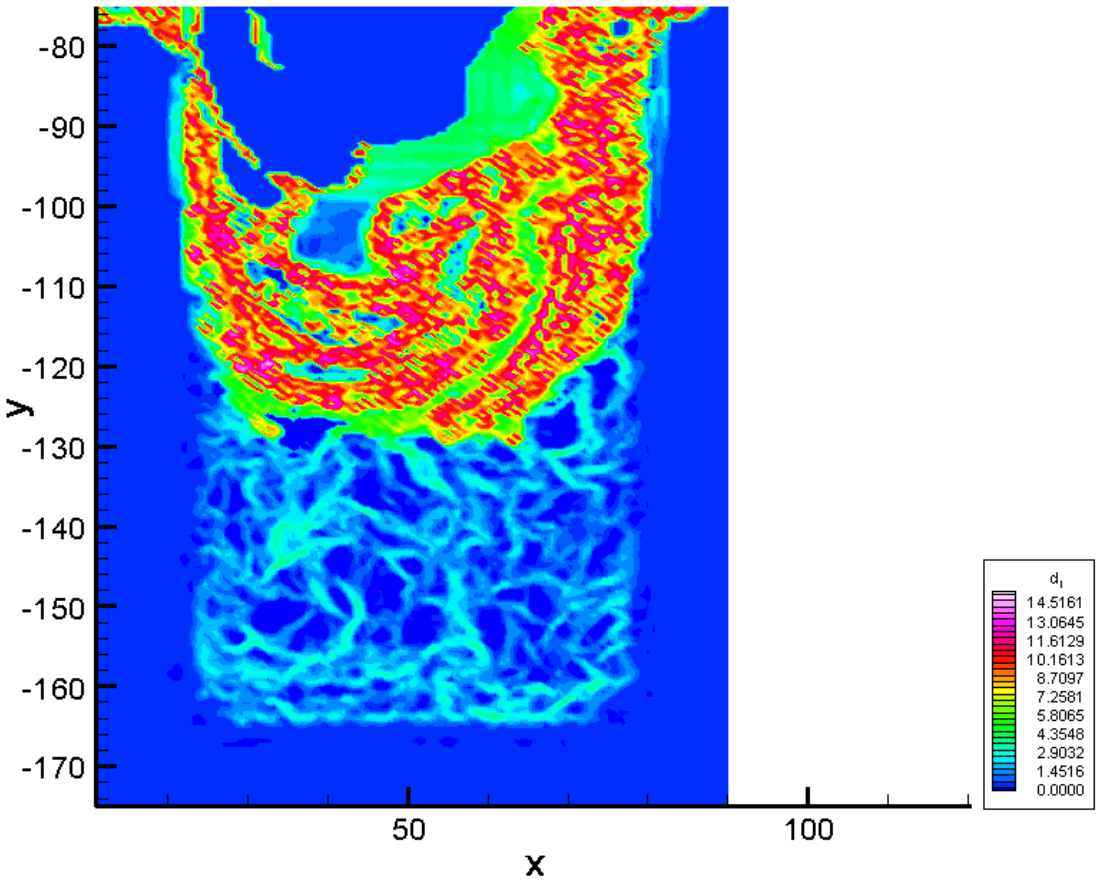

Figure F.197: The forward time LCS during phase increment 5 at 80 Hz.

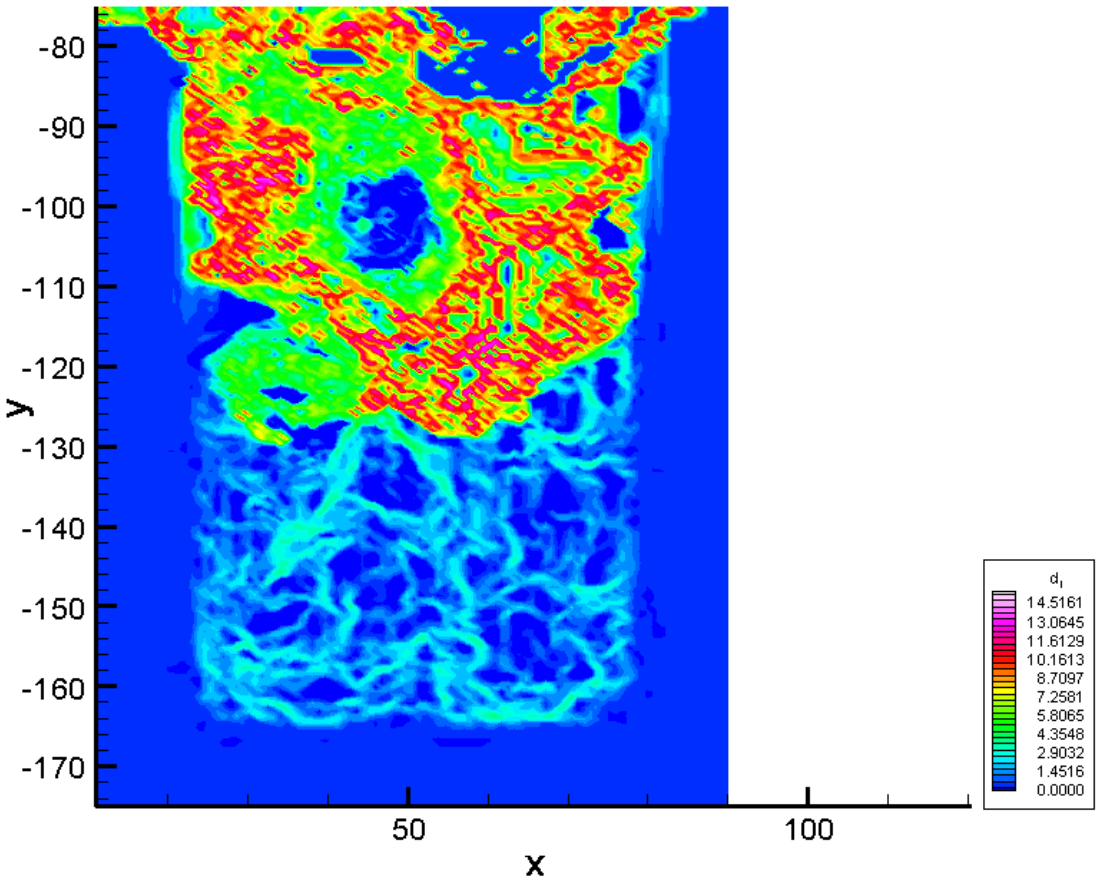

Figure F.198: The forward time LCS during phase increment 6 at 80 Hz.

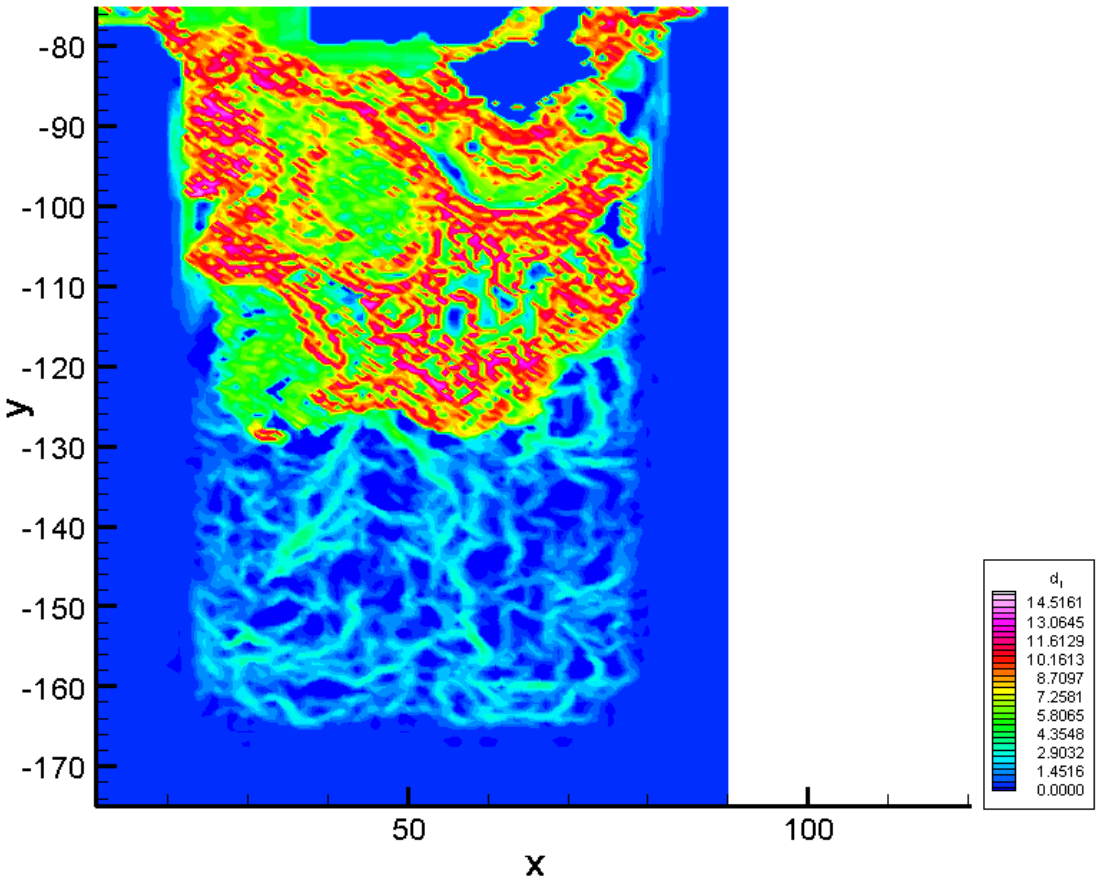

Figure F.199: The forward time LCS during phase increment 7 at 80 Hz.

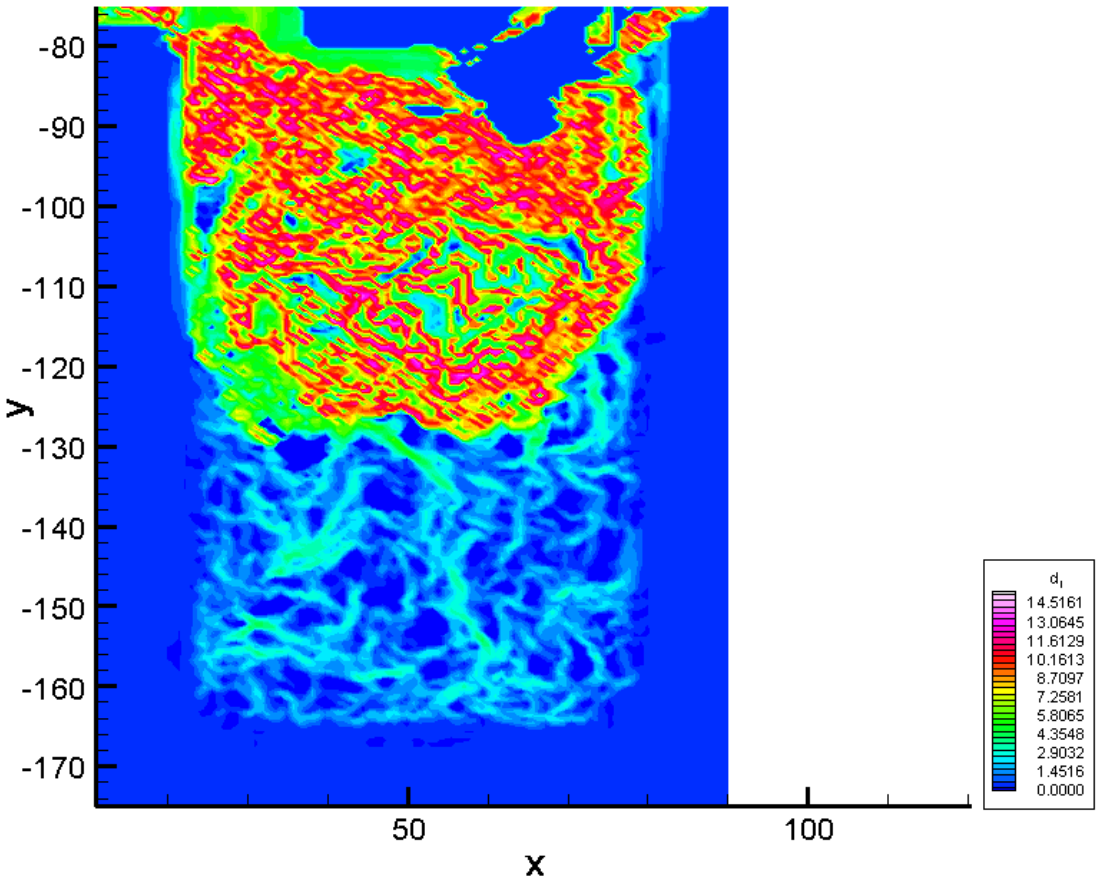

Figure F.200: The forward time LCS during phase increment 8 at 80 Hz.

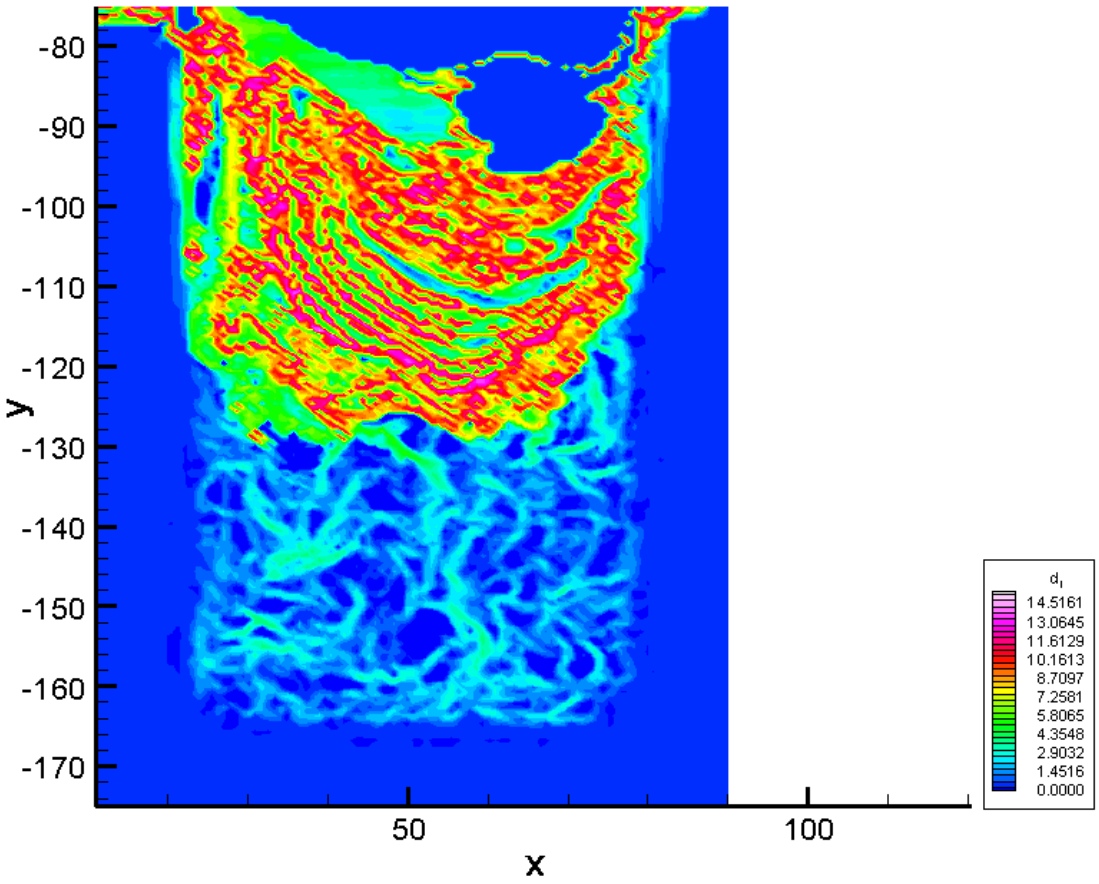

Figure F.201: The forward time LCS during phase increment 9 at 80 Hz.

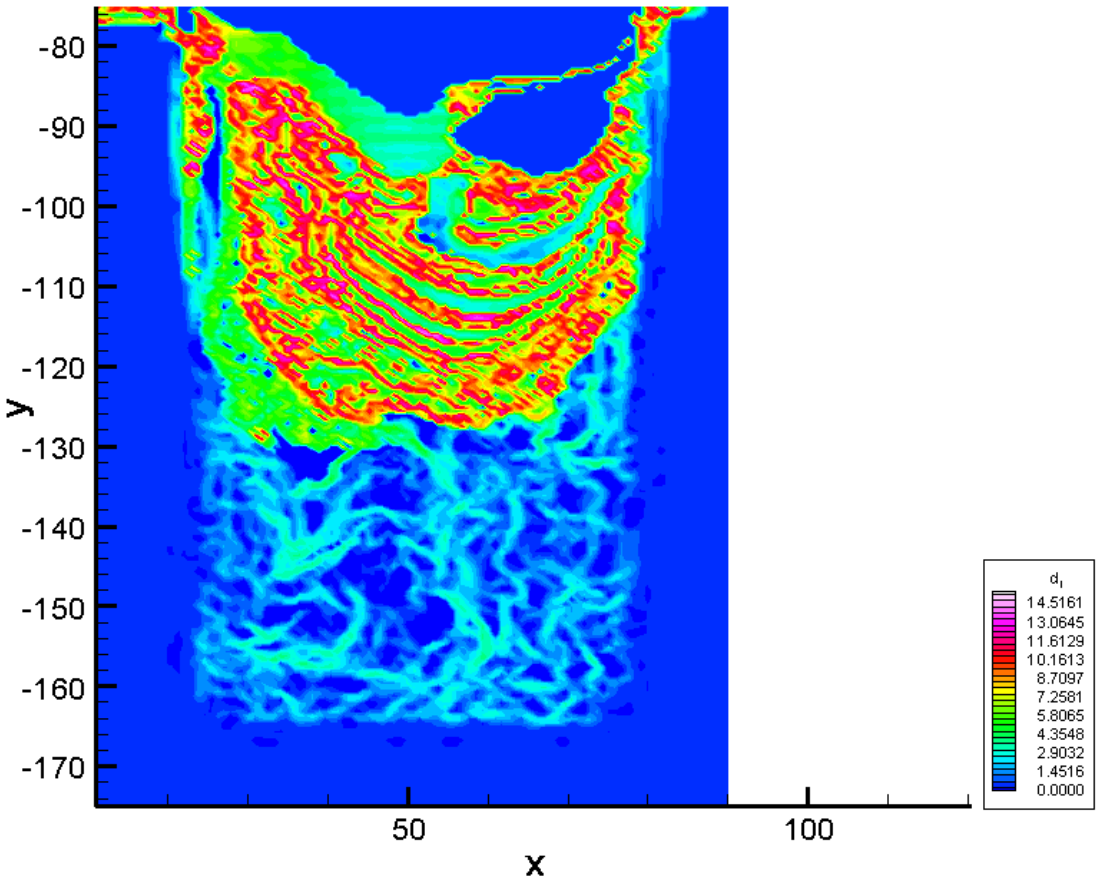

Figure F.202: The forward time LCS during phase increment 10 at 80 Hz.

F.3 113.14 Hz

F.3.1 Velocity field data at 113.14 Hz

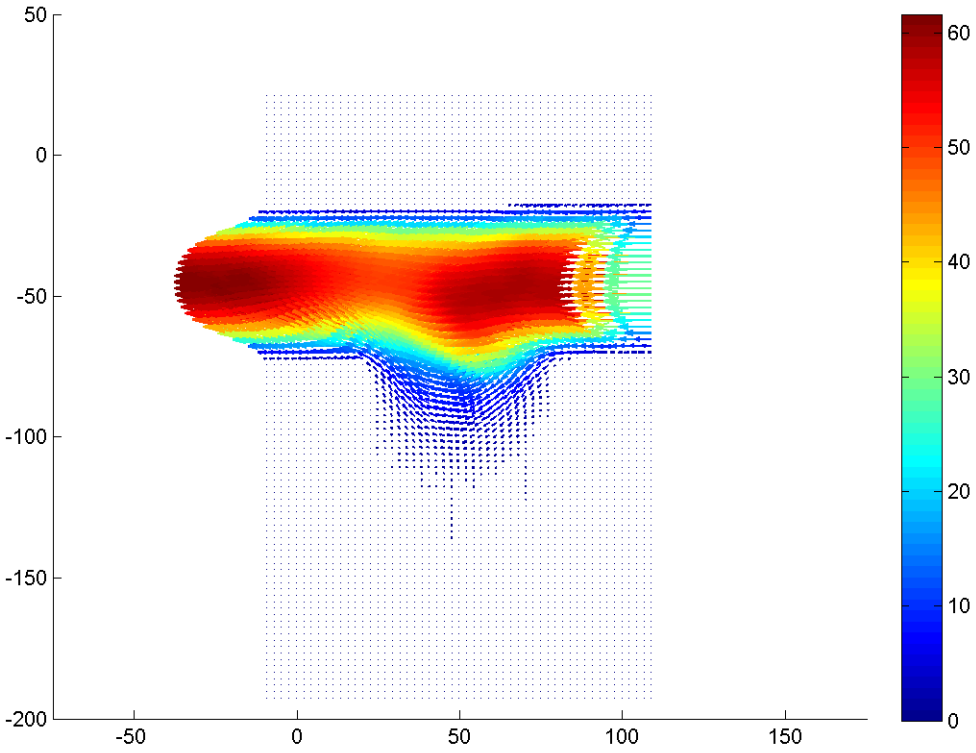

Figure F.203: Velocity field during phase increment 1 at 113.14 Hz with a Re of 0.1.

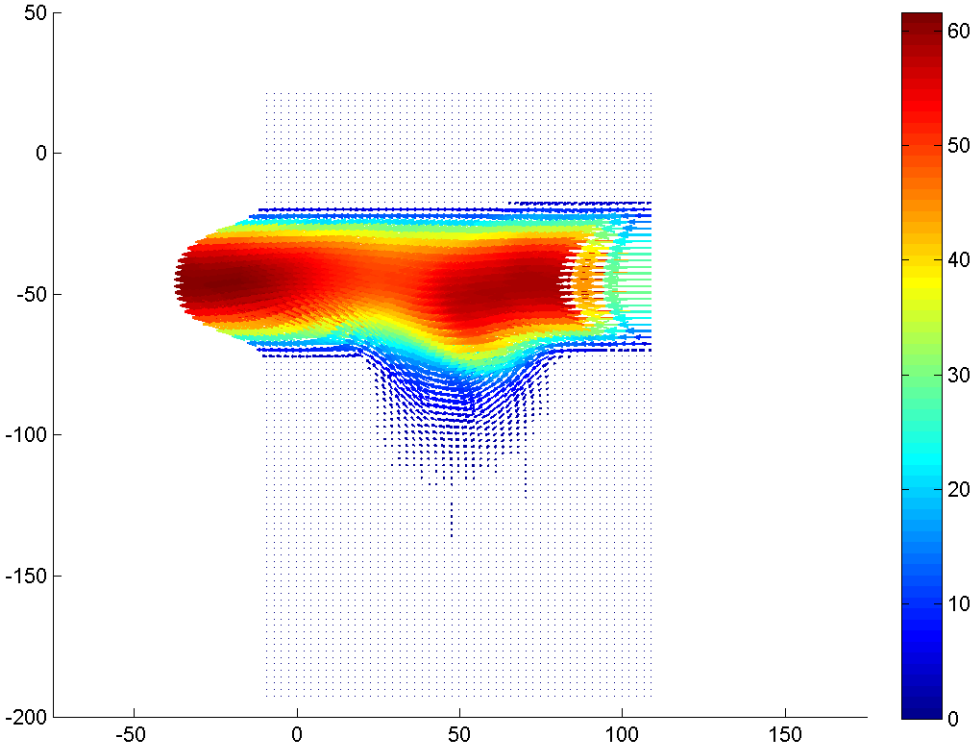

Figure F.204: Velocity field during phase increment 2 at 113.14 Hz with a Re of 0.1.

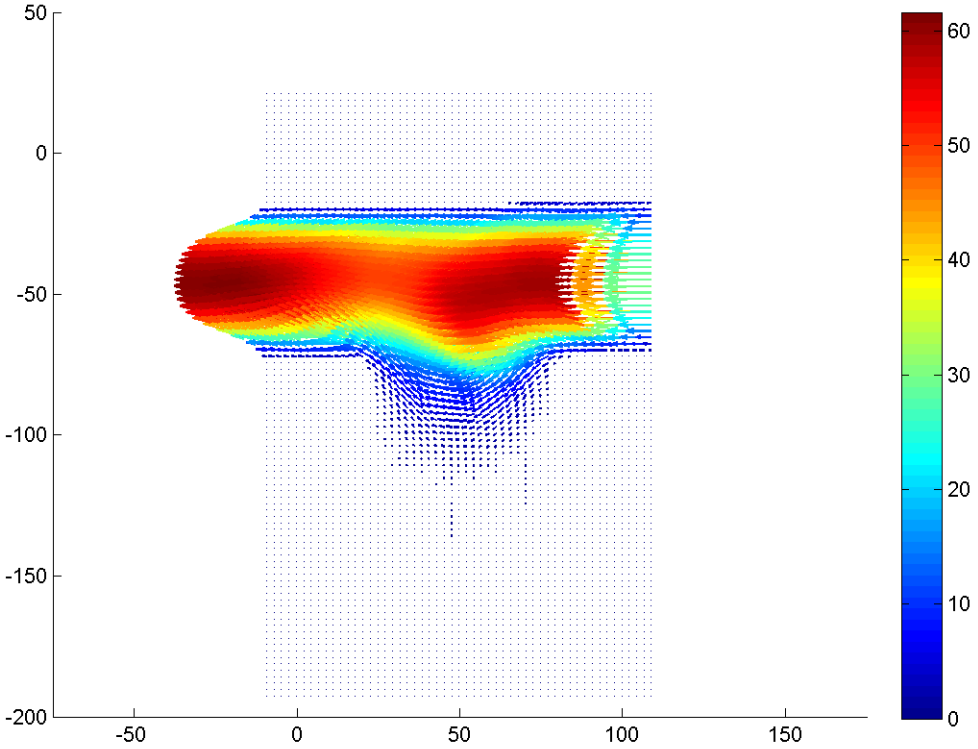

Figure F.205: Velocity field during phase increment 3 at 113.14 Hz with a Re of 0.1.

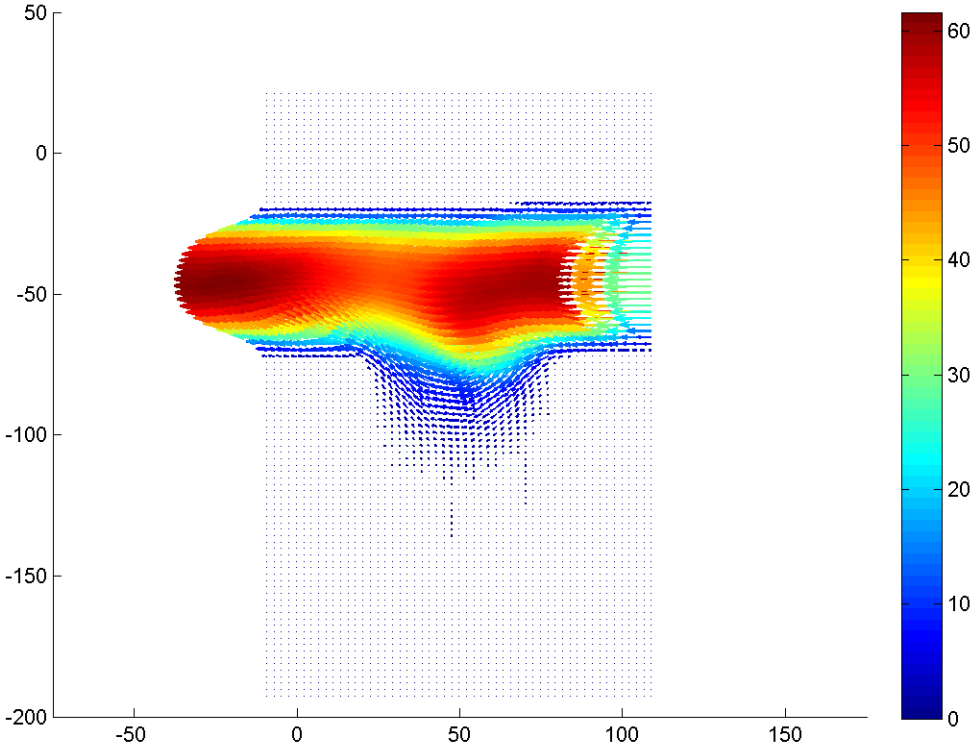

Figure F.206: Velocity field during phase increment 4 at 113.14 Hz with a Re of 0.1.

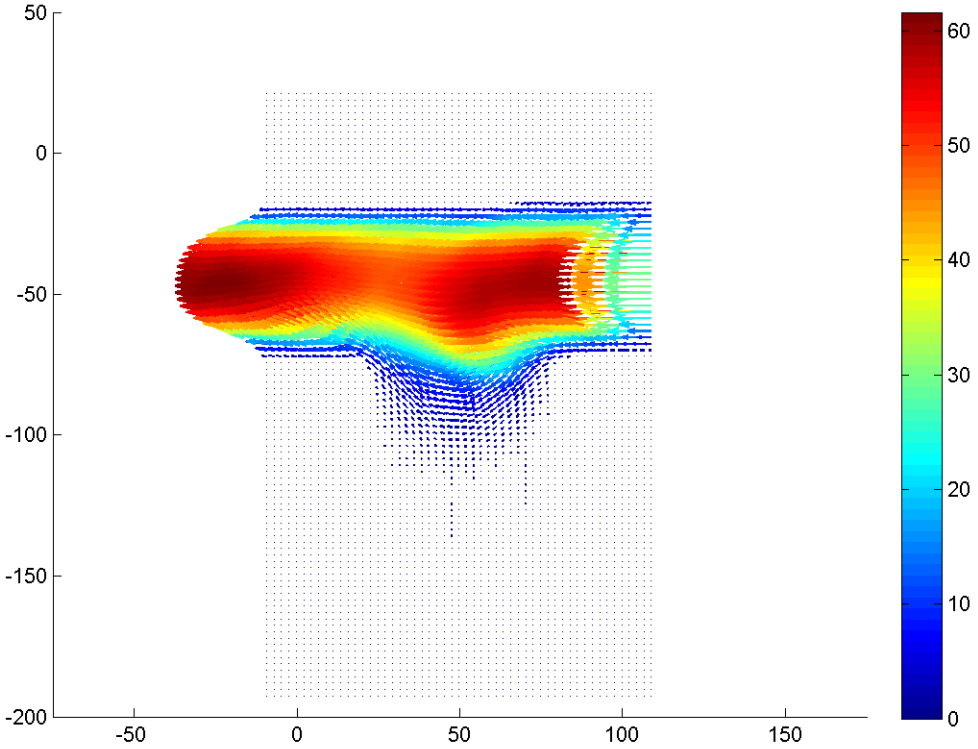

Figure F.207: Velocity field during phase increment 5 at 113.14 Hz with a Re of 0.1.

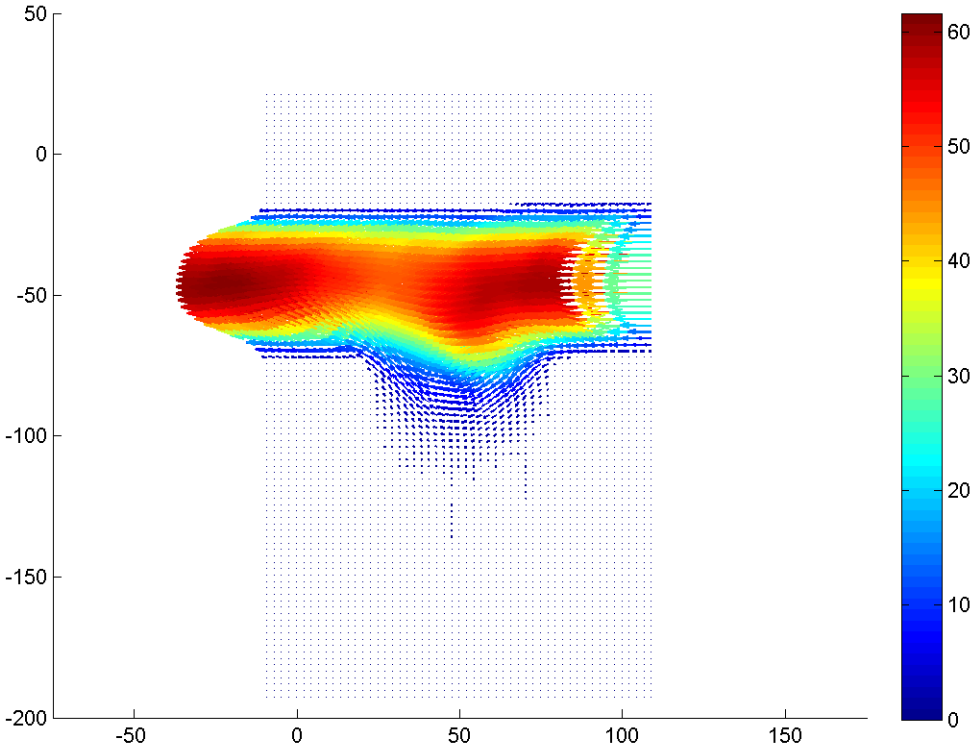

Figure F.208: Velocity field during phase increment 6 at 113.14 Hz with a Re of 0.1.

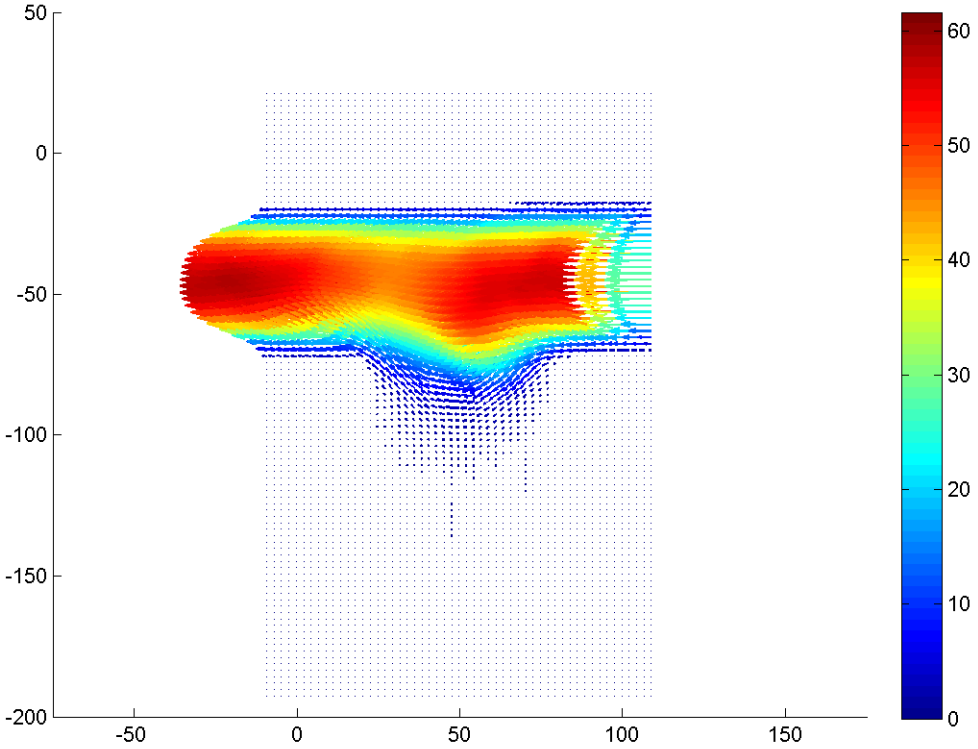

Figure F.209: Velocity field during phase increment 7 at 113.14 Hz with a Re of 0.1.

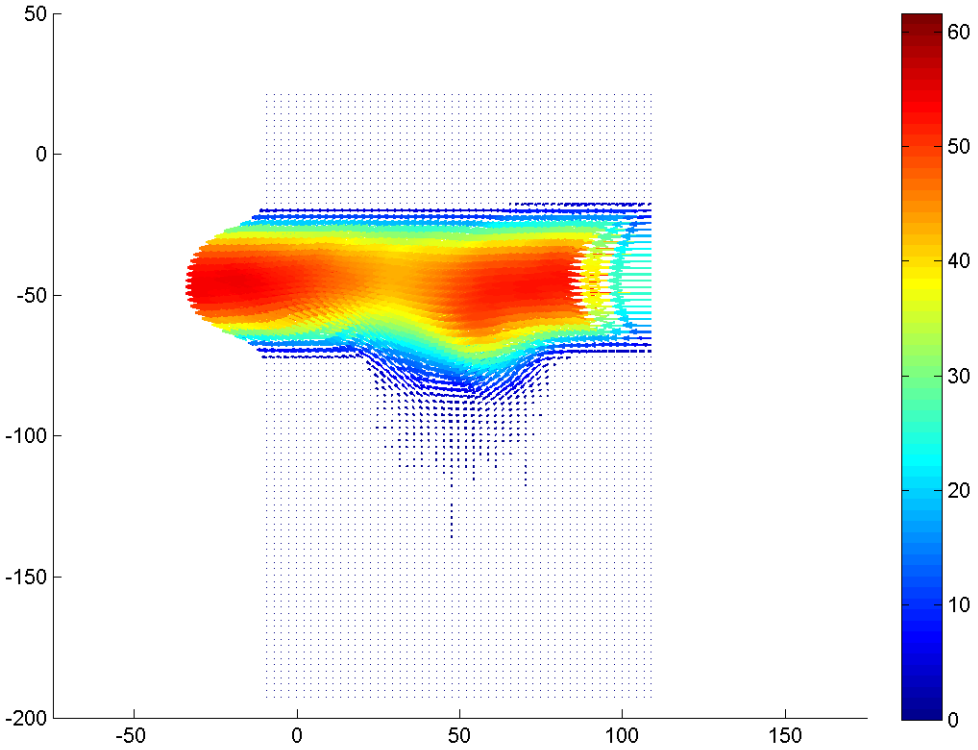

Figure F.210: Velocity field during phase increment 8 at 113.14 Hz with a Re of 0.1.

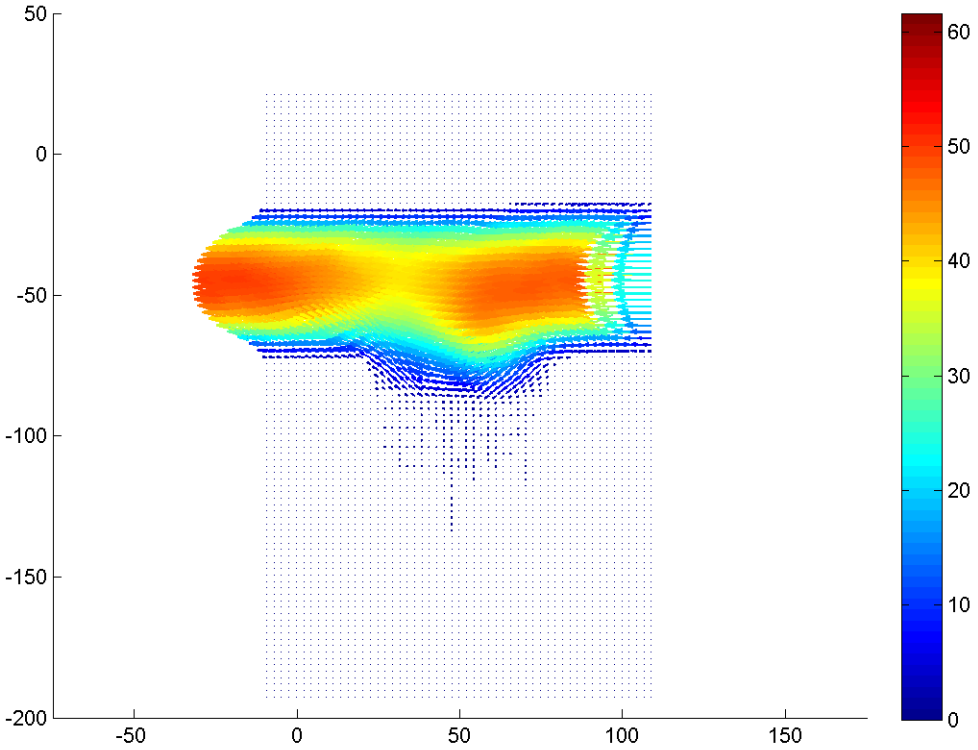

Figure F.211: Velocity field during phase increment 9 at 113.14 Hz with a Re of 0.1.

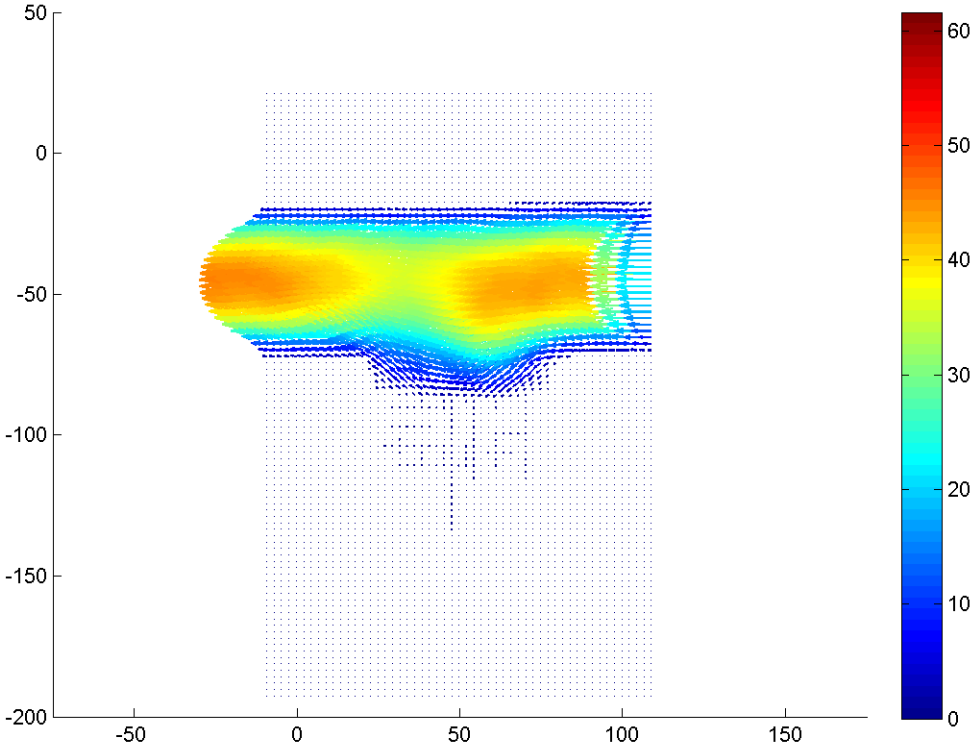

Figure F.212: Velocity field during phase increment 10 at 113.14 Hz with a Re of 0.1.

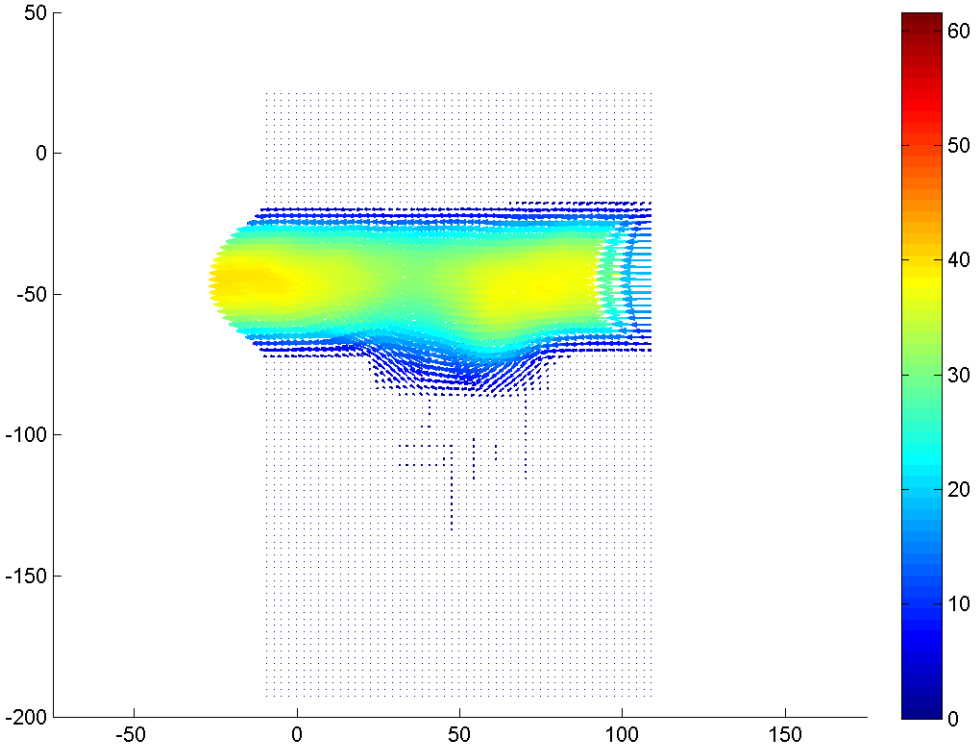

Figure F.213: Velocity field during phase increment 11 at 113.14 Hz with a Re of 0.1.

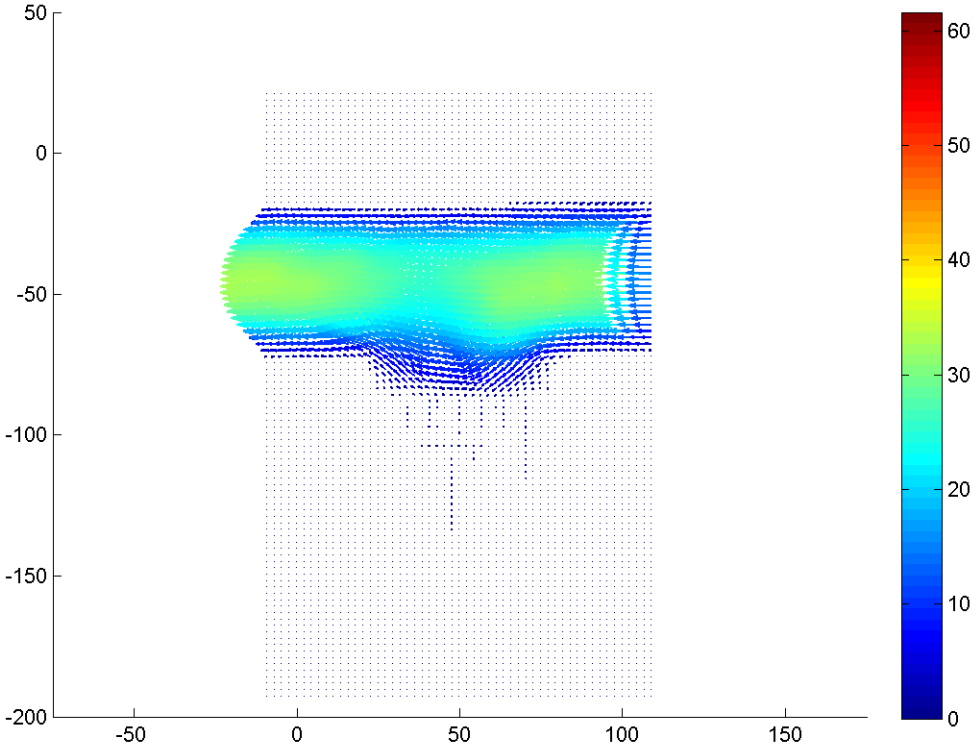

Figure F.214: Velocity field during phase increment 12 at 113.14 Hz with a Re of 0.1.

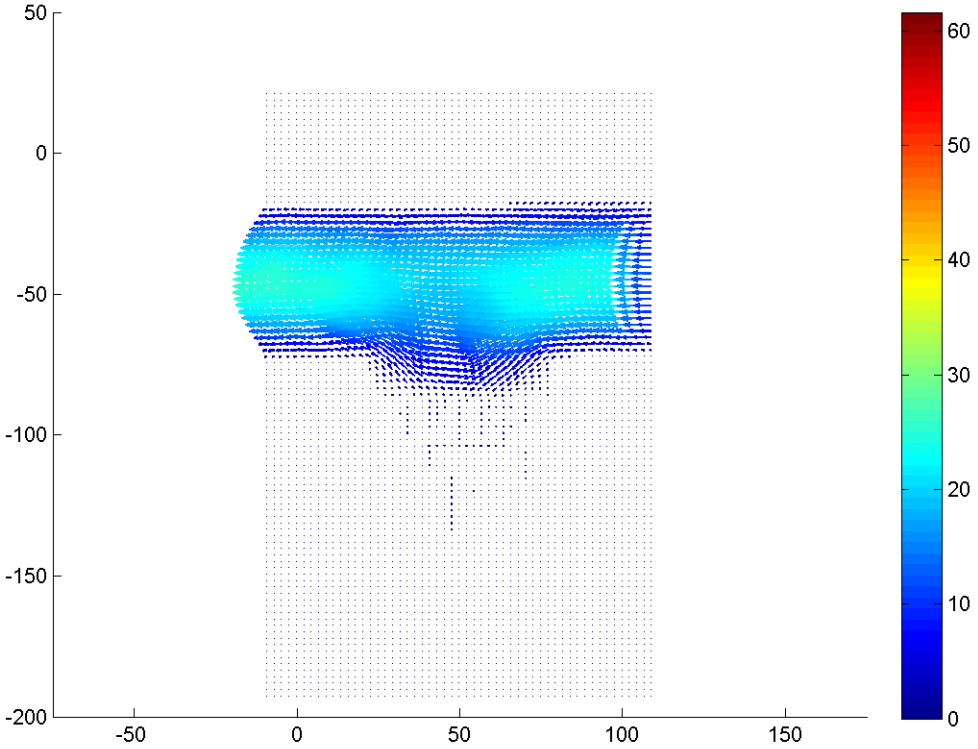

Figure F.215: Velocity field during phase increment 13 at 113.14 Hz with a Re of 0.1.

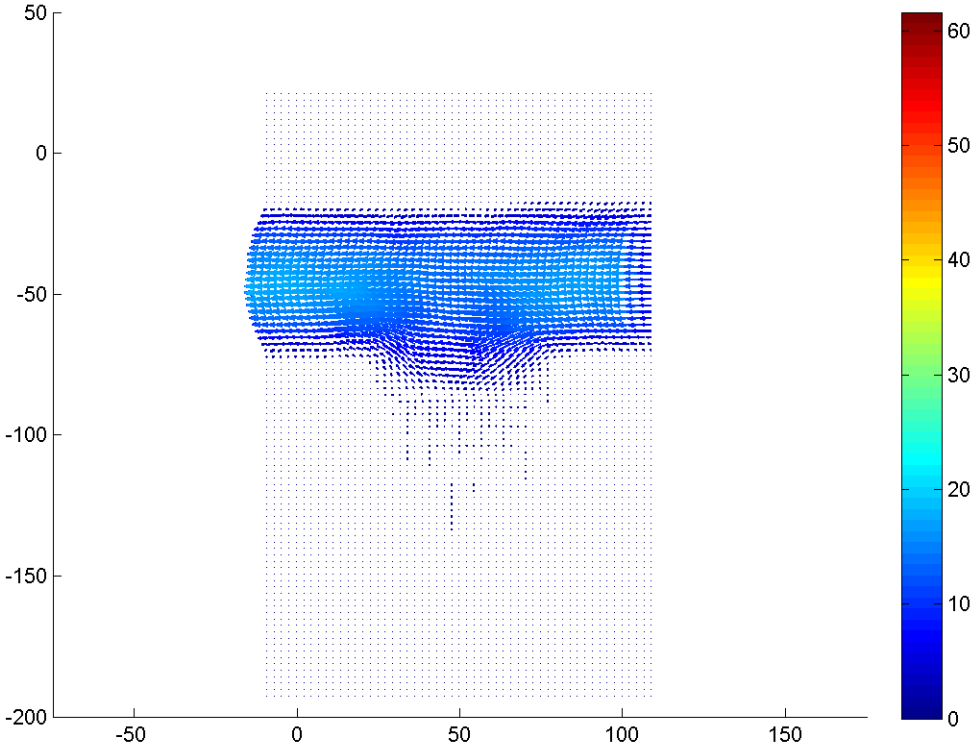

Figure F.216: Velocity field during phase increment 14 at 113.14 Hz with a Re of 0.1.

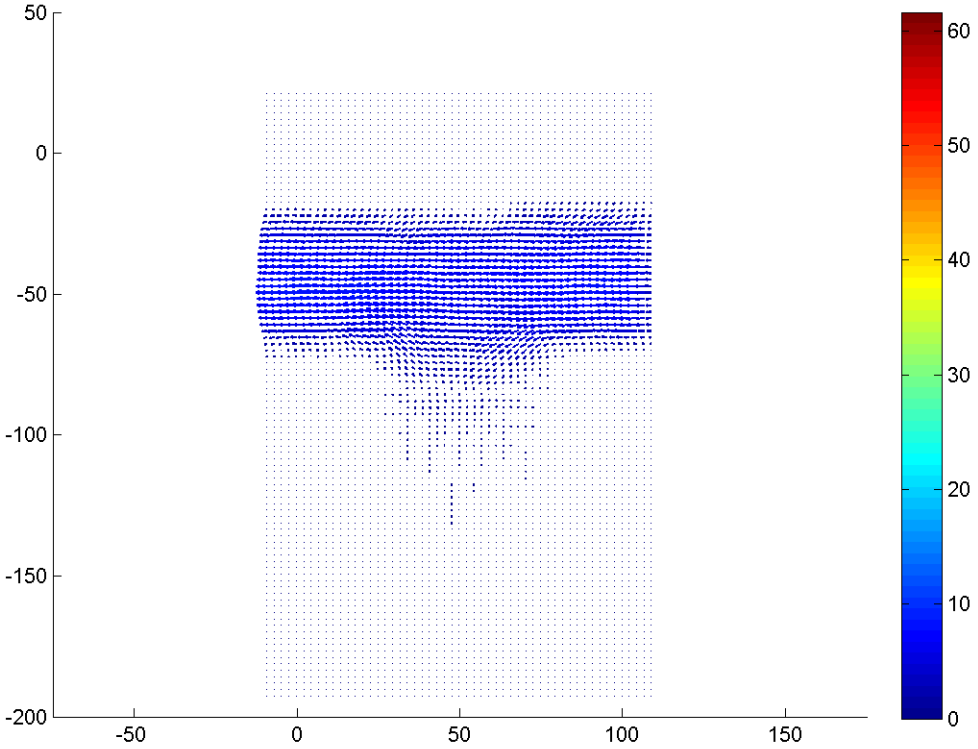

Figure F.217: Velocity field during phase increment 15 at 113.14 Hz with a Re of 0.1.

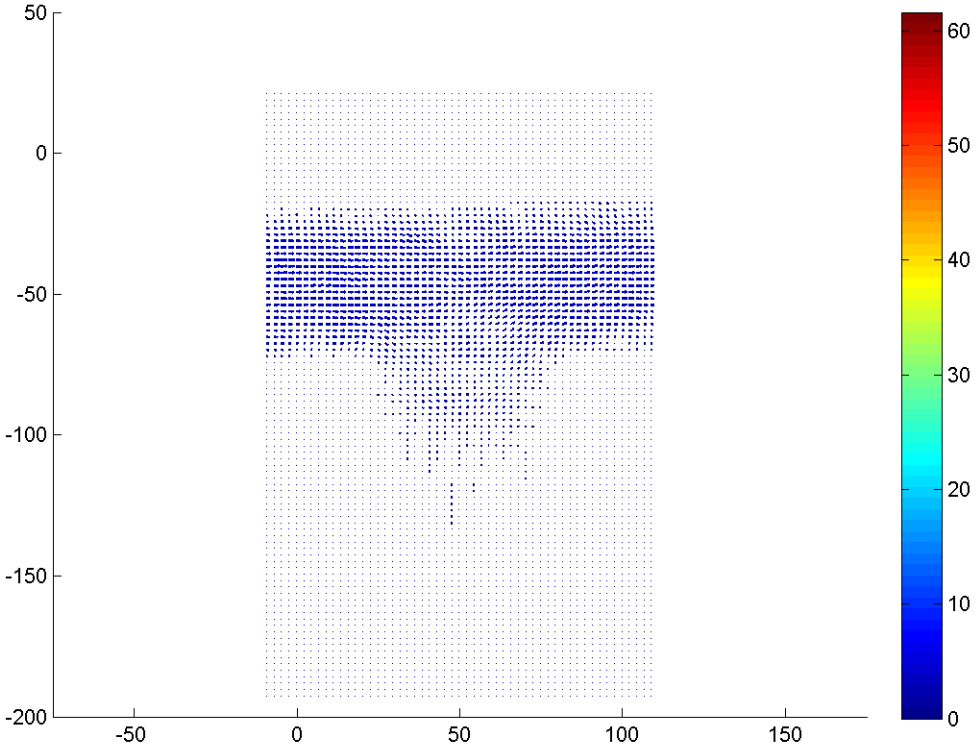

Figure F.218: Velocity field during phase increment 16 at 113.14 Hz with a Re of 0.1.

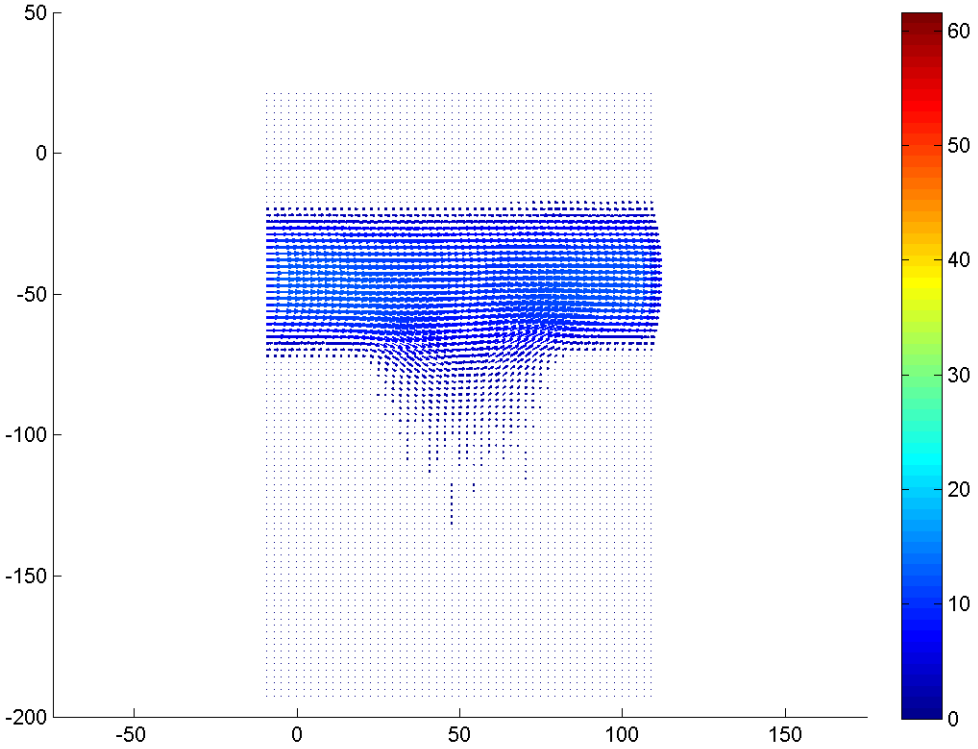

Figure F.219: Velocity field during phase increment 17 at 113.14 Hz with a Re of 0.1.

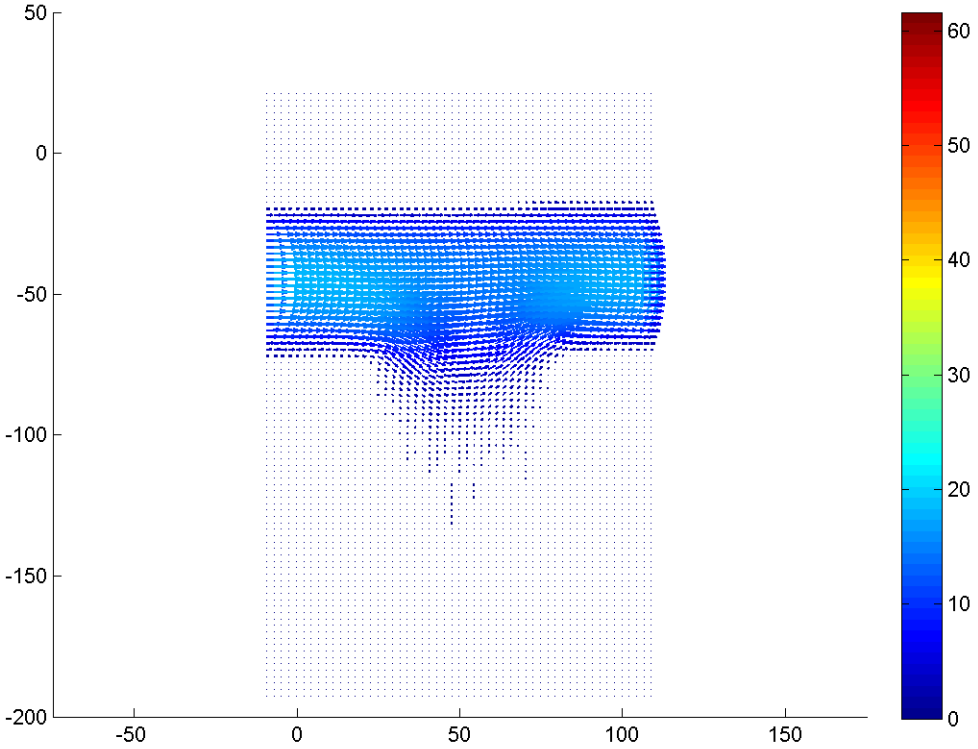

Figure F.220: Velocity field during phase increment 18 at 113.14 Hz with a Re of 0.1.

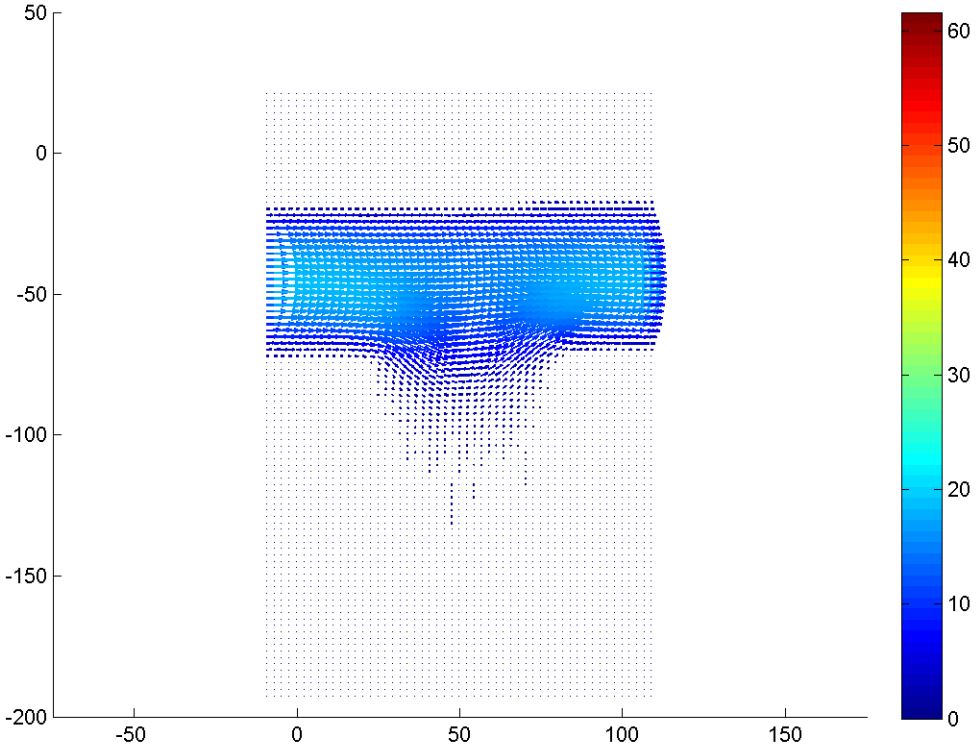

Figure F.221: Velocity field during phase increment 18 at 113.14 Hz with a Re of 0.1.

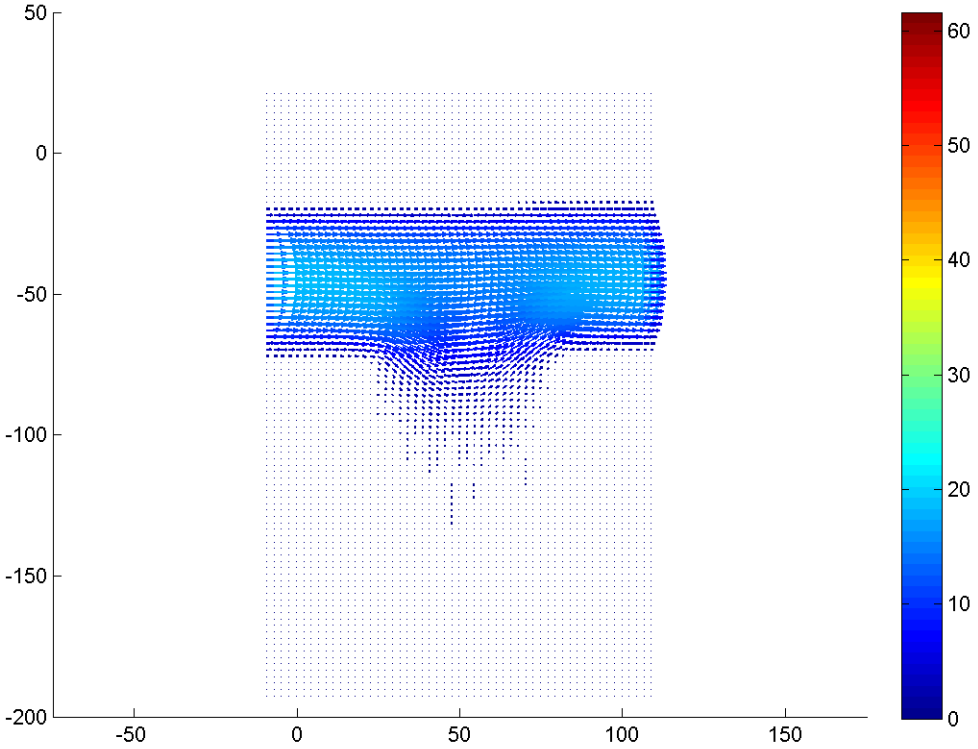

Figure F.222: Velocity field during phase increment 20 at 113.14 Hz with a Re of 0.1.

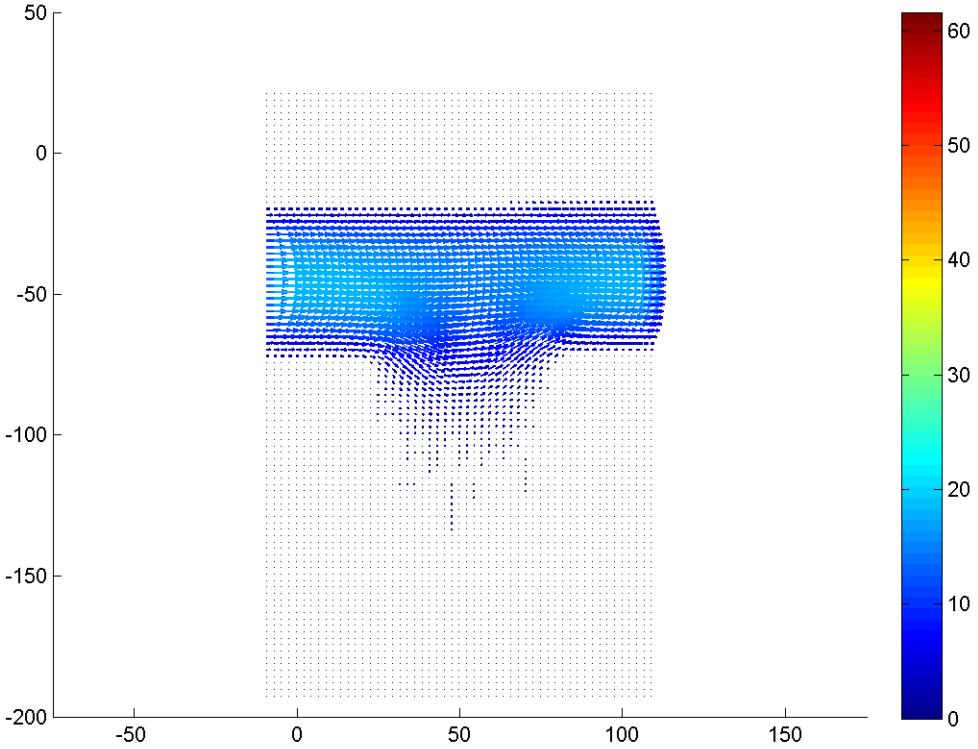

Figure F.223: Velocity field during phase increment 21 at 113.14 Hz with a Re of 0.1.

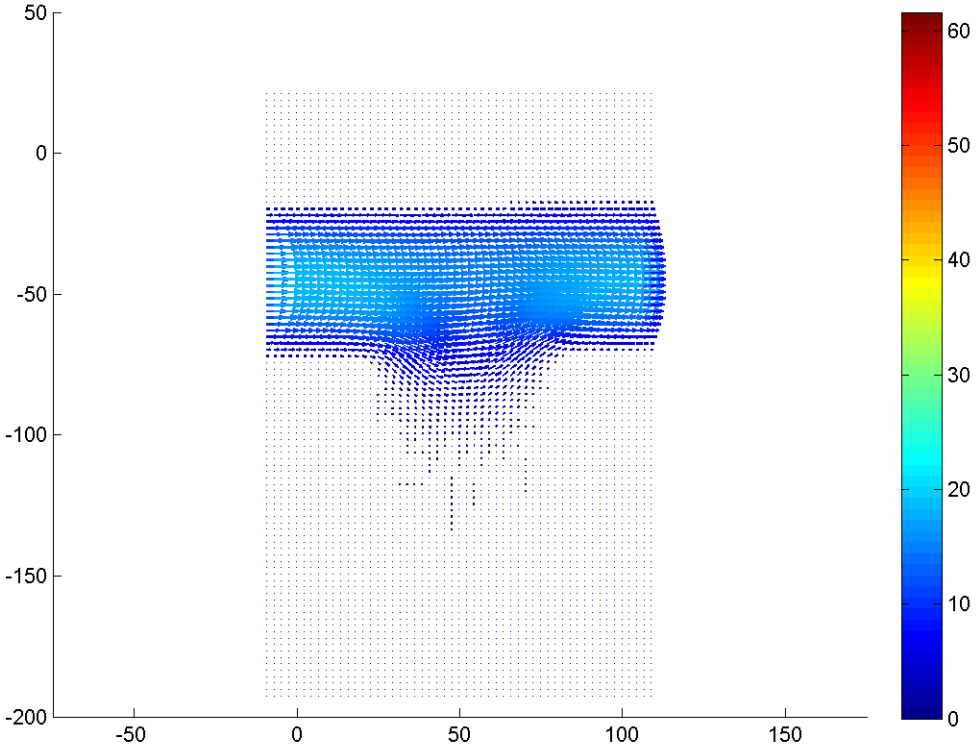

Figure F.224: Velocity field during phase increment 22 at 113.14 Hz with a Re of 0.1.

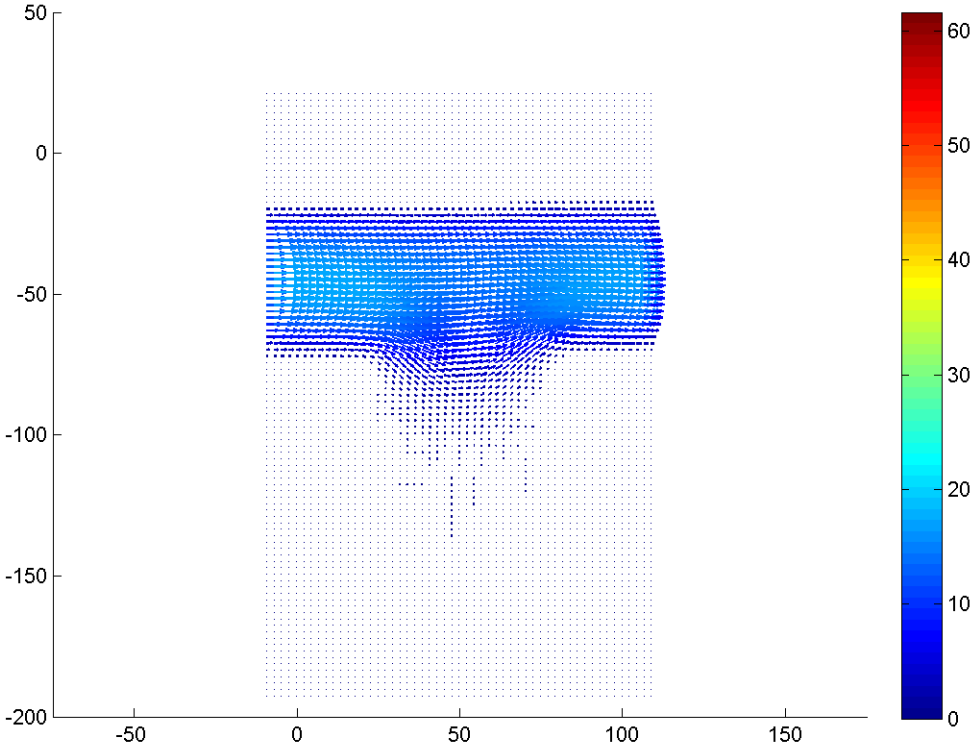

Figure F.225: Velocity field during phase increment 23 at 113.14 Hz with a Re of 0.1.

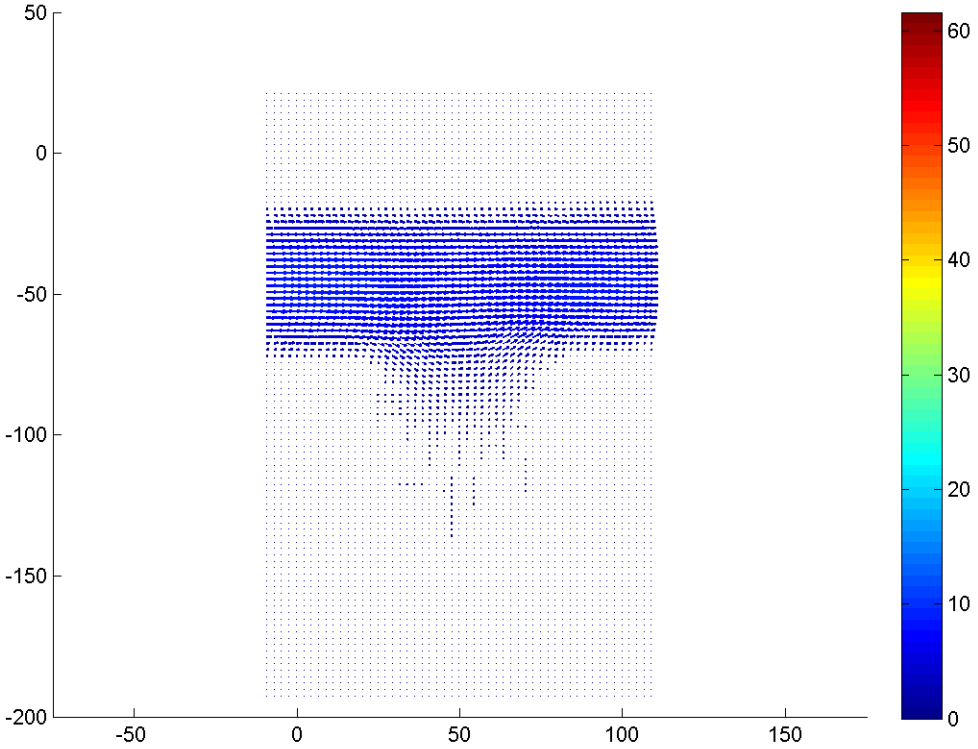

Figure F.226: Velocity field during phase increment 24 at 113.14 Hz with a Re of 0.1.

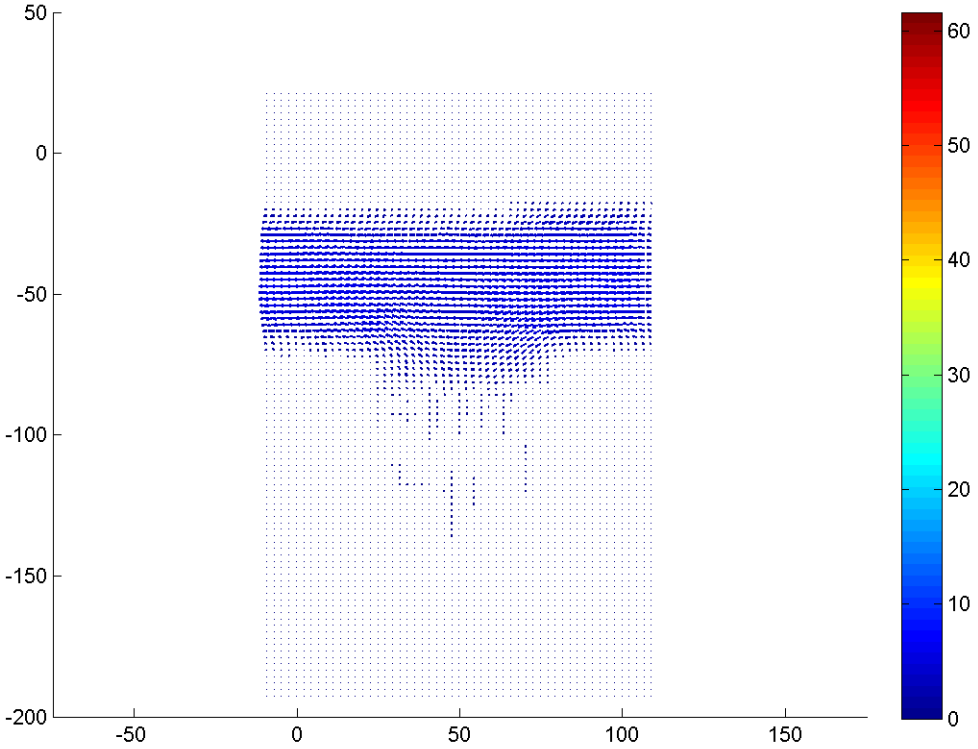

Figure F.227: Velocity field during phase increment 25 at 113.14 Hz with a Re of 0.1.

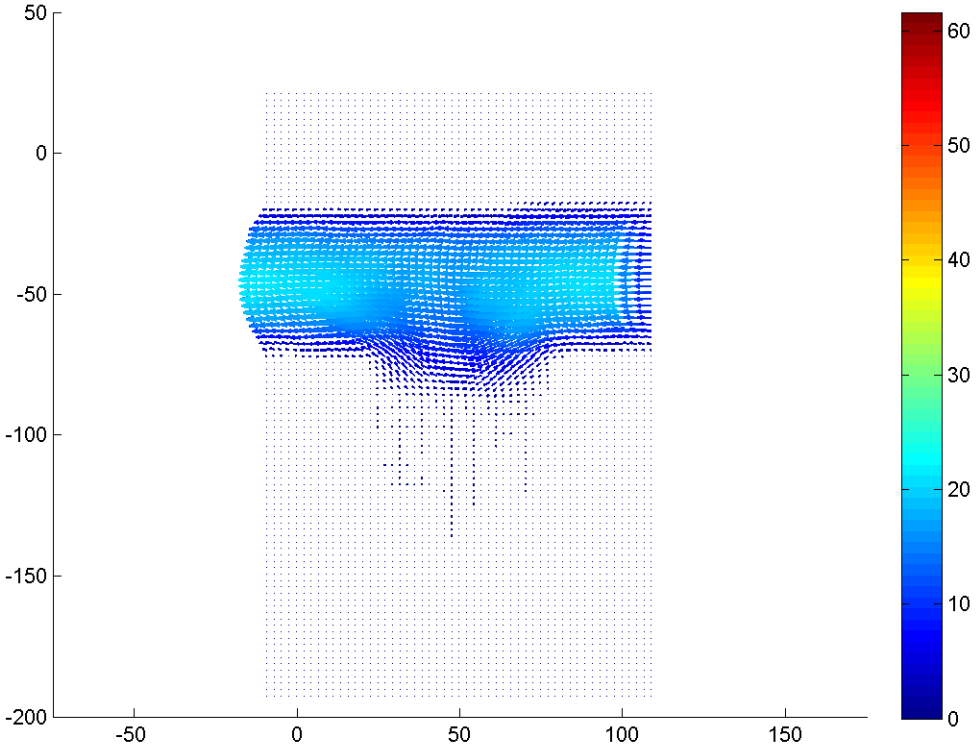

Figure F.228: Velocity field during phase increment 26 at 113.14 Hz with a Re of 0.1.

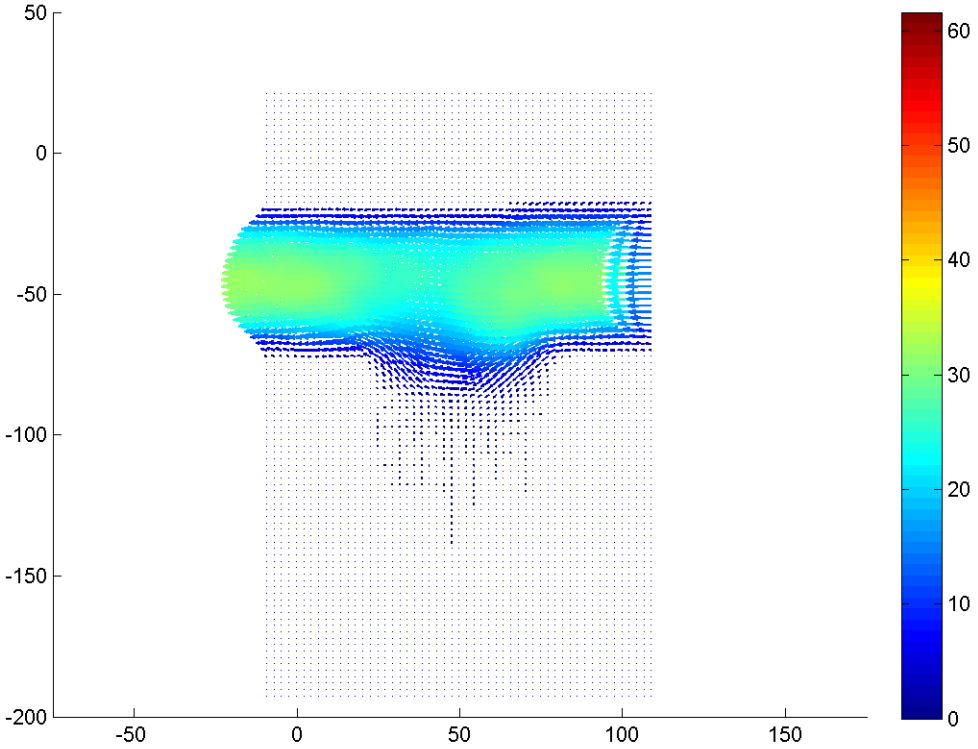

Figure F.229: Velocity field during phase increment 27 at 113.14 Hz with a Re of 0.1.

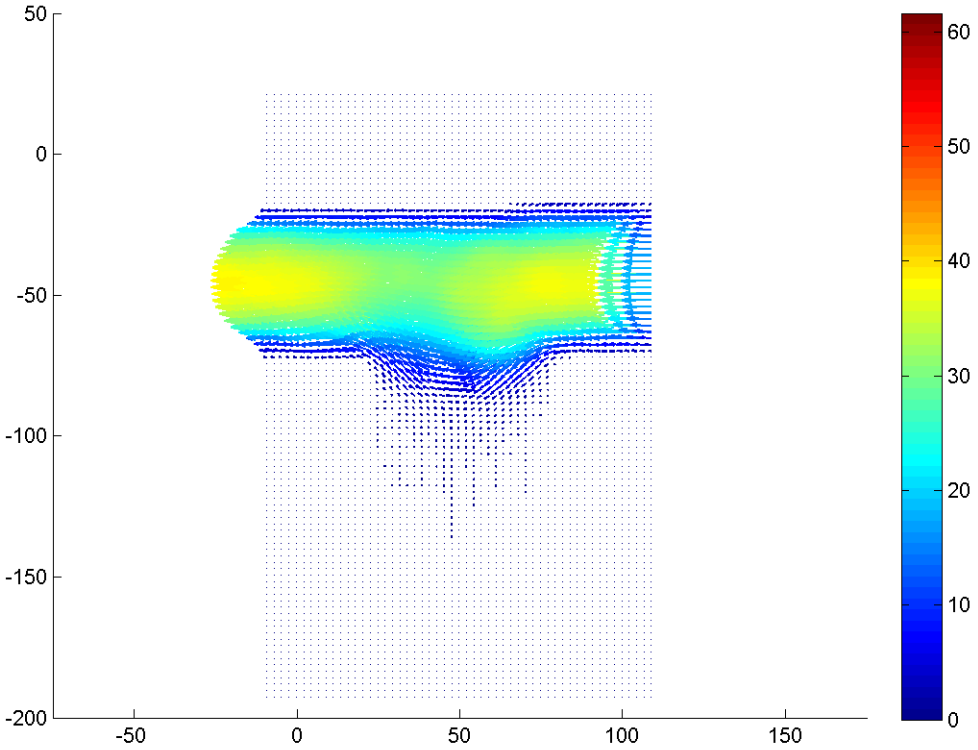

Figure F.230: Velocity field during phase increment 28 at 113.14 Hz with a Re of 0.1.

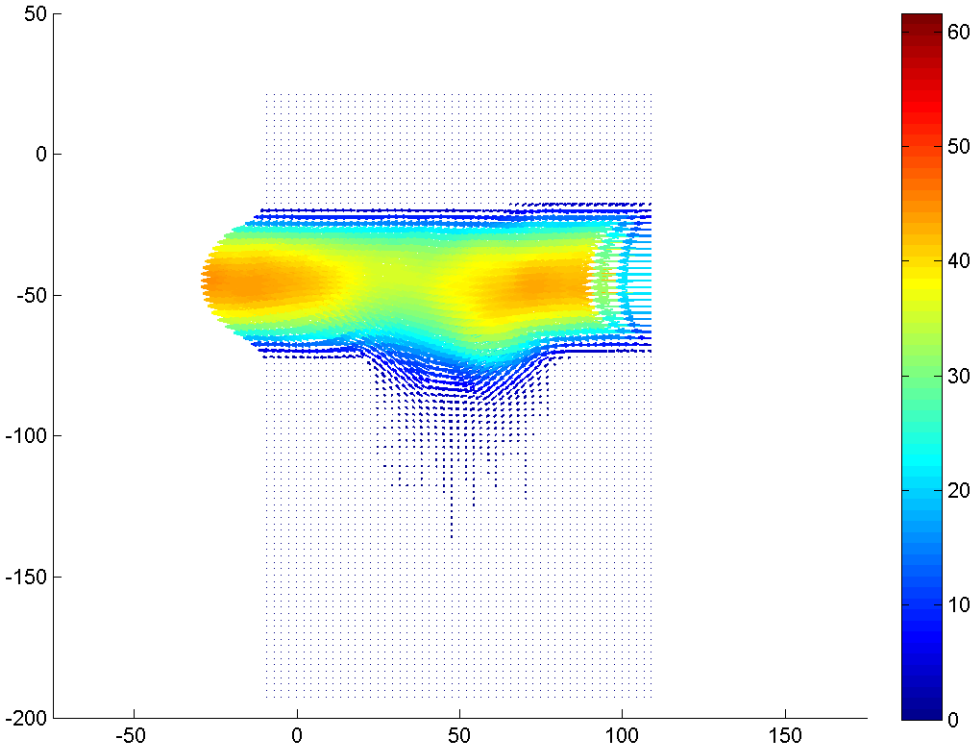

Figure F.231: Velocity field during phase increment 29 at 113.14 Hz with a Re of 0.1.

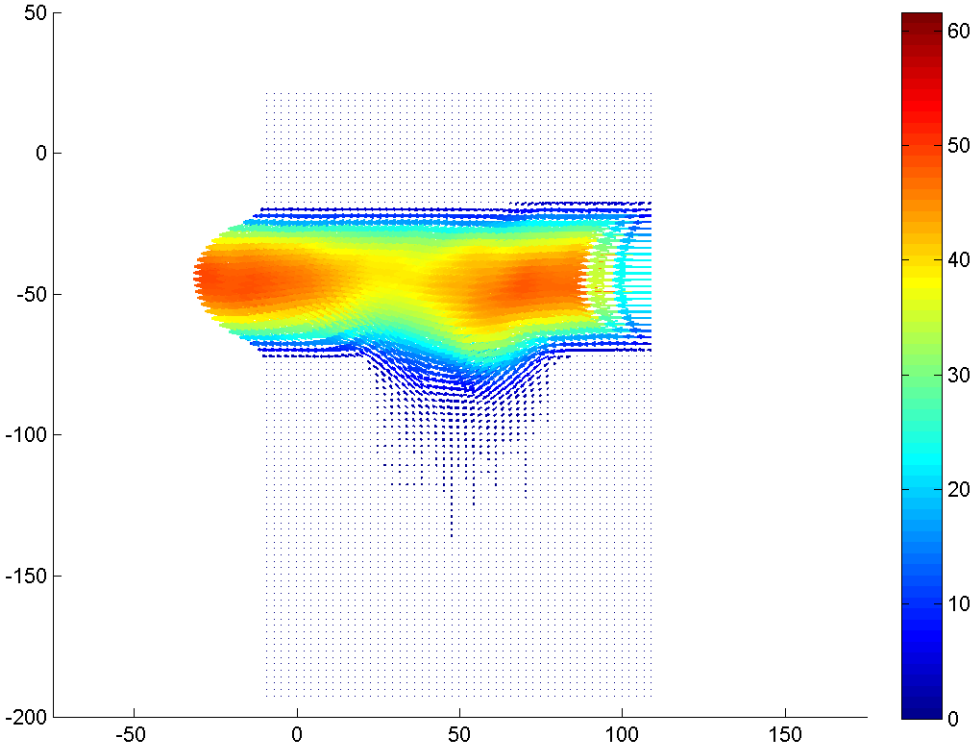

Figure F.232: Velocity field during phase increment 30 at 113.14 Hz with a Re of 0.1.

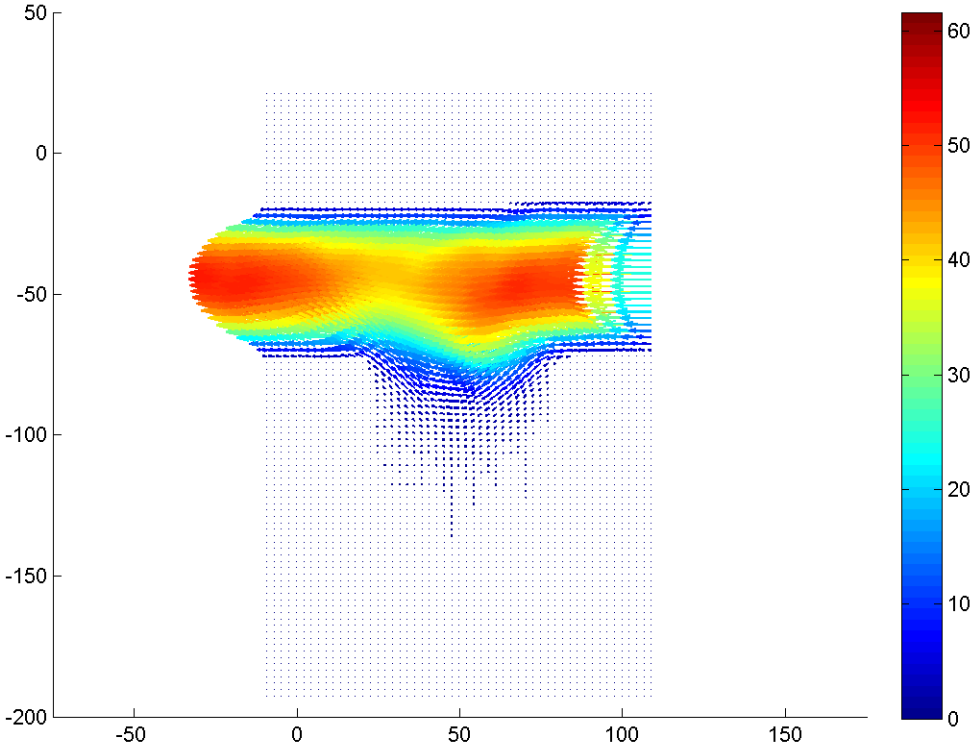

Figure F.233: Velocity field during phase increment 31 at 113.14 Hz with a Re of 0.1.

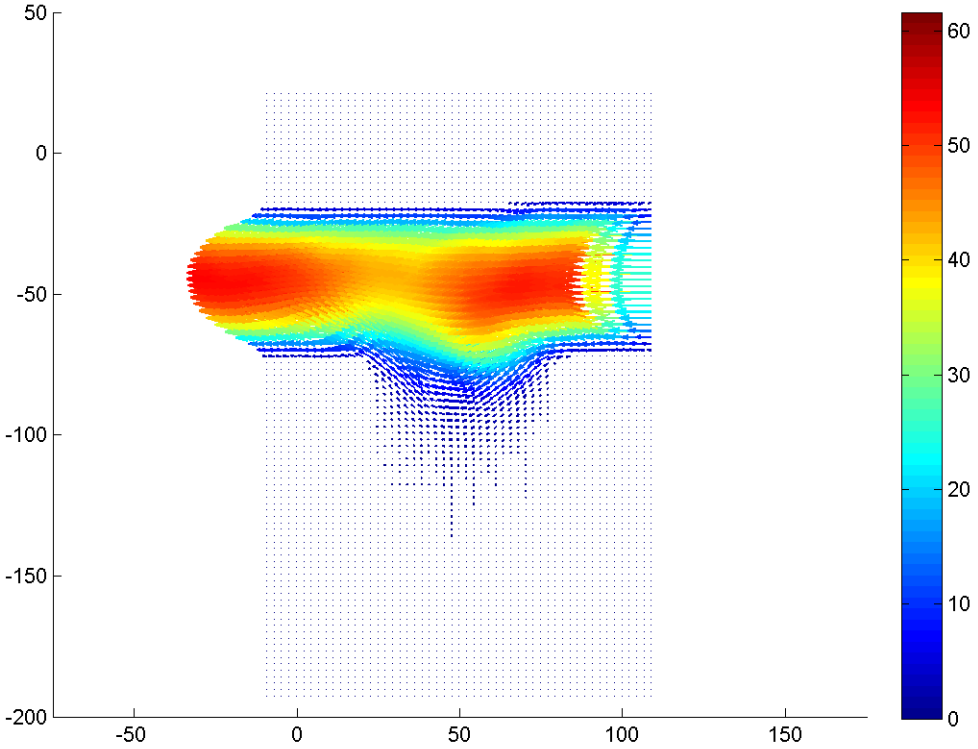

Figure F.234: Velocity field during phase increment 32 at 113.14 Hz with a Re of 0.1.

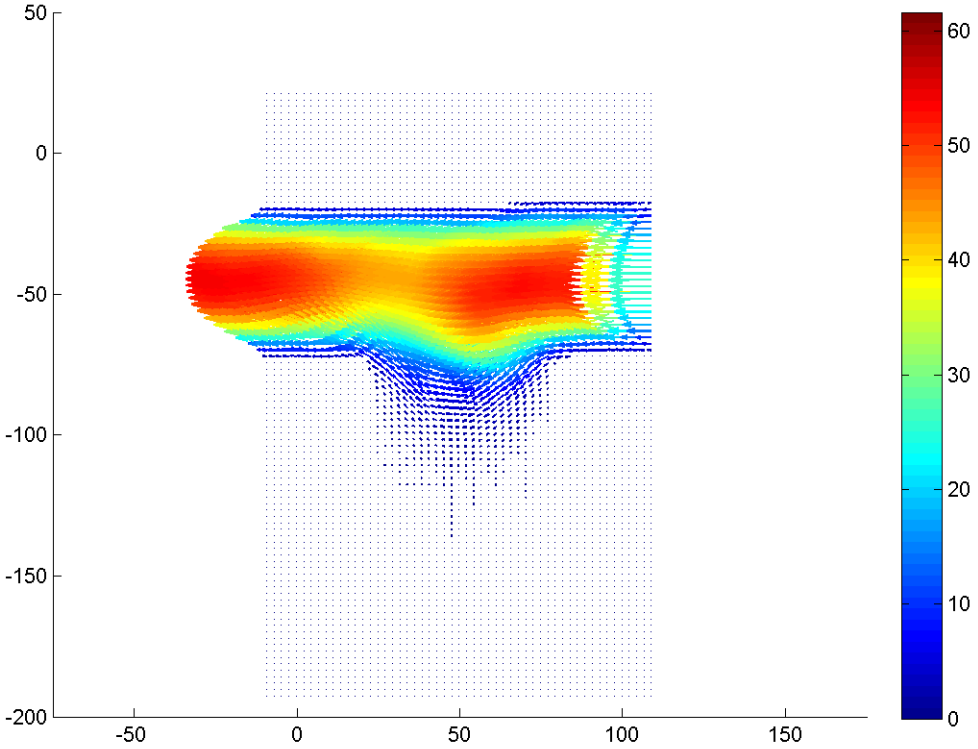

Figure F.235: Velocity field during phase increment 33 at 113.14 Hz with a Re of 0.1.

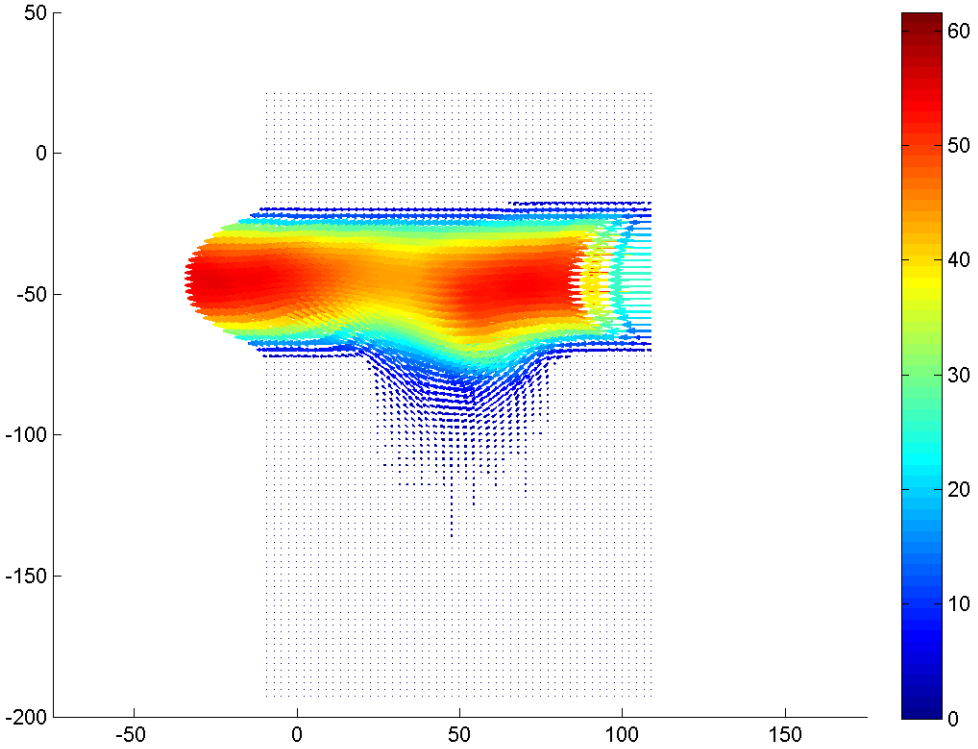

Figure F.236: Velocity field during phase increment 34 at 113.14 Hz with a Re of 0.1.

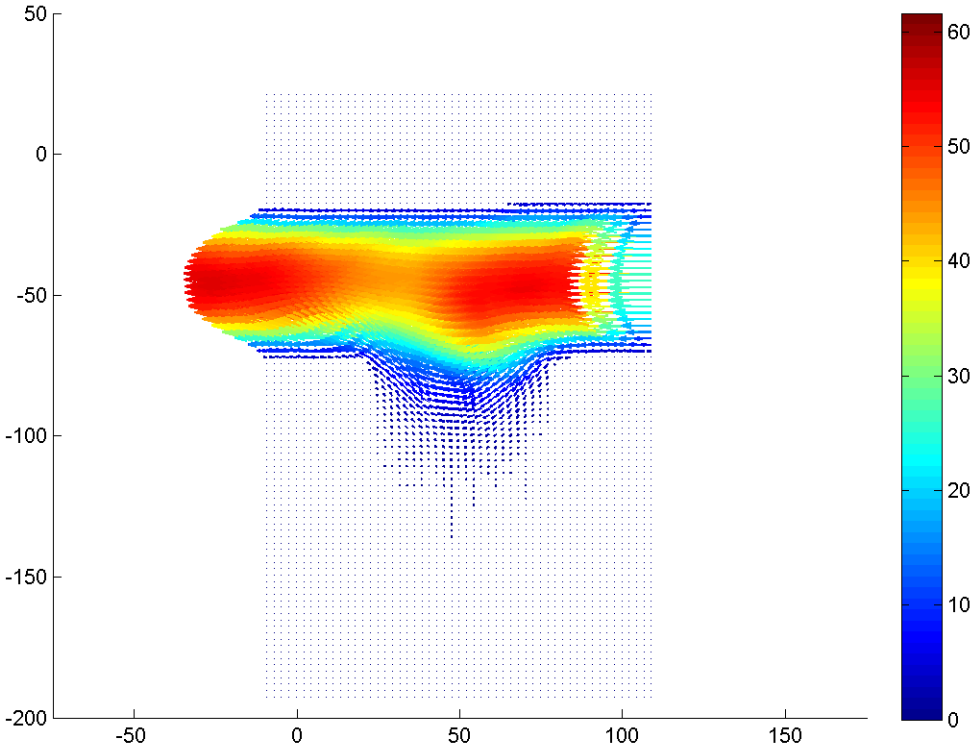

Figure F.237: Velocity field during phase increment 35 at 113.14 Hz with a Re of 0.1.

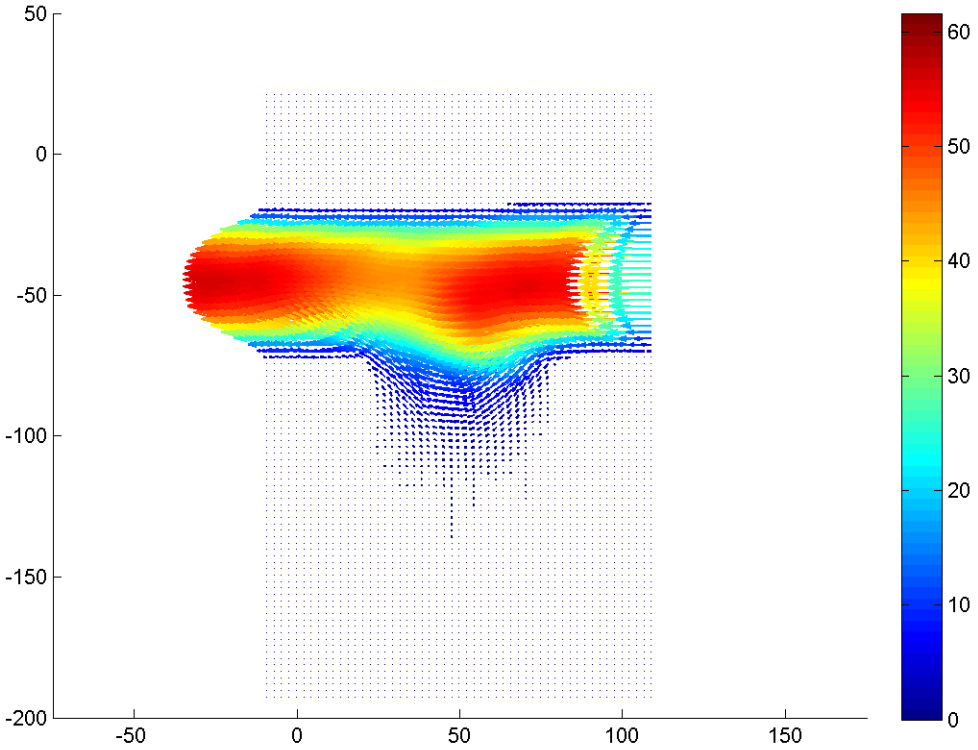

Figure F.238: Velocity field during phase increment 36 at 113.14 Hz with a Re of 0.1.

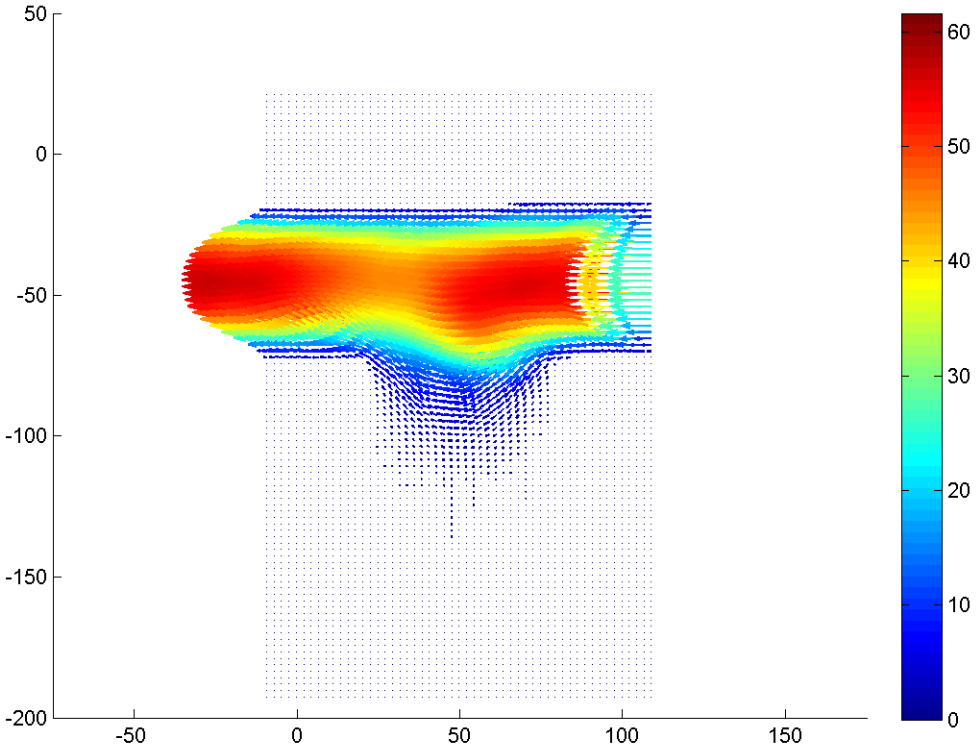

Figure F.239: Velocity field during phase increment 37 at 113.14 Hz with a Re of 0.1.

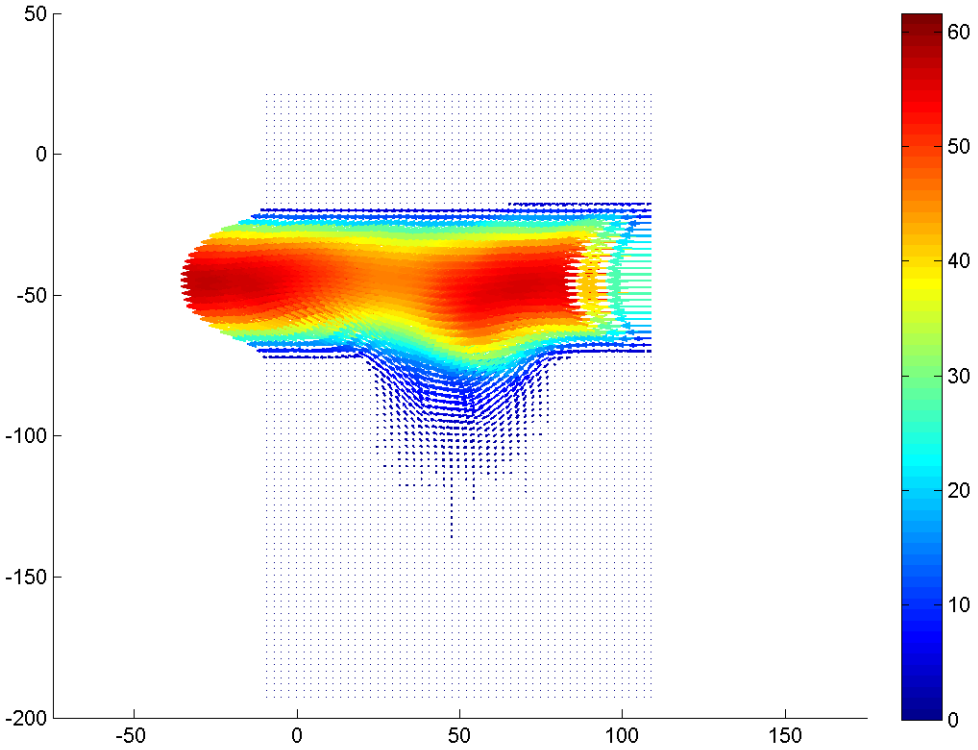

Figure F.240: Velocity field during phase increment 38 at 113.14 Hz with a Re of 0.1.

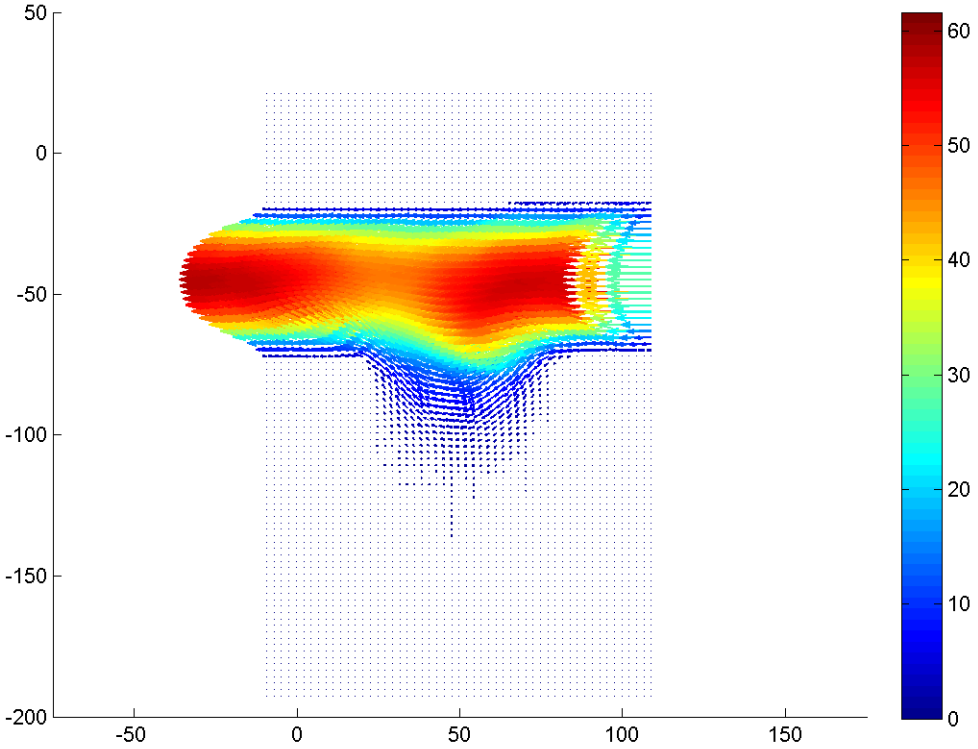

Figure F.241: Velocity field during phase increment 39 at 113.14 Hz with a Re of 0.1.

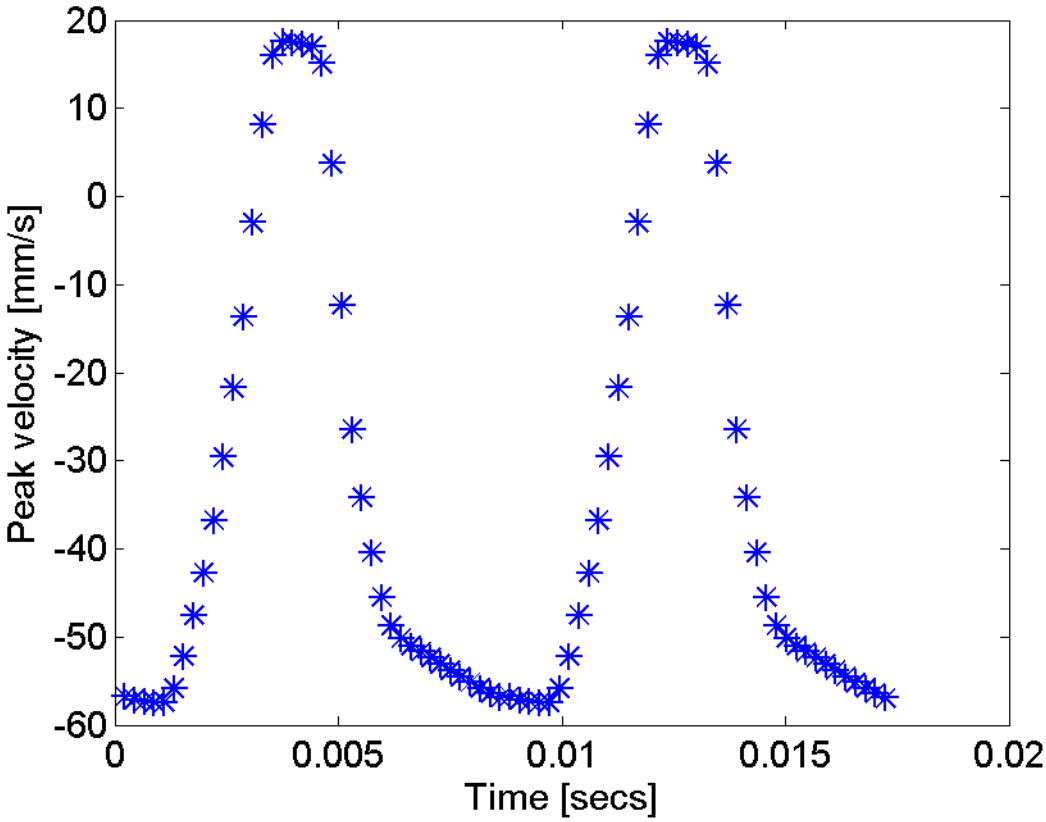

Figure F.242: The peak velocity in the free stream region in time at 113.14 Hz.

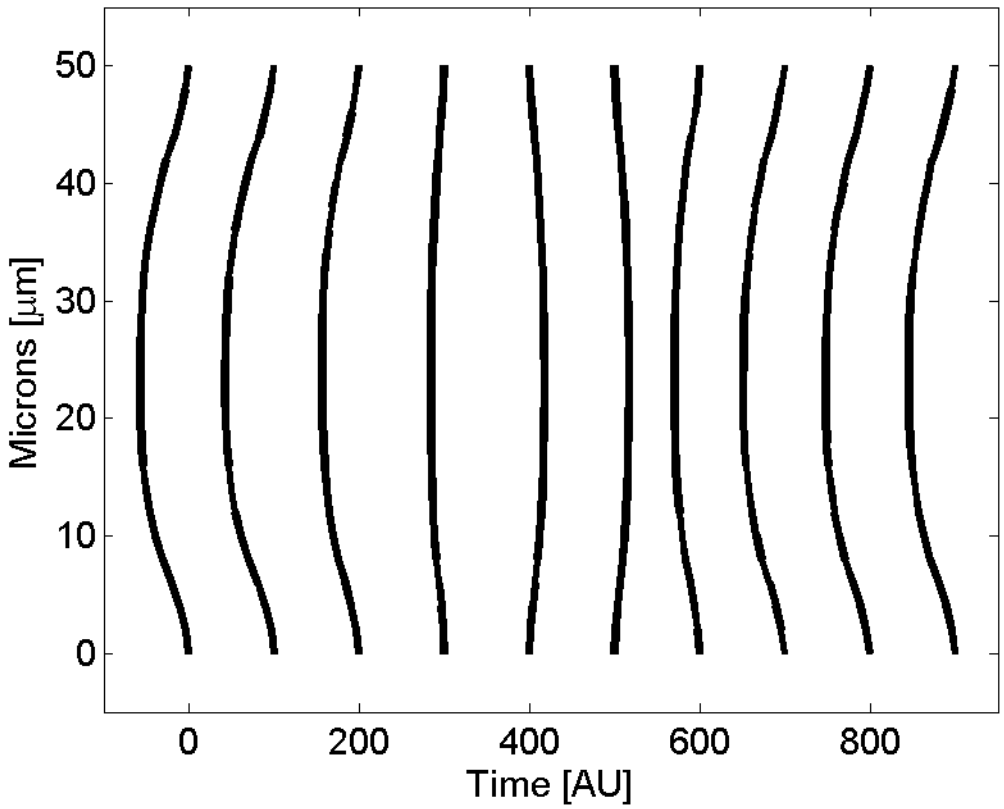

Figure F.243: The velocity profile in the free stream versus time at 113.14 Hz.

F.3.2 Streamline images at 113.14 Hz

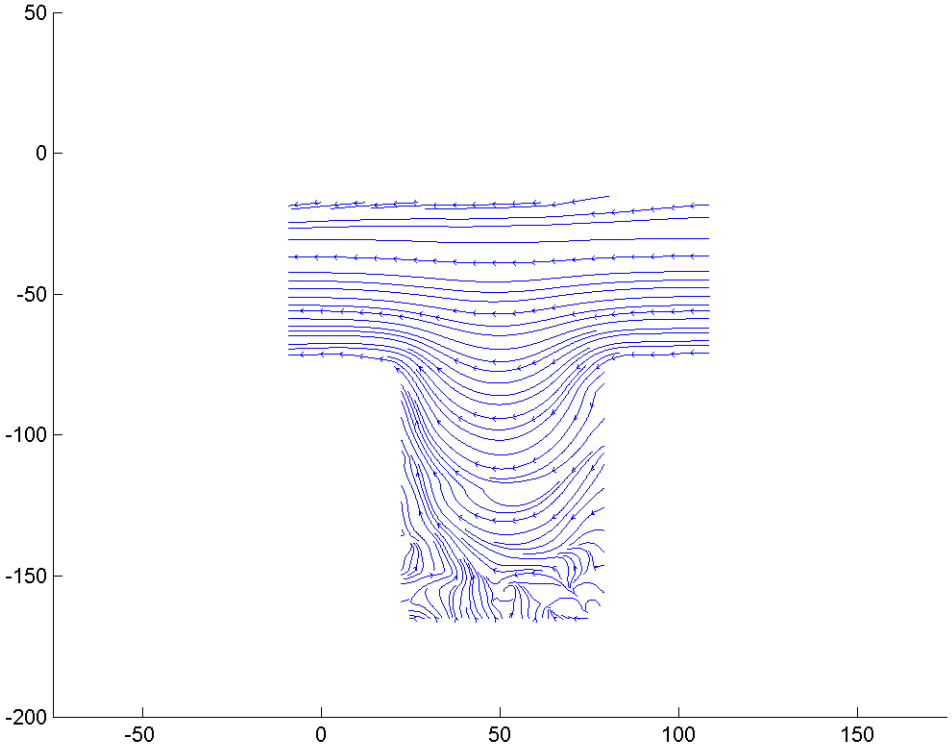

Figure F.244: Streamline image during phase increment 1 at 113.14 Hz and a Re of 0.1.

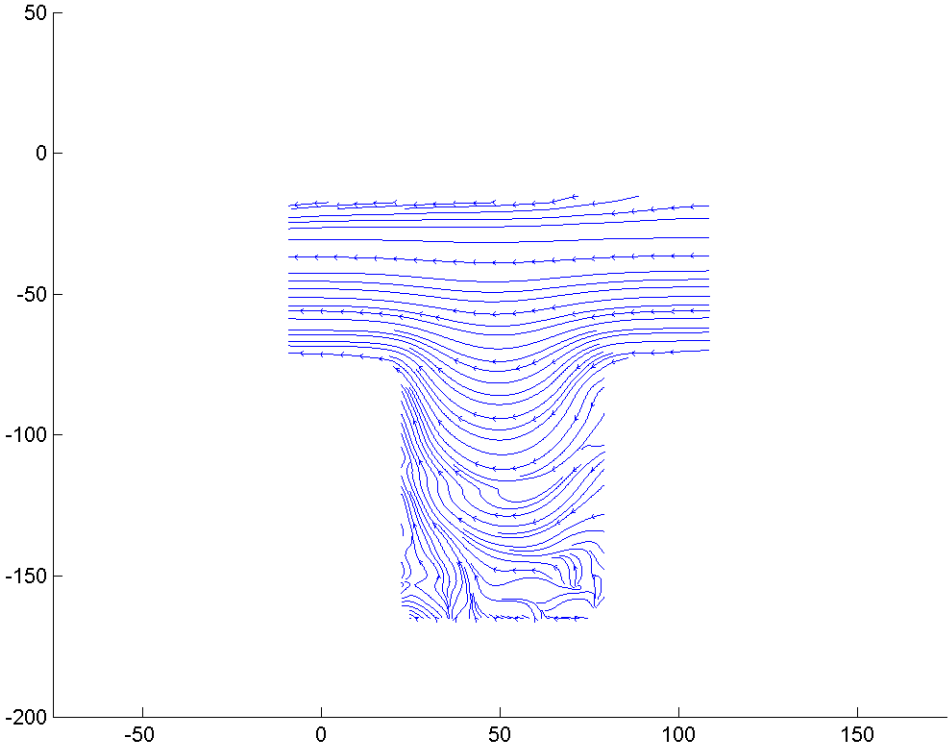

Figure F.245: Streamline image during phase increment 2 at 113.14 Hz and a Re of 0.1.

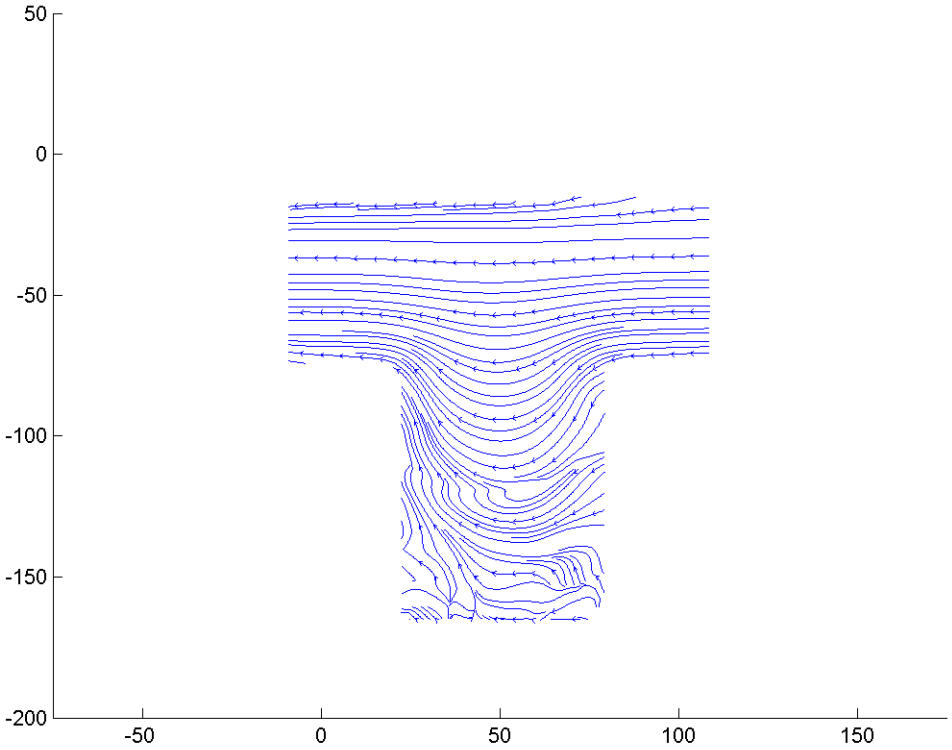

Figure F.246: Streamline image during phase increment 3 at 113.14 Hz and a Re of 0.1.

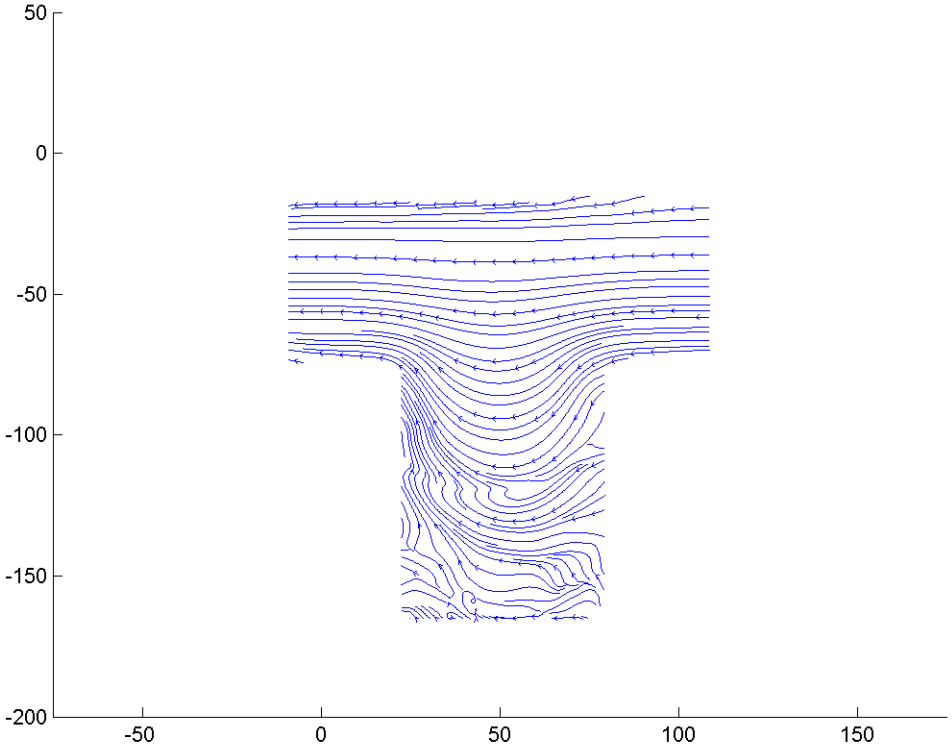

Figure F.247: Streamline image during phase increment 4 at 113.14 Hz and a Re of 0.1.

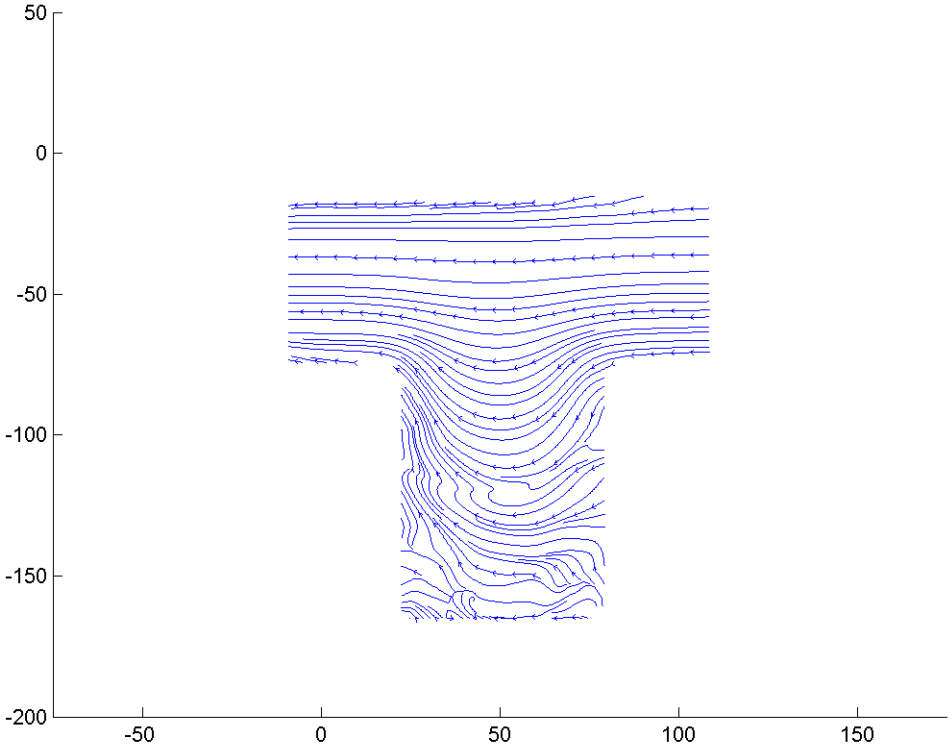

Figure F.248: Streamline image during phase increment 5 at 113.14 Hz and a Re of 0.1.

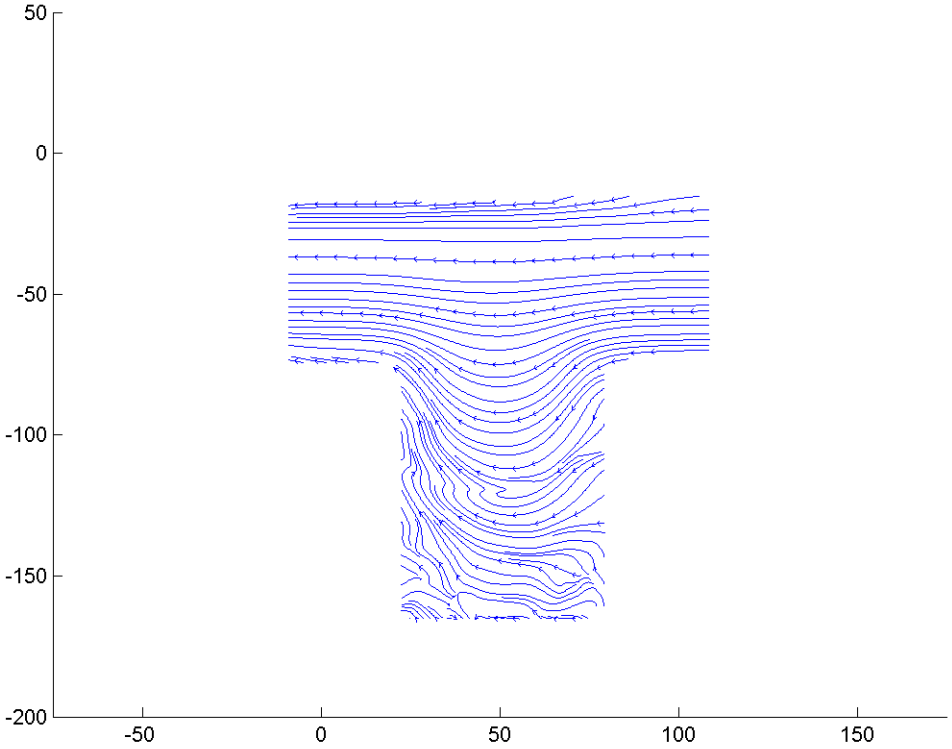

Figure F.249: Streamline image during phase increment 6 at 113.14 Hz and a Re of 0.1.

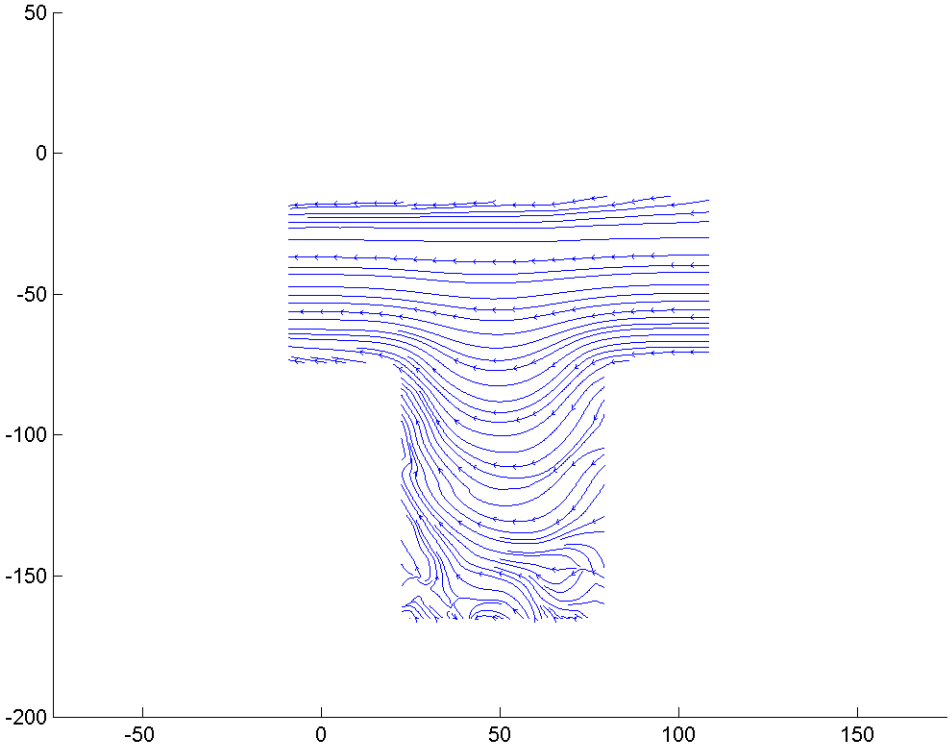

Figure F.250: Streamline image during phase increment 7 at 113.14 Hz and a Re of 0.1.

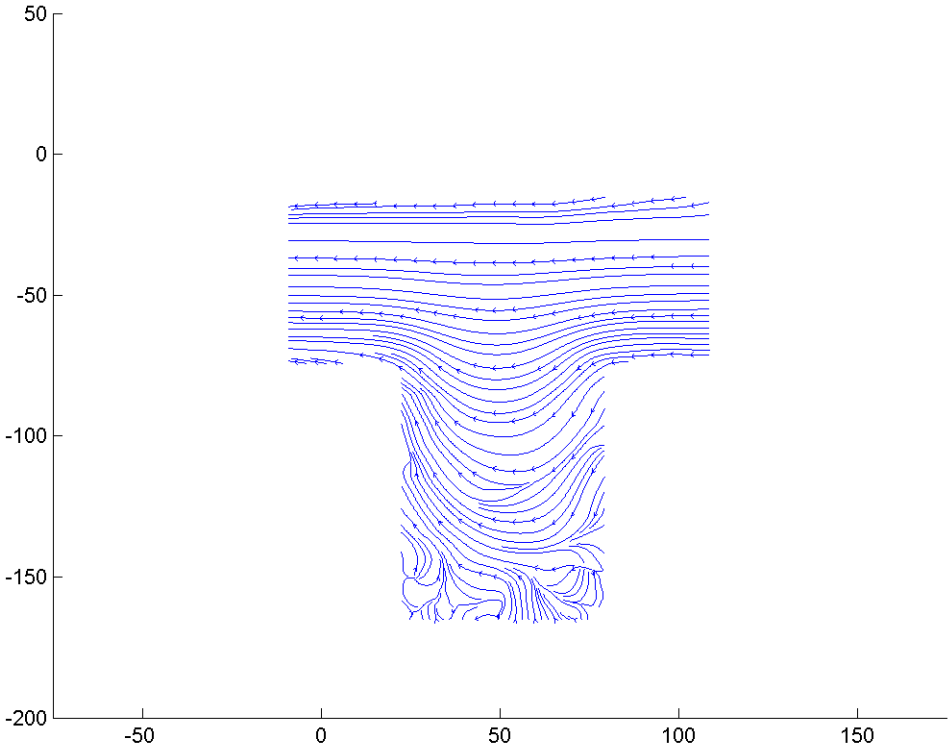

Figure F.251: Streamline image during phase increment 8 at 113.14 Hz and a Re of 0.1.

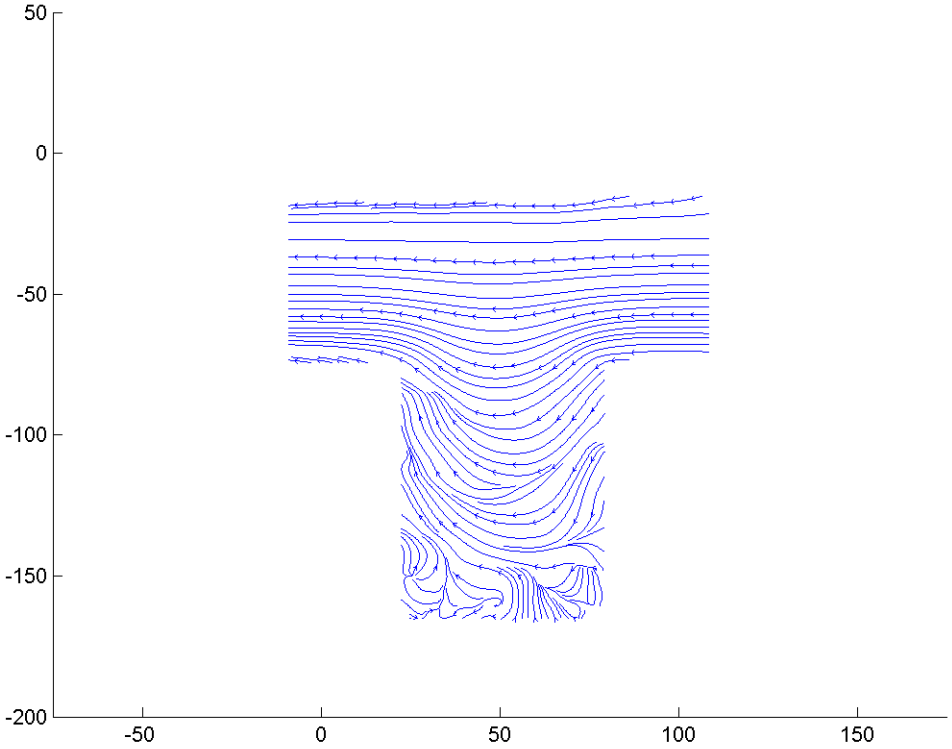

Figure F.252: Streamline image during phase increment 9 at 113.14 Hz and a Re of 0.1.

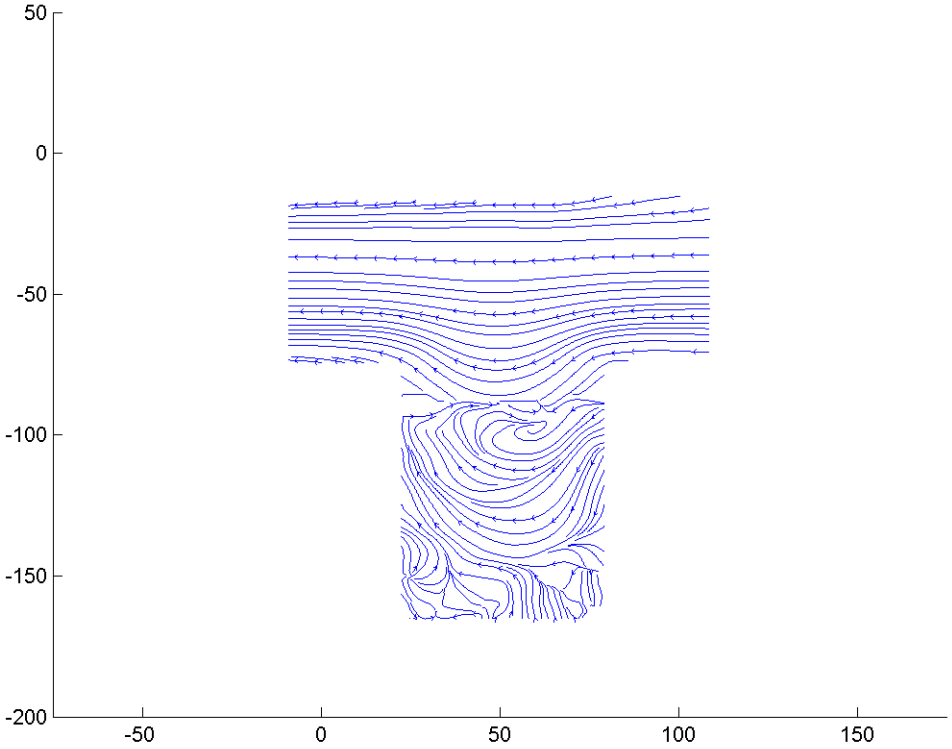

Figure F.253: Streamline image during phase increment 10 at 113.14 Hz and a Re of 0.1.

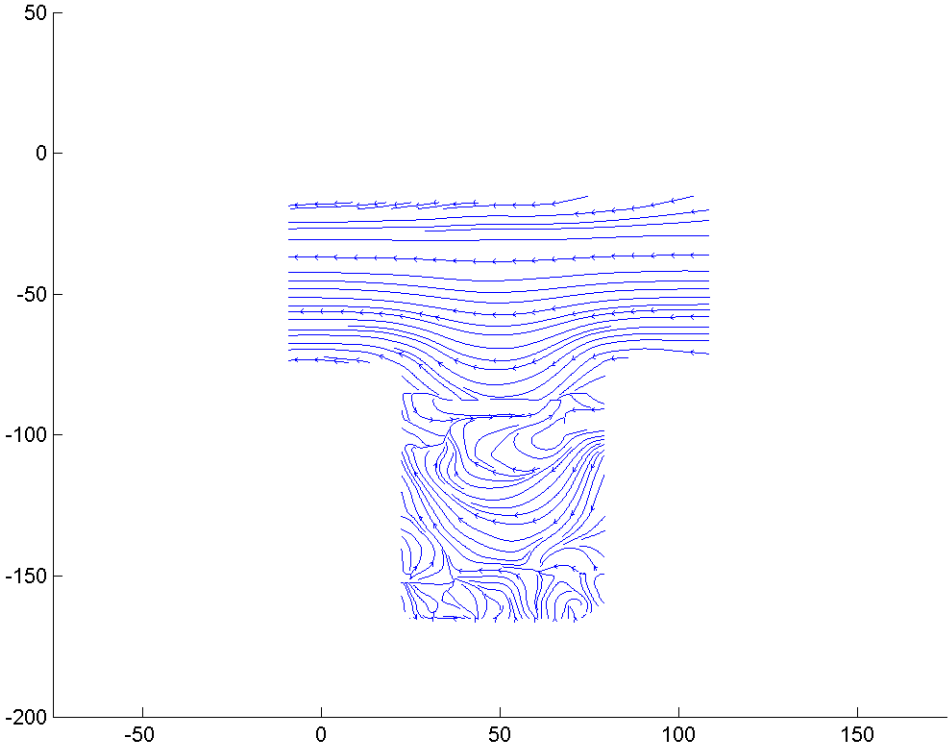

Figure F.254: Streamline image during phase increment 11 at 113.14 Hz and a Re of 0.1.

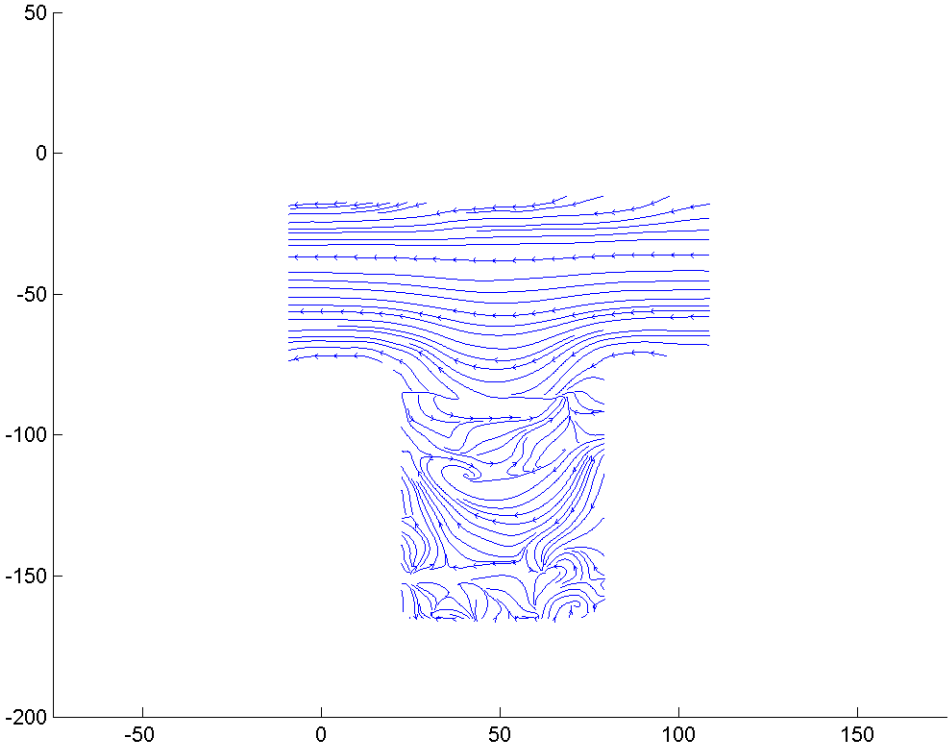

Figure F.255: Streamline image during phase increment 12 at 113.14 Hz and a Re of 0.1.

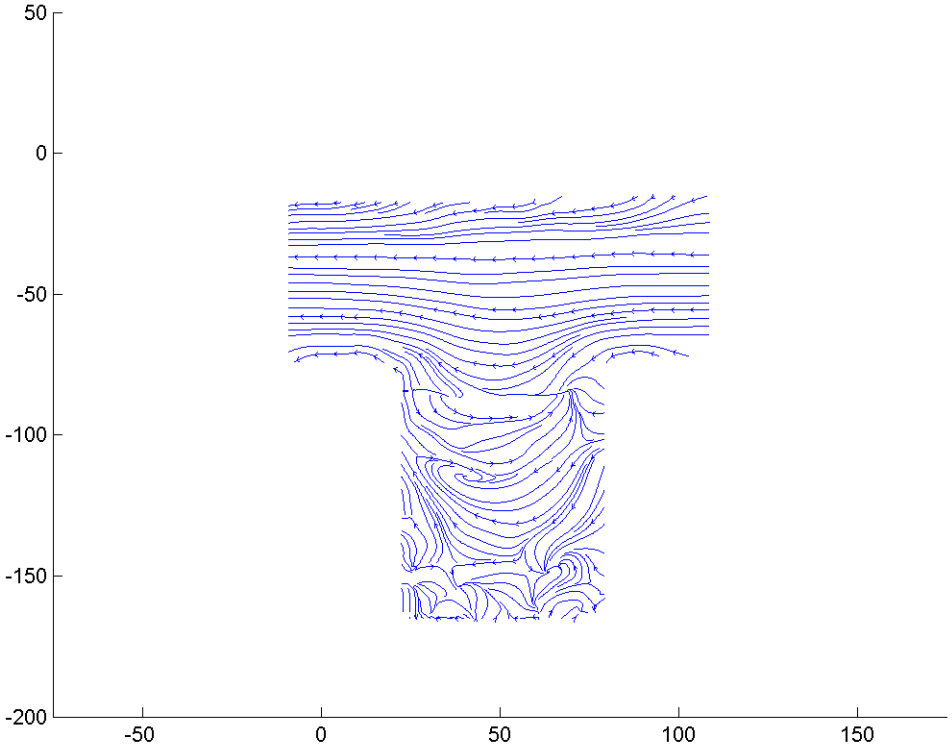

Figure F.256: Streamline image during phase increment 13 at 113.14 Hz and a Re of 0.1.

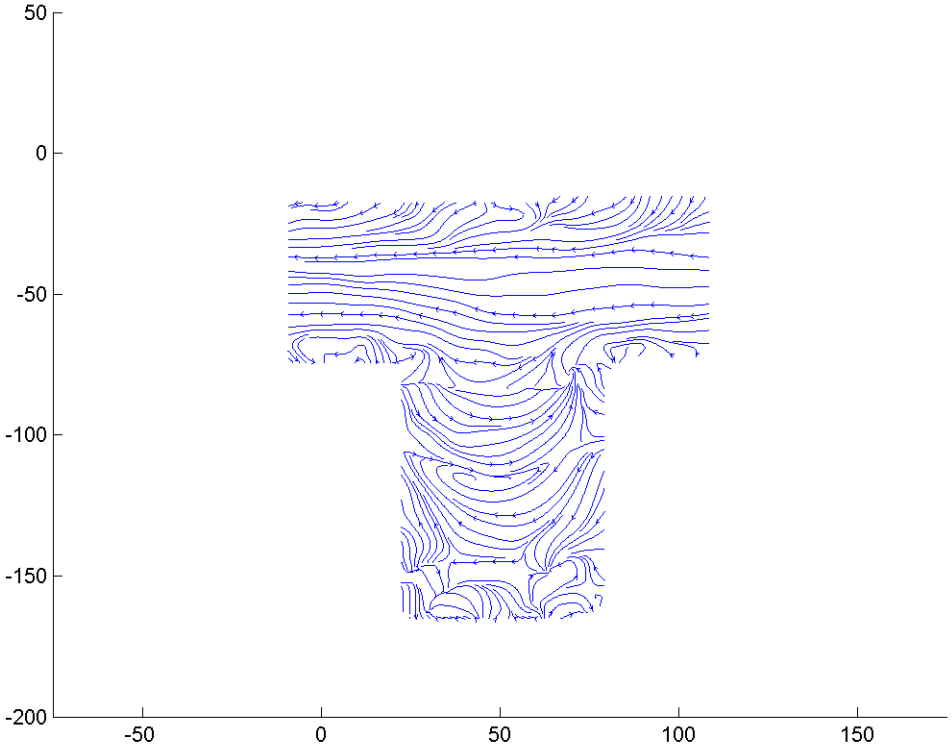

Figure F.257: Streamline image during phase increment 14 at 113.14 Hz and a Re of 0.1.

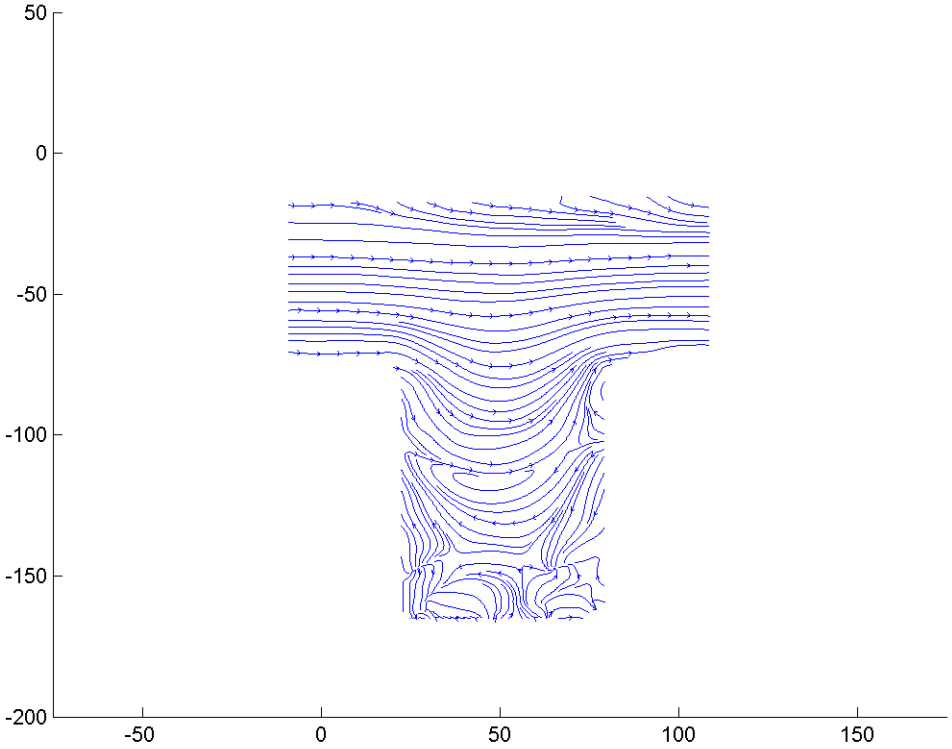

Figure F.258: Streamline image during phase increment 15 at 113.14 Hz and a Re of 0.1.

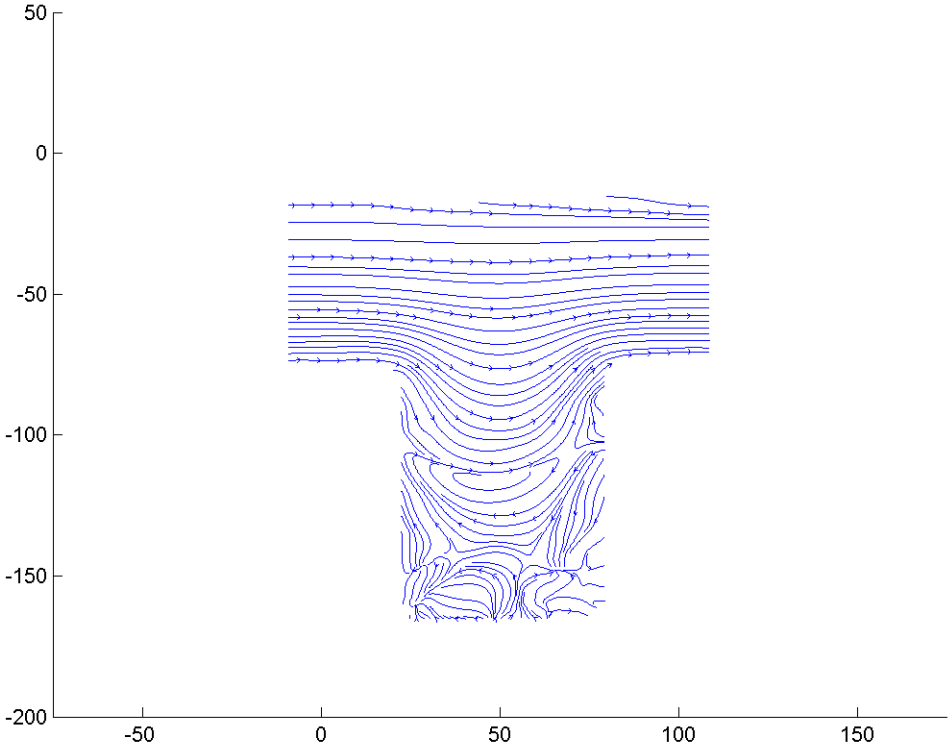

Figure F.259: Streamline image during phase increment 16 at 113.14 Hz and a Re of 0.1.

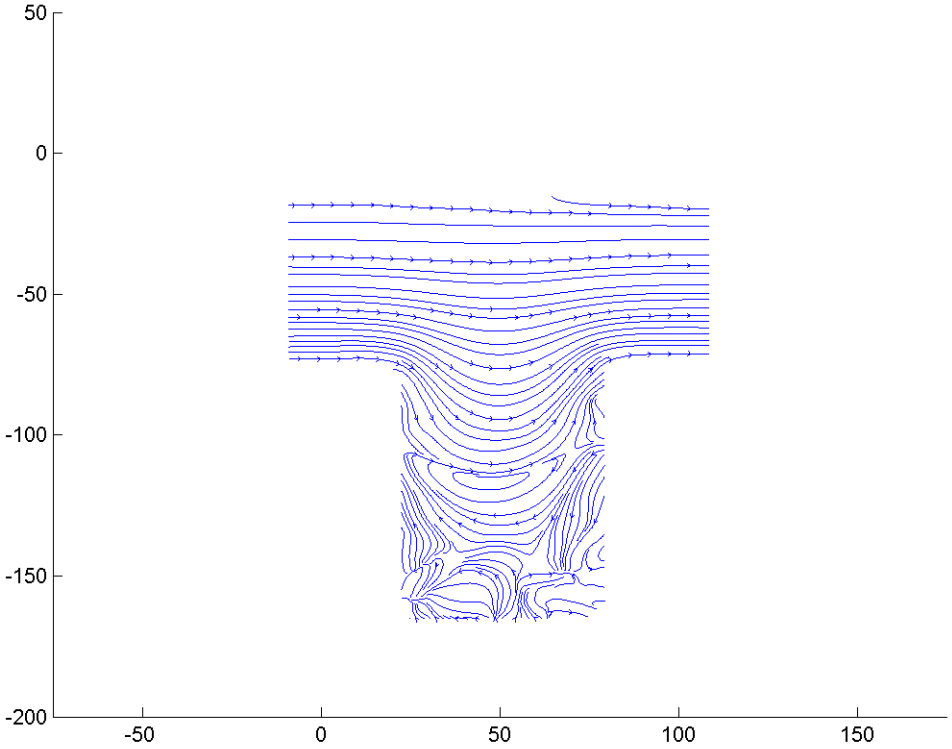

Figure F.260: Streamline image during phase increment 17 at 113.14 Hz and a Re of 0.1.

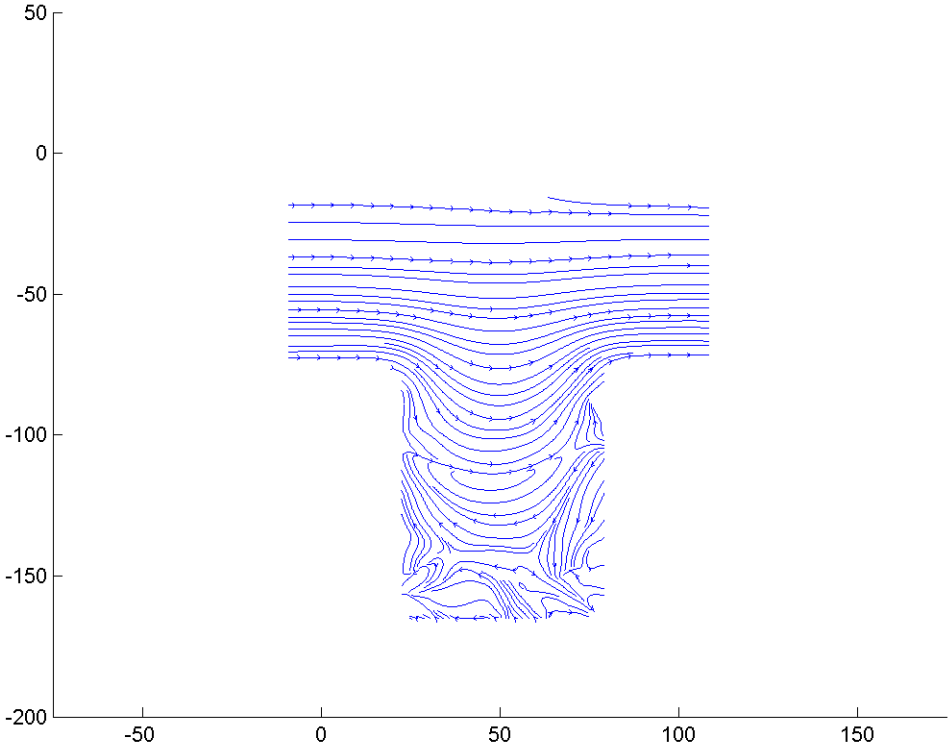

Figure F.261: Streamline image during phase increment 18 at 113.14 Hz and a Re of 0.1.

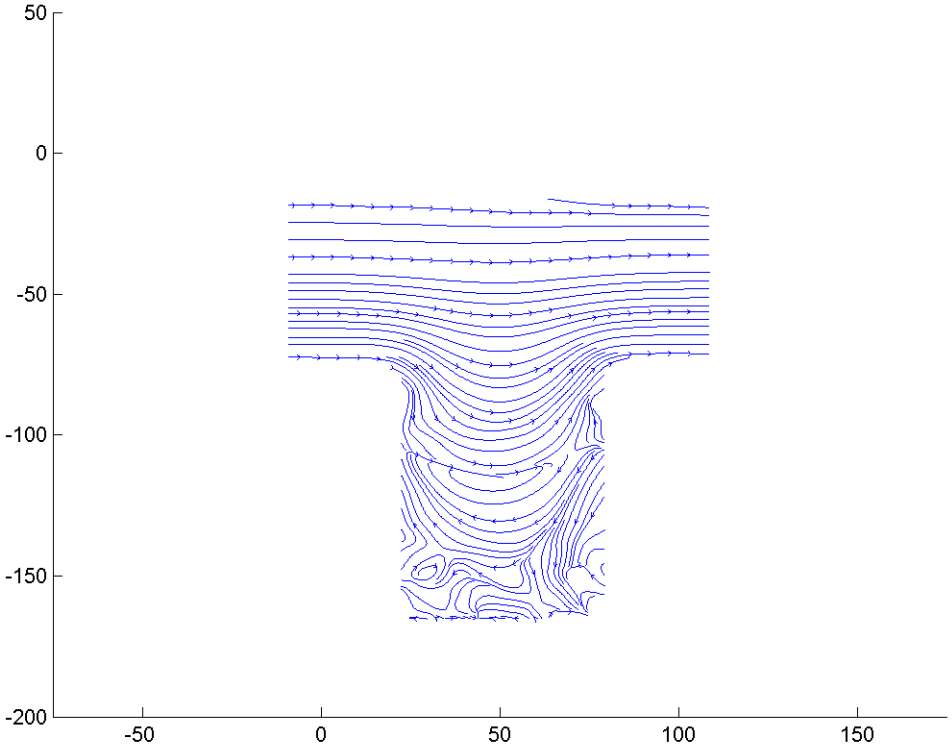

Figure F.262: Streamline image during phase increment 18 at 113.14 Hz and a Re of 0.1.

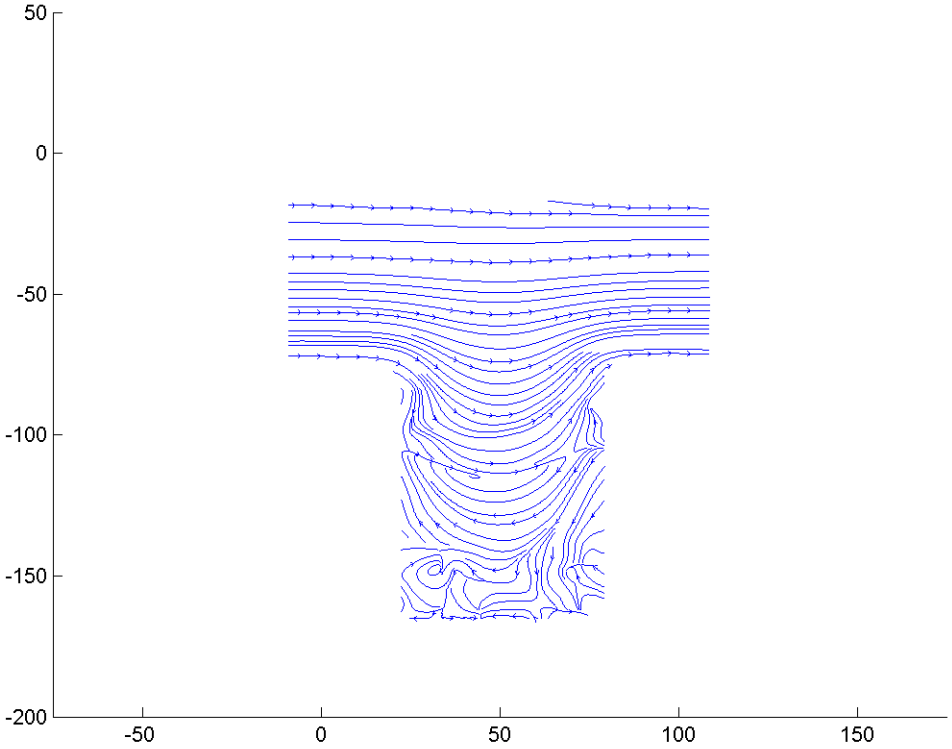

Figure F.263: Streamline image during phase increment 20 at 113.14 Hz and a Re of 0.1.

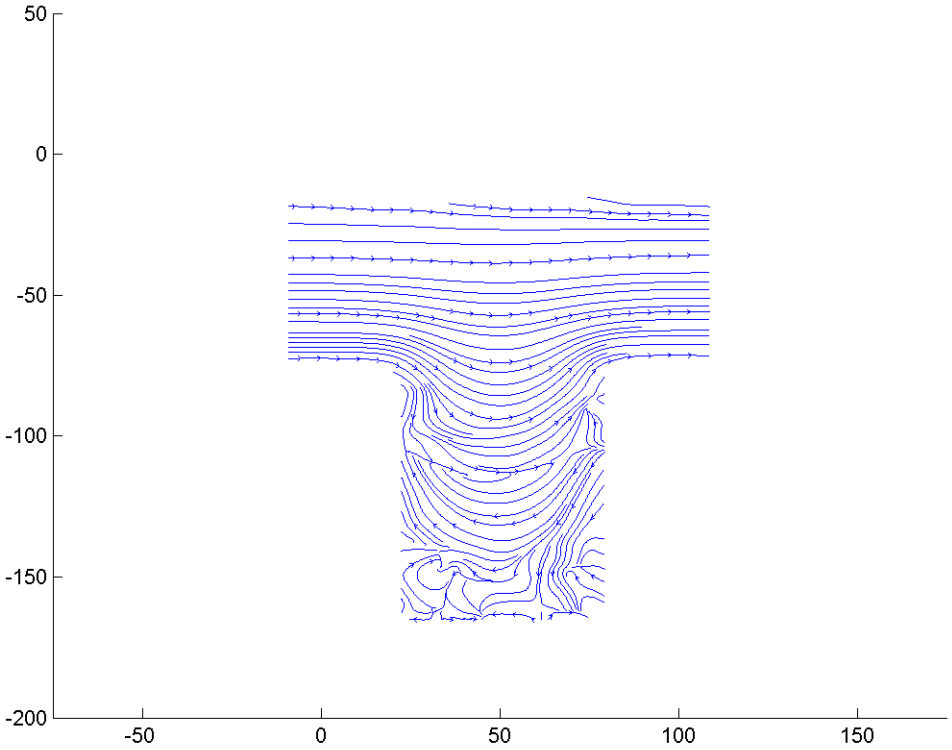

Figure F.264: Streamline image during phase increment 21 at 113.14 Hz and a Re of 0.1.

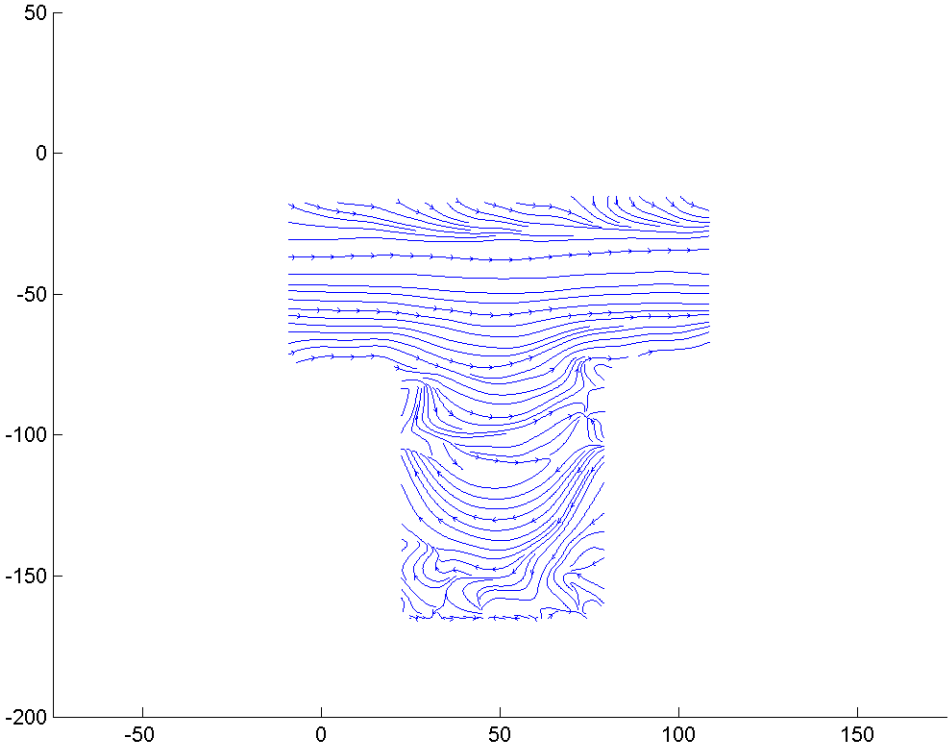

Figure F.265: Streamline image during phase increment 22 at 113.14 Hz and a Re of 0.1.

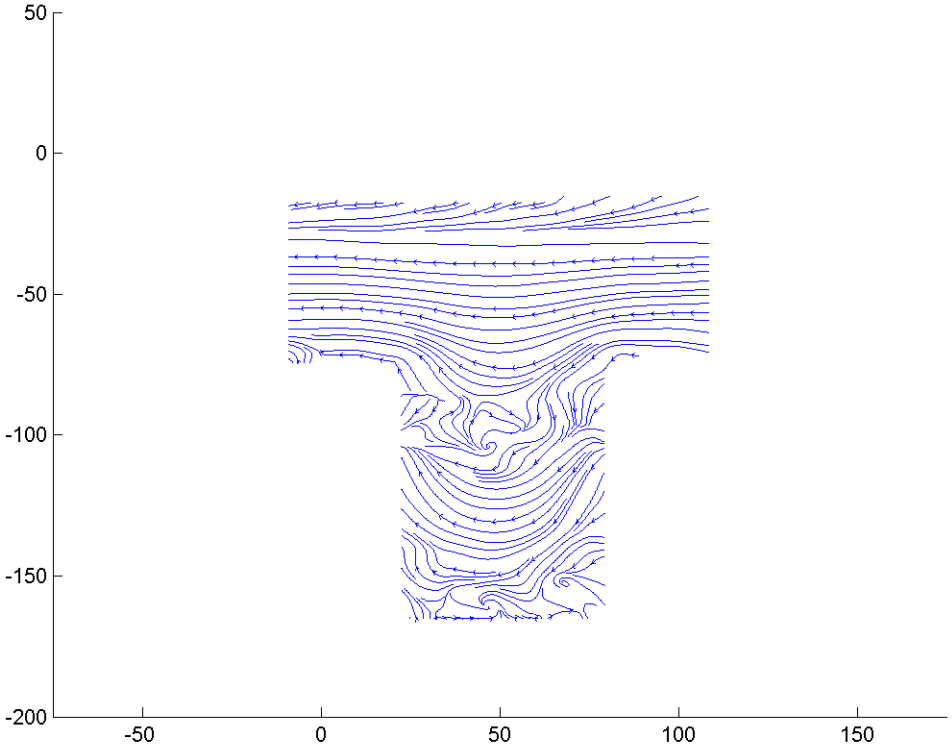

Figure F.266: Streamline image during phase increment 23 at 113.14 Hz and a Re of 0.1.

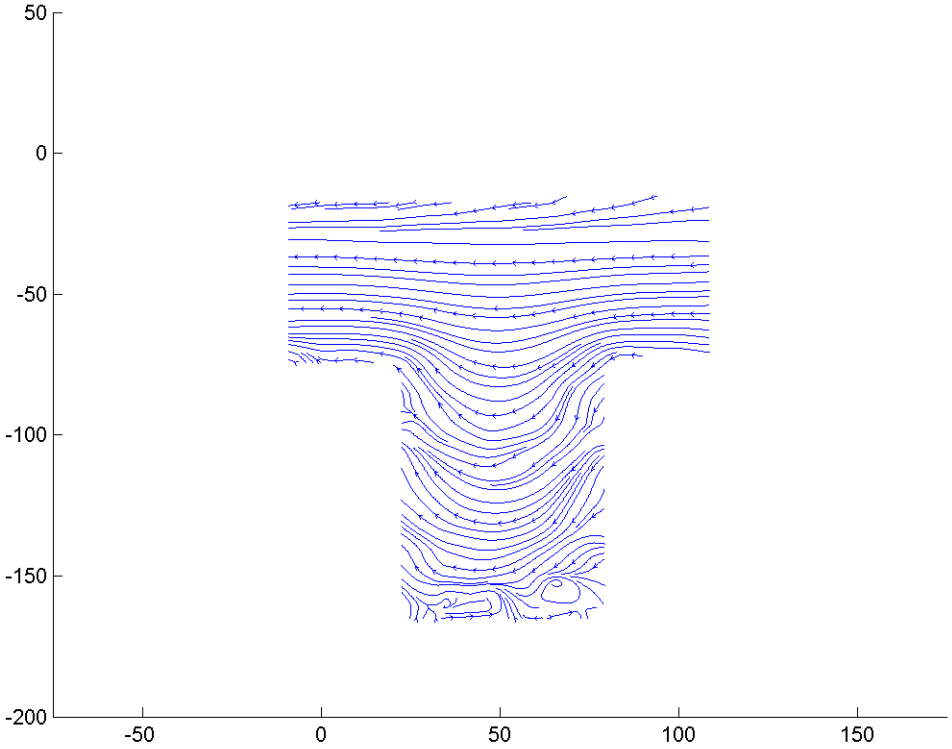

Figure F.267: Streamline image during phase increment 24 at 113.14 Hz and a Re of 0.1.

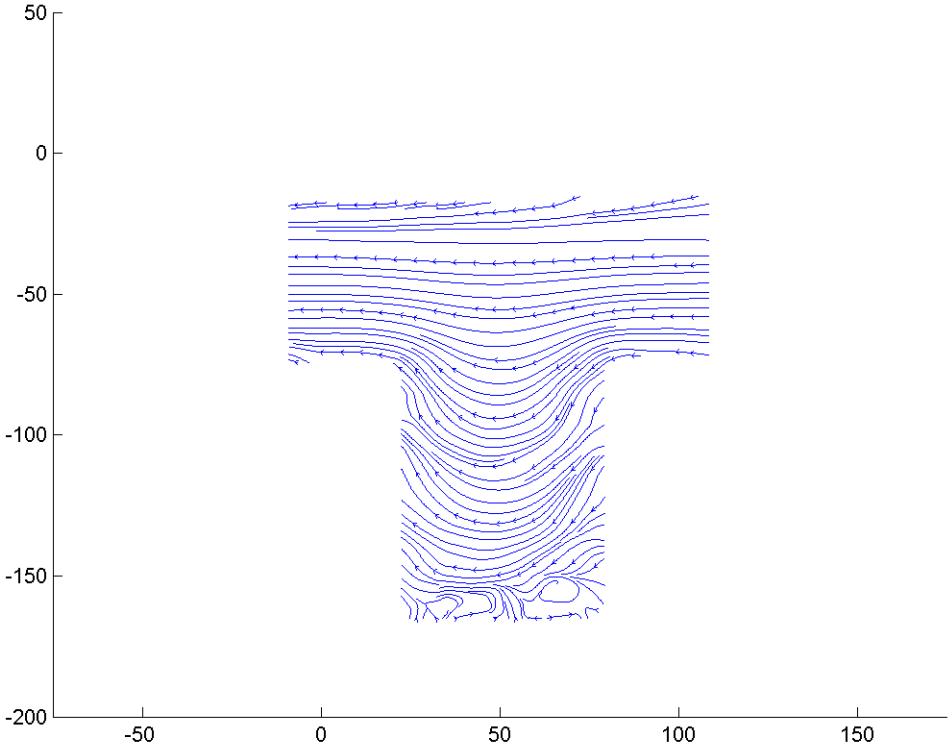

Figure F.268: Streamline image during phase increment 25 at 113.14 Hz and a Re of 0.1.

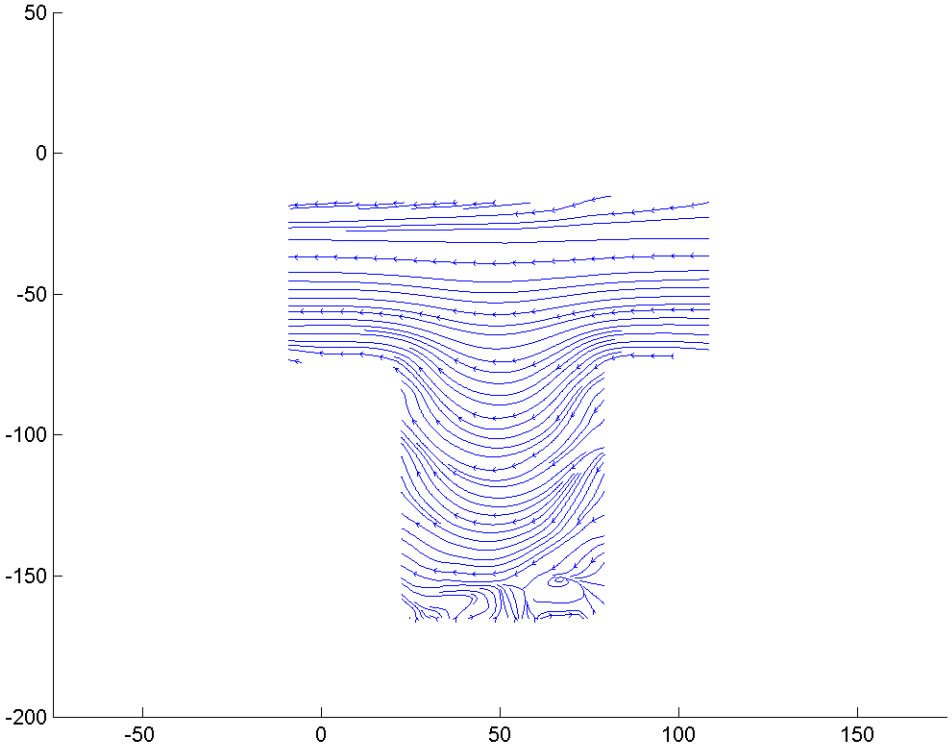

Figure F.269: Streamline image during phase increment 26 at 113.14 Hz and a Re of 0.1.

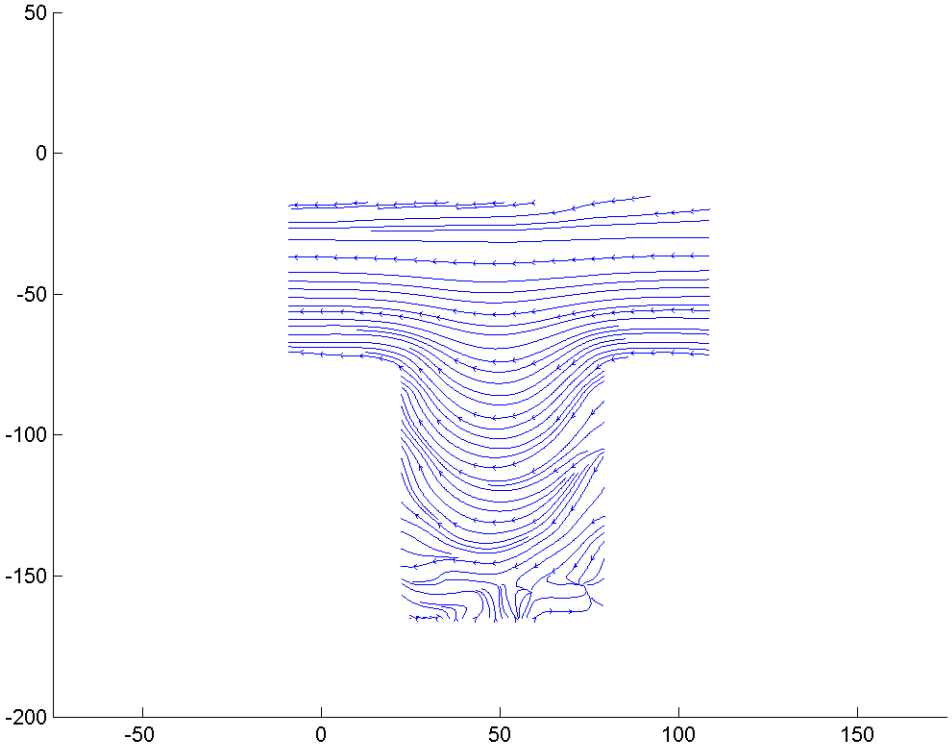

Figure F.270: Streamline image during phase increment 27 at 113.14 Hz and a Re of 0.1.

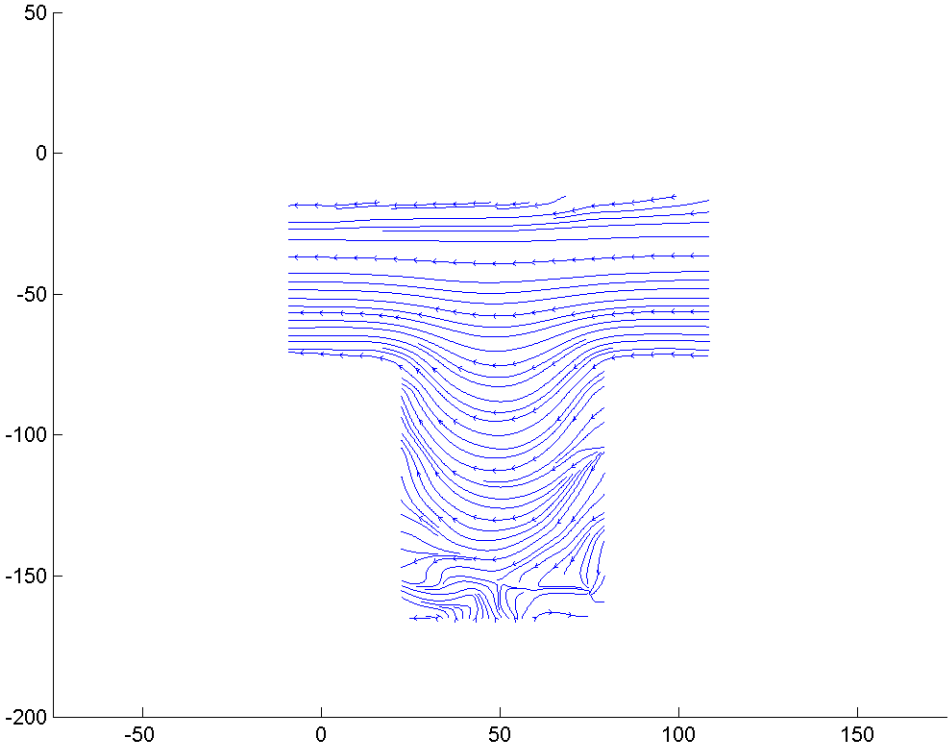

Figure F.271: Streamline image during phase increment 28 at 113.14 Hz and a Re of 0.1.

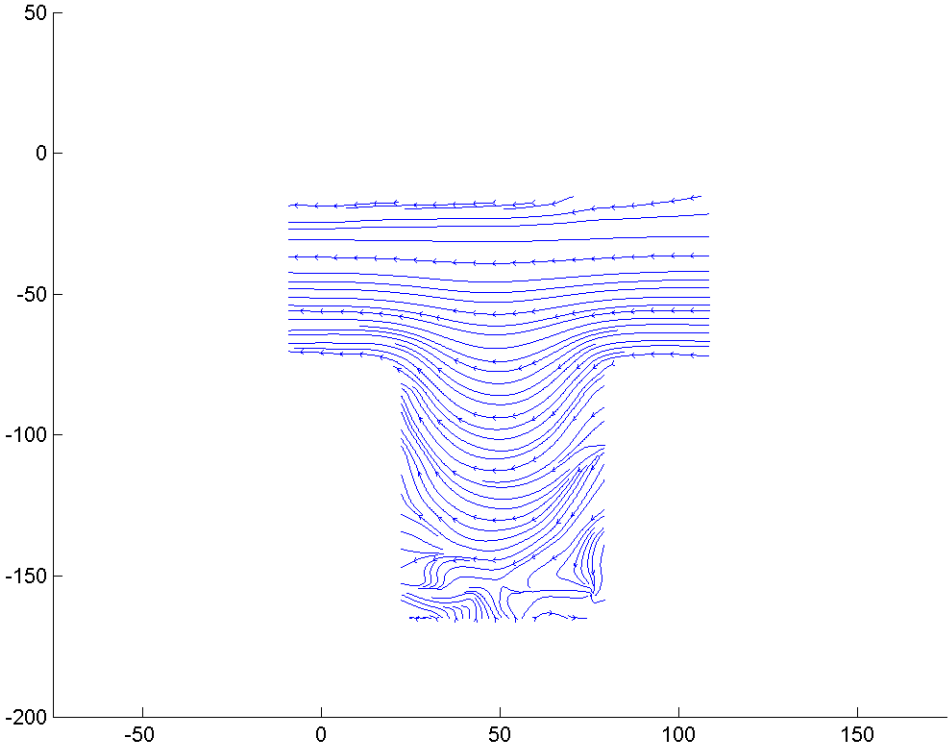

Figure F.272: Streamline image during phase increment 29 at 113.14 Hz and a Re of 0.1.

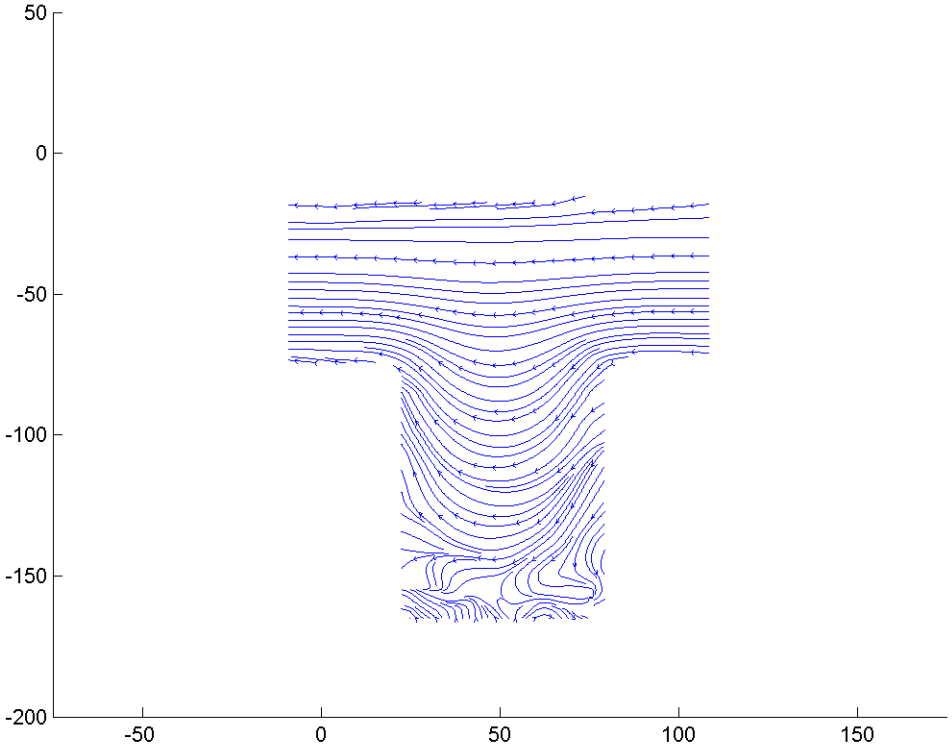

Figure F.273: Streamline image during phase increment 30 at 113.14 Hz and a Re of 0.1.

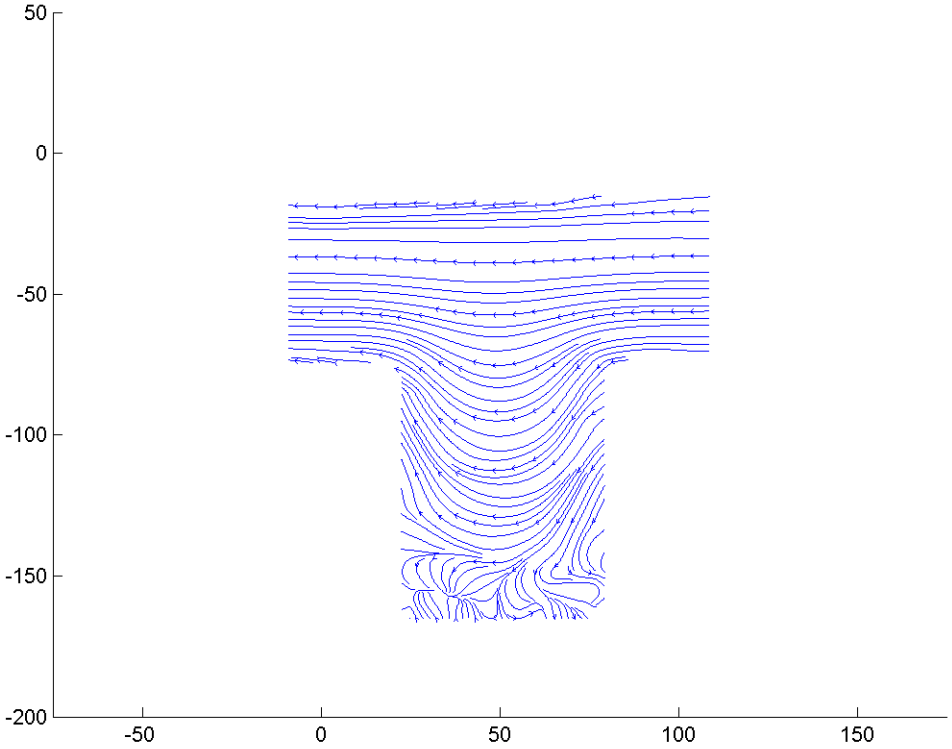

Figure F.274: Streamline image during phase increment 31 at 113.14 Hz and a Re of 0.1.

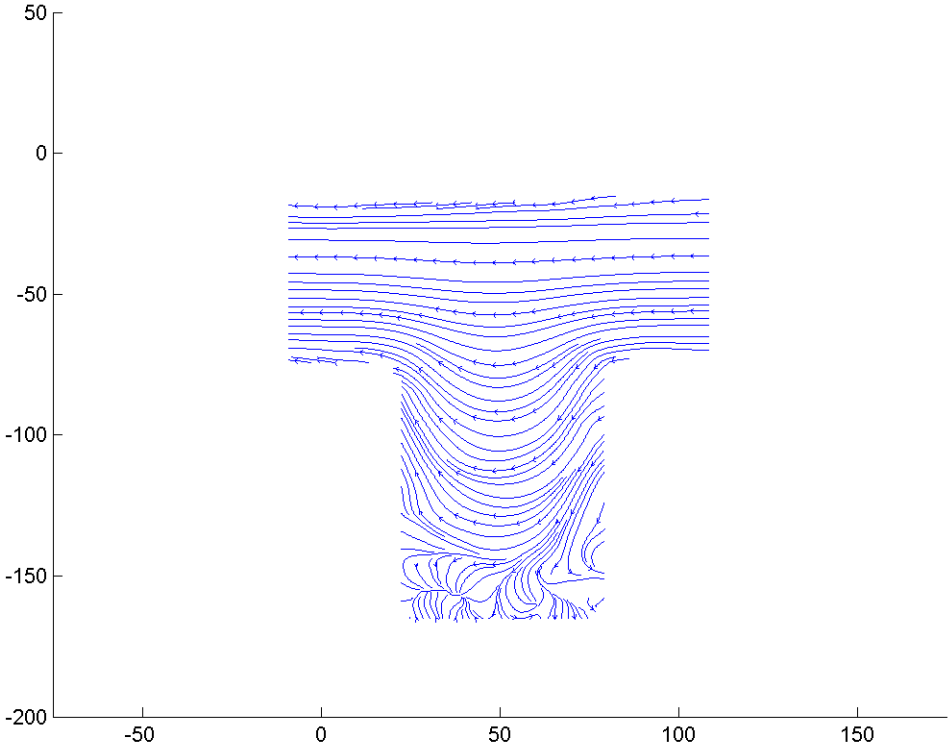

Figure F.275: Streamline image during phase increment 32 at 113.14 Hz and a Re of 0.1.

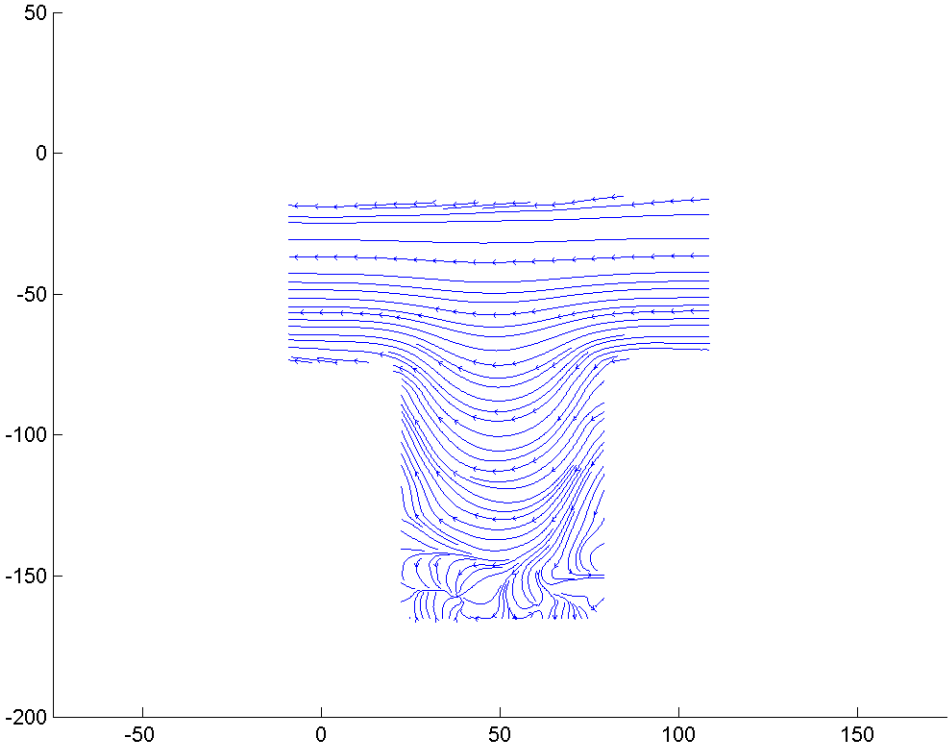

Figure F.276: Streamline image during phase increment 33 at 113.14 Hz and a Re of 0.1.

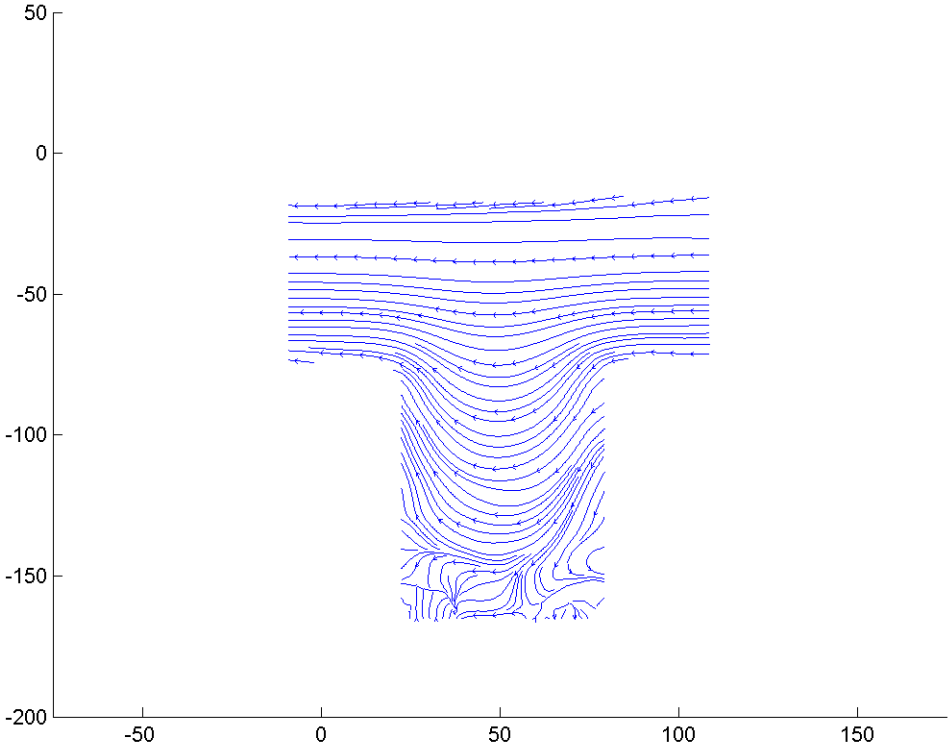

Figure F.277: Streamline image during phase increment 34 at 113.14 Hz and a Re of 0.1.

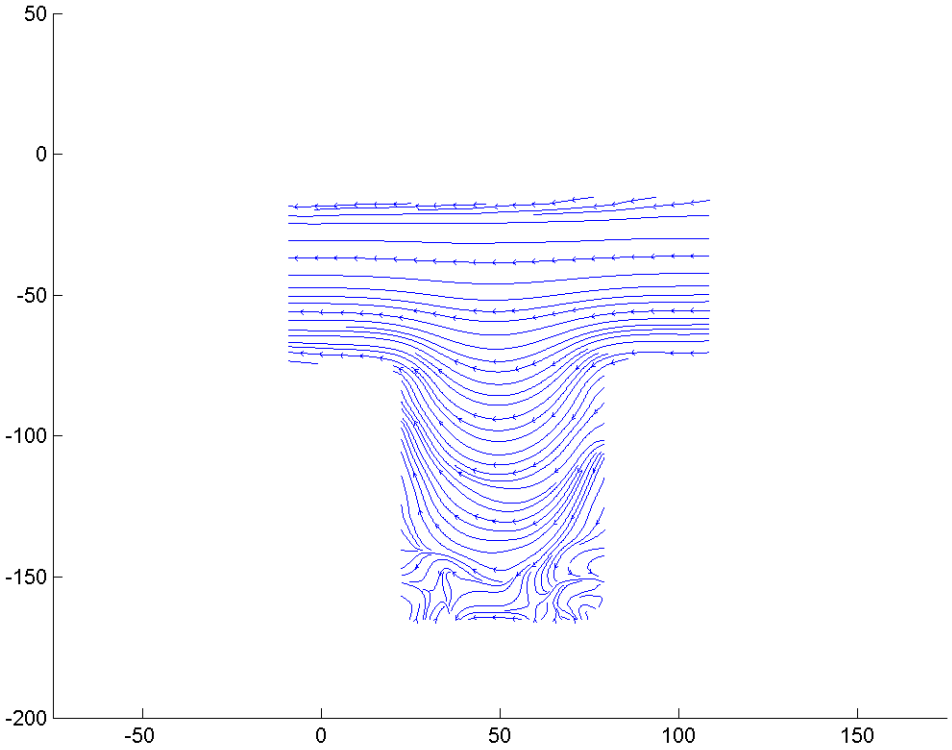

Figure F.278: Streamline image during phase increment 35 at 113.14 Hz and a Re of 0.1.

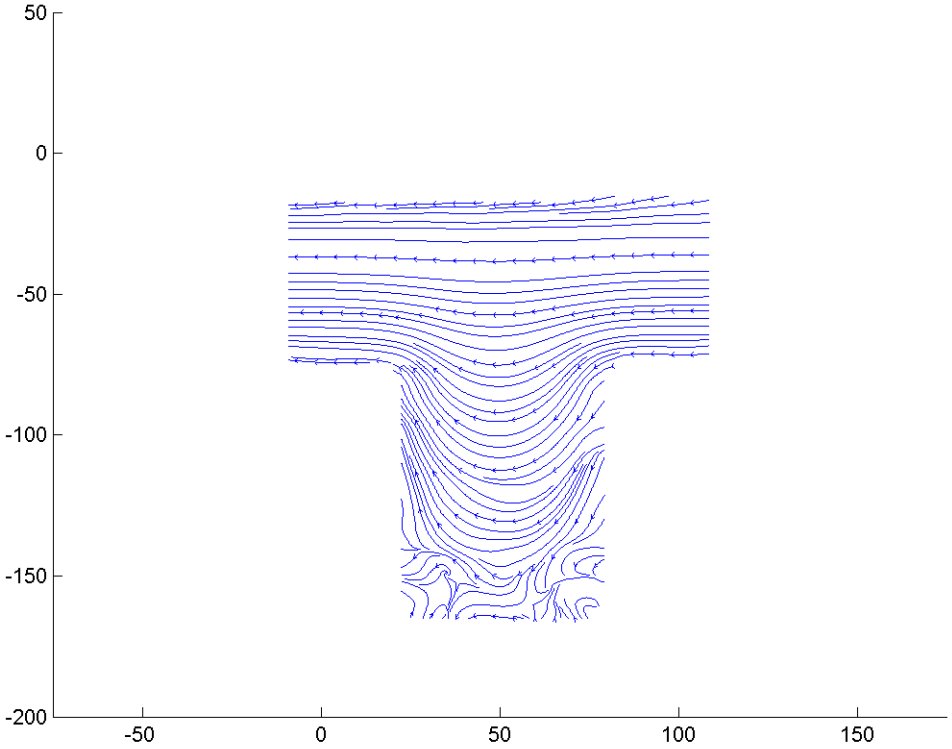

Figure F.279: Streamline image during phase increment 36 at 113.14 Hz and a Re of 0.1.

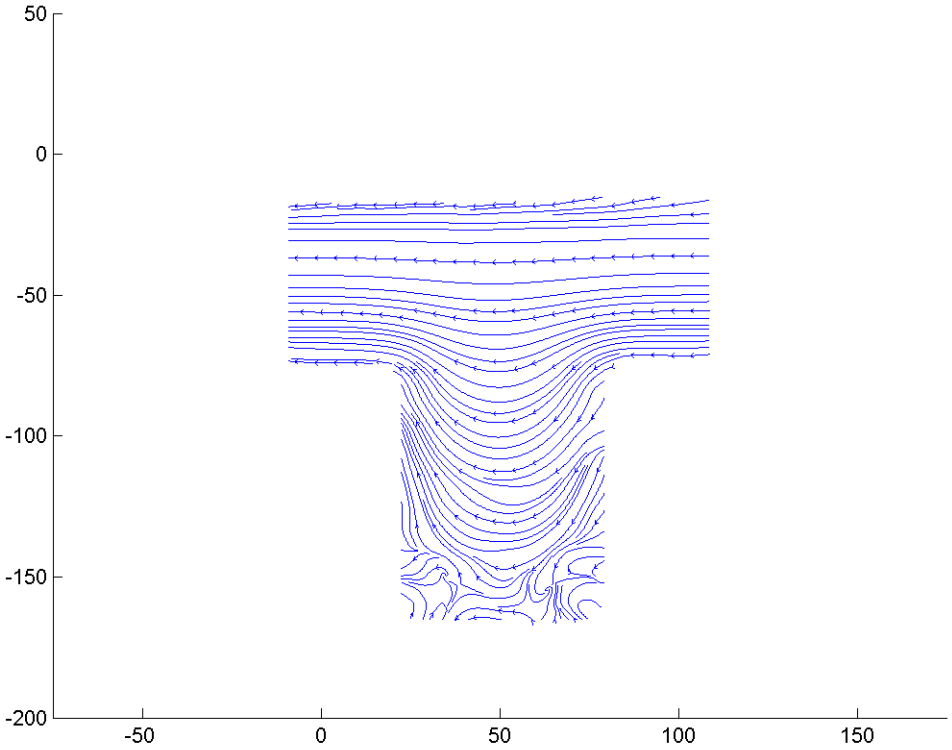

Figure F.280: Streamline image during phase increment 37 at 113.14 Hz and a Re of 0.1.

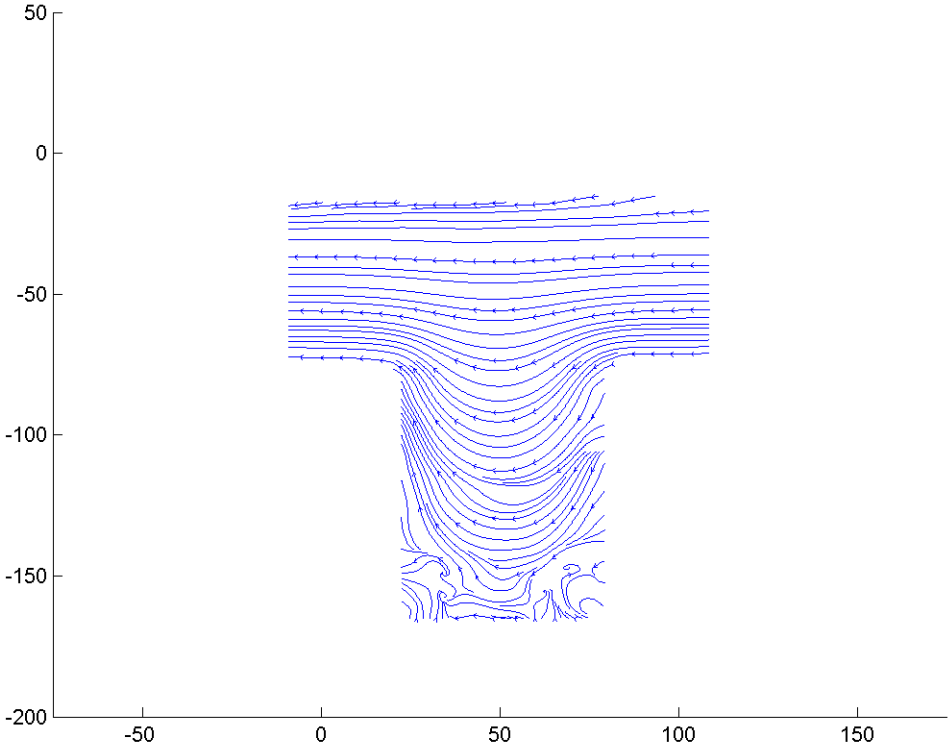

Figure F.281: Streamline image during phase increment 38 at 113.14 Hz and a Re of 0.1.

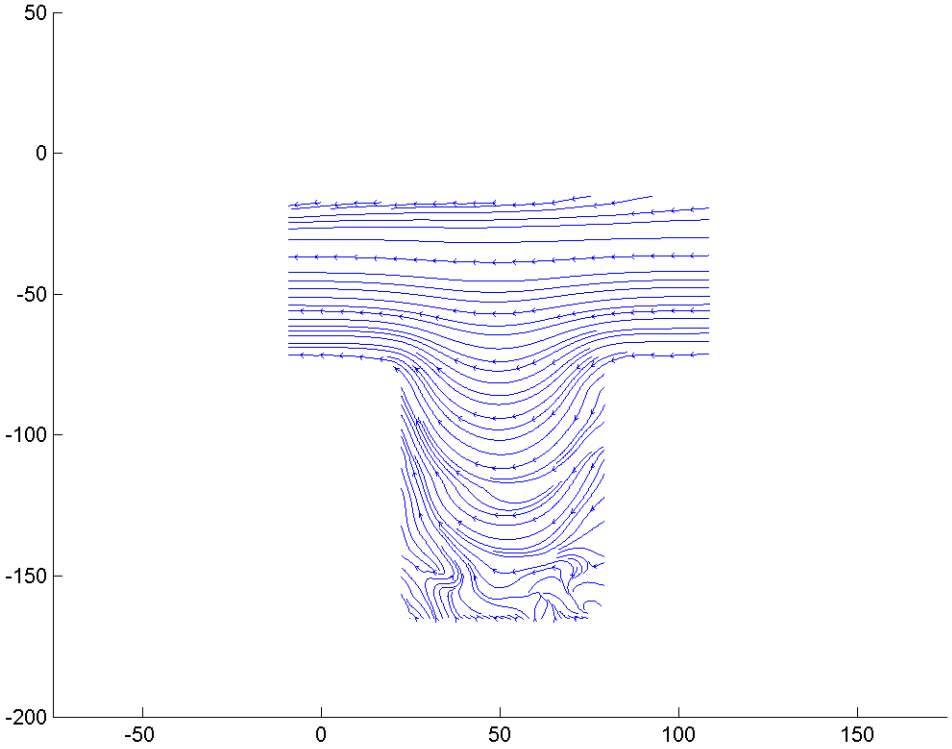

Figure F.282: Streamline image during phase increment 39 at 113.14 Hz and a Re of 0.1.

F.3.3 Residence time of particles in the cavity at 113.14 Hz

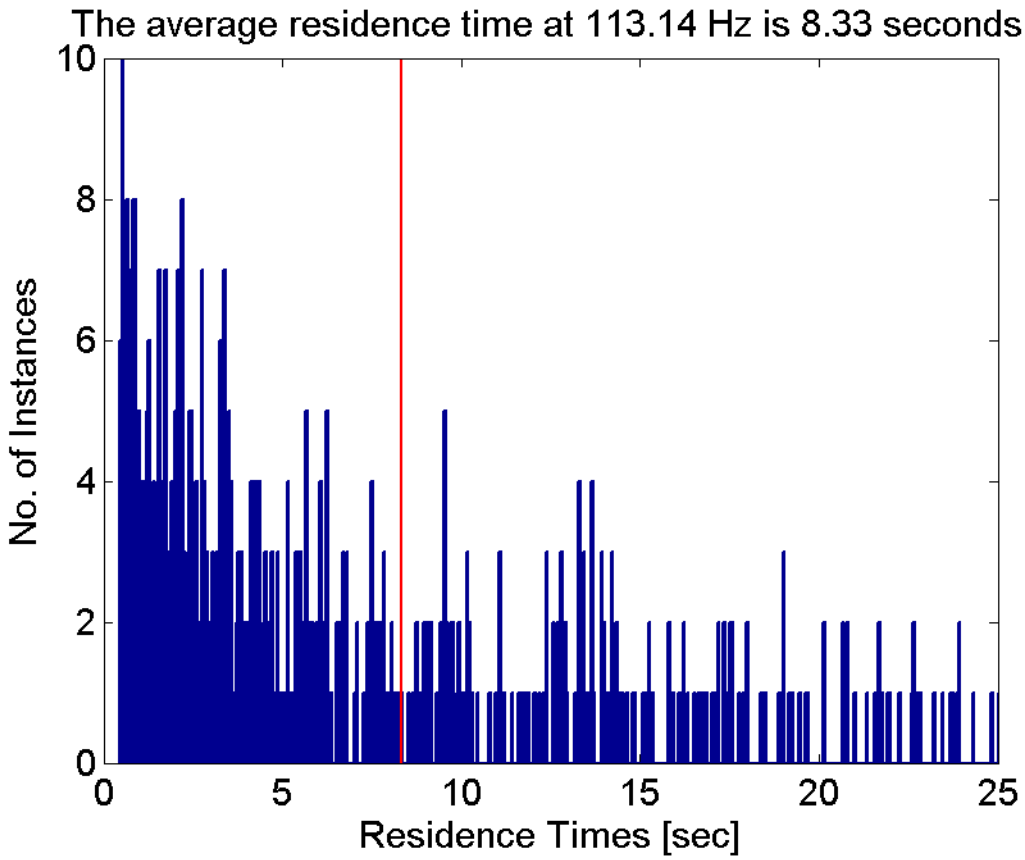

Figure F.283: The residence time distribution for the AR = 0.5 cavity at Re 0.1 at 113.14 Hz. The average residence time is 8.33 secs.

F.3.4 Lagrangian coherent structures at 113.14 Hz

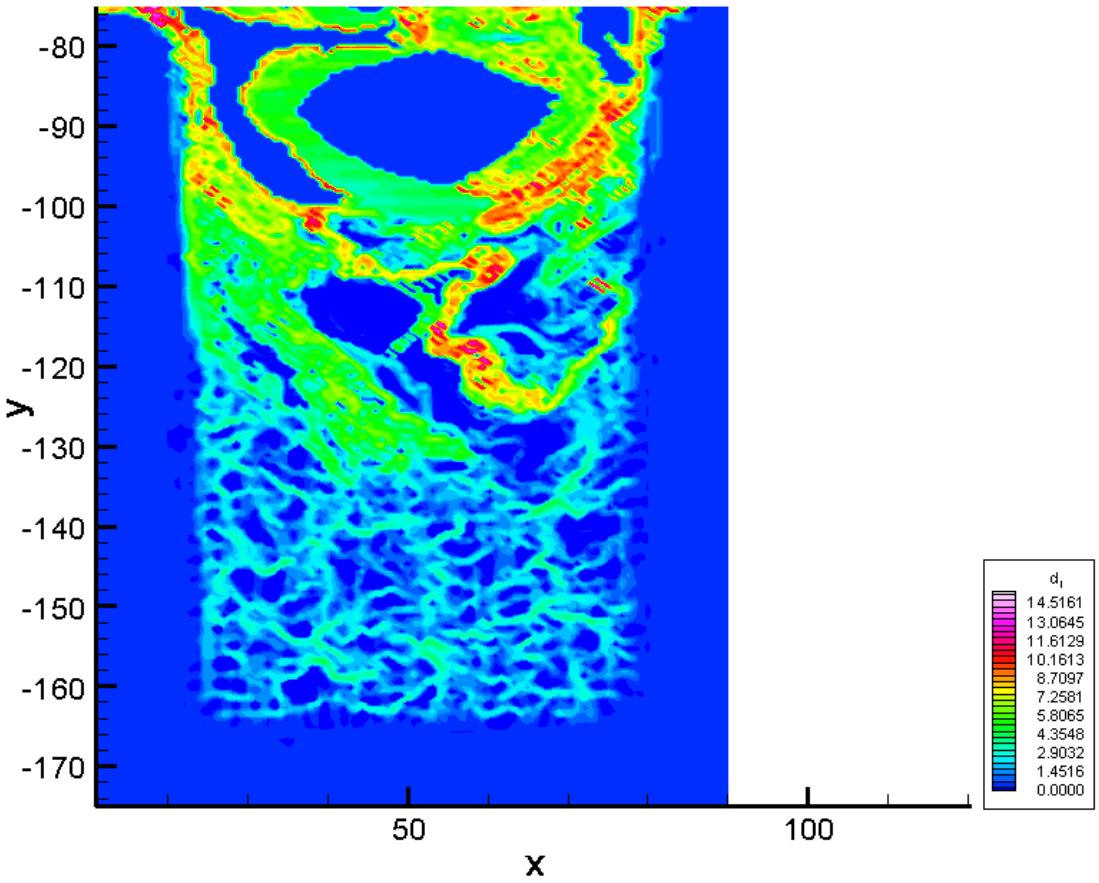

Figure F.284: The backward time LCS during phase increment 1 at 113.14 Hz.

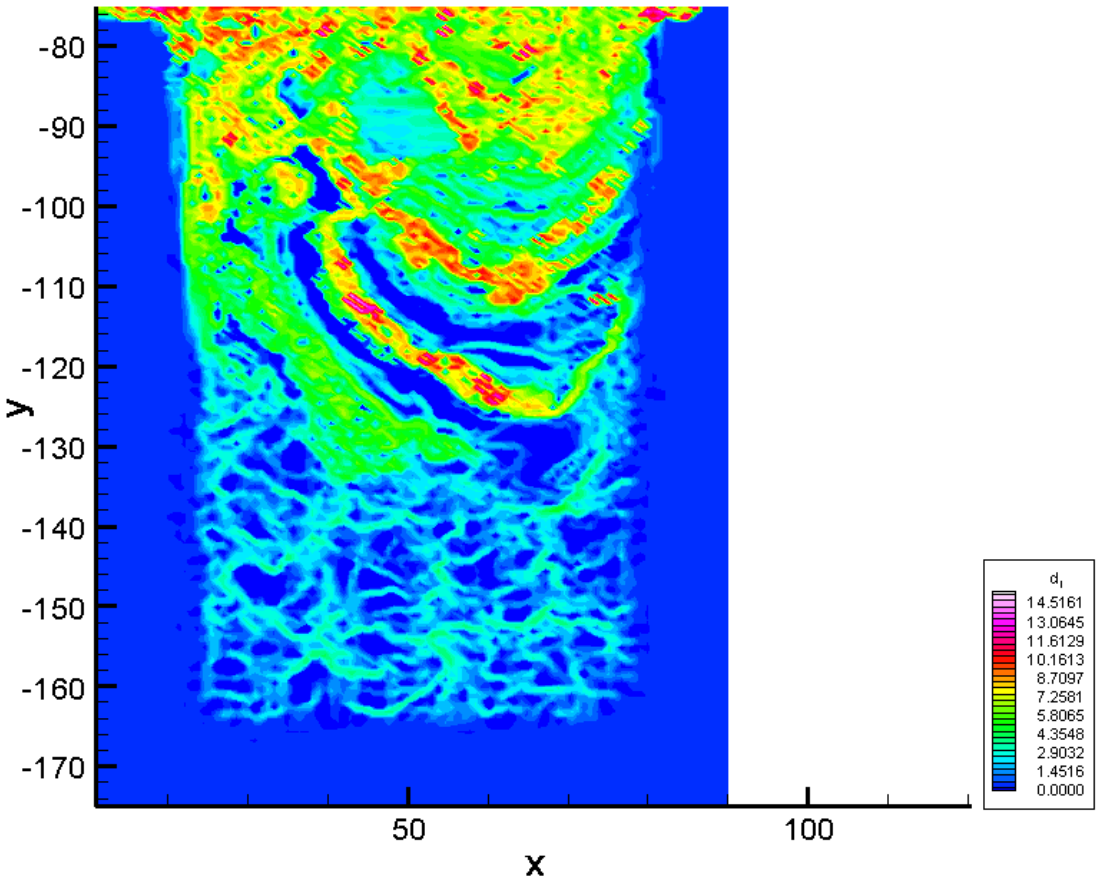

Figure F.285: The backward time LCS during phase increment 2 at 113.14 Hz.

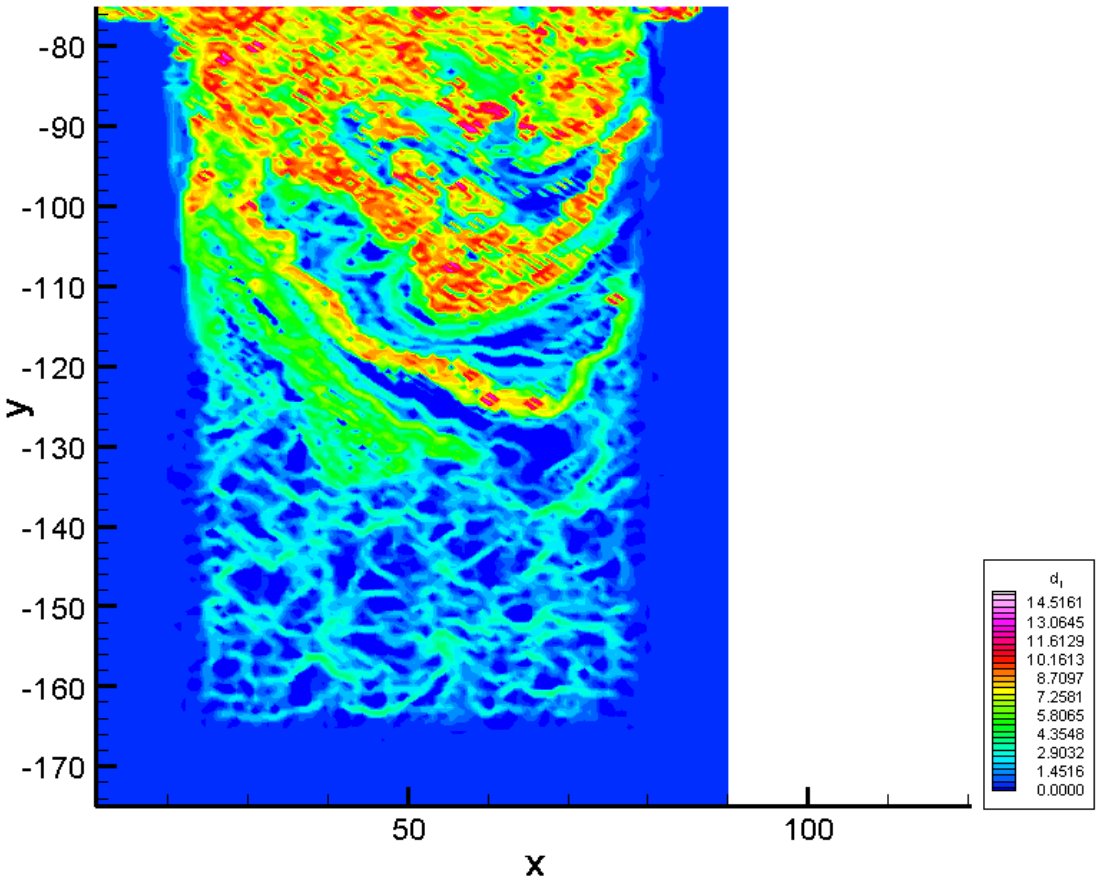

Figure F.286: The backward time LCS during phase increment 3 at 113.14 Hz.

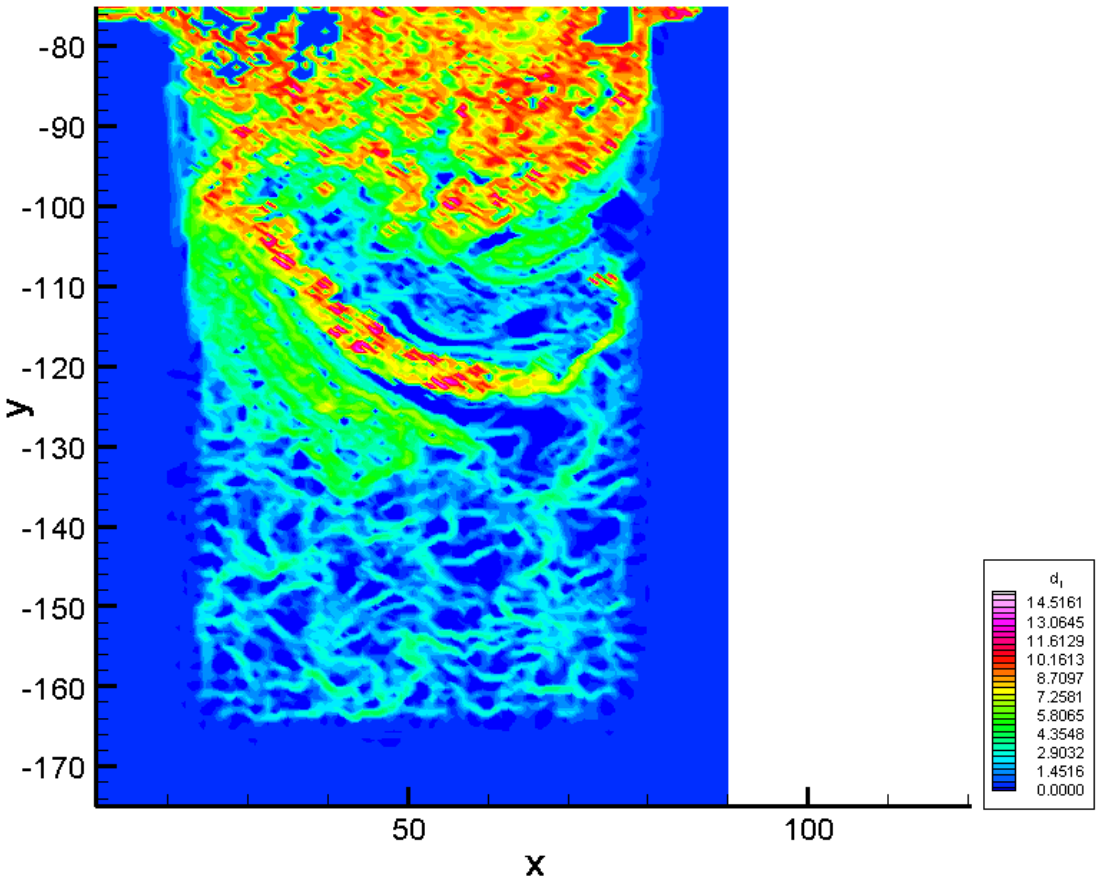

Figure F.287: The backward time LCS during phase increment 4 at 113.14 Hz.

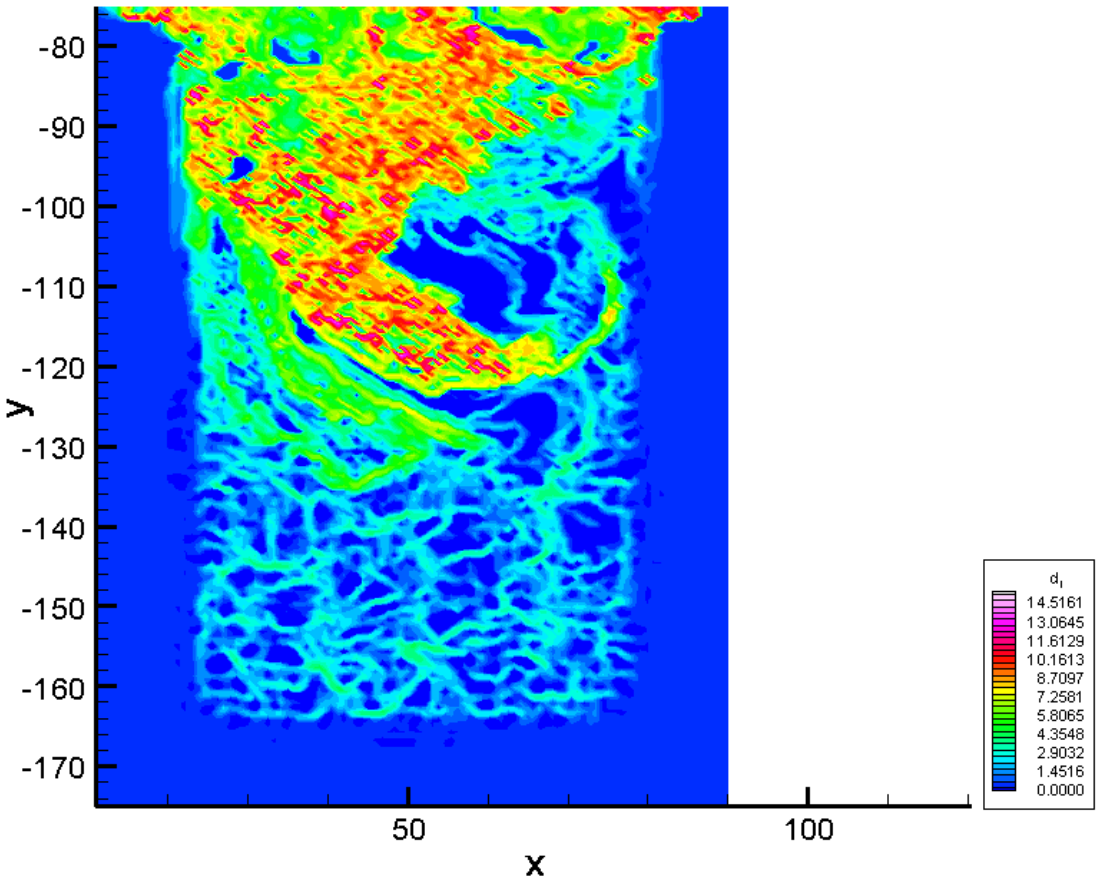

Figure F.288: The backward time LCS during phase increment 5 at 113.14 Hz.

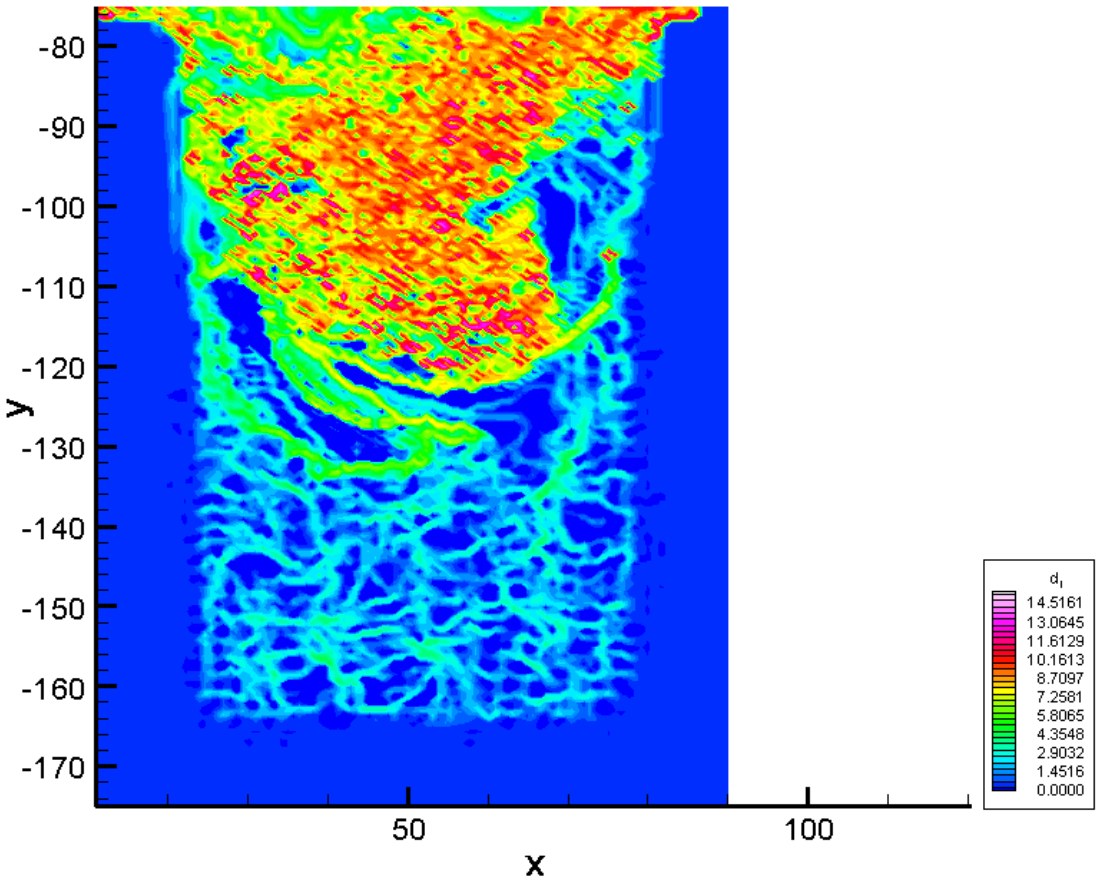

Figure F.289: The backward time LCS during phase increment 6 at 113.14 Hz.

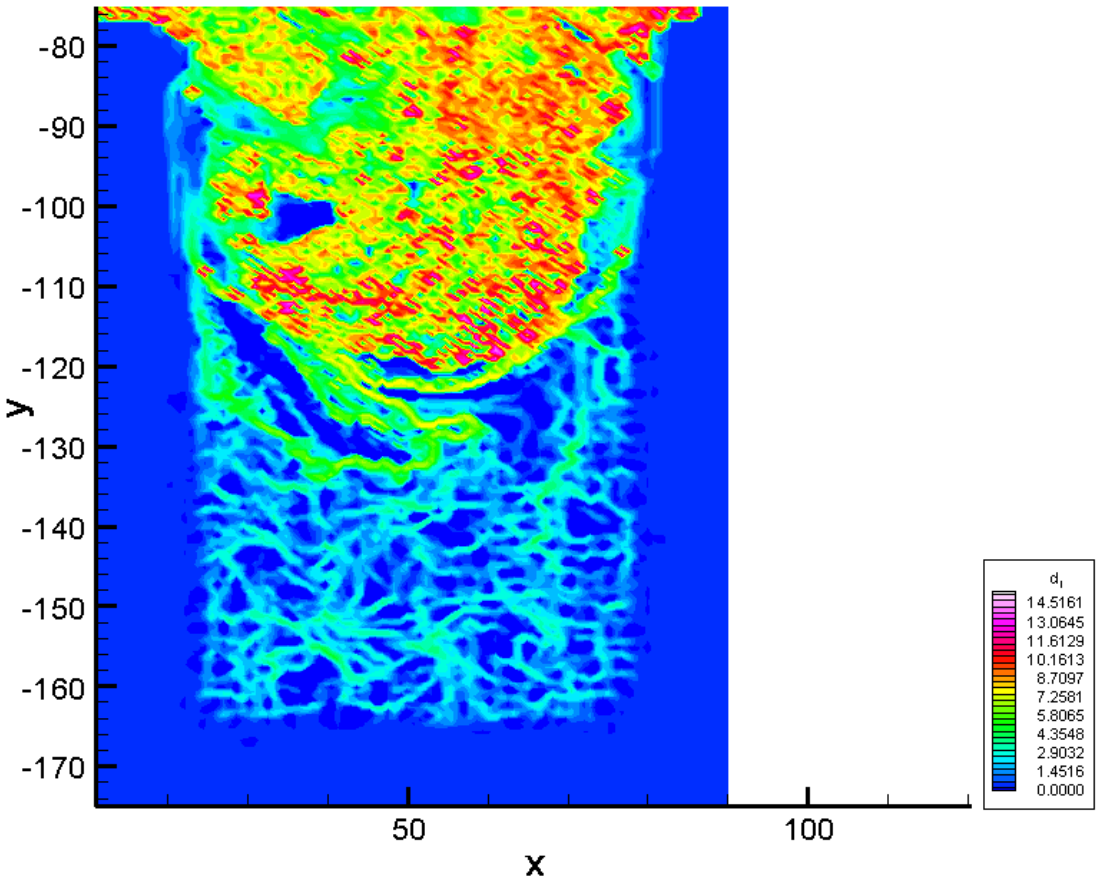

Figure F.290: The backward time LCS during phase increment 7 at 113.14 Hz.

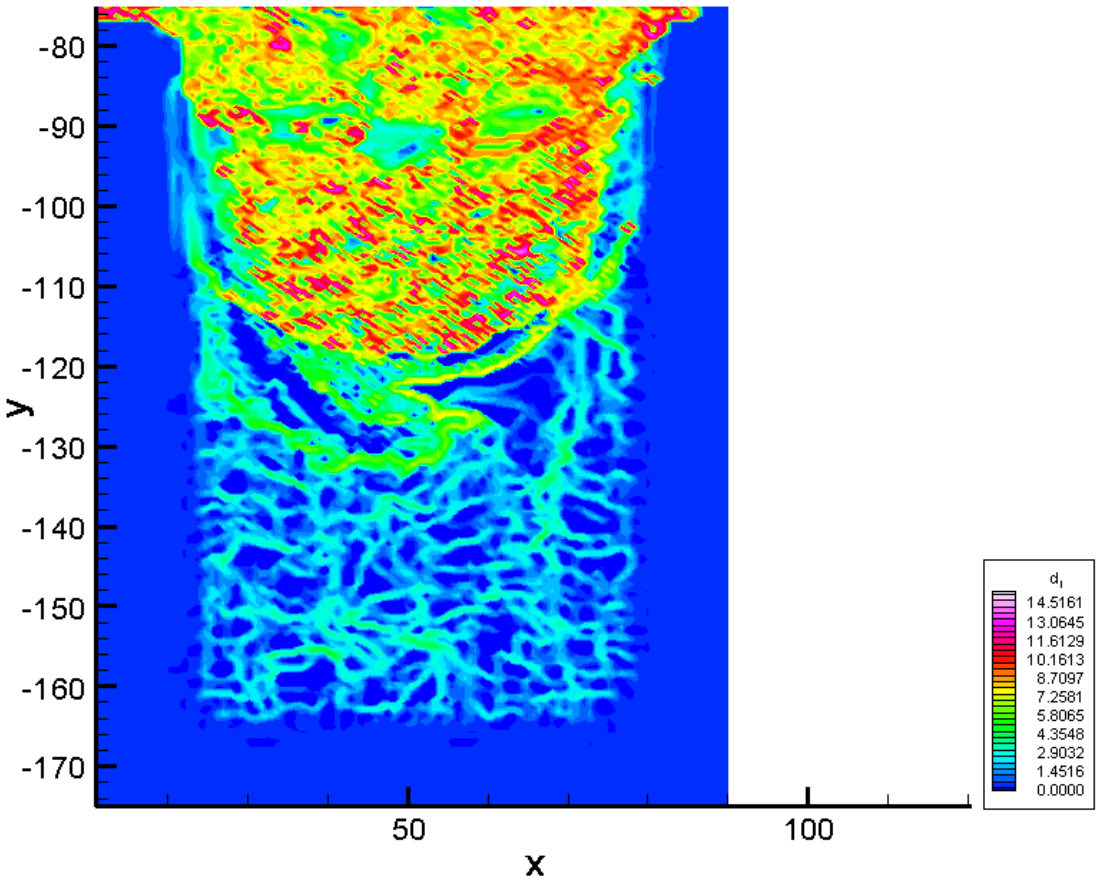

Figure F.291: The backward time LCS during phase increment 8 at 113.14 Hz.

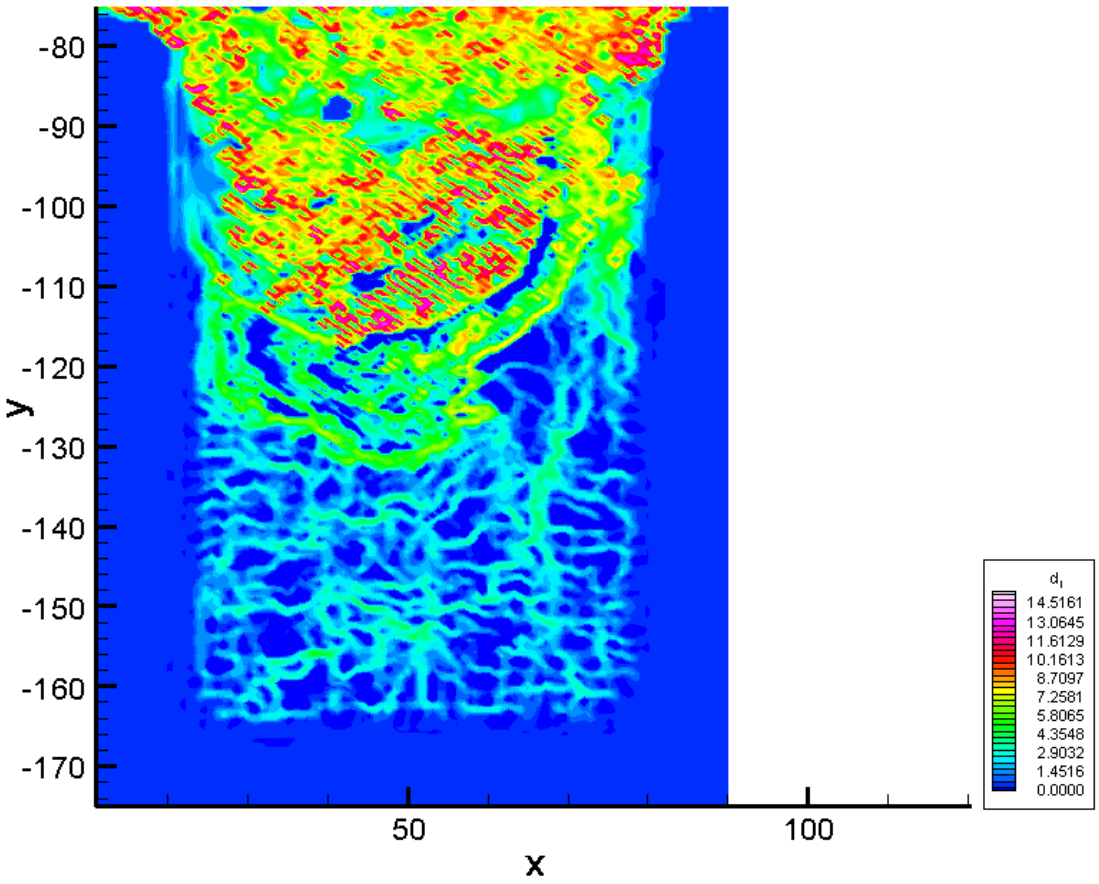

Figure F.292: The backward time LCS during phase increment 9 at 113.14 Hz.

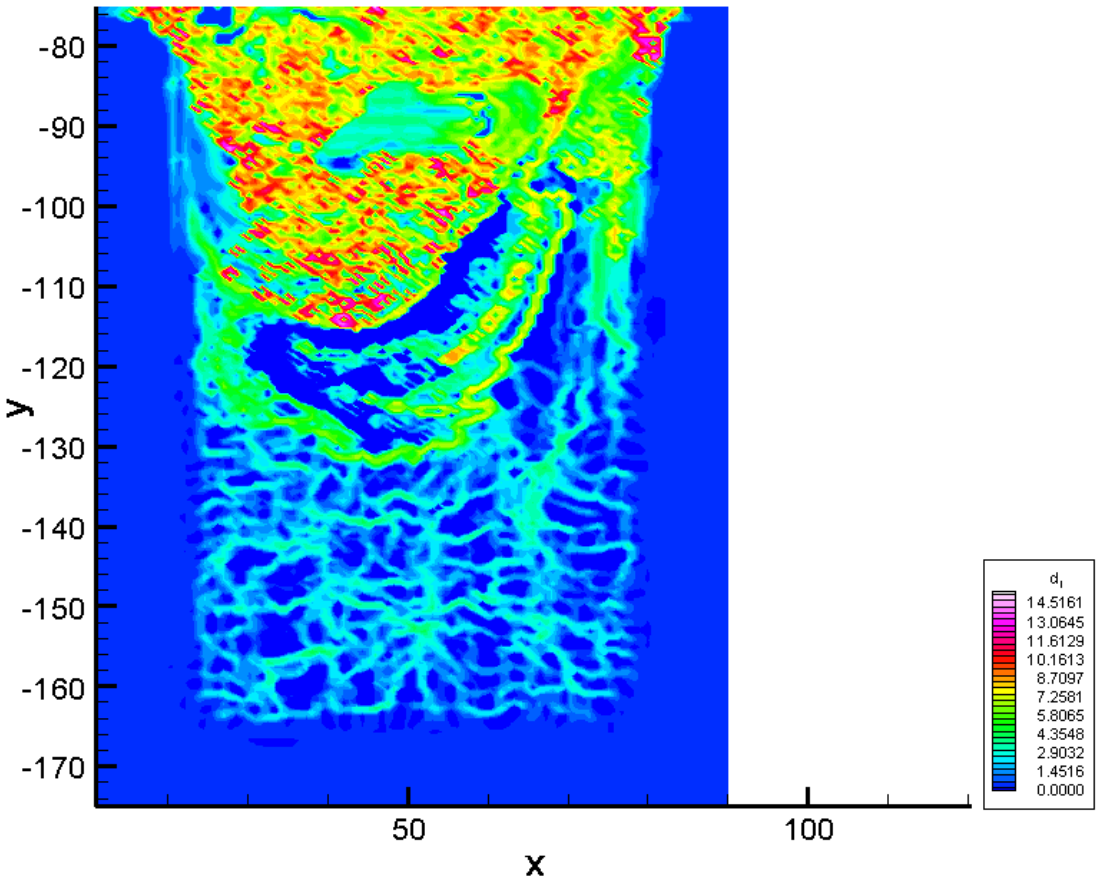

Figure F.293: The backward time LCS during phase increment 10 at 113.14 Hz.

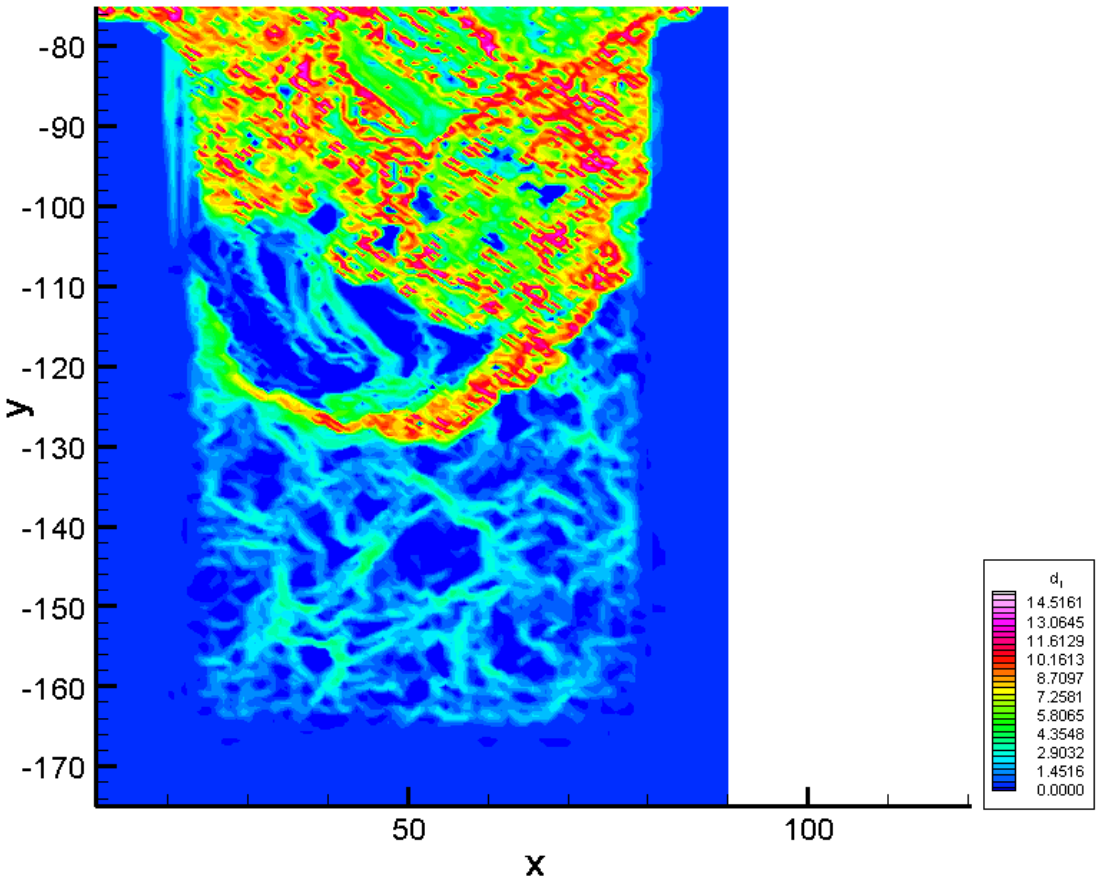

Figure F.294: The forward time LCS during phase increment 1 at 113.14 Hz.

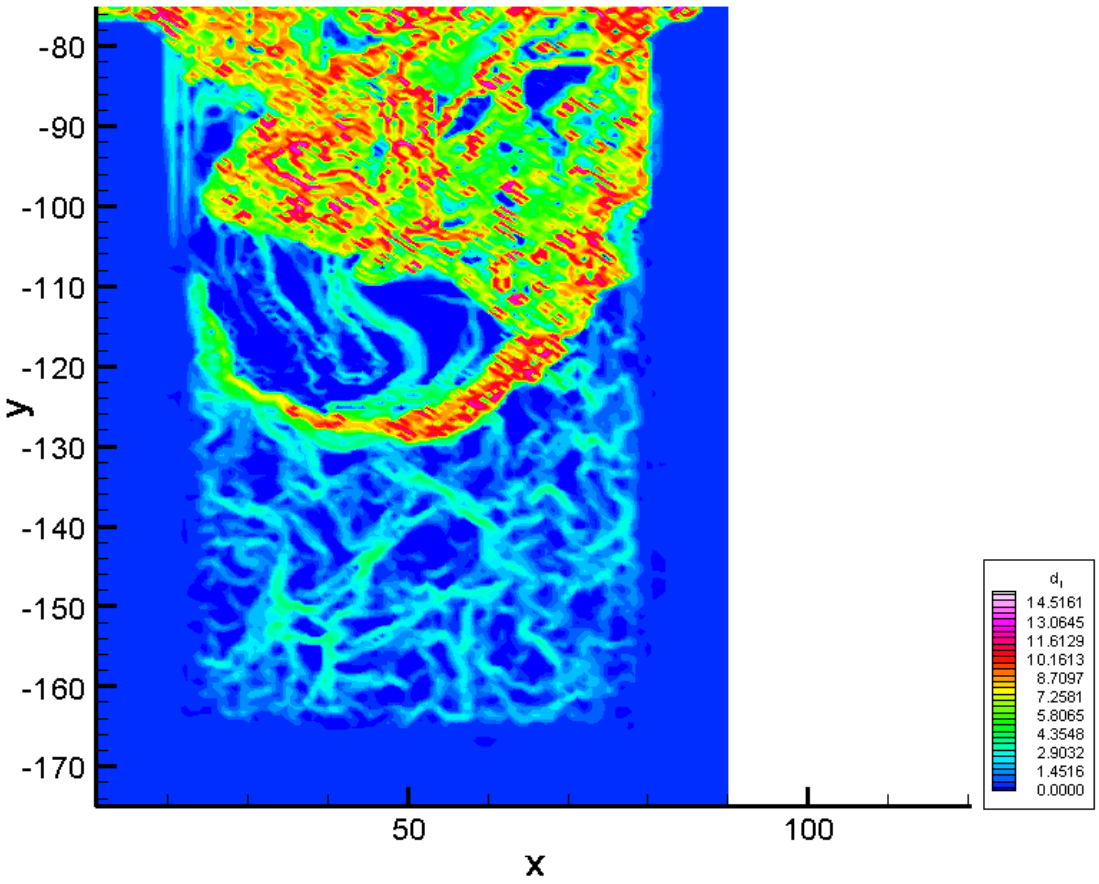

Figure F.295: The forward time LCS during phase increment 2 at 113.14 Hz.

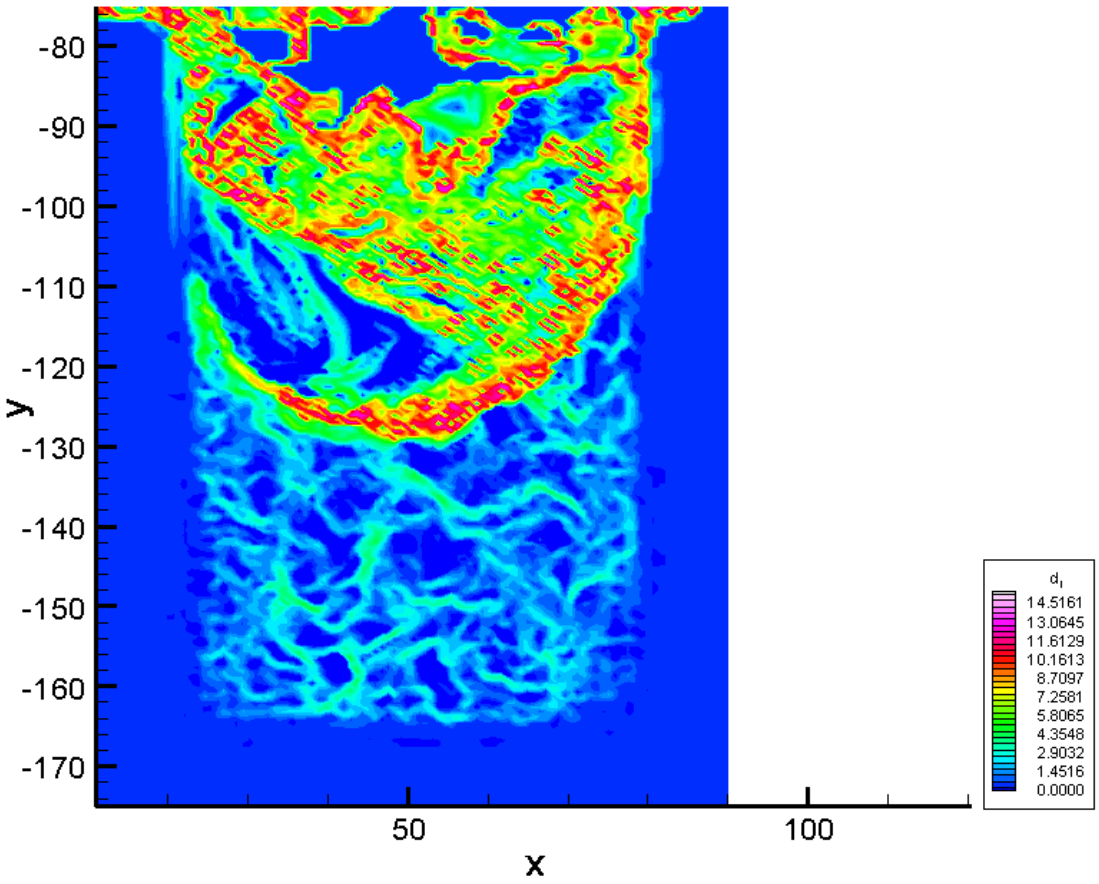

Figure F.296: The forward time LCS during phase increment 3 at 113.14 Hz.

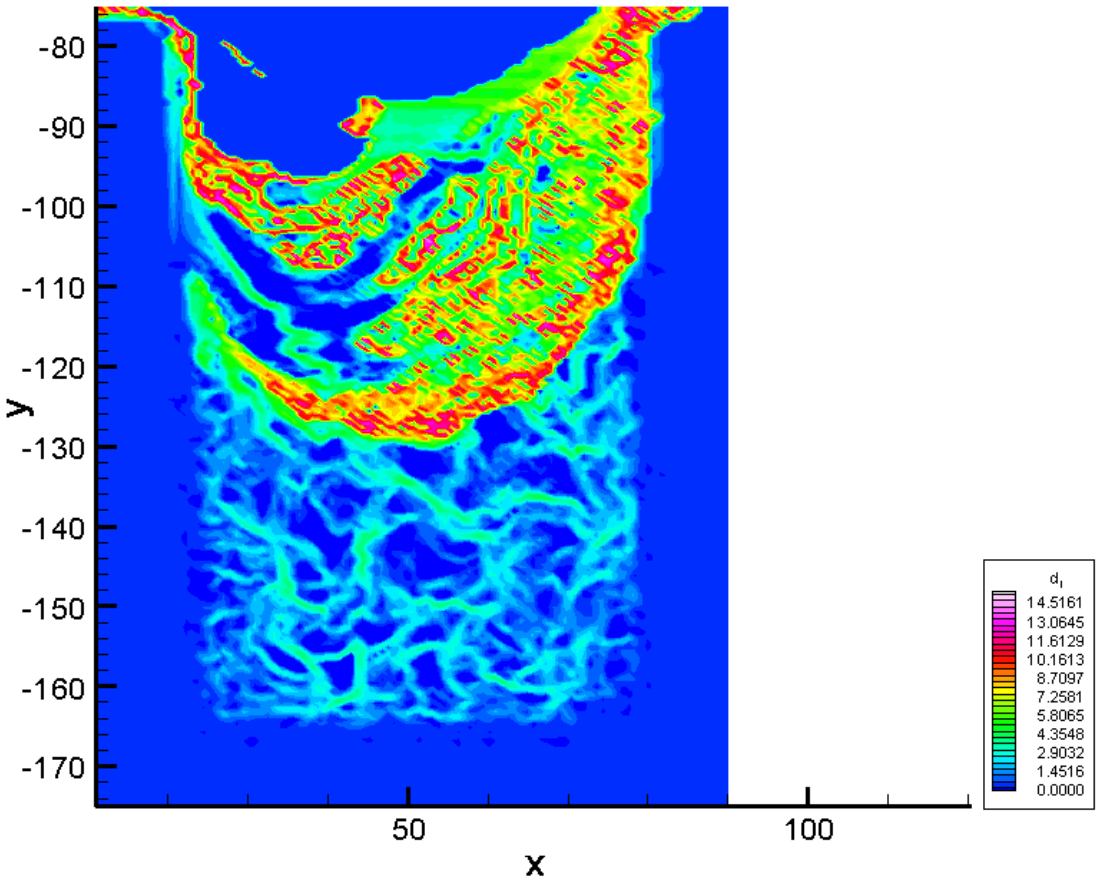

Figure F.297: The forward time LCS during phase increment 4 at 113.14 Hz.

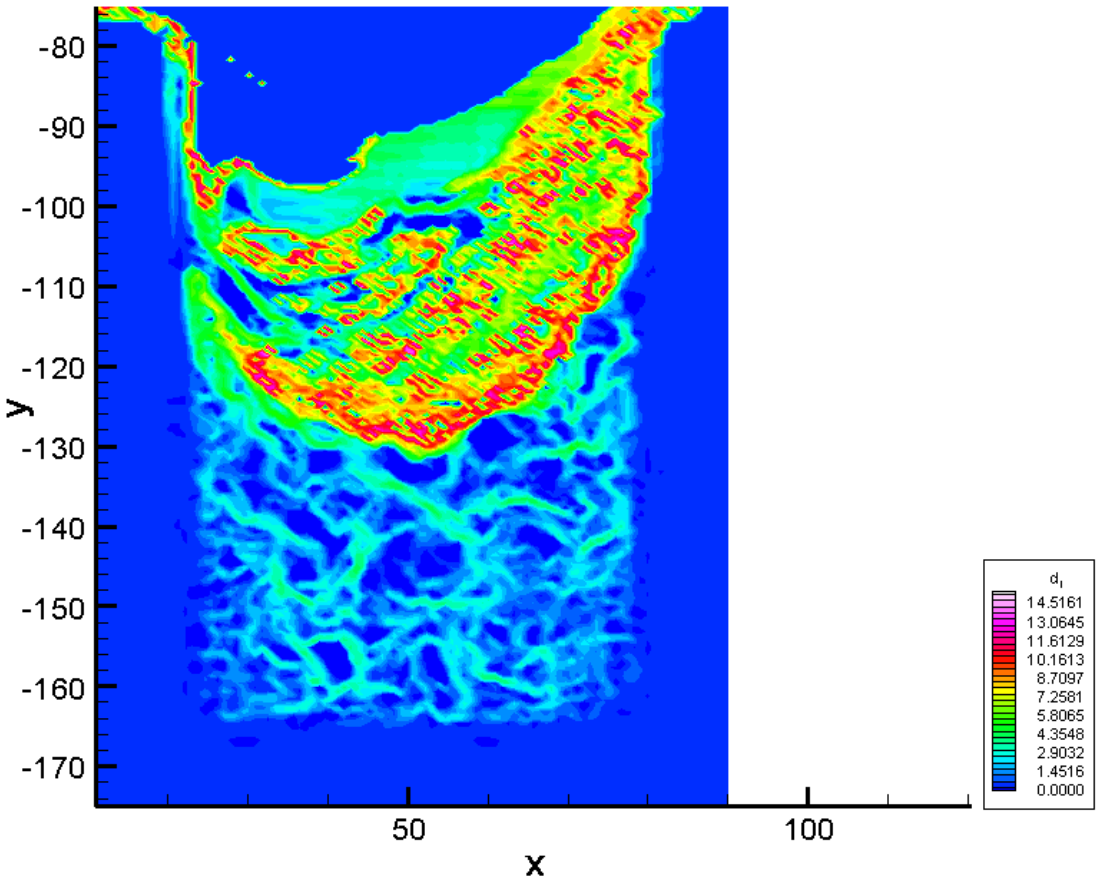

Figure F.298: The forward time LCS during phase increment 5 at 113.14 Hz.

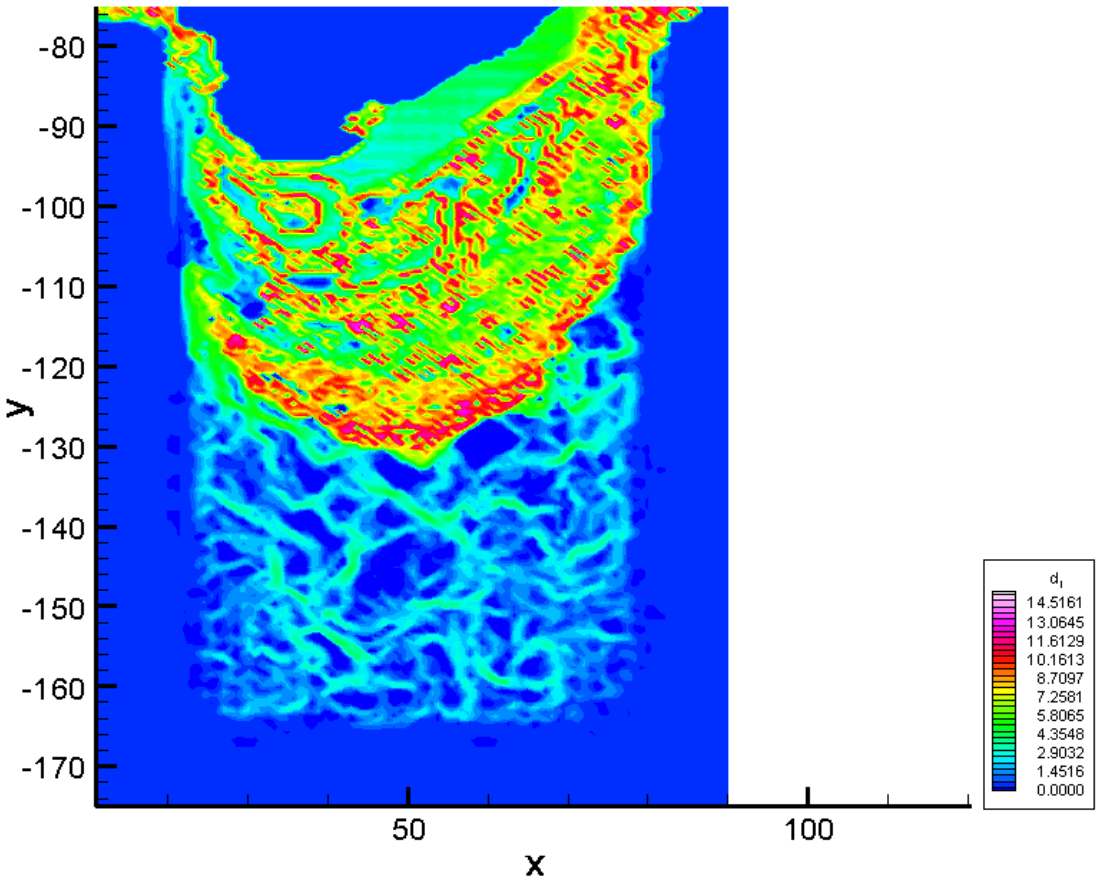

Figure F.299: The forward time LCS during phase increment 6 at 113.14 Hz.

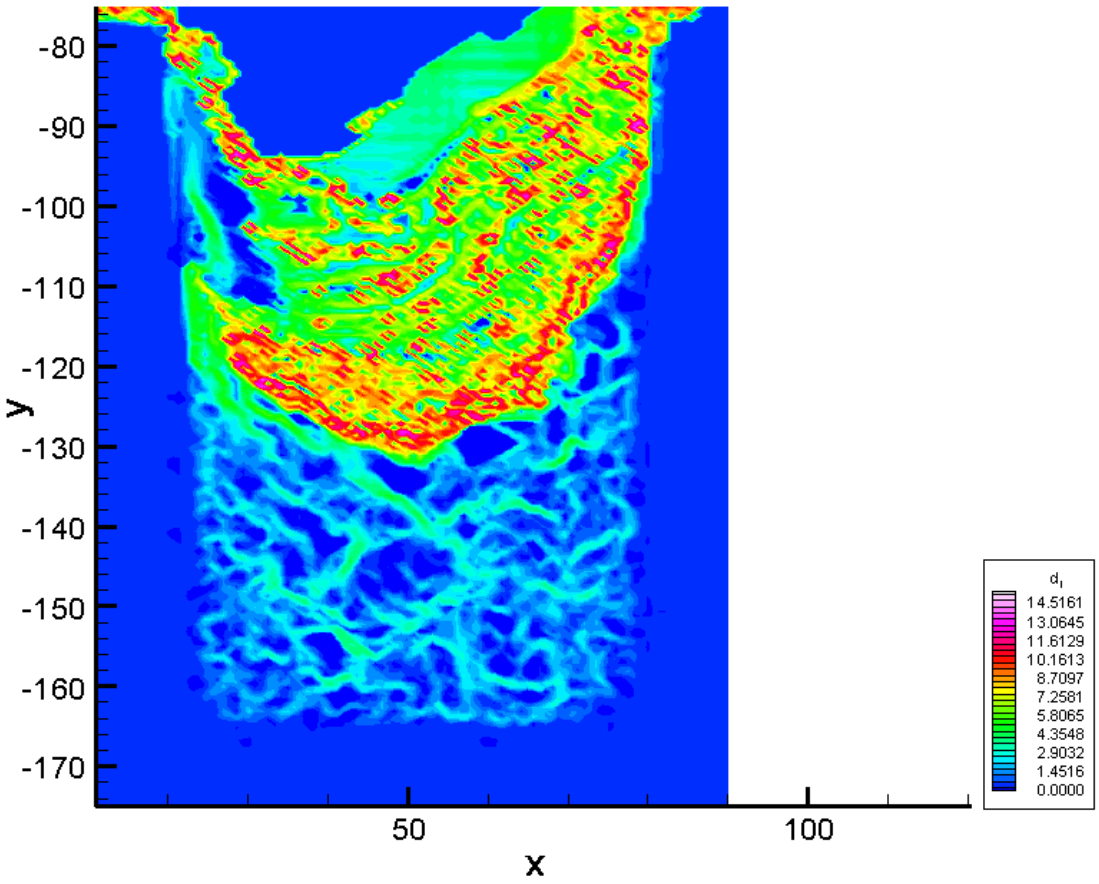

Figure F.300: The forward time LCS during phase increment 7 at 113.14 Hz.

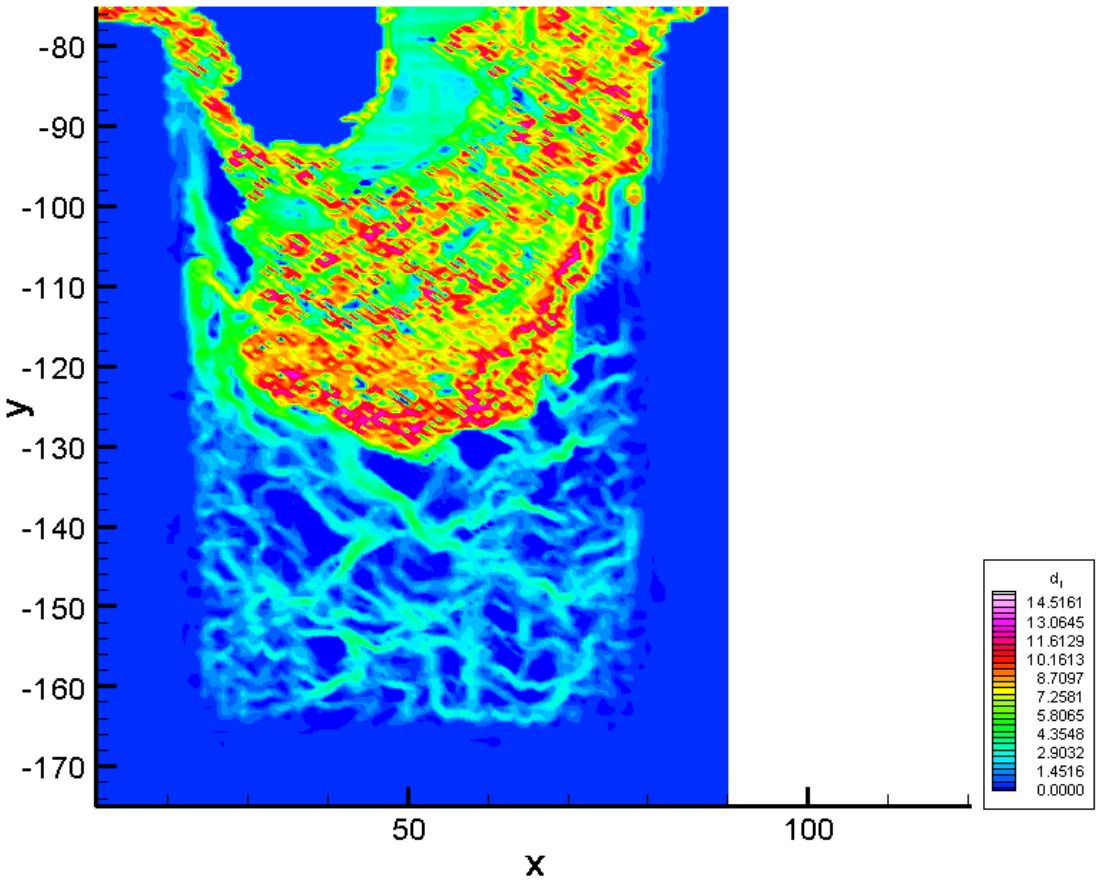

Figure F.301: The forward time LCS during phase increment 8 at 113.14 Hz.

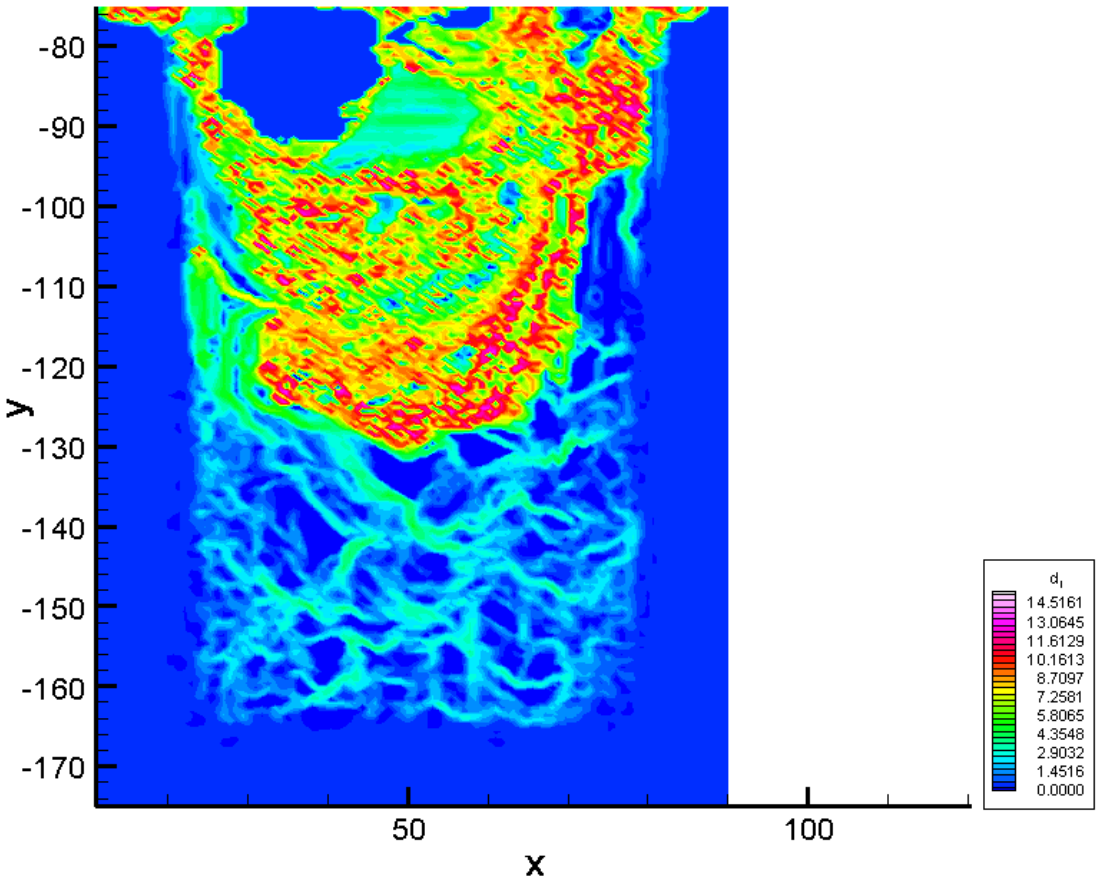

Figure F.302: The forward time LCS during phase increment 9 at 113.14 Hz.

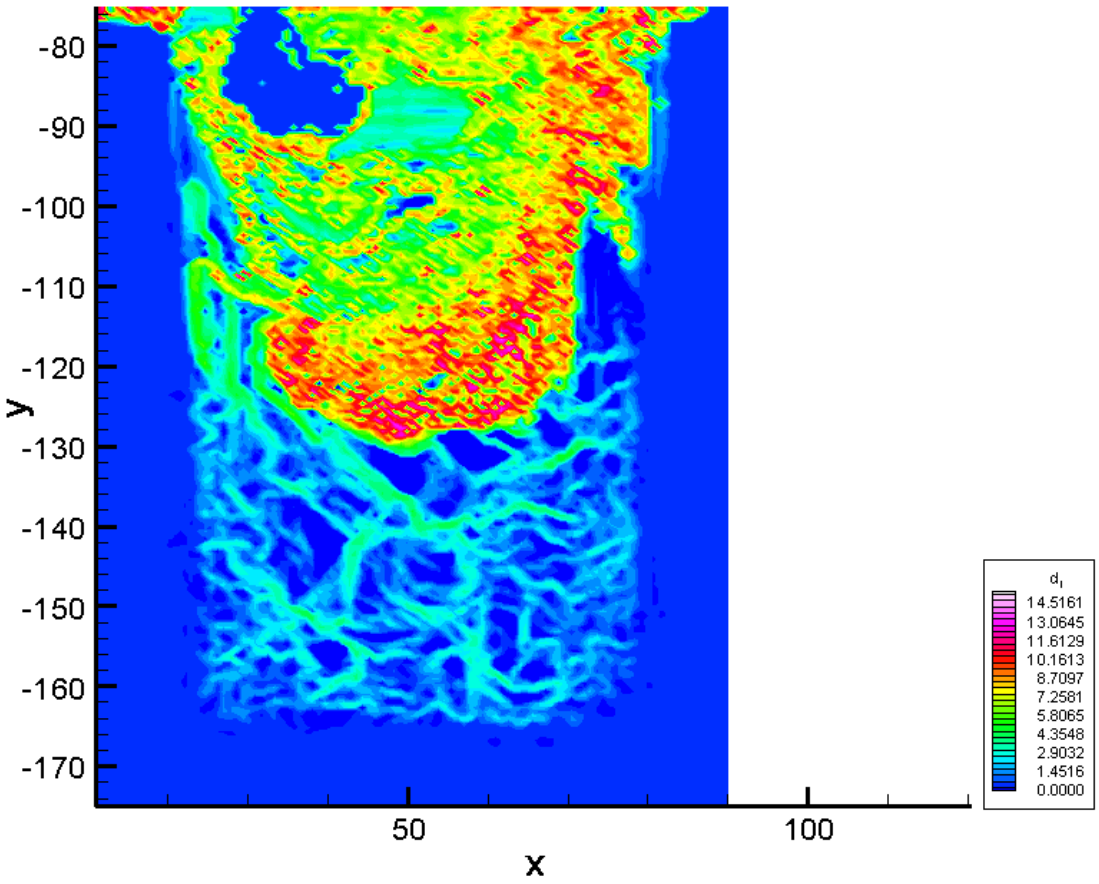

Figure F.303: The forward time LCS during phase increment 10 at 113.14 Hz.

F.4 113.14 Hz with an amplitude of 0.2 mm

F.4.1 Velocity field data at 113.14 Hz with an amplitude of 0.2 mm

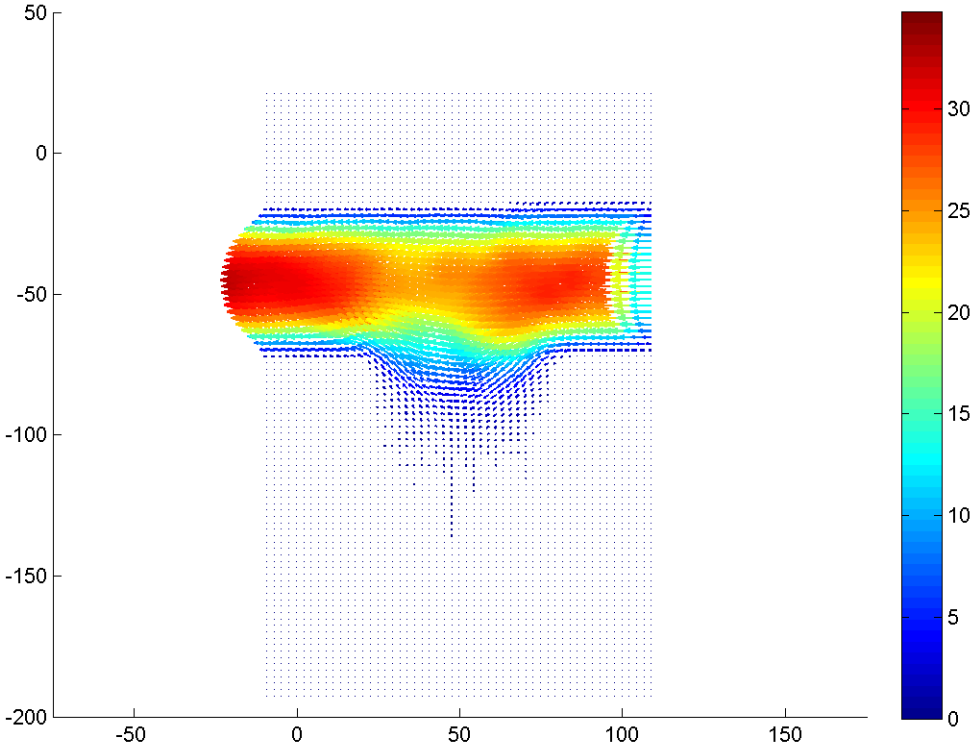

Figure F.304: Velocity field during phase increment 1 at 113.14 Hz with an amplitude of 0.2 mm and a Re of 0.1.

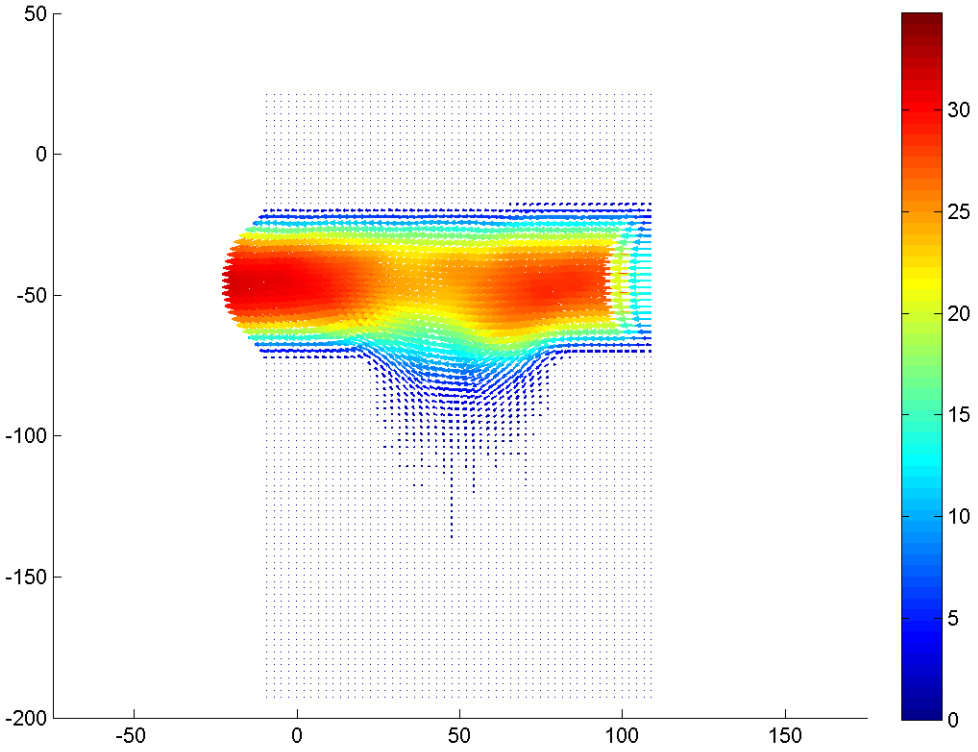

Figure F.305: Velocity field during phase increment 2 at 113.14 Hz with an amplitude of 0.2 mm and a Re of 0.1.

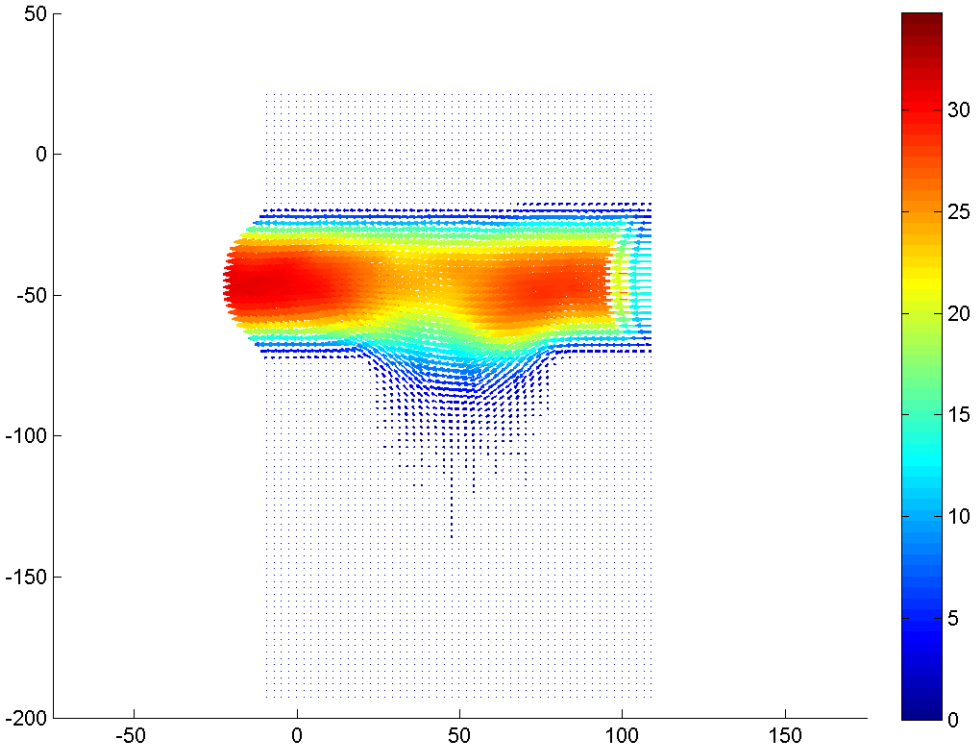

Figure F.306: Velocity field during phase increment 3 at 113.14 Hz with an amplitude of 0.2 mm and a Re of 0.1.

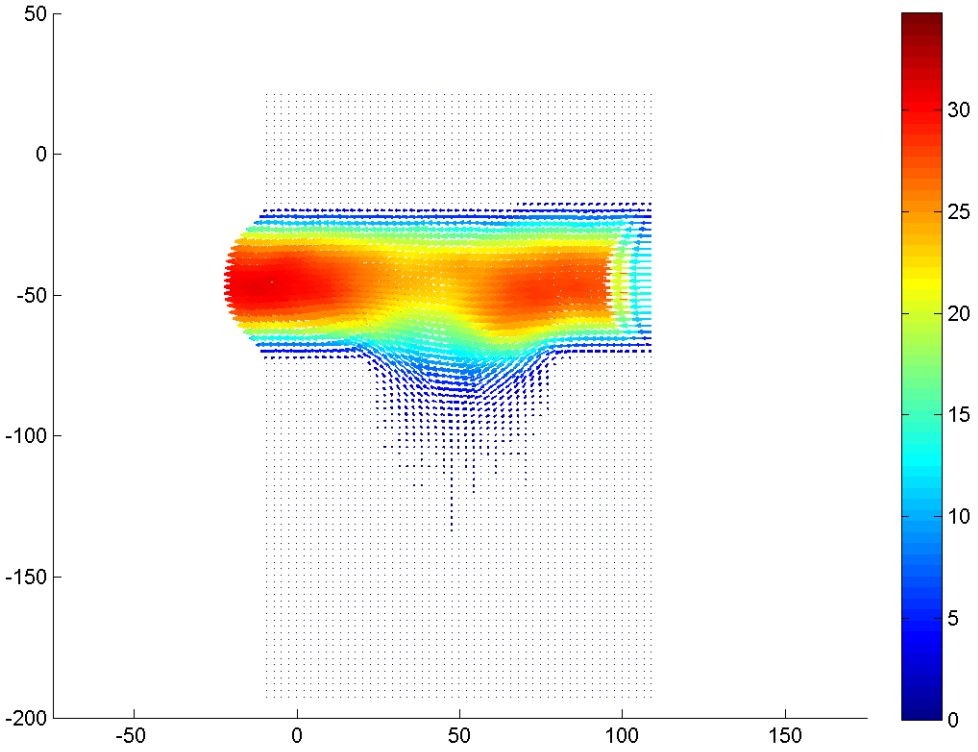

Figure F.307: Velocity field during phase increment 4 at 113.14 Hz with an amplitude of 0.2 mm and a Re of 0.1.

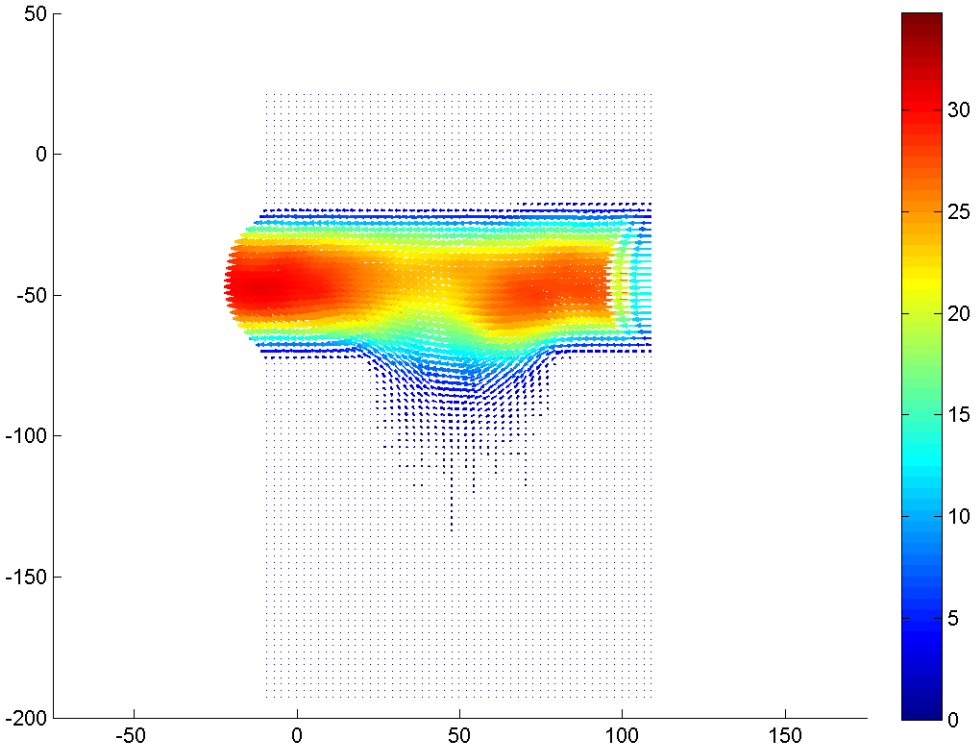

Figure F.308: Velocity field during phase increment 5 at 113.14 Hz with an amplitude of 0.2 mm and a Re of 0.1.

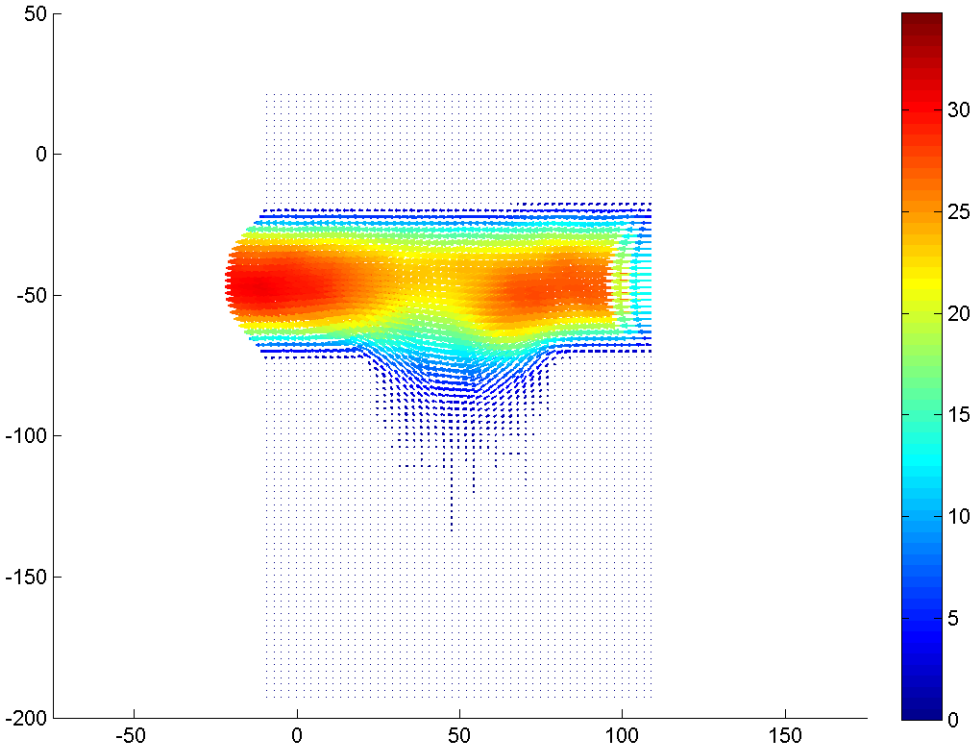

Figure F.309: Velocity field during phase increment 6 at 113.14 Hz with an amplitude of 0.2 mm and a Re of 0.1.

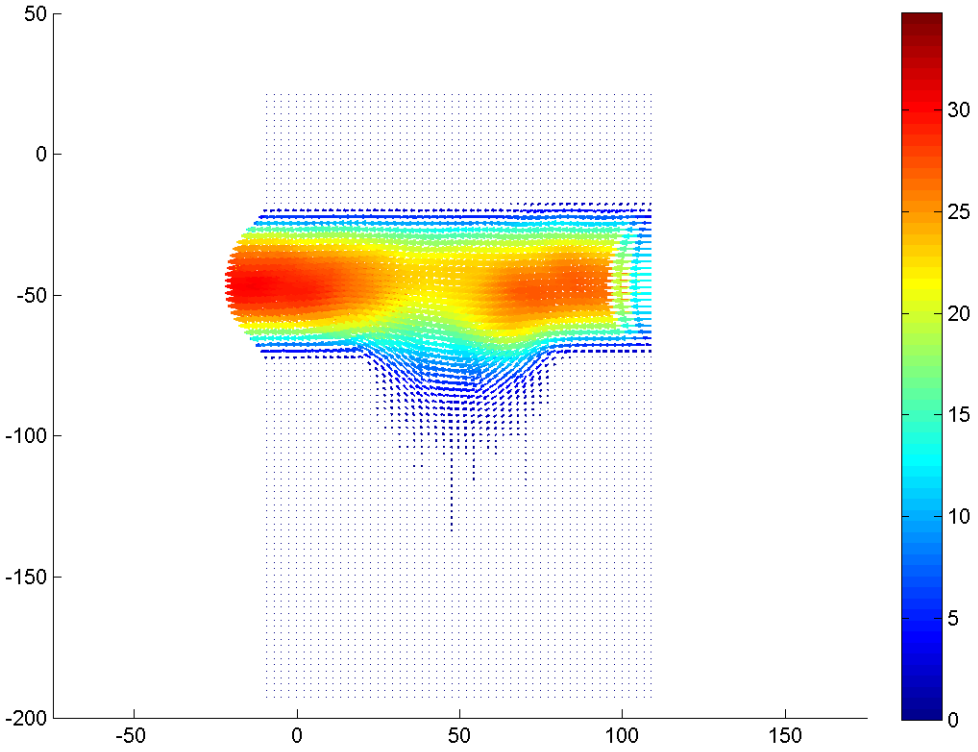

Figure F.310: Velocity field during phase increment 7 at 113.14 Hz with an amplitude of 0.2 mm and a Re of 0.1.

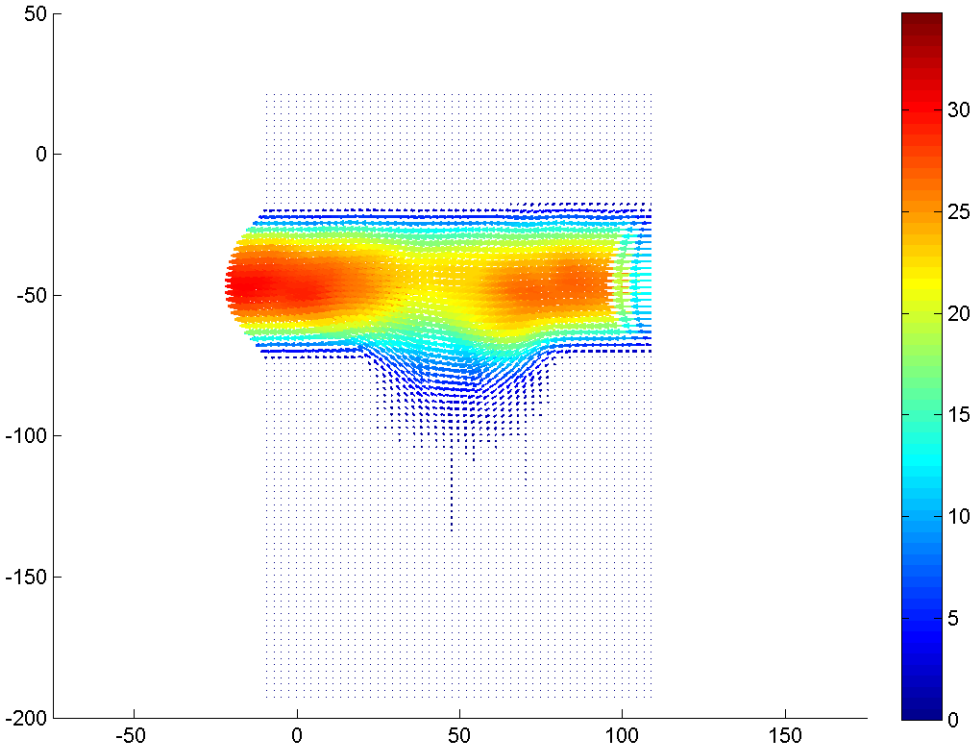

Figure F.311: Velocity field during phase increment 8 at 113.14 Hz with an amplitude of 0.2 mm and a Re of 0.1.

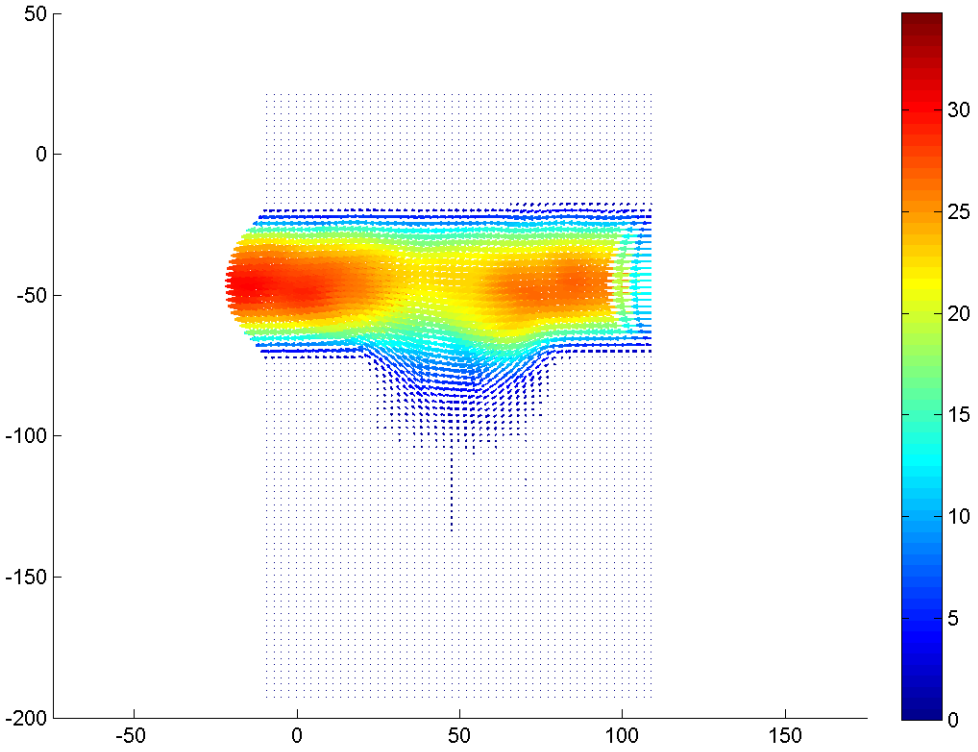

Figure F.312: Velocity field during phase increment 9 at 113.14 Hz with an amplitude of 0.2 mm and a Re of 0.1.

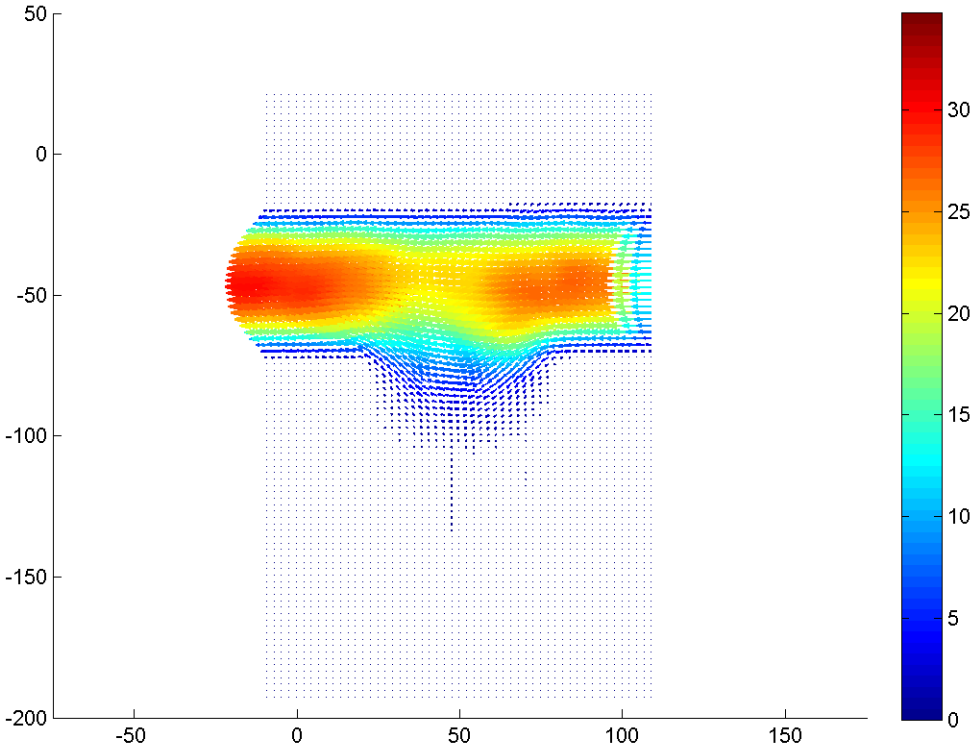

Figure F.313: Velocity field during phase increment 10 at 113.14 Hz with an amplitude of 0.2 mm and a Re of 0.1.

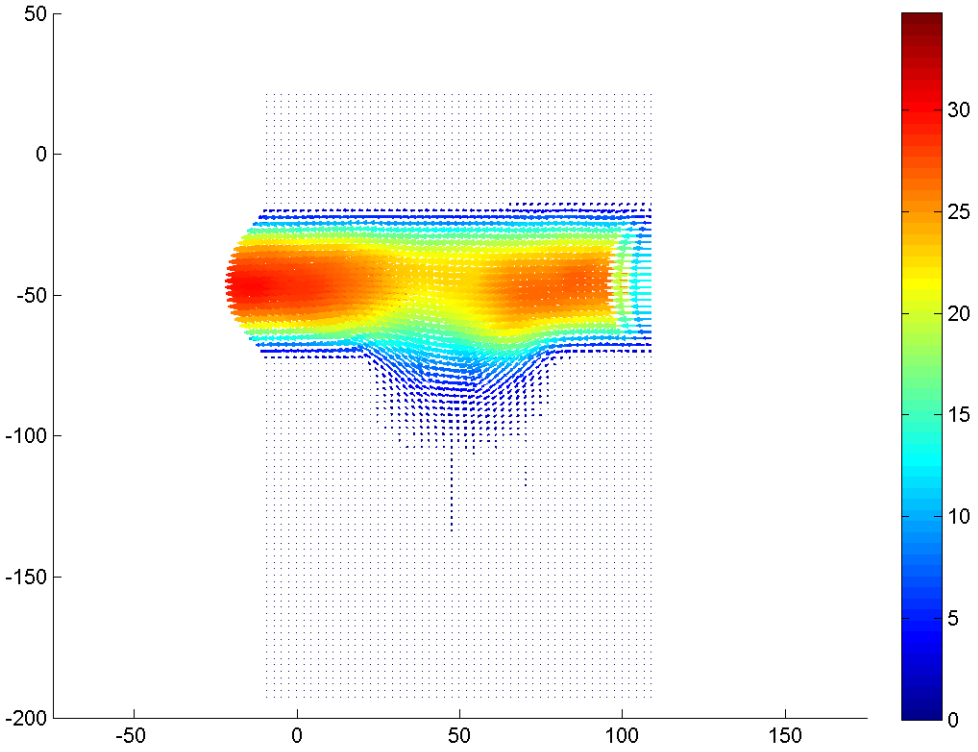

Figure F.314: Velocity field during phase increment 11 at 113.14 Hz with an amplitude of 0.2 mm and a Re of 0.1.

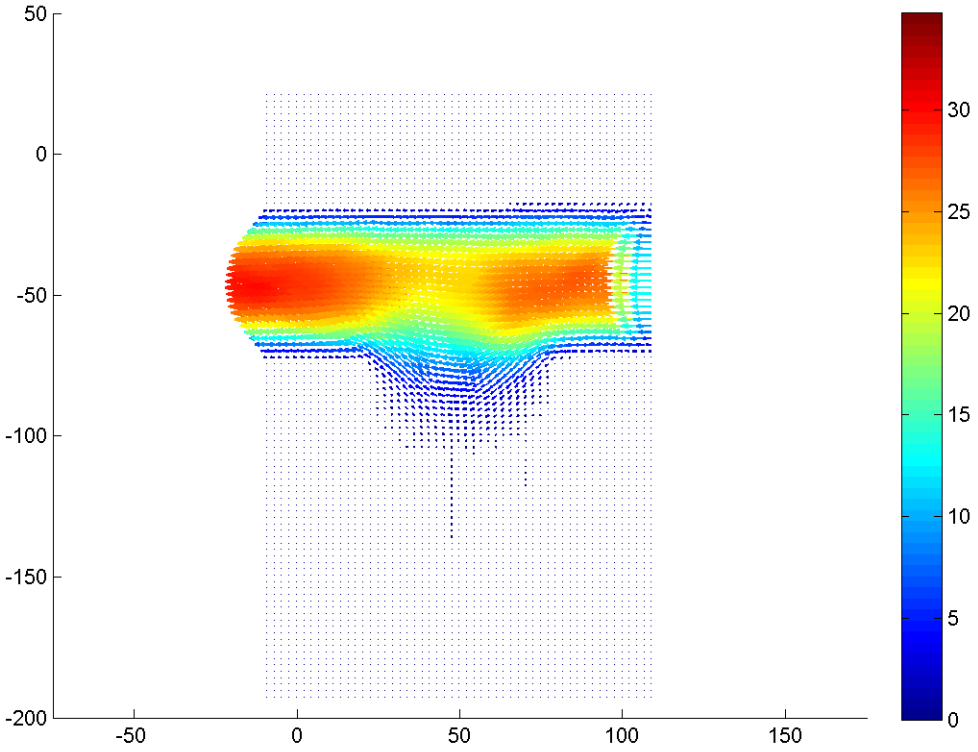

Figure F.315: Velocity field during phase increment 12 at 113.14 Hz with an amplitude of 0.2 mm and a Re of 0.1.

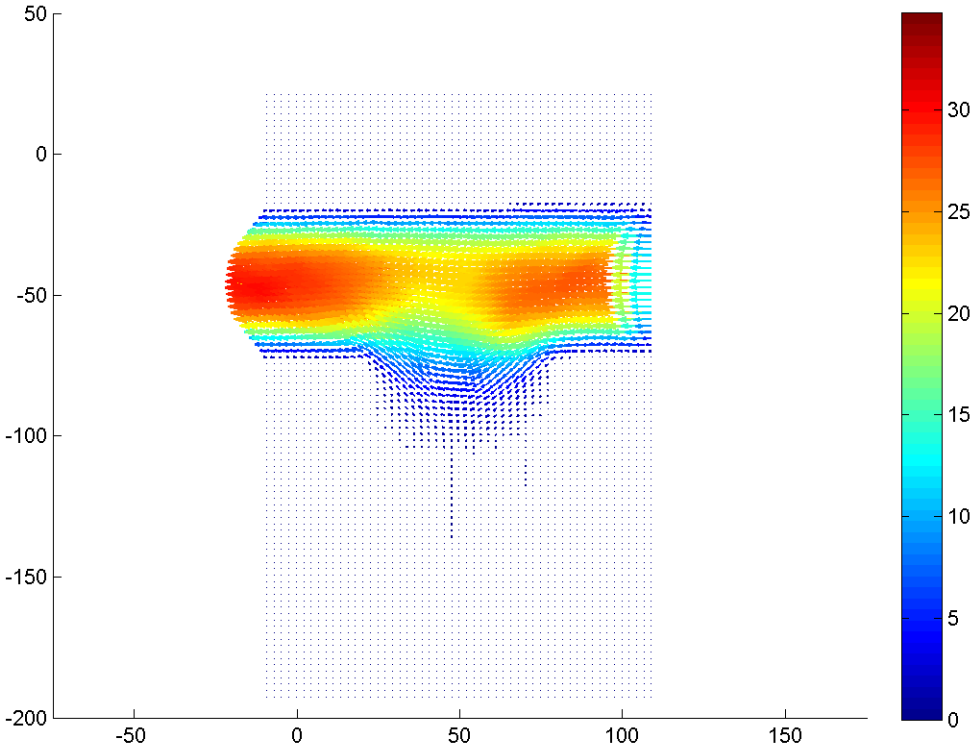

Figure F.316: Velocity field during phase increment 13 at 113.14 Hz with an amplitude of 0.2 mm and a Re of 0.1.

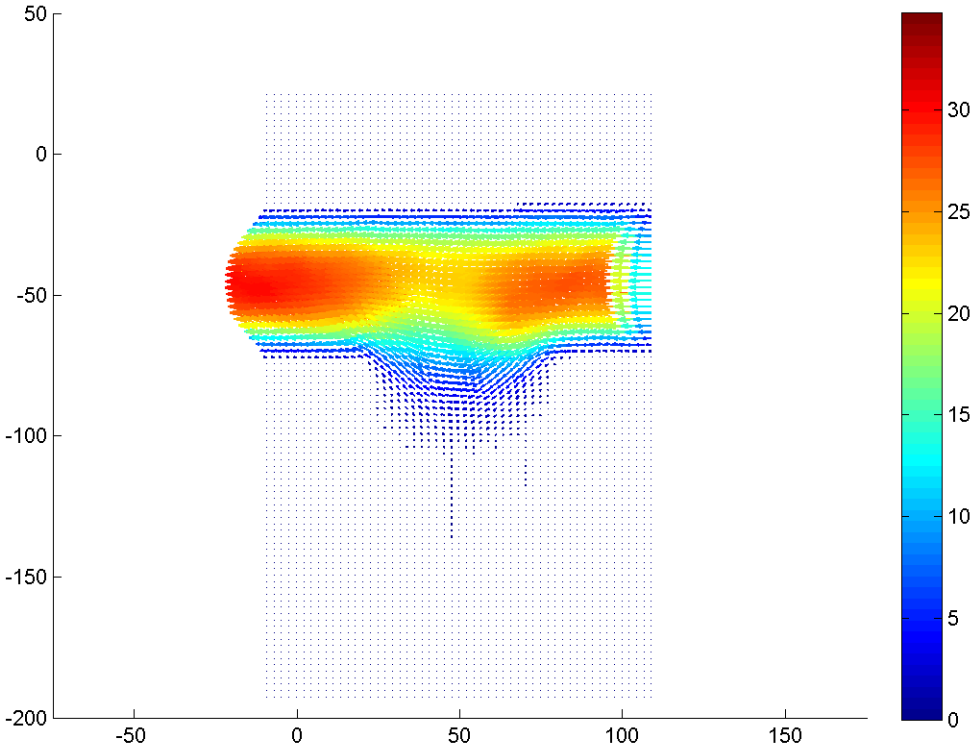

Figure F.317: Velocity field during phase increment 14 at 113.14 Hz with an amplitude of 0.2 mm and a Re of 0.1.

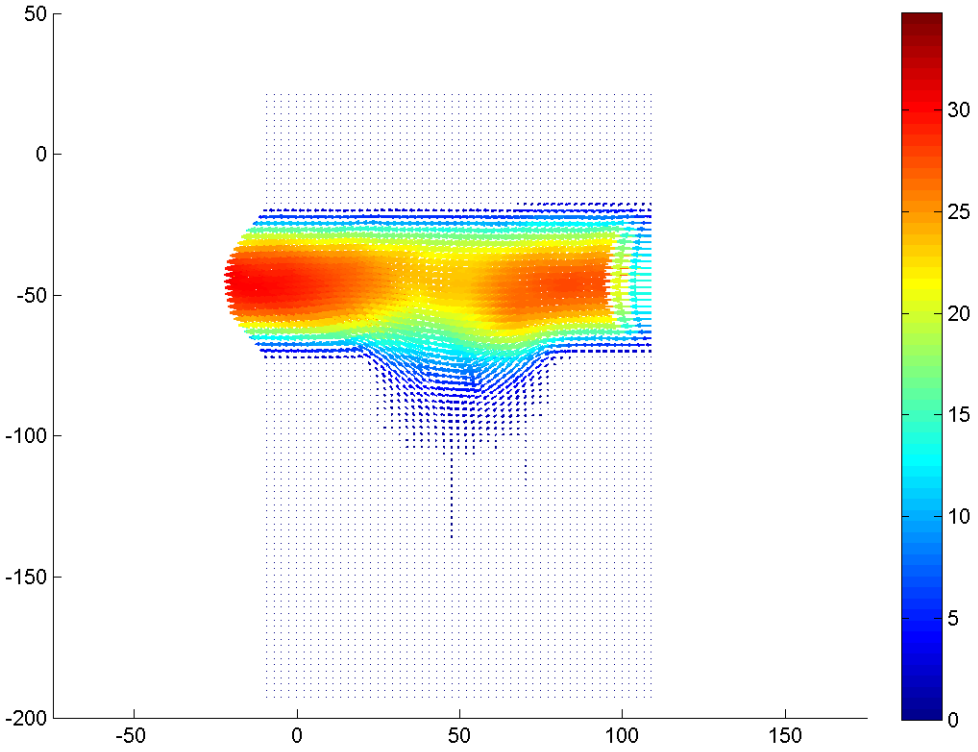

Figure F.318: Velocity field during phase increment 15 at 113.14 Hz with an amplitude of 0.2 mm and a Re of 0.1.

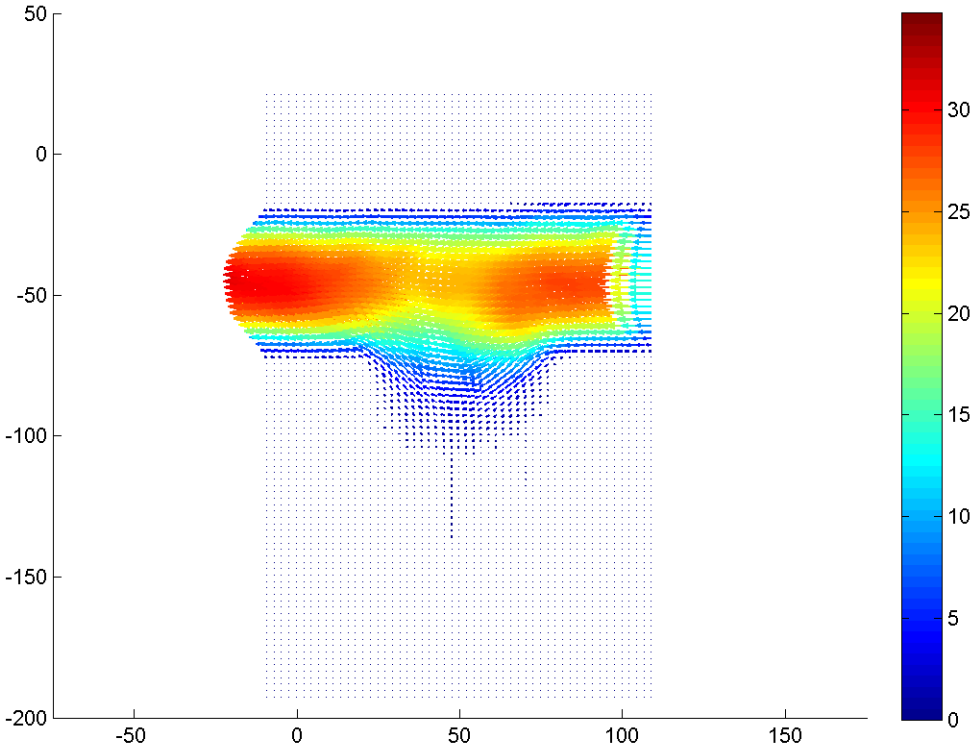

Figure F.319: Velocity field during phase increment 16 at 113.14 Hz with an amplitude of 0.2 mm and a Re of 0.1.

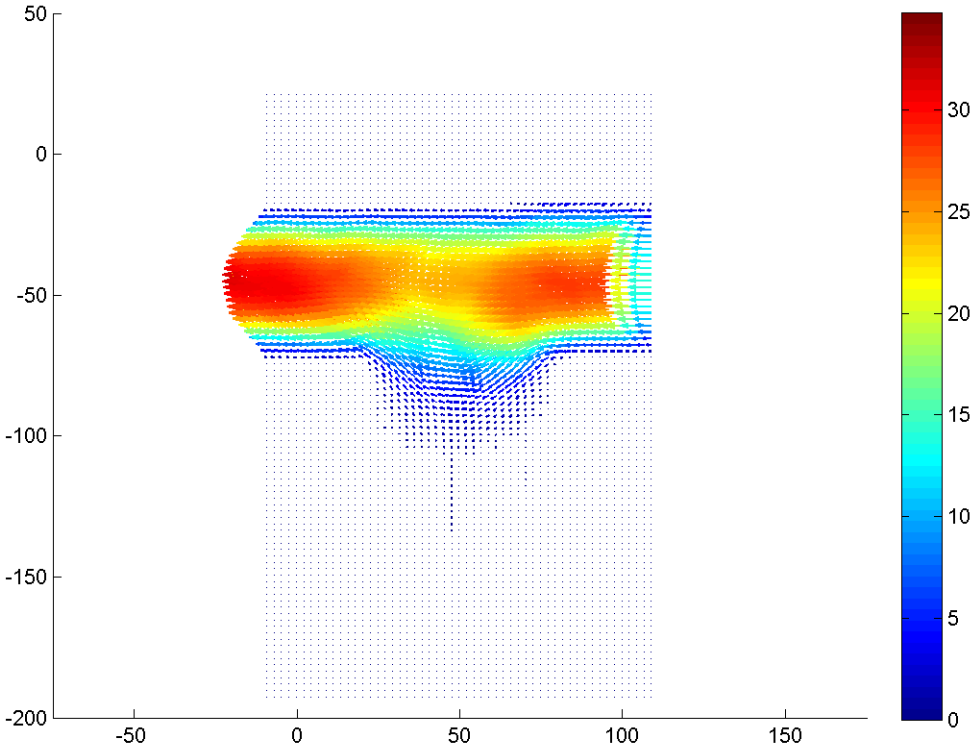

Figure F.320: Velocity field during phase increment 17 at 113.14 Hz with an amplitude of 0.2 mm and a Re of 0.1.

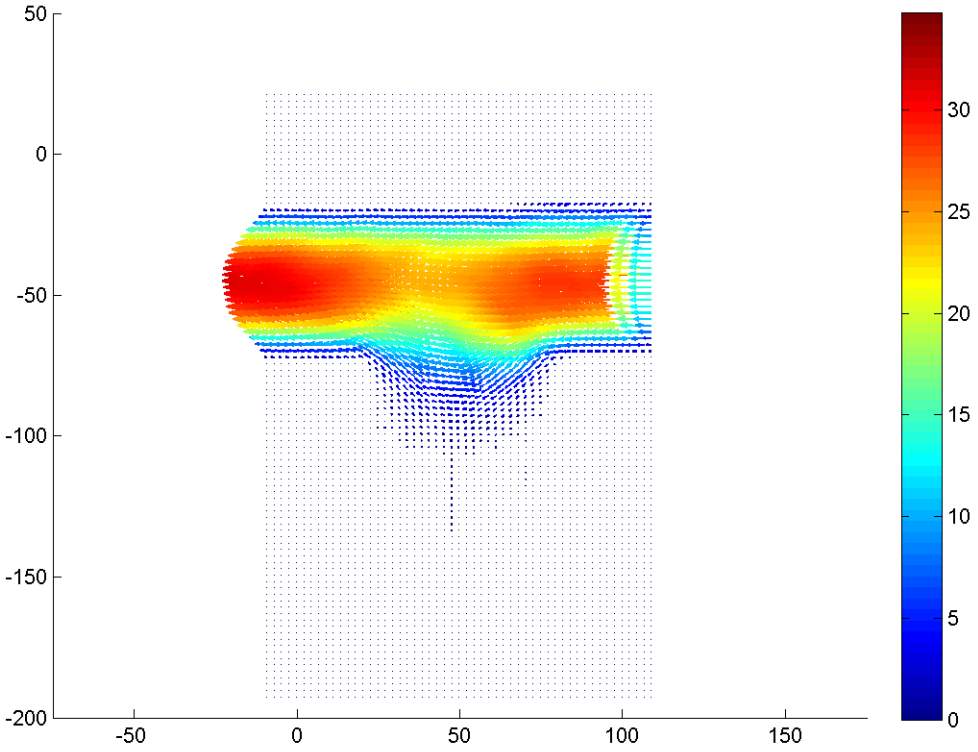

Figure F.321: Velocity field during phase increment 18 at 113.14 Hz with an amplitude of 0.2 mm and a Re of 0.1.

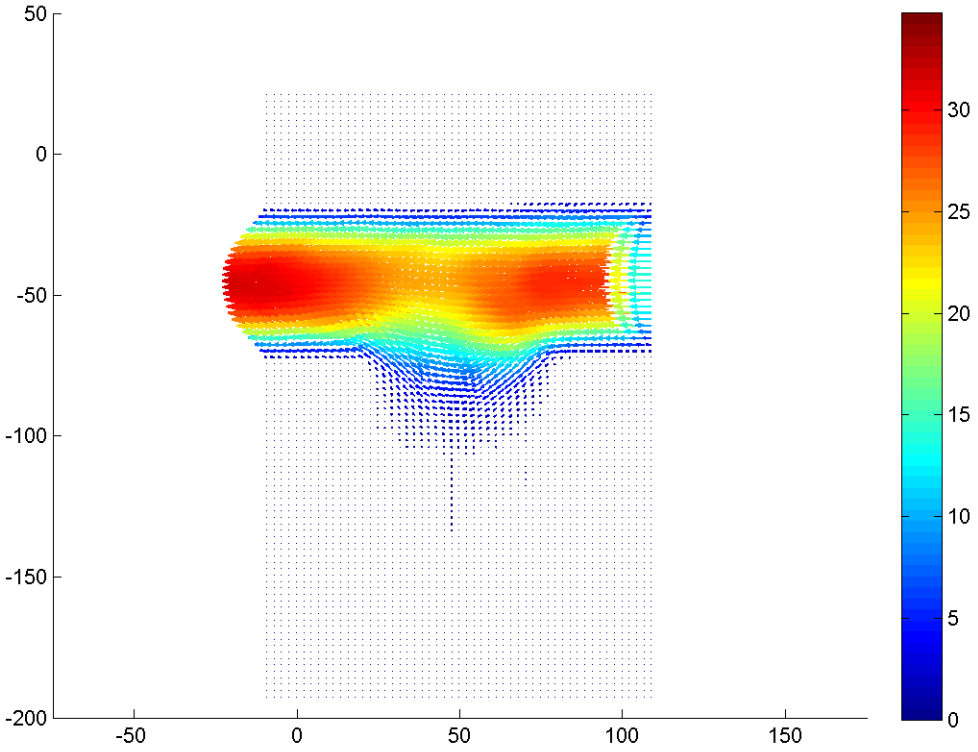

Figure F.322: Velocity field during phase increment 18 at 113.14 Hz with an amplitude of 0.2 mm and a Re of 0.1.

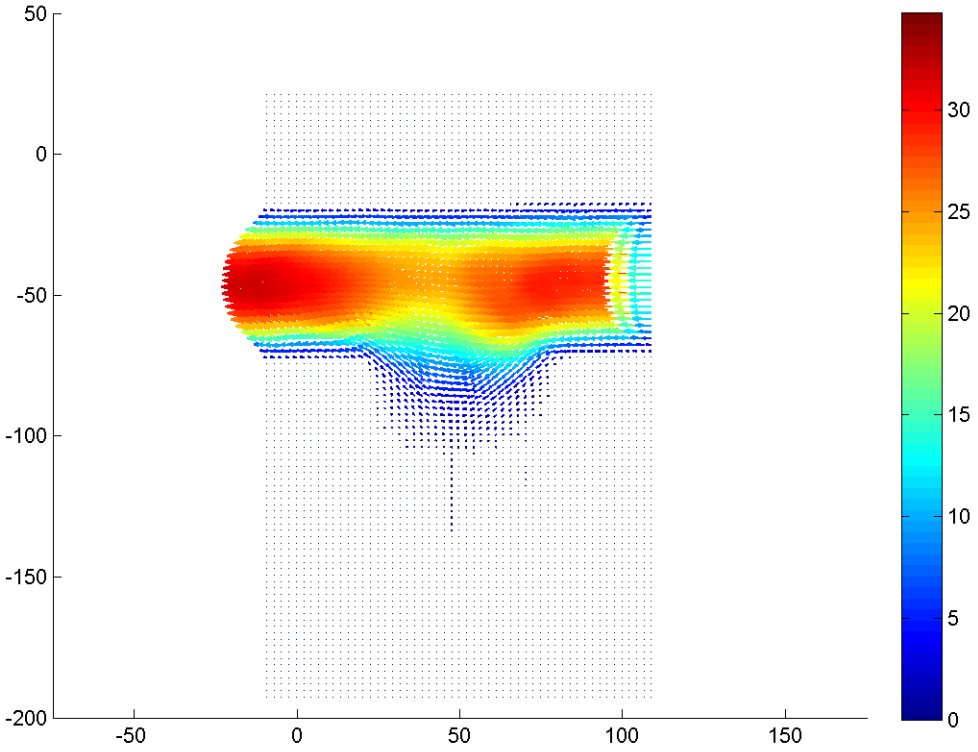

Figure F.323: Velocity field during phase increment 20 at 113.14 Hz with an amplitude of 0.2 mm and a Re of 0.1.

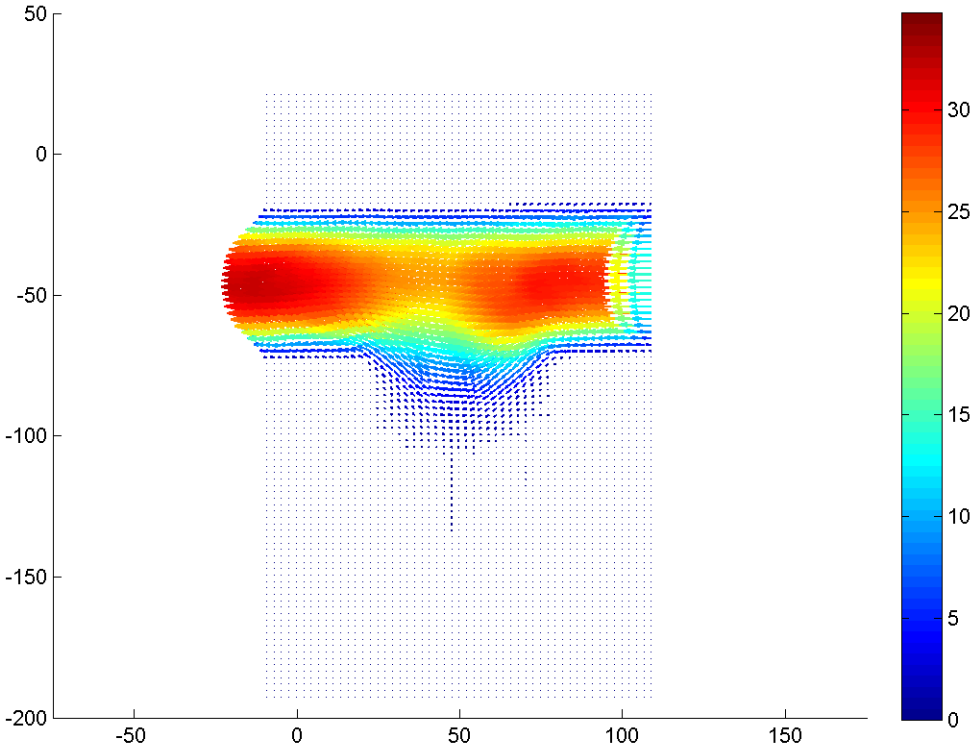

Figure F.324: Velocity field during phase increment 21 at 113.14 Hz with an amplitude of 0.2 mm and a Re of 0.1.

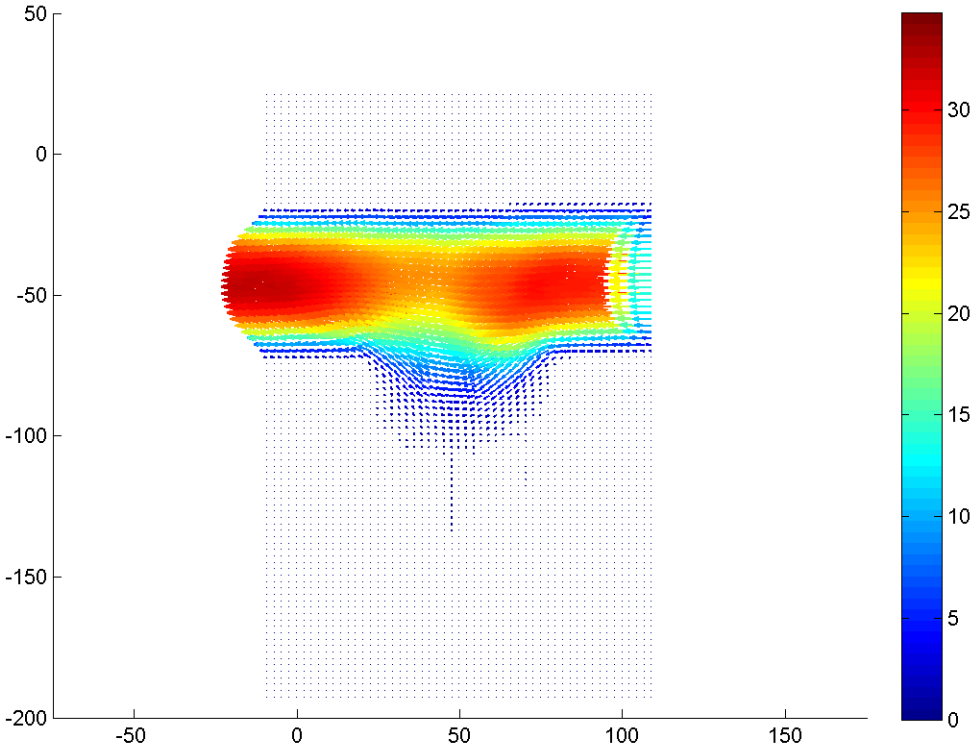

Figure F.325: Velocity field during phase increment 22 at 113.14 Hz with an amplitude of 0.2 mm and a Re of 0.1.

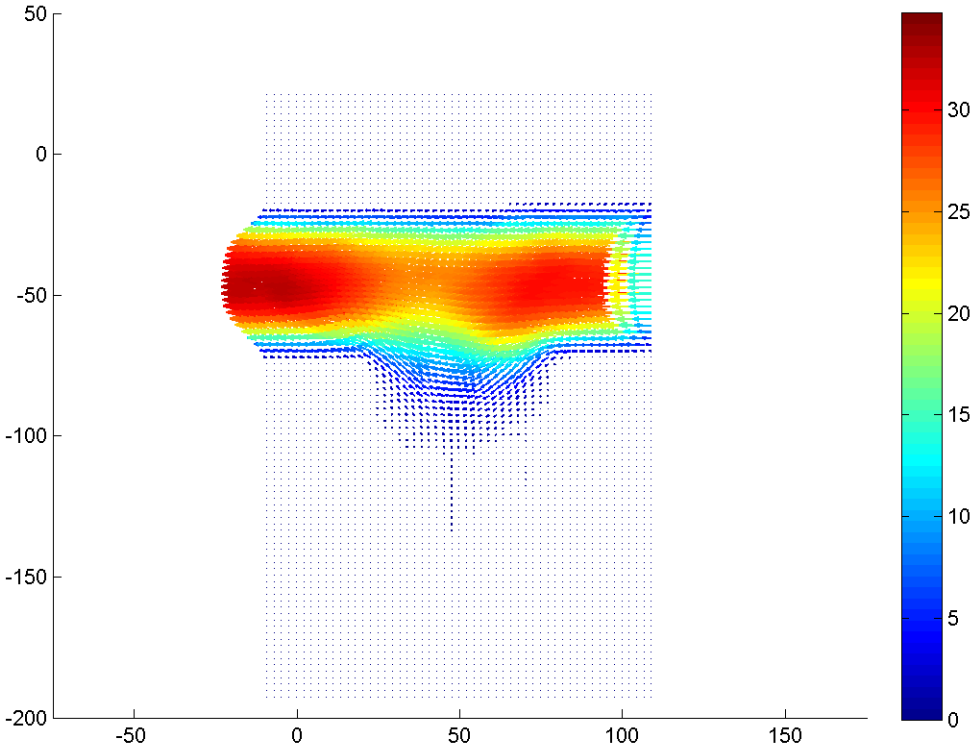

Figure F.326: Velocity field during phase increment 23 at 113.14 Hz with an amplitude of 0.2 mm and a Re of 0.1.

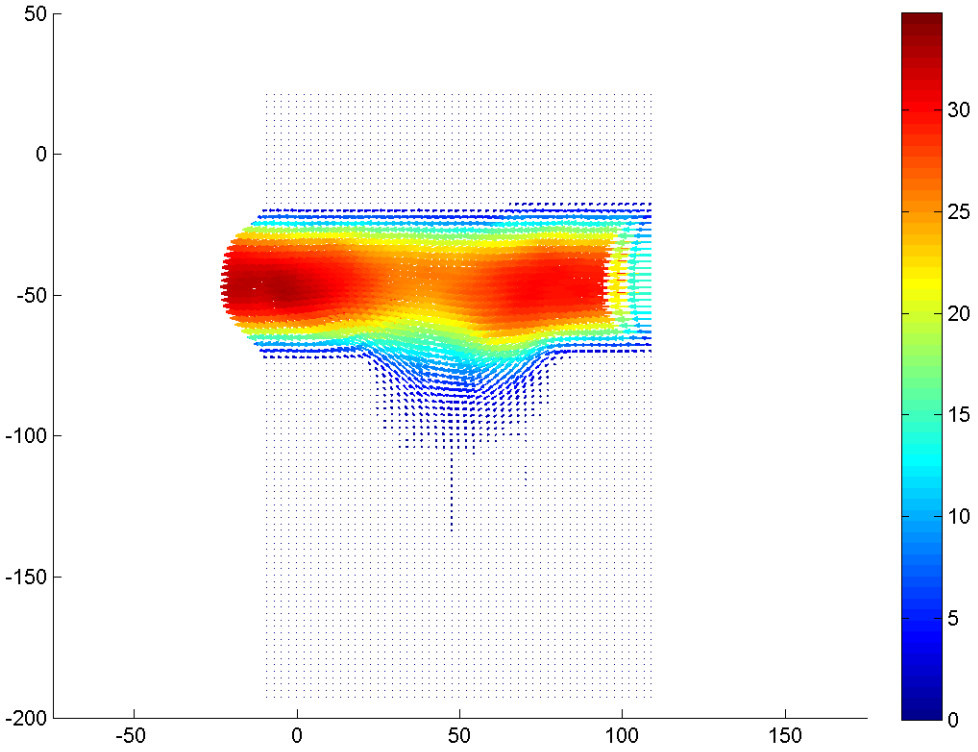

Figure F.327: Velocity field during phase increment 24 at 113.14 Hz with an amplitude of 0.2 mm and a Re of 0.1.

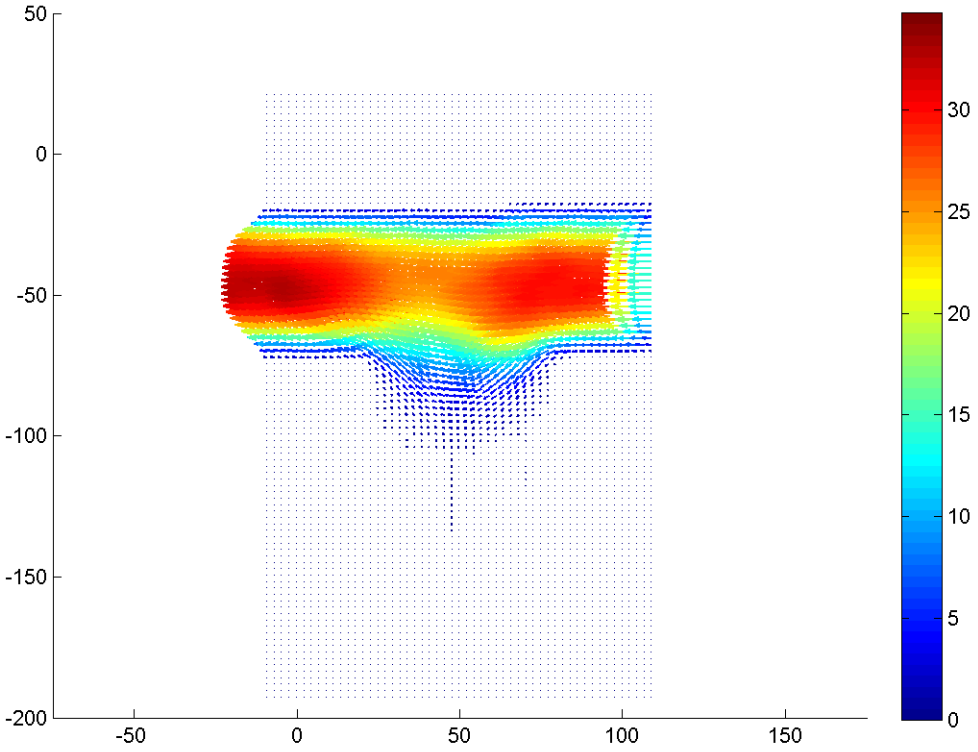

Figure F.328: Velocity field during phase increment 25 at 113.14 Hz with an amplitude of 0.2 mm and a Re of 0.1.

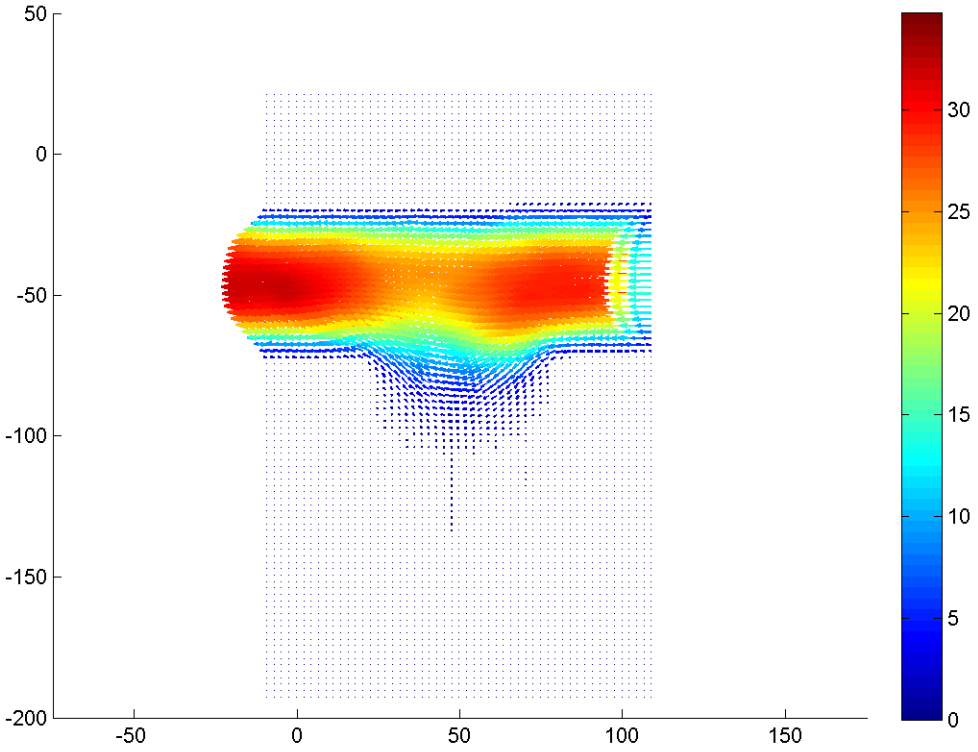

Figure F.329: Velocity field during phase increment 26 at 113.14 Hz with an amplitude of 0.2 mm and a Re of 0.1.

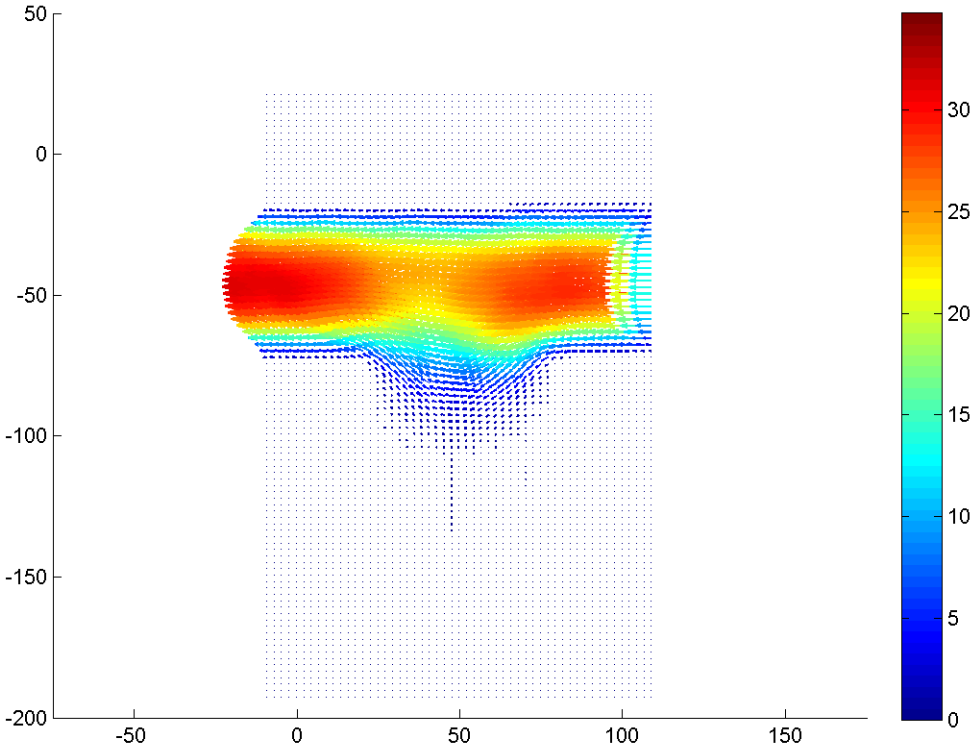

Figure F.330: Velocity field during phase increment 27 at 113.14 Hz with an amplitude of 0.2 mm and a Re of 0.1.

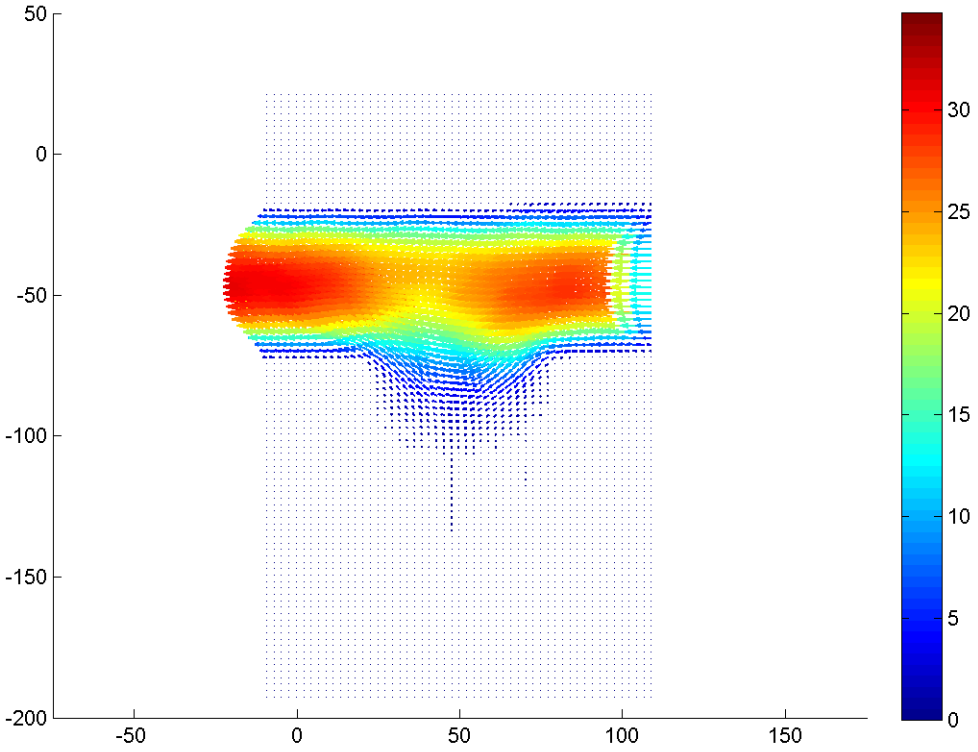

Figure F.331: Velocity field during phase increment 28 at 113.14 Hz with an amplitude of 0.2 mm and a Re of 0.1.

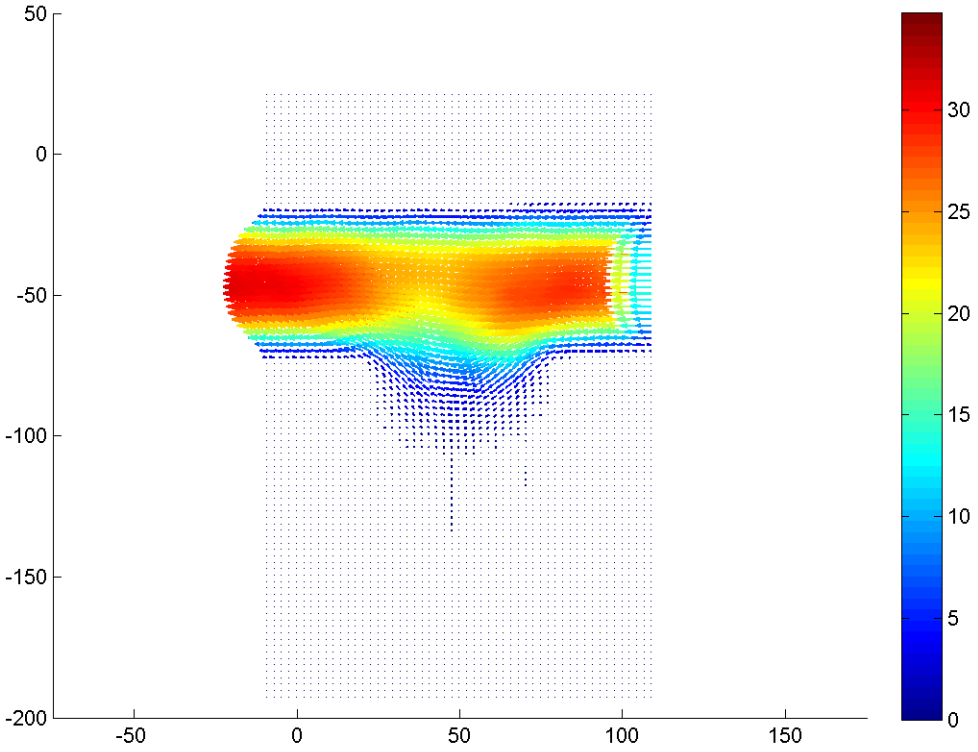

Figure F.332: Velocity field during phase increment 29 at 113.14 Hz with an amplitude of 0.2 mm and a Re of 0.1.

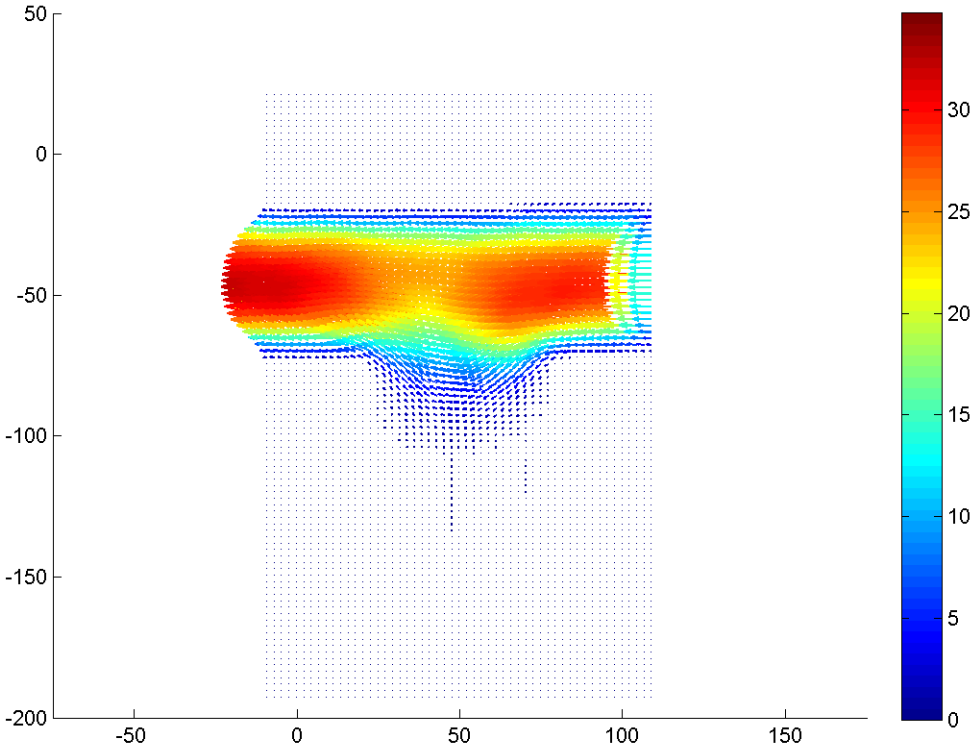

Figure F.333: Velocity field during phase increment 30 at 113.14 Hz with an amplitude of 0.2 mm and a Re of 0.1.

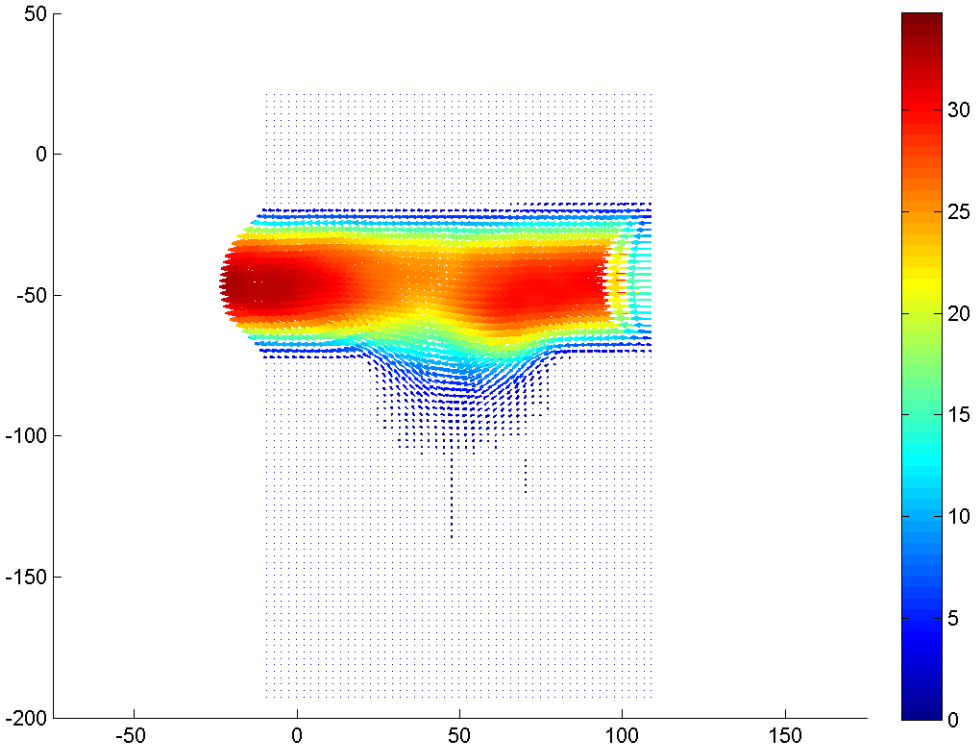

Figure F.334: Velocity field during phase increment 31 at 113.14 Hz with an amplitude of 0.2 mm and a Re of 0.1.

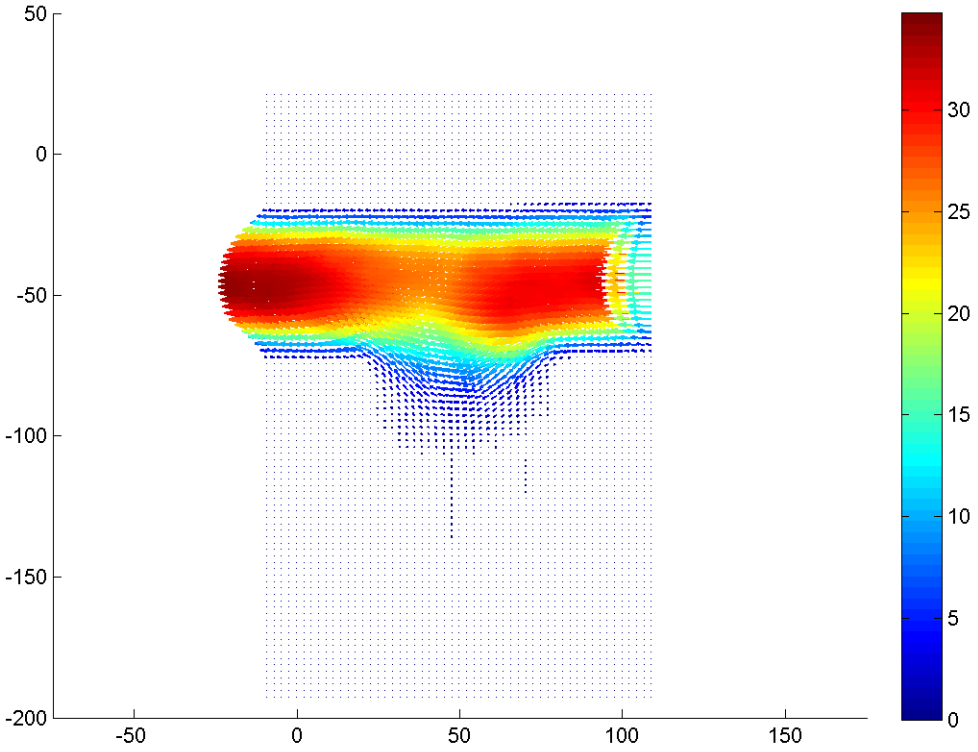

Figure F.335: Velocity field during phase increment 32 at 113.14 Hz with an amplitude of 0.2 mm and a Re of 0.1.

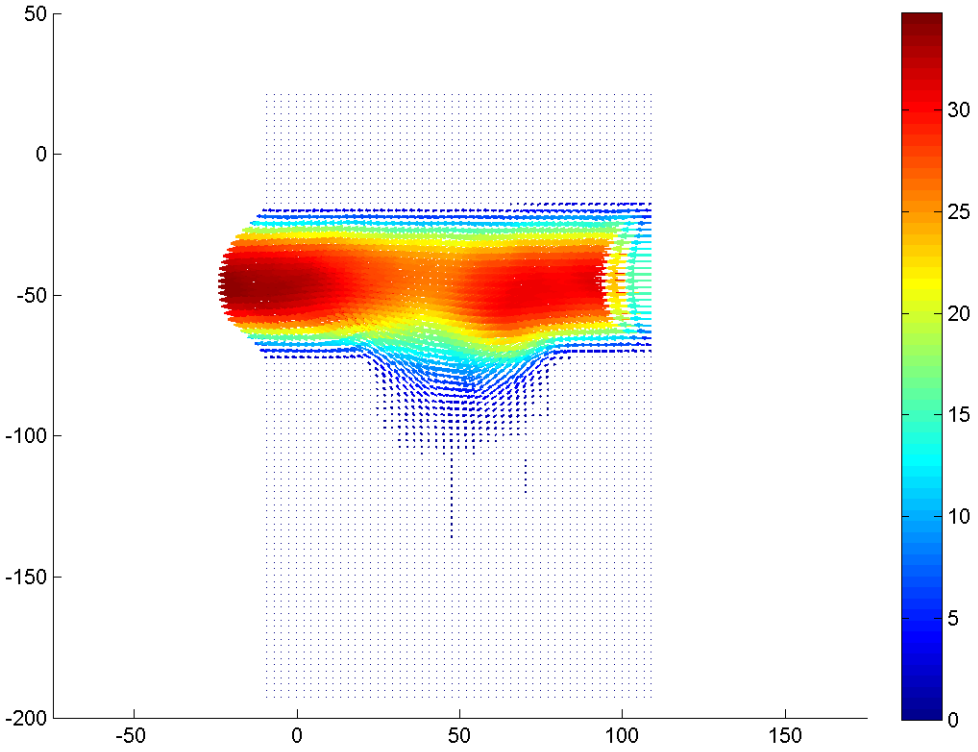

Figure F.336: Velocity field during phase increment 33 at 113.14 Hz with an amplitude of 0.2 mm and a Re of 0.1.

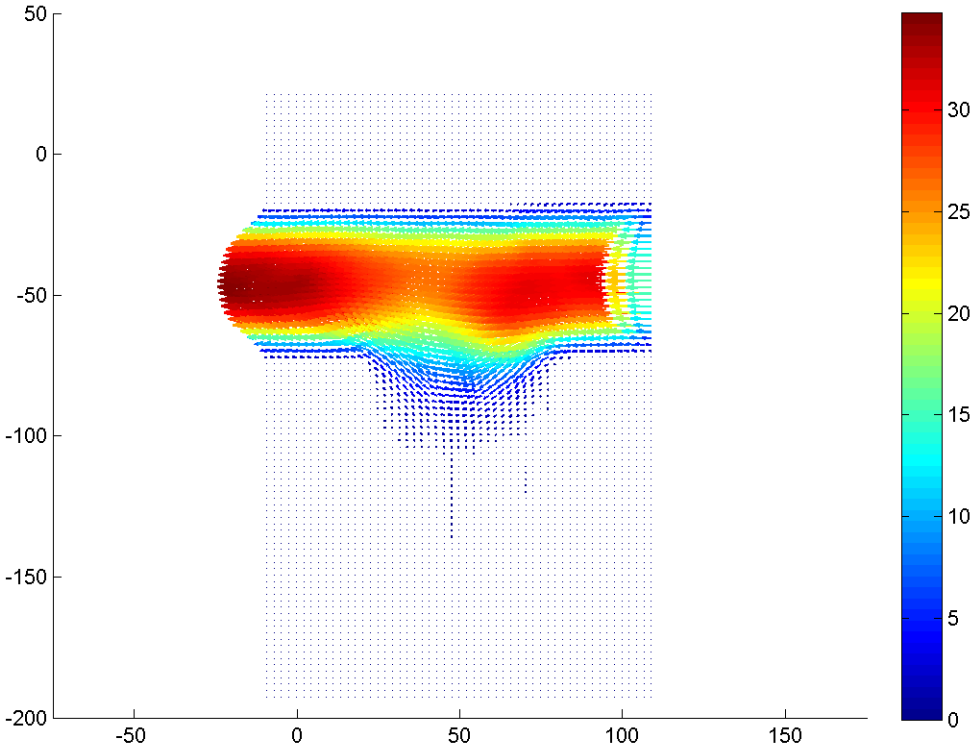

Figure F.337: Velocity field during phase increment 34 at 113.14 Hz with an amplitude of 0.2 mm and a Re of 0.1.

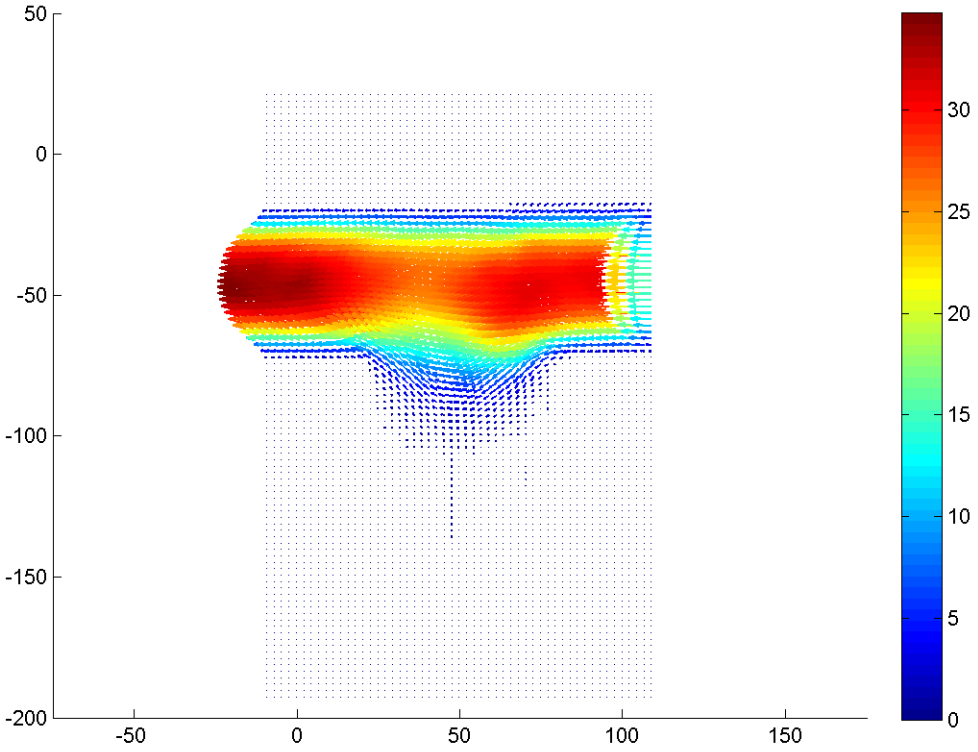

Figure F.338: Velocity field during phase increment 35 at 113.14 Hz with an amplitude of 0.2 mm and a Re of 0.1.

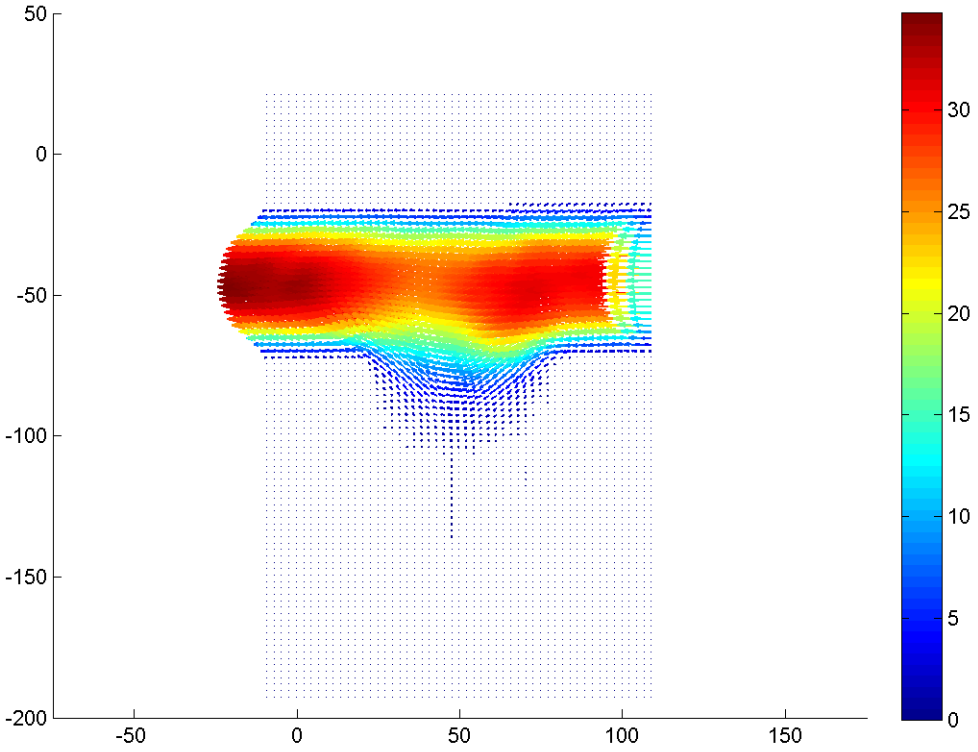

Figure F.339: Velocity field during phase increment 36 at 113.14 Hz with an amplitude of 0.2 mm and a Re of 0.1.

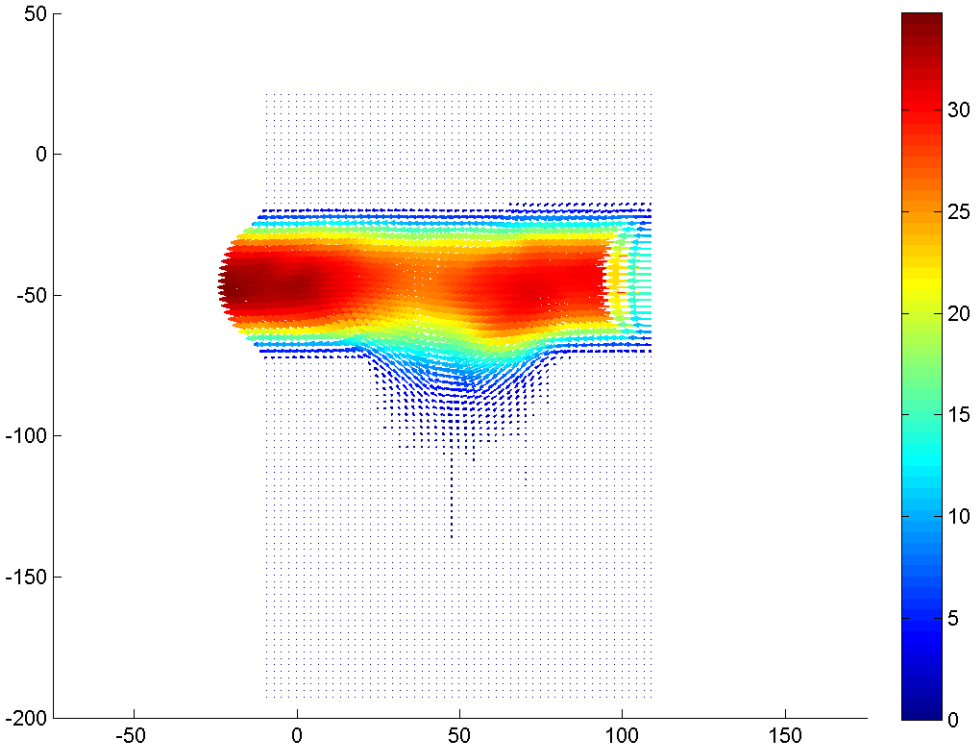

Figure F.340: Velocity field during phase increment 37 at 113.14 Hz with an amplitude of 0.2 mm and a Re of 0.1.

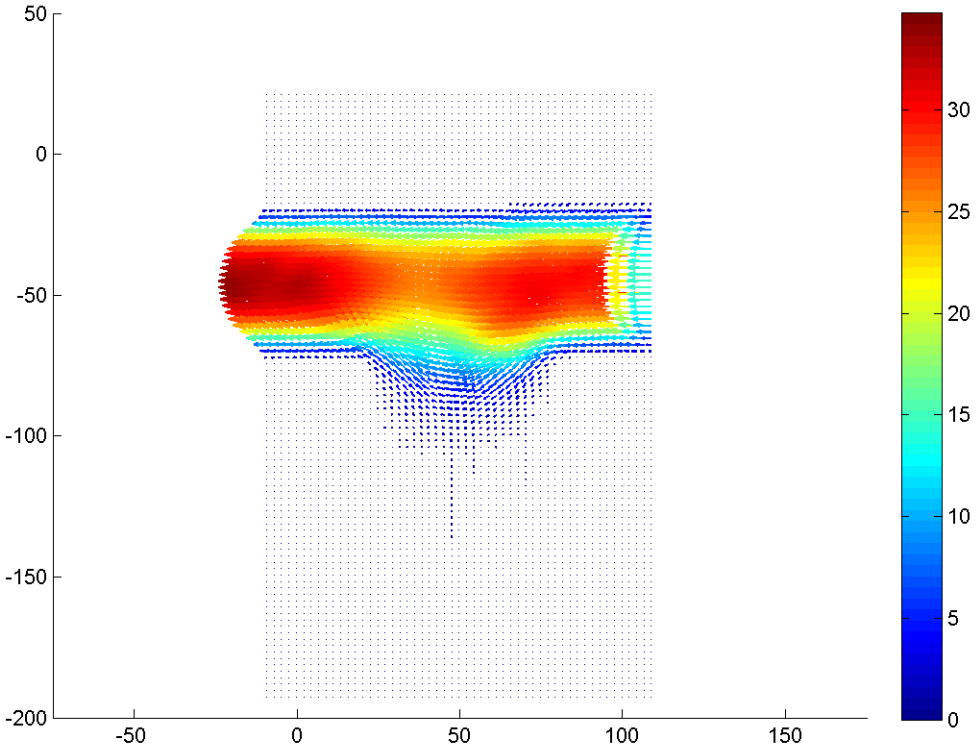

Figure F.341: Velocity field during phase increment 38 at 113.14 Hz with an amplitude of 0.2 mm and a Re of 0.1.

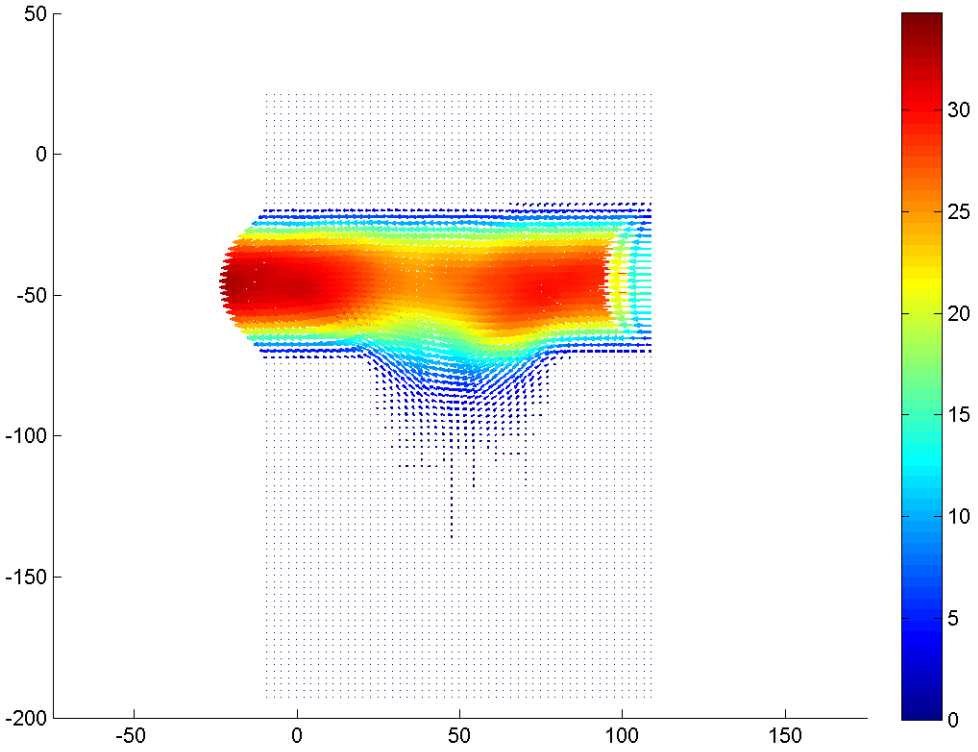

Figure F.342: Velocity field during phase increment 39 at 113.14 Hz with an amplitude of 0.2 mm and a Re of 0.1.

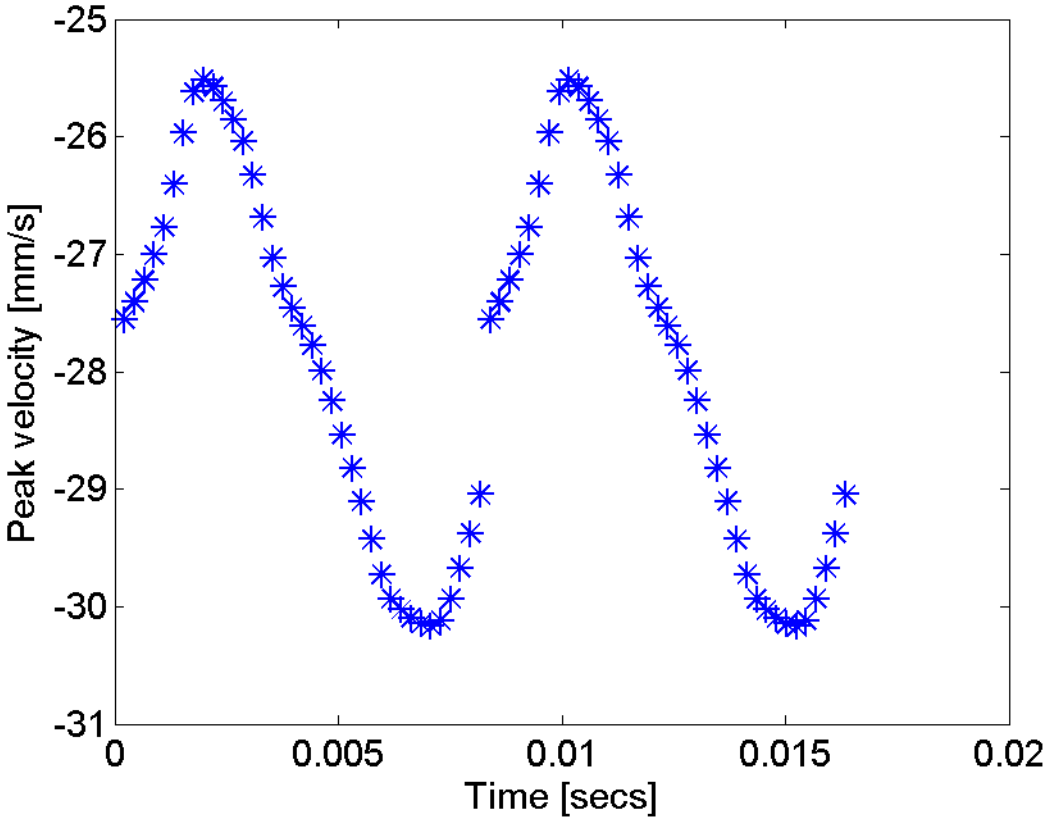

Figure F.343: The peak velocity in the free stream region in time at 113.14 Hz with an amplitude of 0.2 mm.

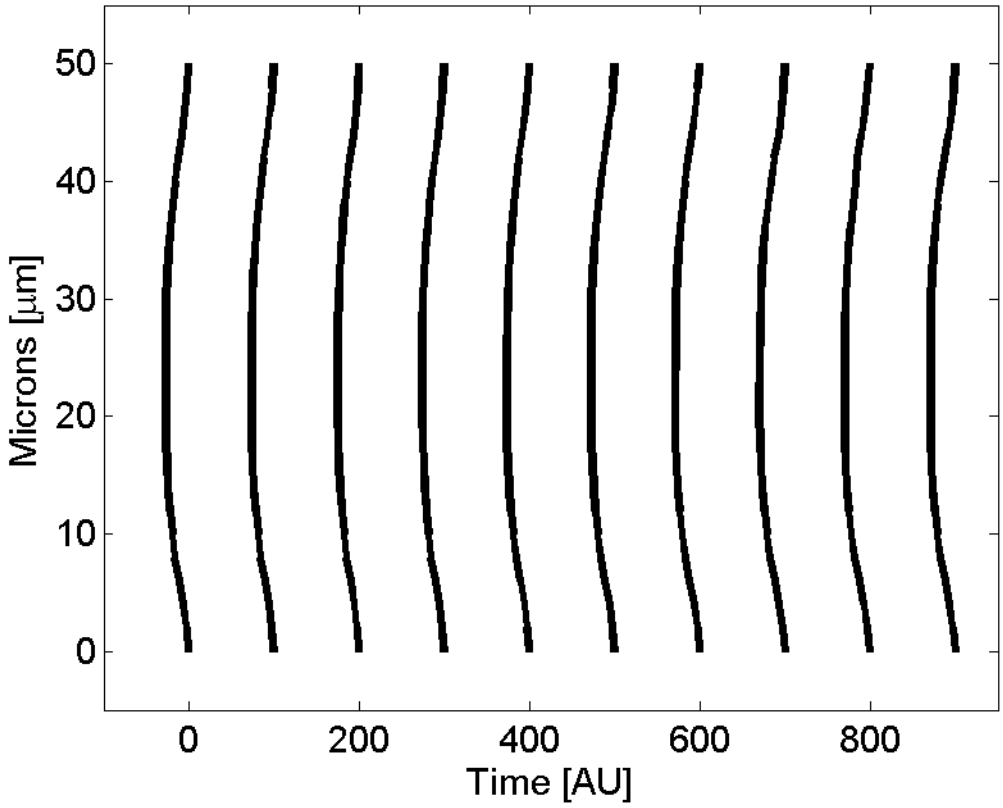

Figure F.344: The velocity profile in the free stream versus time at 113.14 Hz with an amplitude of 0.2 mm.

F.4.2 Streamline images at 113.14 Hz with an amplitude of 0.2 mm

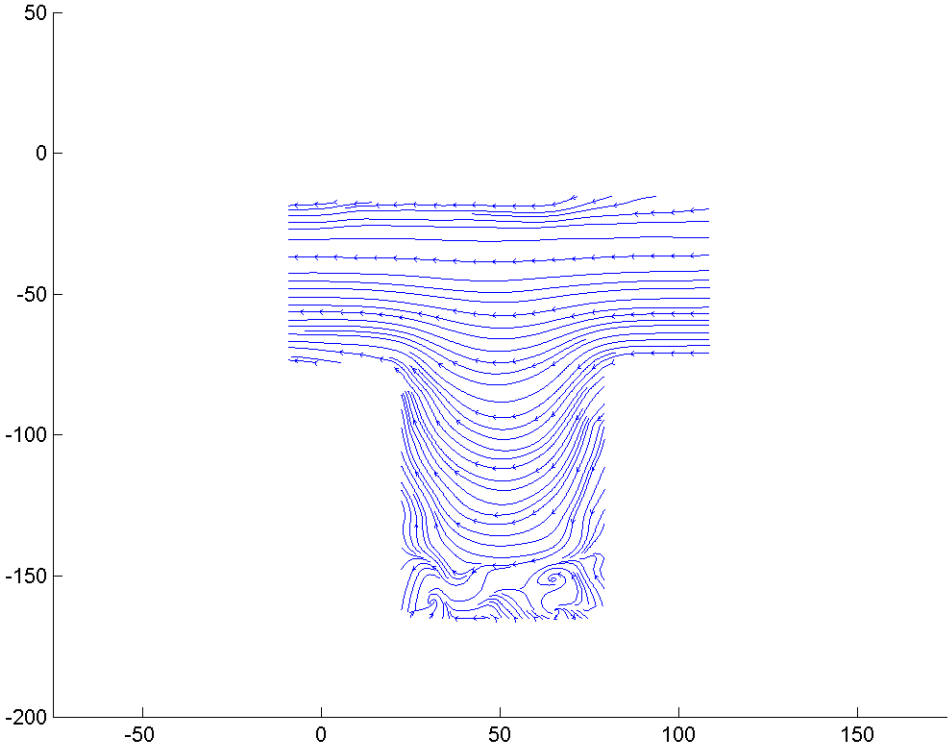

Figure F.345: Streamline image during phase increment 1 at 113.14 Hz with an amplitude of 0.2 mm and a Re of 0.1.

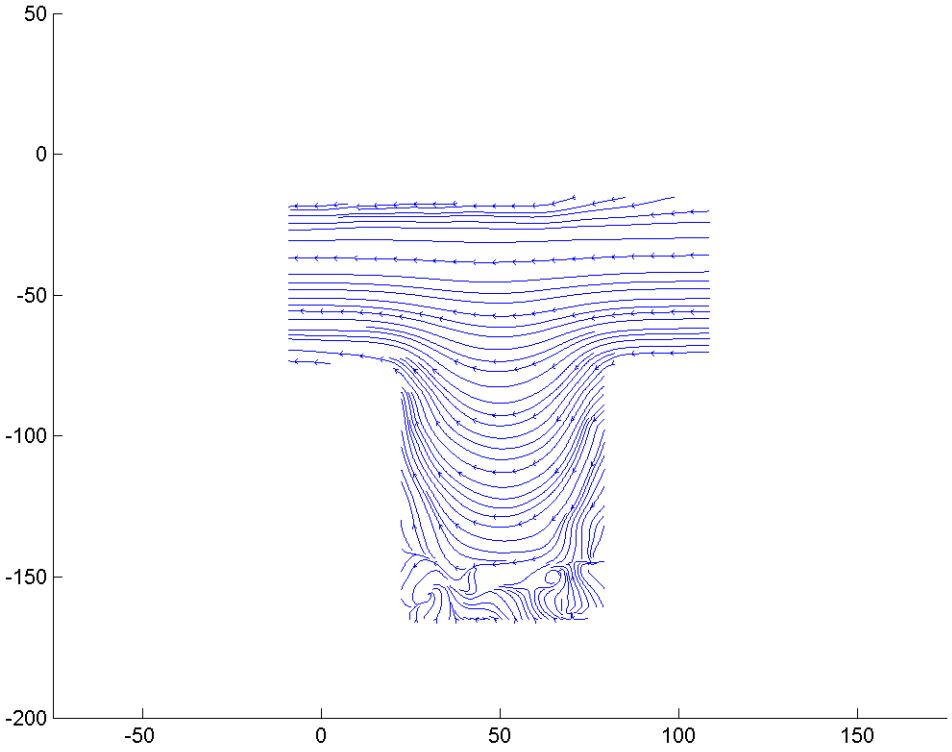

Figure F.346: Streamline image during phase increment 2 at 113.14 Hz with an amplitude of 0.2 mm and a Re of 0.1.

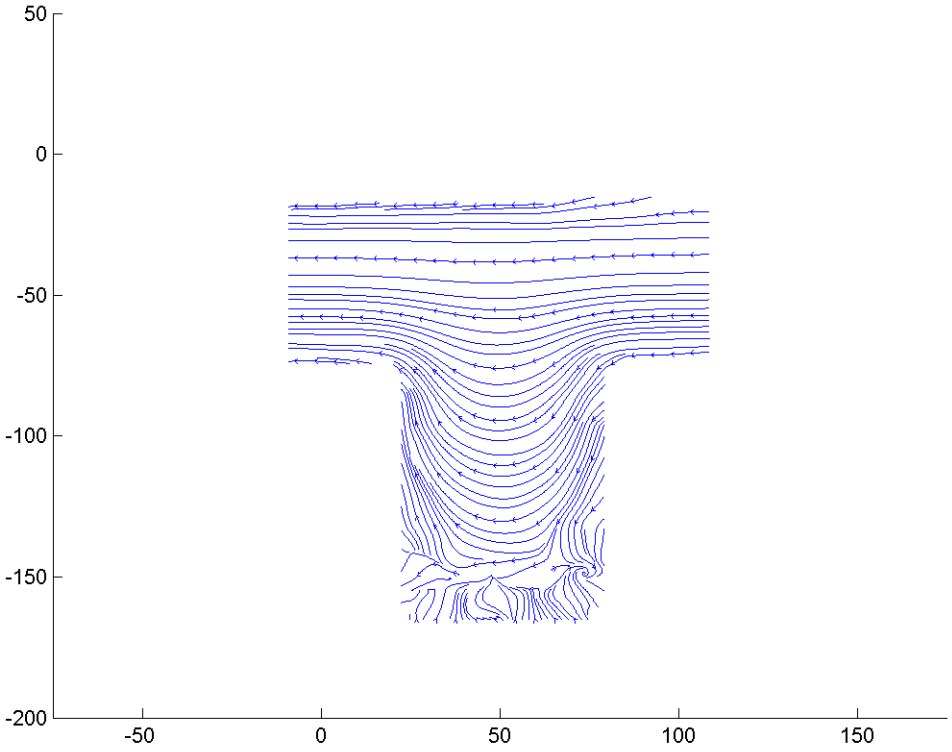

Figure F.347: Streamline image during phase increment 3 at 113.14 Hz with an amplitude of 0.2 mm and a Re of 0.1.

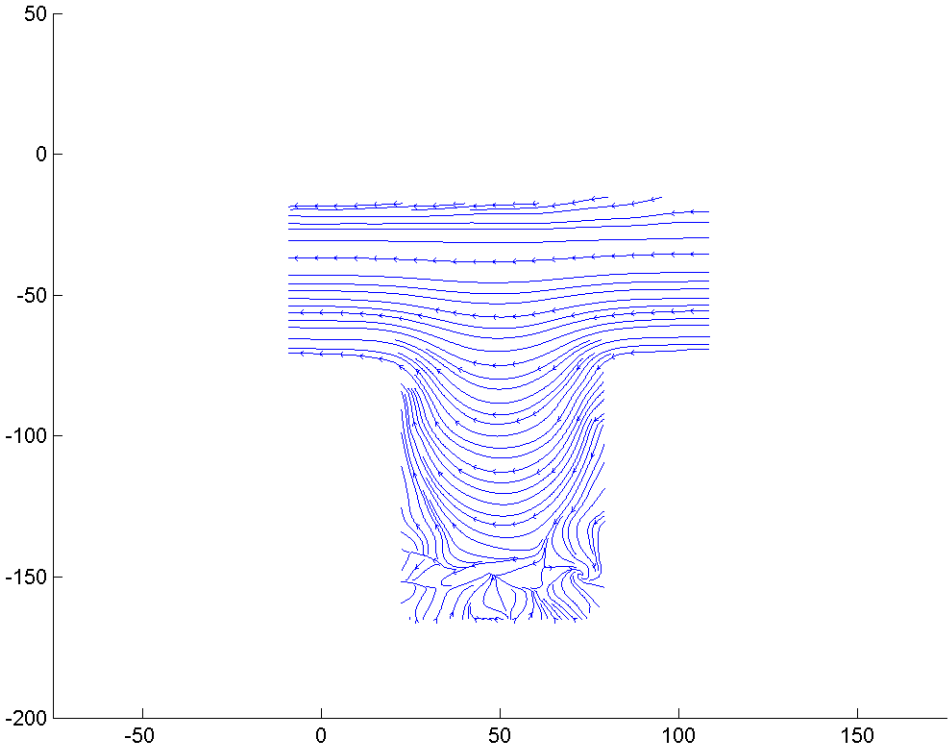

Figure F.348: Streamline image during phase increment 4 at 113.14 Hz with an amplitude of 0.2 mm and a Re of 0.1.

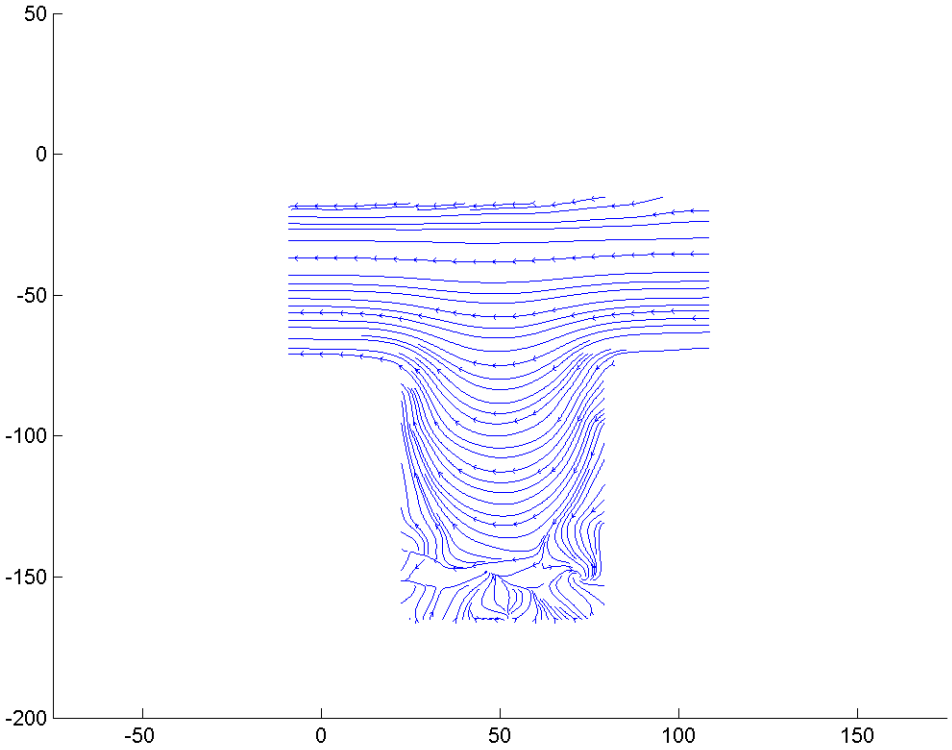

Figure F.349: Streamline image during phase increment 5 at 113.14 Hz with an amplitude of 0.2 mm and a Re of 0.1.

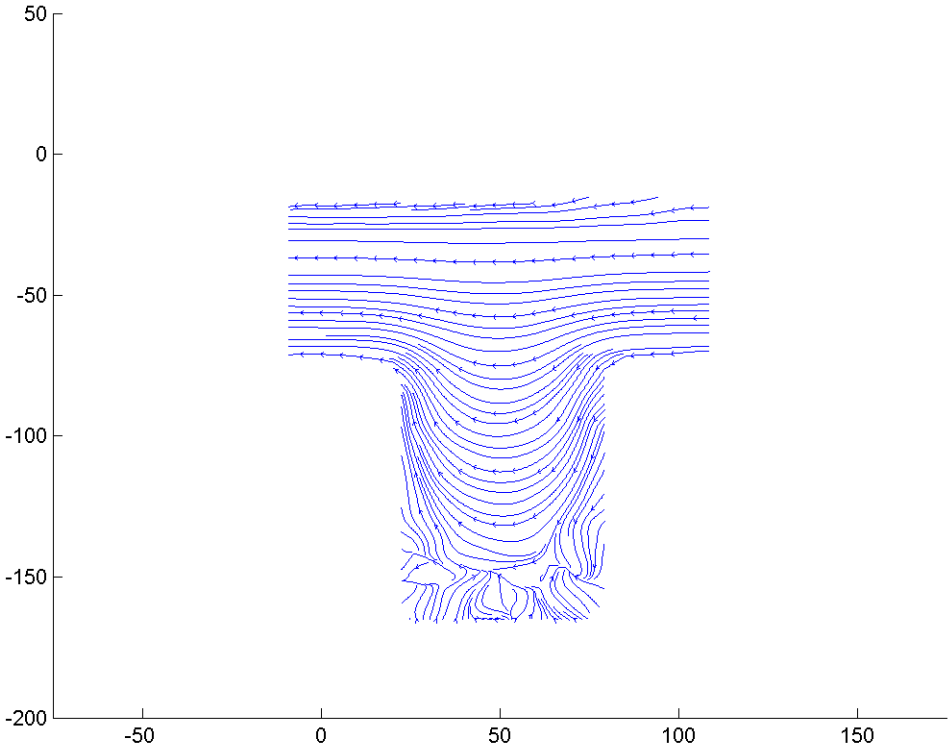

Figure F.350: Streamline image during phase increment 6 at 113.14 Hz with an amplitude of 0.2 mm and a Re of 0.1.

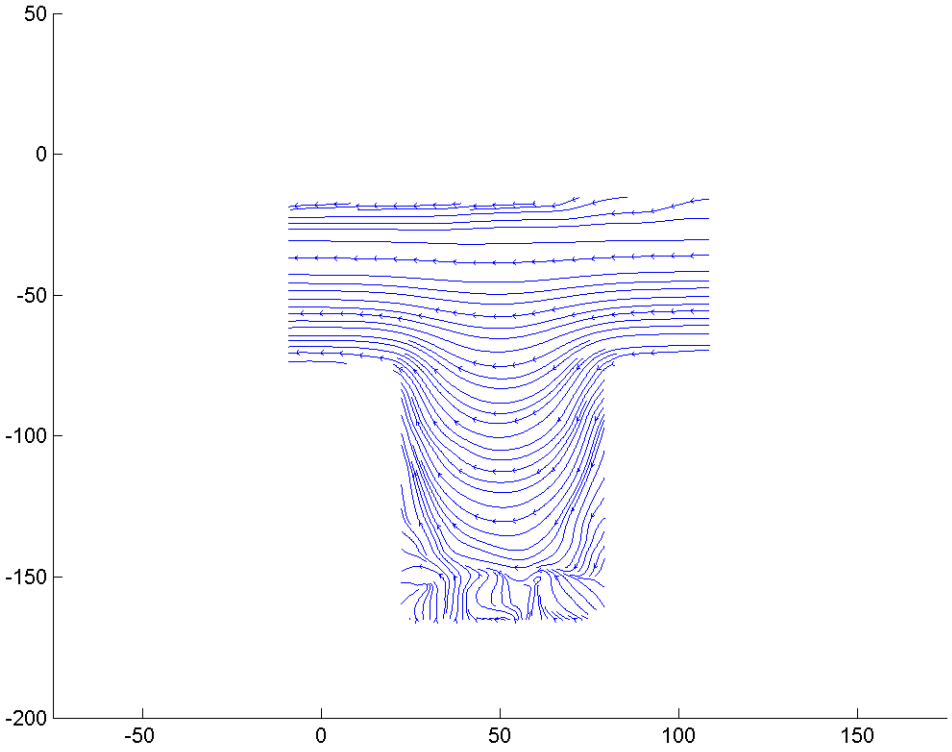

Figure F.351: Streamline image during phase increment 7 at 113.14 Hz with an amplitude of 0.2 mm and a Re of 0.1.

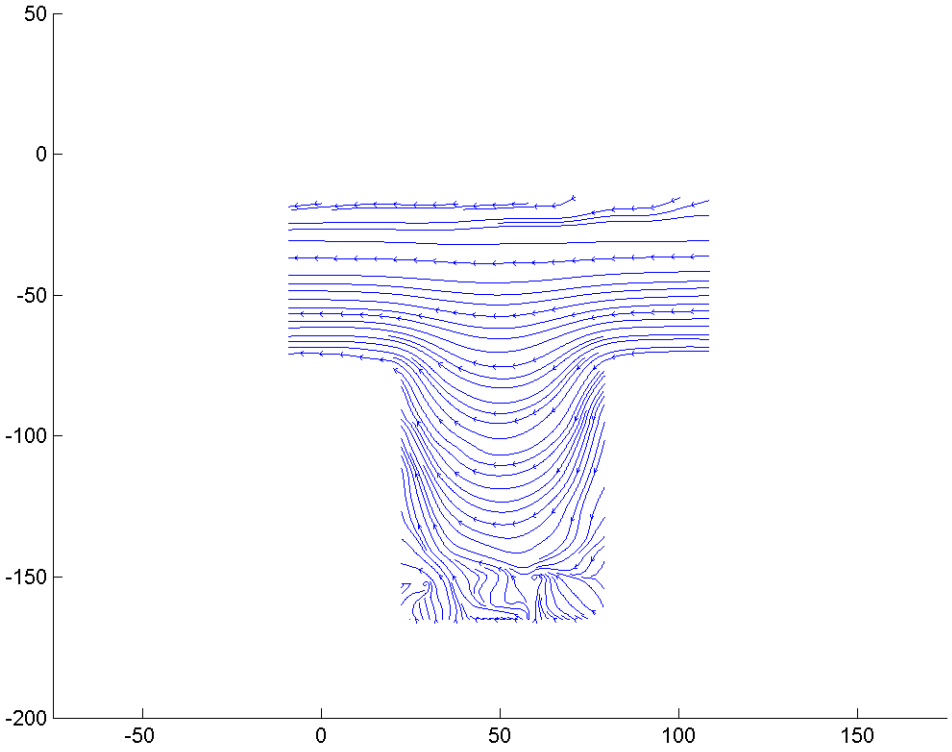

Figure F.352: Streamline image during phase increment 8 at 113.14 Hz with an amplitude of 0.2 mm and a Re of 0.1.

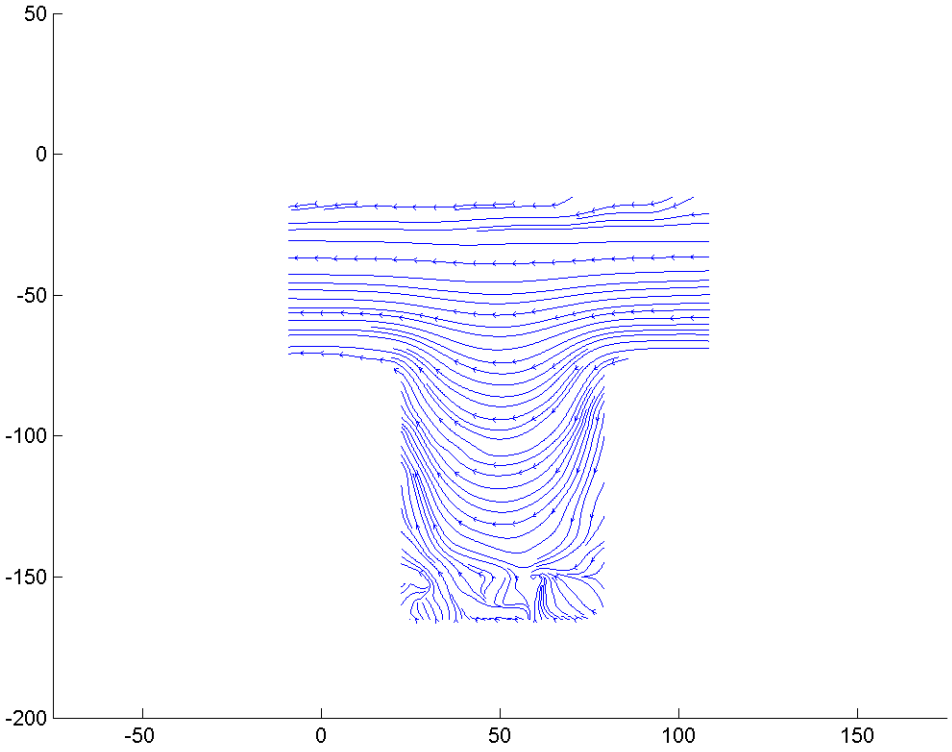

Figure F.353: Streamline image during phase increment 9 at 113.14 Hz with an amplitude of 0.2 mm and a Re of 0.1.

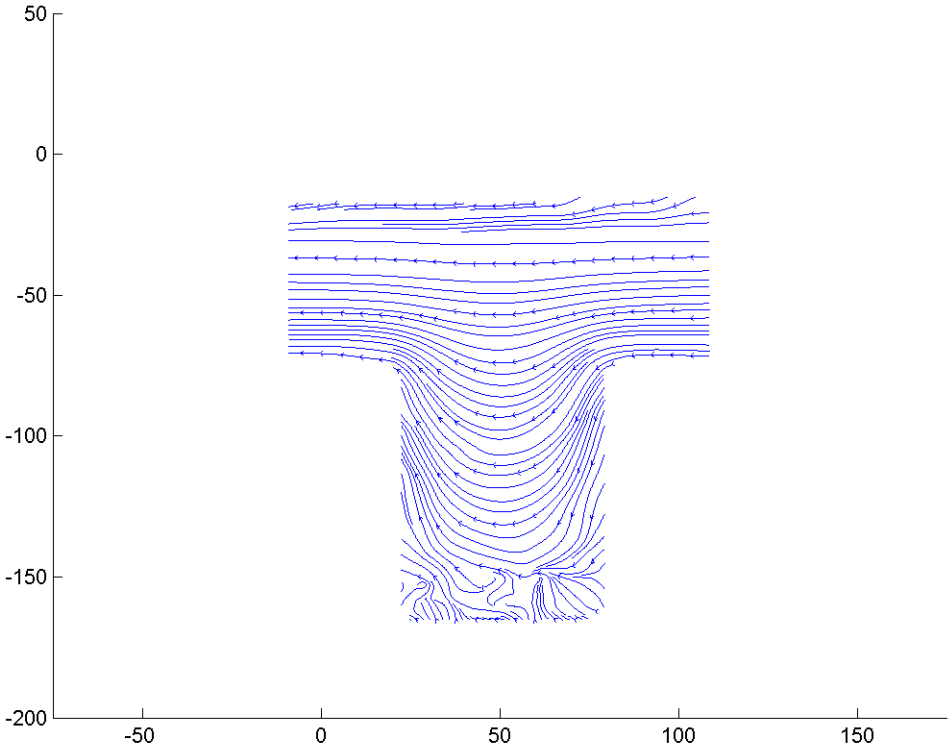

Figure F.354: Streamline image during phase increment 10 at 113.14 Hz with an amplitude of 0.2 mm and a Re of 0.1.

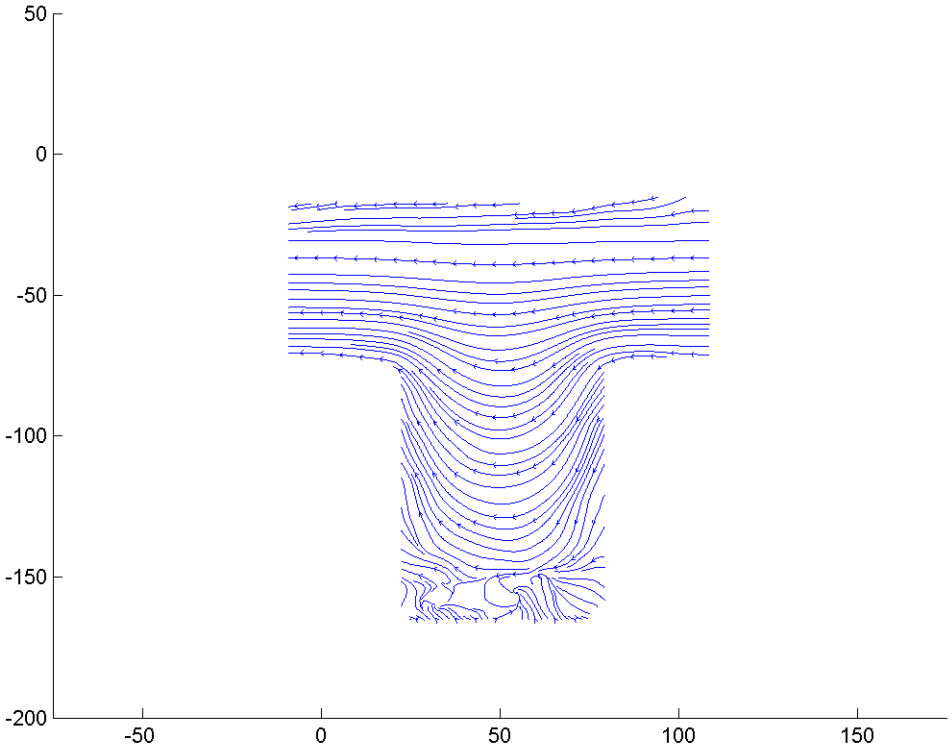

Figure F.355: Streamline image during phase increment 11 at 113.14 Hz with an amplitude of 0.2 mm and a Re of 0.1.

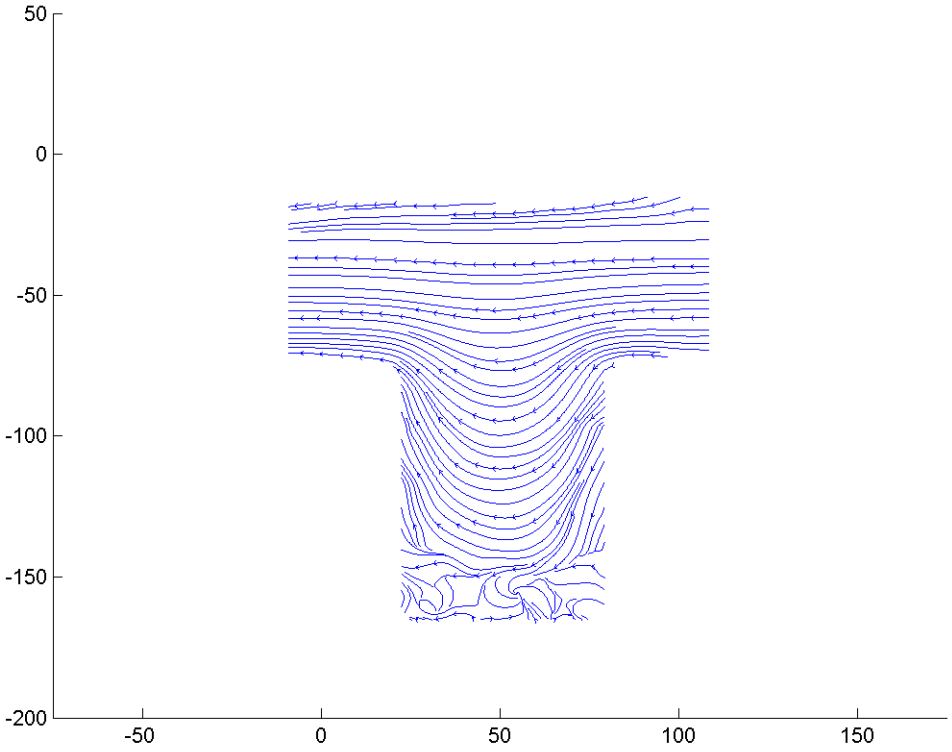

Figure F.356: Streamline image during phase increment 12 at 113.14 Hz with an amplitude of 0.2 mm and a Re of 0.1.

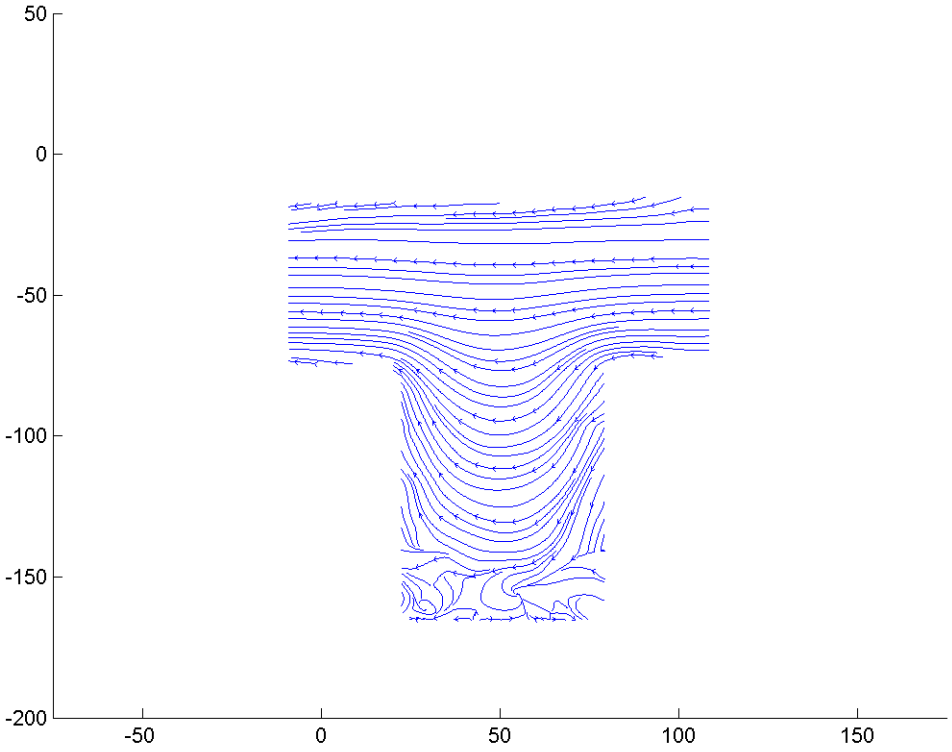

Figure F.357: Streamline image during phase increment 13 at 113.14 Hz with an amplitude of 0.2 mm and a Re of 0.1.

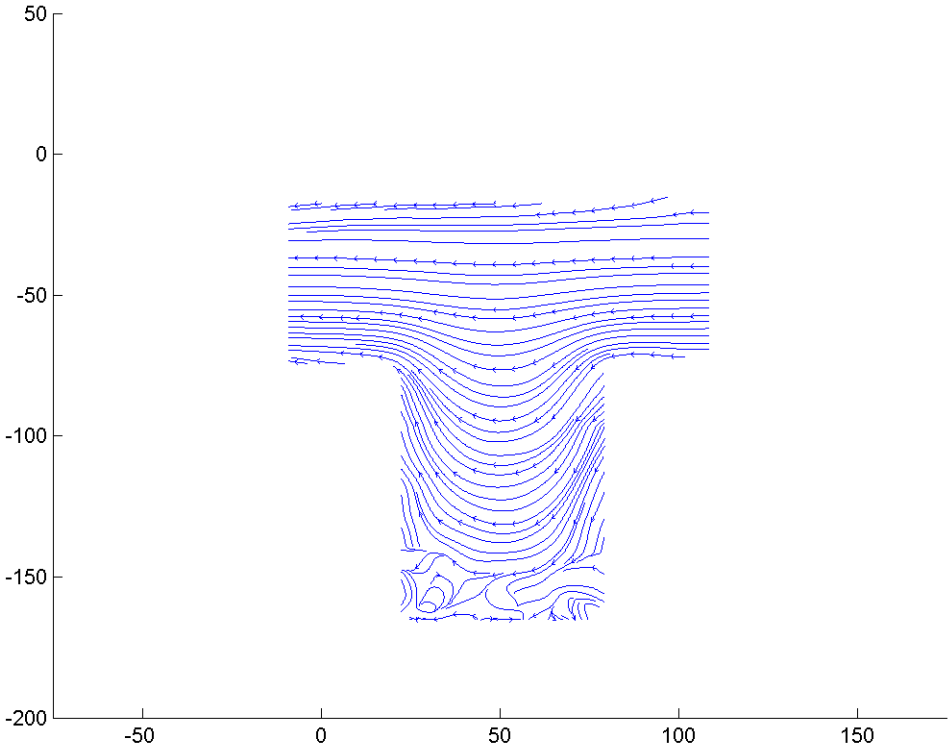

Figure F.358: Streamline image during phase increment 14 at 113.14 Hz with an amplitude of 0.2 mm and a Re of 0.1.

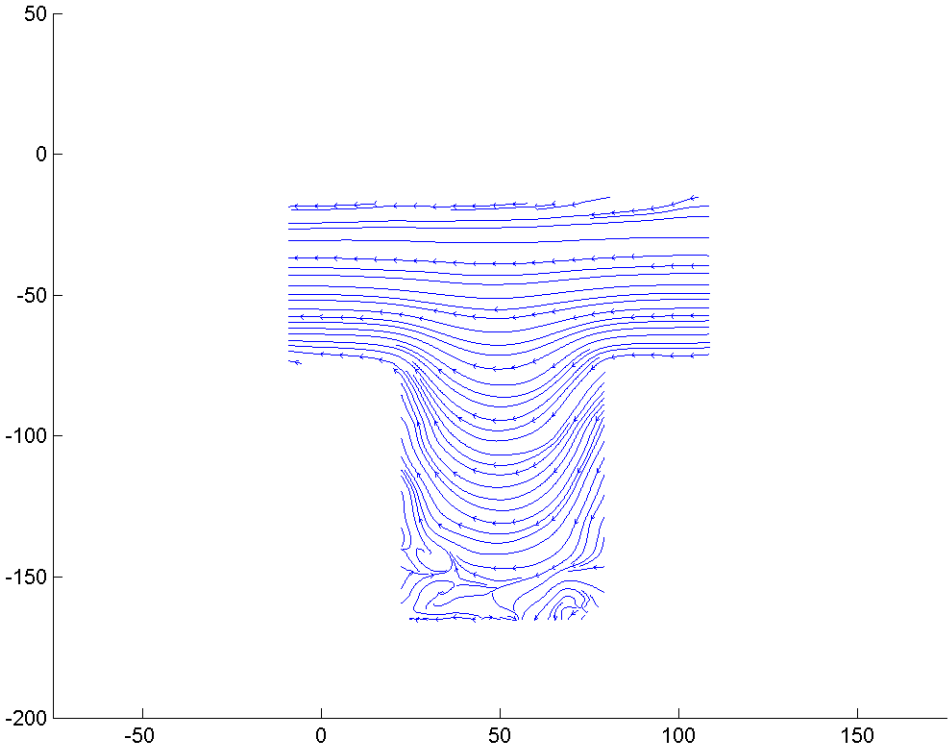

Figure F.359: Streamline image during phase increment 15 at 113.14 Hz with an amplitude of 0.2 mm and a Re of 0.1.

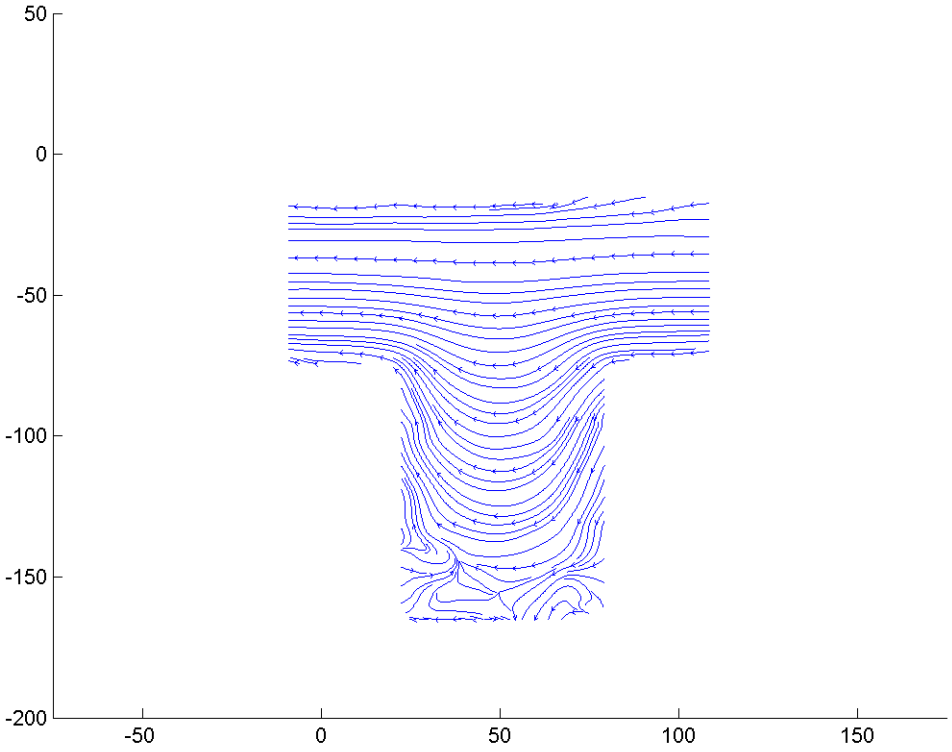

Figure F.360: Streamline image during phase increment 16 at 113.14 Hz with an amplitude of 0.2 mm and a Re of 0.1.

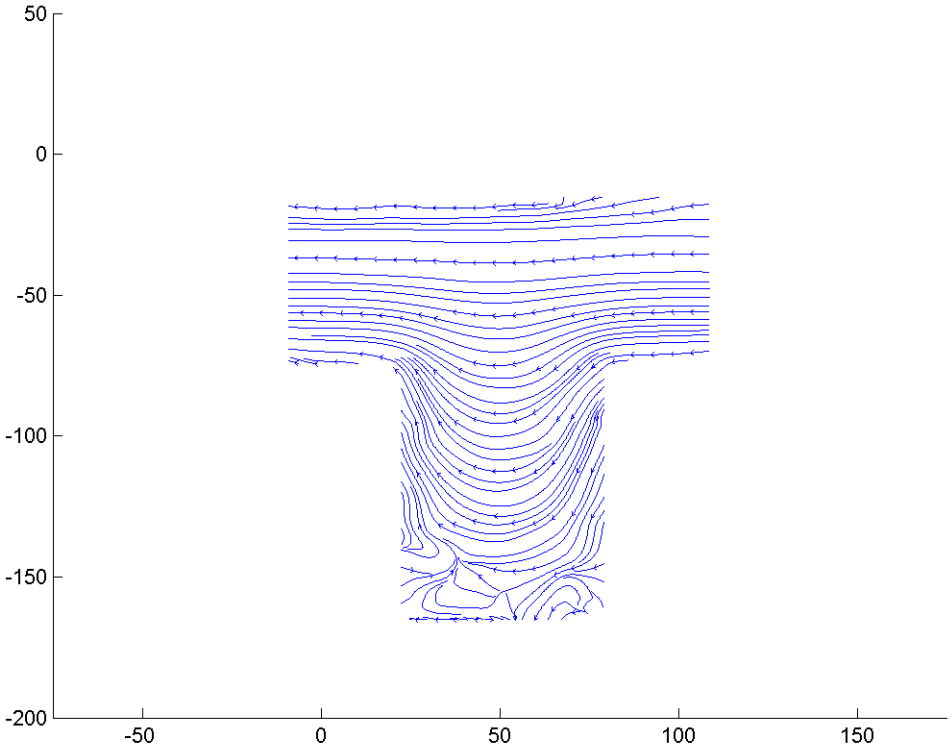

Figure F.361: Streamline image during phase increment 17 at 113.14 Hz with an amplitude of 0.2 mm and a Re of 0.1.

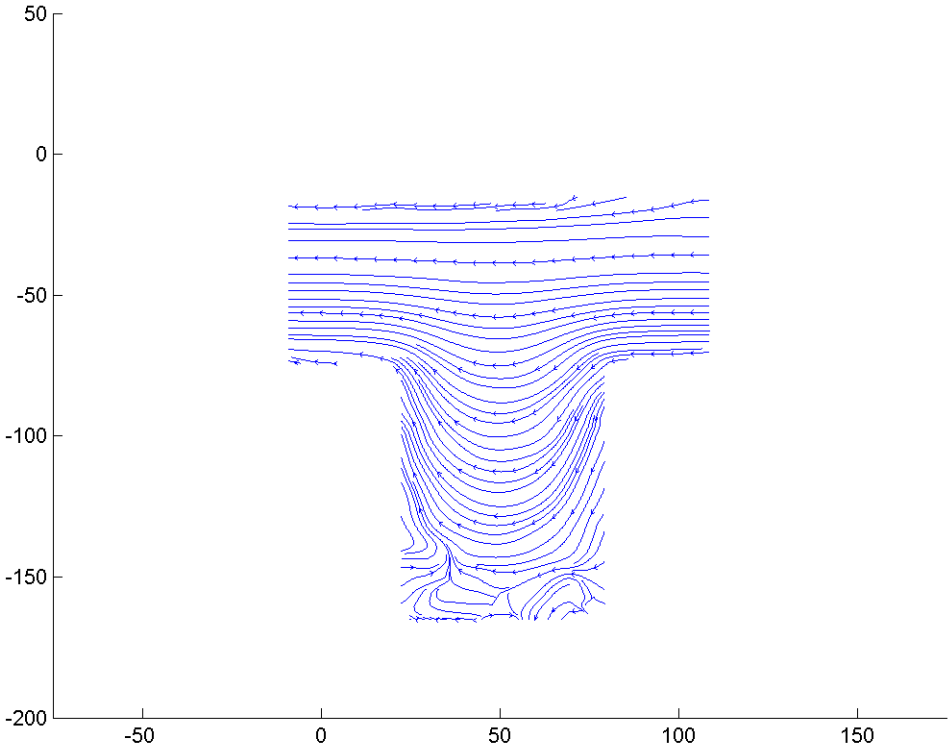

Figure F.362: Streamline image during phase increment 18 at 113.14 Hz with an amplitude of 0.2 mm and a Re of 0.1.

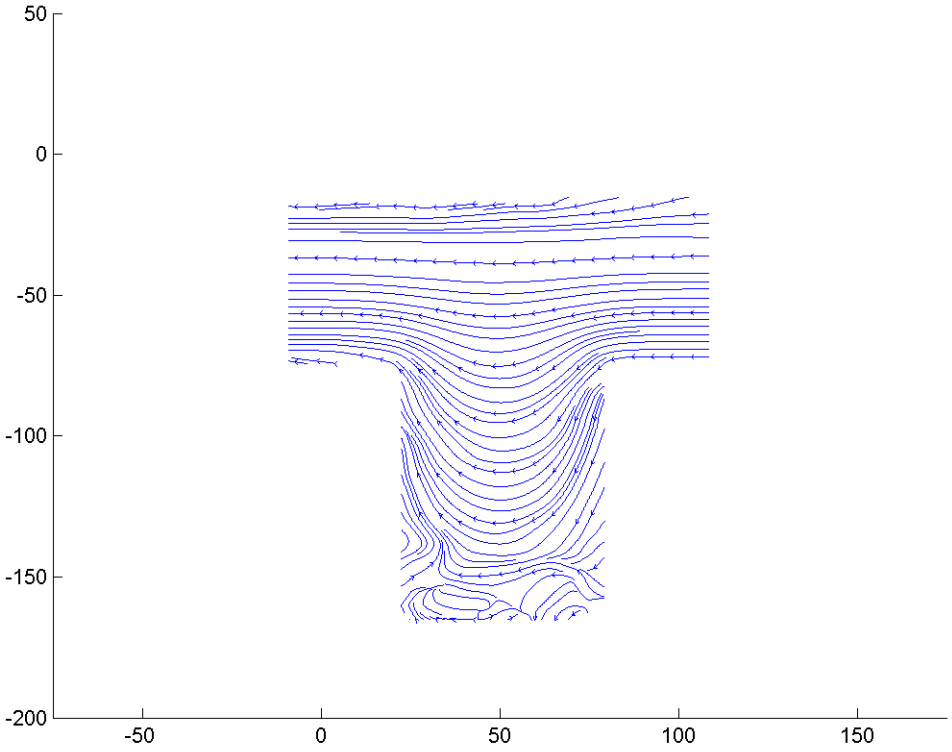

Figure F.363: Streamline image during phase increment 18 at 113.14 Hz with an amplitude of 0.2 mm and a Re of 0.1.

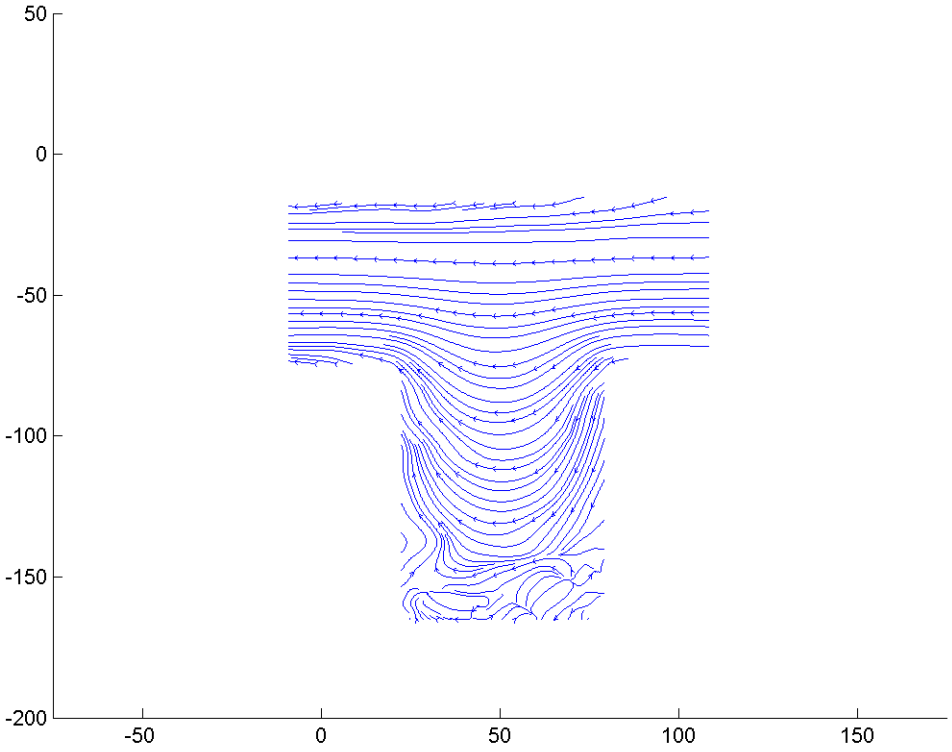

Figure F.364: Streamline image during phase increment 20 at 113.14 Hz with an amplitude of 0.2 mm and a Re of 0.1.

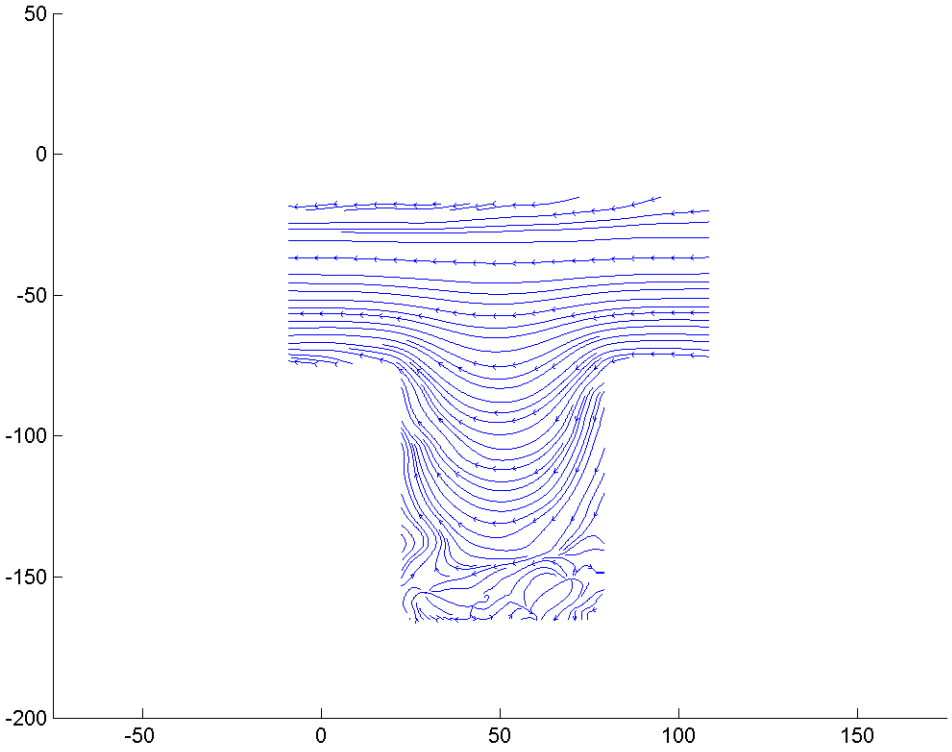

Figure F.365: Streamline image during phase increment 21 at 113.14 Hz with an amplitude of 0.2 mm and a Re of 0.1.

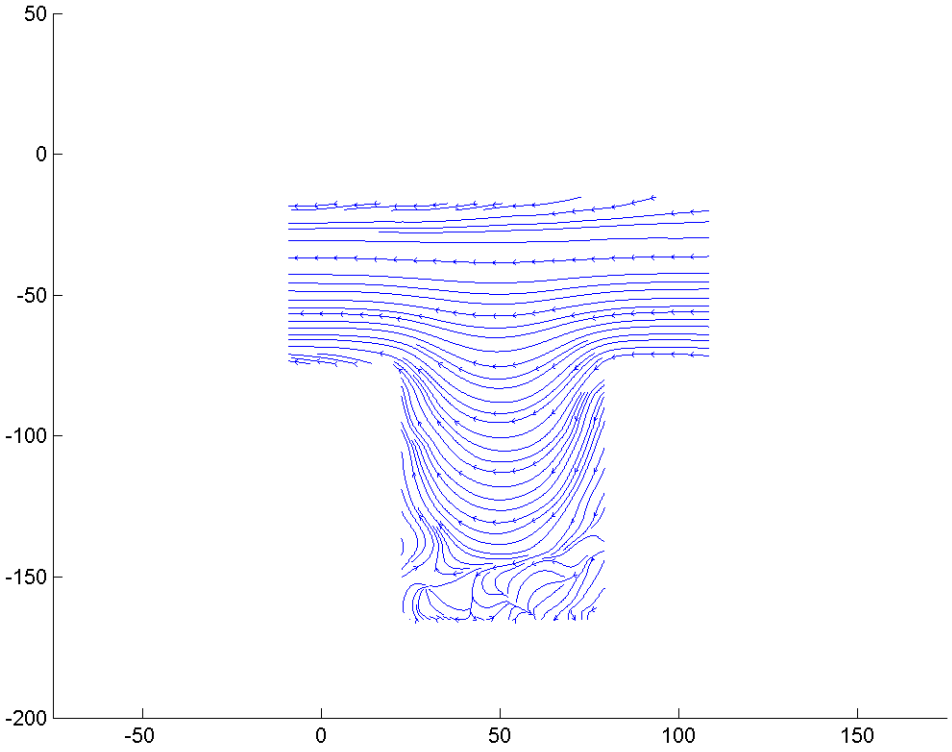

Figure F.366: Streamline image during phase increment 22 at 113.14 Hz with an amplitude of 0.2 mm and a Re of 0.1.

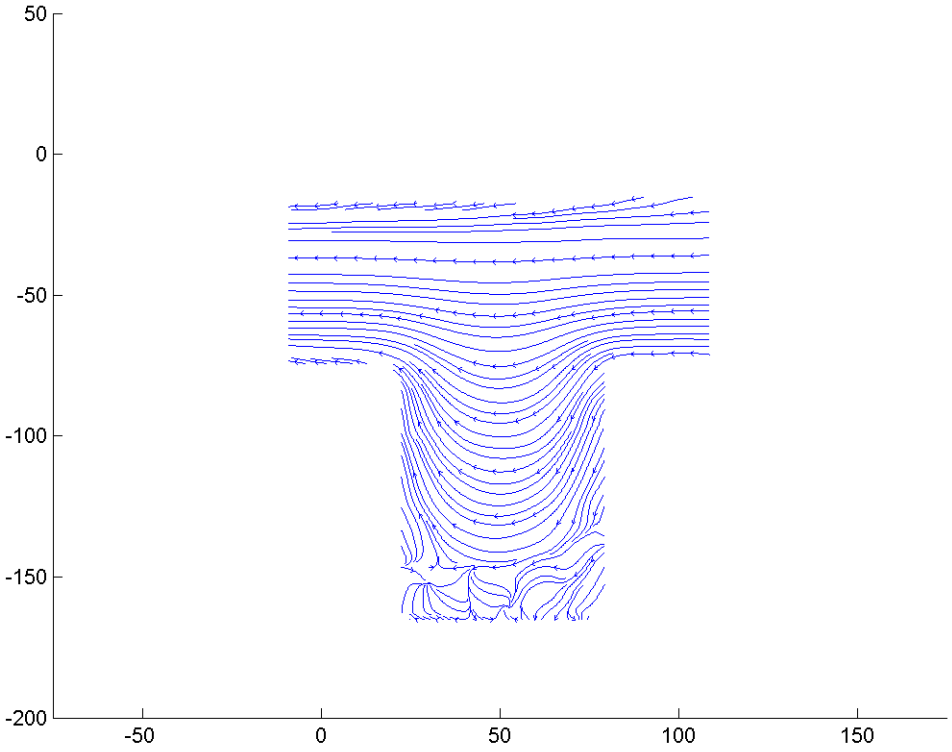

Figure F.367: Streamline image during phase increment 23 at 113.14 Hz with an amplitude of 0.2 mm and a Re of 0.1.

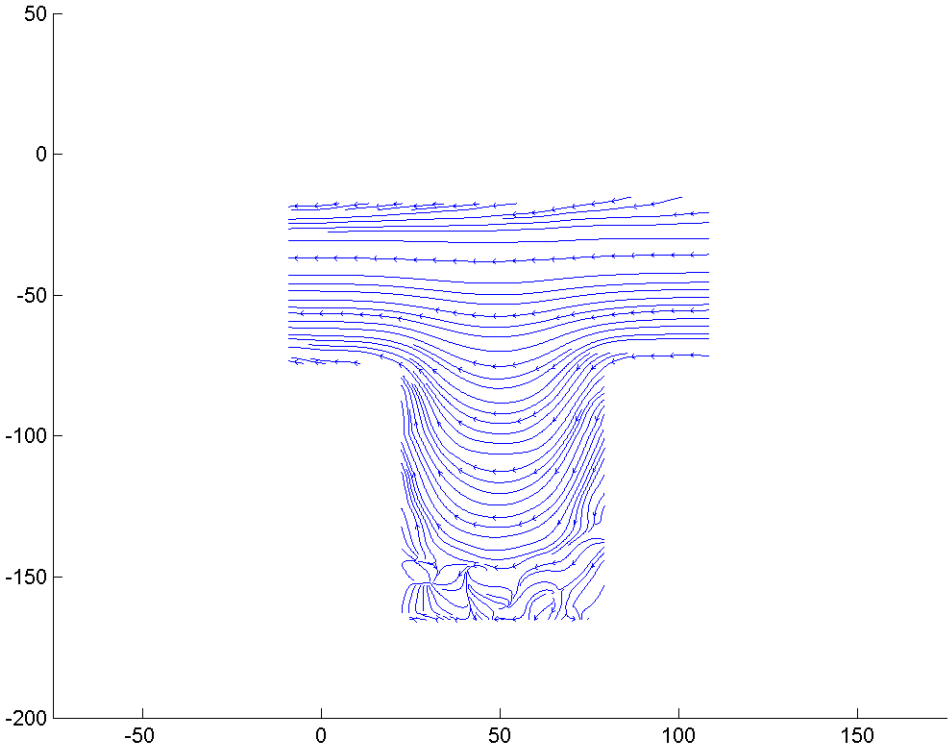

Figure F.368: Streamline image during phase increment 24 at 113.14 Hz with an amplitude of 0.2 mm and a Re of 0.1.

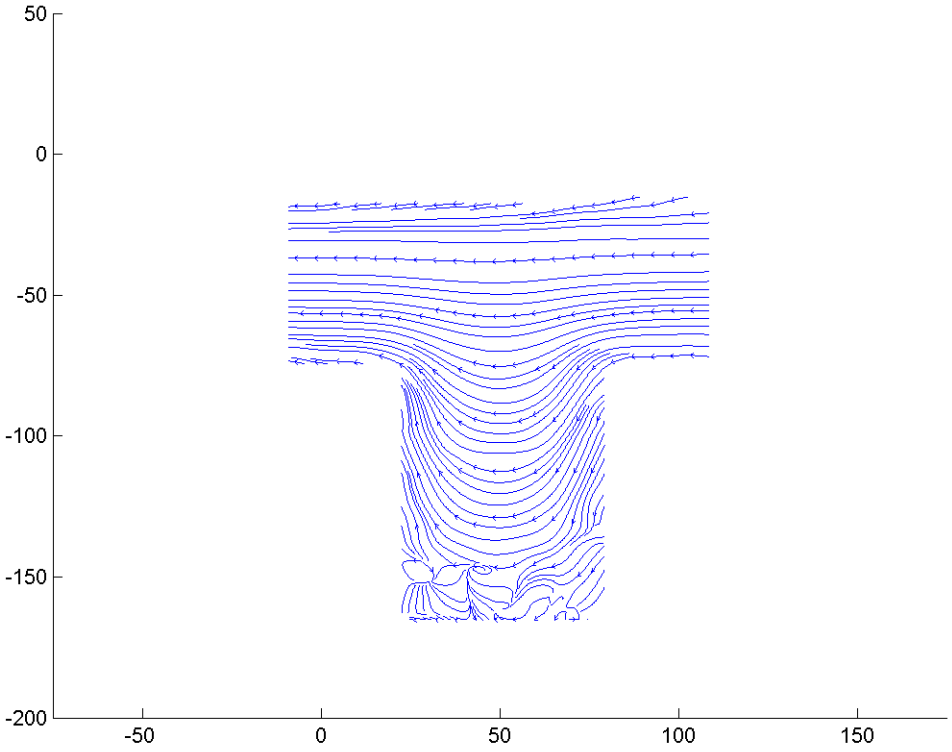

Figure F.369: Streamline image during phase increment 25 at 113.14 Hz with an amplitude of 0.2 mm and a Re of 0.1.

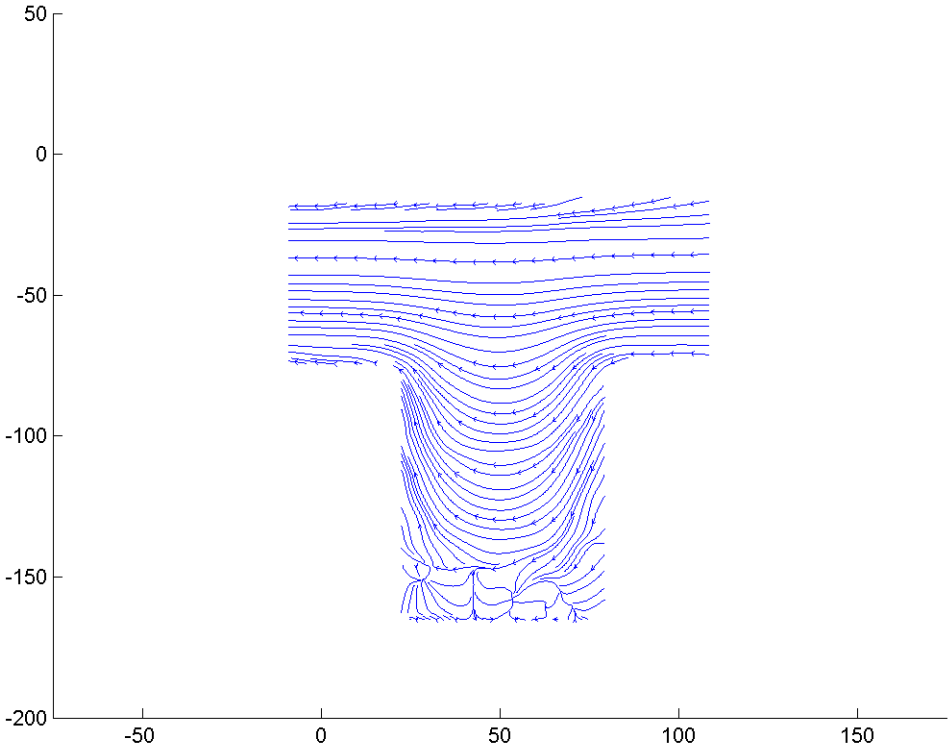

Figure F.370: Streamline image during phase increment 26 at 113.14 Hz with an amplitude of 0.2 mm and a Re of 0.1.

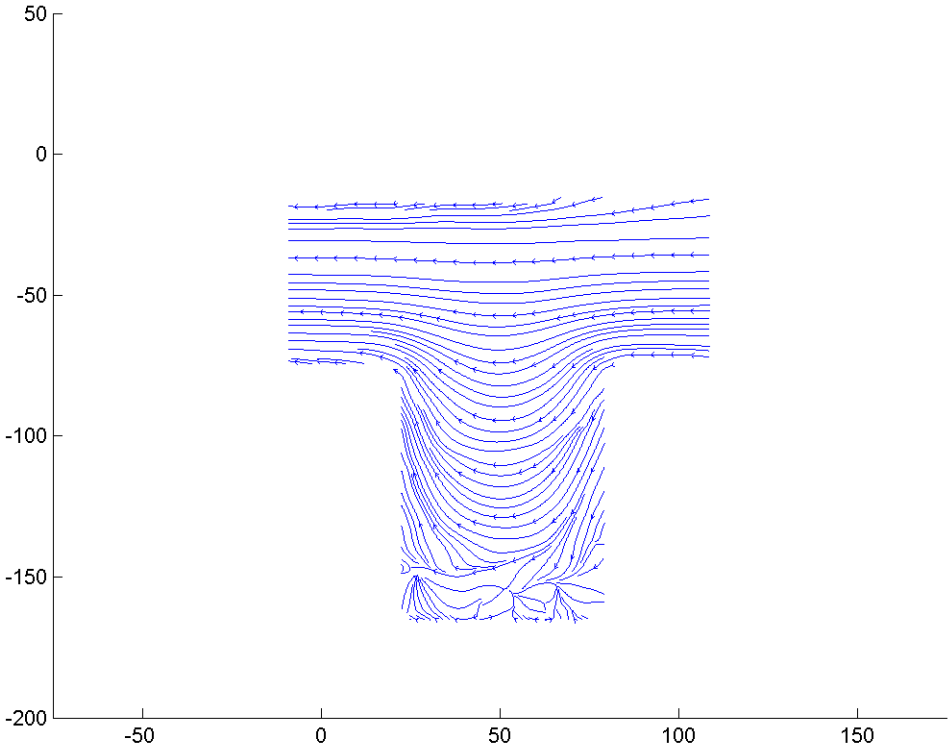

Figure F.371: Streamline image during phase increment 27 at 113.14 Hz with an amplitude of 0.2 mm and a Re of 0.1.

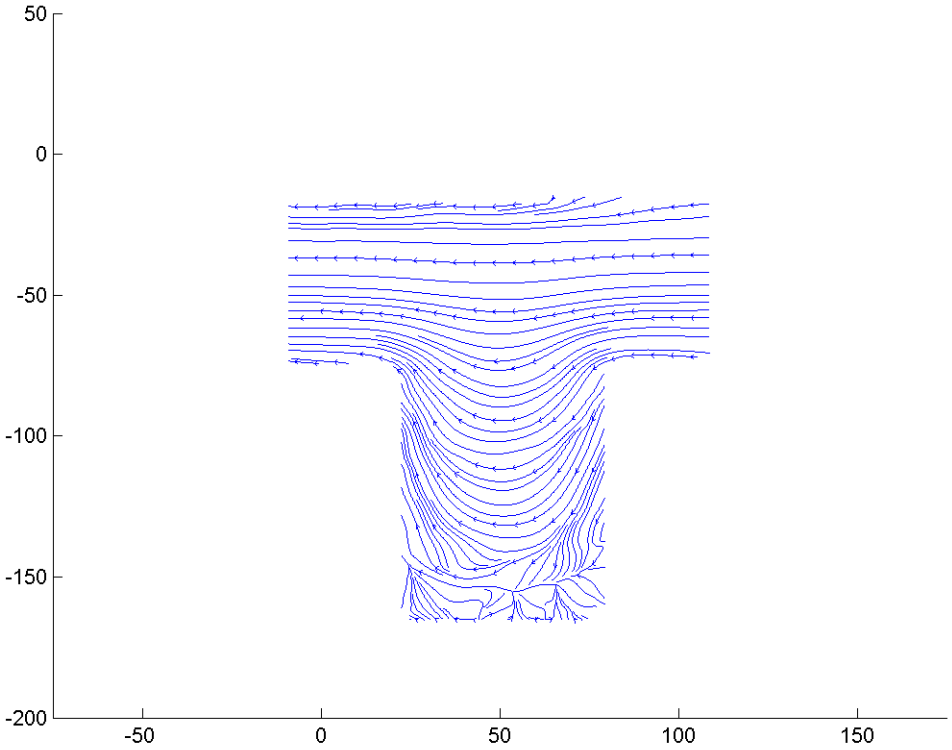

Figure F.372: Streamline image during phase increment 28 at 113.14 Hz with an amplitude of 0.2 mm and a Re of 0.1.

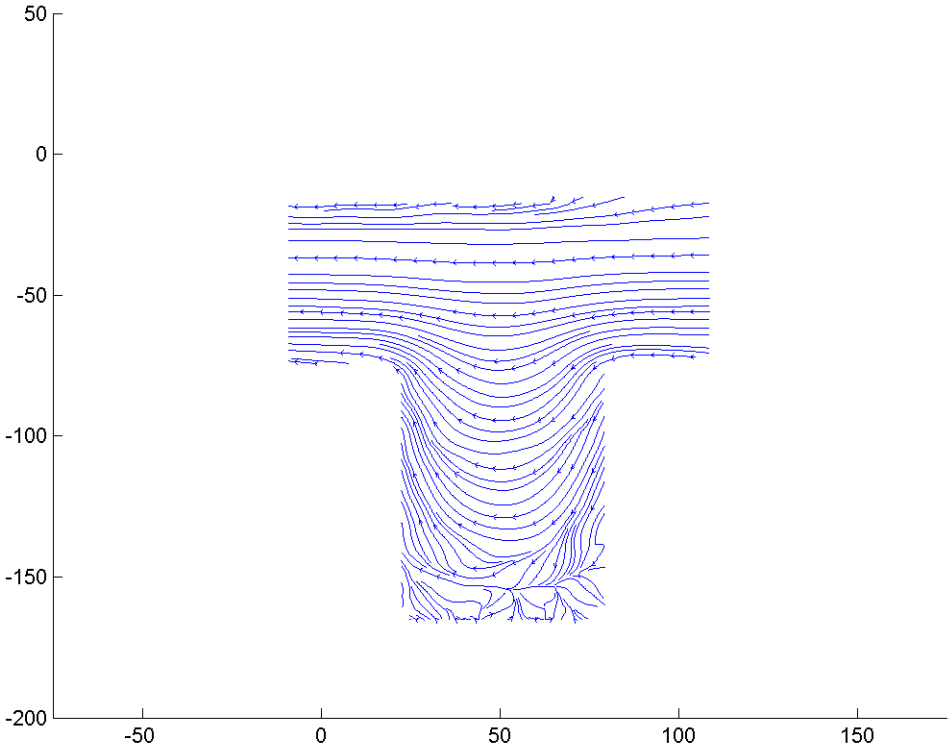

Figure F.373: Streamline image during phase increment 29 at 113.14 Hz with an amplitude of 0.2 mm and a Re of 0.1.

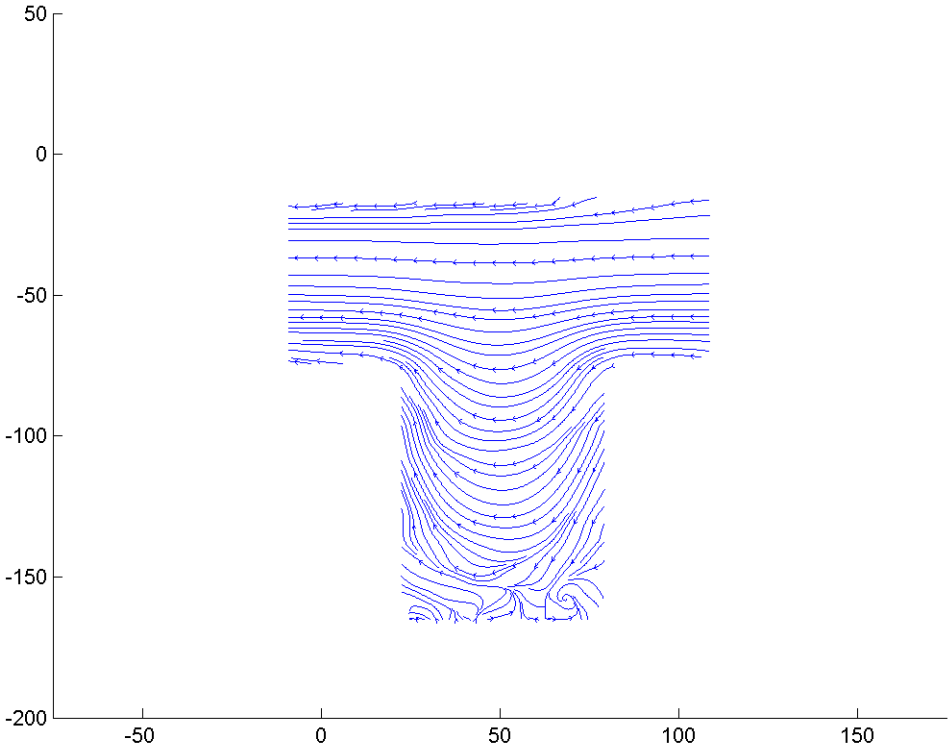

Figure F.374: Streamline image during phase increment 30 at 113.14 Hz with an amplitude of 0.2 mm and a Re of 0.1.

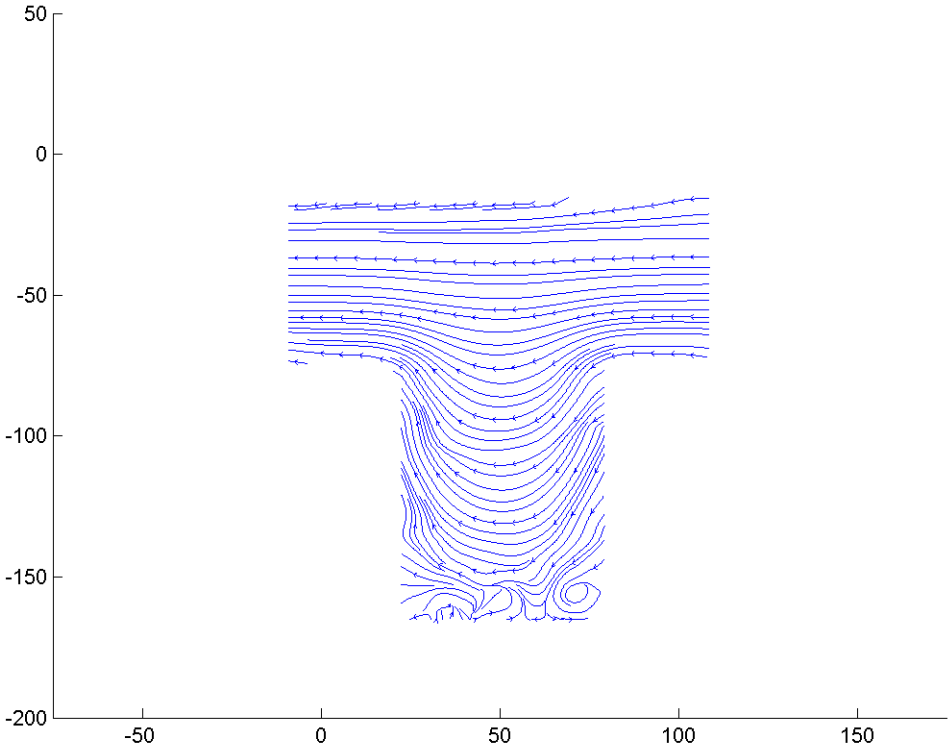

Figure F.375: Streamline image during phase increment 31 at 113.14 Hz with an amplitude of 0.2 mm and a Re of 0.1.

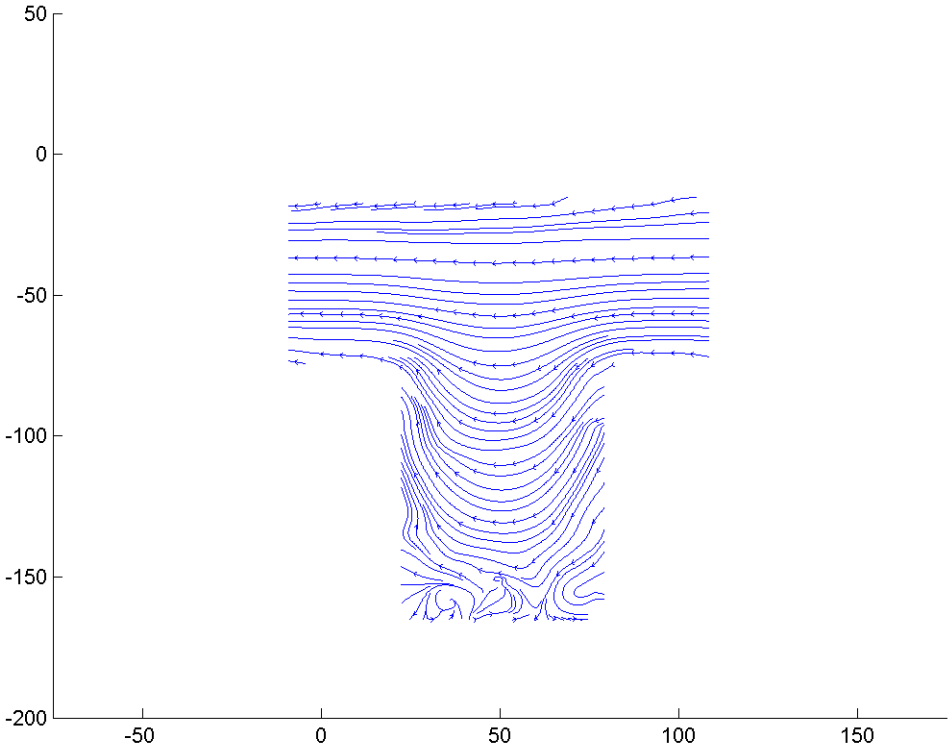

Figure F.376: Streamline image during phase increment 32 at 113.14 Hz with an amplitude of 0.2 mm and a Re of 0.1.

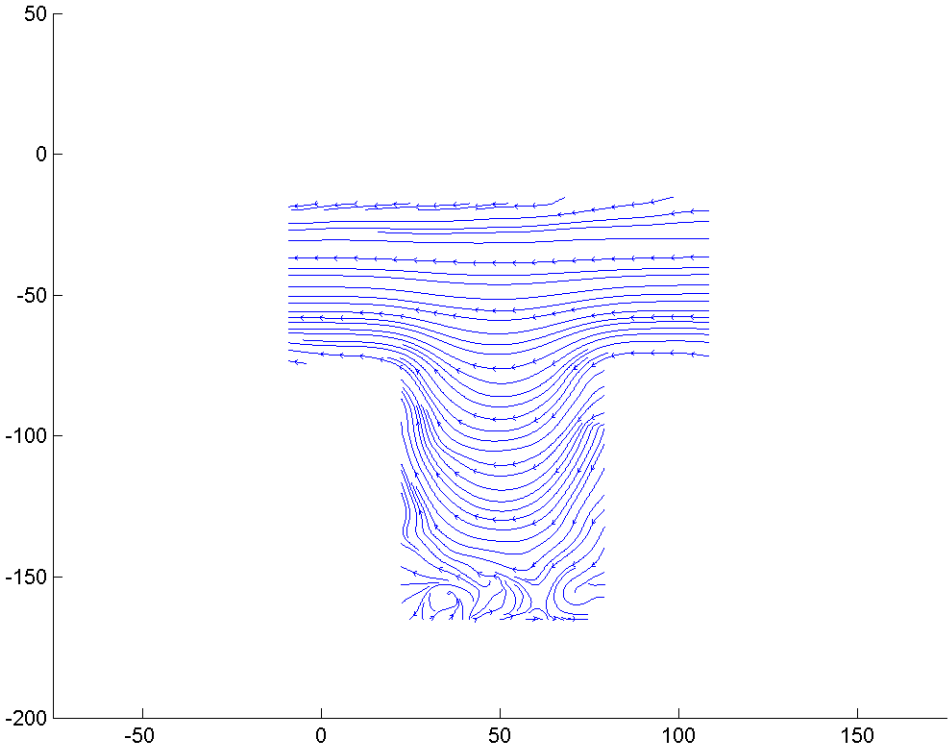

Figure F.377: Streamline image during phase increment 33 at 113.14 Hz with an amplitude of 0.2 mm and a Re of 0.1.

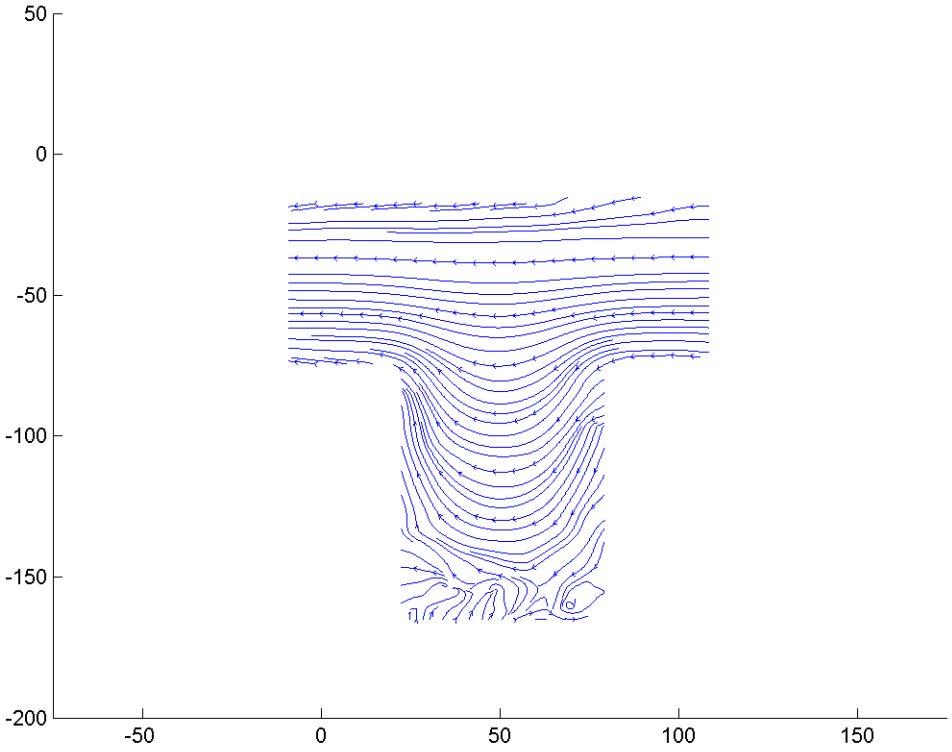

Figure F.378: Streamline image during phase increment 34 at 113.14 Hz with an amplitude of 0.2 mm and a Re of 0.1.

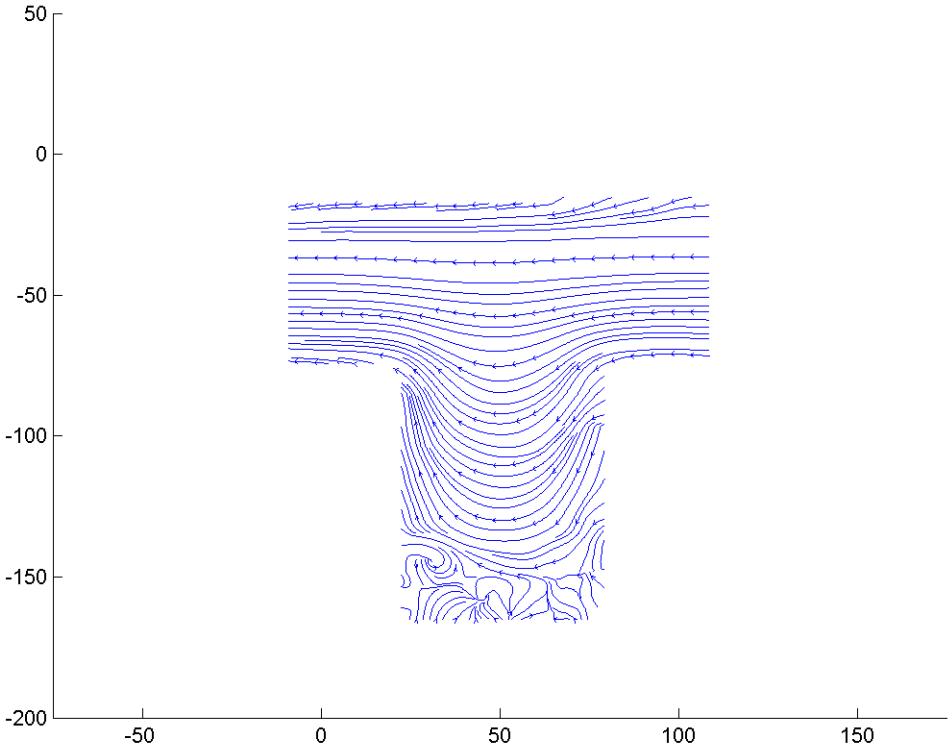

Figure F.379: Streamline image during phase increment 35 at 113.14 Hz with an amplitude of 0.2 mm and a Re of 0.1.

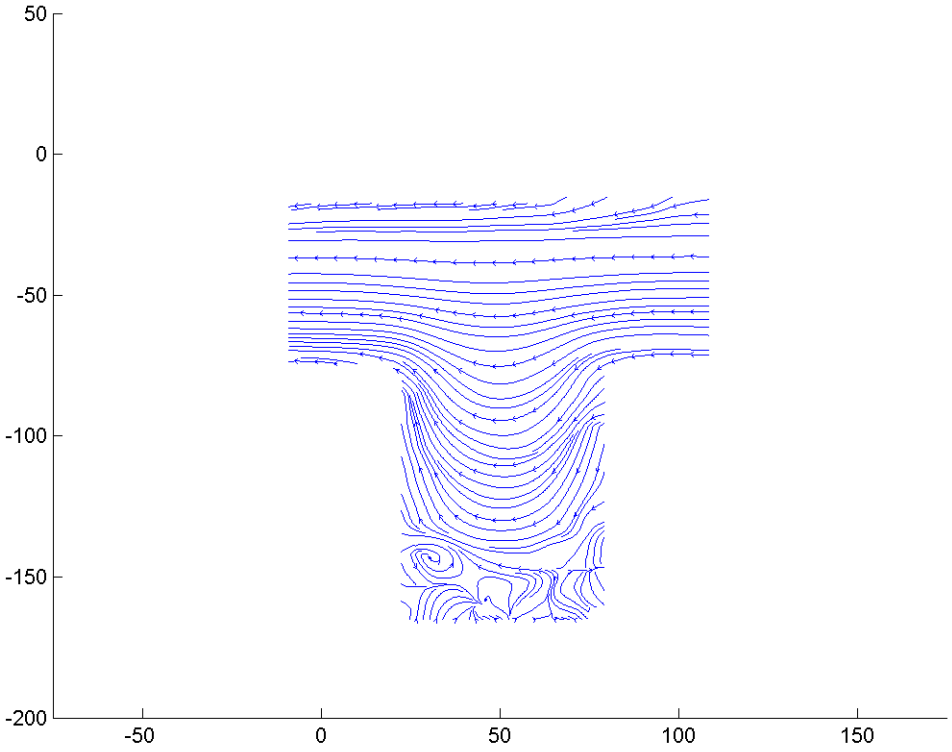

Figure F.380: Streamline image during phase increment 36 at 113.14 Hz with an amplitude of 0.2 mm and a Re of 0.1.

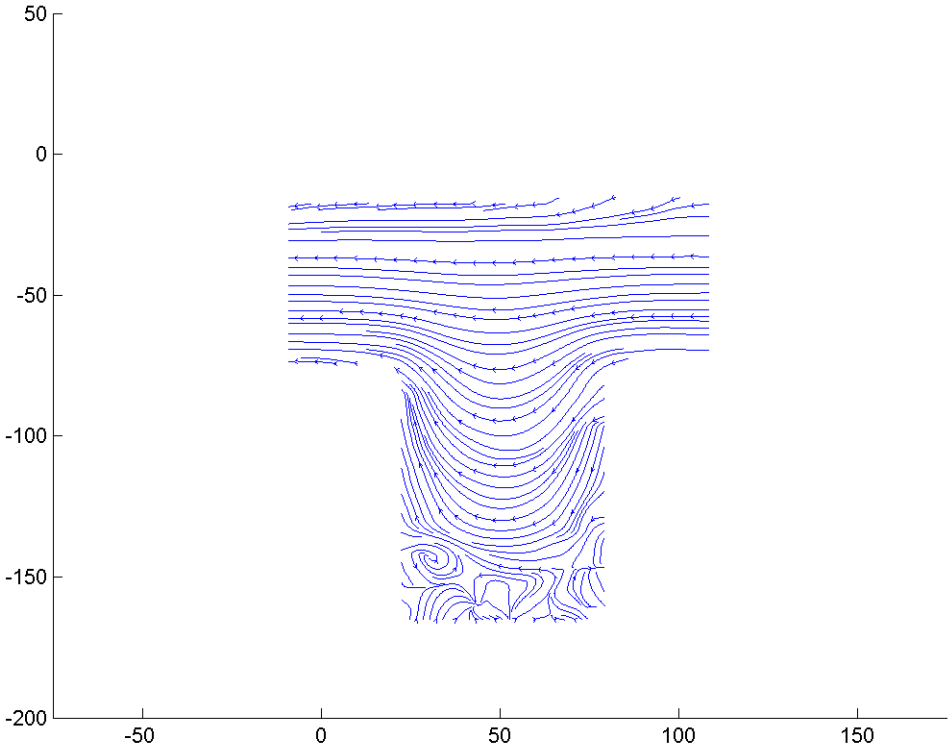

Figure F.381: Streamline image during phase increment 37 at 113.14 Hz with an amplitude of 0.2 mm and a Re of 0.1.

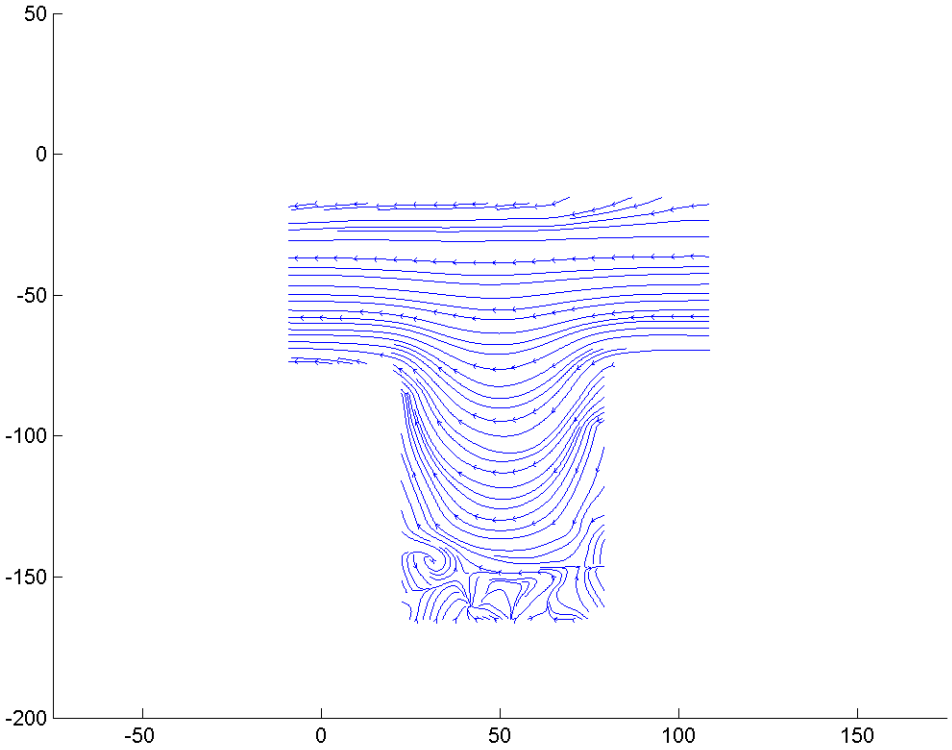

Figure F.382: Streamline image during phase increment 38 at 113.14 Hz with an amplitude of 0.2 mm and a Re of 0.1.

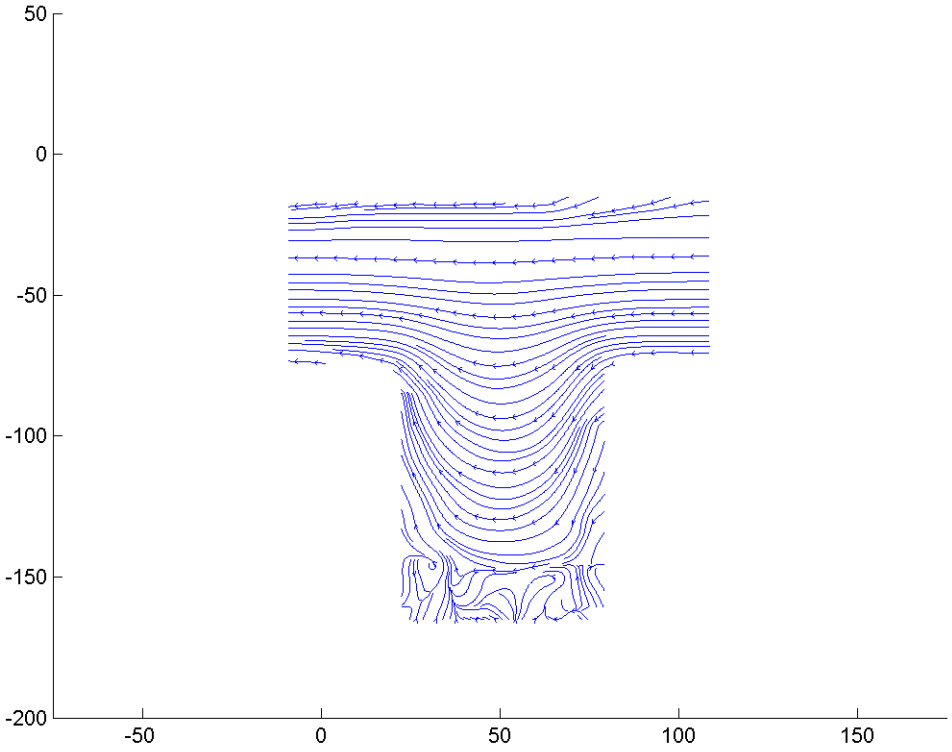

Figure F.383: Streamline image during phase increment 39 at 113.14 Hz with an amplitude of 0.2 mm and a Re of 0.1.

F.4.3 Residence time of particles in the cavity at 113.14 Hz with an amplitude of 0.2 mm

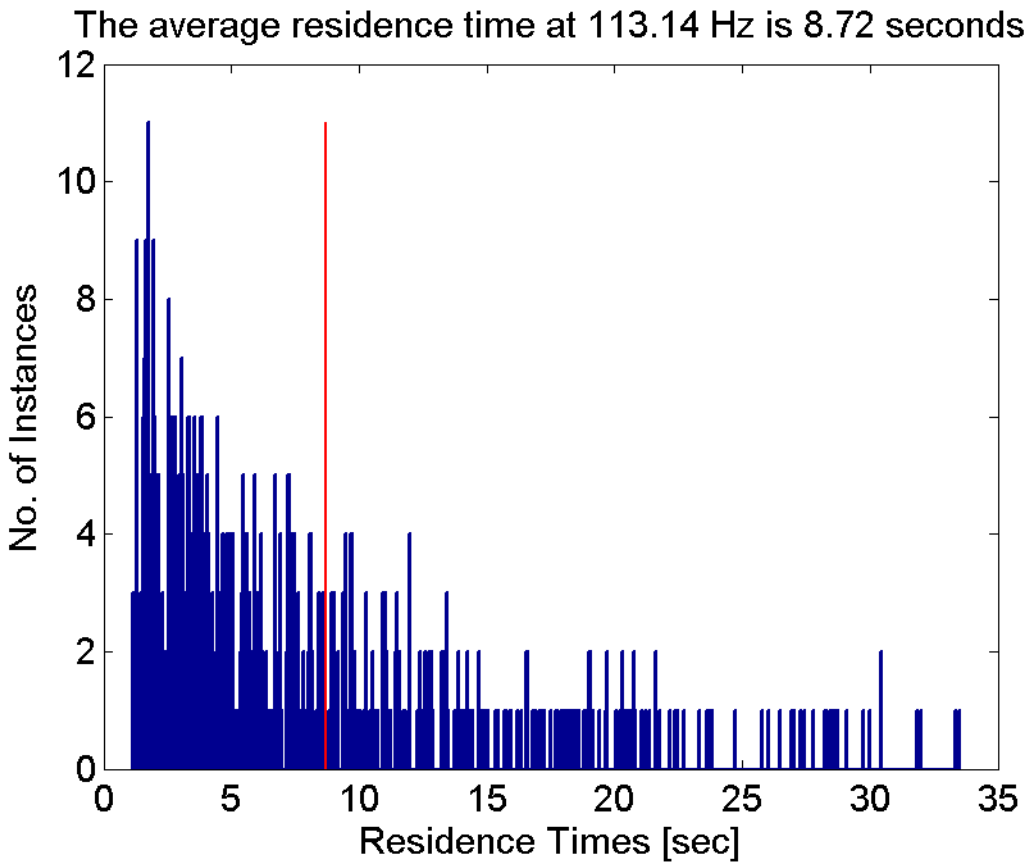

Figure F.384: The residence time distribution for the AR = 0.5 cavity at Re 0.1 at 113.14 Hz. The average residence time is 8.72 secs.

F.4.4 Lagrangian coherent structures at 113.14 Hz with an amplitude of 0.2 mm

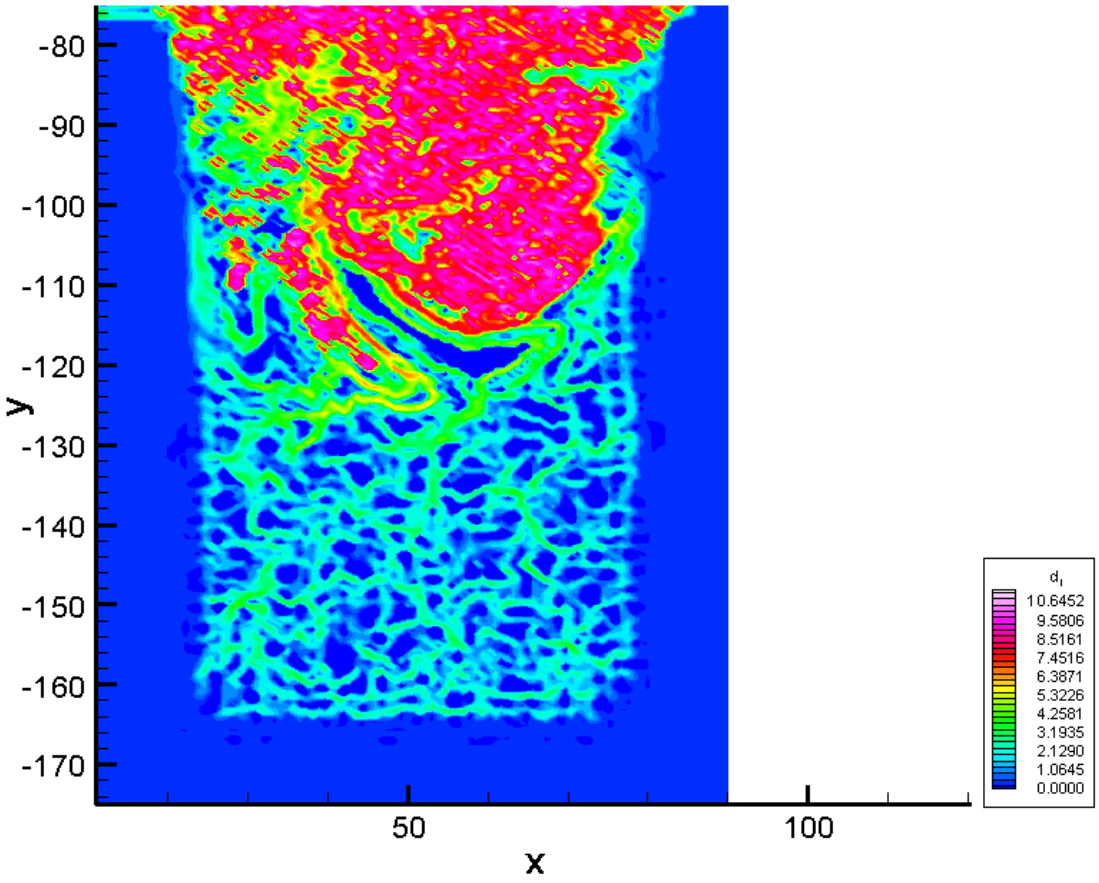

Figure F.385: The backward time LCS during phase increment 1 at 113.14 Hz with an amplitude of 0.2 mm.

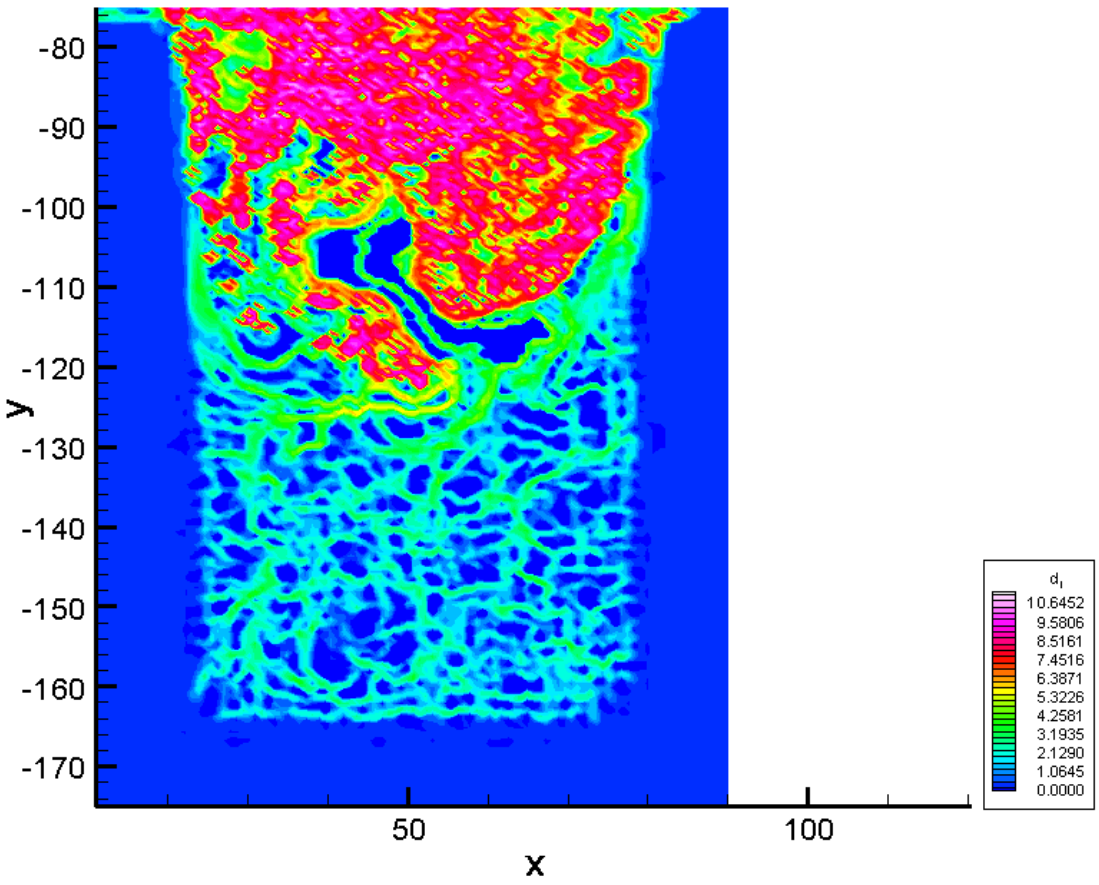

Figure F.386: The backward time LCS during phase increment 2 at 113.14 Hz with an amplitude of 0.2 mm.

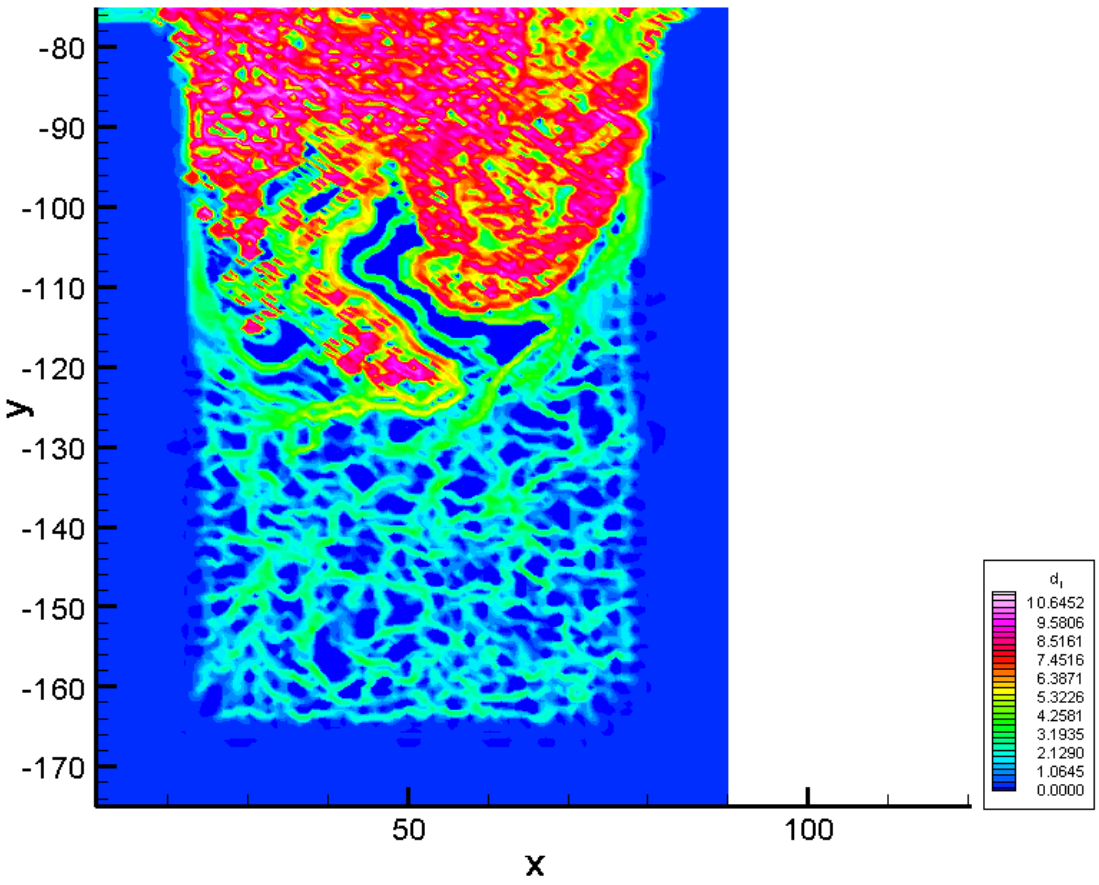

Figure F.387: The backward time LCS during phase increment 3 at 113.14 Hz with an amplitude of 0.2 mm.

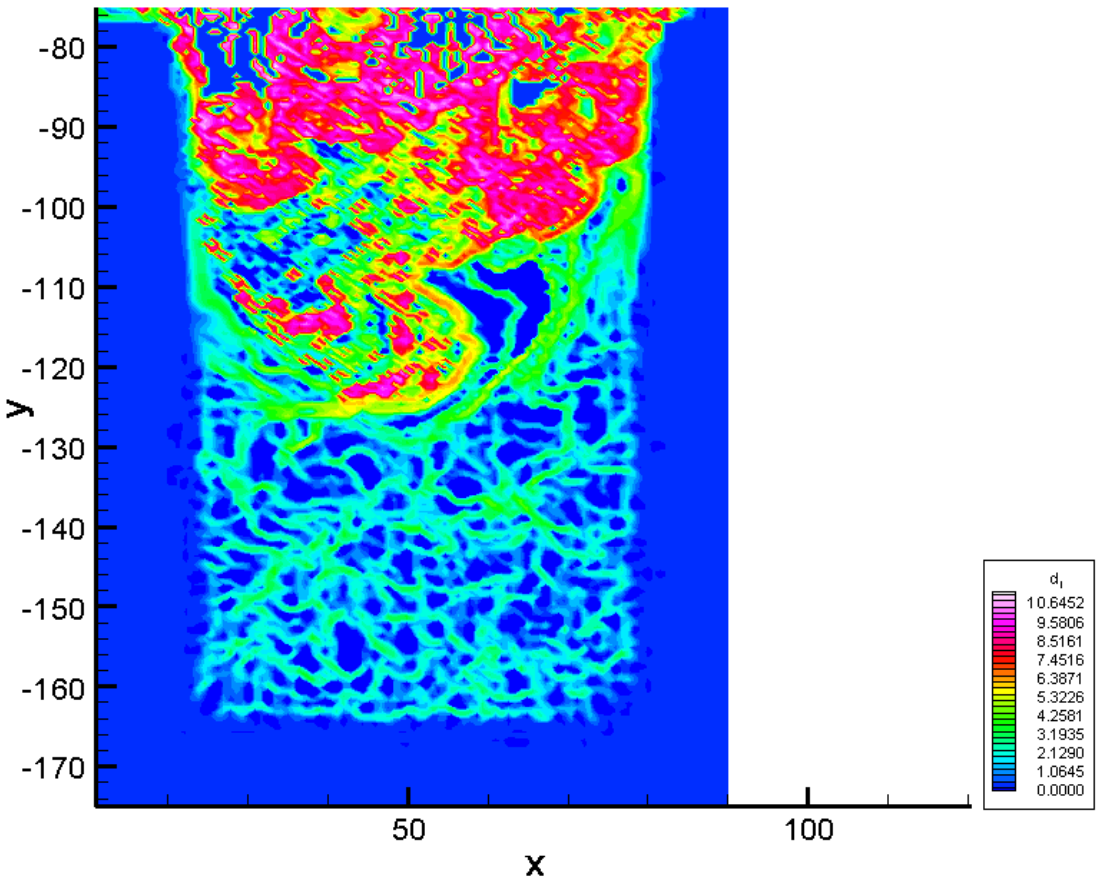

Figure F.388: The backward time LCS during phase increment 4 at 113.14 Hz with an amplitude of 0.2 mm.

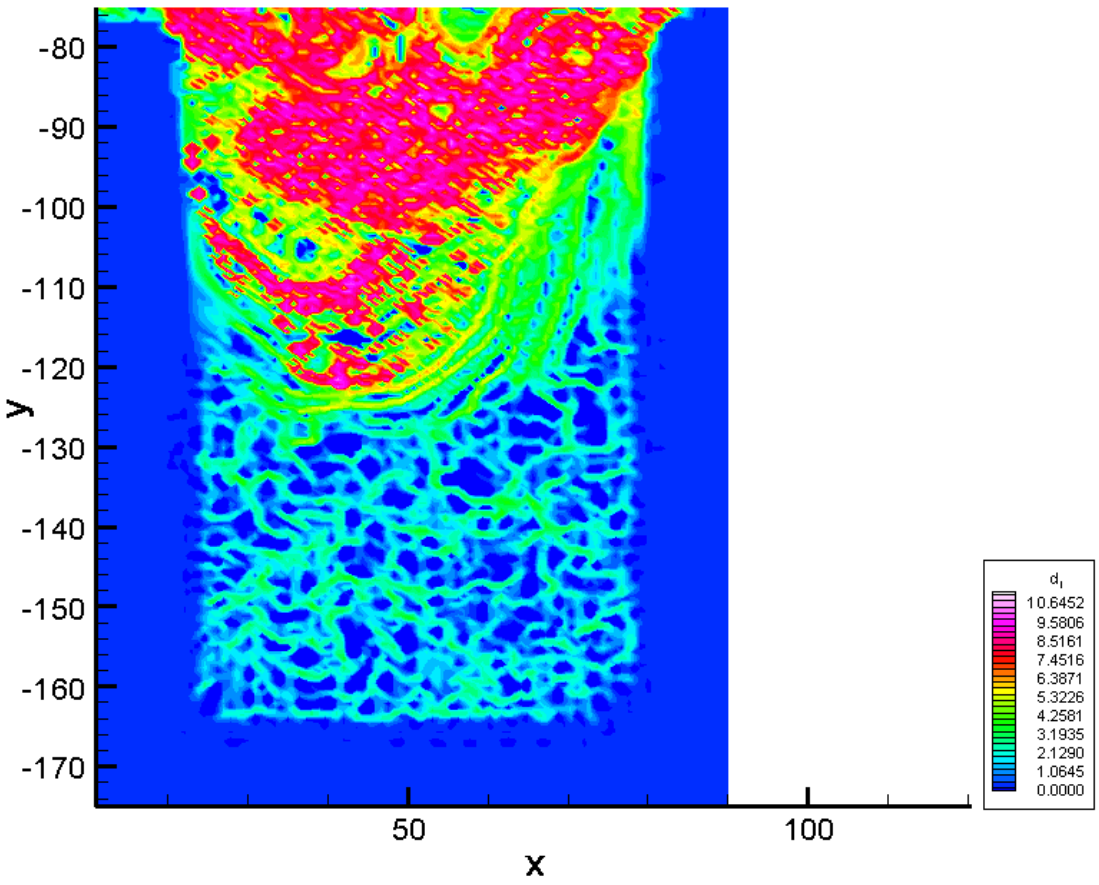

Figure F.389: The backward time LCS during phase increment 5 at 113.14 Hz with an amplitude of 0.2 mm.

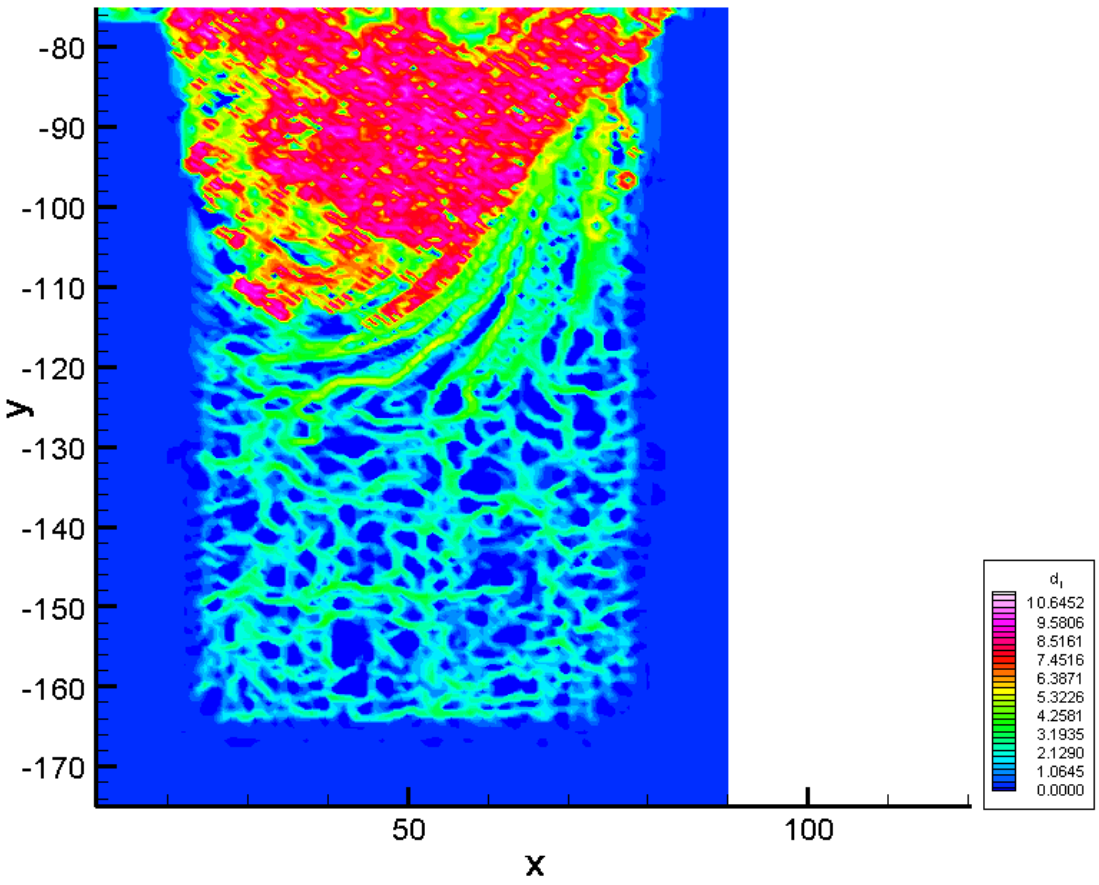

Figure F.390: The backward time LCS during phase increment 6 at 113.14 Hz with an amplitude of 0.2 mm.

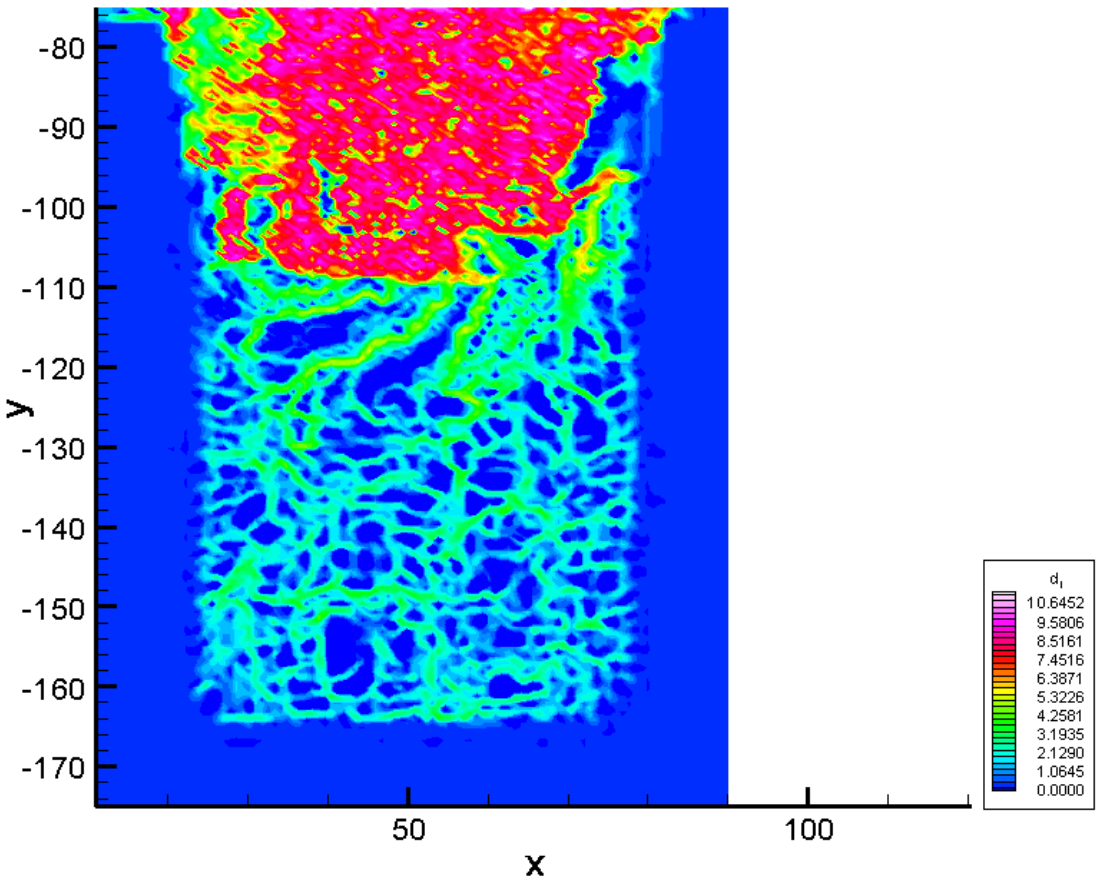

Figure F.391: The backward time LCS during phase increment 7 at 113.14 Hz with an amplitude of 0.2 mm.

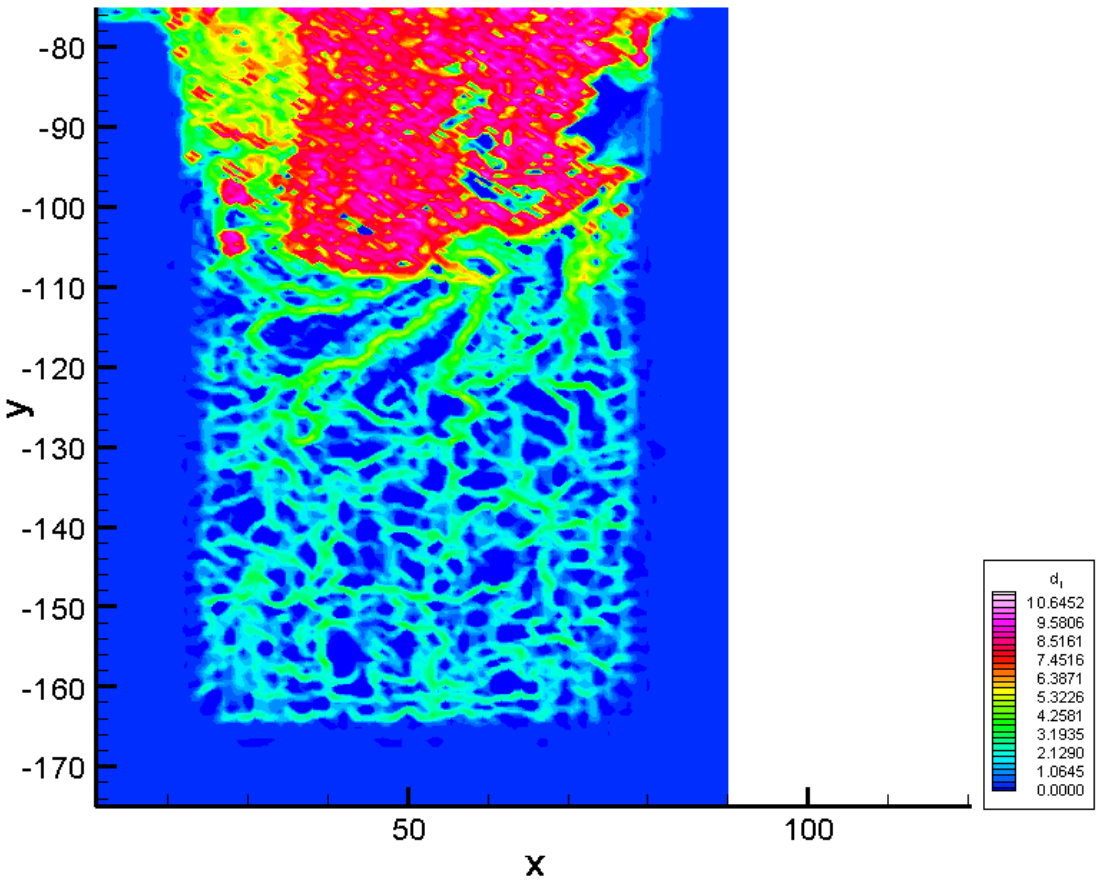

Figure F.392: The backward time LCS during phase increment 8 at 113.14 Hz with an amplitude of 0.2 mm.

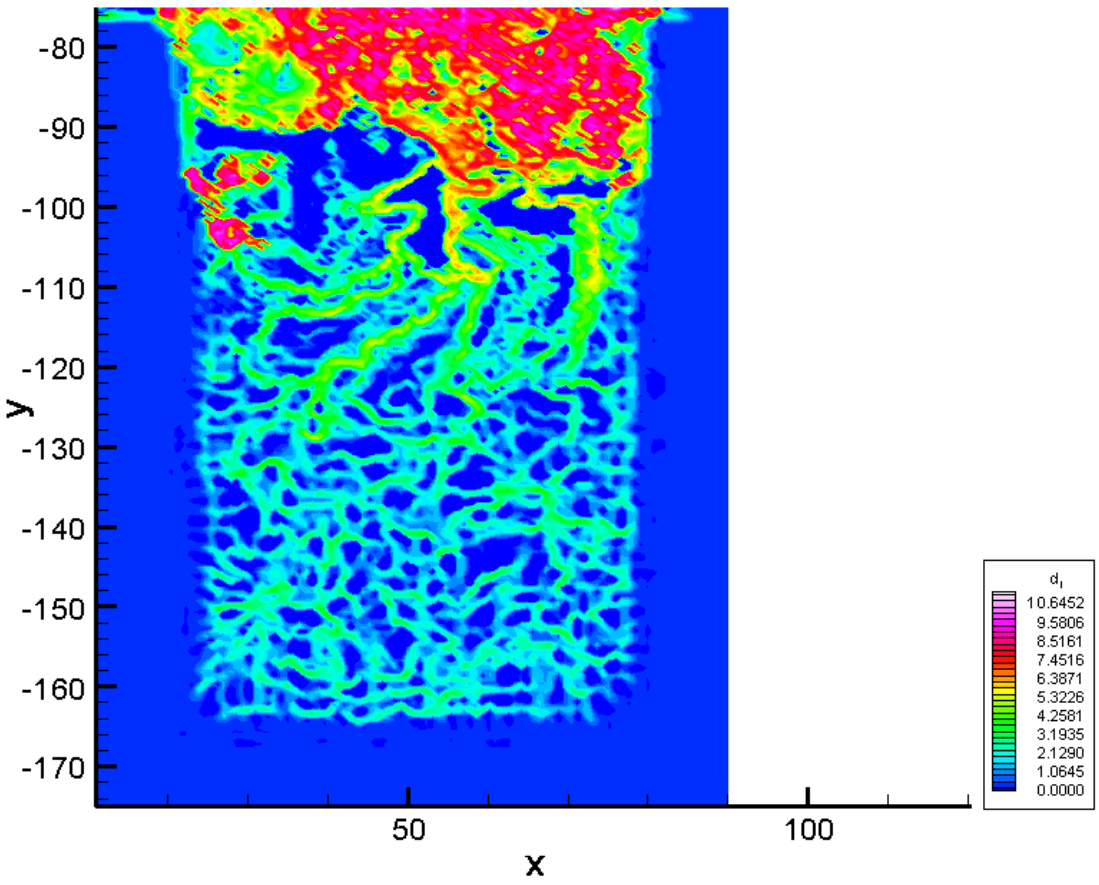

Figure F.393: The backward time LCS during phase increment 9 at 113.14 Hz with an amplitude of 0.2 mm.

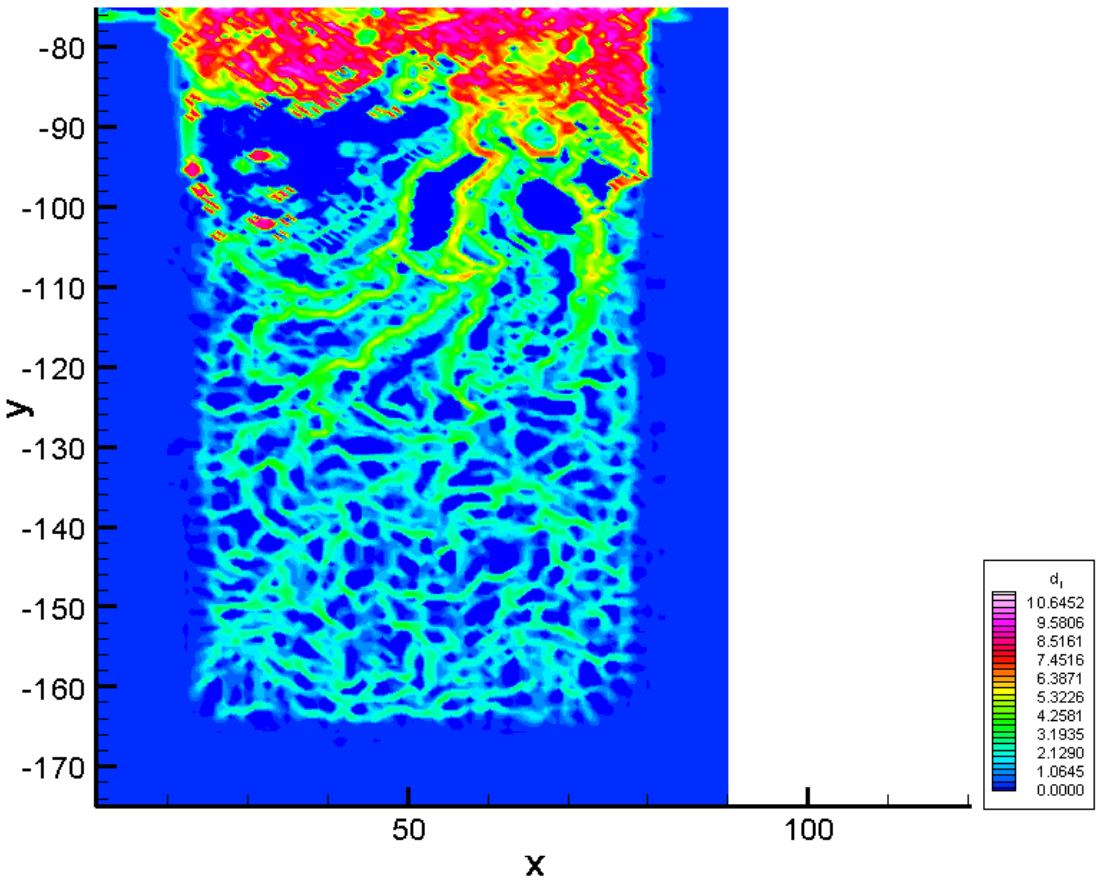

Figure F.394: The backward time LCS during phase increment 10 at 113.14 Hz with an amplitude of 0.2 mm.

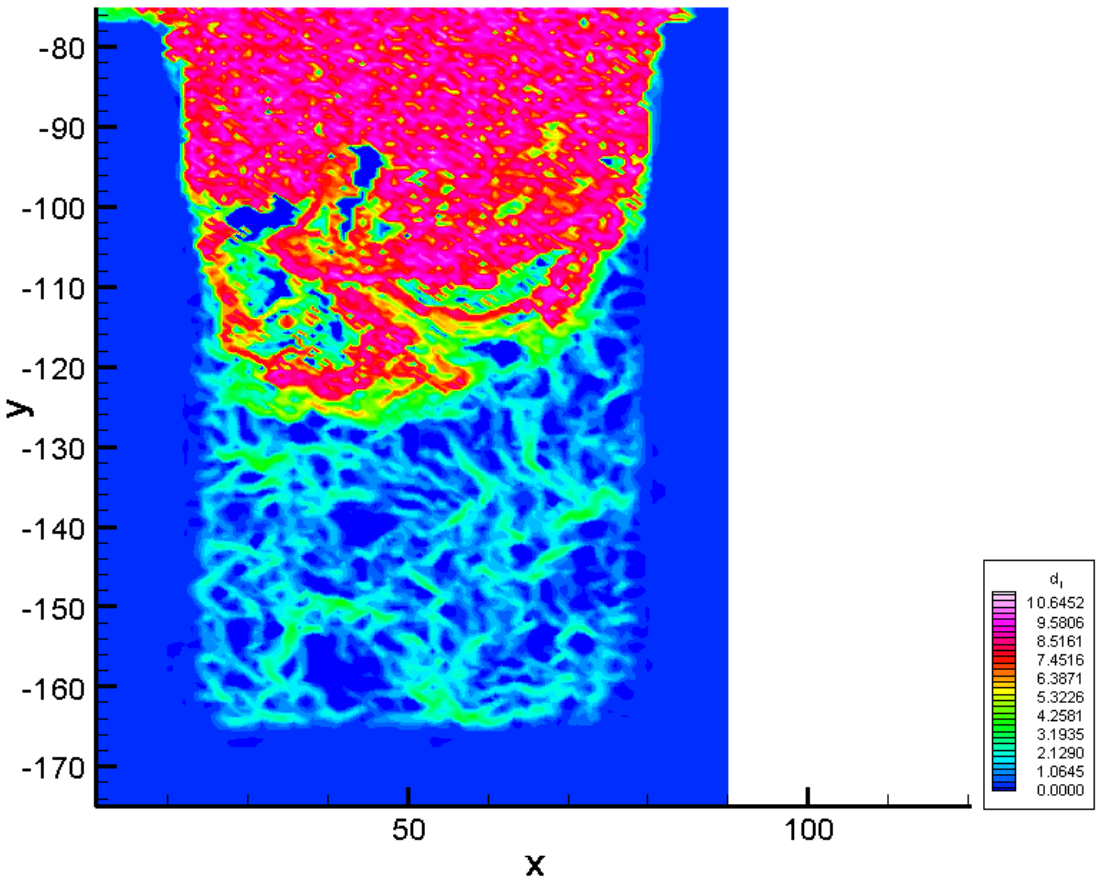

Figure F.395: The forward time LCS during phase increment 1 at 113.14 Hz with an amplitude of 0.2 mm.

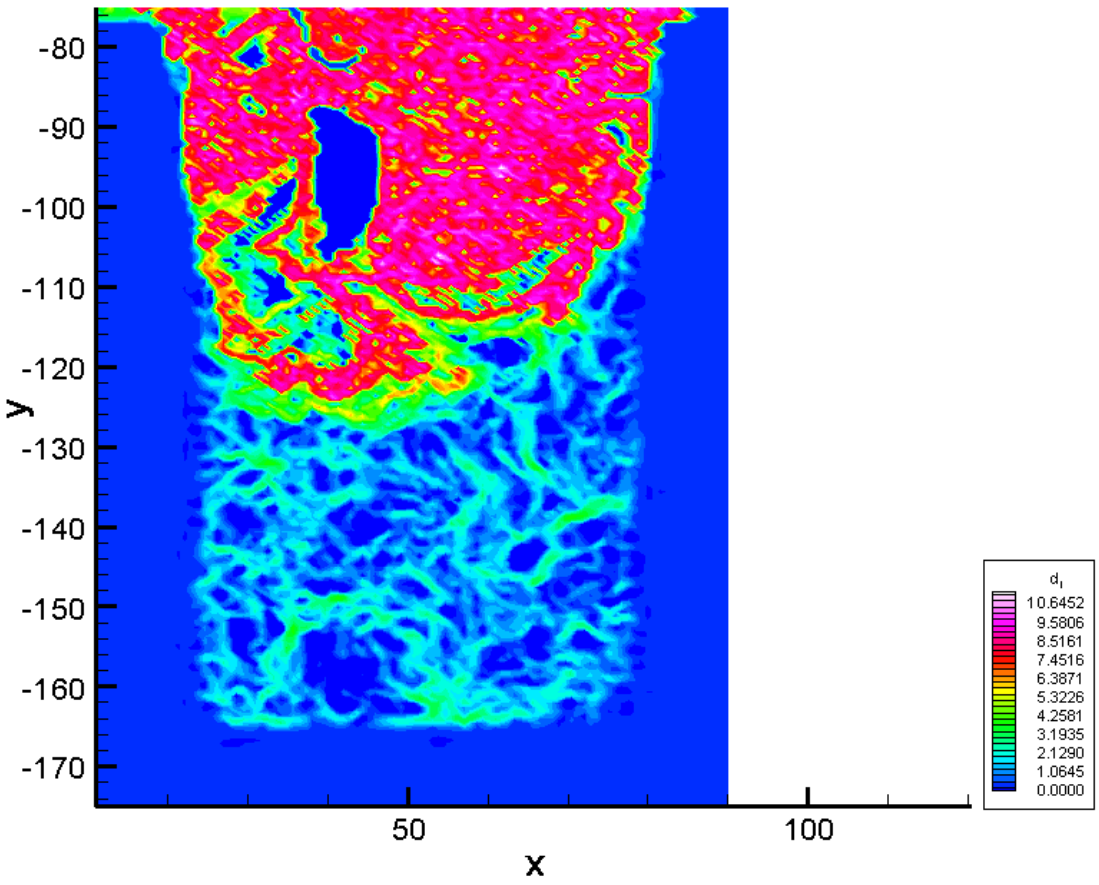

Figure F.396: The forward time LCS during phase increment 2 at 113.14 Hz with an amplitude of 0.2 mm.

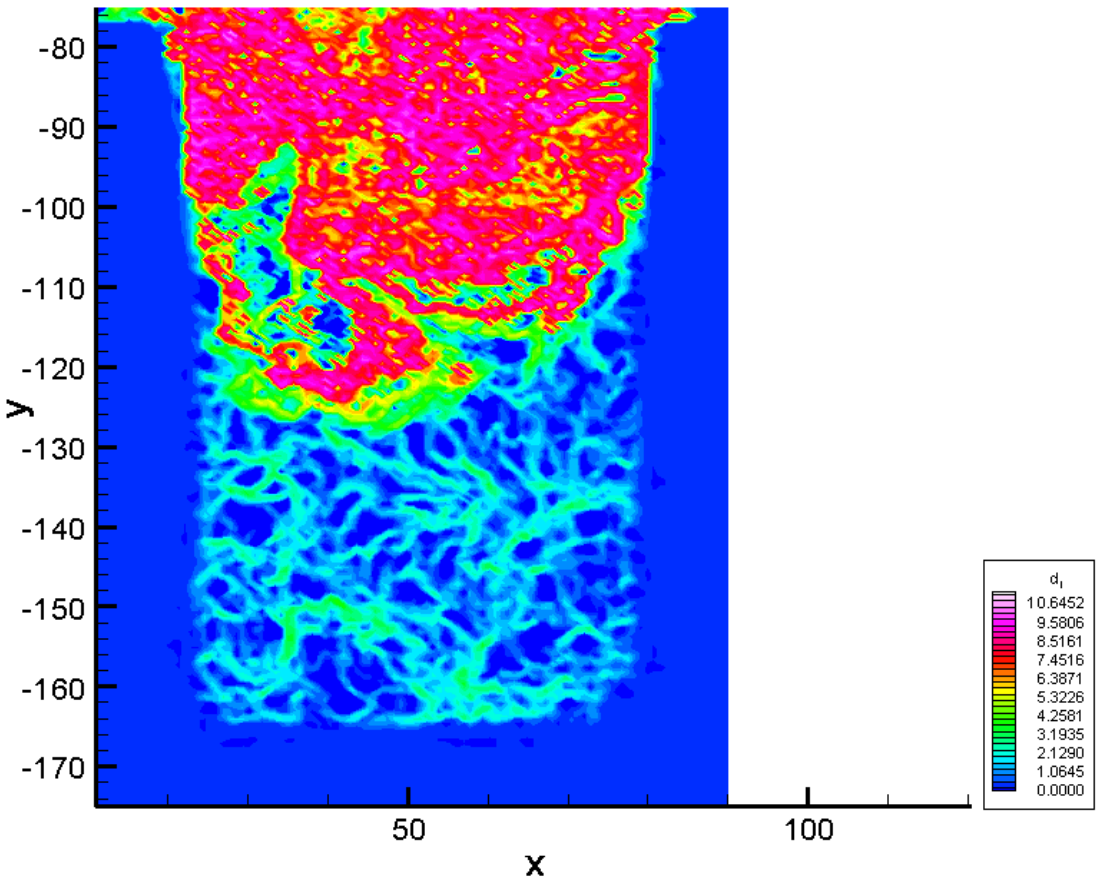

Figure F.397: The forward time LCS during phase increment 3 at 113.14 Hz with an amplitude of 0.2 mm.

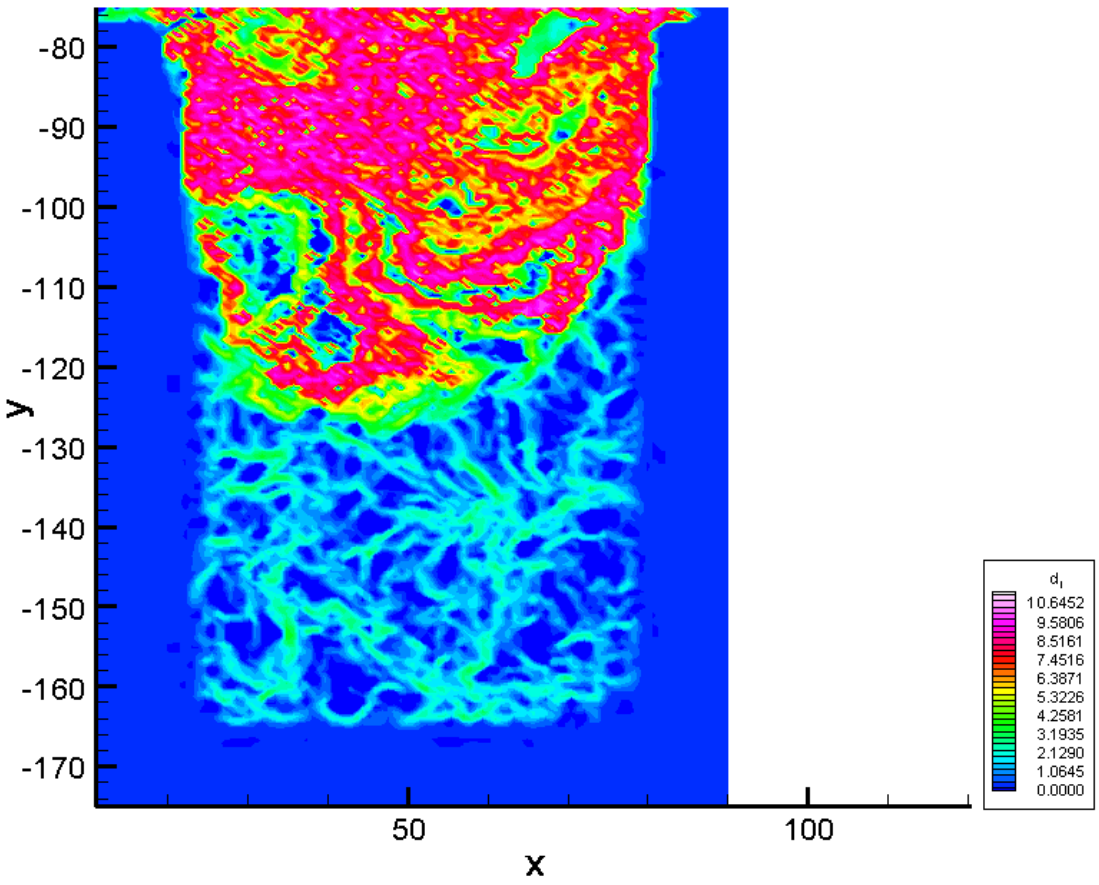

Figure F.398: The forward time LCS during phase increment 4 at 113.14 Hz with an amplitude of 0.2 mm.

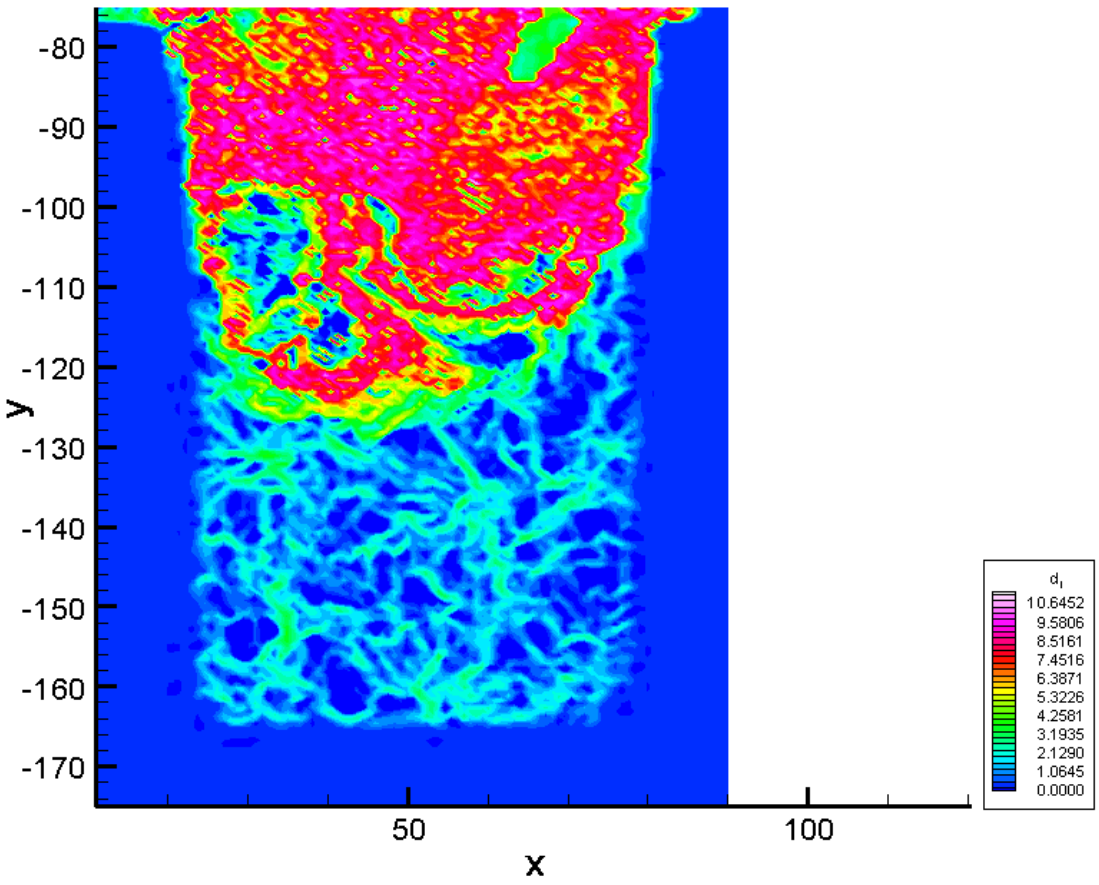

Figure F.399: The forward time LCS during phase increment 5 at 113.14 Hz with an amplitude of 0.2 mm.

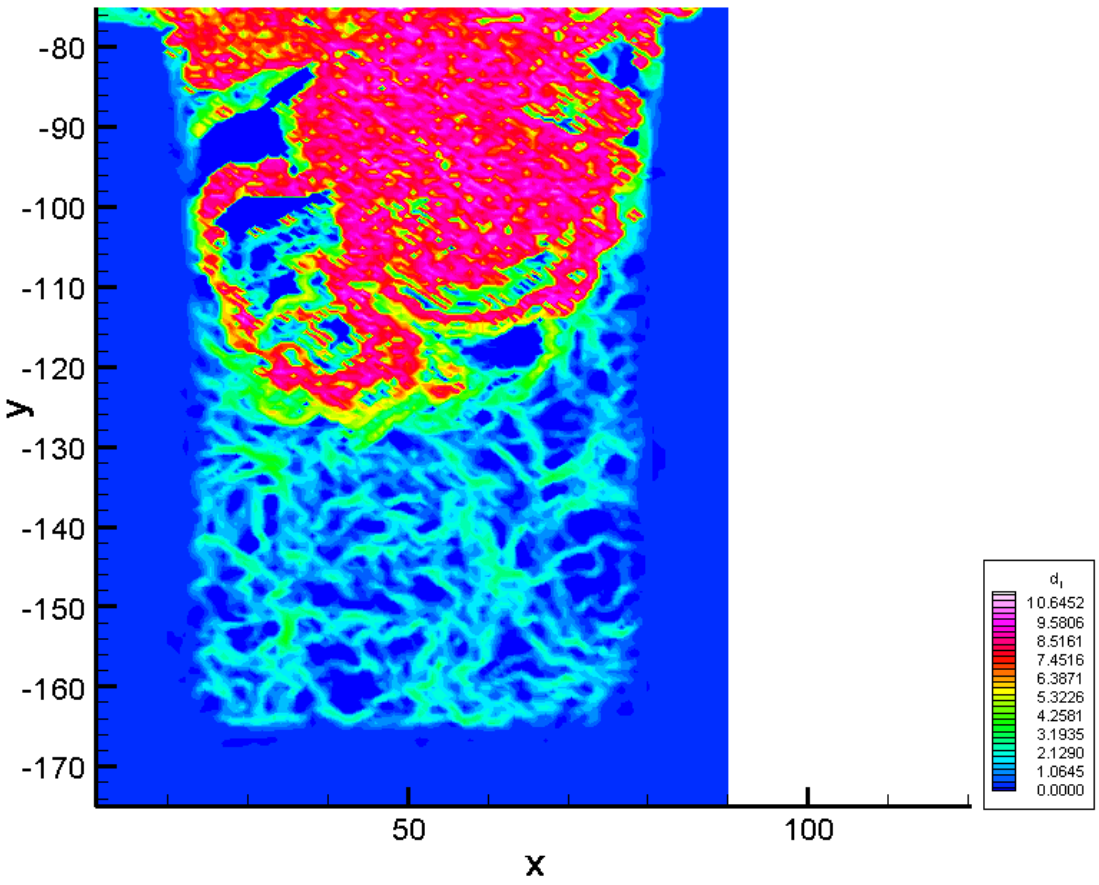

Figure F.400: The forward time LCS during phase increment 6 at 113.14 Hz with an amplitude of 0.2 mm.

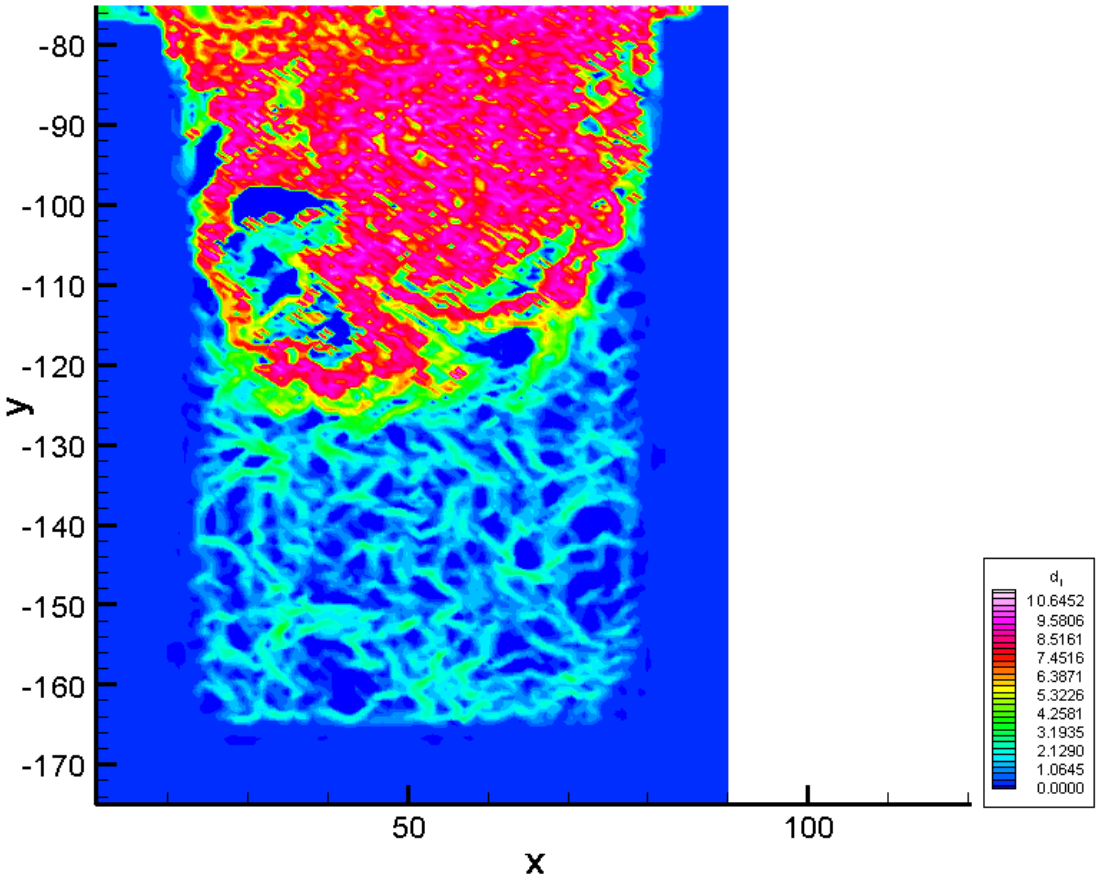

Figure F.401: The forward time LCS during phase increment 7 at 113.14 Hz with an amplitude of 0.2 mm.

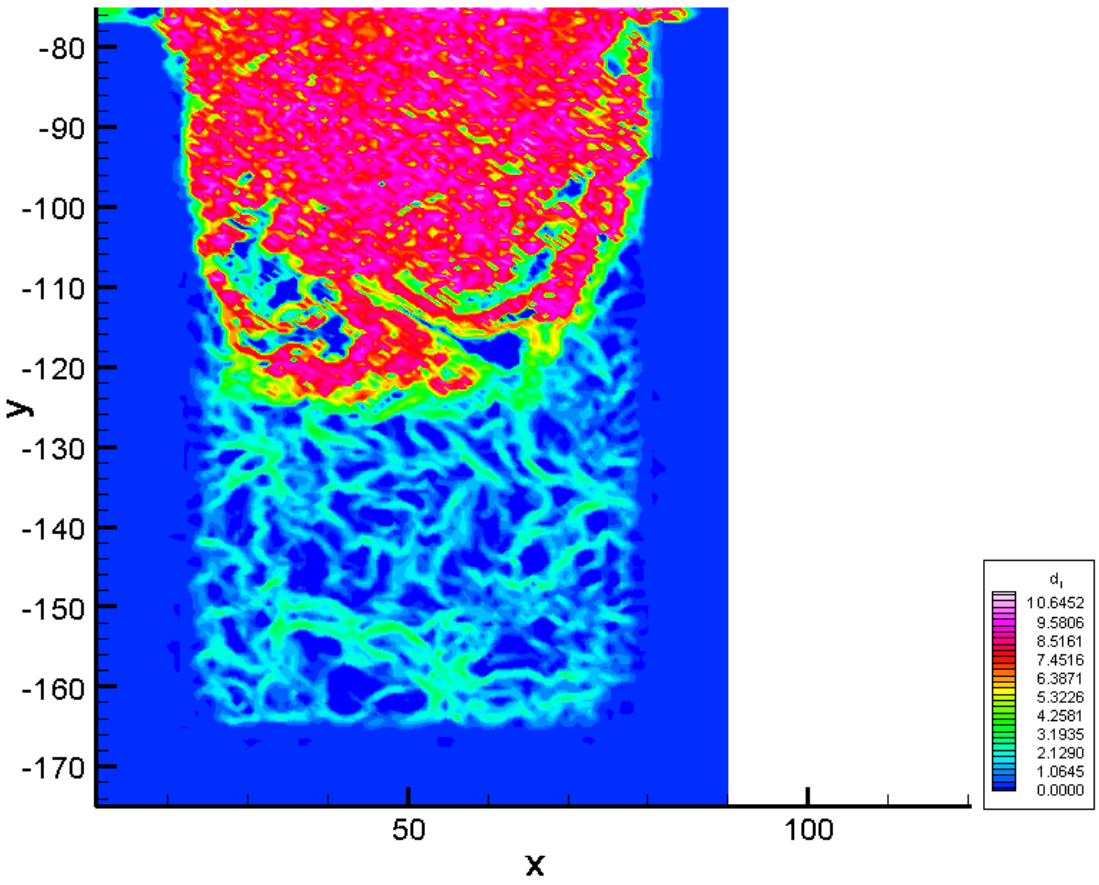

Figure F.402: The forward time LCS during phase increment 8 at 113.14 Hz with an amplitude of 0.2 mm.

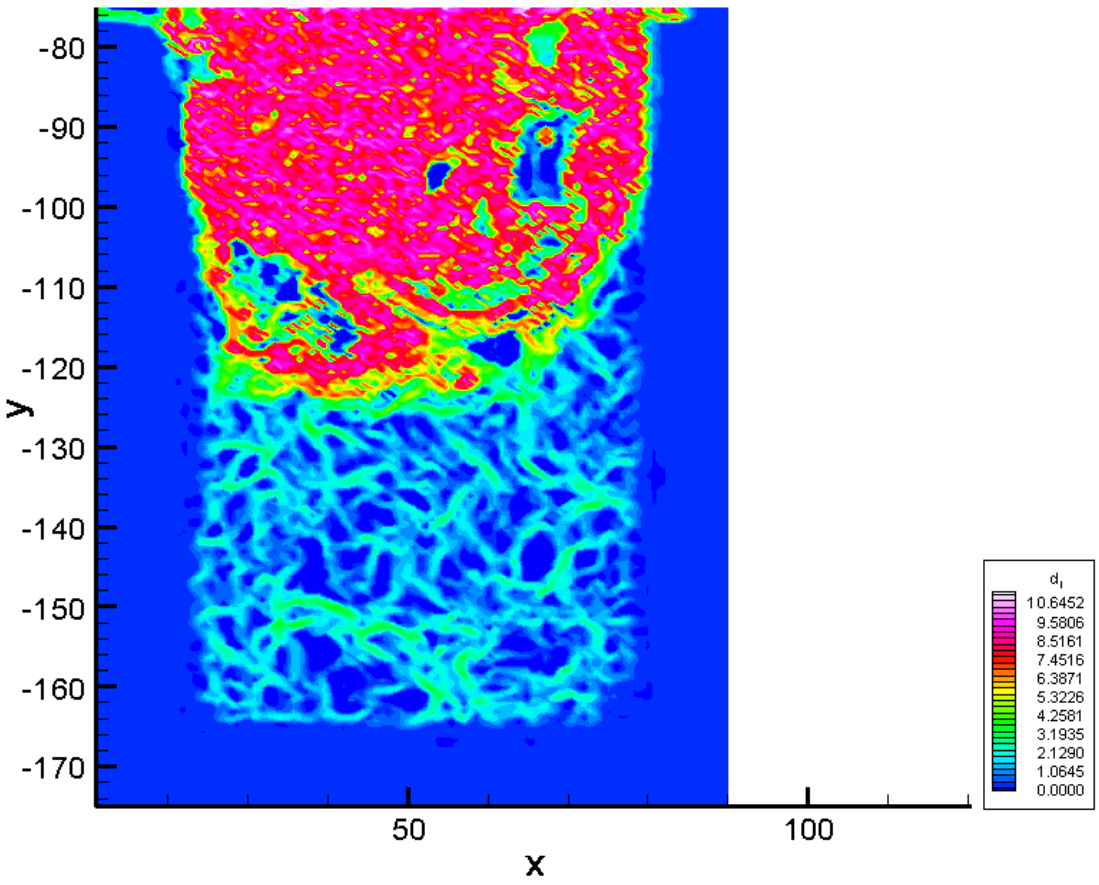

Figure F.403: The forward time LCS during phase increment 9 at 113.14 Hz with an amplitude of 0.2 mm.

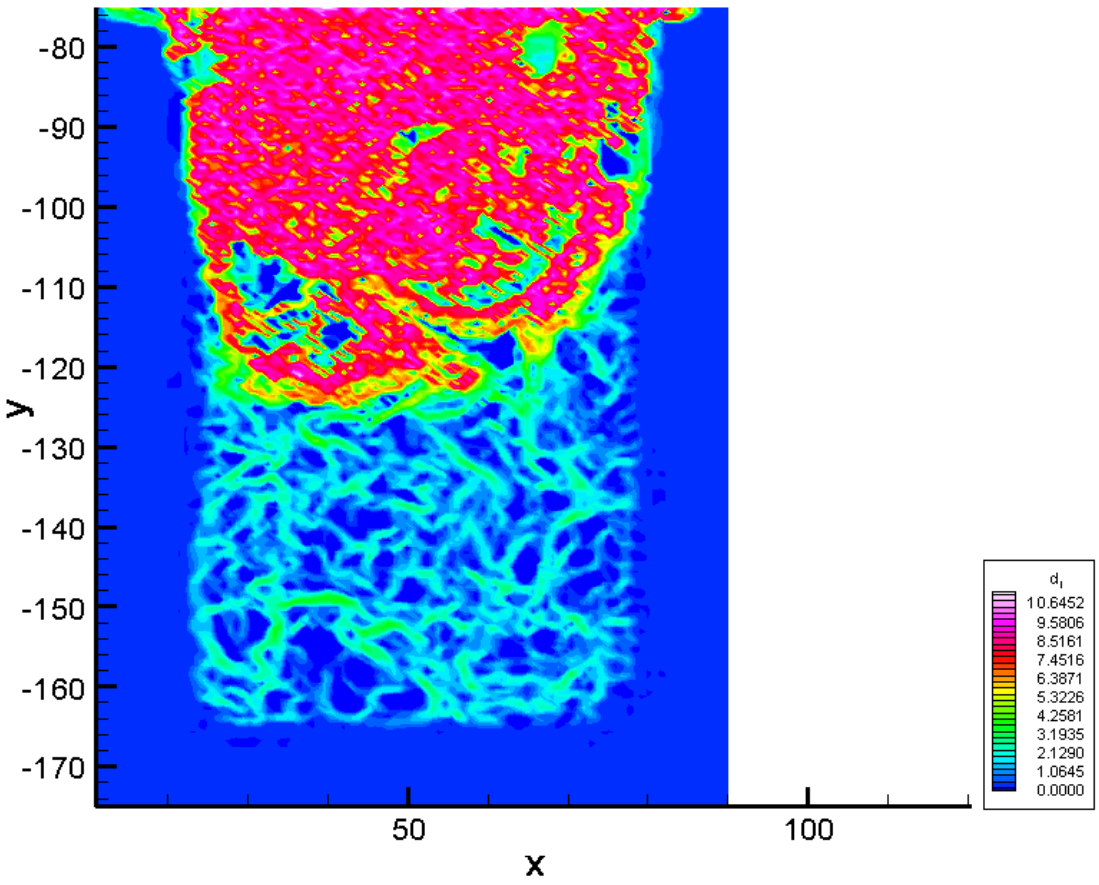

Figure F.404: The forward time LCS during phase increment 10 at 113.14 Hz with an amplitude of 0.2 mm.

References

[1] G. Liebau. Uber ein ventilloses pumpprinzip. *Naturwissenschaften*, 41(14):327–327, 1954.

[2] G. Liebau. Prinzipien kombinierter ventilloser pumpen, abgeleitet vom menschlichen blutkreislauf. *Naturwissenschaften*, 42(11):339–339, 1955.

[3] H Thomann. A simple pumping mechanism in a valveless tube. *Journal of Applied Mathematics and Physics (ZAMP)*, 29:169–177, 1978.

[4] M. Moser, J.W. Huang, G.S. Schwarz, T. Kenner, and A. Noordergraaf. Impedance defined flow generalisation of william harvey's concept of the circulation - 370 years later. *International Journal of Cardiovascular Medicine and Science*, 1(3/4):205 – 211, 1998.

[5] A. Borzi and G. Propst. Numerical investigation of the liebau phenomenon. *Zeitschrift Fur Angewandte Mathematik Und Physik*, 54(6):1050–1072, 2003.

[6] J. T. Ottesen. Valveless pumping in a fluid-filled closed elastic tube-system: one-dimensional theory with experimental validation. *Journal of Mathematical Biology*, 46(4):309–332, 2003.

[7] D. Auerbach, W. Moehring, and M. Moser. An analytical approach to the liebau problem of valveless pumping. *Cardiovascular Engineering: An International Journal*, 4(2):201–207, 2004.

[8] A. I. Hickerson, D. Rinderknecht, and M. Gharib. Experimental study of the behavior of a valveless impedance pump. *Experiments in Fluids*, 38(4):534–540, 2005.

[9] D. Rinderknecht, A. I. Hickerson, and M. Gharib. A valveless micro impedance pump driven by electromagnetic actuation. *Journal of Micromechanics and Microengineering*, 15(4):861–866, 2005.

[10] A. I. Hickerson. *An experimental analysis of the characteristic behaviors of an impedance pump*. PhD thesis, California Institute of Technology, 2005.

[11] I. Avrahami and M. Gharib. Computational studies of resonance wave pumping in compliant tubes. *Journal of Fluid Mechanics*, In press, 2008.

[12] D. J. Laser. A review of micropumps. *Journal of micromechanics and microengineering*, 14(6): R35–R64, 2004. 0960-1317.

[13] M. A. Unger, H. P. Chou, T. Thorsen, A. Scherer, and S. R. Quake. Monolithic microfabricated valves and pumps by multilayer soft lithography. *Science*, 288(5463):113–116, 2000.

[14] H. Andersson, W. van der Wijngaart, P. Nilsson, P. Enoksson, and G. Stemme. A valve-less diffuser micropump for microfluidics analytical systems. *Sensors and actuators. B, Chemical*, 72:259–265, 2001.

[15] T. Gerlach and H. Wurmus. Working principle and performance of the dynamic micropump. *Sensors and actuators. A, Physical*, 50:135–140, 1995.

[16] A. Olsson, G. Stemme, and E. Stemme. A valve-less planar fluid pump with two pump chambers. *Sensors and actuators. A, Physical*, 46-47:549–556, 1995.

[17] A. Olsson, P. Enoksson, G. Stemme, and E. Stemme. A valve-less planar pump isotropically etched in silicon. *J. Micromech Microeng.*, 6:87–91, 1996.

[18] CGJ. Schabmueller, M. Kock, ME. Mokhtari, A.G.R. Evans, A. Brunnschweiler, and H. Sehr. Self-aligning gas/liquid micropump. *J. Micromech Microeng.*, 12:420–424, 2002.

[19] H.R. Upadhye and S.G. Kandlikar. Optimization of microchannel geometry for direct chip cooling using single phase heat transfer. In *The 2nd International Conference on Microchannels and Minichannels*, Rochester, NY, USA, 2004.

[20] W.Q. Tao, Y.L. He, Q.W. Wang, Z.G. Qu, and F.Q. Song. A unified analysis on enhancing single phase convective heat transfer with field synergy principle. *Int. J. Heat Mass Transfer*, 45(24):4871–4879, 2002.

[21] T. Moschandreou and M. Zamir. Heat transfer in a tube with pulsating flow and constant heat flux. *Int. J. Heat Mass Transfer*, 40(10):2461–2466, 1997.

[22] S.Y. Kim, B.H. Kang, and J.M. Hyun. Heat transfer in the thermally developing region of a pulsating channel flow. *Int. J. Heat Mass Transfer*, 36(17):4257–4266, 1993.

[23] M-A. Hessami, A. Berryman, and P. Bandopdhayay. Heat transfer enhancement in an electrically heated horizontal pipe due to flow pulsation. In *ASME International Mechanical Engineering Congress*, pages 49–56, Washington, D.C., 2003. ASME.

[24] T.S. Pottebaum. *The relationship between near-wake structure and heat transfer for an oscillating circular cylinder in cross-flow.* PhD thesis, California Institute of Technology, 2003.

[25] J.M. Ottino. *The kinematics of mixing: stretching, chaos and transport.* Cambridge University Press, New York, NY, 1989.

[26] H. Aref. Stirring by chaotic advection. *Journal of Fluid Mechanics*, 143:1–21, 1984.

[27] S.W. Jones and H. Aref. Chaotic advection in pulsed source-sink systems. *Phys. Fluids*, 31(3): 469–485, 1988.

[28] S. Wiggins and J. M. Ottino. Foundations of chaotic mixing. *Philosophical Transactions of the Royal Society of London Series a-Mathematical Physical and Engineering Sciences*, 362(1818): 937–970, 2004.

[29] D. Gobby, P. Angeli, and A. Gavriilidis. Mixing characteristics of t-type microfluidic mixers. *J. Micromech. Microeng.*, 11:126132, 2001.

[30] J.B. Knight, A. Vishwanath, J.P. Brody, and R.H. Austin. Hydrodynamic focusing on a silicon chip: Mixing nanoliters in microseconds. *Physical Review Letters*, 80(17):3863–3866, 1998.

[31] D.E. Hertzog, J.G. Santiago, and O. Bakajin. Microsecond microfluidic mixing for investigation of protein folding kinetics. In *7th lnternational Conference on Miniaturized Chemical and Biochemical Analysis Systems*, pages 891–894, Squaw Valley, CA., 2003.

[32] Y. Lin, G.J. Gerfen, D.L. Rousseau, and S-R. Yeh. Ultrafast microfluidic mixer and freeze-quenching device. *Anal. Chem.*, 75:5381–5386, 2003.

[33] H. Wang, P. Iovenitti, E. Harvey, and S. Masood. Optimizing layout for obstacles for enhanced mixing in microchannels. *Smart Mater. Struct.*, 11, 2002.

[34] R. Yang, J.D. Williams, and W. Wang. A rapid micro-mixer/reactor based on arrays of spatially impinging micro-jets. *J. Micromech. Microeng.*, 14:1345–1351, 2004.

[35] B. He, B.J. Burke, X. Zhang, R. Zhang, and F.E. Regnier. A picoliter-volume mixer for microfluidic analytical systems. *Anal. Chem.*, 73:1942–1947, 2001.

[36] J. Melin, G. Gimenez, N. Roxhed, W. van der Wijngaart, and G. Stemme. A passive 2-dimensional liquid sample micromixer. In *7th lnternational Conference on Miniaturized Chemical and Biochemical Analysis Systems*, pages 167–170, Squaw Valley, California, USA, 2003.

[37] R.H. Liu, M.A. Stremler, K.V. Sharp, M.G. Olsen, J.G. Santiago, R.J. Adrian, H. Aref, and D.J. Beebe. Passive mixing in a three-dimensional serpentine microchannel. *J. Microelectromech. Syst.*, 9(2):190–197, 2000.

[38] A.D. Stroock, S.K.W. Dertinger, A. Ajdari, I. Mezic, H.A. Stone, and G.M. Whitesides. Chaotic mixer for microchannels. *Science*, 295, 2002.

[39] D.S. Kim, S.W. Lee, T.H. Kwon, and S.S. Lee. A barrier embedded chaotic micromixer. *J. Micromech. Microeng.*, 14:798–805, 2004.

[40] A. D. Stroock and G. J. McGraw. Investigation of the staggered herringbone mixer with a simple analytical model. *Philosophical Transactions of the Royal Society of London Series a-Mathematical Physical and Engineering Sciences*, 362(1818):971–986, 2004.

[41] S. Chang and Y. Cho. Static micromixer using alternating whirls and lamination. *J. Micromech. Microeng.*, 15:1397–1405, 2005.

[42] D. Therriault, S.R. White, and Lewis J. Chaotic mixing in three-dimensional microvascular networks fabricated by direct-write assembly. *Nature Materials*, 2003.

[43] G. A. Mensing, T. M. Pearce, M. D. Graham, and D. J. Beebe. An externally driven magnetic microstirrer. *Philosophical Transactions of the Royal Society of London Series a-Mathematical Physical and Engineering Sciences*, 362(1818):1059–1068, 2004.

[44] M. Bengtsson and T. Laurell. Acoustic streaming - ultrasonic agitation in microchannels. In *7th lnternational Conference on Miniaturized Chemical and Biochemical Analysis Systems*, pages 939–942, Squaw Valley, California, USA, 2003.

[45] J. Voldman, M.L. Gray, and M.A. Schmidt. An integrated liquid mixer/valve. *J. Microelectromech. Syst.*, 9(3):295–302, 2000.

[46] A. A. Darhuber, J. Z. Chen, J. M. Davis, and S. M. Troian. A study of mixing in thermocapillary flows on micropatterned surfaces. *Philosophical Transactions of the Royal Society of London Series a-Mathematical Physical and Engineering Sciences*, 362(1818):1037–1058, 2004.

[47] M.H. Oddy, J.G. Santiago, and J.C. Mikkelsen. Electrokinetic instability micromixing. *Anal. Chem.*, 73:5822–5832, 2001.

[48] Y-K. Lee. Lyapunov exponents of a micro chaotic mixer. *International Journal of Nonlinear Sciences and Numerical Simulation*, 3:561–564, 2002.

[49] W.L.W. Hau, L.M. Lee, Y.K. Lee, and Y. Zohar. Electrokinetically-driven vortical motion for mixing of liquids in a microchannel. In *7th International Conference on Miniaturized Chemical and Biochemical Analysis Systems*, pages 491–494, Squaw Valley, CA., 2003.

[50] J. Deval, P. Tabeling, and Ho Chih-Ming. A dielectrophoretic chaotic mixer. In P. Tabeling, editor, *Micro Electro Mechanical Systems, 2002. The Fifteenth IEEE International Conference on*, pages 36–39, 2002.

[51] J. Evans, D. Liepmann, and A.P. Pisano. Planar laminar mixer. In *Proc. IEEE Int. Workshop Micro Electro Mechanical Systems*, pages 96 – 101, Nagoya, Japan, 1997. IEEE Press.

[52] A. A. Deshmukh, D. Liepmann, and A. P. Pisano. Continuous micromixer with pulsatile micropumps. In *Solid-State Sensor and Actuator Workshop*, Hilton Head Island, SC, USA, 2000.

[53] I. Glasgow and N. Aubry. Pulsed flow mixing for biomems applications. In *7th lnternational Conference on Miniaturized Chemical and Biochemical Analysis Systems*, Squaw Valley, CA. USA, 2003.

[54] Y. Sando, K. Higashino, Y. Fujii, T. Fukuba, S. Usui, and T. Fujii. Generating an alternate pulsed flow for accelerated mixing on a plug and play microfluidic device. In *7th lnternational Conference on Miniaturized Chemical and Biochemical Analysis Systems*, pages 101–104, Squaw Valley, CA., 2003.

[55] F. Bouttausci, F. Mezic, C.D. Meinhart, and C. Cardonne. Mixing in the shear superposition micromixer: three-dimensional analysis. *Phil. Trans. R. Soc. Lond. A*, pages 1–18, 2004.

[56] D. Liepmann and J.D. Evans. Micro-fluidic mixer. *Polym. Mater. Sci. Eng.*, 76:549–550, 1997.

[57] A. Dodge, Jullien M., Okkels F., and P. Tabeling. Mixing and filtering in a cross-channel intersection. In *7th lnternational Conference on Miniaturized Chemical and Biochemical Analysis Systems*, pages 935 – 938, Squaw Valley, California, USA, 2003.

[58] X. Niu and Y-K. Lee. Efficient spatial-temporal chaotic mixing in microchannels. *J. Micromech. Microeng.*, 13, 2003.

[59] F. Okkels and P. Tabeling. Spatiotemporal resonances in mixing of open viscous fluids. *Physical Review Letters*, 92(3):1–4, 2004.

[60] P. Tabeling, M. Chabert, A. Dodge, C. Jullien, and F. Okkels. Chaotic mixing in cross-channel micromixers. *Philosophical Transactions of the Royal Society of London Series a-Mathematical Physical and Engineering Sciences*, 362(1818):987–1000, 2004.

[61] S. Taneda. Visualization of separating stokes flows. *Journal of the Physical Society of Japan*, 46(6):1935–1942, 1979.

[62] A. F. Charwat, J. N. Roos, F. C. Dewey, and J. A. Hitz. An investigation of separated flows .1. the pressure field. *Journal of the Aerospace Sciences*, 28(6):457–470, 1961.

[63] A. F. Charwat, C. F. Dewey, J. N. Roos, and J. A. Hitz. An investigation of separated flows .2. flow in the cavity and heat transfer. *Journal of the Aerospace Sciences*, 28(7):513–527, 1961.

[64] H.K. Moffatt. Viscous and resistive eddies near a sharp corner. *Journal of Fluid Mechanics*, 8: 1, 1964.

[65] V. Sarohia. *Experimental and analytical investigation of oscillations in flows over cavities.* PhD thesis, California Institute of Technology, 1975.

[66] C.W. Knisely. *An experimental investigation of low frequency self-modulation of incompressible impinging cavity shear layers.* PhD thesis, Lehigh University, 1980.

[67] D. Rockwell and E. Naudascher. Review - self-sustaining oscillations of flow past cavities. *Journal of Fluids Engineering-Transactions of the Asme*, 100(2):152–165, 1978.

[68] M. Gharib. *The effect of flow oscillations on cavity drag and a technique for their control.* PhD thesis, California Institute of Technology, 1983.

[69] J.P. Shelby, D.S.W. Lim, J.S. Kuo, and D.T. Chiu. High radial acceleration in microvortices. *Nature*, 425:38, 2003.

[70] J.P. Shelby, S.A. Mutch, and D.T. Chiu. Direct manipulation and observation of the rotational motion of single optically trapped microparticles and biological cells in microvortices. *Anal. Chem.*, 76:2492–2497, 2004.

[71] J.P. Shelby and D.T. Chiu. Controlled rotation of biological micro- and nano- particles in microvortices. *Lab on a Chip*, 4:168–170, 2004.

[72] C. E. Willert and M. Gharib. Digital particle image velocimetry. *Experiments in Fluids*, 10(4): 181–193, 1991.

[73] C. D. Meinhart, S. T. Wereley, and J. G. Santiago. Piv measurements of a microchannel flow. *Experiments in Fluids*, 27(5):414–419, 1999.